Spring 4-21-2016

Improved Methodologies in Modeling and Predicting Failure in AASHTO M-180 Guardrail Steel Using Finite Element Analysis - Phase I

Brandt M. Humphrey
University of Nebraska-Lincoln, brandt.humphrey@huskers.unl.edu

IMPROVED METHODOLOGIES IN MODELING AND PREDICTING FAILURE IN AASHTO M-180 GUARDRAIL STEEL USING FINITE ELEMENT ANALYSIS – PHASE I

by

Brandt M. Humphrey

A THESIS

Presented to the Faculty of

The Graduate College at the University of Nebraska

In Partial Fulfillment of Requirements

For the Degree of Master of Science

Major: Civil Engineering

Under the Supervision of Professor Ronald K. Faller

Lincoln, Nebraska

April, 2016

IMPROVED METHODOLOGIES IN MODELING AND PREDICTING FAILURE IN AASHTO M-180 GUARDRAIL STEEL USING FINITE ELEMENT ANALYSIS – PHASE I

Brandt M. Humphrey, M.S.

University of Nebraska, 2016

Advisor: Ronald K. Faller

Steel guardrail systems have historic and widespread applications throughout the nation's highways and roadways. However, catastrophic system failure can occur if the guardrail element ruptures, thus allowing an errant vehicle to pass uncontrolled through the system and potentially allow fractured ends to pierce the occupant compartment. To aid in the analysis and design of guardrail systems, further efforts are needed to develop and implement more reliable material failure criteria to predict and model guardrail steel rupture under all vehicle impact loading scenarios within impact simulation finite element method (FEM) software, such as LS-DYNA.

This Phase I study accomplished a number of tasks to aid in this objective. First, historical and state-of-the-art failure criteria with emphasis on stress state dependent failure criteria were reviewed. Next, various failure surface methods that provide estimations on the triaxiality and Lode parameter vs. effective plastic strain at failure were review and analyzed. It was determined that more flexible failure surface fitting methods may provide better estimations, and larger more diverse testing programs are required to estimate the failure surface through all stress states. A failure surface method using a Smoothed, Thin-Plate Spline was also proposed to overcome short comings in existing failure surface estimation methods. Based on the review of the existing failure

surfaces' performance, a steel material testing program was developed, and testing was performed on 21 different specimen configurations that represent a range of stress states. The specimens were prepared using ASTM A572 Grade 50 steel with similar material properties as AASHTO M-180 guardrail steel. Test results and calculated material properties were presented herein. Lastly, a preliminary FEM modeling effort was conducted. Various modeling parameters were examined, including the effects from hourglass controls, mesh-size effects, inertial effects from load rate, and solid vs. shell behavior. Based on this analysis, preliminary models of the testing specimen were developed. Also, a preliminary material model was calibrated and presented herein. Conclusions were made, and recommendations were provided for continuing a Phase II effort.

ACKNOWLEDGEMENTS

First, I would like to thank Dr. Ronald Faller for giving me the opportunity to succeed in graduate school. You have helped make this experience invaluable by challenging me and demanding a high quality of work and critical thinking. Furthermore, I deeply appreciate your guidance, support, and advice in all aspects of life.

I would also like to thank the member of my graduate committee, Dr. John Reid, Dr. Mehrad Negahban, and Dr. Jennifer Schmidt. It has been a pleasure working with you all and I am thankful for all of your efforts on my thesis. I would like to thank Mr. Robert Bielenberg for all of your assistance. Thank you for all of your help, time, and patience working with me on this project. I cannot imagine doing any of this without your help.

I would also like to thank all of the MwRSF employees. There are far too many people to list who have made my time here so enjoyable. Bob, Scott, Jennifer, Cody, and Karla, thank you for all of your guidance. Thank you all for always taking the time to address my endless amount of questions. I am surely a better engineer and person after working with you all. I would also like to thank my fellow peers: Tyler, Chaz, Ana, Joe, and Brad for making graduate school so enjoyable. Dylan, Wenlong, and Myles, thank you for all of your assistance during testing.

Finally, I would like to thank my family. To my parents, Mitch and Kim, thank you all of you support and motivating me to always achieve more. I have you to thank for instilling a sense of curiosity in me. From the days of playing with bugs outside through my master's degree graduation, you have always been a cornerstone of unconditional love and support. Finally, to my fiancé, Jessica, thank you for your unending love. Your support has meant the world to me and I cannot imagine life without your smile welcoming me home. Finishing my thesis has been difficult at such a busy time in our life, but your love, patience, and support has made it so much easier.

TABLE OF CONTENTS

LIST OF FIGURES

LIST OF TABLES

1 INTRODUCTION

1.1 Background and Problem Statement

Steel guardrail systems have historic and widespread applications throughout the nation's highways and roadways. They provide a reliable method to redirect errant vehicles by deforming plastically and dissipating the impact energy, while simultaneously maintaining safe occupant ridedown accelerations (ORAs) and occupant impact velocities (OIVs). Catastrophic system failure occurs if the guardrail element ruptures, typically at splice locations, thus allowing the errant vehicle to pass uncontrolled through the system, and potentially allow fractured ends to pierce the occupant compartment.

A recent example of this outcome occurred in a full-scale crash test that was performed by the Midwest Roadside Safety Facility (MwRSF) [1]. In this scenario, a small passenger car impacted a Midwest Guardrail System (MGS) to thrie beam stiffness transition system that was configured with a lower concrete curb at a speed of 62.9 mph (101.2 km/h) and an angle of 25.0 degrees. The vehicle penetrated under the W-beam rail while the wheel climbed the curb. This behavior resulted in the vehicle loading the W-beam rail in both upward and lateral directions, thus causing the rail splice between the W-beam and asymmetrical transition segment to rupture. As a result, the vehicle traveled farther into the transition system where it contacted the ends of stiff rail elements and multiple transition posts, causing the vehicle to stop quickly with excessive longitudinal ORA values. The vehicle and system damage can be seen in Figure 1. The crash test was considered a failure. To further prevent these types of failures, it is important to better understand the failure mechanisms associated with steel guardrails so that system

analysis and design procedures can be improved and become more accurate under variable loading conditions.

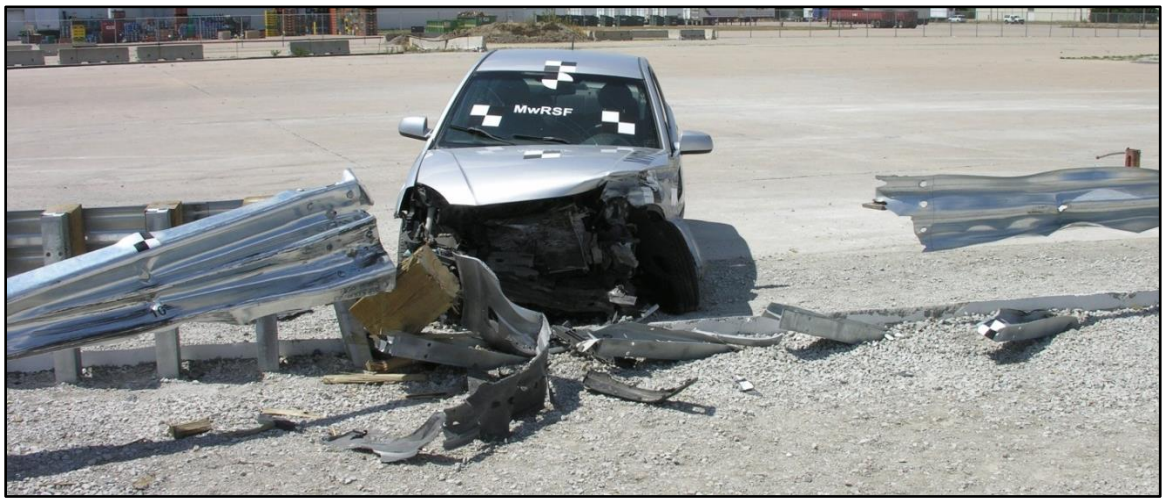

Figure 1. Small Passenger Car and Barrier Damage after Impact into Midwest Guardrail System (MGS) to Thrie Beam Stiffness Transition System [1]

Computer simulation with finite element methods (FEM) modeling programs, such as LS-DYNA [2], are used extensively to investigate and evaluate the dynamic behavior and safety performance of new guardrail systems. However, material failure has been historically difficult to predict using FEM modeling and has not been widely used for investigating rupture in rail elements configured with AASHTO M-180 guardrail steel [3]. A likely cause for this hesitation is that the mechanics and factors contributing to material failure are often debated and not completely understood [4]. Due to the nature of material failure, numerous schools of thought exist, and as a result, countless prediction models have been proposed. Various inconsistencies in material behavior, required loading conditions, and required accuracy have further complicated both predicting and modeling material failure. Some of the various schools of thought, including the state-of-the-art material failure theories, are discussed further in Chapter 3.

In 2001, Ray et al. utilized failure criteria with guardrail material models when evaluating the performance of a W-beam guardrail that was supported by weak posts without the use of blockouts [5]. Initially, a crash test was planned to evaluate dynamic guardrail performance using a pickup truck impacting at a speed of 62 mph (100 km/h) and an angle of 25 degrees. Prior to testing, a FEM simulation was prepared, which did not reveal any barrier performance problems. However, a small nick formed on the lower edge of the guardrail beam at the second post downstream from the impact location during the test. When the front bumper of the pickup truck impacted this nick, the guardrail beam completely ruptured, thus allowing the pickup truck to penetrate through the guardrail system, as seen in Figure 2. This action exposed a possible shortcoming in the material failure criteria that was used to predict the dynamic impact performance of the barrier system within the simulation.

Figure 2. Pickup Truck Impacting Weak-Post W-Beam Guardrail after Rail Rupture [5]

In 1999, Bielenberg et al. attempted to use FEM modeling to investigate guardrail rupture during the development of a thrie beam bullnose median barrier system [6-10]. Initially, a full-scale crash test was performed with a small car impacting head-on into a

bullnose median barrier. Subsequently, simulations were performed with a pickup truck impacting the barrier under similar conditions. However, these preliminary simulations did not utilize any form of material failure criteria for the guardrail steel. As a result, the simulations with the pickup truck failed to accurately represent the impact behavior of the front beam of the guardrail system.

The full-scale crash test later showed that the lower corrugation of the slotted thrie beam rail separated away from the upper two corrugations due to the location of the pickup truck's bumper in the lower valley of the slotted thrie beam. The lower corrugation was then overridden by the vehicle. Due to the reduced area of the guardrail in contact with the vehicle, the upper two corrugations of the thrie beam ruptured. This behavior allowed the vehicle to penetrate into the barrier system. Following the failed full-scale crash test with a pickup truck, an effort was then made to determine the effective plastic strain (EPS) at failure by performing a static tension test on a flattened, slotted, thrie beam and complementary FEM modeling. The failure conditions were then implemented in the FEM model. Load vs. time curves were fairly accurate with the implemented material failure condition. Furthermore, the revised FEM simulation demonstrated separation of the upper two and lower corrugations as well as guardrail rupture. A comparison of the modified computer simulation and full-scale crash test can be found in Figure 3. This model was then used to continue development of the bullnose design. However, it should be emphasized that the noted guardrail rupture criteria were calibrated for this loading case only. It was not expected to produce accurate failure predictions under other impact loading conditions. As shown by these recent examples,

further efforts are needed to develop and implement more reliable material failure criteria to predict and model guardrail steel rupture under all vehicle impact loading scenarios.

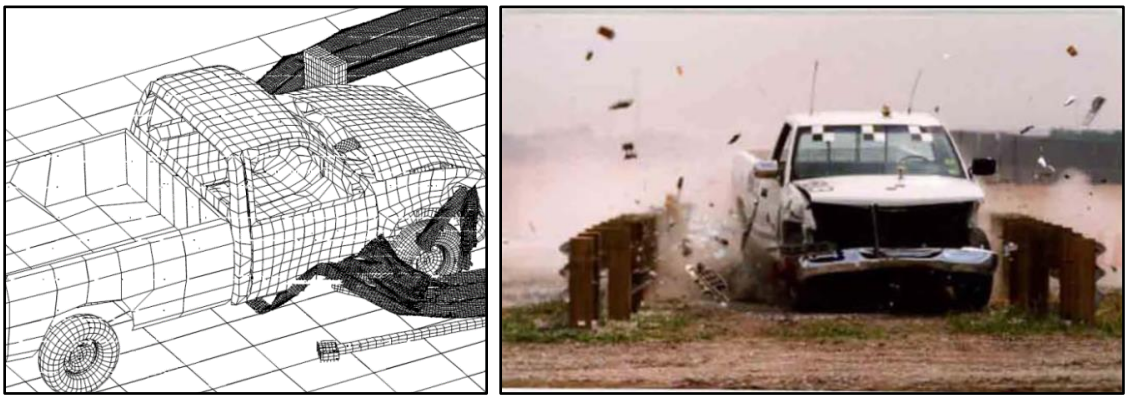

Figure 3. Computer Simulation [7] and Full-Scale Crash Test [8] of Pickup Truck Impacting Thrie Beam Bullnose Guardrail System

1.2 Research Objectives

The objectives of the research study were to advance the knowledge and understanding of failure in AASHTO Specification M-180 guardrail steel. More specifically, it was desired to develop an improved steel material model with material failure criteria, which can be used in common computer simulation programs, such as LS-DYNA, to predict and model failure in vehicle to barrier impact events. The improved material model must be flexible enough to accommodate a range of mesh sizes, loading rates (i.e., strain rates), and stress states.

1.3 Research Scope

The research objectives were accomplished through six tasks. First, a literature review was conducted to garner knowledge on relevant ductile metal failure prediction techniques. Both historical and modern failure prediction methodologies were summarized.

Next, a review of the available LS-DYNA material models was conducted. LS-DYNA offers numerous material models that can be used to represent a wide range of

materials for various applications. The initial round of analysis was filtered to only consider the metallic material models that included a form of element erosion. The material models that were obviously unsuitable for modeling guardrail steel failure were then briefly described and eliminated from further analysis. The second round of analysis considered six criteria that were determined to be critical for a material model to accurately predict ductile steel failure as related to guardrail applications. The final round of analysis involved researching each of the remaining material models to determine, to the best of one's ability without performing testing, the accuracy of the methods used. How each model treated three factors were of particular interest. These factors include: flow stress; failure; and potential additional abilities such as non-local abilities, damage criteria, and strain rate effects.

A number of techniques were reviewed to represent the relationship between the effective plastic strain at failure and the state of stress, as represented by the Lode parameter and triaxiality. Pre-existing data sets were then inputted into the various techniques to evaluate each failure surface methods' ability to fit the data. Reduced data sets were also used in order to evaluate the failure surface methods' ability to predict the full data set. Based on this analysis, a new surface-fitting method utilizing a Smoothed, Thin-Plate Spline (TPS) was also proposed to allow for a potentially more accurate data fit for ranges of stress states not represented by test data.

A comprehensive testing program was developed based on a review of prior variable state of stress testing programs to aid in developing an effective plastic strain at failure as a function of the material stress state. A series of testing specimens were chosen to encompass as many stress states as reasonably possible given the limitations of

available material and testing equipment. Once the physical testing program was defined, steel material was selected to represent the AASHTO M-180 guardrail steel that is available on the market. The test specimens were then machined and subjected to laboratory testing. Results from the comprehensive testing program are presented and discussed herein.

In addition to the physical testing program, FEM models of each test specimen were prepared for use with the LS-DYNA finite element analysis (FEA) software. Simulation parameters, such as mesh sensitivity, hourglassing controls, simulation duration, and element formulation were evaluated. The results from this simulation modeling effort are summarized and discussed herein.

At the ends of the testing and simulation efforts, several conclusions were made pertaining to the modeling and testing of AASHTO M-180 guardrail steel. Several research recommendations were also provided to continue this effort to advance computer simulation modeling involving failure prediction of AASHTO M-180 guardrail steel.

2 MATERIAL FAILURE OVERVIEW

2.1 Historical Strength Theories for Ductile Steel

Failure of ductile materials commonly occurs and is a fundamental principal in engineering design. However, the phenomenon is not fully understood, leaving hundreds of theories and variations of theories attempting to partially explain test data with a model or criteria [4]. Although one of Leonardo da Vinci's earliest goals was to explain material failure, it is unsurprising that the field has a seemingly endless list of scientists attempting to do similar feats. With this in mind, a number of historically significant theories must be reviewed. A notable addition to the field originates from Charles-Augustin de Coulomb, who is generally credited for the origin of maximum shear stress strength theory. In 1773, based on experimentation, Coulomb assumed that failure is caused by sliding along a certain plane, and that failure occurs when the component of the force along this plane becomes larger than the cohesive resistance in shear along the same plane. Coulomb's essay read to the Academy of France later became the basis of the commonly used Mohr-Coulomb Strength Theory [11].

Three major strength theories surfaced. First, the maximum normal stress theory was developed, which related the maximum or minimum principal stress as the criterion of material strength. Lamé and Rankine were two scientists who assumed this condition [12]. The second strength theory was the maximum strain theory, in which Mariotto made the first statement on the maximum elongation or the maximum strain criterion, also known as Saint-Venant's criterion or the Second Strength Theory [13]. While popular at the time, the theory is based on the assumption that material begins to fail when the maximum strain is equal to the yield point strain in simple tension. However, it

is not used today because the criterion does not agree with experimental results [4]. The third major strength theory from the 19th century originates from Henri Édouard Tresca in 1864 [14]. He assumed that the maximum shear stress at flow is equal to a specific constant, now referred to as the Tresca yield criterion. This theory better agrees with experiments for some ductile materials [4]. Later, in 1956, Maxwell determined that the total strain energy per unit volume was a combination of As shown by these recent examples, further efforts are needed to develop and implement more reliable material failure criteria to predict and model guardrail steel rupture under all vehicle impact loading scenarios.

the first part being the strain energy of uniform tension and the second part being the strain energy of distortion [15].

In the 20th century, maximum strength theories split into a number of theories that were developed to attempt to better describe yield and fracture failure conditions of various materials. Yu prepared a well-organized survey of the various strength theories in the 20th century [4]. Some of the more common theories include the single-shear strength (SSS) theory and the octahedral-shear strength (OSS) theory.

The SSS theory was developed when it was hypothesized that fracture occurs on a given plane in the material when a critical combination of shear and normal stress acts on this plane. The expression is given by Equation 2.1.

$$\tau_o = \text{MAX}\left(\frac{|\sigma_1-\sigma_2|}{2}, \frac{|\sigma_2-\sigma_3|}{2}, \frac{|\sigma_1-\sigma_2|}{2}\right) \quad (2.1)$$

where:

$\tau_o = \text{Shear at Yield}$

$\sigma_1, \sigma_2, \sigma_3 = \text{Principal Stresses}$

A variation of the SSS theory is the Mohr-Coulomb theory. The variation is a two parameter criterion in which the failure locus on the deviatoric plane has a hexagonal

threefold-symmetry, as seen in Figure 4. The full three-dimensional representation of the Mohr-Coulomb surface can also be found in Figure 5. The simplified plane stress representation can be found in both Figure 5, as the "tilted" plane represented by the dashed line seen in the three-dimensional plot, as well as in Figure 6. At its simplified form, the expression is given by Equation 2.2.

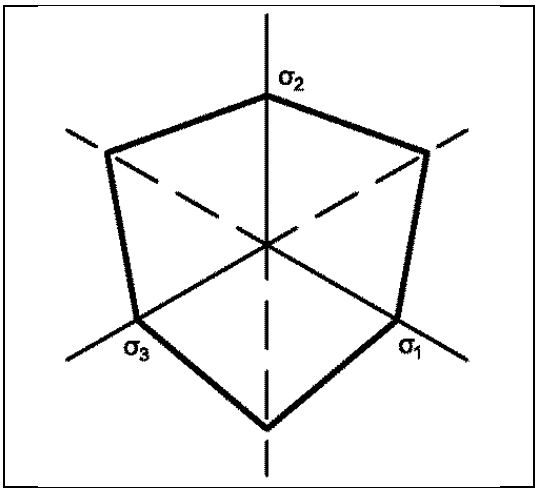

Figure 4. Mohr-Coulomb Failure Surface on Deviatoric Plane

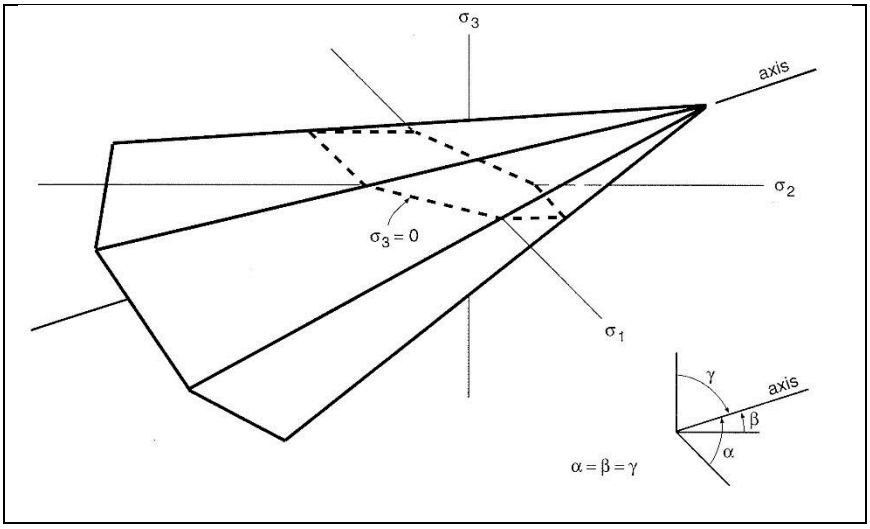

Figure 5. Mohr-Coulomb Three-Dimensional Failure Surface [16]

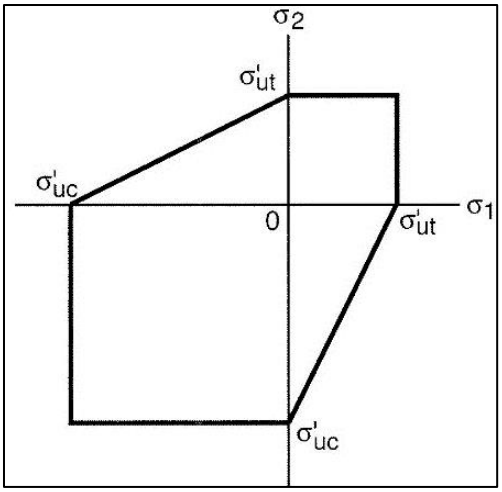

Figure 6. Mohr-Coulomb Failure Surface with Plane Stress Assumptions [16]

$$|\tau| + \mu\sigma = \tau_i \tag{2.2}$$

where:

τ = Shear Stress on Fracture Plane
σ = Normal Stress on Fracture Plane
μ = Slope Constant = $\tan(\phi)$
ϕ = Angle of Internal Friction
τ_i = Cohesion Intercept

The OSS theory encompasses strength theories in which failure is defined as a function of octahedral shear stress and the octahedral normal stress. The most commonly used yield criterion is the one parameter OSS criterion, more often referred to as the von Mises yield criterion. Unlike the Mohr-Coulomb yield surface, the von Mises criterion utilizes a formulation in which the yield strength is the same in both tension and compression. It should be noted that the von Mises failure criteria is also referred to as the J_2 plasticity theory, shear strain theory, equivalent stress criterion, maximum distortion energy criterion, maximum strain energy, or mean root square shear stress theory [4]. The failure surface on the deviatoric plane creates a circle as seen by the two-dimensional and three-dimensional plots found in Figures 7 and 8, respectively. Under plane stress assumptions, the oval-shaped failure surface is produced, as seen in Figure 9.

The plane stress failure surface can also be seen in Figure 8 as the "tilted" plane, as represented by the dashed line when $\sigma_3 = 0$. It should be noted that the von Mises criterion is less conservative than the similar maximum shear stress criterion. The maximum shear stress criterion is represented by the dashed line forming a parallelogram in Figure 9. The von Mises criterion is given by the expression in Equation 2.3.

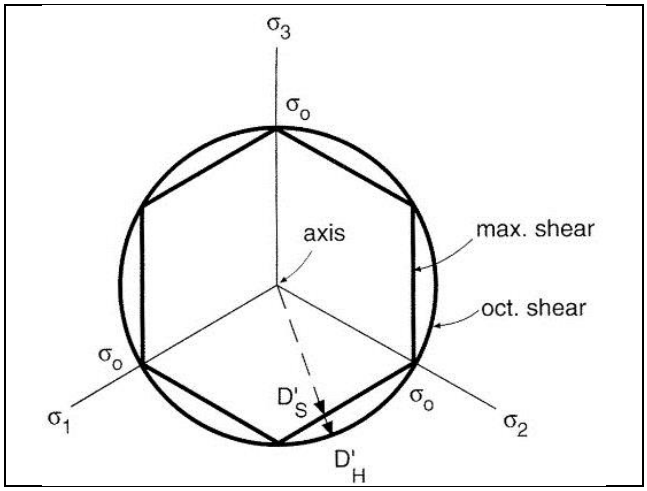

Figure 7. Von Mises Failure Surface on Deviatoric Plane [16]

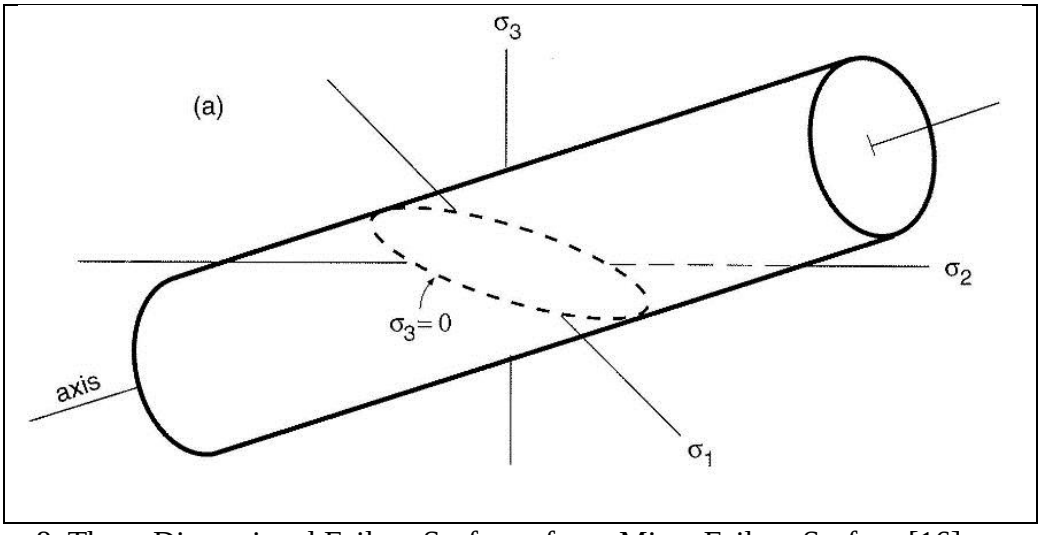

Figure 8. Three-Dimensional Failure Surface of von Mises Failure Surface [16]

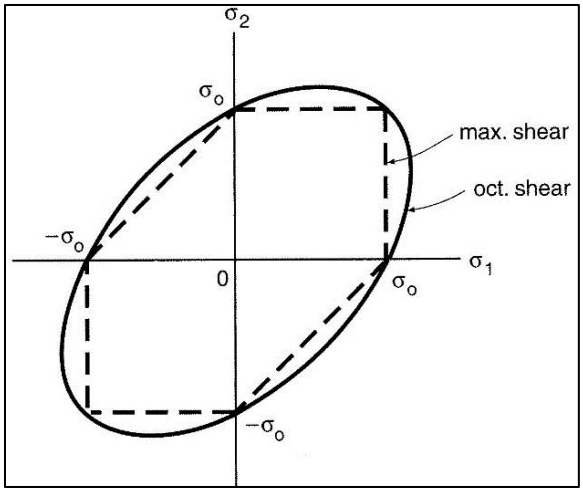

Figure 9. Von Mises Failure Surface (Octahedral Shear) with Plane Stress Assumptions [16]

$$\tau_{oct} = \frac{1}{3}\sqrt{(\sigma_1 - \sigma_2)^2 + (\sigma_2 - \sigma_3)^2 + (\sigma_3 - \sigma_1)^2} = \sqrt{\frac{2}{3} J_2} \tag{2.3}$$

where:

$\tau_{oct} =$ Shear at Octahedral Yield Condition
$\sigma_1, \sigma_2, \sigma_3 =$ Principal Stresses
$J_2 =$ Second Deviatoric Stress Invariant
$J_2 = \frac{1}{2} s_{ij}\, s_{ji} = \frac{1}{6}[(\sigma_1 - \sigma_2)^2 + (\sigma_2 - \sigma_3)^2 + (\sigma_3 - \sigma_1)^2]$
$s_{ij} =$ Deviatoric Stress Tensor

2.2 Modern Ductile Failure Criteria

The previous theories are typically only used to predict, under a given loading condition, when a material will transition from the elastic region to the plastic region. Designing outside of the elastic region is often considered a failure for many structures. As a result, understanding what occurs in the plastic region is of less importance to others. However, it is often also important to understand how the material deforms past the elastic region and when the material will fail completely, especially in the case of guardrail design and analysis.

Ductility is a unique property that relies on material properties, geometric dependencies of stress, strain rate, and temperature, resulting in plastic deformations such

as necking and shear localization. Since ductility is such a complex behavior, it was necessary to focus on a limited subset of the variables, while assuming that the others have a negligent effect on the conditions of interest. For this research effort, temperature effects were not considered. This selection leaves the physical variables of material properties, state of stress, and strain rate, as the remaining variables that affect ductility and ultimately failure.

2.2.1 Physical Material Failure

Fracture involves the breaking of molecular bonds through the propagation of cracks. A generally accepted theory is that ductile failure is controlled by a process of growing microscopic voids. First, necking occurs followed by void nucleation initiated by microscopic flaws. The voids then grow due to a combination of tensile and shear stresses. The voids continue to grow and deform until coalescence of the newly formed micro cracks occurs. Crack growth eventually leads to macroscopic failure [17-20].

2.2.2 Failure Criteria Dependent on State of Stress

Numerous authors have shown that fracture of ductile metals is strongly dependent on hydrostatic stress, beginning prominently with Bridgman's testing under varying hydrostatic pressures [21]. Bridgman documented the effects of a superimposed hydrostatic pressure on a number of material properties, such as flow and fracture behavior. Using round bars being pulled within a pressure chamber, Bridgman found that the ratio of the cross-sectional area at the neck after fracture to the initial cross-sectional area decreased with respect to the imposed confining pressure [21-22]. This environment allowed a fracture envelope, dependent on hydrostatic pressure, to be developed. The hydrostatic pressure is commonly measured as a triaxiality factor defined as the

hydrostatic pressure divided by the effective stress. Furthermore, Hancock and Mackenzie [23] and Rice and Tracey [24] theorized that fracture of ductile metals is dependent on hydrostatic stress by studying the growth and coalescence of microscopic voids where a rapidly decreasing fracture ductility results in an increasing hydrostatic tension. Gurson then implemented this behavior into the well-known Gurson model in which Tvergaard later improved [25-27] . Similar conclusions have been made empirically by Norris et al. [28] and Oyane et al. [29]. Also, the dependence on triaxiality has been shown through continuum damage mechanics models, specifically by Lemaitre [30], and further studied by La Rosa et al. [31]. Norris et al. (1978) and Johnson and Cook (1985) showed that the equivalent fracture strain decreases exponentially with respect to increasing stress triaxiality [28,32-33]. Johnson and Cook then created the well-known Johnson-Cook failure model. Recently, Lewandowski and Lowhaphandu performed an in depth review of the effects of hydrostatic pressure on various materials [34].

2.2.2.1 Triaxiality Dependent Failure Criteria

In the past, researchers have theorized that the material fracture could be predicted as a function of hydrostatic pressure, as represented by triaxiality. The triaxiality, η, is the pressure value normalized by the effective stress, as seen in Equation 2.4.

$$\eta = \frac{p}{\sigma_{eff}} \tag{2.4}$$

where:

$\eta =$ Triaxiality

$p =$ Hydrostatic Pressure $= \frac{\sigma_1+\sigma_2+\sigma_3}{3}$

$\sigma_{eff} =$ Effective Stress $= \sqrt{\frac{(\sigma_1-\sigma_2)^2+(\sigma_2-\sigma_3)^2+(\sigma_3-\sigma_1)^2}{2}}$

The triaxiality dependent failure envelope has been studied extensively, beginning with studies by Bridgman [21]. The resulting relationship between the effective plastic strain at failure and triaxiality typically produces a shape similar to that seen in Figure 10. Note that the curve depicts plane stress assumptions. The shape and values for this curve were taken from the analysis performed in Chapter 4, but the exact shape and values of the effective plastic strain, ε_{eff}^{p}, at failure vary widely depending on material properties, as seen in Bai et al.'s study of pressure and Lode dependence [35], Chinzei et al.'s study of damage modeling in various materials of sheet metal [36], and Lewandowski and Lowhaphandu review of hydrostatic effects in numerous materials [34]. As seen in various papers, aluminum alloys, such as Al2024-T351 and Al6022-T6, as well as 1045 steel, display a large peak under uniaxial tension with lower valleys under shear and laterally confined tension. The effective plastic strain at failure under uniaxial compression then increases quickly toward a value that is unachievably high [35,37-38]. However, some materials, such as DH36 steel, ultra-high strength steels, and the aluminum alloy Al7075-T6, show little to no peak in the effective plastic strain at the uniaxial tension stress state [35-36]. Furthermore, the presentation prepared by Chinzei et al. showed that the as-tested high-strength steel had exhibited a lower effective plastic strain at failure under uniaxial tension loading than observed under pure shear and the tensile lateral confined stress (plane strain) stress states [36].

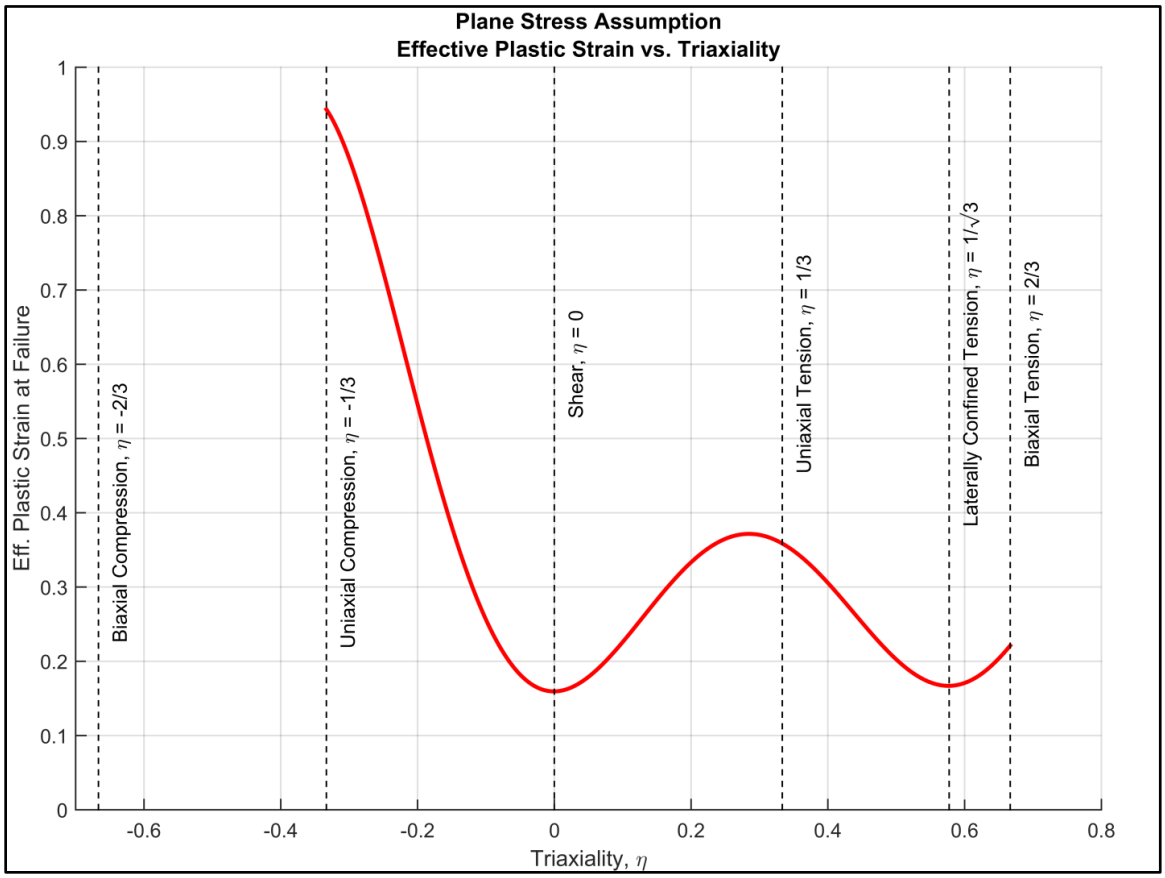

Figure 10. Typical Two-Dimensional Plot of EPS vs. Triaxialities (Plane Stress Assumption)

2.2.2.1 Triaxiality and Lode Parameter Dependent Failure Criteria

More recently, researchers have theorized that the material fracture can be more accurately predicted as a function of state of stress, as represented by triaxiality, and the third deviatoric stress invariant, as typically represented by the Lode parameter [35,37-43]. The Lode parameter, ξ, is given in Equation 2.5. Implementing the Lode parameter dependency allows for a distinction between non-plane stress loading conditions that are present under three-dimensional loading conditions. Note that the Lode angle is sometimes used in place of the Lode parameter. The relationship between the Lode parameter and Lode angle is given in Equation 2.6. A geometrical representation of the

Lode angle in Haigh-Westergaard stress space can be found in Figure 11 [39,44]. In this figure, the radius of the circle is given as $r = \sqrt{2/3}\,\sigma_{eff}$. The Lode angle can be seen as the angle between the vectors OP and OA.

$$\xi = \frac{27}{2}\frac{J_3}{\sigma_{eff}^3} \tag{2.5}$$

where:

$\xi =$ Lode Parameter
$J_3 =$ Third Deviatoric Stress Invariant
$J_3 = \det(\mathrm{s_{ij}}) = \frac{1}{3}s_{ij}s_{jk}s_{ki} = s_1 s_2 s_3$
$J_3 = \frac{2}{27}I_1^3 - \frac{1}{3}I_1 I_2 + I_3$
$I_1, I_2, I_3 =$ Stress Invariants
$\sigma_{eff} =$ Effective Stress$= \sqrt{\frac{(\sigma_1-\sigma_2)^2+(\sigma_2-\sigma_3)^2+(\sigma_3-\sigma_1)^2}{2}}$

and

$$\xi = -\cos 3\theta \tag{2.6}$$

where:

$\xi =$ Lode Parameter
$\theta =$ Lode Angle

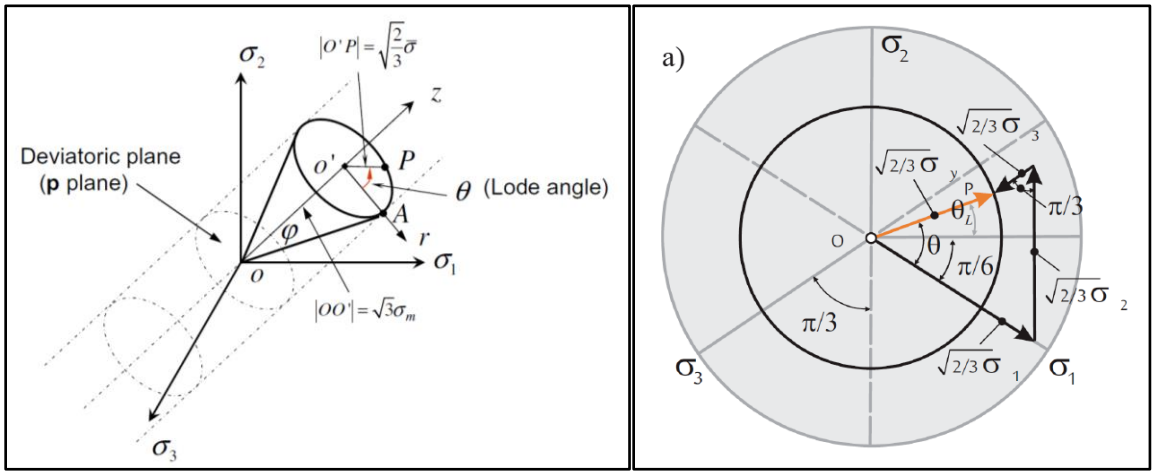

Figure 11. Lode Angle in Haigh-Westergaard Stress Space (Left) [39] and π-Plane (Right) [44]

It should also be noted that due to the physical relationships between the triaxiality, Lode parameter, and Lode angle, the range of values for these three parameters are:

$-\infty < \eta < \infty$,
$-1 \leq \xi \leq 1$, and
$0 \leq \theta \leq \frac{\pi}{3}$

However, the triaxiality range of interest in this report from $-{}^{1}/_{3}$ to 1. This range was chosen because values outside this range become increasingly more difficult to experience under practical loading conditions.

Furthermore, Danas and Ponte Castañeda give the relationships to express the principal stresses as a functions of η, θ, and σ_{eff}, as given by Equation 2.7 [45].

$$\frac{3}{2\sigma_{eff}}\begin{bmatrix}\sigma_1\\ \sigma_2\\ \sigma_3\end{bmatrix} = \begin{bmatrix}-\cos\left(\theta+\frac{\pi}{2}\right)\\ -\cos\left(\theta-\frac{\pi}{2}\right)\\ \cos(\theta)\end{bmatrix} + \frac{3}{2}\eta\begin{bmatrix}1\\1\\1\end{bmatrix} \tag{2.7}$$

Where
$\sigma_{eff} =$ Effective Stress
$\sigma_1, \sigma_2, \sigma_3 =$ Principal Stresses
$\eta =$ Triaxiality
$\theta =$ Lode Angle

Often, plane stress assumptions are inappropriate to use during analysis. When an analysis will be performed on a part that exhibits complex stress states, such as plane strain or partially confined states, a more robust method is needed. To accommodate this kind of analysis, the Lode parameter is often used in conjunction with the triaxiality value to fully represent the state of stress. For reference, a two-dimensional plot is given in Figure 12 to give the location of common load configurations on the triaxiality vs. the Lode parameter plane. This plot was compiled from numerous papers [37-39,43,46-48].

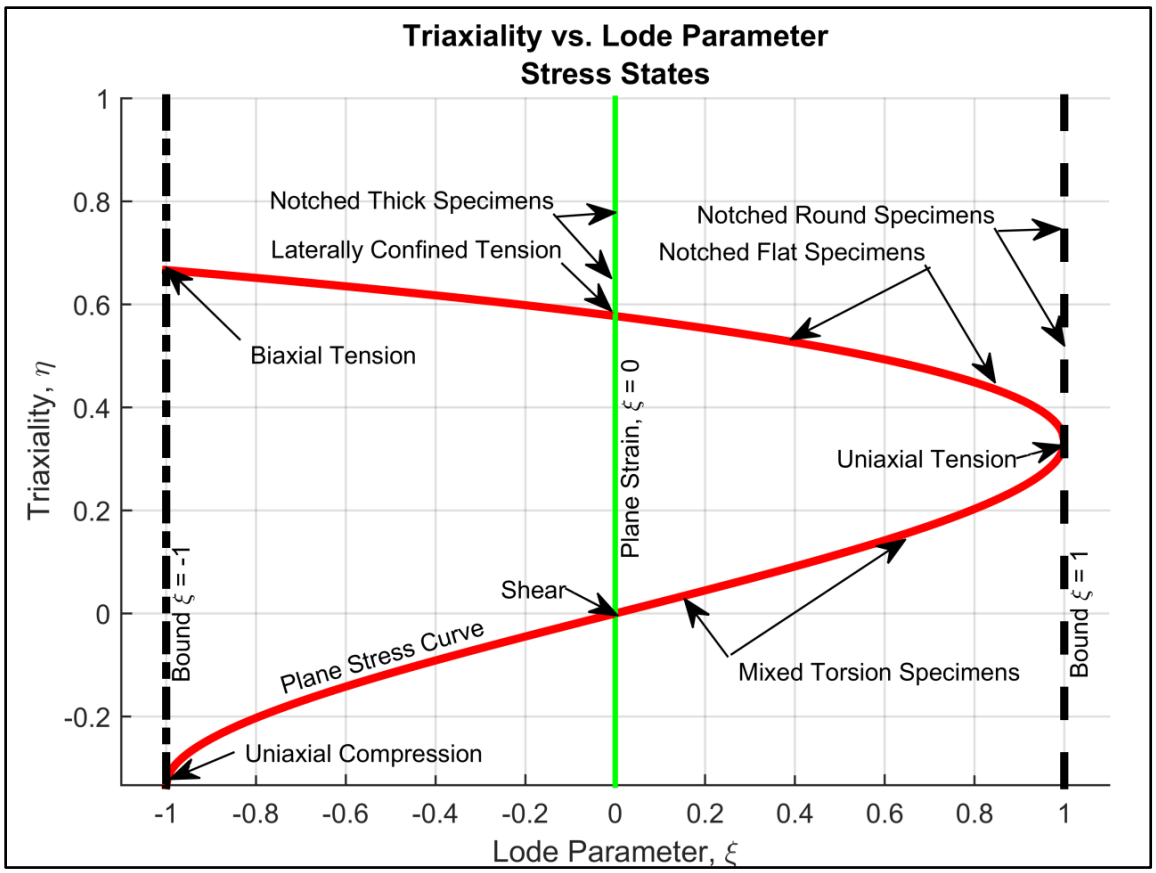

Figure 12. Triaxiality vs. Lode Parameter Stress States

When complex stress states are required in the analysis, the criteria needed to predict the failure condition becomes more complicated. An additional dimension is added to the effective plastic strain at failure vs. triaxiality curve in the form of the Lode parameter. As a result, a failure surface, instead of a failure curve, is required to define failure. Figure 13 shows a typical failure surface dependent on triaxiality and Load parameter where the z-axis represents the effective plastic strain at failure. The details of the surface found in Figure 13 are discussed in Chapter 4.

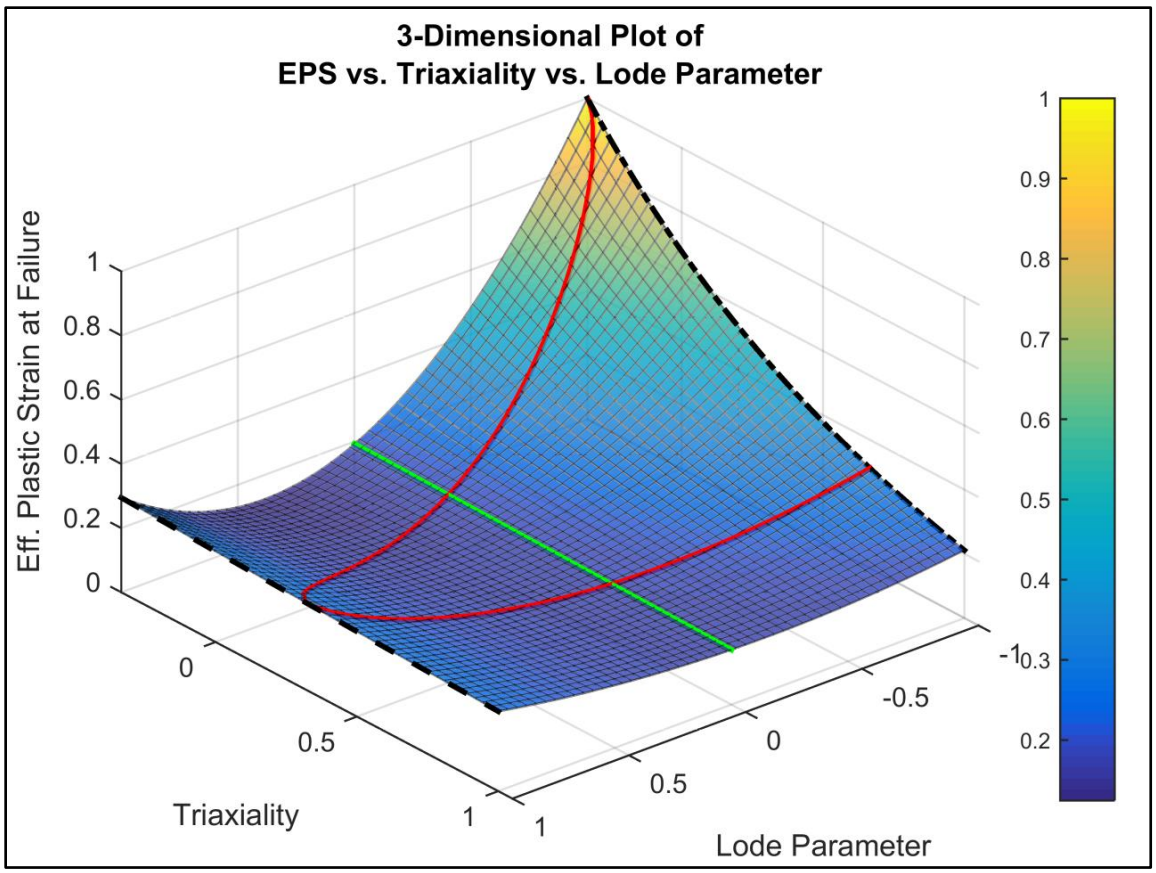

Figure 13. Typical Three-Dimensional Plot of EPS vs. Triaxiality vs. Lode Parameter

The relationship between the one-variable (plane stress) and the two-variable (complex) stress state analysis should become evident as the red curve from Figure 13 is the same as the red curve in Figure 10. However, the red curve seen in Figure 10 is projected such that the curve is independent of the Lode parameter. As previously explained, this two-dimensional plot is adequate in modeling plane stress assumption behavior. Note that the plane stress curve seen in Figures 12 and 13 can be calculated with the triaxiality and Lode parameter relationship given in Equation 2.8 [39].

$$\xi = -\frac{27}{2}\eta\left(\eta^2 - \frac{1}{3}\right) \tag{2.8}$$

where:

$\sigma_3 = 0$

$\xi = \frac{27}{2}\frac{J_3}{\sigma_{eff}^3}$

$\eta = \frac{p}{\sigma_{eff}}$

With the addition of the Lode parameter, other stress states can be represented, specifically those that do not rely on plane stress conditions. As such, a more robust failure surface can be used for modeling complex parts. The additional stress states can be represented in their simplest forms by notched round tension specimens, or thick notched tension specimens as seen in Figure 12. However, parts with unique geometries or complex loading conditions can exhibit stress states anywhere in the plotted area.

Numerous methods have been recently proposed to fill the gaps between the tested data points representing relatively-simple stress states and complex stress states that are more difficult to isolate while conducting physical testing. These methods are discussed in detail in Chapter 4.

2.2.3 Failure Criteria Dependent on Strain Rate

As discussed in the study performed by Wright and Ray, strain rate can have a large effect on AASHTO Specification M-180 guardrail steel [49]. As shown in Figure 14, the strain at failure typically decreases as the strain rate increases. Furthermore, the stress vs. strain behavior shifts upward for both the elastic and plastic regions as strain rate increases. The common method of applying strain rate effects to the yield stress is through the use of Cowper-Symonds relationship [2,49-50]. Typical coefficient values are provided for mild steel and AASHTO Specification M-180 guardrail steel, as seen in

Table 1. The Cowper-Symonds relationship, as used in LS-DYNA, is given in Equation 2.9.

It should be noted that the Cowper-Symonds relationship does not allow for a generalized scaling of the stress vs. strain curve, and an effective plastic strain at failure vs. strain rate dependence was not available in LS-DYNA3D at the time of the Wright and Ray study. As a result, strain rate effects were not simulated as part of the research effort. However, the modern material formulations, such as the common MAT_24 (Isotropic Piecewise Linear Plasticity) [2], allow for a generalized curve to be defined to scale the yield stress vs. strain rate as well as a table to define the stress vs. strain curves for each given strain rate. Unfortunately, the modern MAT_24 material model does not allow for an effective plastic strain at failure vs. strain rate to be defined without the MAT_ADD_EROSION option [2]. The MAT_ADD_EROSION option allows for more customized failure options to be applied in addition to the material models in LS-DYNA. MAT_ADD_EROSION is detailed in Chapter 3.

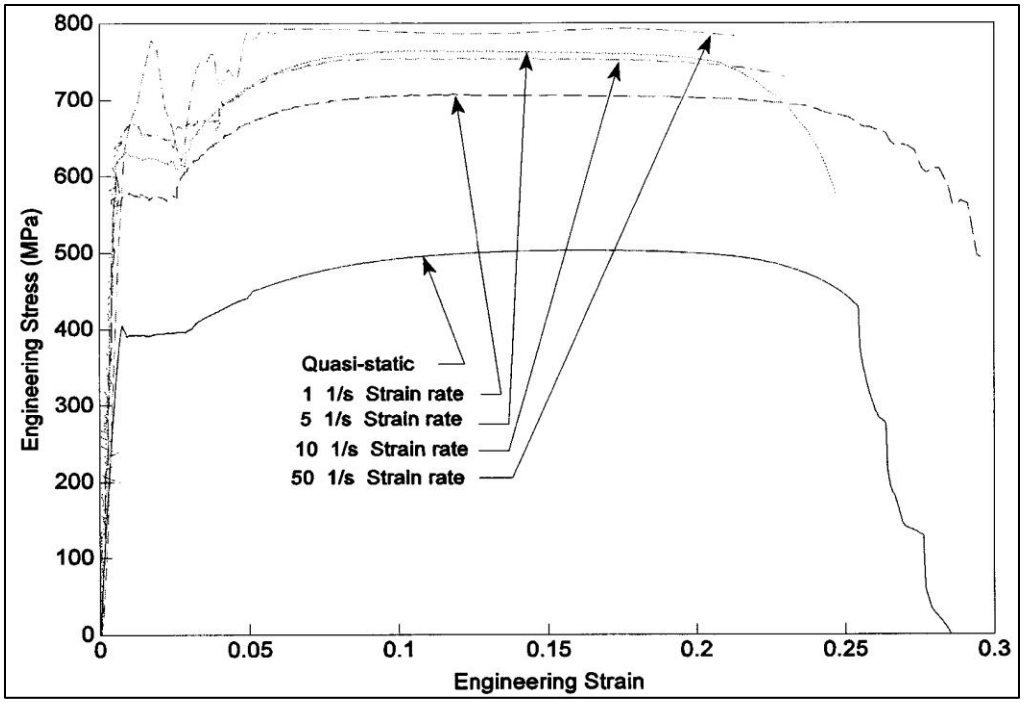

Figure 14. AASHTO Specification M-180 Type II Class A Guardrail Steel Engineering Stress vs. Strain Behavior at Various Strain Rates [49]

Table 1. Cowper-Symonds Coeficient Values [49-50]

Material	**C** $\mathbf{sec^{-1}}$	**p**
Mild Steel	40.4	5.0
AASHTO Specification M-180 Guardrail Steel	100.4	4.9

$$\sigma_y\left(\varepsilon_{eff}^p, \dot{\varepsilon}_{eff}^p\right) = \sigma_y^s\left(\varepsilon_{eff}^p\right) + SIGY * \left(\frac{\dot{\varepsilon}_{eff}^p}{C}\right)^{1/p} \quad (2.9)$$

where:

$\sigma_y =$ Yield Stress Function
$\varepsilon_{eff}^p =$ Effective Plastic Strain
$\dot{\varepsilon}_{eff}^p =$ Effective Plastic Strain Rate
$\sigma_y^s =$ Static Stress Function
SIGY = Initial Yield Stress
$C =$ Cowper − Symonds Strain Rate Parameter
$p =$ Cowper − Symonds Strain Rate Parameter

2.3 Modern Metal Failure Prediction Simulation

In the last decade, great advances in modeling metal failure have been made. While a number of failure criteria are available, as reviewed by Du Bois et al. [51], reliable prediction of failure continues to pose a challenge. The focus of current research efforts are on stress state dependent failure conditions, typically defined by a Lode parameter and triaxiality. While the triaxiality-only failure criterion has been researched extensively in the last half century, recent research has shifted to examining failure surfaces dependent on complex stress states. These complex stress states are commonly represented by triaxiality and Lode parameter. A more detailed description of the various metallic material fracture modeling methods, with and without stress state dependent failure criteria is provided in Chapter 3.

3 LS-DYNA MATERIAL MODEL REVIEW

3.1 Material Model Review Scope

LS-DYNA offers a large number of material models that can be used to simulate a wide range of materials and accommodate a number of applications. In this study, the behavior of AASHTO M-180 steel through the failure regime is of interest. For this reason, all metallic material models that include a form of element erosion were included in the initial material model research. A total of 40 methods of element erosion for metallic materials were aggregated, as per the LS-DYNA User Manual [2]. As part of the initial review, a brief background review was performed to eliminate 22 material models that were inadequate for modeling failure in Specification M-180 steel, or models that focused on effects outside the scope of this research. After this initial round of elimination, a second round of analysis was performed. In the second round, the remaining material models were reviewed and rated based on their ability to handle the following six criteria:

- ability to arbitrarily input stress vs. strain curves through failure;
- ability to implement damage accumulation (tracking of damage);
- ability to couple damage with a reduction of stiffness and/or strength prior to failure;
- inclusion of failure criterion parameters as a function of stress state, strain rate, and temperature; (However, temperature effects are not of critical importance to roadside safety applications at this time due to the relatively lower energy impacts witnessed in vehicular impacts. Adiabatic temperature effects are assumed to be negligible in this report.)
- ability to regularize the material model to adjust failure based on element size or the inclusion of some form of non-local failure criteria; and
- ability to delete elements after a failure criterion has been met.

Based on the performance of the material models in regards to the six criteria, eight material models were retained and the other material models were eliminated from further research at this time. As part of the final round of analysis, each model was further investigated. The purpose of the final round of analysis was to determine, to the best of one's ability without performing material tests, the accuracy of the methods used and how the following factors are accounted for:

- flow stress behavior;
- failure; and
- potential additional abilities such as non-local abilities, damage criteria, and strain rate effects.

Also, the number of tests needed to calibrate each model was considered as well as the difficulty required to determine each model's input parameters. Based on these results, two material models were selected for further research as well as the MAT_ADD_EROSION (GISSMO) failure criteria. The majority of the research was based on the LS-DYNA (Draft) Theory Manual [52] as well as the LS-DYNA Keyword User's Manual [2].

3.2 Initial Round – Material Model Elimination

A brief explanation is given for each material model that was eliminated as part of the initial round of analysis. The material models that were determined to warrant further investigation are not included in this section, as they are described in the following sections.

3.2.1 MAT_3 – Elastic Plastic with Kinematic Hardening

The material model offers a simple and effective application when limited material data is present, especially when only small plastic strains are present. However,

due to its inability to arbitrarily define stress vs. plastic strain curves, as the model is only a bilinear approximation of the elastic and plastic regions, the model may not be well suited for roadside safety applications.

3.2.2 MAT_10 - Elastic Plastic Hydrodynamic

The model can effectively model post yield stress-strain curves. It offers numerous spall options and is applicable to a wide range of materials, including those with pressure dependent yield behavior. However, due to its inability to model strain rate effects, the model is not the best suited for roadside safety applications. As such, this model was not considered for further evaluation.

3.2.3 MAT_11 - Steinberg Elastic-Plastic with Thermal Softening

The material model is useful for a wide range of materials and applications. However, the Steinberg model is oriented for extremely high strain rates ($> 10^5$) and material melting. It is unlikely that roadside safety applications will exhibit strain rates of this magnitude, or material melting due to high-energy impacts. The model is similar to MAT_10, including spalling effects, with the addition of high strain rate effects. As such, this model was not considered for further evaluation.

3.2.4 MAT_13 - Isotropic Elastioplastic with Failure

The model is a highly-simplistic failure model where failure occurs when either the effective plastic strain reaches a determined failure strain or when the pressure reaches a specified failure pressure. Accurately modeling failure of materials in roadside safety applications with this material model is not ideal due to the model's over simplified failure criteria as well as the material model's reliance on assuming simplified

material properties, such as the use of the plastic hardening modulus. As such, this model was not considered for further evaluation.

3.2.5 MAT_17 - Oriented Crack

As the *LS-DYNA Theory Manual* states, "This model is applicable to elastic or elastoplastic material under significant tensile or shear loading when fracture is expected. Potential applications include brittle materials, such as ceramics, as well as porous materials, such as concrete, in cases where pressure hardening effects are not significant [52]." Because the model utilizes the oriented-crack fracture model, based on the maximum principal stress criteria, the model has limited use predicting the fracture behavior of ductile guardrail steel. As such, this model was not considered for further evaluation.

3.2.6 MAT_19 - Strain Rate Dependent Isotropic Plasticity

The material model is similar to MAT_24 Piecewise-Linear Plasticity, except MAT_19 offers additional strain rate dependencies. This model is able to model simplistic failure through the use of an effective stress at failure. Also, an optional strain-rate dependency can be applied to the failure condition. This option can alter the modeled material's behavior greatly by allowing a tabulation of the effective stresses at failure dependent on the strain rate. Additionally, Young's modulus and the tangent modulus can optionally be made functions of strain rate. However, as the failure option of defining an effective stress at failure is not used to predict failure in guardrail steel, the material model may not be well suited for roadside safety applications.

3.2.7 MAT_52 - Bammann Damage/Sandia's Damage Model

MAT_52 is complex and includes many input parameters in order to allow modeling of temperature and rate dependent plasticity with the Bammann damage model [53-54]. The model may warrant further investigation based on its implementation on modelling foreign object debris (FOD) impacts [55]. However, the use of this model appears limited due to its complexity. As such, this model was not considered for further evaluation.

3.2.8 MAT_65 - Zerilli-Armstrong (Rate/Temperature Plasticity)

The material model is a rate and temperature sensitive plasticity model which is sometimes preferred in ordnance design calculations. The model is often used in applications involving elevated temperatures due to its ability to model flow stress for body centered cubic (BCC) and face centered cubic (FCC) metals at elevated temperatures [56-57]. This dependency is typically unnecessary in roadside safety applications. Failure options include failure strain and three spalling options. As such, this model was not considered for further evaluation.

3.2.9 MAT_103_P - Anisotropic Plastic

MAT_103_P is a simplified version of MAT_103 that does not include the viscoplastic strain rate formulation and can only be applied to shells. MAT_103 would be preferred over MAT_103_P due to its limited modeling abilities. As such, this model was not considered for further evaluation.

3.2.10 MAT_107 - Modified Johnson Cook

The modified Johnson-Cook model is typically used in elevated temperature analysis, such as hot rolled formed metals or ordnance impact analysis due to the additive

decomposition of the rate-of-deformation tensor (including elastic, plastic, and thermal parts). It is unlikely that roadside safety applications will be subjected to the thermally activated and viscous regimes that the model was meant to address. As such, this model was not considered for further evaluation.

3.2.11 MAT_124 – Tension-Compression Plasticity

The material model allows different yield stress vs. strain values in compression and tension by defining two different curves. However, the difference in compression and tension curves may not be beneficial for metal materials used in roadside safety applications. As such, this model was not considered for further evaluation. However, due to its similarity to MAT_24, the material model may warrant further research if a model with independent compression and tension flow behavior is required.

3.2.12 MAT_131 - Isotropic Smeared Crack

The smeared crack method is typically used to model brittle materials. As such, little to no information was found on this being used to model ductile metal materials. Also, the model does not allow any strain rate effects or shell elements so it is unsuitable for roadside safety applications. As such, this model was not considered for further evaluation.

3.2.13 MAT_132 - Orthotropic Smeared Crack

The material model can be used to model brittle material with options to model delamination of brittle composites. No information could be found on this technique being used to model ductile metal materials. Also, similar to the isotropic smeared crack material model, MAT_131, the model does not allow any strain rate effects so it is

unsuitable for roadside safety applications. As such, this model was not considered for further evaluation.

3.2.14 MAT_135 - Weak and Strong Texture Model

This model allows YLD2003 (Artez [58]), YLD89 (Barlat [59]), or an orthotropic anisotropic eight parameter yield surface card to be used to model the material. However, these yield prediction techniques are usually only reserved for metal forming simulations due to their efficiency at defining orthotropic effects with plane stress assumptions. As the steel guardrail material is assumed to be isotropic, this material model is unnecessary. Failure is based on three options including the Cockcroft and Latham (CL) fracture, Bressan-Williams shear fracture, or critical thickness. Cockcroft-Latham fracture criterion was developed for the bulk forming operations and therefore only applicable to the range of small and negative stress triaxiality. Similarly, the Bressan-Williams criterion defines a critical shear value for shear fracture. Furthermore, the critical thickness criterion defines a plastic thickness strain at failure. As such, this model was not considered for further evaluation.

3.2.15 MAT_151 - Evolving Microstructural Model of Inelasticity (EMMI)

As EMMI is an extension of the Bammann material model, it may be worth further research. However, no literature, besides the original Sandia National Laboratory report [60], could be found that provided practical use of this model. The model is a temperature and rate dependent model with a porosity-based isotropic damage state variable to describe the progressive deterioration of the strength and mechanical properties of metals induced by deformation. As such, this model was not considered for further evaluation.

3.2.16 MAT_153 - Damage 3

The model is designed to model low rate, hysteretic behavior of steel structures focused on the prediction of local bucking and the evolution of damage due to low-cycle fatigue (i.e. earthquakes) [61]. While the model may warrant more research, little to no literature could be found pertaining to this material outside of larger structures undergoing earthquake-like loading. As such, this model was not considered for further evaluation.

3.2.17 MAT_165 - Plastic Nonlinear Kinematic

MAT_165 is a simplified version of MAT_153 with one back stress tensor component, linear isotropic hardening, and critical equivalent plastic strain damage criterion. Due to its simplified focus on cyclic loading, it is not deemed suitable for roadside safety applications. Also, no strain rate dependency options are available. As such, this model was not considered for further evaluation.

3.2.18 MAT_190 - Flow limit diagram 3-Parameter Barlat

The model is a complex model that was developed by Barlat and Lian to model sheets with anisotropic materials under plane stress conditions [59]. The model was modified to include Forming Limit Diagram (FLD) failure criterion. While further research may be warranted, the model fails to account for strain rate effects or damage, and it is typically used in forming simulations. As such, this model was not considered for further evaluation.

3.2.19 MAT_225 - Viscoplastic Mixed Hardening

MAT_225 is a model with kinematic or isotropic hardening as well as arbitrary stress vs. strain curve and strain rate dependency based on a user defined table. The

model focuses on mixed forms of isotropic and kinematic hardening of the material. The added complexity to account for cyclic loading is not necessary in roadside safety applications at this time. As such, this model was not considered for further evaluation.

3.2.20 MAT_238 – Piecewise Linear Plasticity with Perturbation

MAT_238 is a near duplicate of MAT_24, modified for use with *PERURBATION_MATERIAL. The perturbation, also known as a stochastic field, is typically used to add imperfections in the material in order to better model situations, such as buckling. Due to the limited increase in overall accuracy with the addition of accurate buckling modeling, at the cost of a 10 percent increase in computational time, applications of this material have limited use in roadside safety applications. As such, this model was not considered for further evaluation.

3.2.21 MAT_251 - Tailored Properties

The model is almost identical to MAT_24, except additional material history variable data is written using *INTERFACE_SPRINGBACK_LSDYNA. The model is intended for crash simulation with additional emphasis on recording historical material effects. The additional material history variables typically represent a local stress-strain behavior applied to the part by techniques such as bake hardening or other history effects developed through part forming. At this time, modeling part forming effects are beyond the immediate research scope of this project, but may pose as a useful material model when considering residual local stress-strain behavior from part forming. The material model is limited to shells, so the model was eliminated from further research at this time.

3.2.22 MAT_255 - Thermal Piecewise Linear Plastic

The material model is similar to MAT_24, except this model includes thermal properties to be accounted for by assigning two tables that give the yield stress in tension and compression as load curves for different temperatures. Also, a thermal coefficient of expansion can be defined. While temperature may play a role in affecting the load curves in roadside safety applications, the effect is not a primary concern at this time and will largely not affect the model accuracy. As such, this model was not considered for further evaluation.

3.3 Second Round – Material Model Elimination

A brief explanation is provided for each material model that was eliminated as part of the second round of analysis. However, the material models that were determined to warrant further investigation are not included as part of the brief explanations, as they are described in the following section. Also, Table 2 is included to give the findings of the six-criteria-review for all the remaining material models that were not eliminated in the first round elimination. It should be noted that the ability to delete elements after failure is not included in the table as all of the remaining models have the ability to delete an element after some form of failure criteria has been met.

3.3.1 MAT_ADD_EROSION (DIEM) - Damage Initiation and Evolution Criteria

The Damage Initiation and Evolution Criteria (DIEM) is an alternative to GISSMO that is implemented through MAT_ADD_EROSION. The model allows the user to arbitrarily invoke any number of damage-initiation and evolution criteria to create a phenomenological failure model. The damage initiation options include: ductile; shear; Müschenborn-Sonne forming limit diagram (MSFLD); and form limit diagram (FLD).

Two linear algorithms can be used to model the damage parameter. This model may be a useful addition to a material model. However, GISSMO is preferred due to the regularization option and the ability to add Lode parameter dependency. As such, this model was not considered for further evaluation.

Table 2. Six Criteria Review as Part of Second Round Elimination.

Name	Accuracy of Stress vs. Strain Curve	Damage Accumulation	Coupled Damage	Failure Criterion: Strain Rate Dependent	Failure Criterion: Stress State Dependent	Regularization of Failure
GISSMO (MAT_ADD_EROSION)	NA	Yes	Optional	No	Yes	Yes- Load curve defining element size factor vs. EPS at failure. And scaling factor at two triaxiality values
DIEM (MAT_ADD_EROSION)	NA	Yes	Yes	Yes	Yes	No
MAT_ADD_EROSION (Standard Failure Criteria)	NA	No	No	No	No	Yes- Load curve defining element size factor vs. standard failure options.
MAT_15	Phemenological model	Yes	No	Yes	Yes	No
MAT_24	Arbitrary stress vs. strain and strain rate dependency	No	No	No	No	No
MAT_81/82	Arbitrary stress vs. strain	Yes	Yes	No	No	No
MAT_81/82_RCDC	Arbitrary stress vs. strain	Yes	Yes	No	Yes	The Wilkins method is a nonlocal model (damage gradient depends on behavior of surrounding elements), so mesh size should be independent of failure.
MAT_98	Phemenological model	No	No	Yes	No	No
MAT_99	Phemenological model	No	No	Yes	No	No
MAT_103	Arbitrary stress vs. strain	No	No	No	No	No
MAT_104	Arbitrary stress vs. strain	Yes	Yes	Yes	Yes	No
MAT_105	Arbitrary stress vs. strain	Yes	Yes	Yes	Yes	No
MAT_120	Arbitrary stress vs. strain	Yes	Yes	Yes	Yes	Yes- through load curves defining Gurson void volume parameters vs. element length
MAT_120_JC	Arbitrary stress vs. strain	Yes	Yes (Gurson)	Yes	Yes	Yes- through a load curve defining Gurson void volume parameters vs. element length
MAT_120_RCDC	Arbitrary stress vs. strain	Yes	Yes (Gurson and Rc-Dc)	No	Yes	Yes- through a load curve or 4 point correlation defining Gurson' failure void volume fraction vs. element length. The Wilkins method is a nonlocal model (damage gradient depends on behavior of surrounding elements), so failure should be less dependent on mesh size
MAT_123	Arbitrary stress vs. strain and strain rate dependency	No	No	No	No	No
MAT_123_RTCL	Arbitrary stress vs. strain and strain rate dependency	Yes	No	No	Yes	No
MAT_224	Arbitrary stress vs. strain and strain rate dependency	Yes	No	Yes	Yes	Yes- Load curve defining plastic failure strain as a function of element size (with a curve for each triaxiality)

3.3.2 MAT_ADD_EROSION - Standard Erosion Criteria

MAT_ADD_EROSION allows failure or erosion to be added to material models that may or may not contain failure criterion. There are ten additional failure criteria supported that may be applied, and once an arbitrary number of those criteria are satisfied, the element is deleted. The ten criteria include maximum pressure at failure, minimum principal strain at failure, minimum pressure at failure, maximum principal strain at failure, equivalent stress at failure, maximum principal strain at failure, shear strain at failure, Tuler-Butcher criterion (stress impulse for failure), and the non-local windshield impact method. However, none of these criteria account for damage effects or stress state dependent failure. As such, this model was not considered for further evaluation.

3.3.3 MAT_15 - Johnson-Cook Plasticity Model

The Johnson-Cook model offers a well-proven phemenological model to incorporate material effects throughout a wide range of applications. The model has been used extensively since it was proposed in 1983 [32]. However, it should be noted that the model does not account for the Lode parameter and, as a result, cannot predict failure under complex loading accurately. MAT_224 offers a similar approach, except MAT_224 replaces the analytical formulations with tabulated generalizations of stress state dependencies, strain rate dependencies, stress vs strain input curves, and includes regularization. For these reasons, MAT_224 would be preferred over MAT_15. As such, this model was not considered for further evaluation.

3.3.4 MAT_81/82 - Plasticity with Damage

The material model is similar to MAT_24. However, this model incorporates a damage coefficient that allows linear damage as a function of plastic strain to allow softening of the material to begin at a determined failure plastic strain that continues until strain reaches a rupture value. After the rupture strain is reached, the material fails and the element is deleted. The standard damage procedure is replicated in the ductile failure damage procedure (DITYP.EQ.0) in the DIEM option in MAT_ADD_EROSION DIEM offers more diverse failure options. As a result, MAT_24 with the MAT_ADD_EROSION DIEM option is more comprehensive and is preferred over the standard damage model included in MAT_81. Also, an option to include the Rc-Dc failure prediction model is available and may provide more accurate results than the standard material model. As such, this model was not considered for further evaluation.

3.3.5 MAT_98 - Simplified Johnson Cook

MAT_98 is a simplified version of Johnson Cook with approximately 50 percent reduction in computational cost. Thermal and damage effects are ignored, and elements only fail when the plastic strain exceeds a predetermined value. It may be valuable to examine this model further if the original Johnson Cook was determined to be adequate. However, exclusion of the damage parameter will likely reduce material failure modeling performance considerably. As such, this model was not considered for further evaluation.

3.3.6 MAT_99 - Simplified Johnson Cook Orthotropic Damage

MAT_99 is an extension of MAT_98 with defined failure strain in tension in one of the two orthogonal directions. The model is intended to be used to model failure in

aluminum panels with orthotropic material properties. As such, this model was not considered for further evaluation.

3.3.7 MAT_103 - Anisotropic Viscoplastic

MAT_103 accounts for anisotropic effects in the material. The failure provides strain rate effects and is meant to provide superior results to MAT_03 and MAT_24 for anisotropic materials. If the tested material shows significant anisotropic properties, this material model may perform better than MAT_24. However, it should be noted that the model has similar limitations as MAT_24 for failure criteria, except anisotropic failure conditions are included. As such, this model was not considered for further evaluation.

3.3.8 MAT_104 - Damage 1

The model includes a continuum damage mechanics (CDM) model from Lemaitre which also includes an option to model anisotropic damage behavior and viscoplastic effects [30]. The focus of the CDM model is the prediction of the unloading at a degraded stiffness, in contrast to elastic-plasticity which assumes unloading parallel to the initial stiffness. CDM models are used extensively to model initiation and growth of cracks as material degrades due to cyclical loading. However, as this behavior is outside the scope of this research, the material model may not be well suited to model material failure in roadside safety applications. As such, this model was not considered for further evaluation.

3.3.9 MAT_120 - Gurson

The Gurson model is very popular in modeling damage based failure. MAT_120 is a micromechanical model that is able to predict both homogeneous and localized dilation deformation phases. The Gurson model, as used in MAT_120, is dependent on

triaxiality. Also, the model is able to predict material softening behavior due to nucleation and growth of voids. However, the large number of parameters due to the complex function of flow rule and damage evolution adds considerable time for preparation. In addition, there is no shear consideration because the hydrostatic pressure remains constant in simple shear and there is no macroscopic dilation. To account for shear, MAT_120_JC or MAT_120_RCDC are more ideal. MAT_120_JC includes the Johnson-Cook criterion in the shear region triaxiality by combining a Johnson-Cook damage parameter with the Gurson damage. Also, the Rc-Dc fracture criterion by Wilkins is added in MAT_120_RCDC, which adds additional damage formulation that is dependent on stress asymmetry and hydrostatic pressure. As shown in the experimental program and simulation effort performed by Feucht et al., the Gurson model tends to overestimate displacements at failure of the losipescu specimens to test shear strength [62]. This error is a result of the void growth in the Gurson model depending only on the hydrostatic stress. Thus, shear deformations do not influence the damage process in the Gurson model. For more information, a valuable study with a comparison between the Gurson and GISSMO model was performed by Hauge et al. and presented at the 2010 International LS-DYNA Conference [63]. As potentially better options are available, the base MAT_120 model was not considered for further evaluation.

3.3.10 MAT_123 - Modified Piecewise Linear Plasticity

MAT_123 is an extension of MAT_24 with enhanced failure criterion using an optional incremental Rice–Tracey and Cockcroft–Latham (RTCL) damage calculation based on a piecewise-triaxiality dependent function. However, the base material model only offers element erosion at an effective plastic strain at failure and a thinning strain at

failure as a function of the plastic strain rate. Due to the limited enhancements over MAT_24, the material model was eliminated. As such, this model was not considered for further evaluation.

3.4 Final Round – Material Model Elimination

A brief explanation is provided for each material model that was eliminated as part of the third round of analysis. Based on this evaluation, it was determined that MAT_224 – Tabulated Johnson-Cook as well as the MAT_ADD_EROSION optional GISSMO failure criteria warranted further research, testing, and validation. The MAT_24 Piecewise-Linear Plasticity material model was also included to act as a baseline model due to its prevalence in modeling guardrail steel in crash simulations.

3.4.1 MAT_81/82_RCDC - Plasticity with Damage with Rc-Dc Option

The model is similar to MAT_24. However, this model incorporates a damage coefficient that allows linear damage as a function of plastic strain to allow softening of the material to begin at a determined plastic strain that continues until the plastic strain reaches a rupture value. After the rupture strain is reached, the material fails and the element is deleted. The standard damage procedure is replicated in the ductile failure damage procedure (DITYP.EQ.0) in the DIEM option in MAT_ADD_EROSION.

An option to include the Rc-Dc model, as developed by Wilkins, is included. Because the Rc-Dc model considers triaxiality and the maximum ratio of first and second deviatoric principal stresses (1980 model [64]) or the minimum ratio of the second and third principal stresses (1977 model [65]), the Wilkins (Rc-Dc) option may be worth additional research. Also, MAT_81 gives options for an orthotropic damage model in which damage is accumulated along the two orthotropic directions. The 1980 version of

the Rc-Dc model is preferred as it accounts for the maximum ratio of the first and second deviatoric stress instead of the minimum ratio of the two lesser principal stresses.

While this failure prediction model may warrant further research, the model has some limitations. First, the model only allows three parameters to calibrate the state of stress vs. failure surface. As shown by the analysis performed in Chapter 4, the higher degree of freedom surface fitting methods fit the data sets better than the lower degree of freedom surface fitting methods. Furthermore, instead of utilizing the Lode parameter, which is a function of the third deviatoric stress invariant, the Rc-Dc method uses only two of the principal stress deviators to define the state of stress. As recent research has shown a preference toward defining the state of stress dependent failure surfaces with the triaxiality and Lode parameter due to their ability to capture complex loading conditions, the Rc-Dc method has limited use. Due to these limitations it was determined that the material model may not be well suited to predict material failure for guardrail steel. As such, this model was not considered for further evaluation.

3.4.2 MAT_105 - Damage 2

The model is an elastic-viscoplastic material model with similar behavior to MAT_24, but the model utilizes a CDM model by Lemaitre similar to MAT_104 [30]. CDM models are used extensively to model initiation and growth of cracks as material degrades due to cyclical loading. However, as this behavior is outside the scope of this research, the material model may not be well suited to model material failure in roadside safety applications. As such, this model was not considered for further evaluation. However, further research of MAT_104 or MAT_105 may be warranted if a cyclical loading condition with material softening is present.

3.4.3 MAT_120_JC - Gurson with Johnson Cook

As discussed previously, the Gurson model is a very popular micromechanical model that is able to predict both homogeneous and localized deformation phases. However, there is no shear consideration in the standard Gurson model because under shear loading the hydrostatic pressure remains constant and there is no macroscopic dilation. To overcome this shortcoming MAT_120_JC combines the Johnson-Cook damage with the Gurson damage in the shear region of the triaxiality range. This change was proposed by Nahshon and Hutchinson to include the new void growth term that accounts for shear [66]. The original Gurson model, as used in LS-DYNA, neglects void growth in the shear regime. As recent research has shown a preference toward defining the state of stress dependent failure surfaces with the triaxiality and Lode parameter due to their ability to capture complex loading conditions, the Gurson with Johnson-Cook criteria method has limited use. Due to these limitations it was determined that the material model may not be well suited to predict material failure for guardrail steel. As such, this model was not considered for further evaluation.

3.4.4 MAT_120_RCDC - Gurson with Rc-Dc Option

This model is similar to the MAT_120_JC option. However, instead of the additional Johnson-Cook damage in the shear triaxiality range, the Rc-Dc fracture criterion by Wilkins is added in MAT_120_RCDC. The Rc-Dc fracture criterion adds additional damage formulation that is dependent on stress asymmetry and hydrostatic pressure [64]. As recent research has shown a preference toward defining the state of stress dependent failure surfaces with the triaxiality and Lode parameter due to their ability to capture complex loading conditions, the Gurson with Johnson-Cook criteria

method has limited use. Due to these limitations it was determined that the material model may not be well suited to predict material failure for guardrail steel. As such, this model was not considered for further evaluation.

3.4.5 MAT_123_RTCL - Modified Piecewise Linear Plasticity (RTCL Option)

The optional RTCL failure criterion of MAT_123 is damage parameter based. The RTCL criterion is composed of a void growth model developed by Rice and Tracey [24], and a shear failure model developed by Cockcroft and Latham [67]. The Cockcroft-Latham fracture criterion was developed for the bulk forming operations and therefore only applicable to the range of small and negative stress triaxiality. Since the Rice-Tracey criterion predicts fracture from void growth and Cockcroft-Latham predicts ductile shear fracture, the combination of these two theories is a natural combination. The material failure model produced from combining the two methods is a piecewise damage accumulation model in which the damage factor increases in a piecewise form as a function of triaxiality through plastic deformation to failure.

Only one test is required to calibrate the model as the RTCL piecewise damage accumulation curve shape is predefined. Only the effective plastic strain at failure is used to calibrate the curve, which allows for easy implementation of a material model. However, the model does not include any Lode parameter dependence or any adjustment to the shape of the curve if test data shows that the given RTCL curve does not fit test data. As a result, other material models that allow adjustable triaxiality and Lode parameter dependent failure surfaces are preferred. As such, this model was not considered for further evaluation.

3.5 Selected Material Models

It was determined that MAT_224 – Tabulated Johnson-Cook as well as the MAT_ADD_EROSION optional GISSMO failure criteria warranted further research, testing, and validation. The MAT_24 Piecewise-Linear Plasticity material model was also included to act as a baseline model due to its prevalence in modeling guardrail steel in crash simulations.

3.5.1 MAT_24 - Isotropic Piecewise-Linear Plasticity

MAT_24 is a popular material model that is used widely in crash simulations. The model treats plasticity similar to MAT_10, but it includes three options to account for strain rate effects and does not use an equation of state. Strain rate effects is accounted for either by the Cowper-Symonds model, a load curve with a scale factor vs. strain rate defined, or a series of stress vs. strain curves tabulated for various strain rates. It should be noted that the failure criteria is overly simplified, as the only element erosion methods available are failure based on a defined constant effective plastic strain or a minimum time step size. However, the material failure capabilities of this material model can be enhanced with the various failure criteria available in MAT_ADD_EROSION.

3.5.2 MAT_ADD_EROSION - GISSMO

Generalized Incremental Stress-State dependent damage Model (GISSMO) is a damage formulation model that is added through MAT_ADD_EROSION that includes failure through damage effects with a coupled damage-stress relationship and a measure of instability through the state of stress that leads to a coupled reduction in an element's ability to carry an external stress. GISSMO is ideal for predicting ductile failure through the input of a failure curve as a function of triaxiality and Lode parameter, where the

surface is used to define failure with damage accumulation. More specifically, arbitrary effective plastic strain at failure can be defined for each triaxiality and Lode parameter to create a failure envelope that varies with triaxiality and Lode parameter. Opposed to MAT_224, damage is accumulated by accounting for stress, and damage coupling is included. As previously explained, the options to include damage coupling and state of stress failure criteria may be necessary to provide accurate material failure predictions.

3.5.3 MAT_224 - Tabulated Johnson Cook

This material model resembles the original MAT_15 but with the possibility of general tabulated input parameters. Arbitrary stress vs. strain curves as a function of strain rate and temperature can be inputted. Also, plastic strain at failure can be defined as a function of triaxiality and lode parameter, strain rate, temperature, and/or element size (regularization). Also, the element size scaling of the effective plastic strain at failure can be inputted as a function of triaxiality. MAT_224 is a broad material model that offers many options and accounts for many various aspects that increase its usefulness in modeling failure in roadside safety applications. Failure is accumulated over an integral of the ratio of effective plastic strain to effective plastic strain at failure. When this integral exceeds a value of one, element erosion occurs. Note, while the material model was intended to be an extension of the Johnson-Cook material model, the new reliance on tabulated input tables and curves allow for arbitrary failure envelopes to be implemented.

4 FAILURE SURFACE REVIEW AND ANALYSIS

4.1 Introduction

As part of an initial investigation to develop a failure surface that defines the effective plastic strain at failure as a function of the state of stress given by the triaxiality and Lode parameter, four existing failure surface methods that assume this dependency were reviewed and analyzed. This analysis was based solely on preexisting test data. As part of the review, the governing equations defining each failure surface method are given as well as a brief overview of the methodology and reasoning used during each failure surface methods' development. The analysis of each failure surface method consisted of an attempt to recreate the proposed method with both the physical test data from the original paper as well as with the physical test data that was published in other material testing programs. In doing so, the failure surface methods' ability to accurately represent material testing results at various stress states could be accessed. This process also gave insight into the quantity and type of specimens needed for a testing program in order to accurately represent a failure surface as a function of the state of stress given by the triaxiality and Lode parameter.

4.2 Existing Failure Surface Method Review

4.2.1 Xue-Wierzbicki Failure Surface Method

The failure surface proposed by Xue and Wierzbicki is a triaxiality and Lode parameter dependent failure surface [37,68]. Failure is expected to occur when the accumulation of the effective plastic strain, modified by the function of the stress triaxiality and the Lode parameter, reaches a limiting value equal to one, as seen in Equation 4.10. Furthermore, as the values of the triaxiality and Lode parameter typically

change through the deformation process, integrating the modified effective plastic strain value is required. It should be noted that during calibration, the effects of the triaxiality and Lode parameter are meant to be averaged out by using the average triaxiality and Lode parameter found in Equations 4.11 and 4.12. An alternative, simpler, yet possibly less accurate, approach would be to use a static failure surface given by triaxiality and Lode parameter in which failure occurs based only on the final triaxiality and Lode parameter exhibited in the specimen, as seen in Equation 4.13.

Failure Occurs When $\widehat{\varepsilon_f^p} = \int_0^{\varepsilon_f^p} \frac{d\varepsilon^p}{F(\eta,\xi)} = 1$ (4.10)

Where

$\widehat{\varepsilon_f^p} =$ Accumulated Modified Effective Plastic Strain
$\varepsilon_f^p =$ Effective Plastic Strain At Failure
$\varepsilon^p =$ Effective Plastic Strain
$\varepsilon^p = \sqrt{2/3\,(\varepsilon_1^2 + \varepsilon_2^2 + \varepsilon_3^2)}$
$\varepsilon_1, \varepsilon_2, \varepsilon_3 =$ Principal Strains
$F(\eta, \xi) =$ Failure Value Dependent on Triaxiality and Lode Parameter

and

$\eta_{ave} = \frac{1}{\varepsilon_f^p} \int_0^{\varepsilon_f^p} \eta(\varepsilon^p)\, d\varepsilon^p$ (4.11)

where

$\eta_{ave} =$ Average Triaxiality
$\varepsilon_f^p =$ Effective Plastic Strain At Failure
$\varepsilon^p =$ Effective Plastic Strain
$\eta(\varepsilon^p) =$ Triaxiality at Current Plastic Strain Value

and

$$\xi_{ave} = \frac{1}{\varepsilon_f^p}\int_0^{\varepsilon_f^p} \xi(\varepsilon^p)\, d\varepsilon^p \tag{4.12}$$

where

ξ_{ave} = Average Lode Parameter
ε_f^p = Effective Plastic Strain At Failure
ε^p = Effective Plastic Strain
$\xi(\varepsilon^p)$ = Lode Parameter at Current Plastic Strain Value

and

$$\varepsilon_f^p = F(\eta, \xi) \tag{4.13}$$

where

ε_f^p = Effective Plastic Strain At Failure
$F(\eta, \xi)$ = Failure Function Dependent on Triaxiality and Lode Parameter

The function, $F(\eta, \xi)$, as proposed by Xue and Wierzbicki, is defined by two bounding equations – an upper and lower bound for the failure surface. The upper bound is defined by the axial symmetrical Lode parameter in which $\xi = -1$ and $\xi = 1$. The lower bound is defined by plane strain conditions in which $\xi = 0$. Xue and Wierzbicki determined that both of these bounding curves can be described by the exponential functions given in Equations 4.14 and 4.15. A graphical representation of these upper and lower bound equations can be seen in Figure 15. Furthermore, Xue and Wierzbicki assumed that the drop in ductility due to the Lode parameter can be described by a family of elliptic functions given by Equation 4.16, where m is the even integer closest to $1/n$, and n is the hardening exponent. Combining these two sets of equations (Equations 4.14 through 4.16) creates the surface defining the effective plastic strain at failure as a function of triaxiality and Lode parameter, as given in Equation 4.17. It is important to note that using an ellipsoidal approach to describe the relationship between the change in ductility and the Lode parameter assumes that the surface will be axial-symmetric along the $\xi = 0$ axis. Therefore, the resulting equation describing the surface can be calibrated

with the four coefficients, C_1, C_2, C_3, C_4, where C_2 and C_4 are related to the hardening exponent, n.

$$\varepsilon_f^{p\ axial} = C_1 e^{-C_2 \eta}\ when\ \xi = -1\ and\ \xi = 1 \tag{4.14}$$

where

$\varepsilon_f^{p\ axial}$ = Effective Plastic Strain at Failure Under Axial Loading Conditions
C_1, C_2 = Coefficients
η = Triaxiality
ξ = Lode Parameter

and

$$\varepsilon_f^{p\ plane\ strain} = C_3 e^{-C_4 \eta}\ when\ \xi = 0 \tag{4.15}$$

where

$\varepsilon_f^{p\ plane\ strain}$ = Eff. Plastic Strain at Failure Under Plane Strain Conditions
C_3, C_4 = Coefficients
η = Triaxiality
ξ = Lode Parameter

and

$$\left(\frac{\Delta\varepsilon_f^p}{\varepsilon_f^{p\ axial} - \varepsilon_f^{p\ plane\ strain}}\right)^{1/m} + \xi^{1/m} = 1 \tag{4.16}$$

where

ε_f^p = Effective Plastic Strain at Failure
$\varepsilon_f^{p\ axial}$ = Effective Plastic Strain at Failure Under Axial Loading Conditions
$\varepsilon_f^{p\ plane\ strain}$ = Effective Plastic Strain at Failure Under Plane Strain Conditions
m = Hardening Coefficient

and

$$\varepsilon_f^p = F(\eta_{av}, \xi_{av}) = C_1 e^{-C_2\eta} - (C_1 e^{-C_2\eta} - C_3 e^{-C_4\eta})(1-\xi^n)^n \quad (4.17)$$

where

ε_f^p = Effective Plastic Stress at Failure

$F(\eta_{av}, \xi_{av})$ = Failure Function Dependent on Average Triaxiality and Average Lode Parameter

C_1, C_2, C_3, C_4 = Coefficients

η = Triaxiality

ξ = Lode Parameter

n = Hardening Exponent

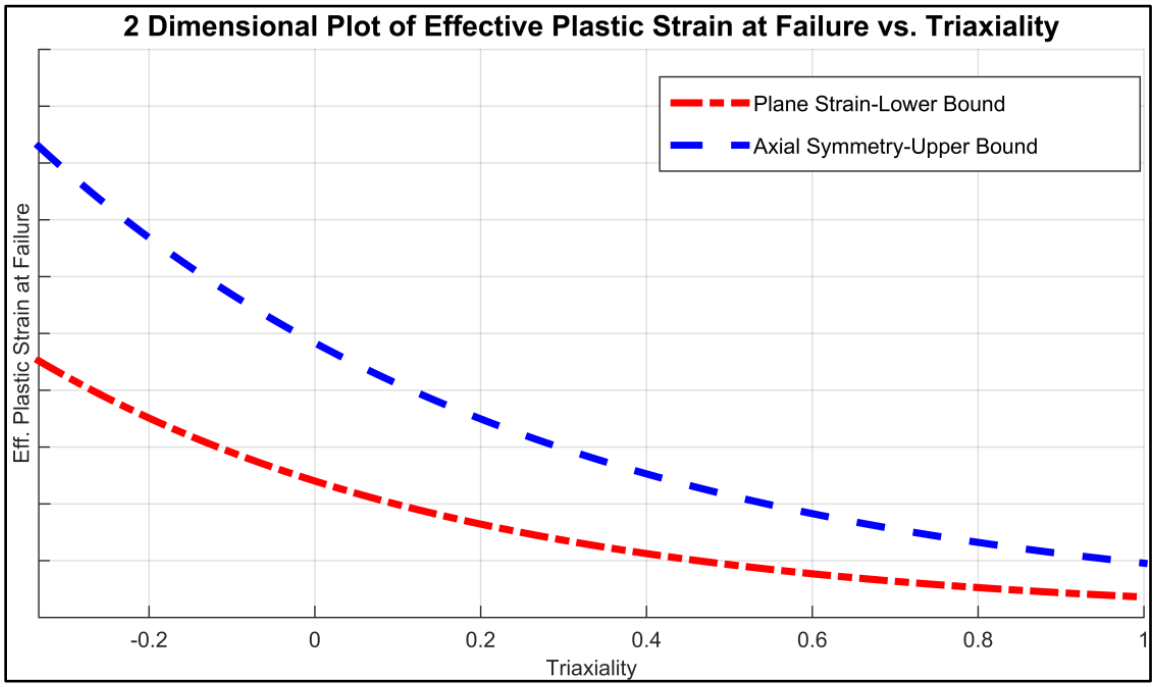

Figure 15. Xue-Wierzbicki Method Upper and Lower Bounds

4.2.2 Bai Failure Surface Method (Asymmetric and Symmetric Approach)

The failure surface proposed by Bai is a triaxiality and Lode parameter dependent failure surface similar to the Xue-Wierzbicki failure surface [35,39,69]. However, Bai proposed a number of changes compared to the Xue-Wierzbicki failure surface. First, Bai proposed that the relationship between the changes in ductility in relation to the Lode parameter can be described by a parabolic function, as opposed to the ellipsoidal function used in the Xue-Wierzbicki failure surface. While both the ellipsoidal and parabolic

functions are conic sections, the parabolic function, as used by Bai, allows for increased flexibility to describe the failure surface by allowing asymmetry along the $\xi = 0$ axis. Furthermore, the hardening exponent is removed from the failure surface equation. Instead, two additional coefficients are used to describe the failure surface. This results in the six coefficient equation as seen in Equation 4.18. It should be noted that Bai presents this failure surface as a function of triaxiality and a normalized Lode angle parameter, $\bar{\theta}$, as given in Equation 4.19. However, for the comparison and analysis performed in this chapter, the standard Lode parameter that is utilized throughout this report is used. This change should alter the shape of the failure surface slightly as compared to using the Lode angle parameter to describe one of the stress-state axes, but it should not greatly affect the analysis or conclusion.

$$\varepsilon_f^p = F(\eta_{av}, \xi_{av}) = \left[\frac{1}{2}(D_1 e^{-D_2\eta} + D_5 e^{-D_6\eta}) - D_3 e^{-D_4\eta}\right]\bar{\theta}^2 + \frac{1}{2}(D_1 e^{-D_2\eta} - D_5 e^{-D_6\eta})\bar{\theta} + D_3 e^{-D_4\eta} \tag{4.18}$$

where

ε_f^p = Effective Plastic Stress at Failure
$F(\eta_{av}, \xi_{av})$ = Failure Function Dependent on Average Triaxiality and Average Lode Parameter
$D_1, D_2, D_3, D_4, \mathrm{D}_5, \mathrm{D}_6$ = Coefficients
η = Triaxiality
$\bar{\theta}$ = Normalized Lode Angle

and

$$\bar{\theta} = 1 - {}^{6\theta}/_{\pi} = 1 - \frac{2}{\pi}\arccos(\xi) \tag{4.19}$$

where

$\bar{\theta}$ = Normalized Lode Angle
θ = Lode Angle
ξ = Lode Parameter

Bai proposed an asymmetric failure surface that would allow for a more flexible surface to be fitted. However, if the testing data shows that an asymmetric approach is

not needed, or test data along $\xi = -1$ is not available, the function describing the failure surface in the state of stress space can be simplified to a symmetric surface about the $\xi = 0$ axis. This simplification has the advantage of only needing to calibrate four coefficients to describe the failure surface, as opposed to the six coefficients that are needed to calibrate the asymmetric surface function. To derive this alternate function, the $D_1 e^{-D_2\eta}$ term defining the $\xi = 1$ bounding curve will replace the $D_5 e^{-D_6\eta}$ term defining the $\xi = -1$ bounding curve so that both curves will be equal along the $\xi = 1$ and $\xi = -1$ axes. The resulting symmetric function is given in Equation 4.20.

$$\varepsilon_f^p = F_{sym}(\eta_{av}, \xi_{av}) = [D_1 e^{-D_2\eta} - D_3 e^{-D_4\eta}]\bar{\theta}^2 + D_3 e^{-D_4\eta} \quad (4.20)$$

where

$\varepsilon_f^p =$ Effective Plastic Stress at Failure
$F_{sym}(\eta_{av}, \xi_{av}) =$ Symmetric Failure Function Dependent on Average Triaxiality and Average Lode Parameter
$D_1, D_2, D_3, D_4 =$ Coefficients
$\eta =$ Triaxiality
$\bar{\theta} =$ Normalized Lode Angle

4.2.3 Buyuk Failure Surface Method

Buyuk defined a different approach to define a state of stress dependent failure surface. He proposed a least-squares approximation to find a bivariate spline approximation of the effective plastic strain at failure by carefully selecting testing specimens through a range of stress states [38,70]. The failure surface is bounded by four stress meridians (plane stress, axial-symmetric tension, axial-symmetric compression, and plane strain) constructed by three-dimensional, smoothing spline functions, as seen in Figure 16. Note that Buyuk used the opposite sign convention for triaxiality than what is used in this report. These meridians act as a ruled surface that is meant to define the boundary of the region of interest. Then, three-dimensional B-spines are constructed

using a least-squares approximation of the test data to develop a failure surface that is a bounded by the stress meridians. Buyuk utilizes the bivariate approach in order to control the knots used to construct the splines. A preferred approach for constructing splines involves manually specifying the internal knots to coincide with the repeating triaxiality and Lode parameter values in the testing program. Ideally, these should be intentionally spaced at nearly equidistance intervals. Buyuk refers to this relationship as "bridging" states of stress. This approach is meant to reduce the bias from more inflexible failure surfaces, such as the Xue-Wierzbicki and Bai methods. However, a large number of unique stress state tests are required to calibrate the model.

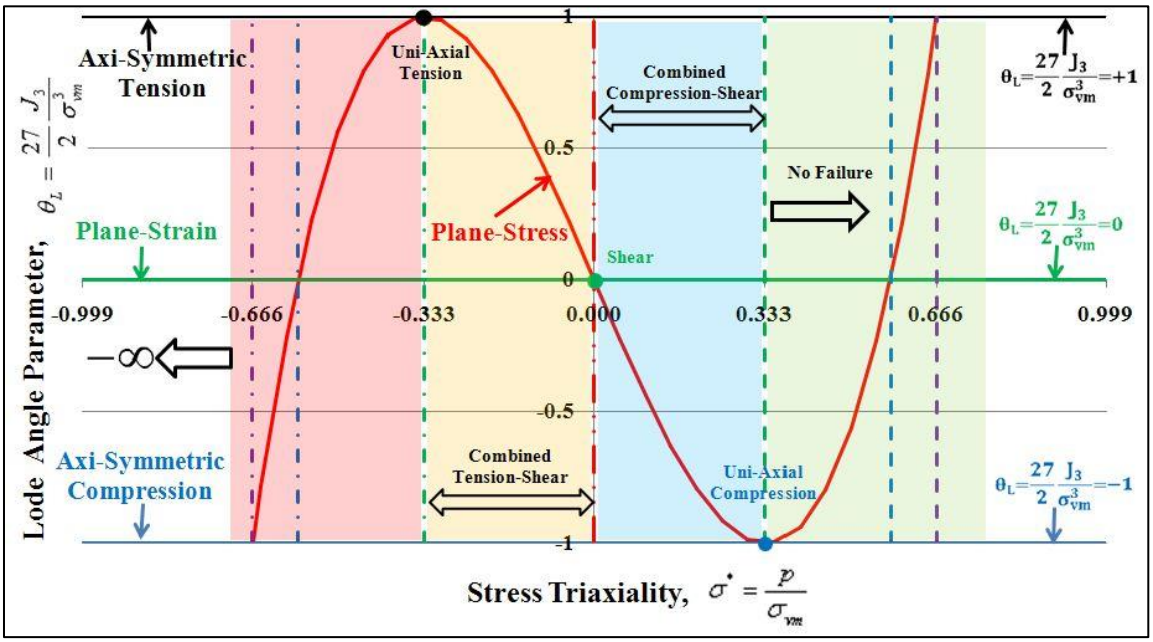

Figure 16. Stress Meridians in Triaxiality vs. Lode Parameter State of Stress [38]

It should be noted that the knot sequence Buyuk proposes does not meet the Shoenberg-Whitney conditions, as seen in Equation 4.21, to develop the splines due to the lack of an adequate number of data sites (i.e. unique stress state specimen tests). Thus, a unique bivariate spline approximation cannot be developed using B-splines and Buyuk's recommended internal knot sequence, as given in Equation 4.22. To meet the

Schoenberg-Whitney conditions, the number of polynomial pieces used to describe the spline is given in Equation 4.23. This equation governs the maximum number of polynomial pieces that are able to be used. For example, if a cubic-order spline is used per Buyuk's recommendation, then three data sites will be required along each spline if only one polynomial piece is used. Likewise, four data sites will be required to produce a spline with two polynomial pieces and so on. As seen with this trend, a large number of data sites are required to produce a cubic-order spline that will accurately describe the failure surface. Furthermore, even with Buyuk's large testing program, splines in the Lode parameter direction have a minimum of two and a maximum of six data sites, while splines in the triaxiality direction have a minimum of one and a maximum of three data sites. This finding greatly limits the flexibility of bivariate splines to either a lower order of spline or a low number of polynomial pieces. Due to the limitations inherent in constructing multivariable, bivariate splines, Buyuk's method of producing a failure surface based on bivariate splines was unable to be reproduced. However, the failure surface that Buyuk developed using the data set provided in the accompanying report is analyzed and discussed in Section 4.3.4 [38,43].

$$knots(j) < x(j) < knots\ (j + k) \tag{4.21}$$

where

$$j = 1, \dots, \text{length}(x) = \text{length}(knots) - k$$
$$k = \text{order of spline}$$

and

$$knot_{Lode} = [-1.0, 0.0, 0.617, 0.9145, 1.0] \tag{4.22}$$
$$knot_{triaxiality} = [-0.333, 0.0, 0.1466, 0.2505, 0.333, 0.41, 0.49, 0.577, 0.666, 0.8, 0.999]$$

and

$$\text{Number of Polynomial Pieces} \leq length(x) - k + 1 \quad (4.23)$$

4.3 Existing Failure Surface Method Analysis

Four existing state of stress dependent failure surfaces were analyzed to determine their effectiveness at predicting the effective plastic strain at failure against previously reported testing programs. These failure surface methods include the Xue-Wierzbicki, Bai Symmetrical, Bai Asymmetrical, and the Buyuk methods. MATLAB [71] programs were written to perform a surface fit using the various proposed methods, and can be found in Appendices A through D. MATLAB's Curve-Fitting Toolbox was utilized to solve for the various coefficients in the Xue-Wierzbicki and Bai failure surfaces. A non-linear least squares method was utilized to solve for the coefficients.

Three stress-state testing programs were used from literature in order to replicate and analyze the existing failure surface methods. These testing programs included: the Wierzbicki et al. data set; the Bai et al. data set; and the Buyuk data set. The Wierzbicki et al. data set, as provided by Bao, included a number of complex flat and round pieces with an additional four compression cylinders, as seen in Table 3 and Figure 17 [37,46]. The Bai et al. data set was comprised of six unique specimens: three flat-grooved plane strain specimens; two round specimens; and a pure torsion shear specimen, as seen in Table 4 and Figure 18 [39]. Lastly, the Buyuk data set, as provided by Seidt, included four flat specimens, six round specimens, three thick specimens, one torsion specimen, and a number of mixed loading and punch tests, as seen in Table 5 and Figure 19 [38,43].

The Wierzbicki et al., Bai et al., and Buyuk data sets comprised of 6, 15, and 20 specimens, respectively, and can be seen in Tables 3 through 5. The Buyuk testing matrix is the most comprehensive, while the Wierzbicki et al. and Bai et al. testing matrices

consist of fewer unique specimen tests. As such, the Buyuk testing matrix allows for a higher resolution, stress-state dependent, failure surface to be constructed. As part of the analysis performed in this research effort, all three data sets were used as part of a surface-fitting effort to evaluate each of the four methods. However, only the testing program used in the failure surface development and the Buyuk testing program are reported in the following section. This selection allows for a manageable-sized analysis to be presented and discussed. This process allowed insight into the required number and type of unique specimens that were needed to accurately represent a stress-state dependent failure model.

Furthermore, in the following subsection, subsets of the Wierzbicki et al. and the Buyuk testing programs were carefully selected, analyzed, and used to determine the number and type of unique specimens needed to accurately represent a stress state dependent failure surface. The first subset was chosen as a minimalistic approach. The specimens were chosen so that the least amount of specimens would be required to calibrate a stress-state dependent failure surface. The second subset includes a selection of flat specimens that could potentially be machined from thin pieces of material, such as guardrail steel. This additional analysis is meant to predict the results of a limited testing program compared to a full testing matrix seen in the existing testing programs.

Table 3. Wierzbicki et al. Testing Matrix as provided by Bao [37,46]

Specimen Description	Average Lode Parameter	Average Triaxiality	Effective Plastic Strain at Failure
#1 Round, Smooth	1.00	0.40	0.46
#2 Round, Large Notch	1.00	0.63	0.28
#3 Round, Small Notch	1.00	0.93	0.17
#4 TPS (Flat Grooved)	0.10	0.61	0.21
#5 Cylinder d/h=0.5	-0.91	-0.28	0.45
#6 Cylinder d/h=0.8	-0.81	-0.23	0.38
#7 Cylinder d/h=1.0	-0.82	-0.23	0.36
#8 Cylinder d/h=1.5	-0.80	-0.22	0.34
#9 Round, Notched Compression	-0.84	-0.25	0.62
#10 Flat Dog Bone Tension (Shear)	0.06	0.01	0.21
#11 Flat Dog Bone Tension (Shear/Tension mix)	0.50	0.12	0.26
#12 Plate with Circular Hole	1.00	0.34	0.31
#13 Simple Dog Bone Tension	0.98	0.36	0.48
#14 Pipe	0.98	0.36	0.33
#15 Solid Rectangular Bar	1.00	0.37	0.36

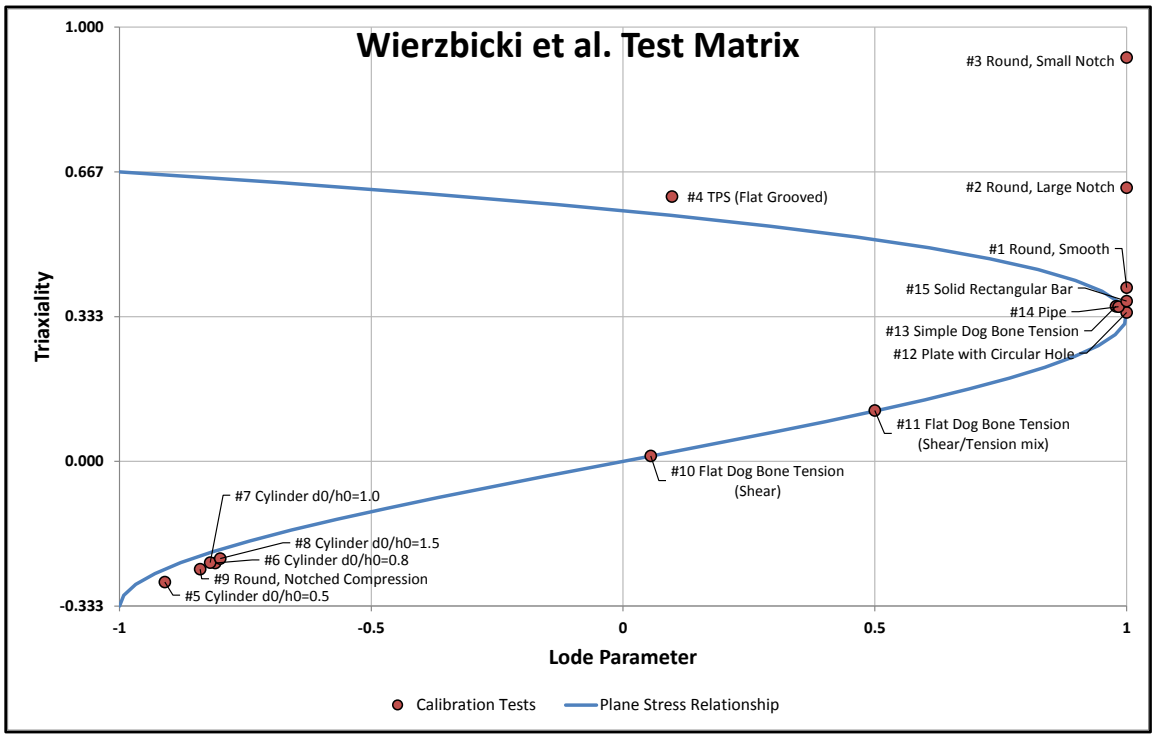

Figure 17. Wierzbicki et al. Graphical Test Matrix

Table 4. Bai et al. Testing Matrix [39]

Specimen Description	Idealized Lode Parameter	Idealized Triaxiality	Average Lode Parameter	Average Triaxiality	Effective Plastic Strain at Failure
TPS (t/R=0.1260)	0.00	0.61	0.00	0.67	0.14
TPS (t/R=0.4030)	0.00	0.68	0.00	0.78	0.10
TPS (t/R=1.006)	0.00	0.84	0.00	1.02	0.07
Round Smooth	1.00	0.33	1.00	0.50	0.43
Round Notched	1.00	0.55	1.00	0.81	0.26
Pure Torsion Shear	0.00	0.00	0.00	0.00	0.48

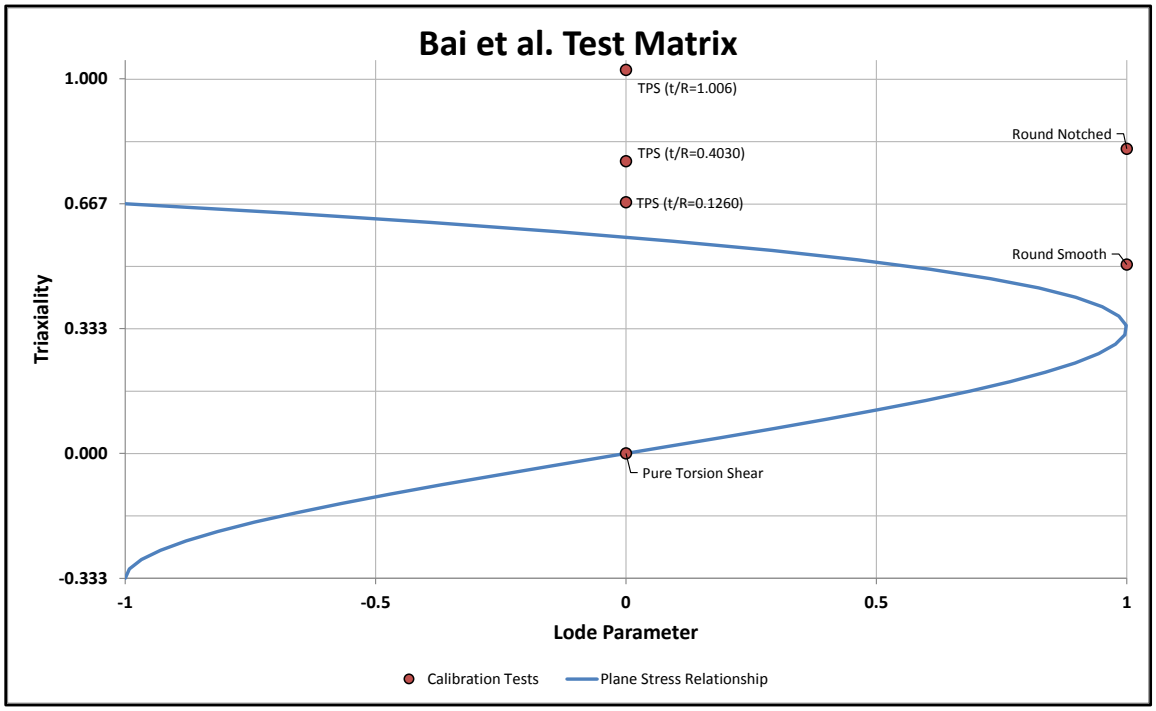

Figure 18. Bai et al. Graphical Test Matrix

Table 5. Buyuk Testing Matrix [38,43]

Specimen Description	Idealized Lode Parameter	Idealized Triaxiality	Average Lode Parameter	Average Triaxiality	Effective Plastic Strain at Failure
Flat Specimen #1 Standard Dog Bone	1.00	0.33	1.00	0.34	0.25
Flat Specimen #2 Large Notch	0.91	0.41	0.89	0.43	0.25
Flat Specimen #3 Small Notch	0.62	0.49	0.65	0.50	0.21
Flat Specimen # 4 Sharp Notch	0.00	0.58	-0.02	0.58	0.10
Round Specimen #5 Un-notched	1.00	0.33	1.00	0.35	0.32
Round Specimen #6 Notched	1.00	0.41	1.00	0.53	0.31
Round Specimen #7 Notched	1.00	0.49	1.00	0.61	0.29
Round Specimen #8 Notched	1.00	0.58	1.00	0.68	0.27
Round Specimen #9 Notched	1.00	0.67	1.00	0.76	0.25
Round Specimen #10 Notched	1.00	0.80	1.00	0.86	0.20
Thick Specimen #11 Thick Dog Bone	0.00	0.58	0.15	0.56	0.20
Thick Specimen #12 Large Round Notched	0.00	0.67	0.21	0.61	0.19
Thick Specimen #13 Small Round Notched	0.00	0.80	0.10	0.73	0.21
Cylinder Specimen #14	-1.00	-0.33	-1.00	-0.33	1.00
Torsion/Shear Specimen #15	0.00	0.00	0.04	0.00	0.18
Mixed Loading Specimen #16 (Axial/Shear Stress =1.973)	0.92	0.25	0.95	0.28	0.18
Mixed Loading Specimen #17 (Axial/Shear Stress =0.848)	0.62	0.15	0.73	0.18	0.20
Punch Specimen #18	-1.00	0.58	-0.99	0.59	0.32
Punch Specimen #19	-1.00	0.67	-0.99	0.67	0.33
Punch Specimen #20	0.00	0.00	-0.01	0.01	0.20

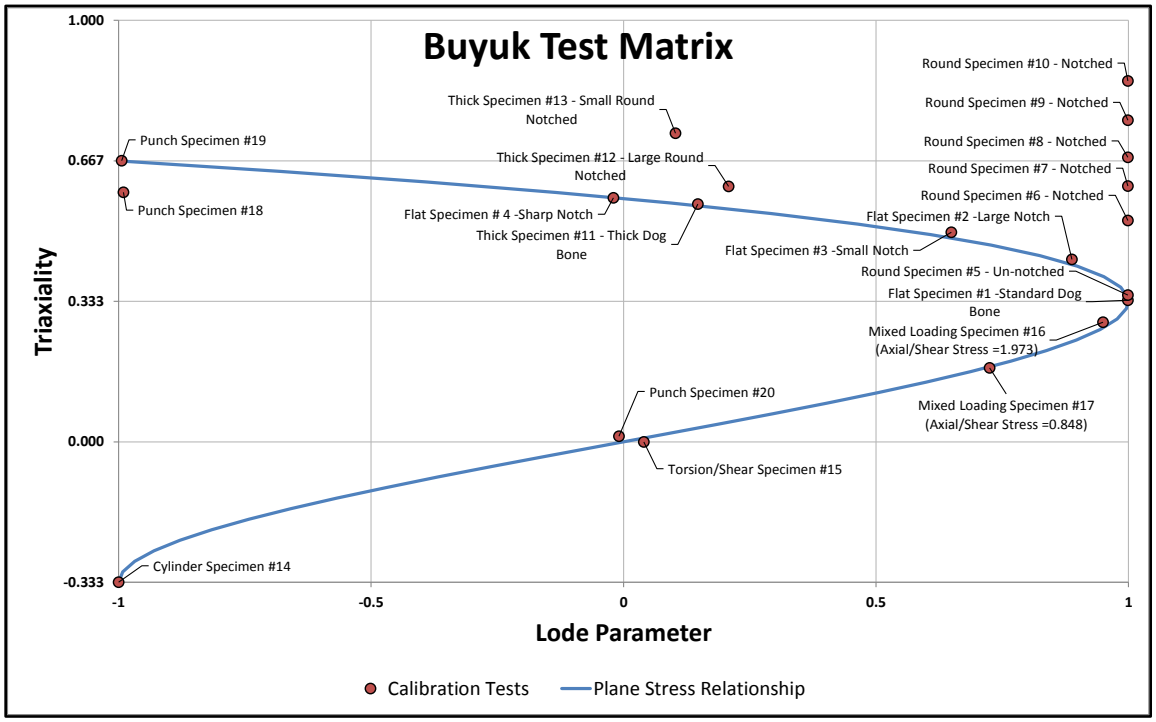

Figure 19. Buyuk Graphical Test Matrix

4.3.1 Xue-Wierzbicki Failure Surface Method Analysis

The Xue-Wierzbicki failure surface method offers a simple Lode-axis symmetric four coefficient model that can ideally be calibrated with four carefully-selected specimens. A surface fit was obtained when the Wierzbicki et al. data set was used for calibration, as seen in Figure 20. Note that the data points utilized the averaged triaxiality and Lode parameter to construct the surface fit utilizing Equation 4.17. It is clear from the two-dimensional plot of triaxiality vs. effective plastic strain at failure, found in Figure 20(a) that the surface provided a biased estimation of the failure surface for specimens along the plane stress curve. However, it is clear that as triaxiality increased, the overall trend of the effective plastic strain at failure decreased. This property was captured well with the Xue-Wierzbicki failure surface.

It should be noted that a number of the test's data points had a large residual from the fitted Xue-Wierzbicki failure surface, as seen by the Residual Plot in Figure 20(d). The largest of the residuals are focused along the $\xi = -1$ and $\xi = 1$ axes due to the failure surface being unable to capture the highly-variable data in these regions. These residuals resulted in a high residual sum of squares (SSE) of 0.111. Furthermore, the Xue-Wierzbicki failure surface produced a relatively low R-squared equal to 44.1 percent. The relatively high bias produced with this data set can be attributed to the low variation allowed by the Xue-Wierzbicki failure surface equation. A three-dimensional view and a contour plot of the fitted surface can also be found in Figure 20(b) and (c).

A similar surface fitting performed on the Buyuk data set also produced similar results, as seen in Figure 21. Similar to the Wierzbicki et al. data set, it is clear from the two-dimensional plot of triaxiality vs. effective plastic strain at failure, found in Figure

21(a), that the surface provided a slightly-biased estimation of the failure surface for specimens along the plane stress curve. Furthermore, unlike the Wierzbicki et al. data set, the trend for plane strain curve actually exhibited an increasing effective plastic strain at failure as triaxiality increased. Lastly, similar to the Wierzbicki et al. data set, the majority of the data points with larger residuals are grouped along the $\xi = -1$ and $\xi = 1$ axes. However, the more uniform data resulted in a lower SSE of 0.036 and a much higher R-squared value of 94.1 percent. A three-dimensional view and a contour plot of the fitted surface can also be found in Figure 21(b) and (c).

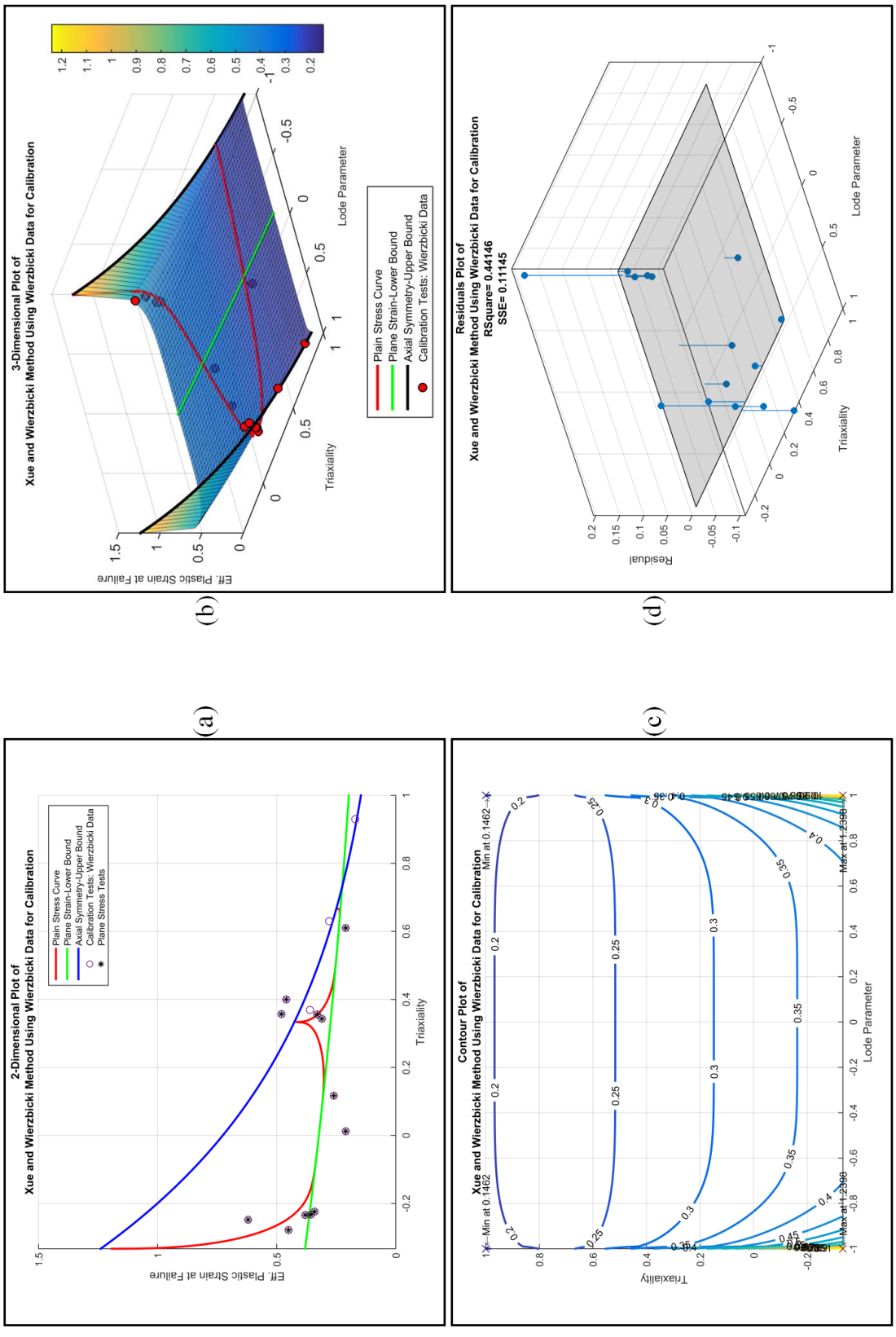

Figure 20. Xue-Wierzbicki Failure Surface Method Using Wierzbicki et al. Data for Calibration

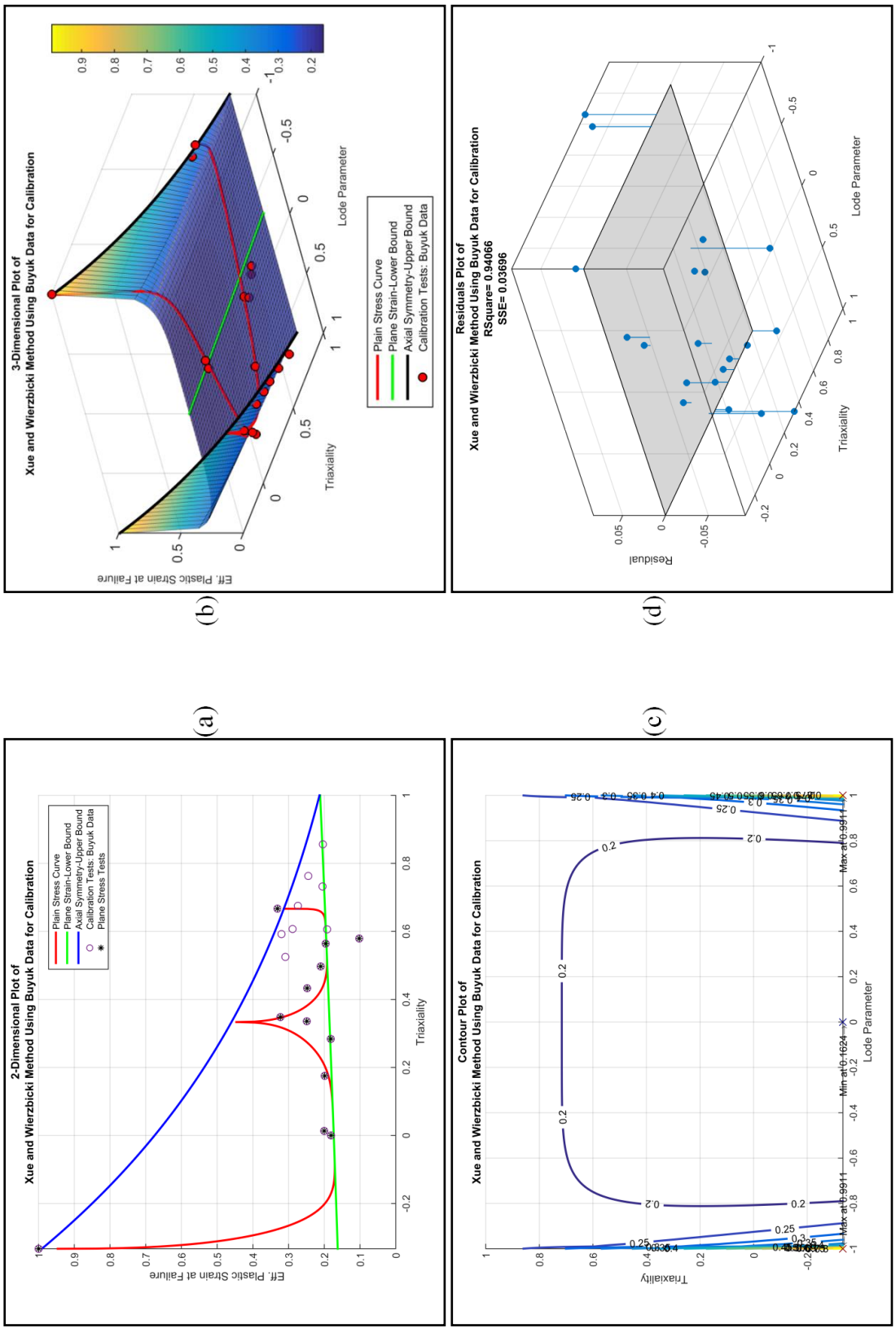

Figure 21. Xue-Wierzbicki Failure Surface Method Using Buyuk Data for Calibration

4.3.2 Bai Failure Surface Method Analysis (Symmetric Approach)

The Bai failure surface method with the symmetric approach offers a similar method to the Xue-Wierzbicki method that is Lode-axis-symmetric, and a four coefficient model that can ideally be calibrated with four carefully-selected specimens. As such, Bai calibrated his model with five tests and used a sixth test to check the fit. A similar approach, in which all six tests were used for calibration, can be seen in Figure 22. As seen by the two-dimensional and three-dimensional plots found in Figure 22(a) and (b), the six data points aligned with the Bai (Symmetrical) failure surface. This outcome resulted in a nearly perfect fit with the SSE equal to nearly zero and the R-squared value of nearly 100 percent, as seen by the residual plot found in Figure 22(d). However, due to the limited data set, limited conclusions can be made about the accuracy of the Bai failure surface with the symmetrical approach.

When the more comprehensive data set given by Buyuk was used to calibrate the failure surface method, more conclusions could be made about the failure surface method. As seen in the two-dimensional and three-dimensional plots given in Figure 23(a) and (b), the method produced heavily-biased results. The model was unable to capture the region of high variation around the intersection of the plane stress curve and the $\xi = 1$ axis. Furthermore, the model produced a fairly substantial bias along the $\xi = 1$ and $\xi = -1$ axes due to the symmetrical nature of the defining equation. These residuals resulted in a fairly large SSE of 0.100 and an R-squared value of 83.9 percent, as seen in the residual plot found in Figure 23(d). Lastly, the model provided a questionably accurate estimation of the failure surface for specimens along the plane strain curve as the effective plastic strain at failure increased as triaxiality increased.

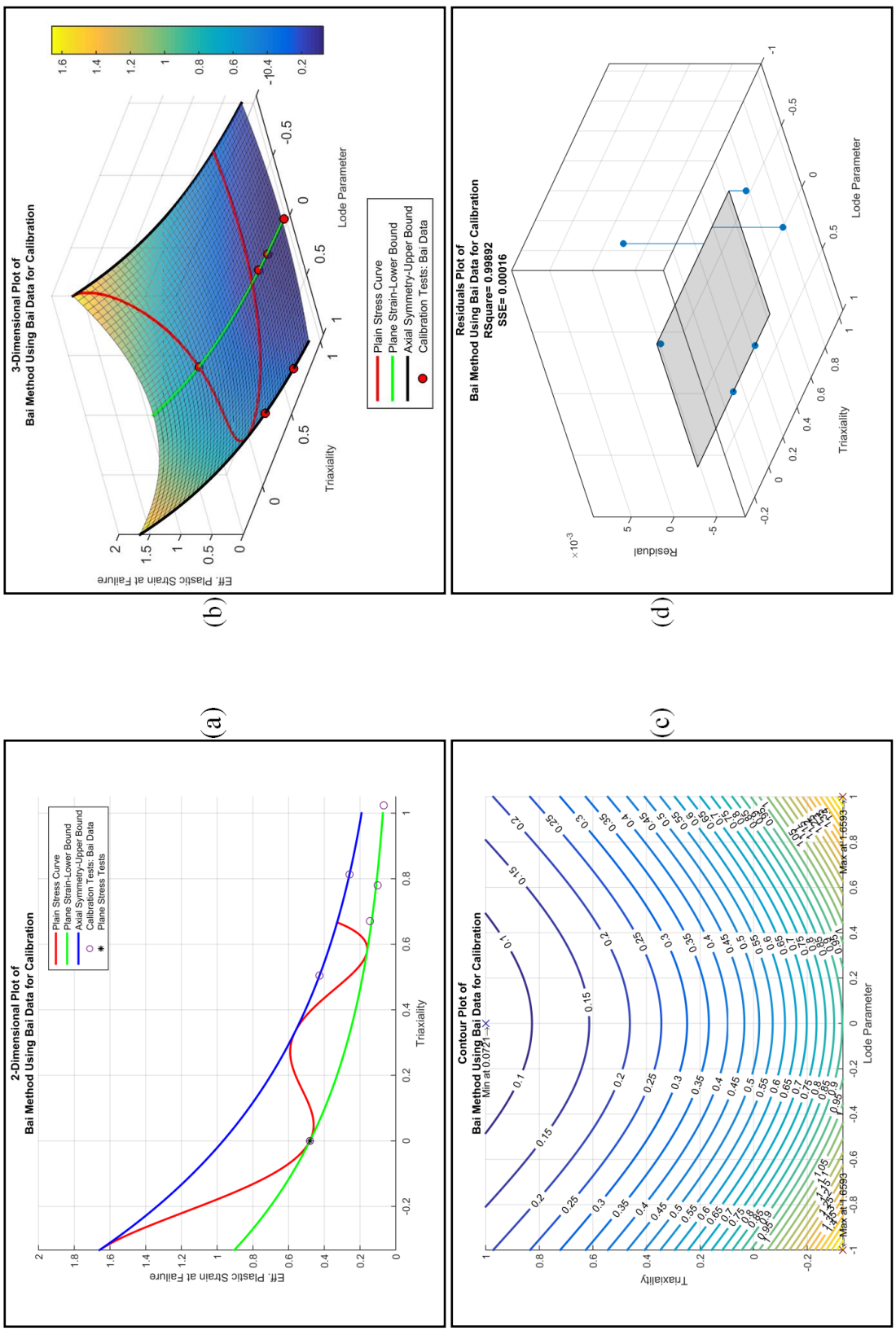

Figure 22. Bai (Symmetrical) Failure Surface Method Using Bai et al. Data for Calibration

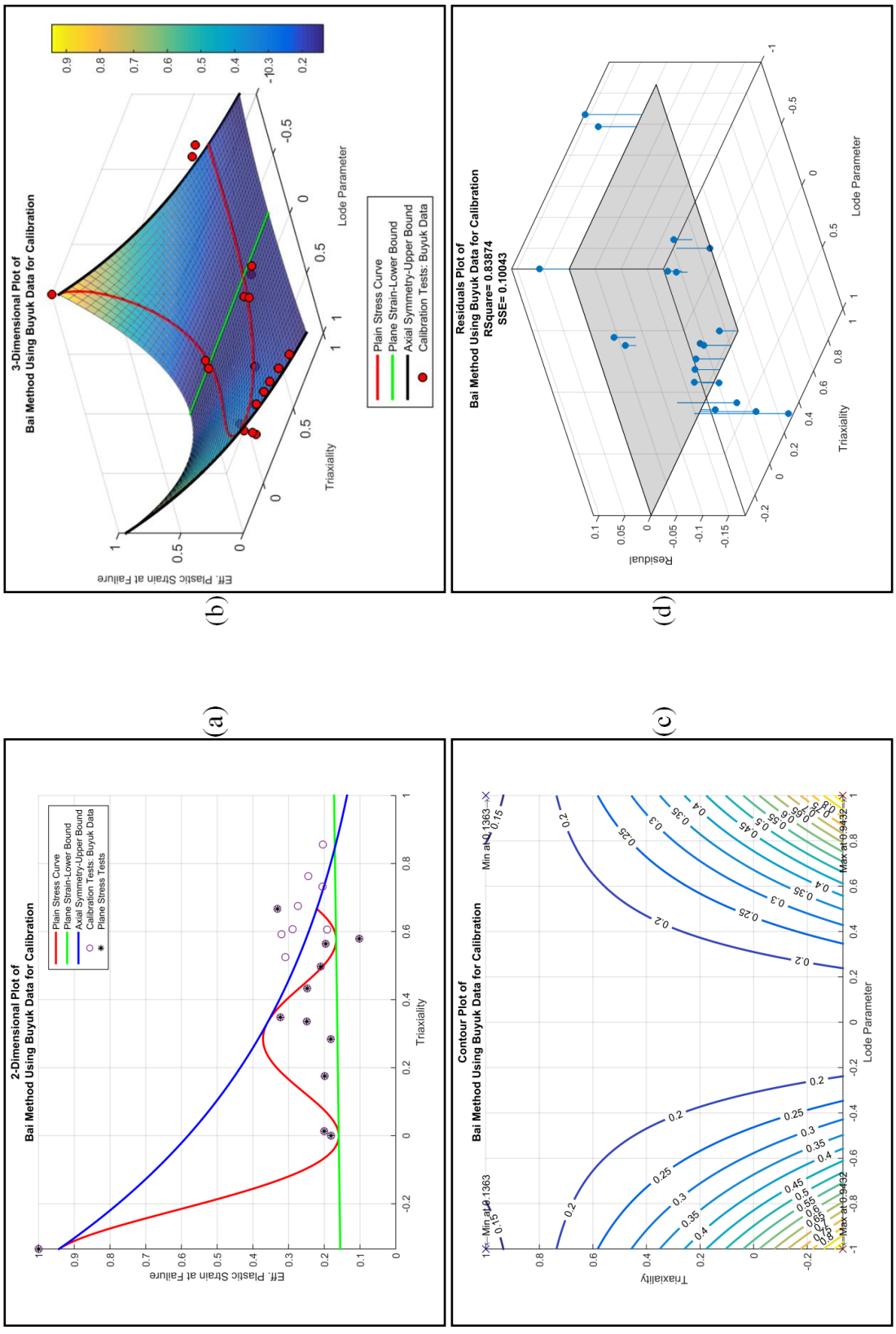

Figure 23. Bai (Symmetrical) Failure Surface Method Using Buyuk Data for Calibration

4.3.3 Bai Failure Surface Method Analysis (Asymmetric Approach)

The Bai failure surface method with the asymmetric approach is meant to offer a more flexible failure surface than the simplified symmetric approach. As such, a minimum of six tests are needed to calibrate the surface. The calibration of the Bai failure surface method using the Bai et al. data set can be seen in Figure 24. As seen by the two-dimensional and three-dimensional plots found in Figure 24(a) and (b), the six data points aligned with the Bai (Asymmetric) failure surface. This outcome resulted in a nearly perfect fit with the SSE equal to nearly zero and the R-squared value of nearly 100 percent, as seen in the residual plot found in Figure 24(d). However, due to the limited data set, limited conclusions can be made about the accuracy of the Bai failure surface with the asymmetrical approach. Also, it should be noted that because data was lacking where $\xi < 0$, the surface in the positive Lode parameter region can only be taken as an extrapolation and may differ greatly from the true values if tests were performed in that region.

The more comprehensive Buyuk data set offered much greater insight into the performance of the Bai (Asymmetric) failure surface method. As seen in the two-dimensional and three-dimensional plots in Figure 25(a) and (b), the Bai (Asymmetric) surface failure method performed fairly-reasonable at predicting the plane stress curve, but the method resulted in a slightly biased fit. As similarly seen in the symmetrical approach, the model exhibited difficulty with the highly-variable data in the region around the intersection of the plane stress curve and the $\xi = 1$ axis. However, due to the asymmetric properties of the surface failure method, the $\xi = 1$ and $\xi = -1$ axes were much better estimators of the data along the curves when compared to the symmetrical

approach. These residuals resulted in a smaller SSE of 0.023 and an R-squared value of 96.3 percent, as seen in the residual plot found in Figure 25(d).

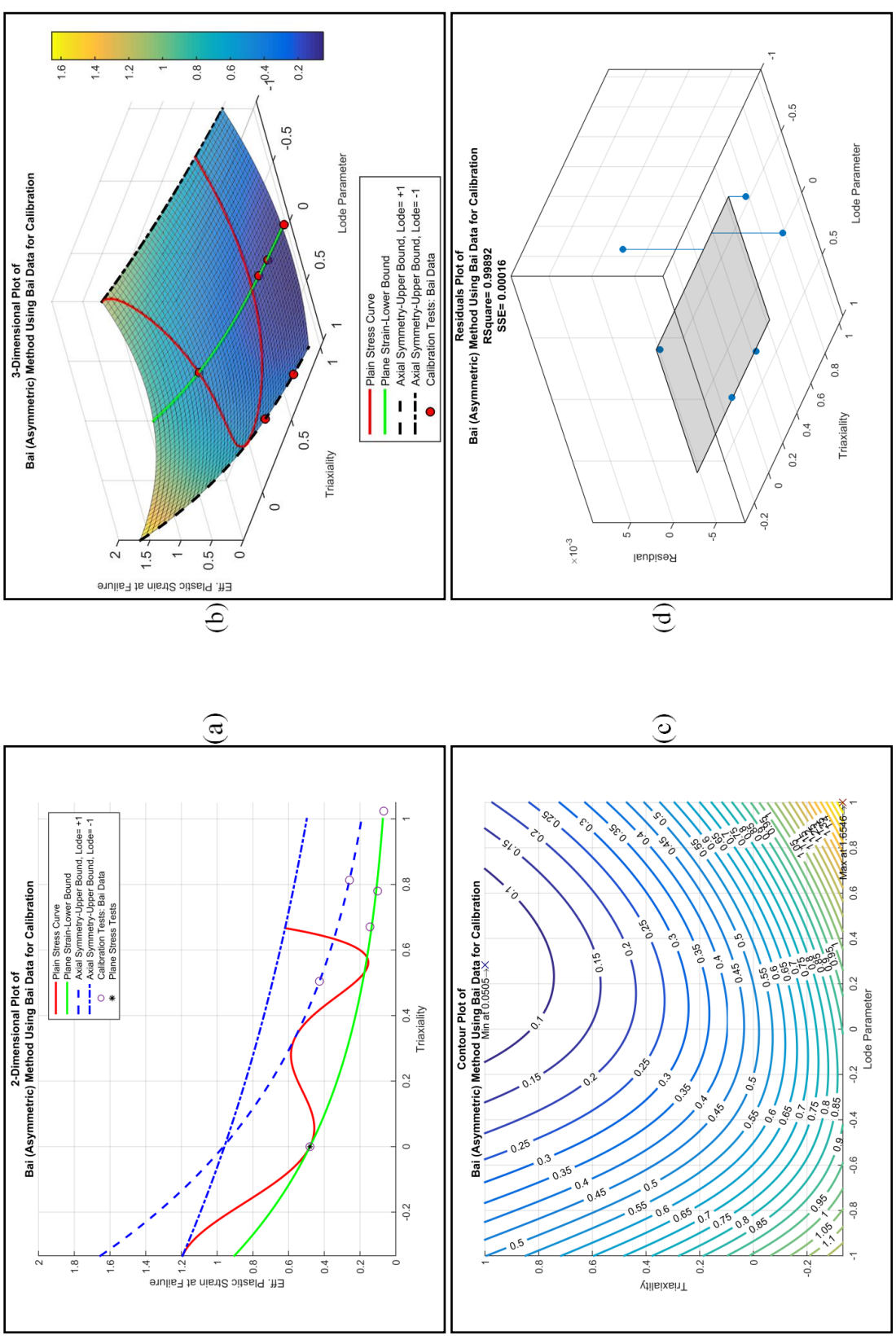

Figure 24. Bai (Asymmetrical) Failure Surface Method Using Bai et al. Data for Calibration

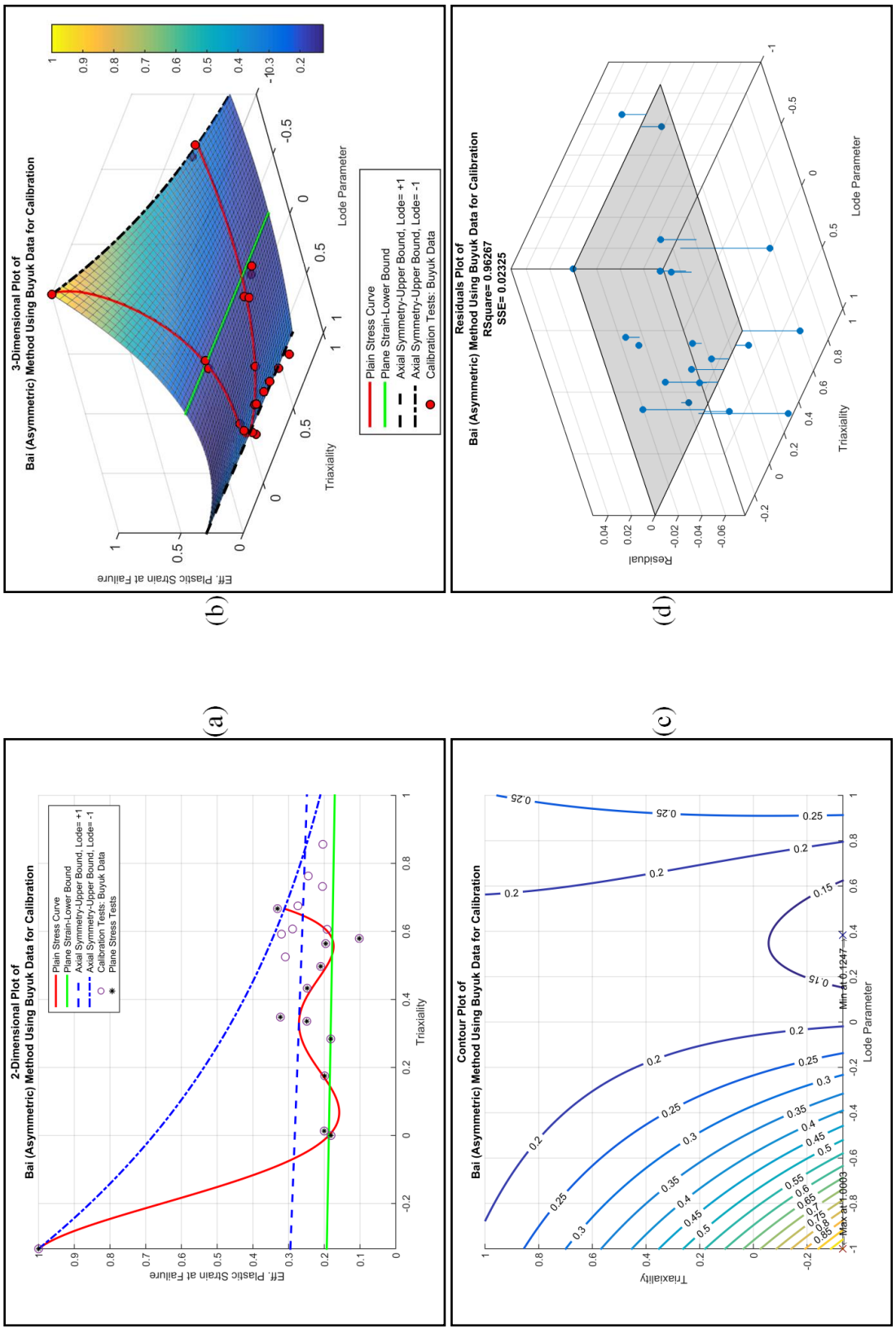

Figure 25. Bai (Asymmetrical) Failure Surface Method Using Buyuk Data for Calibration

4.3.4 Buyuk Failure Surface Method Analysis

The Buyuk failure surface method is meant to be flexible enough to fit a highly-variable data set, while also limiting both high variance and over-fitting by utilizing cubic splines. As previously explained, Buyuk's method was unable to be reproduced. As such, the failure surface provided by Buyuk is shown in Figure 26 [70]. It should be noted that Buyuk used the idealized values of triaxiality and the Lode parameter, as opposed to the averaged values used in the previous analyses. This selection may have slightly changed the resulting failure surface, specifically around the stress states represented by the thick specimen geometries where the difference between the average Lode parameter and the idealized Lode parameter was the largest. The largest variation between idealized and averaged Lode parameter was exhibited in the Thick Specimen No. 12 – Large Round Notch with a difference of 0.21, as seen in Table 5. Note that Buyuk used the opposite sign convention for positive hydrostatic pressure. As a result, the sign convention for the triaxiality values was opposite of what was used in this report. This convention choice would have no effect on the performance of the failure surface, but one should be aware of this discrepancy.

Some of Buyuk's test specimens shared idealized stress states with other test specimens, such as the Flat Specimen No. 4 – Sharp Notch with the Thick Specimen No. 11 – Thick Dog Bone and the Torsion/Shear Specimen No. 15 with the Punch Specimen No. 20, as seen in Table 5. As this provided two data points at the same stress state, it is necessary to either eliminate one of the data points or average out the effective plastic strain at failure values for the matching pairs. Interestingly, it appears that Buyuk selectively eliminated one of the data points. As seen in Figure 26, the Flat Specimen No.

4 – Sharp Notch with a very low effective plastic strain at failure of 0.102, compared to the Thick Specimen No. 11 – Thick Dog Bone with a substantially higher effective plastic strain at failure of 0.196, was not included in the failure surface calculation. The reasoning for picking one test specimen's results over the other was not immediately clear.

The failure surface, as seen in Figure 26, reasonably modeled the $\xi = 1$ axis and the plane stress curve. However, the $\xi = -1$ and plane strain curves exhibited an uncharacteristic dip in the effective plastic strain at failure that has not been witnessed in testing or theorized mechanically. This dip in the surface is a sign of overfitting the data from either poorly chosen knots for the B-spline fitting method, too high of an order spline, or lack of sufficient data points. A summary of the existing failure surface method analyses as well as conclusions based on comparisons of the results presented herein are given in Section 4.6.

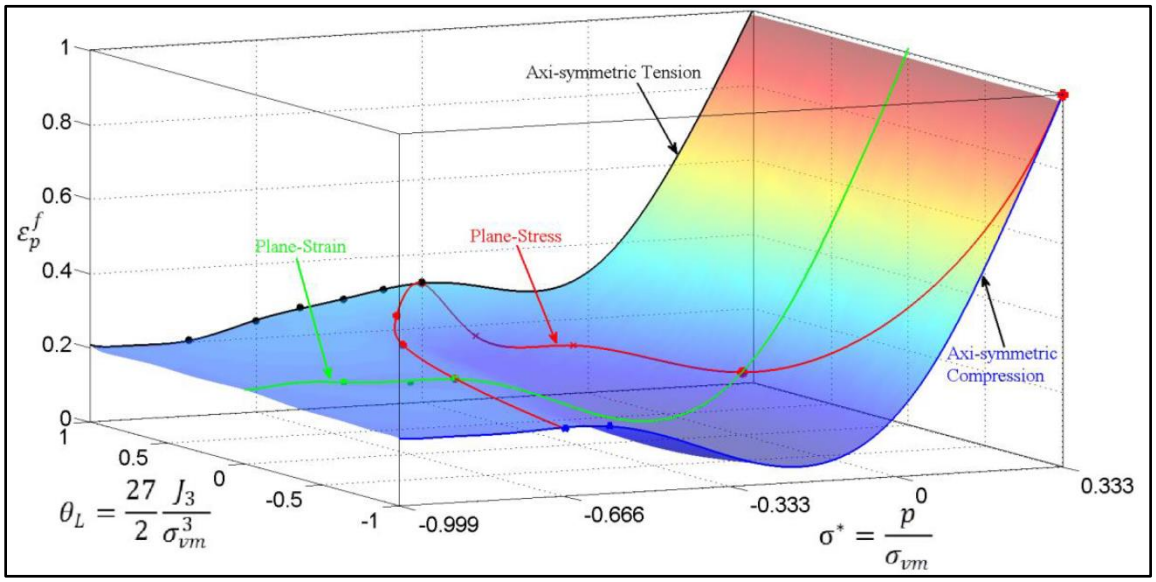

Figure 26. Buyuk Method Using Buyuk Data for Calibration [70]

4.4 Subset Data Sets Analysis

Two reduced-size data sets were used to create stress-state dependent failure surfaces to determine the importance of a large data set compared to a small, or reduced, data set. The first analysis consisted of a data set from Wierzbicki et al. as recommended by Xue[72], as seen in Table 6 and Figure 27. The aim of this analysis was to determine if a small minimalistic data set (i.e., fewer specimen geometries) could be utilized to calibrate the failure surface while still producing similar results as the failure surface calibrated with the full data set. The second analysis was conducted to determine if a failure surface calibrated with a test matrix comprised of only flat specimens that could be fabricated from thin steel, such as that from a guardrail, can accurately predict the failure surface calibrated with the full data set. The data points were taken from the Buyuk data set, shown in Table 7 and Figure 28. The following subsections summarize these findings by comparing the two reduced data sets with their respective full data set.

Table 6. Wierzbicki et al. Reduced Data Set [37,46]

Specimen Description	Average Lode Parameter	Average Triaxiality	Effective Plastic Strain at Failure
#1 Round, Smooth	1.00	0.40	0.46
#3 Round, Small Notch	1.00	0.93	0.17
#4 TPS (Flat Grooved)	0.10	0.61	0.21
#7 Cylinder d0/h0=1.0	-0.82	-0.23	0.36

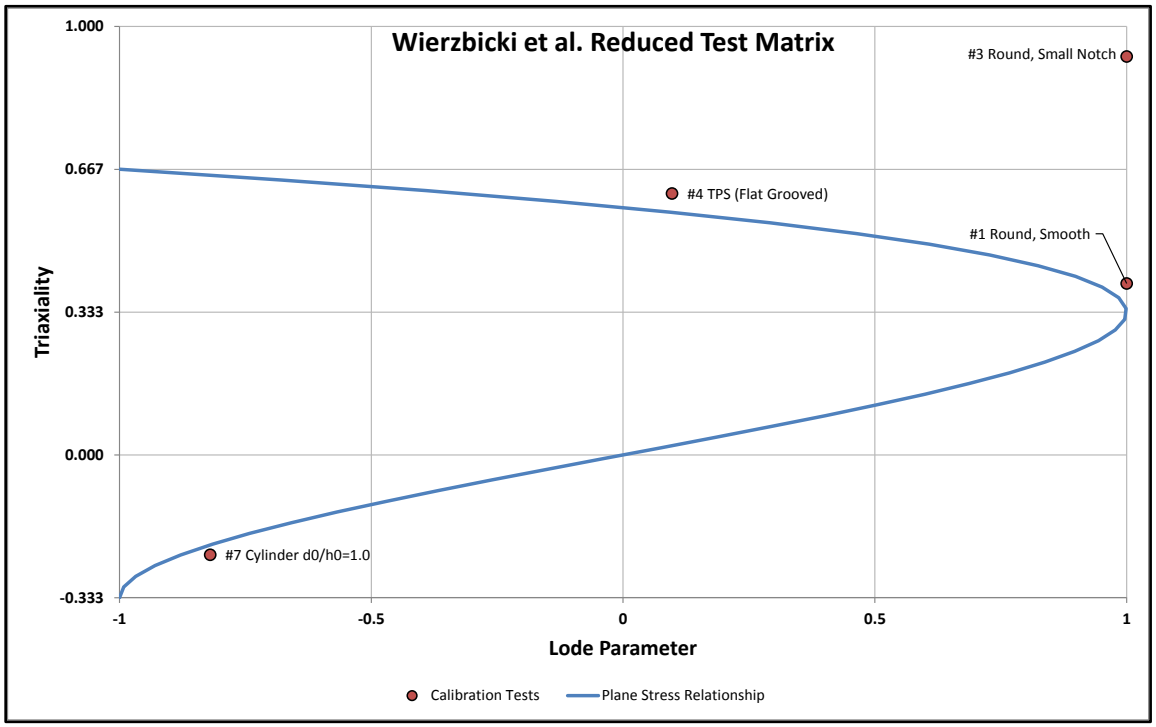

Figure 27. Wierzbicki et al. Graphical Reduced Test Matrix

Table 7. Buyuk Flat Specimen Data Set [38,43]

Specimen Description	Idealized Lode Parameter	Idealized Triaxiality	Average Lode Parameter	Average Triaxiality	Effective Plastic Strain at Failure
Flat Specimen #1 -Standard Dog Bone	1.00	0.33	1.00	0.34	0.25
Flat Specimen #2 -Large Notch	0.91	0.41	0.89	0.43	0.25
Flat Specimen #3 -Small Notch	0.62	0.49	0.65	0.50	0.21
Flat Specimen # 4 -Sharp Notch	0.00	0.58	-0.02	0.58	0.10
Punch Specimen #18	-1.00	0.58	-0.99	0.59	0.32
Punch Specimen #19	-1.00	0.67	-0.99	0.67	0.33
Punch Specimen #20	0.00	0.00	-0.01	0.01	0.20

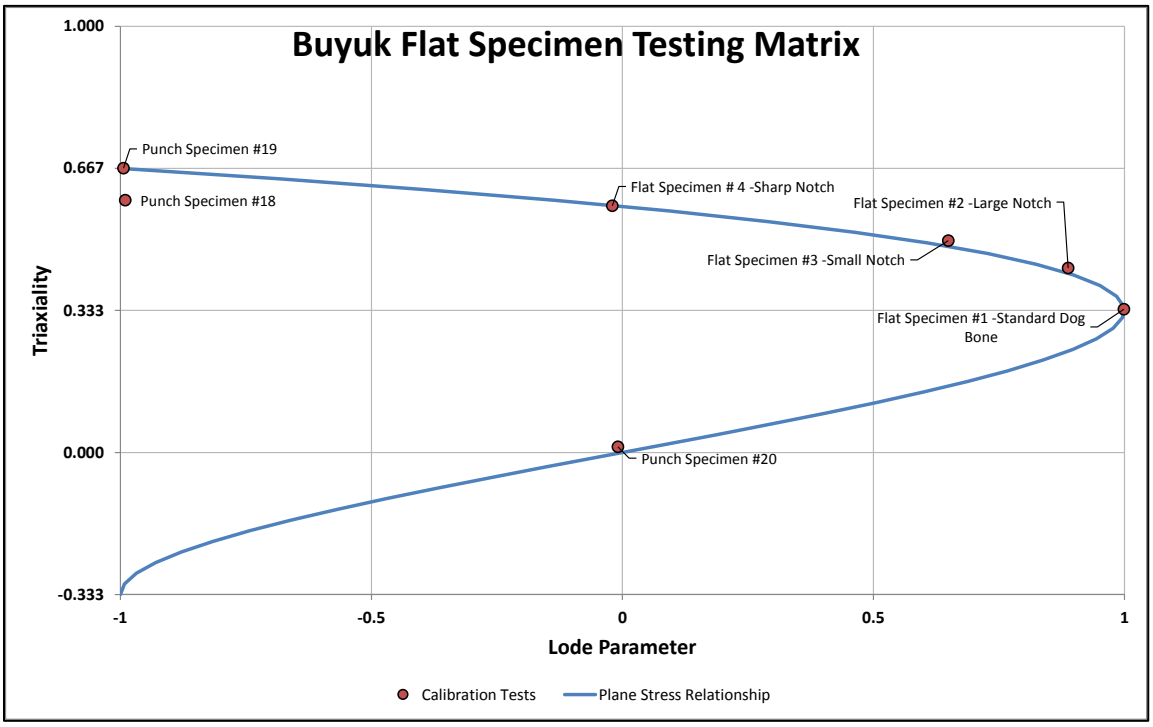

Figure 28. Buyuk Graphical Flat Specimen Test Matrix

4.4.1 Reduced Data Set Analysis from Wierzbicki et al. Data Set as Recommended by Xue

A reduced data set was utilized to calibrate the failure surface methods to analyze the performance of the failure surfaces calibrated with reduced data sets, particularly in comparison to the respective failure surfaces calibrated with full data set.

4.4.1.1 Xue-Wierzbicki Failure Surface Method

A comparison of the failure surfaces calibrated with the reduced and the full Wierzbicki et al. data set using the Xue-Wierzbicki failure surface method can be seen in Figure 29. Figure 29(a) and (b) depict the failure surface calibrated with the full data set, while Figure 29(c) and (d) depict the failure surface calibrated with the reduced-data set. Both two-dimensional and three-dimensional plots are included. The plane stress curve was roughly similar for the two data sets. Furthermore, both the plane strain and the $\xi = 1$ and $\xi = -1$ curves of the reduced-data set followed the same general trends as the full data set failure surface. However, the $\xi = 1$ and $\xi = -1$ curves of the reduced-data set overestimated the effective plastic strain at failure through the majority of the stress states. The most substantial variation was seen when $\eta = -{}^{1}/_{3}$ where the peak effective plastic strain at failure was approximately 0.6 greater in the reduced-data set compared to the full-data set.

4.4.1.2 Bai (Symmetric) Failure Surface Method

The same reduced Wierzbicki et al. data set was used to calibrate a failure surface using the Bai Symmetric failure surface mothed. This produced vastly different results as compared to failure surface calibrated with the full-data set, as seen in the comparison in Figure 30. Figure 30(a) and (b) depict the failure surface calibrated with the full-data set, while Figure 30(c) and (d) depict the failure surface calibrated with the reduced-data set. Both two-dimensional and three-dimensional plots are included. The failure surface calibrated with the reduced-data set failed to predict the full data set failure surface along the plane strain curve. This was likely caused by providing only one data point along the $\xi = 0$ axis. As a result, where the plane stress curve intersects the plane strain curve at

$\eta = \xi = 0$, the reduced-data set failure surface failed to predict similar values to the full-data set failure surface. However, the plane stress and the $\xi = 1$ and $\xi = -1$ curves followed the same general trends as the full data set failure surface such that, the values of the effective plastic strain at failure along the $\xi = 1$ and $\xi = -1$ curves matched fairly well.

It should be noted that calibration using the reduced-data set with the Bai Asymmetrical approach was not possible as the method requires at least six unique data points to calibrate the six-coefficient asymmetric surface and only four data points were available.

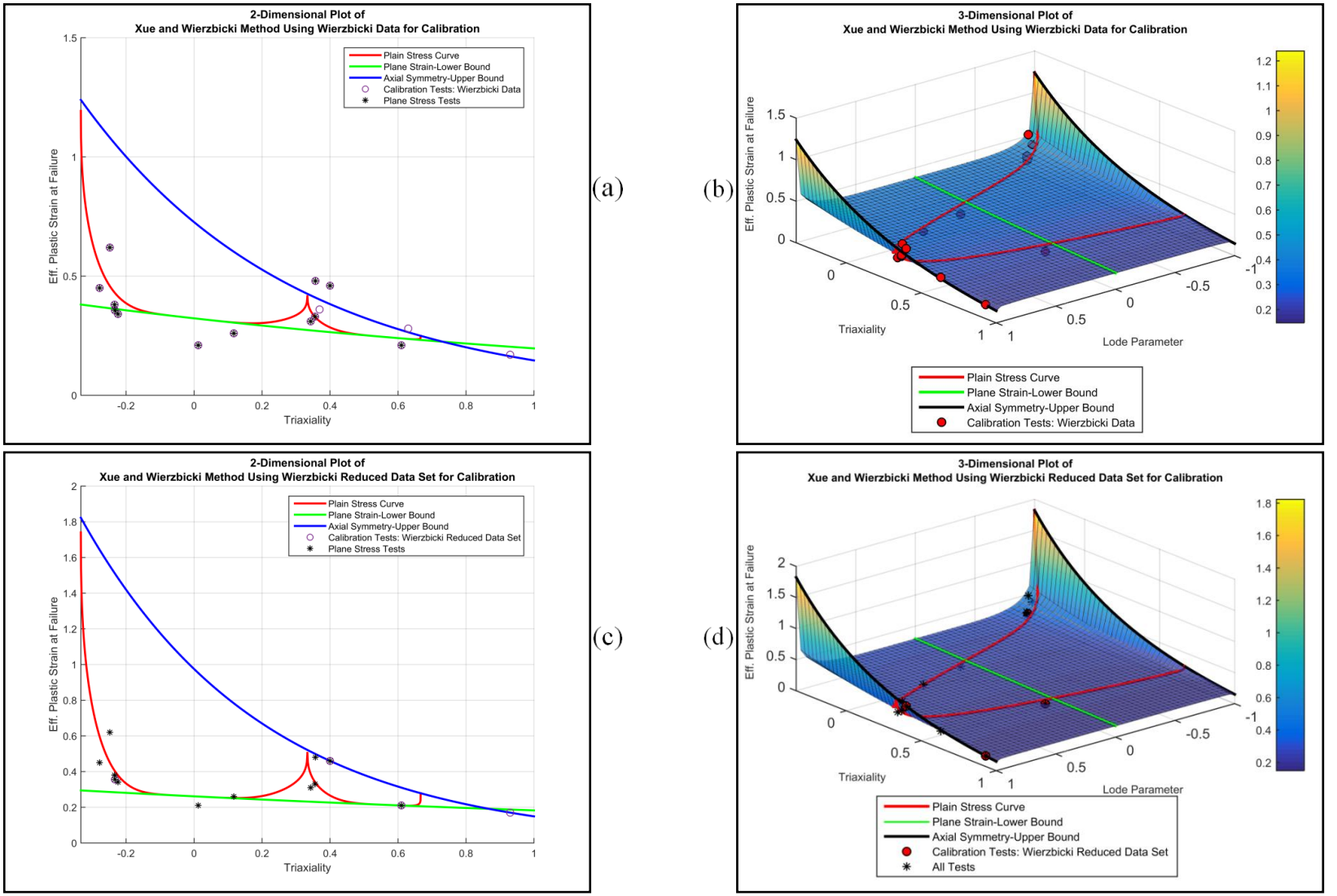

Figure 29. Comparison of Wierzbicki et al. Full (Top) and Reduced (Bottom) Data Set with the Xue-Wierzbicki Failure Surface

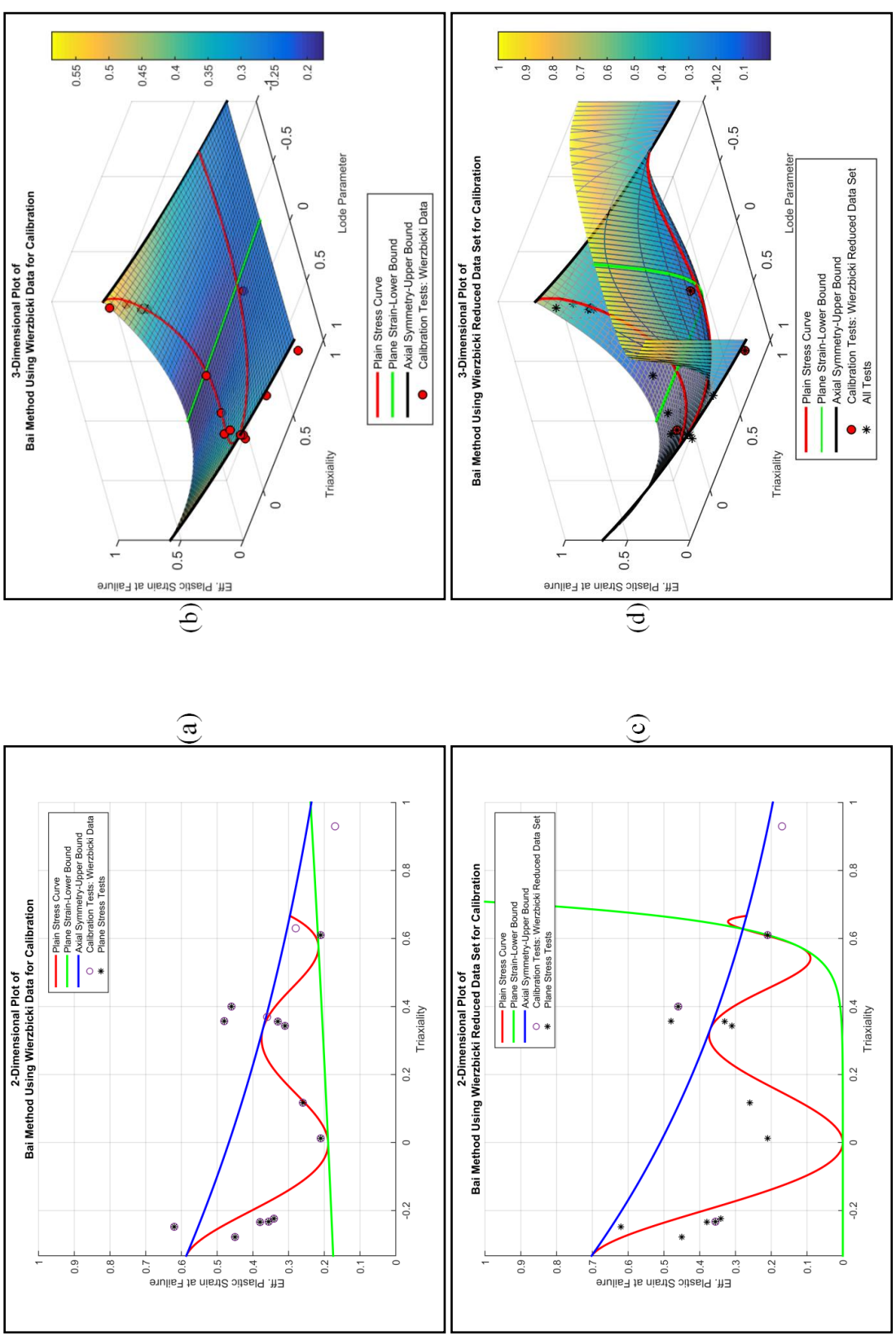

Figure 30. Comparison of Wierzbicki et al. Full (Top) and Reduced (Bottom) Data Set with the Bai Symmetrical Failure Surface

4.4.2 Flat Specimen Reduced Data Set from Buyuk Data Set

A data set comprising of only flat specimens was utilized to calibrate the failure surface methods to analyze the performance of the failure surfaces calibrated with reduced data sets, particularly in comparison to the respective failure surfaces calibrated with full data set.

4.4.2.1 Xue-Wierzbicki Failure Surface Method

A comparison of failure surfaces calibrated with the flat specimen data set and the full Buyuk data set using the Xue-Wierzbicki failure surface method was conducted. The results can be found in Figure 31. Figure 31(a) and (b) depict the failure surface calibrated with the full data set, while Figure 31(c) and (d) depict the failure surface calibrated with the flat specimen-data set. Both two-dimensional and three-dimensional plots are included.

The two failure surfaces along the plane stress curve followed roughly similar trends when the triaxiality is greater than zero. However, with the lack of any compression specimens, the flat specimen data set failure surface is an inaccurate extrapolation in the negative triaxiality region. As a result, the failure surface calibrated with the flat specimen data set was unable to accurately replicate the full data set failure surface in the negative triaxiality range. Furthermore, the flat specimen failure surface along both the plane strain and the $\xi = 1$ and $\xi = -1$ axes are both inversely related to the full data set failure surface. Interestingly, the failure surface along the plane strain curve decreased as the triaxiality increased, in agreement to previous research efforts as opposed to the failure surface calibrated with the full Buyuk data set [21]. Similar to the region along the plane stress curve, the lack of any compression specimen data resulted in

a failure surface with a lower effective plastic strain at failure in the negative triaxiality region when compared to the same region of the full-data set failure surface. Due to the limitation inherent in the defining equation, this trend resulted in a higher effective plastic strain at failure in the positive triaxiality range than what was witnessed in the full data set failure surface.

4.4.2.2 Bai (Symmetric) Failure Surface Method

Using the flat specimen data set to calibrate the surface, similar trends and comparisons found in the failure surface built using the Xue-Wierzbicki failure surface method were seen in the failure surface built using the Bai Symmetric failure surface method. A comparison of the failure surfaces calibrated with the flat specimen and full-data set using the Bai Symmetric failure surface method can be found in Figure 32. Figure 32(a) and (b) depict the failure surface calibrated with the full data set, while Figure 32(c) and (d) depict the failure surface calibrated with the flat specimen-data set. Both two-dimensional and three-dimensional plots are included.

The two failure surfaces along the plane stress curve followed roughly similar trends when the triaxiality was greater than zero. However, as previously seen in the failure surface built with the Xue-Wierzbicki method, due to the lack of any compression specimens, the reduced data set failure surface was unable to accurately replicate the full data set failure surface in the negative triaxiality region. Furthermore, the flat specimen failure surface along both the plane strain and the $\xi = 1$ and $\xi = -1$ axes were both inversely related to the failure surface calibrated with the full-data set. Due to the limitation inherent in the defining equation, this trend resulted in an effective plastic

strain at failure in the positive triaxiality range along the $\xi = 1$ and $\xi = -1$ curves that was higher than what was witnessed in the full data set failure surface.

4.4.2.3 Bai (Asymmetric) Failure Surface Method

Using the flat specimen-data set to calibrate the surface, similar trends and comparisons found in the failure surface built using the previously discussed failure surface methods were seen in the failure surface built using the Bai Asymmetric failure surface method. A comparison of the failure surfaces calibrated with the flat specimen and full-data set using the Bai Asymmetric failure surface method can be found in Figure 33. Figure 33(a) and (b) depict the failure surface calibrated with the full data set, while Figure 33(c) and (d) depict the failure surface calibrated with the flat specimen-data set. Both two-dimensional and three-dimensional plots are included.

Similar to the symmetric approach, the region of the failure surfaces along the plane stress curve was roughly similar for the two data sets when the triaxiality was greater than zero. However, some slight variation is present due to the fewer data points in the flat specimen-data set. Furthermore, as seen previously, the reduced data set failure surface was unable to accurately replicate the full data set failure surface in the negative triaxiality region due to the lack of any compression specimen. This is particularly evident on the failure surface along the plane stress, plane strain, and $\xi = -1$ curves. Interestingly, this did not affect the failure surface along the $\xi = 1$ curve as the constitutive equation allows for the $\xi = 1$ and $\xi = -1$ axes to be independent of each other. As a result, the failure surface along the $\xi = 1$ axis was nearly similar to the full data set failure surface. Lastly, it should be noted that the failure surface calibrated with the flat specimen data set along the plane strain curve underestimated the effective plastic

strain at failure in the positive triaxiality region and overestimated the effective plastic strain at failure in the negative triaxiality region. A summary of the findings from the subset data set analysis as well as conclusions pertaining to the required number of data points to accurately calibrate a reasonable failure surface is given in Section 4.6.

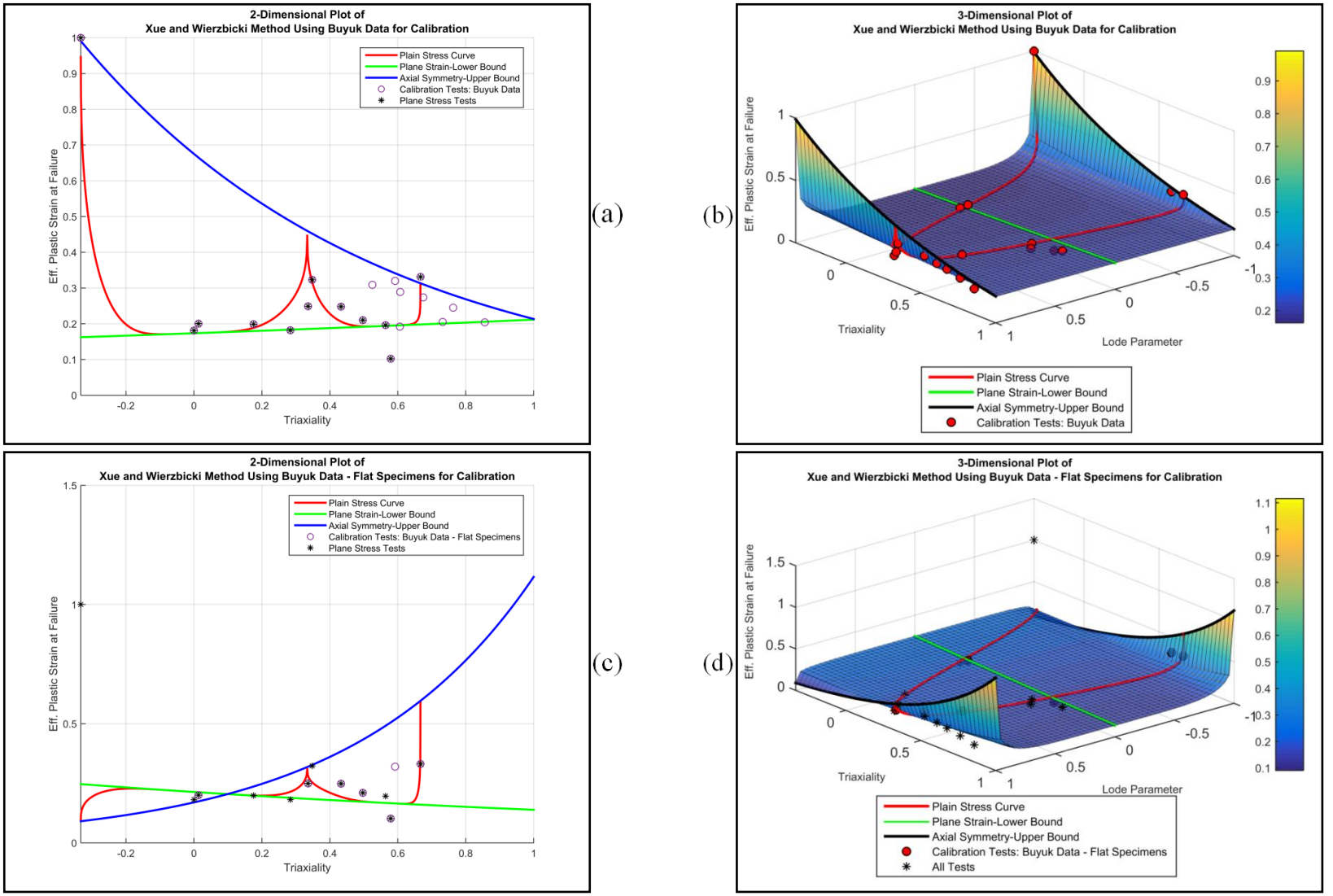

Figure 31. Comparison of Full Buyuk Data (Top) and Flat Specimens (Bottom) with the Xue-Wierzbicki Failure Surface Method

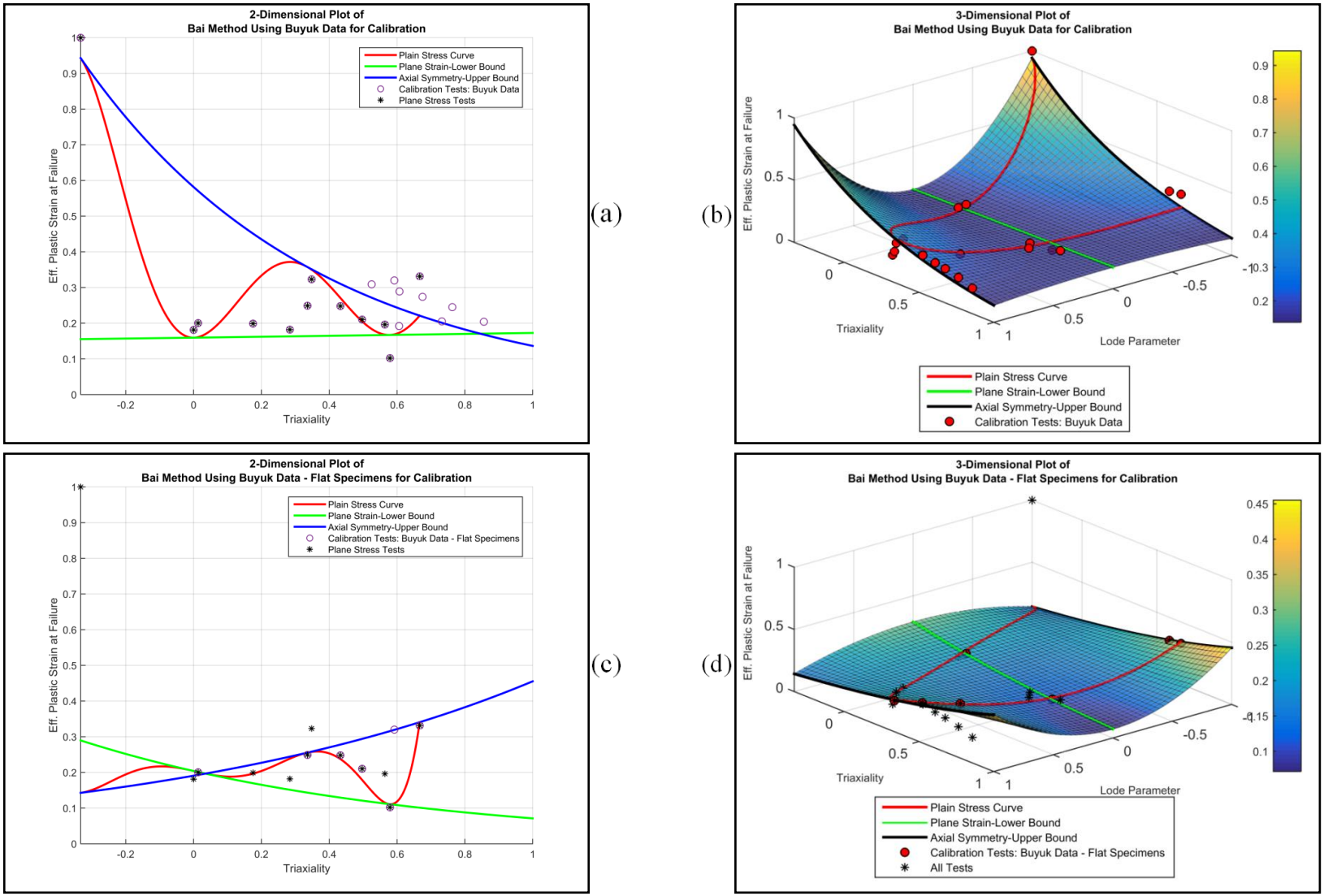

Figure 32. Comparison of Full Buyuk Data (Top) and Flat Specimens (Bottom) with the Bai Symmetric Failure Surface Method

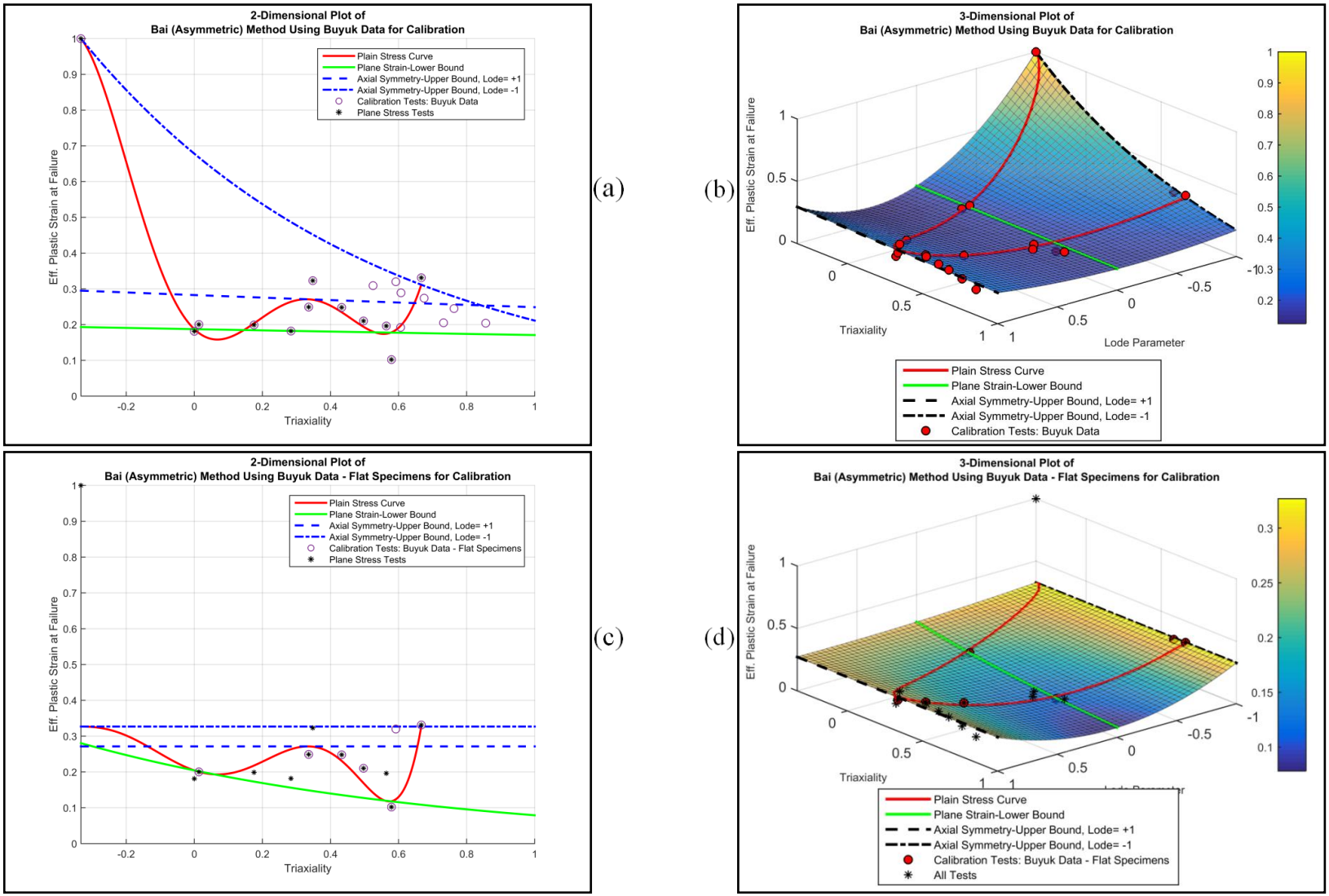

Figure 33. Comparison of Full Buyuk Data (Top) and Flat Specimens (Bottom) with the Bai Asymmetric Failure Surface Method

4.5 Proposed Technique to Define a Failure Surface Using a Smoothed, Thin-Plate Spline

An alternative method to define a surface to predict the effective plastic strain at failure as a function of triaxiality and Lode parameter is to use a Smoothed, Thin-Plate Spline (TPS). A thin plate spline is often referred to the physical analogy involving the bending of a thin sheet of metal. Similar to a piece of sheet metal, the Smoothed, Thin-Plate Spline fit resists bending by imposing a penalty involving the smoothness of the fitted surface. The flexibility of the TPS allows a highly-variable data set to be fit, while the smoothing factor can be adjusted manually until a satisfactory fit is achieved. However, a large testing matrix is required to potentially provide a superior stress-state dependent failure surface.

In this report, the Smoothed, Thin-Plate Spline formulation included in MATLAB's Curve-Fitting Toolbox was utilized [73]. The Smoothed, Thin Plate Spline *f* is the unique minimizer of the weighted sum given in Equation 4.24. The error measure is given by Equation 4.25, and the roughness measure is given by Equation 4.26.

$$pE(f) + (1-p)R(f) \tag{4.24}$$

where

$p = \text{Smoothing Parameter}$
$E(f) = \text{The Error Measure}$
$R(f) = \text{The Roughness Measure}$

and

$$E(f) = \sum_j \left| y(:,j) - f\left(x(:,j)\right)\right|^2 \tag{4.25}$$

where

$x(:,j) = \text{The Given Data Sites}$
$y(:,j) = \text{The Given Data Values}$

and

$$R(f) = \int \left(\left| D_{1,1}^{f} \right|^2 + 2 \left| D_{1,2}^{f} \right|^2 + \left| D_{2,2}^{f} \right|^2 \right) \tag{4.26}$$

where

$D_{i,j}^{f} =$ Second Partial Derivative of f with Respect to its ith and jth Argument

4.5.1 Proposed Surface Analysis

It is believed that the TPS method has the ability to better represent experimental data and give more accurate estimations of effective plastic strain in stress states where experimental data is not available. If the smoothing parameter is set to 1, the spline creates an interpolation where the TPS passes through the given effective plastic strain value at each given data site. However, it is believed that a more satisfactory surface could be produced if a smoothing value less than 1 is used to prevent over fitting of the data.

The full Buyuk data set was chosen to analyze this method, because the spline method requires a large number of data sites to provide a reasonable surface. Two attempts at creating a surface were performed in order to bracket the smoothing parameter's performance. The first attempt utilized a smoothing parameter of 0.700. The resulting surface reduced the risk of over fitting the data at the cost of a higher variance. The second attempt used a smoothing parameter of 0.999 and as a result, the surface was very close to an interpolation. However, evidence of overfitting the data was exhibited. A comparison of these two attempts using the full Buyuk data set to calibrate the surface is shown in Figure 34. Figure 34(a), (c), and (e) depict the three-dimensional, two-dimensional, and contour plots of the Smoothed, Thin-Plate Spline with a smoothing parameter of 0.700. Figure 34(b), (d), and (f) depict the three-dimensional, two dimensional, and contour plots of the Smoothed, Thin-Plate Spline with a smoothing

parameter of 0.999. Unfortunately, at this time, it was impossible to determine which surface would perform better over a range of stress states. While the second attempt will likely provide more accurate effective plastic strain results at the known test sites, the first attempt may possibly provide more reasonable effective plastic strain results at stress states that were not tested. The best performing surface likely utilizes a smoothing parameter value between these two examples.

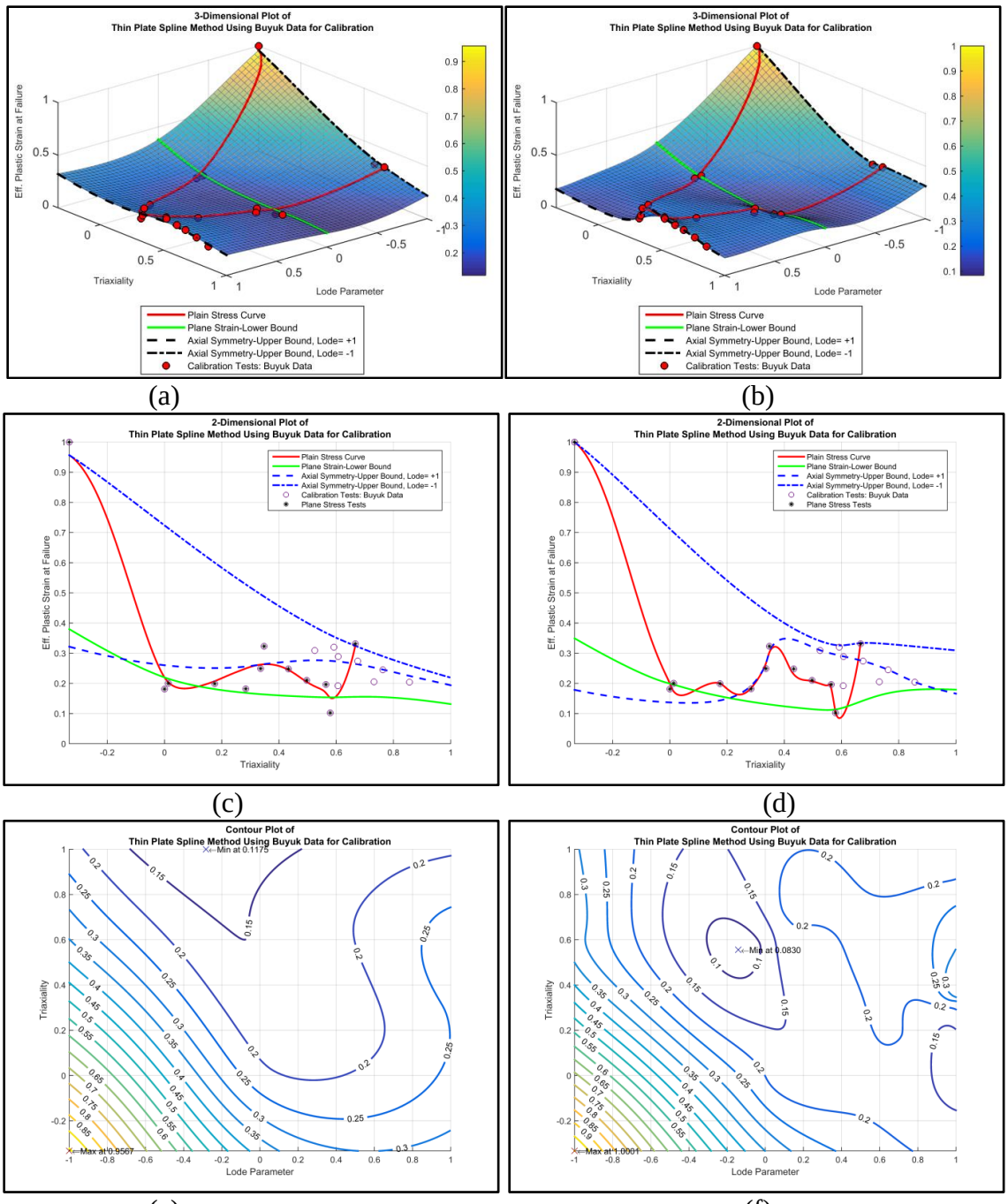

Figure 34. Comparison of Proposed TPS Method with p=0.700 (Left) and p=0.999 (Right)

4.6 Conclusions

As seen in the previous sections, four different approaches which aim to accurately define and predict the effective plastic strain at failure as a function of

triaxiality and Lode parameter were analyzed with a number of test matrices varying in size and specimen geometry. The performance of the four failure surface methods varied widely between each method and test matrix used for calibration. The most extreme case was the failure surfaces built using the Bai Symmetrical failure surface method calibrated with the Bai et al. data set and Buyuk data set. As seen in Figures 22 and 23, the Bai Symmetrical approach matched the Bai et al. data nearly perfectly with little bias or variance. However, when the more complex Buyuk data set was used to calibrate the failure surface, the surface had a much higher bias; so much that in areas on the failure surface, such as the intersection of the plane stress and $\xi = 1$ curves, the surface failed to accurately represent the data points. This lack of flexibility in the surface can be attributed to the failure surface method's symmetrical equation. As such, the asymmetric Bai failure surface method addressed this shortcoming by allowing the $\xi = 1$ and $\xi = -1$ curves to be independent of each other. As a result, a better calibrated failure surface was configured, as seen in Figure 25. Unfortunately, the Xue-Wierzbicki, symmetric Bai, and asymmetric Bai failure surface methods' defining equations all rely on terms defining the surface in the triaxiality direction with an exponential function similar to Equation 4.27. As a result of using this assumption, the surfaces exhibtied limited flexibility, and a biased fit to the highly fluctuating data points was present.

$$\varepsilon_f^{p\,triaxiality\ direction} = C_1 e^{-C_2 \eta} \quad (4.27)$$

where

$\varepsilon_f^{p\,triaxiality\ direction}$ = Effective Plastic Strain At Failure along Triaxiality Axis

C_1, C_2 = Coefficients

η = Triaxiality

In conclusion, it is clear that it is important to choose a failure surface method that is able to accurately define a reasonable failure surface with enough flexibility to limit excessive residuals. The Buyuk method, while unable to be reproduced, allowed the most natural surface fit by fitting every data point with no residual. However, this method requires a large number of tests to determine the failure surface of the material in question. Unfortunately, due to the nature of spline fitting, the method is prone to over fitting the data, thus creating a high variance solution. The uncharacteristic dip around the $\xi = -1$ and plane strain curves in the positive triaxiality region was likely inaccurate and only the result of overfitting the splines.

In conclusion to the full data set analysis with the existing failure surface methods, the Asymmetric Bai failure surface produced the most reasonable results. The method provided a surface that limited bias, while also providing relatively low variance. At the cost of requiring at least six carefully-selected, unique, stress-state specimens to calibrate the surface fitting, the resulting surface allowed for a fairly accurate representation of both the Buyuk and Wierzbicki et al. data sets, as seen in Figures 25 and 33, respectively.

In addition to the full data sets analysis, two partial data sets were used to evaluate the ability of the failure surface methods to produce surfaces similar to those produced using the full data sets. The first reduced data set consisted of four specimens from the

Wierzbicki et al. data set, as recommended by Xue [72]. While the results from the reduced calibration using the Xue-Wierzbicki failure surface method may have been within acceptable tolerances, the surface fit produced using this method did not completely reproduce the full data set failure surface. Furthermore, the symmetrical Bai failure surface method calibrated with the reduced data set was unable to accurately reproduce the failure surface created with the full data set.

The second reduced data set was comprised of the flat specimens from Buyuk's test matrix. Neither the Xue-Wierzbicki, the Asymmetric Bai, nor the Symmetric Bai failure surface methods were able to predict the effective plastic strain at failure in the negative triaxiality region. Furthermore, the symmetrical approach used in the Xue-Wierzbicki failure surface and the Symmetrical Bai failure surface caused inaccurate $\xi = 1$ and $\xi = -1$ curves that were inversely proportional to the full data set surfaces. Interestingly, the Asymmetric Bai failure surface method allowed the most accurate comparison to the full data set surface, as seen in Figure 33. However, the lack of a compression test resulted in an inaccurate negative triaxiality range and allowed the $\xi = -1$ curve to underestimate the effective plastic strain at failure. However, the plane stress, plane strain, and $\xi = 1$ curves remained relatively accurate when compared to the full data set surface. The accuracy of the plane stress curve was likely a result of the plane stress (flat) specimen used to calibrate the failure surface. The failure surface was a moderately-accurate prediction of the full data set in the positive triaxiality region only.

To summarize, it is clear that large test matrices are preferred when defining a stress-state dependent failure surface. While simple defining equation surfaces with a limited number of data points produce surfaces with little to no residual values, the

resulting surface may not accurately predict the failure surface through all stress states. Furthermore, no existing failure surface method that was reproduced and analyzed in this report can be said to accurately define and predict the whole of each data set. Thus, it may be beneficial to use more flexible surfaces, similar to that seen in the Buyuk method. This decision would of course come at the cost of needing a large test matrix with carefully-selected specimens to reproduce critical stress states. One method that could achieve a more flexible surface fit, while allowing an adjustment to balance bias and overfitting, is with a Smoothed, Thin-Plate Spline Method. The penalty approach used in creating the surface reduces the risk of uncharacteristic surface dips from overfitting of the data. Furthermore, the adjustability added with the smoothness parameter allows a balance to be calibrated between a highly-variable, low-bias surface and a stiff, high-bias surface. However, further analysis is needed to determine the effectiveness of the Smoothed, Thin-Plate Spline Method.

5 MATERIAL TESTING PLAN – STEEL SPECIMENS

5.1 Material Selection

The material selection process was critical to accurately represent AASHTO M-180 guardrail steel. A number of important issues in selecting an appropriate material were considered. First, the component testing program would require several complex shapes with dimensions much thicker than typically provided for standard W-beam rail sections. Thus, a substitute material would need to be selected that has similar mechanical and chemical properties. Furthermore, the AASHTO M-180 steel specification provides minimum values of acceptable mechanical properties, including yield strength, tensile strength, and elongation, as seen in Table 8. As such, a survey of guardrail available in the market was used to determine a range of usable mechanical properties. The material certificates and material properties were compiled as part of a recent effort by Schmidt et al. [74]. This data allowed for median values as well as 15^{th} and 85^{th} percentile values of yield strength, tensile strength, and elongation to be computed and used for reasonable bounds during the material search, as seen in Figure 35. Lastly, the AASHTO specification does not reference a specific ASTM specification for which the guardrail must meet, besides those specific to bolts, nuts, and Zinc coatings. Therefore, a steel specification was needed to define the material that should be acquired for the component testing program. Similar to the research report by Schrum et al. [75-76], it was determined that ASTM A572 steel [77] is typically similar to the AASHTO Specification M-180 guardrail steel available on the market in regards to chemical and mechanical properties.

After an extensive search, a material was obtained that meets both the requirements to match the material properties of available guardrail steel available and also be commonly available in sufficient dimensions to allow for component testing within the described testing program. The chosen material was a 0.5 in. (12.7 mm) thick, 60 in. (1,524 mm) wide, and conformed to ASTM A572 Grade 50 steel plate with material properties similar to the median values of the compiled material that was available on the market, as seen in Table 8 and Figure 35. The selected material falls within the 15th and 85th percentile ranges for both yield and ultimate strength, but exhibits an elongation 1.3 percent greater than the 85th percentile range. It was determined that the slightly higher ductility was acceptable, because it still fell within the range of the compiled data. The material certificate for the selected material can be found in Appendix E.

Table 8. AASHTO M-180 and Selected Material Mechanical Properties

	Yield Strength, ksi (MPa)	Ultimate Strength, ksi (MPa)	Elongation, (in 2 in.)
AASHTO Specification M-180 Minimum Values	50 (345)	70 (483)	12%
Median Values of Compiled Material Available on Market	63.2 (436)	74.8 (516)	27.1%
Selected Material Mean Values from Material Certificate	65 (448)	74 (510)	30.5%

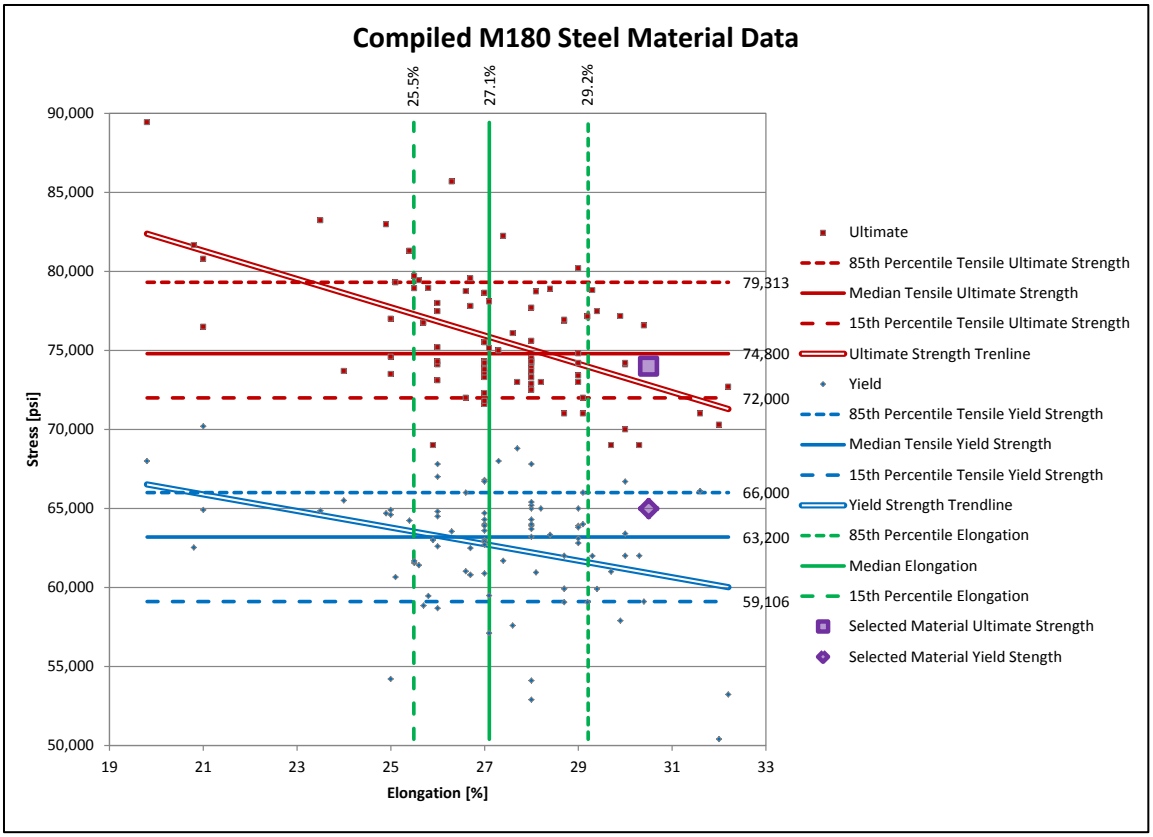

Figure 35. Compiled AASHTO Specification M-180 Steel Material Data [74]

5.2 Development of Component Testing Program

The material testing program was developed based on the assumption that the selected material used to represent the AASHTO M-180 guardrail steel will fail at an effective plastic strain dependent on triaxiality and Lode parameter. Furthermore, the test matrix was developed based on available testing equipment, knowledge of existing specimen geometries noted in the literature, and the time required to test and model each specimen. The majority of the utilized specimen geometries were similar to those used by Buyuk and Seidt [38,43]. However, the specimen geometries have been commonly used by other researchers as well. Recently, researchers at the Impact and Crashworthiness Laboratory at the Massachusetts Institute of Technology utilized a testing matrix comprised of: round, notched, axial-symmetric tensile and compression specimens;

cylindrical compression specimens; a solid bar specimen; a pipe specimen; a flat grooved specimen; and various shaped flat specimens [35,37,40]. Mirone conducted a study with un-notched and notched specimens with various dimensions [78]. Carney et al.'s test matrix consisted of various flat plane stress specimens, two thick plane strain specimens, various axial symmetric round specimens, and a biaxial punch specimen [47]. Ebelsheiser et al.'s study included three different shear tests, various flat plane stress tensile specimens, and a biaxial punch specimen [79]. Gao et al. provided a testing matrix consisting of a notch round bar specimen, a circular-notched plane strain specimen, a flat plane stress specimen, a modified flat plane stress specimen, and a torsion specimen [41]. In the following subsections, each specimen's geometry is reviewed, and then the final testing matrix is provided.

5.2.1 Specimen Geometry No. 1: Flat Standard Dog Bone Specimen

The Flat Standard Dog Bone Specimen is a common tension specimen in which the narrowed middle length, as seen in Figure 36, allows for simple tension tests to be performed. Due to this shape being the simplest and most common specimen shape, it allows for a baseline comparison between the material tested in this report and other steel materials. Furthermore, the simple tension geometry is often used in the determination of material properties, such as strain rate sensitivity, hardening curve shape, elastic modulus, and yield strength. The stress state of this specimen is given by a triaxiality of $^1/_3$ and a Lode parameter of 1 [37, 38,43,46].

Figure 36. Flat Standard Dog Bone Specimen

5.2.2 Specimen Geometry Nos. 2 Through 4: Notched Flat Specimen

Notched specimens have been used to study the effect of varying stress states along the plane stress curve in numerous testing programs, beginning with Bridgman's experiments in which he showed that hydrostatic forces develop in the neck region [21]. The notch is meant to induce a confinement on the material that affects the state of stress along the reduced cross section. As the radius of the notch changes, the state of stress will shift along the plane stress curve. Testing a number of flat specimens with various notch sizes allows for a number of unique plane stress states to be studied. As seen in Figure 37, the curve defined by the thick green line can be represented by the four flat specimens with stress states ranging between $\eta = \frac{1}{3}$ to $\frac{1}{\sqrt{3}}$ and $\xi = 0$ to 1. While an infinite number of notch radii could be used to produce a high resolution curve, only three additional flat specimens were selected to allow for reasonable resolution along this portion of the plane stress curve. The notched flat specimens as well as the Flat Standard Dog Bone Specimen can be seen in Figure 38.

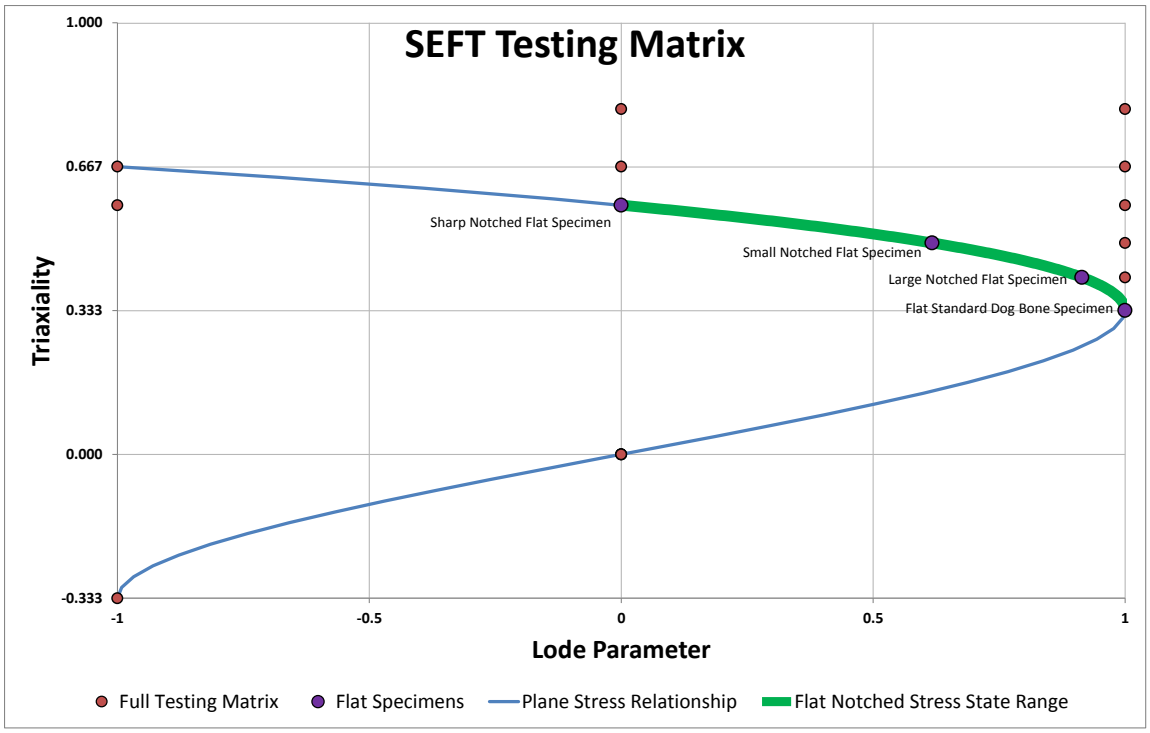

Figure 37. Flat Specimen Stress States

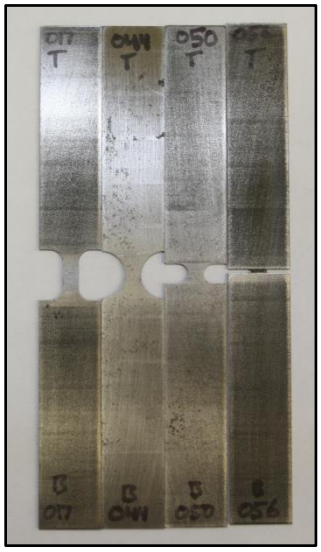

Figure 38. Flat Standard and Notched Specimen Nos. 1-4

5.2.3 Specimen Geometry No. 5: Axial-Symmetric Round Smooth Specimen

The Axial-Symmetric Round Smooth Specimen, as shown in Figure 39, is a common tension specimen similar to the Flat Standard Dog Bone Specimen. The round rod with a narrowed middle length allows for simple tension tests to be performed.

Similar to the Flat Standard Dog Bone Specimen, the specimen can be used in the determination of material properties, such as strain rate sensitivity, hardening curve shape, elastic modulus, and yield strength. As the stress state is also identical to that of the Flat Standard Dog Bone Specimen, material properties such as yield strength, elastic modulus, hardening curve shape, strain rate sensitivity, and effective plastic strain at failure, should be similar between the two specimens.

Figure 39. Axial-Symmetric Round Smooth Specimen No. 5

5.2.4 Specimen Geometry Nos. 6 Through 10: Notched Round Specimens

Similar to the three Flat Notched Specimens, a similar approach can be used to produce various stress states with axial-symmetric round specimens. The confinement produced by a notch affects the stress state, and by changing the radius of the notch, different stress states can be produced. Five additional round specimens with notches were included to represent the range given by the green curve along $\xi = 1$, as seen in Figure 40. The notched axial-symmetric specimens as well as the Axial-Symmetric Round Smooth Specimen can be seen in Figure 41.

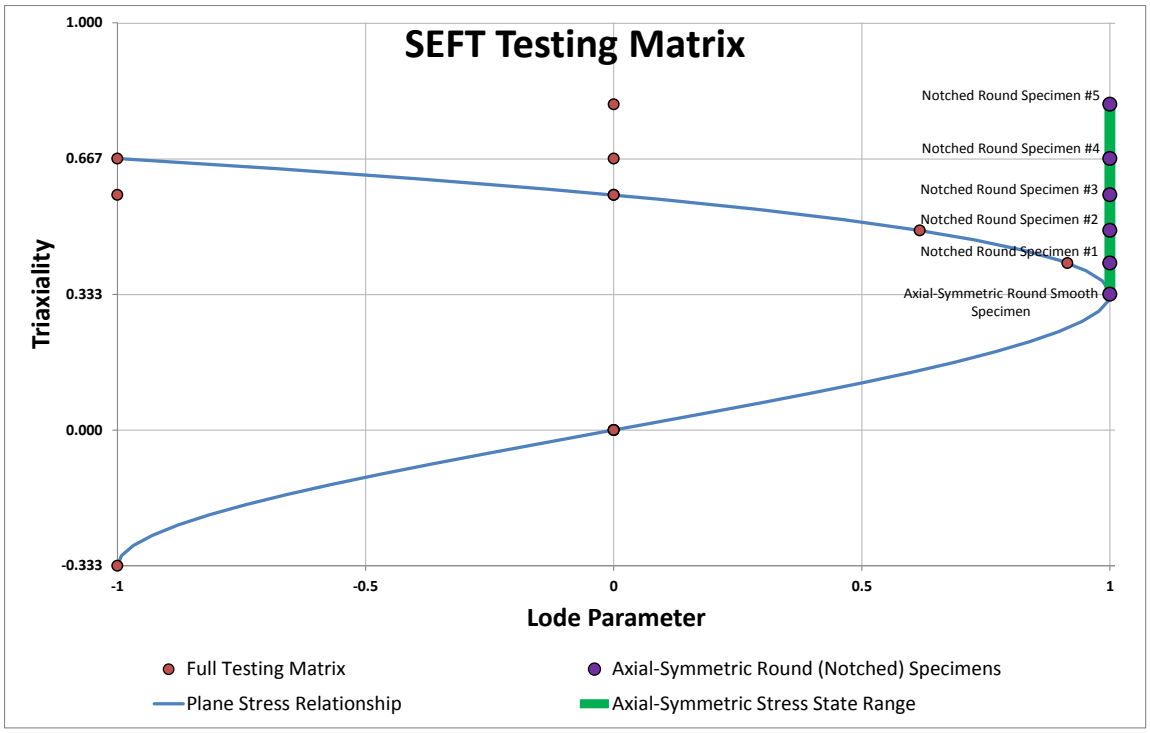

Figure 40. Axial-Symmetric Round Specimen Stress States

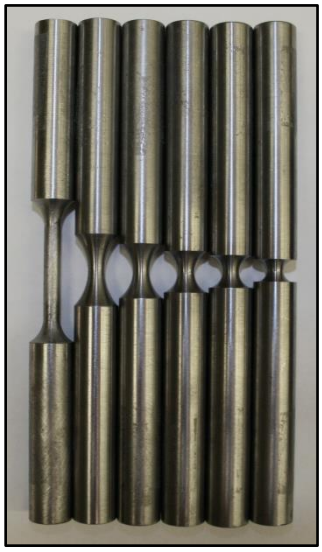

Figure 41. Axial-Symmetric Round Specimen Nos. 5-10

5.2.5 Specimen Geometry No. 11: Thick Dog Bone Specimen

The Thick Dog Bone Specimen is meant to predict plane strain conditions and is similar to the Thin Plane Strain (TPS) Specimen, as presented by Clausing [80]. The TPS Specimen includes a notch in the lateral direction of the base material. The specimen

shape and thickness can be seen in Figure 42. This notch allows for a state of stress in which strain can be assumed to be zero in the z-direction, which is in agreement with plane strain assumptions. The specimen's stress state lies along the plane strain, $\xi = 0$ curve, with a triaxiality of $\frac{1}{\sqrt{3}}$ and a Lode parameter of 0. It is interesting to note that this specimen shares the same geometry as the Flat Standard Dog Bone Specimen, except this specimen is more than 33 times thicker than the Flat Standard Dog Bone Specimen. Also, the Thick Dog Bone Specimen shares a stress state with the plane stress curve, as represented by triaxiality and Lode parameter at the intersection of the plane stress and plane strain curves at $\eta = \frac{1}{\sqrt{3}}$ and $\xi = 0$. Furthermore, these are the same stress state coordinates of the Sharp Notched Flat Specimen. With the assumptions of a state of stress dependent failure, this means that both of these tests should fail at similar effective stress states. Although, variations in the internal stress states across the two cross sections during necking may influence the results.

Increasing the thickness of the specimen further would allow for a specimen that converges towards the theoretical plane strain condition. However, the finite element method study conducted by Buyuk [70] shows that at 32 times the thickness of the plane stress specimen, both the triaxiality and Lode parameter values converge very closely for the tested AL2024-T351 material. While thicker specimens could be fabricated and tested to provide more accurate results based on Buyuk's study, it was determined that the thickness of 1 in. (25.4 mm) would provide adequate results.

Figure 42. Thick Dog Bone Specimen No. 11

5.2.6 Specimen Geometry Nos. 12 and 13: Thick Notched Specimen

Similar to the axial-symmetric notched and flat notched specimens, adding a notch, or in this case changing the shape of the notch, allows for different stress states to be tested and evaluated. Two additional thick specimens were chosen, both of which include round notches with different size radii. A visual comparison of the three thick specimens can be found in Figure 44. Similar to the Thick Dog Bone Specimen, both of the round notched thick specimens have stress states in agreement to plane strain conditions. As such, they lie on the plane strain, $\xi = 0$ curve. Combined, the three thick specimens represent the range along the plane strain curve between the triaxiality range $\frac{1}{\sqrt{3}}$ to 0.8, as seen by the thick green curve in Figure 43.

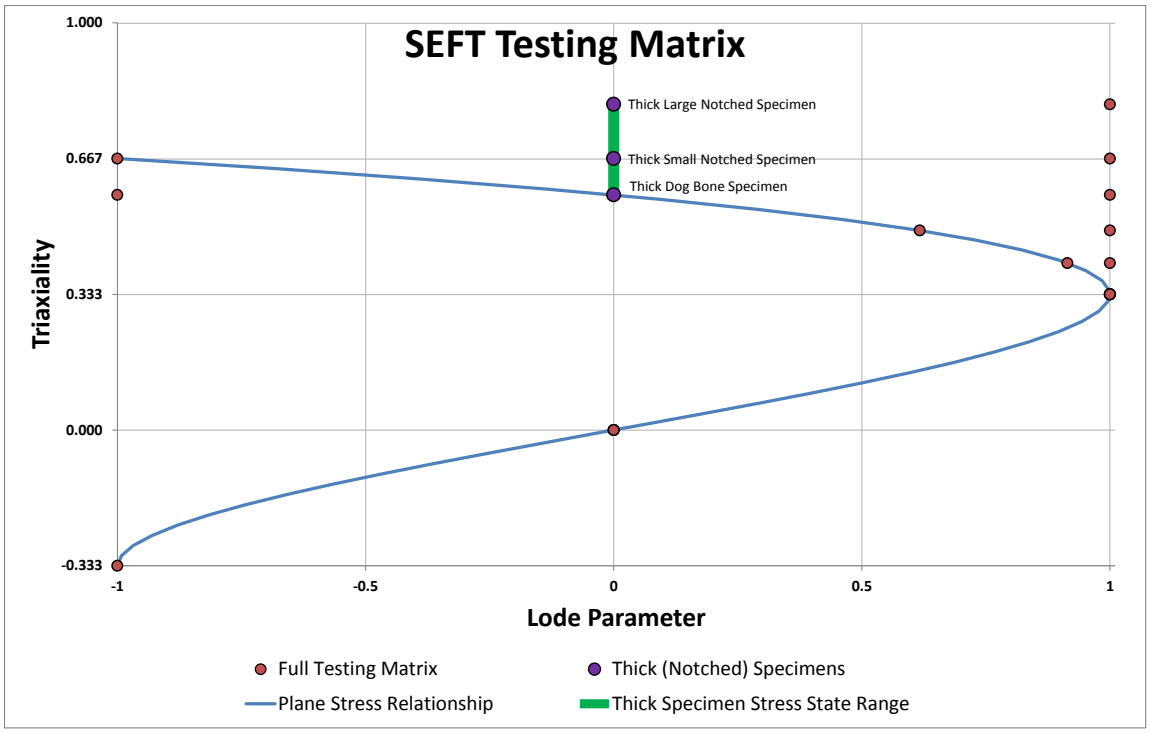

Figure 43. Thick Specimen Stress States

Figure 44. Thick Specimen Nos. 11-14

5.2.7 Specimen Geometry No. 14: Cylinder Upsetting Specimen

The Cylinder Upsetting Specimen is the only compression specimen used in this testing matrix, and it is used to represent the negative triaxiality range. The generally-accepted cut off value for triaxiality is $\eta = -\frac{1}{3}$ as determined by Bridgman [21], and

more recently by both Bao [46] and Bao and Wierzbicki [81]. As such, the idealized state of stress for the compression cylinder is represented by $\eta = -\frac{1}{3}$ and $\xi = -1$. The uniaxial compression specimen has equal length and diameter to give a ratio of $^{d}/_{h} = 1$, as seen in Figure 45. To attempt to reduce the barreling effect that causes shear zones to develop and the specimen to fail, a lubricant was applied to both platen-specimen interfaces, which was similar to the testing performed by Seidt [82]. This process allows for a more uniform stress field throughout the specimen and a more true stress state to be reported.

Figure 45. Cylinder Upsetting Specimen No. 14

5.2.8 Specimen Geometry Nos. 15, 16, 17, 20, and 21: Punch Specimens

Similar to the Buyuk testing matrix, three punch tests were fabricated with unique punch head shapes that were intended to induce varying methods of failure, as represented by a range of stress states, provided in Figure 46. These specimens included a Standard Punch Head, a Round Punch Head, and a Sharp Punch Head.

Similar punch tests using servo-hydraulic load frames have been performed by Lee, Woertz, and Wierzbicki [83], Grytten et al. [84], and Seidt [43]. As such, the punch fixture used in this test matrix was similar to those used in previous research. The dimensions of the punch fixture and the initial punch heads were similar to those used by Buyuk and Seidt [38,43]. However, instead of using epoxy to hold the punch specimen within the fixture, the specimen was held in place by a clamping compressive load

similar to tests performed by Walters [85], Lee, Woertz, and Wierzbicki [83], and Grytten et al. [84].

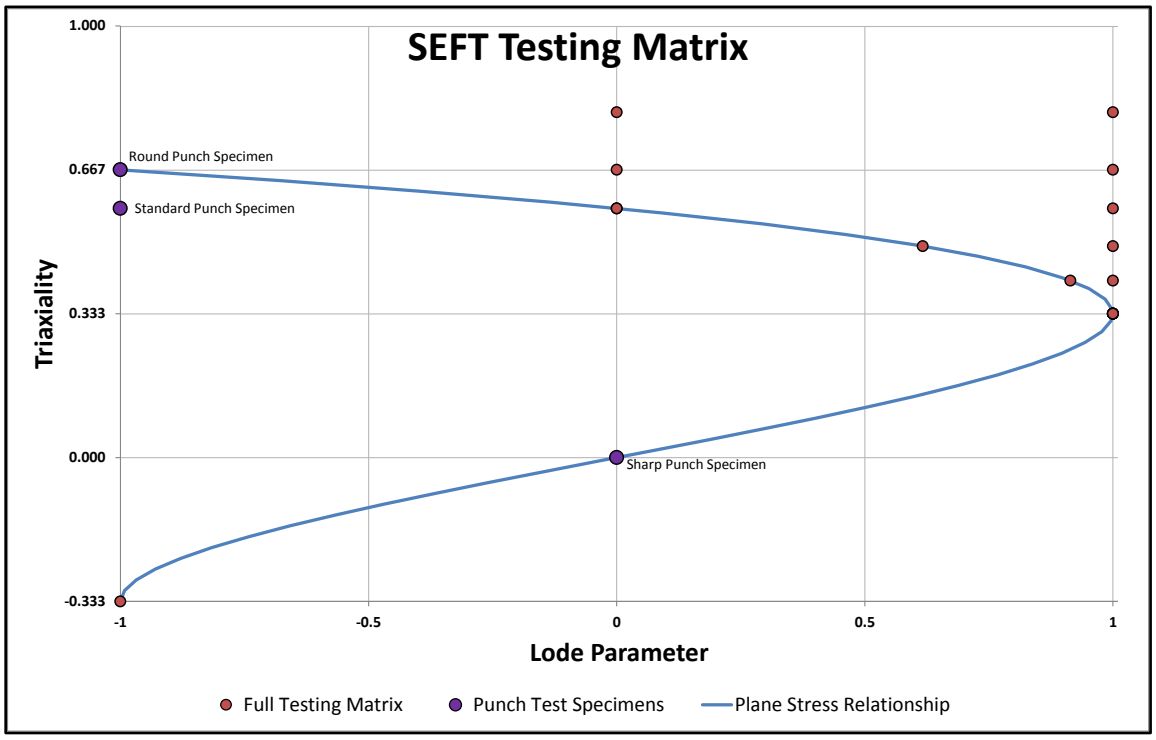

Figure 46. Punch Tests Stress States

The punch fixture was designed to accommodate the Landmark 22-kip servo-hydraulic load frame, while also allowing for the fixture to be reusable. The punch fixture utilizes three separate sections. The top two sections allow for a clamping force to be applied to the punch specimen by four $^{1}/_{4}$-in. (6.4-mm) diameter UNF Grade 5 bolts, each with a maximum pre-load force of 2,300 lb (10.2 kN). A recessed area in the middle fixture section was used to center the punch specimens, which is slightly less deep than the specimen thickness. The third section, a base, was meant to allow for a flat surface for the fixture to sit on a compression platen. A pair of serrated vee-grips were used to hold the different punch rods. A blockout disk equal in diameter to the fixture was attached to the punch rods to allow for the laser extensometer, retro-reflective tape to be used to

measure punch movement. The assembled fixture with a punch rod can be seen in Figure 47. Varying amounts of bolt tightening torque was investigated with, and it was determined that 80 in.-lb (9.0 kN-mm) of torque gave a balance between minimizing fixture separation through specimen leverage and preventing crushing of the specimen.

During testing, it was found that the original standard and round punch heads were causing shear around the edge of the fixture prior to the intended failure mechanism occurring. Upon closer examination, it was believed that this behavior was due to interference between the punch head and fixture. A FEM model, configured with an Isotropic Piecewise Linear Plasticity material model calibrated with the existing Axial-Symmetric Round Smooth Specimen test data, was used to confirm this theory. Unlike the material used in the Buyuk and Seidt [38,43] testing program, the ASTM A572 Grade 50 steel material showed a much higher effective plastic strain at failure. As a result, an increased draw down distance was required to produce the intended failure in the specimens. However, prior to reaching the critical effective plastic strain at failure, the original diameter of the punches caused a shearing action around the punch rod-fixture interface.

A number of simulations were run with varying punch rod diameters until it was believed that failure would occur in the center of the specimen disk with reduced risk of shearing. Based on these computer simulations, two new punch heads were designed with diameters of 0.2756 in. (7.000 mm); 0.0984 in (2.500 mm) smaller than the original punch rods. The Revised Standard Punch Rod utilized the same head shape as the original, withholding the reduced diameter. However, the Revised Round Punch Head was designed with an axial-symmetric head radius equal to the radius of the shaft. A

visual comparison of the five punch rods can be found in Figure 48. A new upper fixture was also designed with a tighter tolerance center punch-hole to allow easier and more consistent alignment of the fixture.

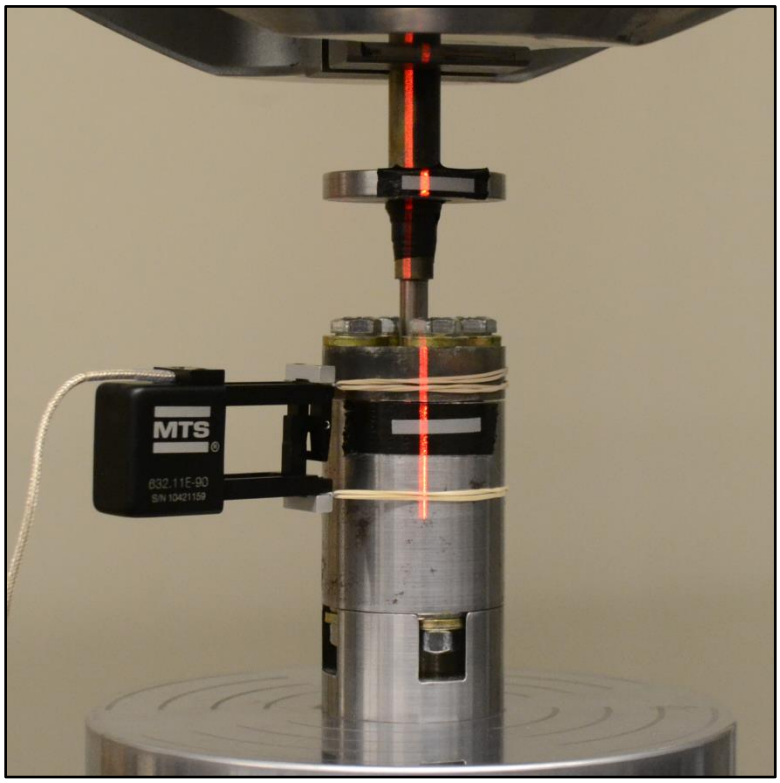

Figure 47. Assembled Punch Fixture Placed on Compression Platen and Punch Rod in Vee-Grips

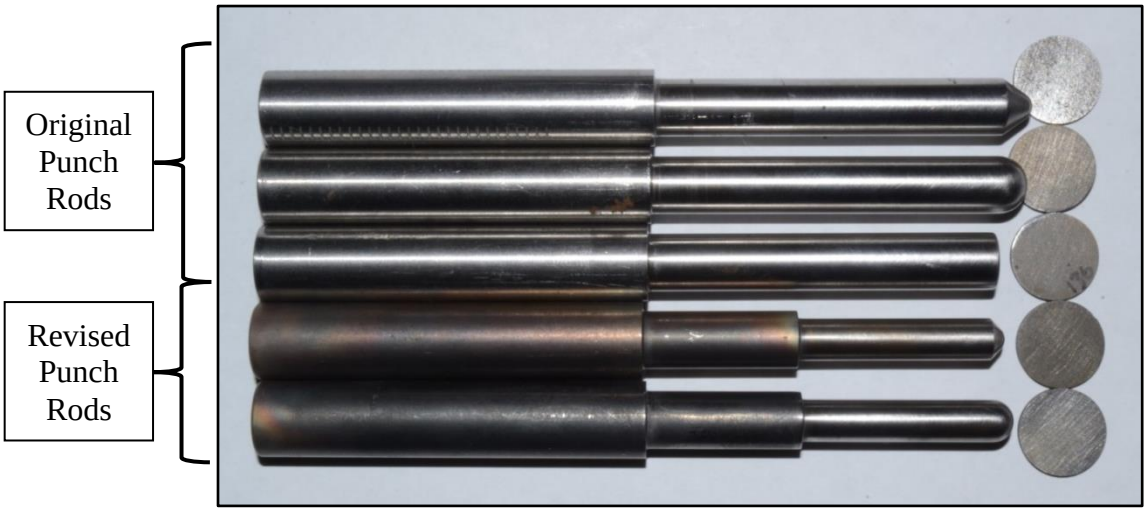

Figure 48. Punch Rods for Specimen Nos. 15, 16, 17, 20, and 21

5.2.9 Specimen Geometry No. 18: Dual-Point Shear

A Dual-Point Shear Fixture, as seen in Figure 49 with an inside diameter of 0.394 in. (10.00 mm) and obtained from MTS Systems Corporation, was used to shear the 0.393-in. (9.97-mm) diameter rod. A shear rod specimen can be seen in Figure 50. A blockout was machined to allow retro-reflective tape to be attached to the upper mount so that the laser extensometer was equidistance from both the upper and lower retro-reflective tapes. While similar tests setups are typically used to test the double shear strength of fasteners [86], a similar test setup was used to provide data at the shear stress state of $\eta = \xi = 0$.

Figure 49. Dual-Point Shear Fixture

Figure 50. Dual-Point Shear Rod Specimen No. 18

5.2.10 Specimen Geometry No. 19: Torsion Specimen

A thin, hollow, cylindrical-tube specimen was tested in torsion with a stress state identical to the Sharp Punch and Dual-Point Shear Specimens at $\eta = \xi = 0$. A thin material thickness was selected in order to assume plane stress conditions so that the specimen could approach pure torsion shear conditions. The specimen can be seen in Figure 51. Due to the limitations of the mechanically-driven torsion frame used during testing, reliable torque measurements could not be recorded. However, the angle at failure was recorded by measuring the differential angle between two rods attached to either side of the gauge length before and after testing. Testing occurred under slow loading conditions where the test duration was between 8 and 10 minutes.

Figure 51. Torsion Specimen, No. 19

5.3 Test Matrix

A total of 103 tests were conducted on the 21 test configurations, as seen in the test matrix found in Table 9 and the specimen types depicted in Figure 52. The testing matrix provided a wide range of tests that are necessary to develop a material model with accurate material properties and a stress state dependent failure surface. Test nos. SEFT-14 through SEFT-16, SEFT-66 through SEFT-69, SEFT-79, and SEFT-88 through SEFT-89, allowed for a determination of the basic material properties such as Young's modulus, yield stress, and isothermal hardening curve. The remaining tests allowed for a stress state dependent failure surface to be developed.

The test matrix found in Table 9 provides details for load rate, gauge length, load frame, fixtures, and measurement devices that were used in each test. The complete two-dimensional plot of the targeted stress states, as represented by triaxiality and Lode parameter, for each specimen type can be found in Figure 53. It is important to note that this graph is dissimilar to those graphs shown in Chapter 4 as it gives the targeted stress states as opposed to the average stress states determined by modeling and testing. The drawings of the specimens, punch fixture, and punch heads are provided in Figures 54 through 84.

Table 9. SEFT Test Matrix

Test ID	Specimen Name	Specimen Geometry No.	Load Rate in./sec - rad/min (mm/sec)	Primary Measurement Gauge Length in. (mm)	Target Lode Parameter	Target Triaxiality	Load Frame	Fixture/Grips	Measurement Devices
SEFT 14-16, 69	Flat Standard Dog Bone Specimen	1	0.000400 (0.01016)	Varies	1.0000	0.3333	Landmark 22 kip	0-0.30" Surfalloy Flat Grips	LX 500 Laser Extensometer, 1 in. Axial Extensometer, 22 and 2.2 kip Load Cell
SEFT 70-72, 74, 76, 77, 79	Flat Standard Dog Bone Specimen	1	0.000400 (0.01016)	1.0000 (25.4000)	1.0000	0.3333	Landmark 22 kip	0-0.30" Surfalloy Flat Grips	1 in. Axial Extensometer, ARAMIS 2M DIC, 22 kip Load Cell
SEFT 17-19	Large Notched Flat Specimen	2	0.000250 (0.00635)	1.0000 (25.4000)	0.9145	0.4100	Landmark 22 kip	0-0.30" Surfalloy Flat Grips	LX 500 Laser Extensometer, 1 in. Axial Extensometer, 22 and 2.2 kip Load Cell
SEFT 73, 75	Large Notched Flat Specimen	2	0.000250 (0.00635)	1.0000 (25.4000)	0.9145	0.4100	Landmark 22 kip	0-0.30" Surfalloy Flat Grips	1 in. Axial Extensometer, ARAMIS 2M DIC, 22 kip Load Cell
SEFT 20-22	Small Notched Flat Specimen	3	0.000170 (0.00432)	1.0000 (25.4000)	0.6170	0.4900	Landmark 22 kip	0-0.30" Surfalloy Flat Grips	LX 500 Laser Extensometer, 1 in. Axial Extensometer, 22 and 2.2 kip Load Cell
SEFT 83	Small Notched Flat Specimen	3	0.000170 (0.00432)	1.0000 (25.4000)	0.6170	0.4900	Landmark 22 kip	0-0.30" Surfalloy Flat Grips	1 in. Axial Extensometer, ARAMIS 2M DIC, 22 kip Load Cell
SEFT 23-25	Sharp Notched Flat Specimen	4	0.000108 (0.00274)	1.0000 (25.4000)	0.0000	0.5774	Landmark 22 kip	0-0.30" Surfalloy Flat Grips	LX 500 Laser Extensometer, 1 in. Axial Extensometer, 22 and 2.2 kip Load Cell
SEFT 84	Sharp Notched Flat Specimen	4	0.000108 (0.00274)	1.0000 (25.4000)	0.0000	0.5774	Landmark 22 kip	0-0.30" Surfalloy Flat Grips	1 in. Axial Extensometer, ARAMIS 2M DIC, 22 kip Load Cell
SEFT 66-68	Axial-Symmetric Round Smooth	5	0.001180 (0.02997)	Varies	1.0000	0.3333	Landmark 22 kip	0.43-0.65" Serrated Vee Grips	LX 500 Laser Extensometer, 2 in. Axial Extensometer, 22 kip Load Cell
SEFT 88-89	Axial-Symmetric Round Smooth	5	0.001180 (0.02997)	2.0000 (50.8000)	1.0000	0.3333	Landmark 22 kip	0.43-0.65" Serrated Vee Grips	2 in. Axial Extensometer, ARAMIS 2M DIC, 22 kip Load Cell
SEFT 27-29	Notched Round Specimen #1	6	0.000564 (0.01433)	2.0000 (50.8000)	1.0000	0.4100	Landmark 22 kip	0.43-0.65" Serrated Vee Grips	LX 500 Laser Extensometer, 2 in. Axial Extensometer, 22 kip Load Cell
SEFT 86	Notched Round Specimen #1	6	0.000564 (0.01433)	2.0000 (50.8000)	1.0000	0.4100	Landmark 22 kip	0.43-0.65" Serrated Vee Grips	2 in. Axial Extensometer, ARAMIS 2M DIC, 22 kip Load Cell
SEFT 30-32	Notched Round Specimen #2	7	0.000496 (0.01260)	2.0000 (50.8000)	1.0000	0.4900	Landmark 22 kip	0.43-0.65" Serrated Vee Grips	LX 500 Laser Extensometer, 2 in. Axial Extensometer, 22 kip Load Cell
SEFT 87	Notched Round Specimen #2	7	0.000496 (0.01260)	2.0000 (50.8000)	1.0000	0.4900	Landmark 22 kip	0.43-0.65" Serrated Vee Grips	2 in. Axial Extensometer, ARAMIS 2M DIC, 22 kip Load Cell
SEFT 33-35	Notched Round Specimen #3	8	0.000447 (0.01135)	2.0000 (50.8000)	1.0000	0.5774	Landmark 22 kip	0.43-0.65" Serrated Vee Grips	LX 500 Laser Extensometer, 2 in. Axial Extensometer, 22 kip Load Cell
SEFT 80	Notched Round Specimen #3	8	0.000447 (0.01135)	2.0000 (50.8000)	1.0000	0.5774	Landmark 22 kip	0.43-0.65" Serrated Vee Grips	2 in. Axial Extensometer, ARAMIS 2M DIC, 22 kip Load Cell
SEFT 36-38	Notched Round Specimen #4	9	0.000404 (0.01026)	2.0000 (50.8000)	1.0000	0.6667	Landmark 22 kip	0.43-0.65" Serrated Vee Grips	LX 500 Laser Extensometer, 2 in. Axial Extensometer, 22 kip Load Cell
SEFT 78	Notched Round Specimen #4	9	0.000404 (0.01026)	2.0000 (50.8000)	1.0000	0.6667	Landmark 22 kip	0.43-0.65" Serrated Vee Grips	2 in. Axial Extensometer, ARAMIS 2M DIC, 22 kip Load Cell
SEFT 39-41	Notched Round Specimen #5	10	0.000404 (0.01026)	2.0000 (50.8000)	1.0000	0.8000	Landmark 22 kip	0.43-0.65" Serrated Vee Grips	LX 500 Laser Extensometer, 2 in. Axial Extensometer, 22 kip Load Cell
SEFT 82	Notched Round Specimen #5	10	0.000404 (0.01026)	2.0000 (50.8000)	1.0000	0.8000	Landmark 22 kip	0.43-0.65" Serrated Vee Grips	2 in. Axial Extensometer, ARAMIS 2M DIC, 22 kip Load Cell
SEFT 42-44	Thick Dog Bone Specimen	11	0.000400 (0.01016)	2.0000 (50.8000)	0.0000	0.5774	Landmark 22 kip	0.46-0.75" Diamond Flat Grips	LX 500 Laser Extensometer, 2 in. Axial Extensometer, 22 kip Load Cell
SEFT 81	Thick Dog Bone Specimen	11	0.000400 (0.01016)	2.0000 (50.8000)	0.0000	0.5774	Landmark 22 kip	0.46-0.75" Diamond Flat Grips	2 in. Axial Extensometer, ARAMIS 2M DIC, 22 kip Load Cell
SEFT 45-47	Thick Large Notched Specimen	12	0.000312 (0.00792)	2.0000 (50.8000)	0.0000	0.6667	Landmark 22 kip	0.46-0.75" Diamond Flat Grips	LX 500 Laser Extensometer, 2 in. Axial Extensometer, 22 kip Load Cell
SEFT 85	Thick Large Notched Specimen	12	0.000312 (0.00792)	2.0000 (50.8000)	0.0000	0.6667	Landmark 22 kip	0.46-0.75" Diamond Flat Grips	2 in. Axial Extensometer, ARAMIS 2M DIC, 22 kip Load Cell
SEFT 48-50	Thick Small Notched Specimen	13	0.000250 (0.00635)	2.0000 (50.8000)	0.0000	0.8000	Landmark 22 kip	0.46-0.75" Diamond Flat Grips	LX 500 Laser Extensometer, 2 in. Axial Extensometer, 22 kip Load Cell
SEFT 101	Thick Small Notched Specimen	13	0.000250 (0.00635)	2.0000 (50.8000)	0.0000	0.8000	Landmark 22 kip	0.46-0.75" Diamond Flat Grips	2 in. Axial Extensometer, ARAMIS 2M DIC, 22 kip Load Cell
SEFT 51	Cylinder Upsetting Specimen	14	0.000400 (0.01016)	-	-1.0000	-0.3333	Landmark 22 kip	Compression Platens	LX 500 Laser Extensometer, 2 in. Axial Extensometer, 22 kip Load Cell
SEFT 59-61	Cylinder Upsetting Specimen	14	0.000400 (0.01016)	-	-1.0000	-0.3333	Criterion 220 kip	Compression Platens	LX 500 Laser Extensometer, 220 kip Load Cell
SEFT 99	Cylinder Upsetting Specimen	14	0.000400 (0.01016)	-	-1.0000	-0.3333	Criterion 220 kip	Compression Platens	LX 500 Laser Extensometer, ARAMIS 2M DIC, 220 kip Load Cell
SEFT 52-56	Standard Punch Specimen	15	0.000400 (0.01016)	-	-1.0000	0.5774	Landmark 22 kip	Punch Fixture	LX 500 Laser Extensometer, 1 in. Axial Extensometer, 22 kip Load Cell
SEFT 57-58	Round Punch Specimen	16	0.000400 (0.01016)	-	-1.0000	0.6667	Landmark 22 kip	Punch Fixture	LX 500 Laser Extensometer, 1 in. Axial Extensometer, 22 kip Load Cell
SEFT 96-98	Sharp Punch Specimen	17	0.001300 (0.03302)	-	0.0000	0.0000	Landmark 22 kip	Punch Fixture	LX 500 Laser Extensometer, 1 in. Axial Extensometer, 22 kip Load Cell
SEFT 62-65	Dual Point Shear	18	0.000400 (0.01016)	-	0.0000	0.0000	Criterion 220 kip	Dual Point Shear Fixture	LX 500 Laser Extensometer, 220 kip Load Cell
SEFT 102-104	Torsion Specimen	19	0.1	-	0.0000	0.0000	Torsion	F Grips	Angle Tripmeter
SEFT 90-92	Standard Punch Specimen R1	20	0.001300 (0.03302)	-	-1.0000	0.5774	Landmark 22 kip	Punch Fixture R1	LX 500 Laser Extensometer, 1 in. Axial Extensometer, 22 kip Load Cell
SEFT 93-95	Round Punch Specimen R1	21	0.001300 (0.03302)	-	-1.0000	0.6667	Landmark 22 kip	Punch Fixture R1	LX 500 Laser Extensometer, 1 in. Axial Extensometer, 22 kip Load Cell

Figure 52. Composite Photograph of Test Specimens

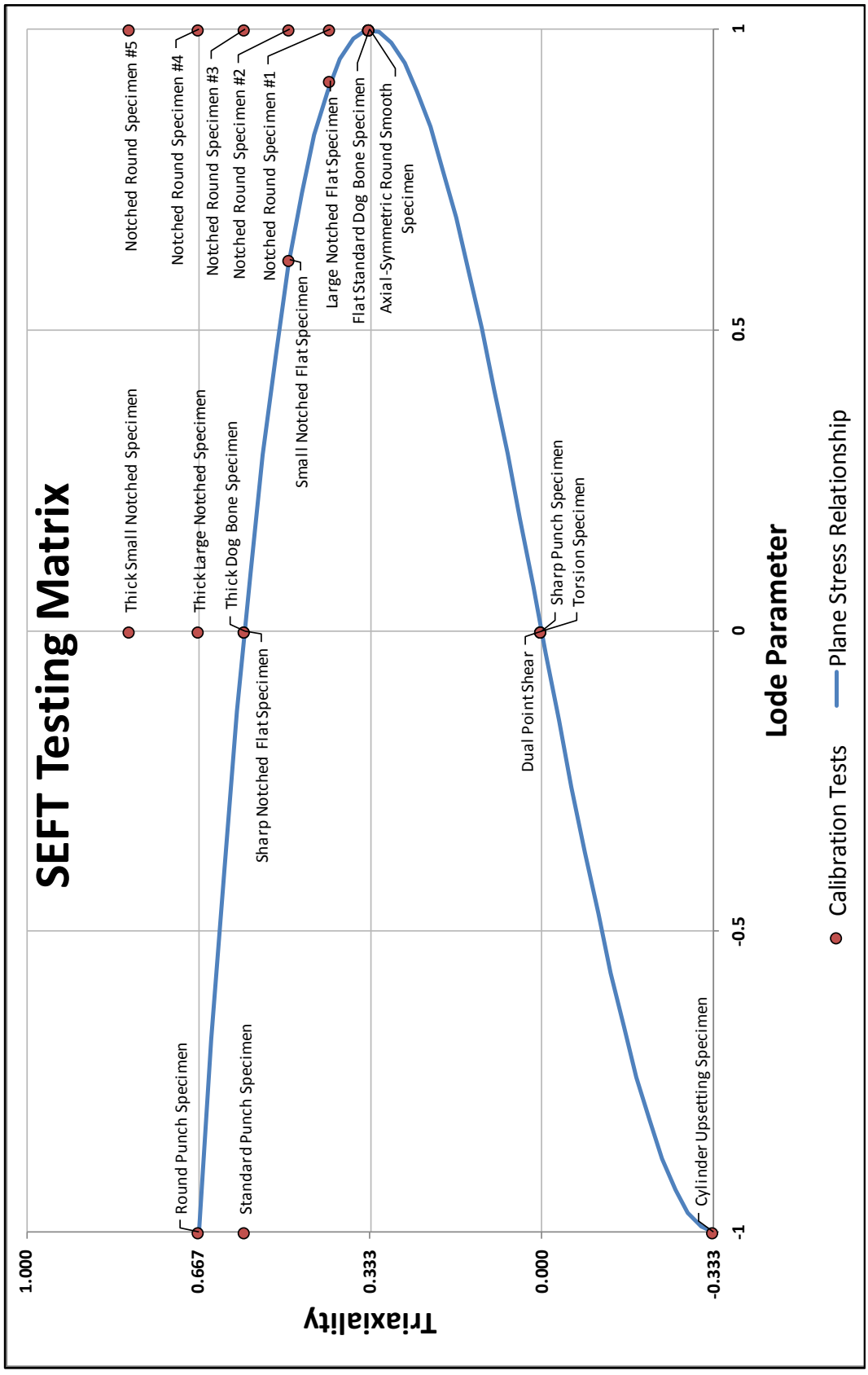

Figure 53. SEFT Specimen Stress States

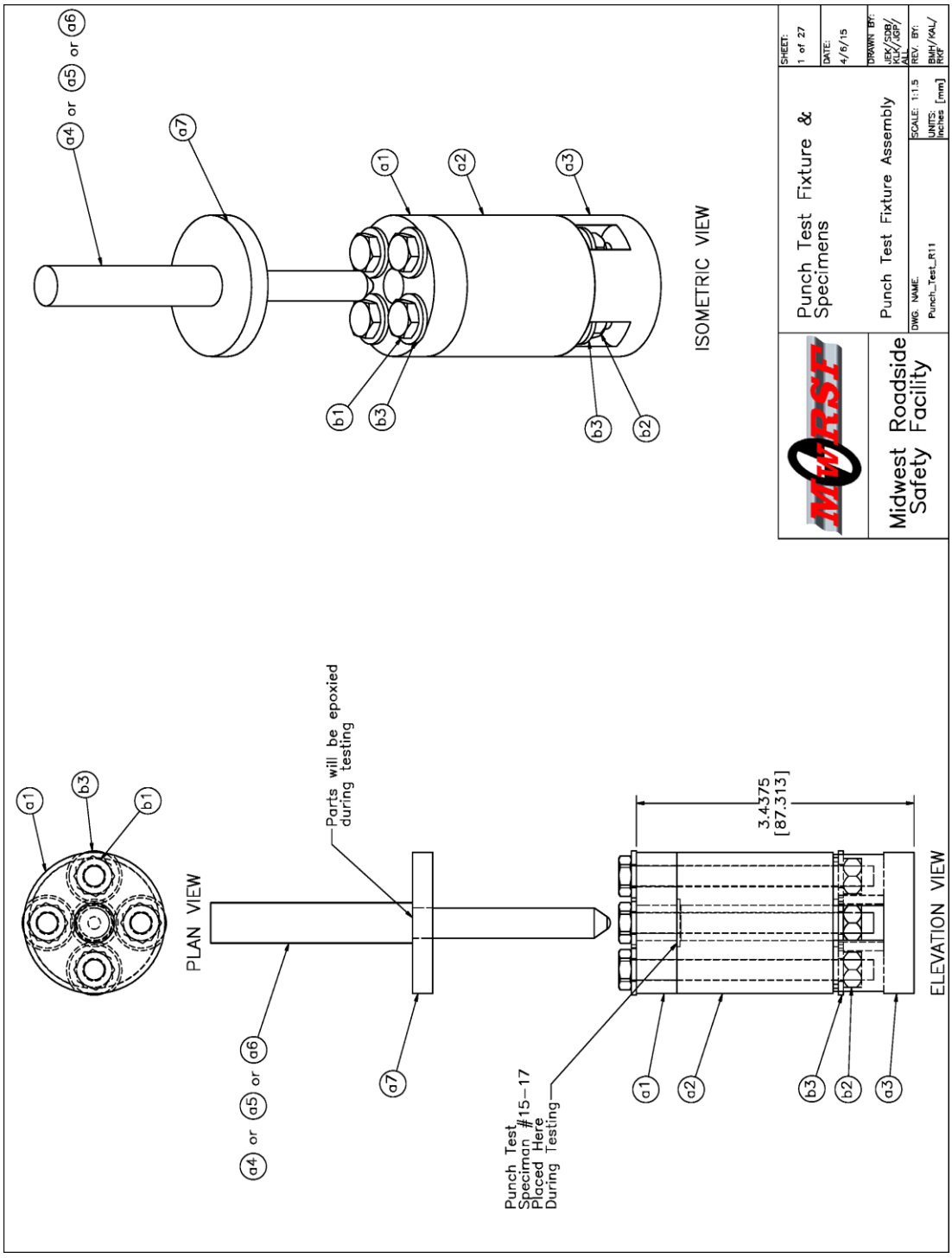

Figure 54. Punch Test Fixture Assembly

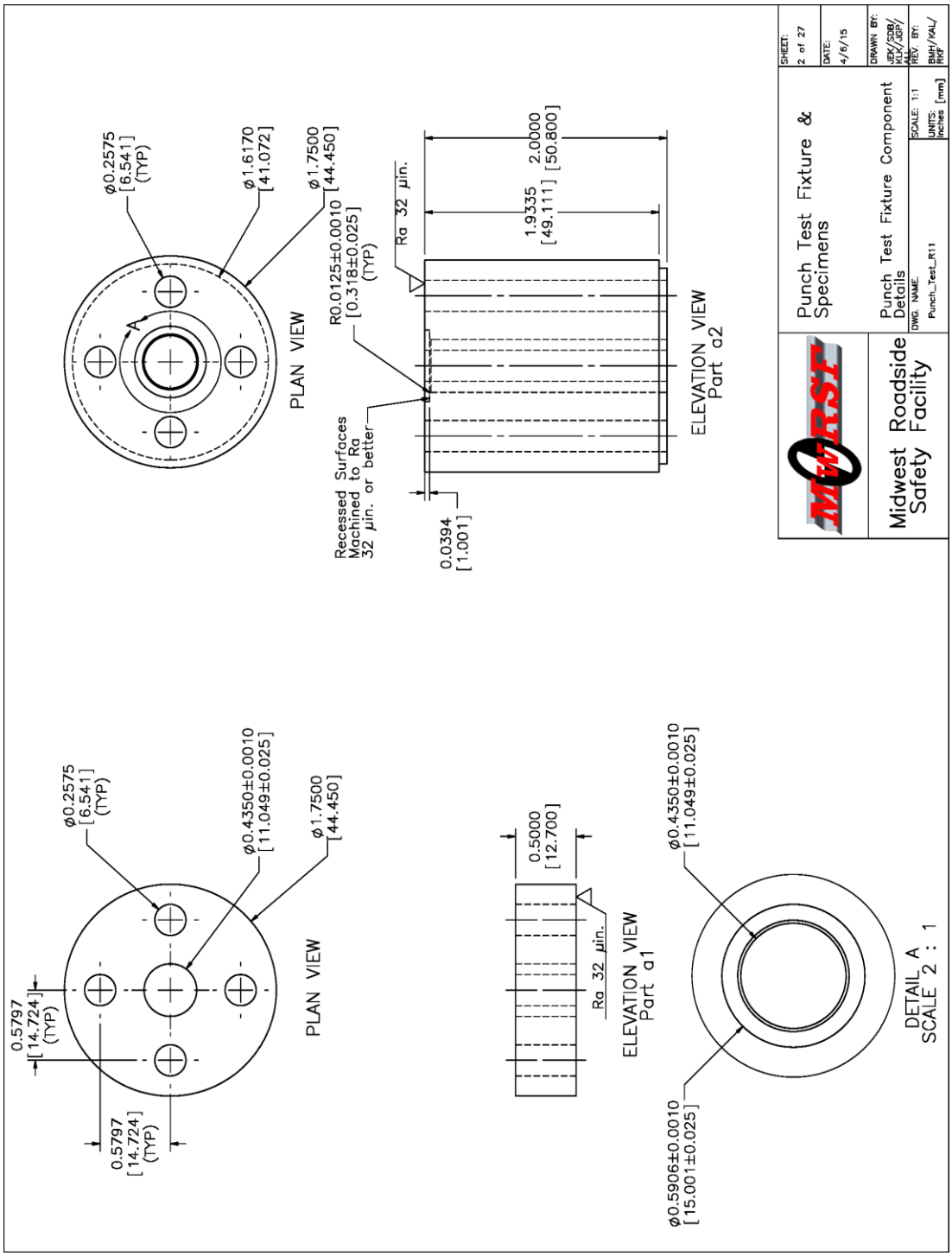

Figure 55. Punch Test Fixture Component Details

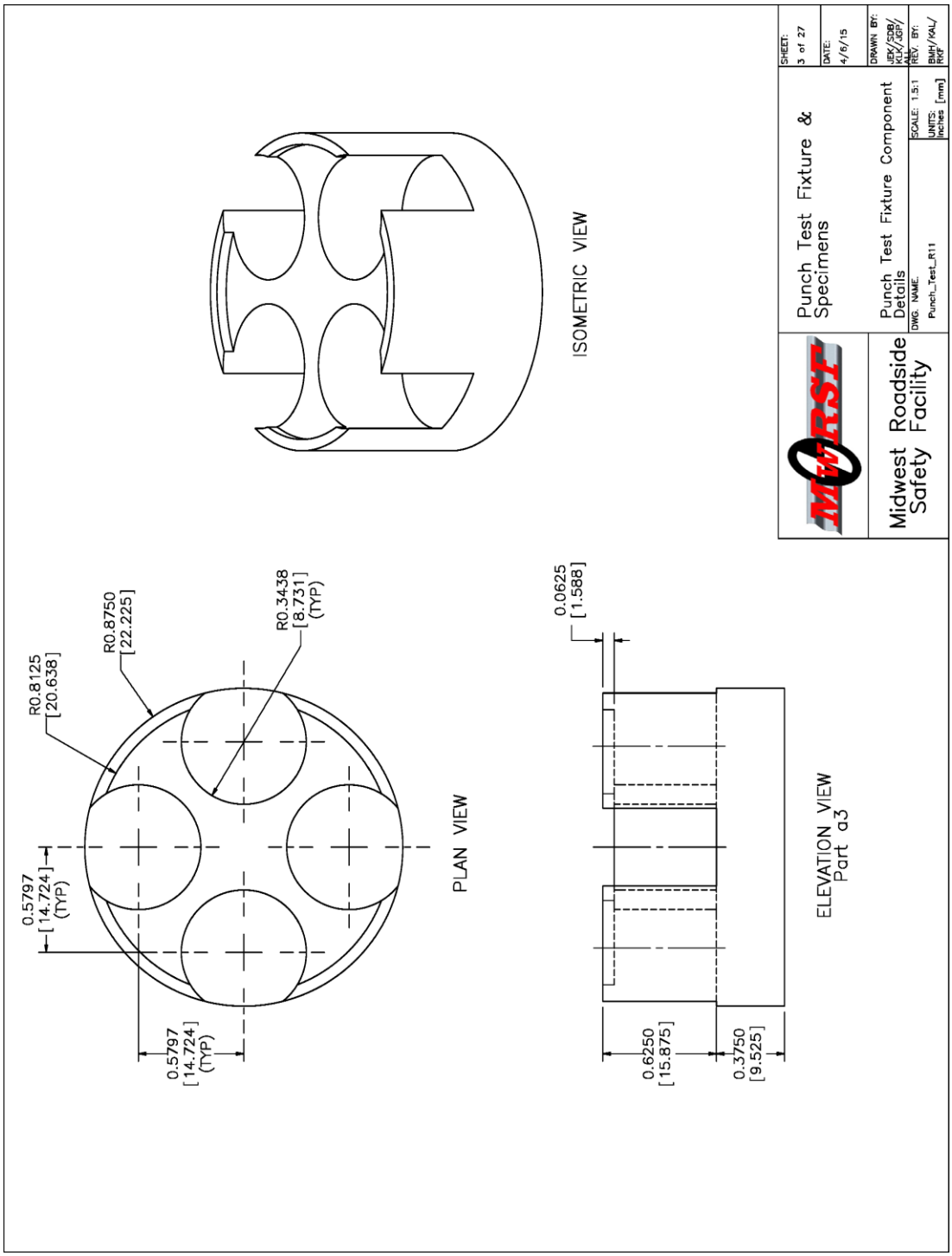

Figure 56. Punch Test Fixture Component Details

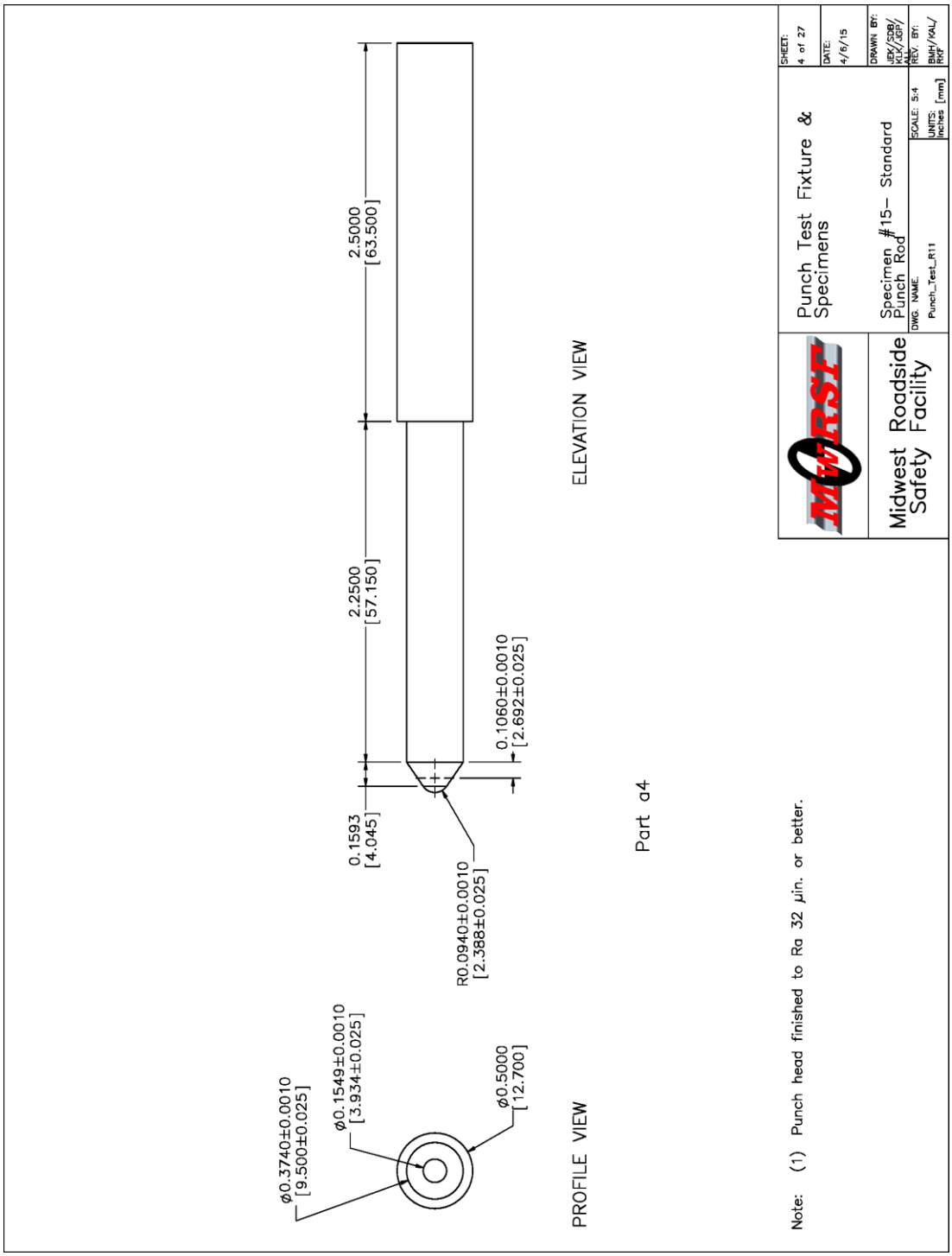

Figure 57. Specimen No. 15 – Standard Punch Rod

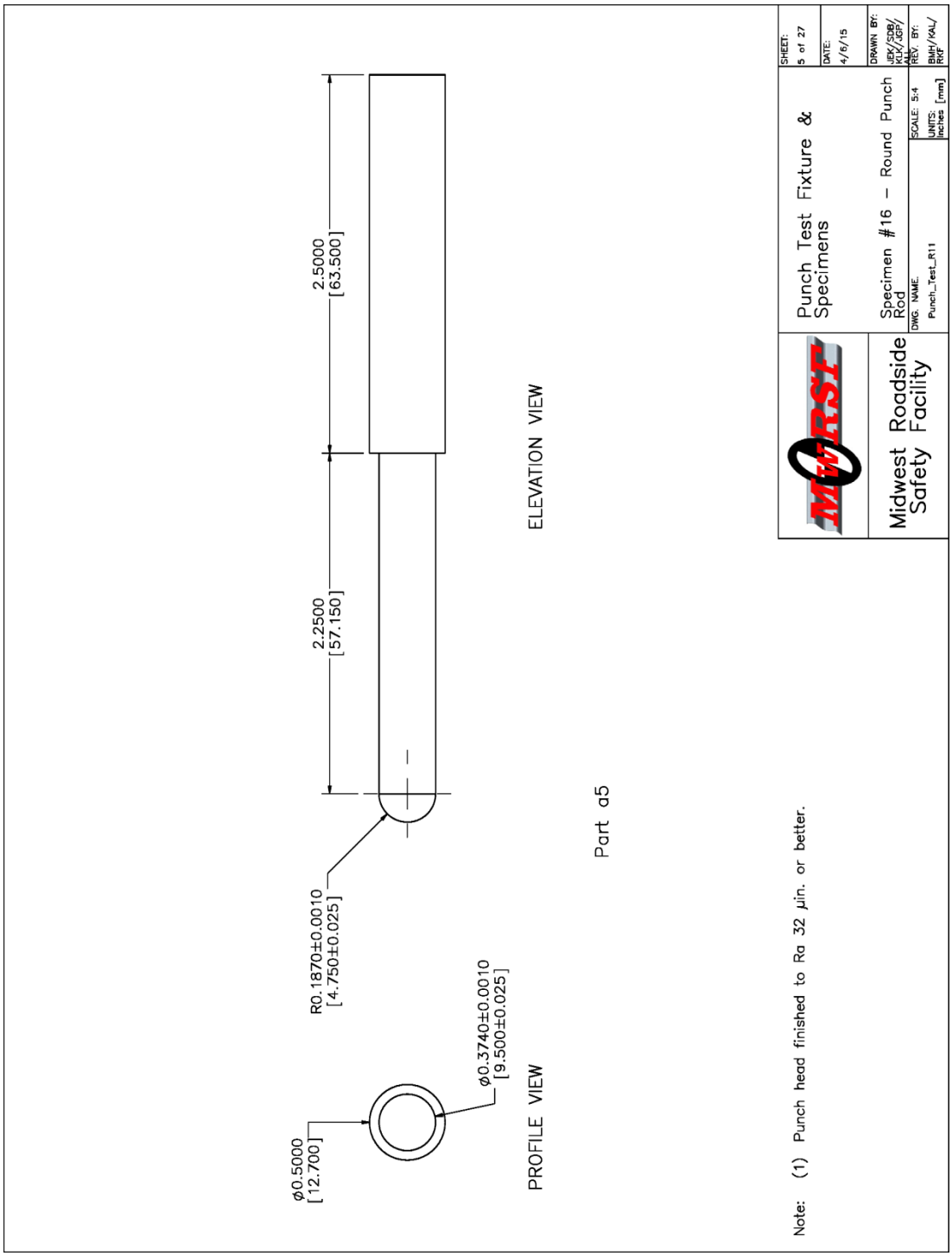

Figure 58. Specimen No. 16 – Round Punch Rod

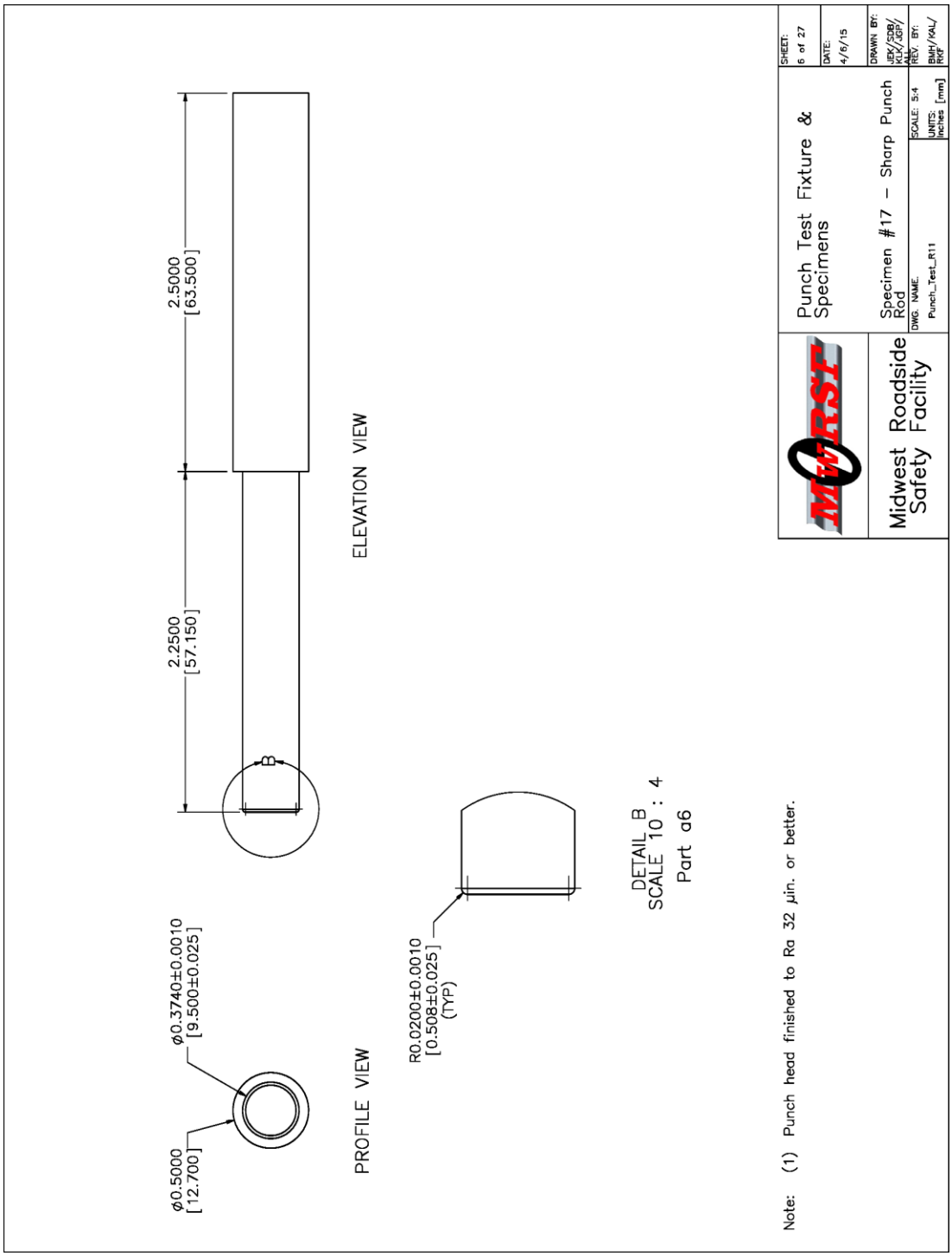

Figure 59. Specimen No. 17 – Sharp Punch Rod

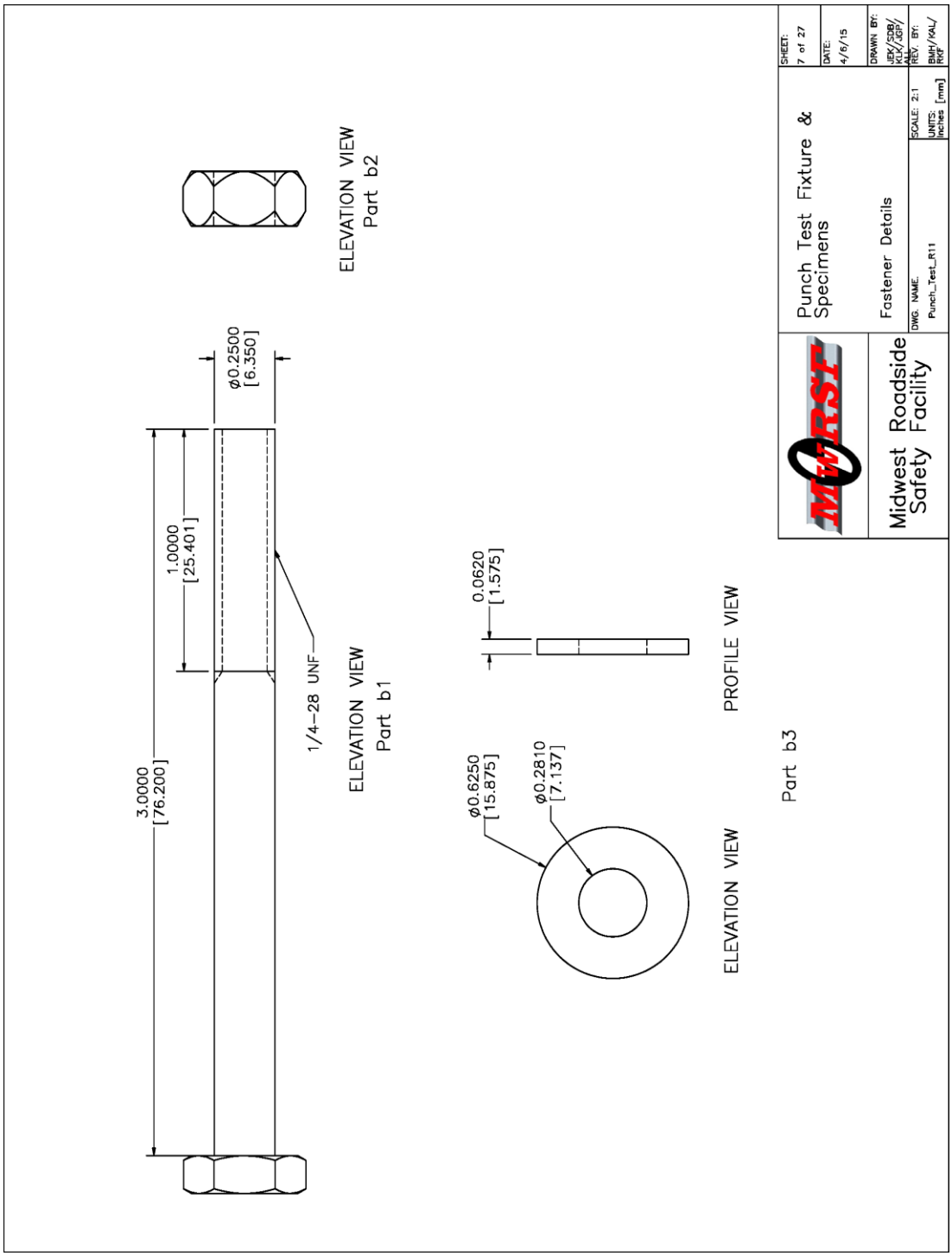

Figure 60. Fastener Details

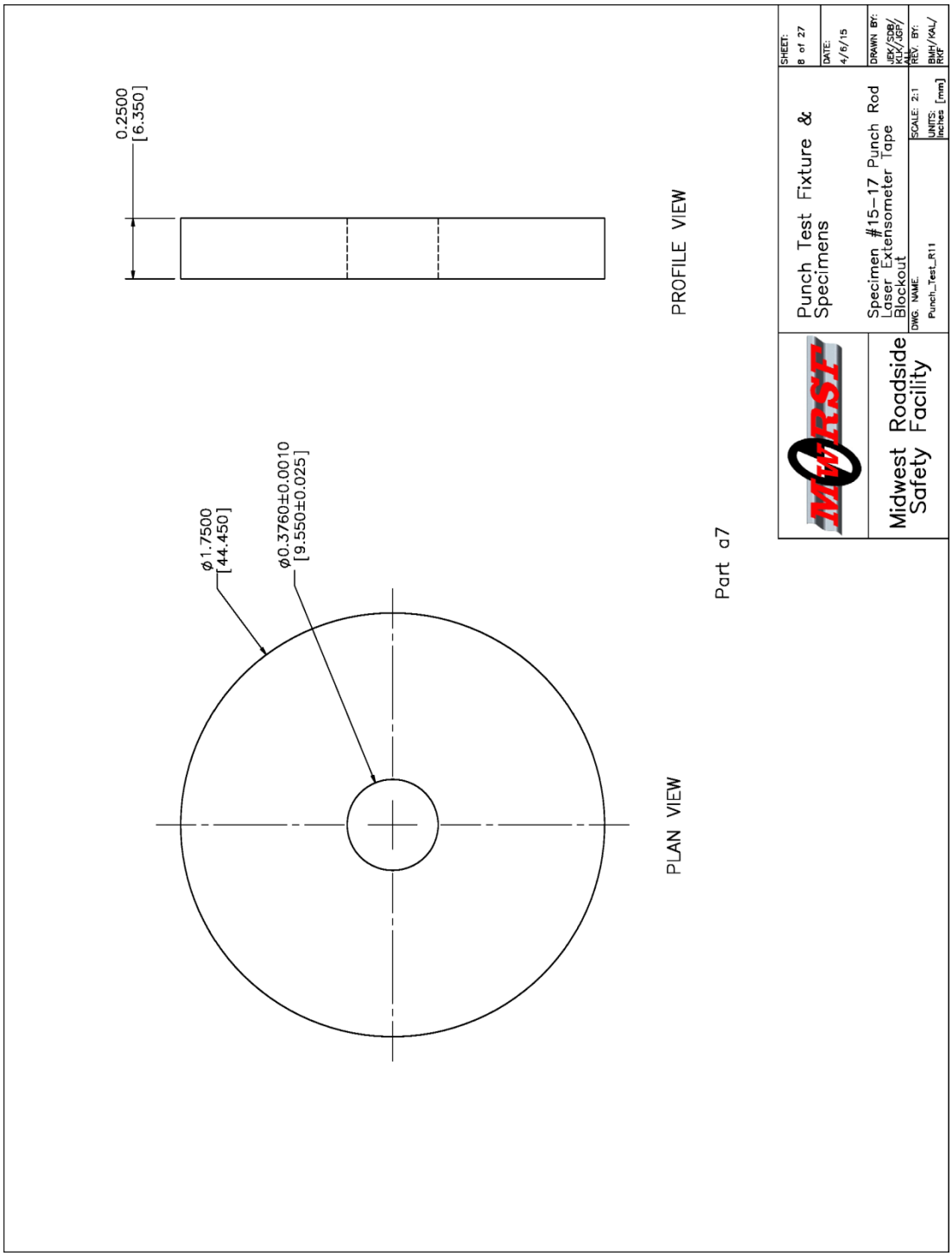

Figure 61. Specimen Nos. 15-17 Punch Rod Laser Extensometer Tape Blockout

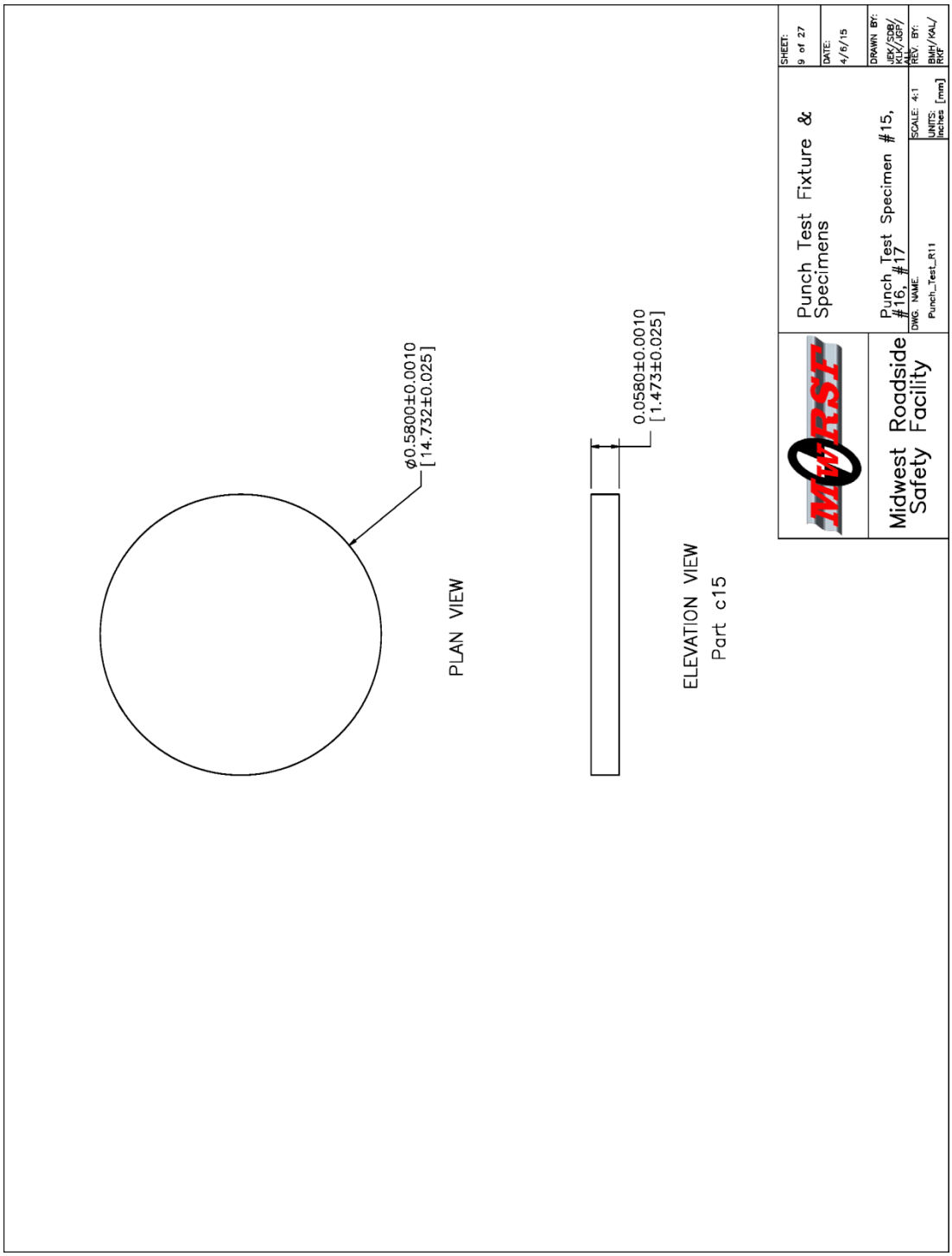

Figure 62. Punch Test Specimen Nos. 15-17

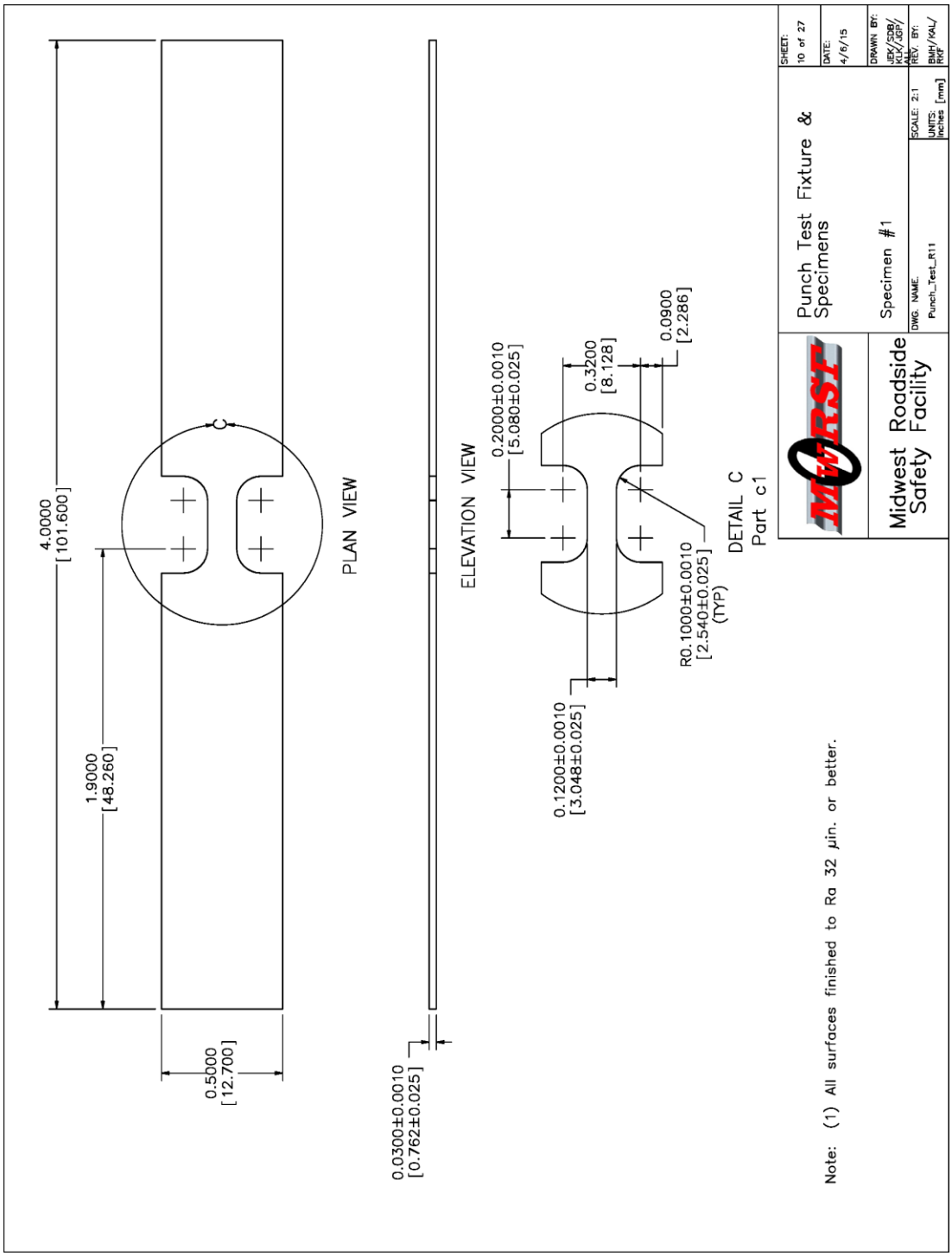

Figure 63. Specimen No. 1

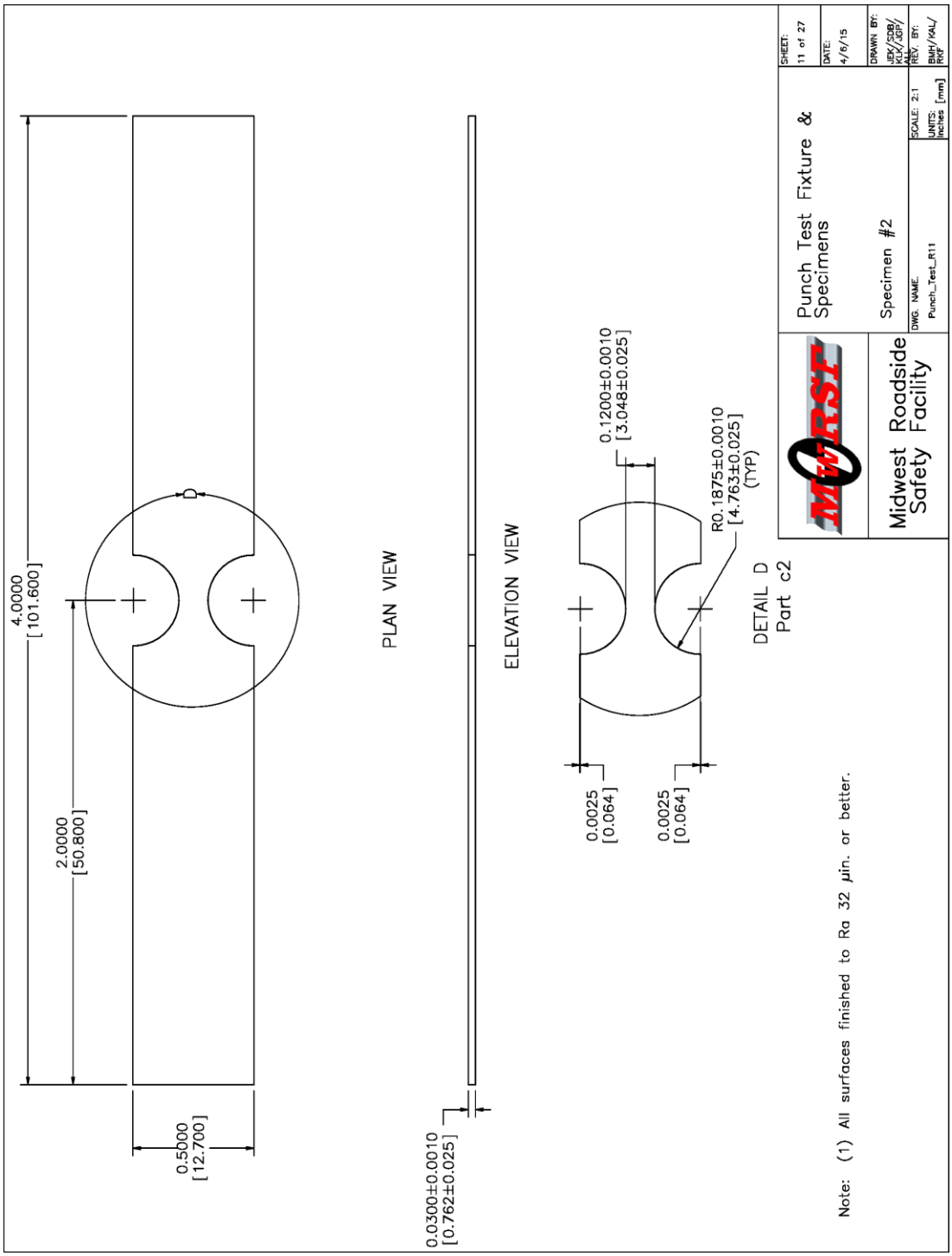

Figure 64. Specimen No. 2

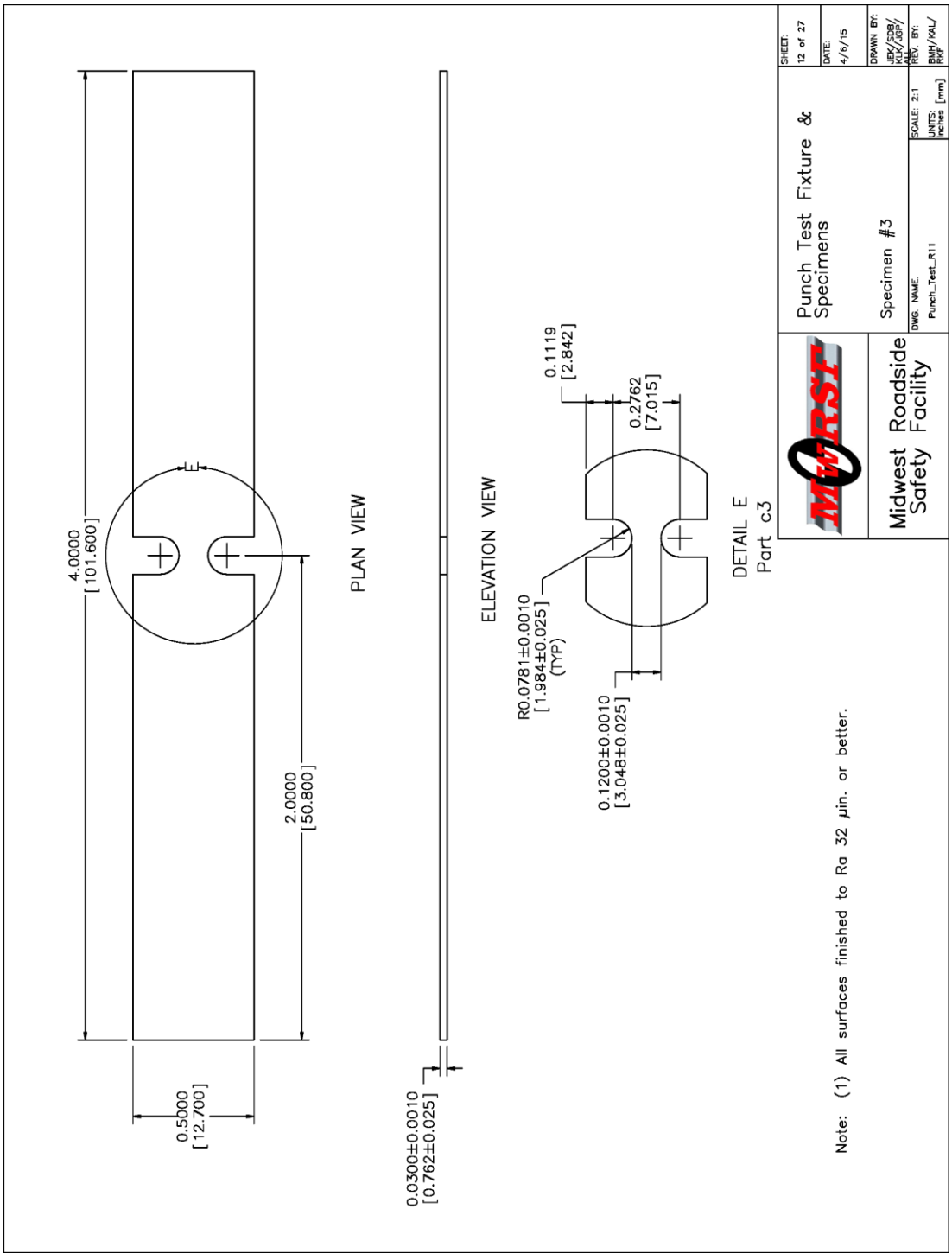

Figure 65. Specimen No. 3

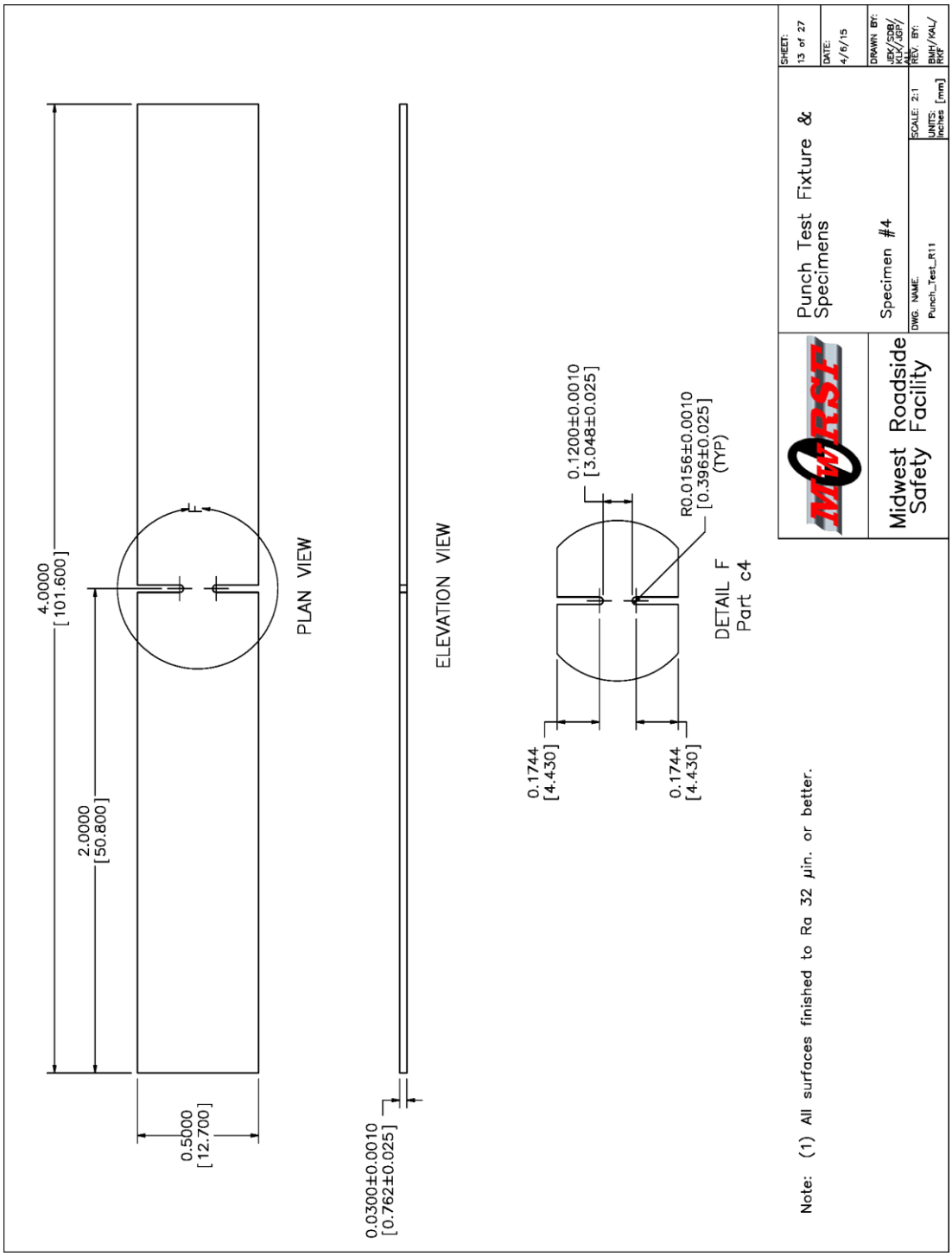

Figure 66. Specimen No. 4

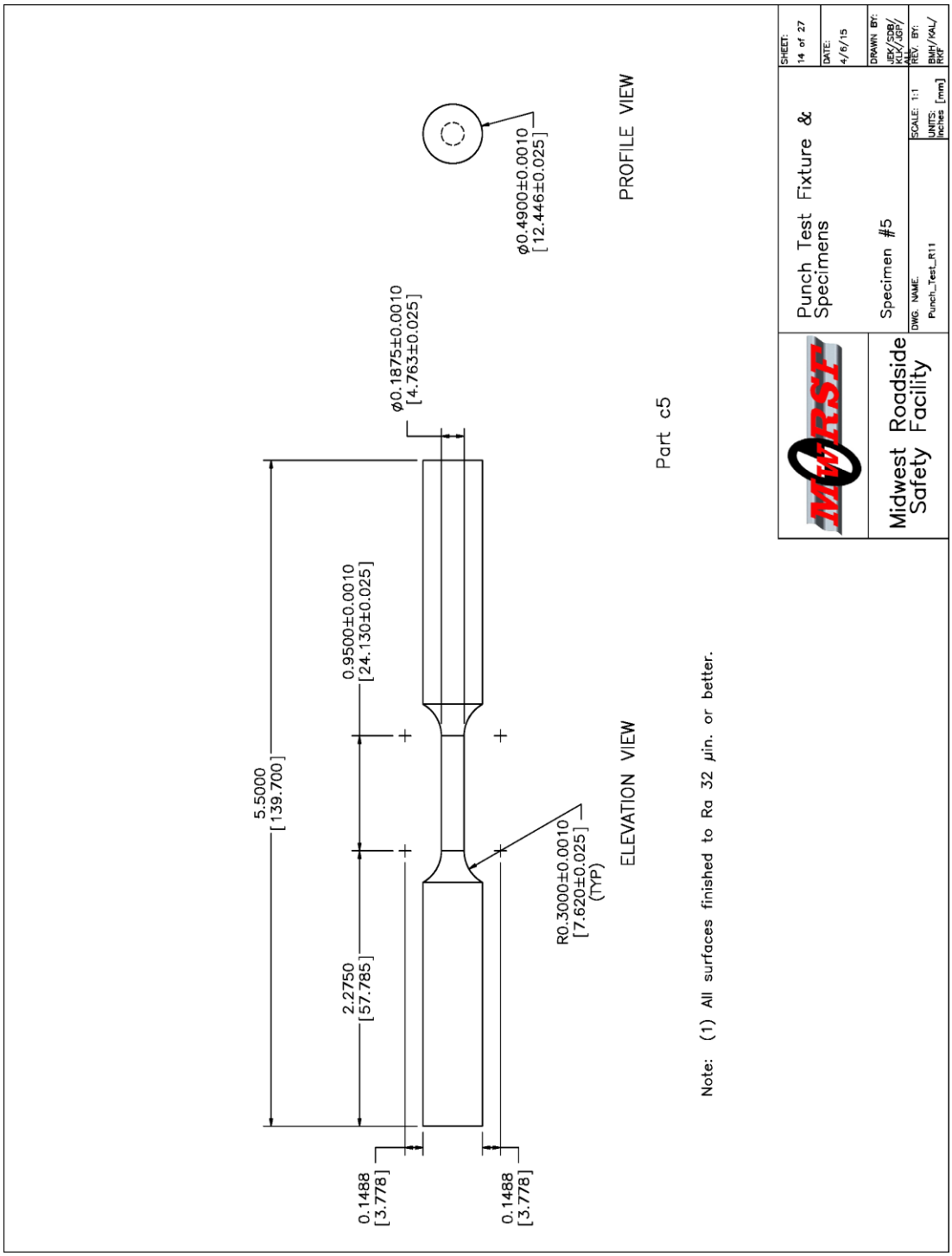

Figure 67. Specimen No. 5

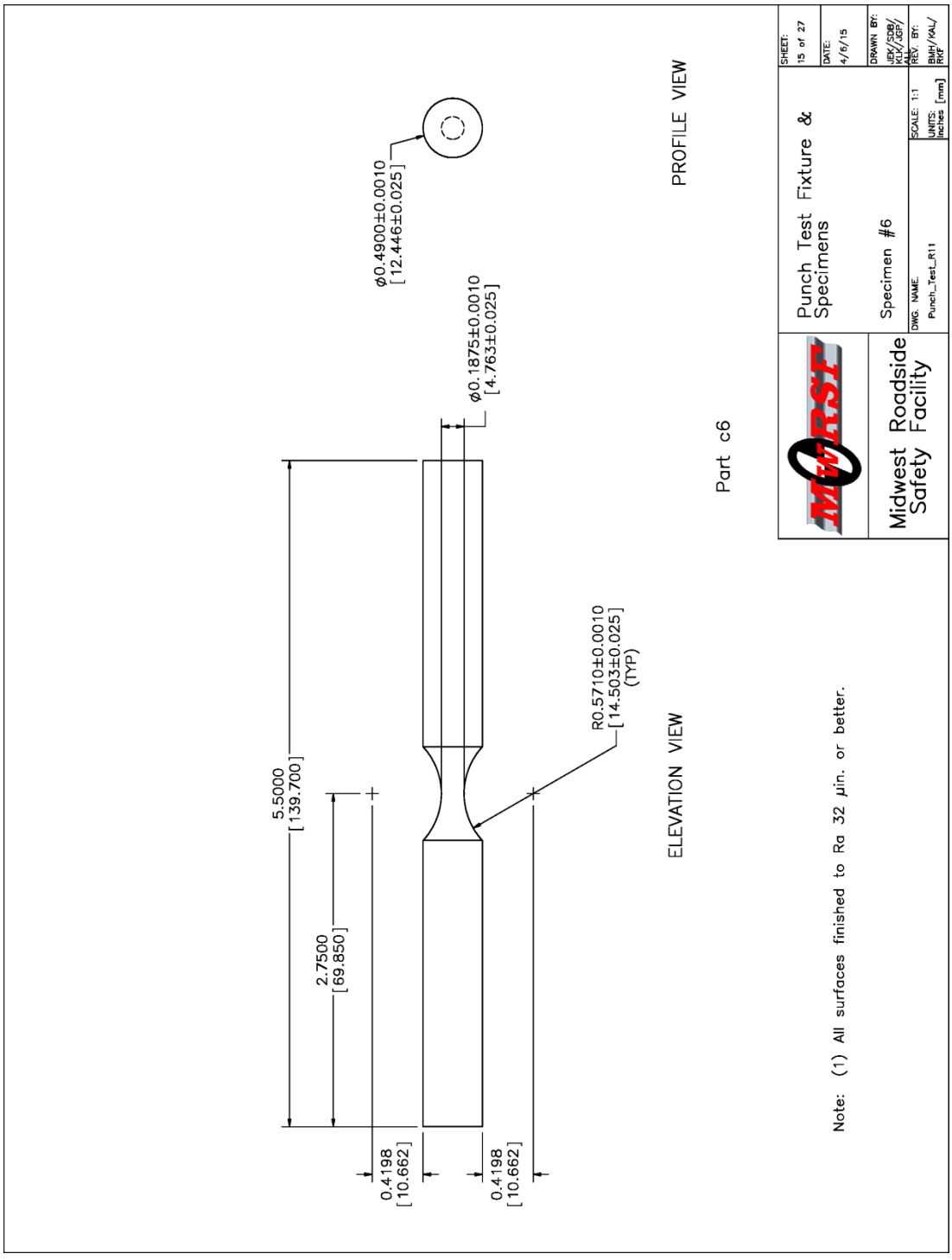

Figure 68. Specimen No. 6

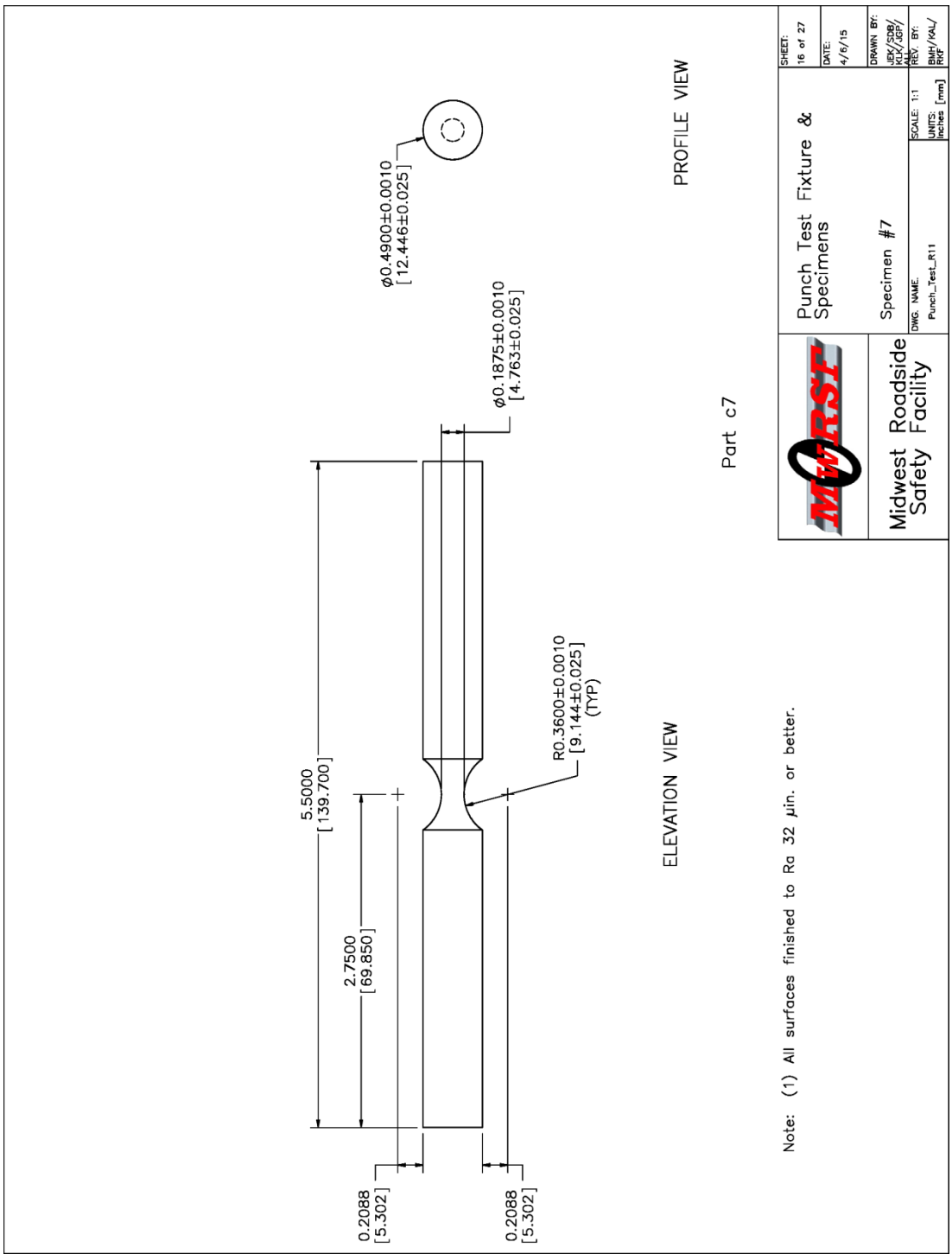

Figure 69. Specimen No. 7

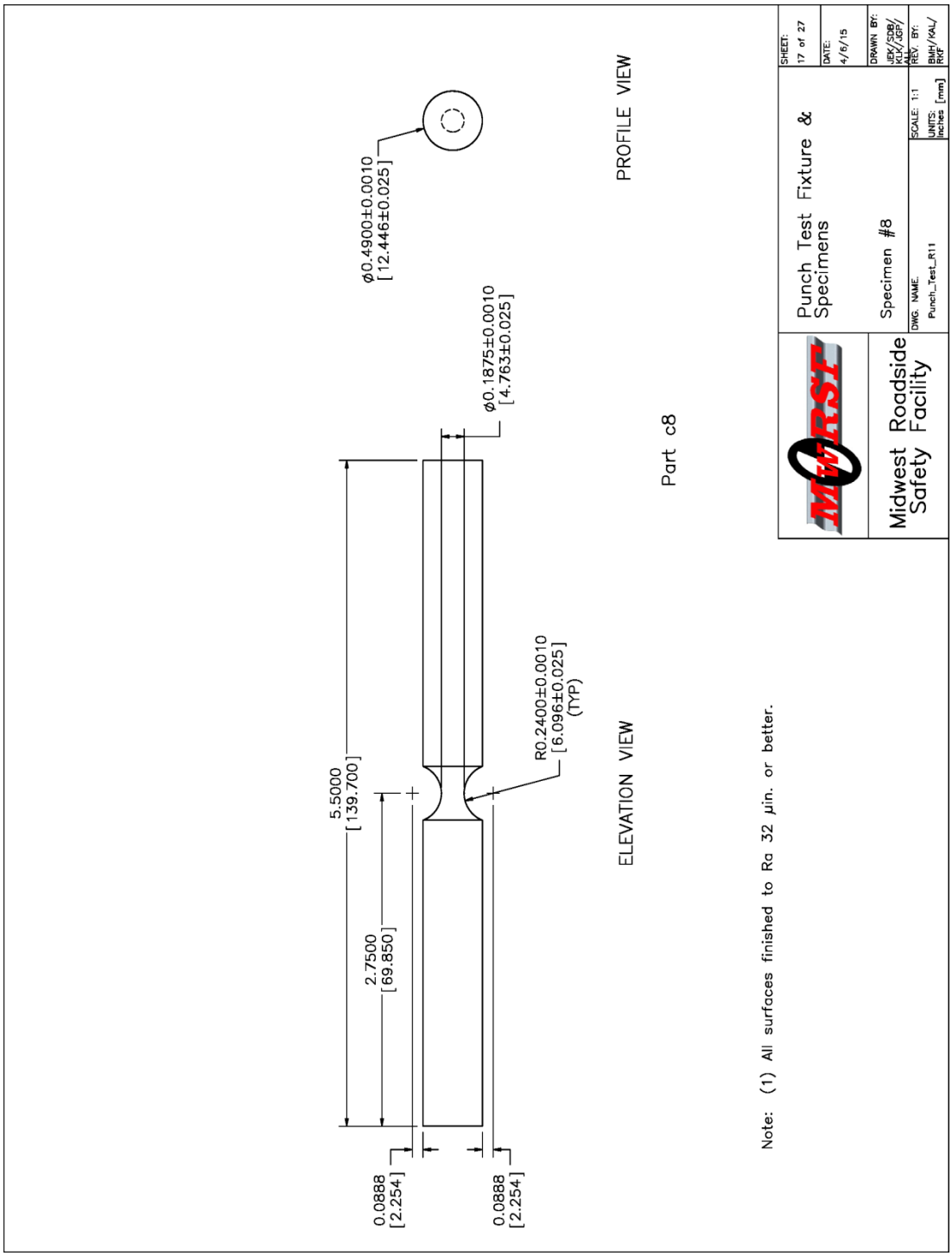

Figure 70. Specimen No. 8

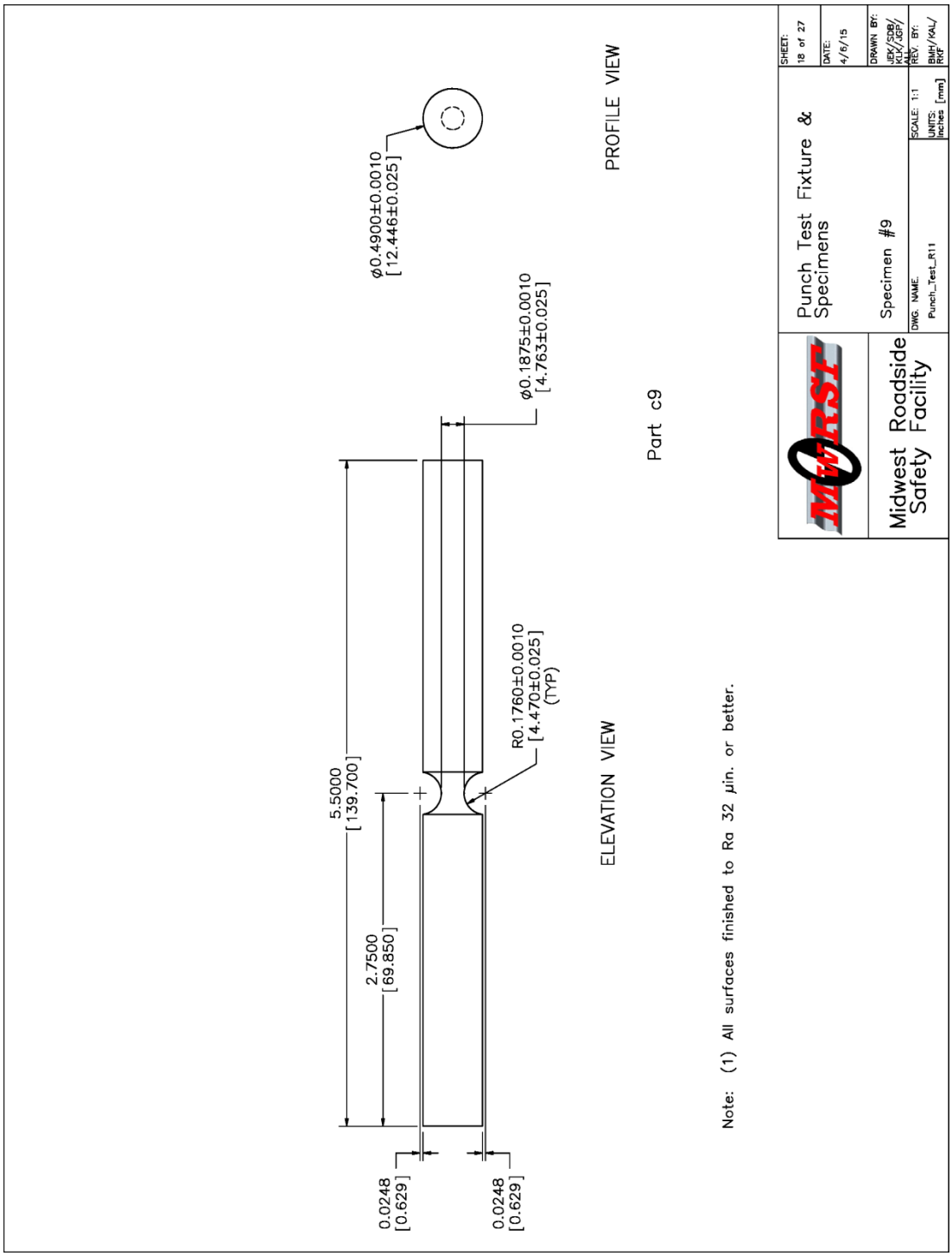

Figure 71. Specimen No. 9

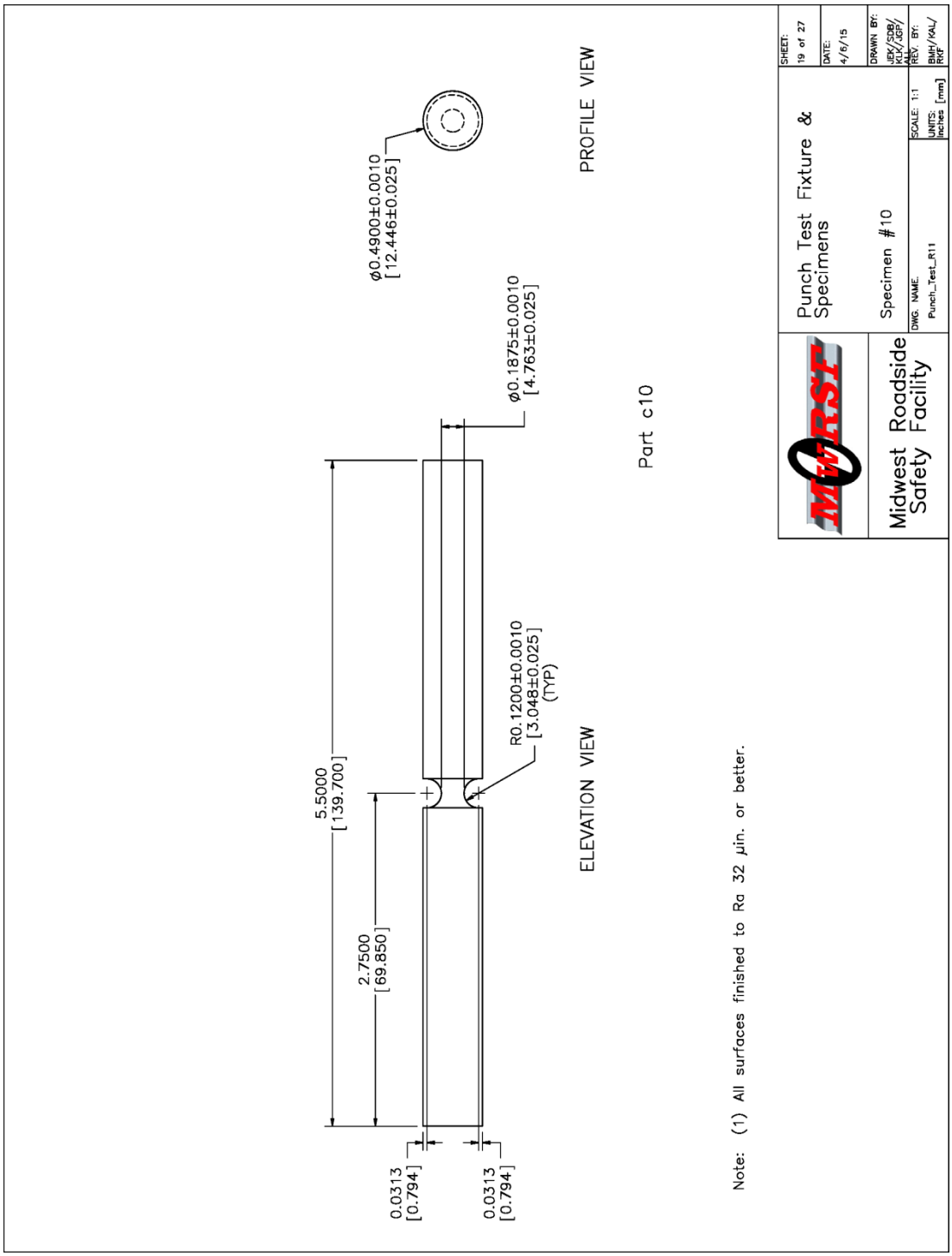

Figure 72. Specimen No. 10

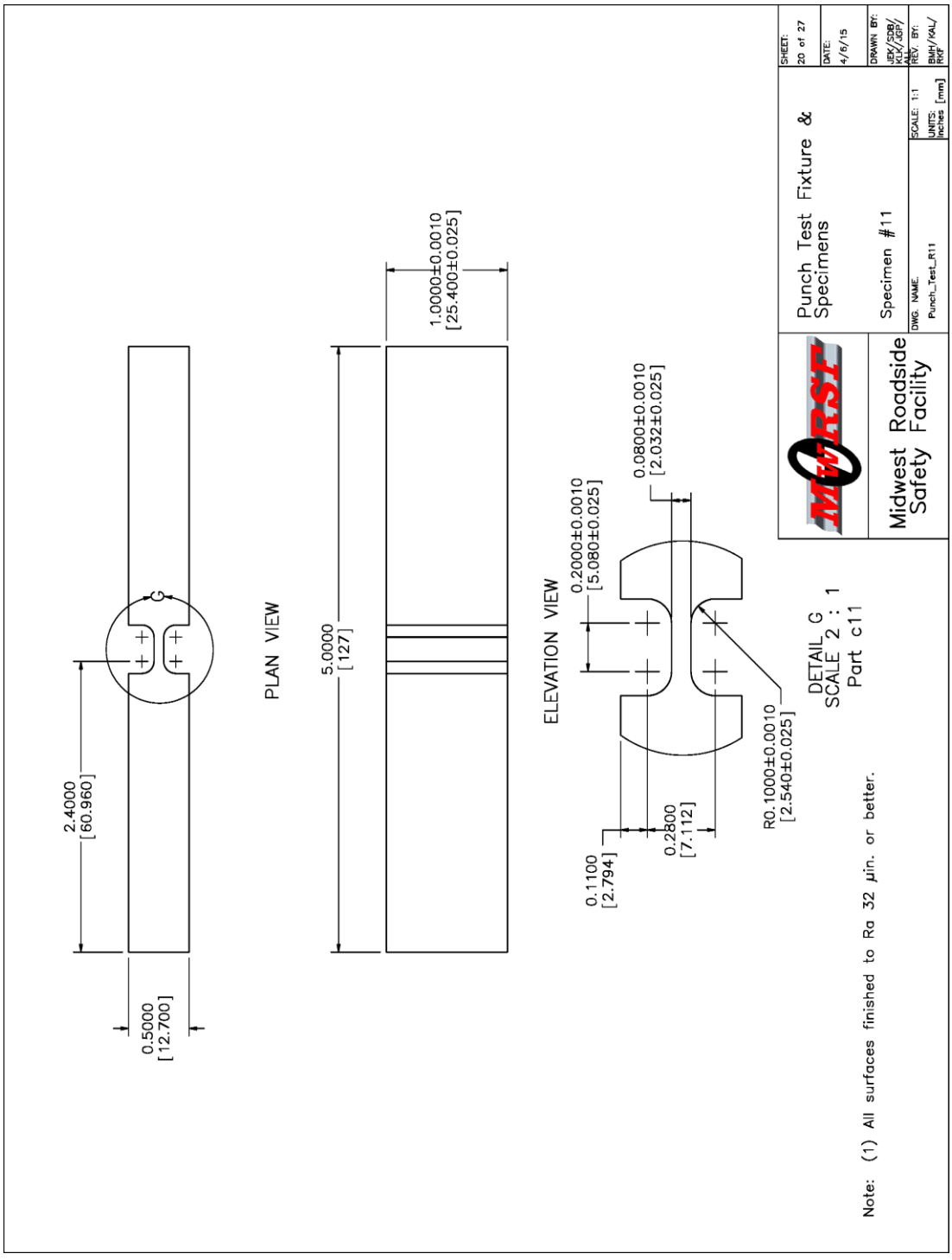

Figure 73. Specimen No. 11

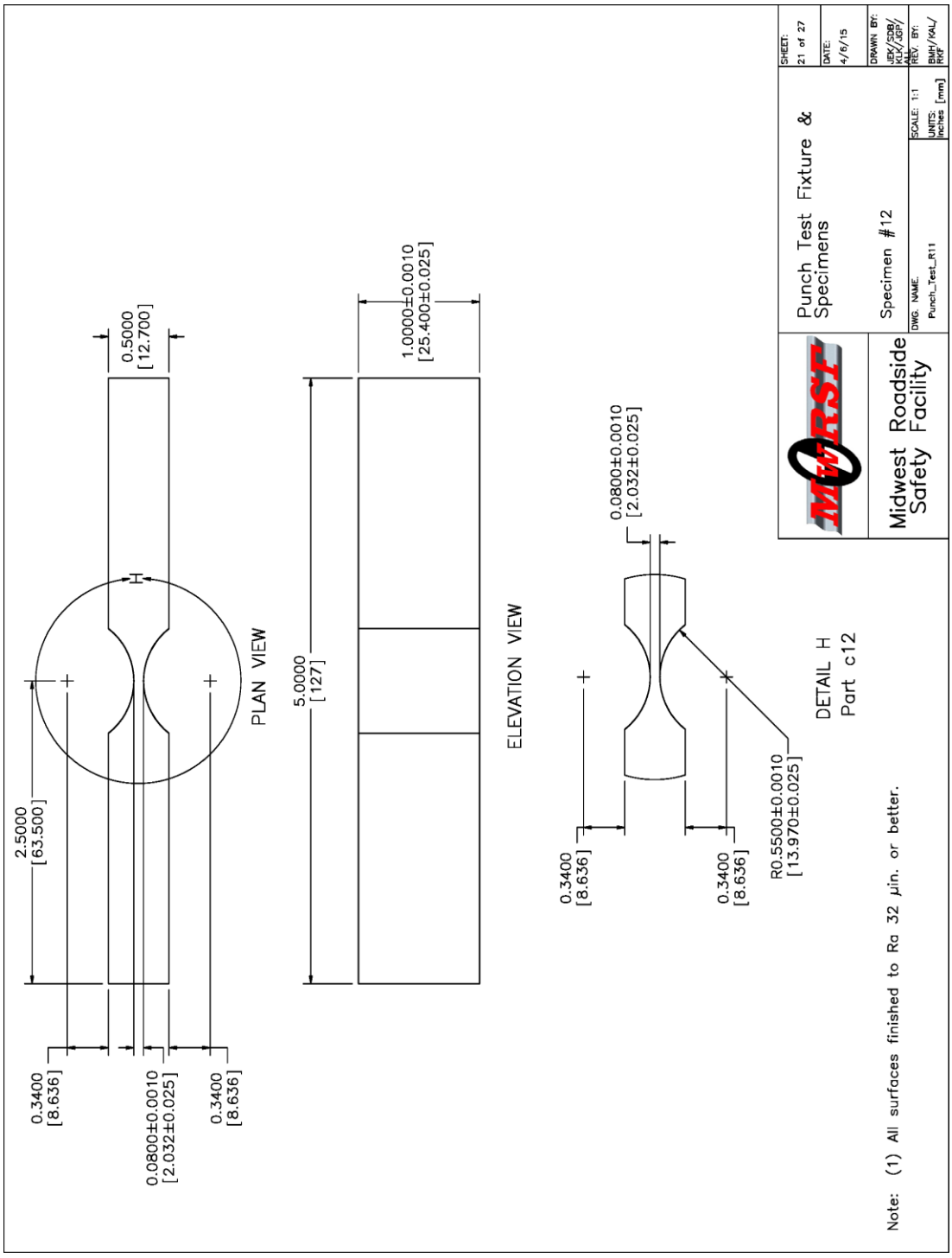

Figure 74. Specimen No. 12

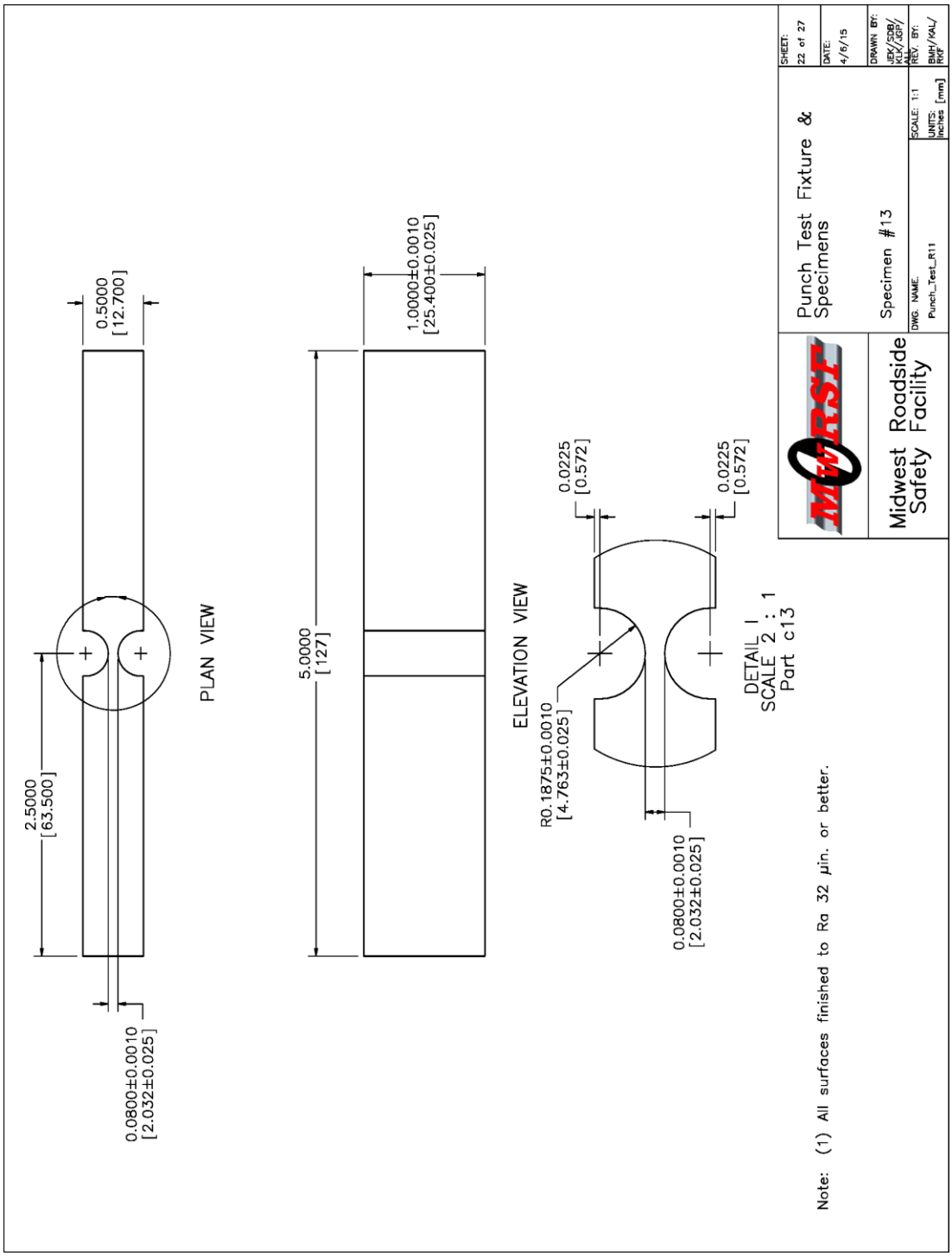

Figure 75. Specimen No. 13

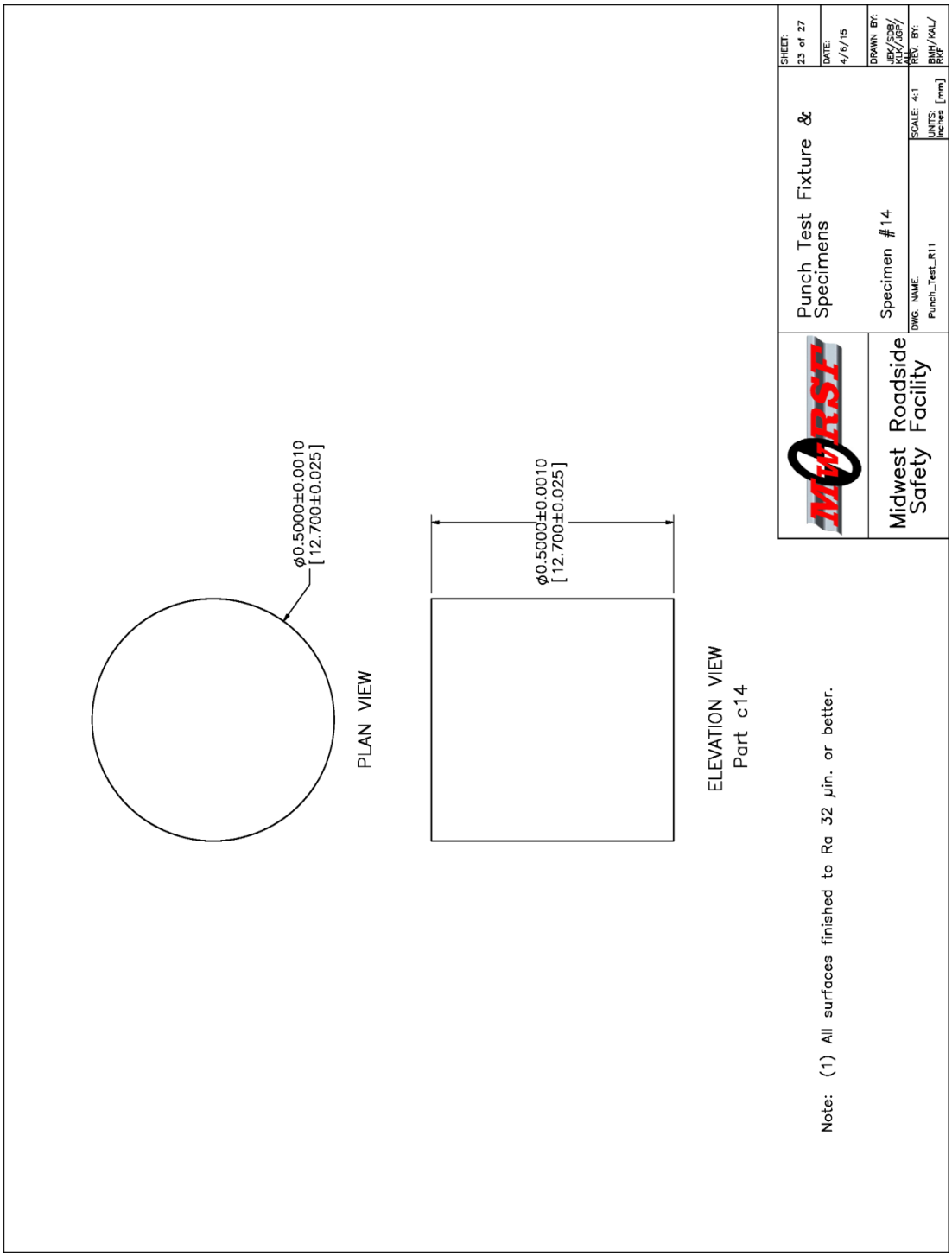

Figure 76. Specimen No. 14

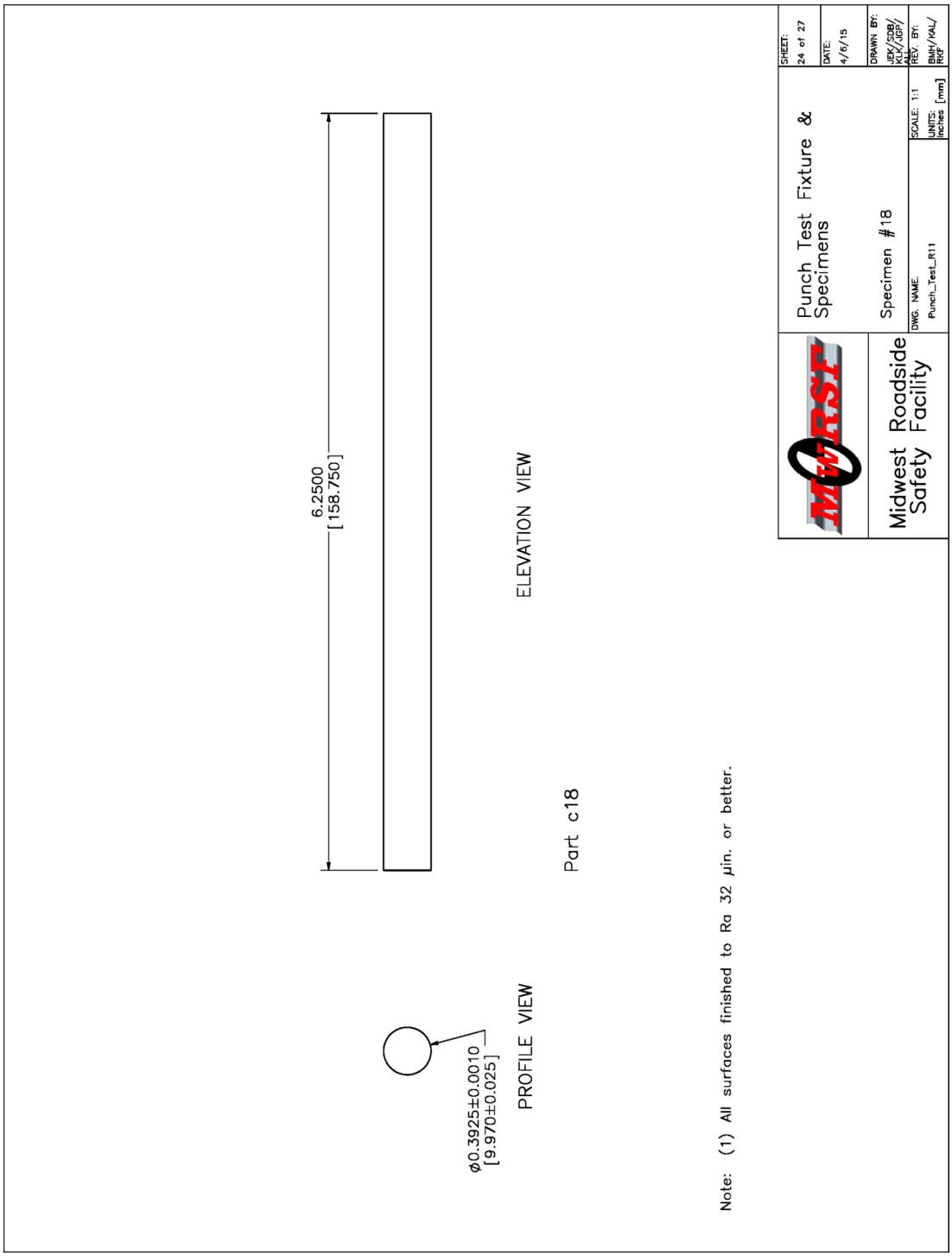

Figure 77. Specimen No. 18

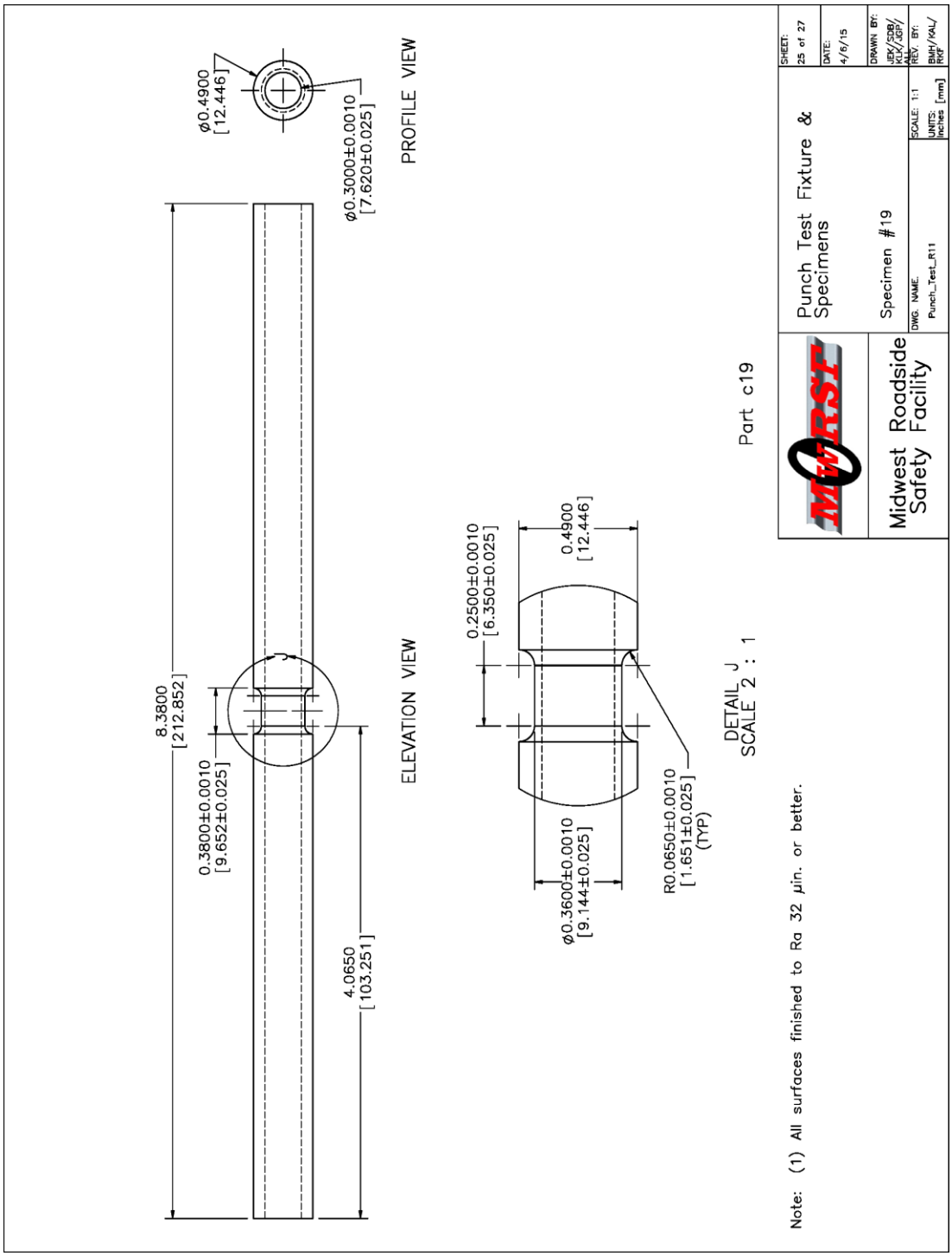

Figure 78. Specimen No. 19

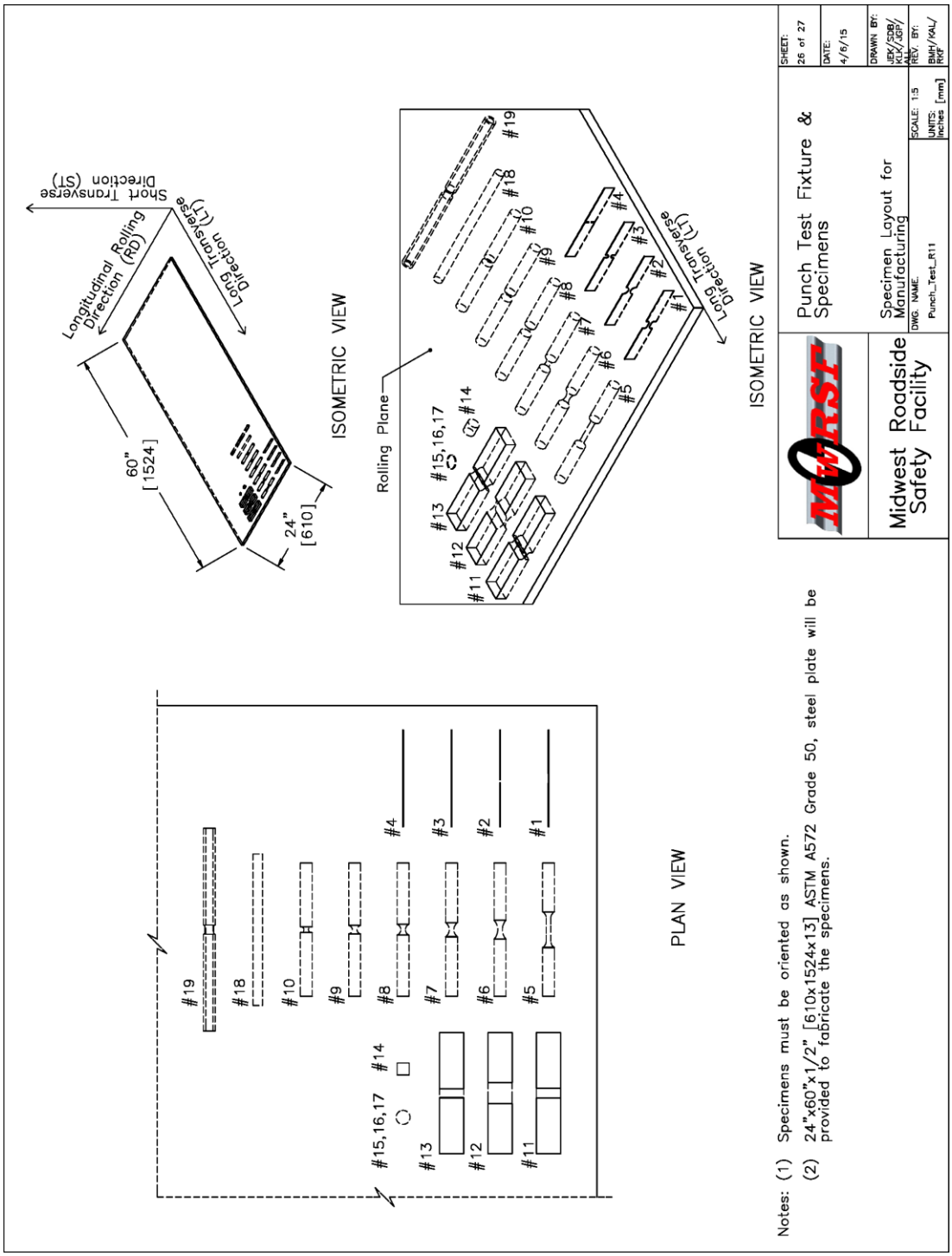

Figure 79. Specimen Layout for Manufacturing

Item No.	QTY.	Description	Material Spec
a1	2	Punch Test Fixture Top	01 Tool Steel
a2	2	Punch Test Fixture Center	01 Tool Steel
a3	2	Punch Test Fixture Base	01 Tool Steel
a4	2	Specimen #15 – Standard Punch Rod	01 Tool Steel
a5	2	Specimen #16 – Round Punch Rod	01 Tool Steel
a6	2	Specimen #17 – Sharp Punch Rod	01 Tool Steel
a7	6	Specimen #15–17 Punch Rod Laser Extensometer Tape Blockout	ASTM A36
b1	4	1/4" [6] Dia. UNF, 3" [76] Long Hex Bolt	SAE J429 Grade 5/ASME B18.2.1
b2	8	1/4" [6] Dia. UNF Hex Nut	SAE J995 Grade 5/ASME B18.2.2
b3	16	1/4" [6] SAE Flat Washer	ASTM F436
c1	40	Specimen #1	ASTM A572 Grade 50 (Material Provided)
c2	6	Specimen #2	ASTM A572 Grade 50 (Material Provided)
c3	6	Specimen #3	ASTM A572 Grade 50 (Material Provided)
c4	6	Specimen #4	ASTM A572 Grade 50 (Material Provided)
c5	6	Specimen #5	ASTM A572 Grade 50 (Material Provided)
c6	6	Specimen #6	ASTM A572 Grade 50 (Material Provided)
c7	6	Specimen #7	ASTM A572 Grade 50 (Material Provided)
c8	6	Specimen #8	ASTM A572 Grade 50 (Material Provided)
c9	6	Specimen #9	ASTM A572 Grade 50 (Material Provided)
c10	6	Specimen #10	ASTM A572 Grade 50 (Material Provided)
c11	6	Specimen #11	ASTM A572 Grade 50 (Material Provided)
c12	6	Specimen #12	ASTM A572 Grade 50 (Material Provided)
c13	6	Specimen #13	ASTM A572 Grade 50 (Material Provided)
c14	6	Specimen #14	ASTM A572 Grade 50 (Material Provided)
c15	25	Punch Test Specimen #15–17	ASTM A572 Grade 50 (Material Provided)
c18	6	Specimen #18	ASTM A572 Grade 50 (Material Provided)
c19	6	Specimen #19	ASTM A572 Grade 50 (Material Provided)

MWRSF

Midwest Roadside Safety Facility

Punch Test Fixture & Specimens

Punch Test Fixture and Specimens Bill of Materials

DWG. NAME. Punch_Test_R11

SCALE: 1:2

UNITS: Inches [mm]

SHEET: 27 of 27

DATE: 4/6/15

DRAWN BY: JEK/SDB/ KLK/JGP/ AH

REV. BY: BMH/KAL/ RKF

Figure 80. Punch Test Fixture and Specimens Bill of Materials

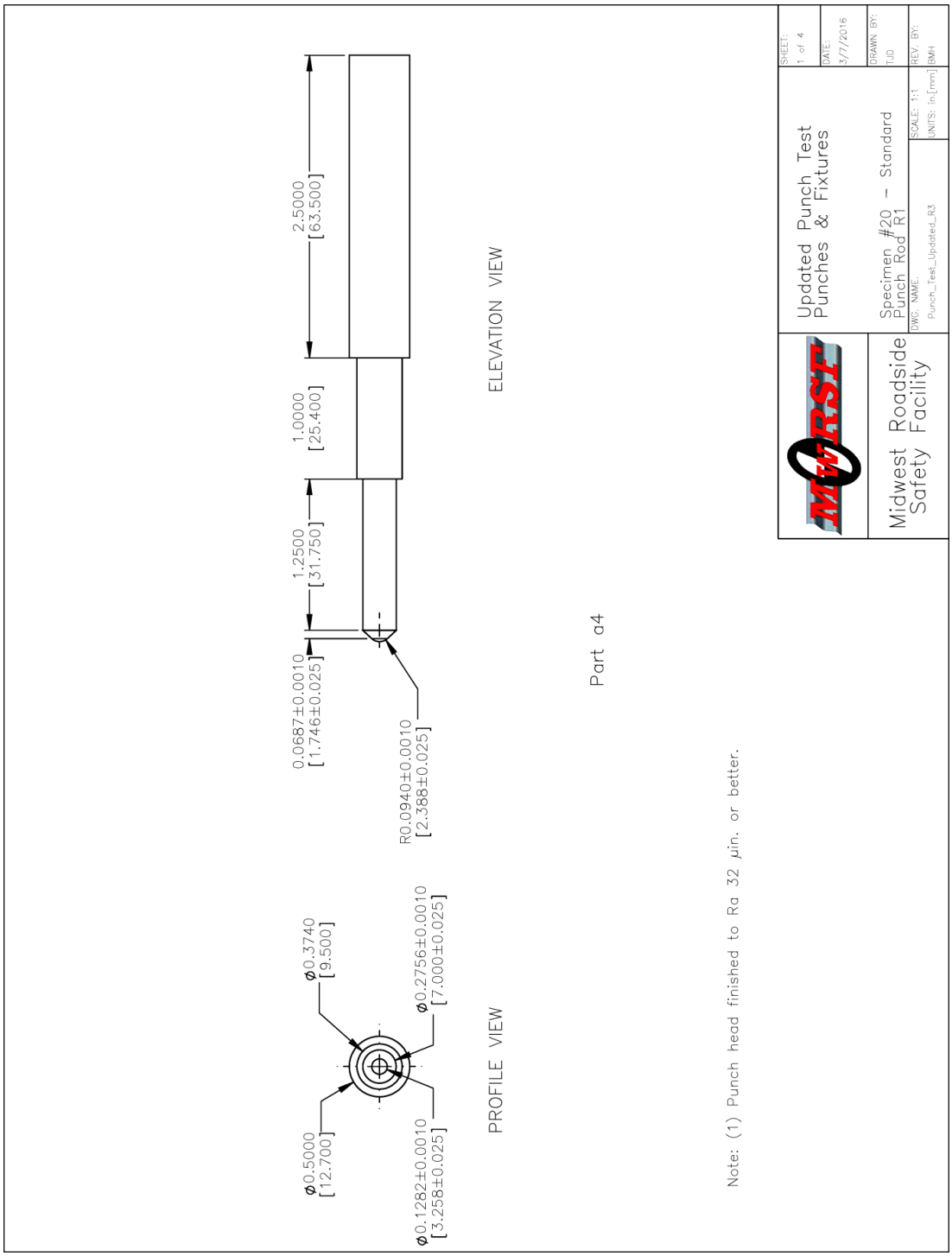

Figure 81. Specimen No. 20 Standard Punch Rod R1

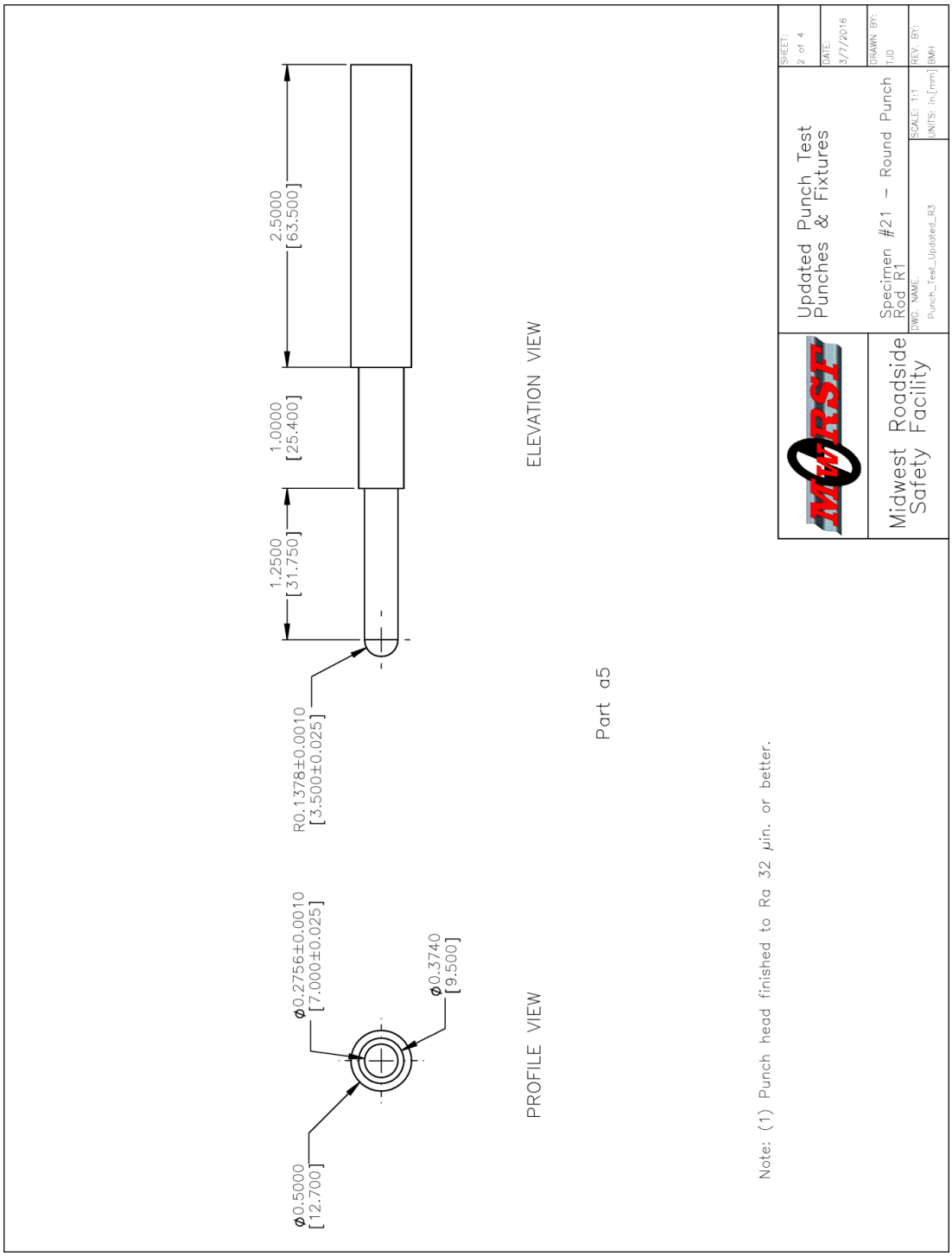

Figure 82. Specimen No. 21 Round Punch Rod R1

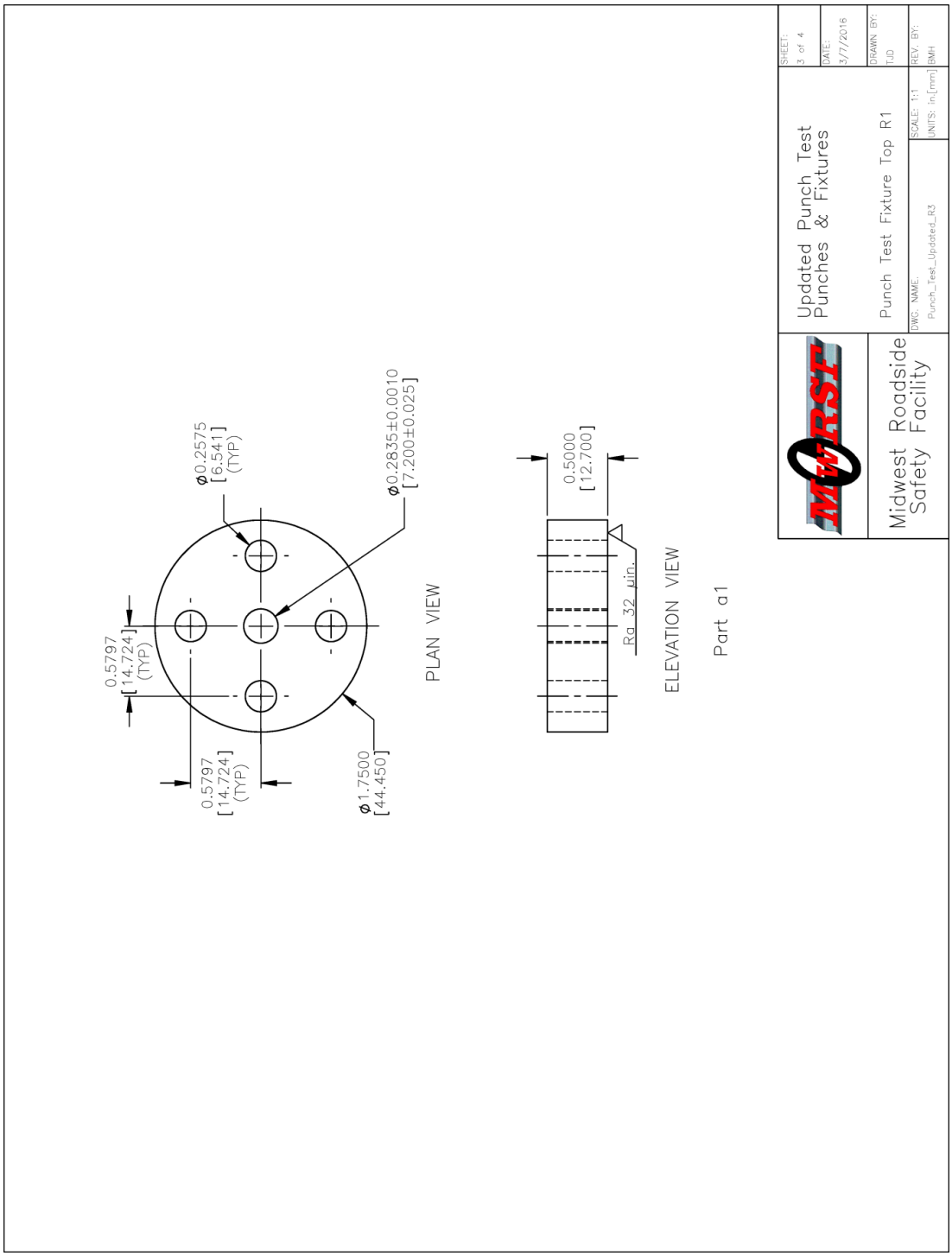

Figure 83. Punch Test Fixture Top R1

Item No.	QTY.	Description	Material Spec
a1	1	Punch Test Fixture Top	A-2 Tool Steel Hardened to 55 HRC
a4	2	Specimen #20 - Standard Punch Rod	A-2 Tool Steel Hardened to 55 HRC
a5	2	Specimen #21 - Round Punch Rod	A-2 Tool Steel Hardened to 55 HRC

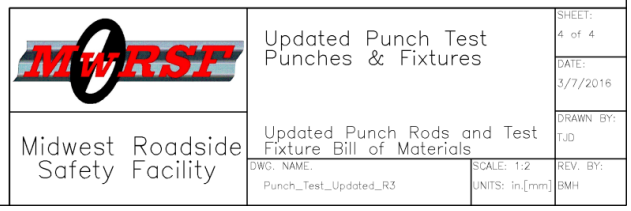

Figure 84. Updated Punch Rods and Test Fixture Bill of Materials

5.4 Equipment and Instrumentation

5.4.1 Load Frames

Three load frames were utilized during testing. The selection of each load frame depended on the specimen size, loading type, and fixture required for testing.

5.4.1.1 22-kip Landmark Fatigue Testing System

The 22-kip Landmark Fatigue Testing System is a servo hydraulic testing frame manufactured by MTS Systems Corporation, as seen in Figure 85. The platform was designed to perform static and dynamic testing including: durability; fatigue crack growth; high cycle fatigue; low cycle fatigue; fracture toughness; tension; compression; and others. The 370 series load frame includes an axial actuator powered by a SilentFlo Model 505 hydraulic power unit (HPU) with a FlexTest 40 controller. The actuator is rated at 22 kip (100 kN) with a dynamic stroke of 10 in. (250 mm). The software, TestsWorks Elite, was used to design, run, and report the tests.

Both compression platens and hydraulic wedge grips were used during testing. The compression platens, model no. 643.15B-02 are rated with maximum dynamic and static pressures of 40 and 100 ksi (276 and 690 MPa), respectively. The servo-hydraulic wedge grips, model no. 647.10A, are rated with maximum dynamic and static grip forces of 22 and 27 kip (100 and 120 kN), respectively. Integrated hydraulic grip controls are available with up to 3,000 psi (21 MPa) grip pressure. Various flat diamond tip and SurfAlloy surface grips as well as numerous serrated-vee grips were used. Threaded mounts were custom made from 17-4 PH H1150 Stainless steel to allow the compression platens to be installed without the need to remove the servo-hydraulic wedge grips. One

end of the mount was threaded into the compression platen and the mount was gripped with the appropriately sized serrated-vee grips.

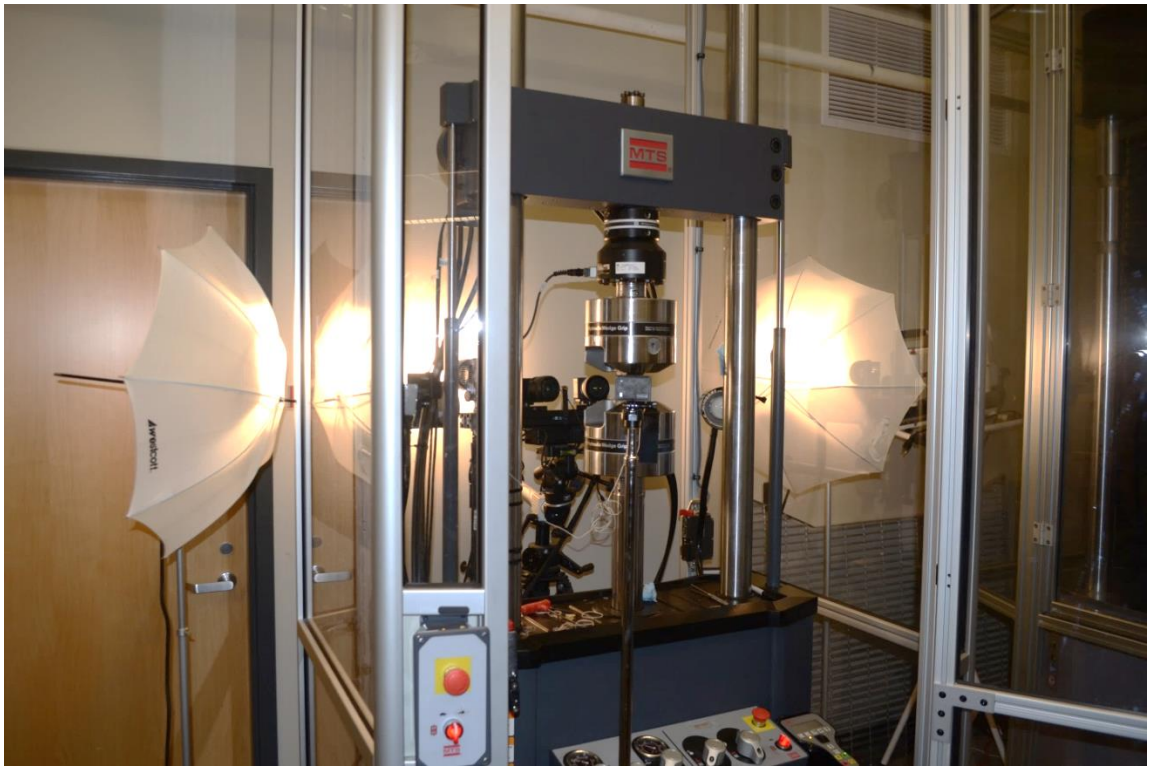

Figure 85. Landmark 22-kip Load Frame

5.4.1.2 220-kip Criterion Static Testing System

The 220-kip Criterion Static Testing System is a servo-hydraulic testing frame manufactured by MTS Systems Corporation. The platform was designed to perform high load static testing. The six column load frame includes tension and compression test zones capable of a maximum load of 220 kip (1,000 kN). For this testing, only the compression zone was used. The series 60 integrated operations platform includes a hydraulic power unit, system electronics and digital controls, and a computer controlling the testing system with the "TestSuite TW Elite" software.

Figure 86. Criterion 220-kip Load Frame

5.4.1.3 Torsion Frame

A torsion frame, manufactured by Tinius Olsen & Company of Philadelphia, was used to test the torsion specimen, as seen in Figure 87. Electric motors were available to apply torsion to the rotating head. However, a hand crank was used to apply a slower rotation rate to better detect when failure occurred. Torque measurements using a balance

beam were recorded during testing. However, the accuracy of the measurements could not be verified, so they were not reported. It should also be noted that the non-rotating head allowed some translational movement in the radial direction and some pivoting away from the central axial direction.

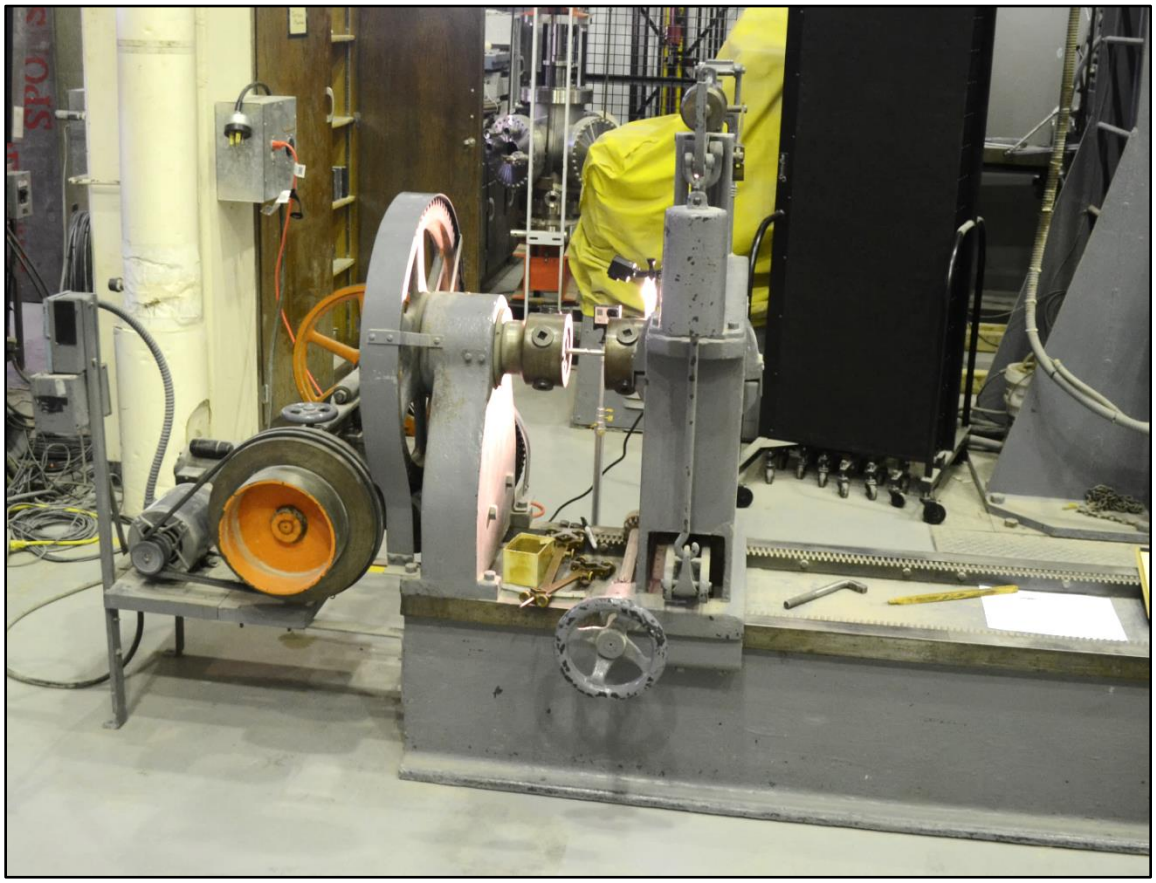

Figure 87. Torsion Load Frame

5.4.2 Data Acquisition Systems

5.4.2.1 Extensometers

Three different MTS Systems Corporation extensometers were utilized. The first two were axial extensometers. The first extensometer, model no. 634.25E-24, has a 2-in. (50.8-mm) gauge length with extensions ranges of -10 percent to 50 percent and is shown in Figure 88. The extensometer meets or exceeds calibration requirements according to

ASTM E83 Class B1 and ISO 9513 Class 0.5. The extensometer is designed to be left on through failure without damaging the unit. Knife edges were used with quick-attach spring clamps or rubber bands to hold onto the specimen. The second extensometer, model no. 632.11E-90, has a 1-in. (25.4-mm) gauge length with an overall travel distance of ±0.16 in. (±4.0 mm) and is shown in Figures 89 and 90. Knife edges were used with elastic bands to hold onto the specimen. The last extensometer was a LX 500 Laser Extensometer, as shown in Figure 90. The laser system utilized retro-reflective tape to reflect a parallel beam laser to measure the distance between the lower edges of two retro-reflective tape strips. These tape strips can be seen clearly in Figure 88. The scanner has a resolution of 0.0001 in. (0.001 mm), non-linearity of 0.0004 in. (0.009 mm), repeatability of 0.0002 in. (0.003 mm), and a minimum and maximum gauge length of 0.3 and 5 in. (8 and 127 mm), respectively. The system meets accuracy requirements as stated in ASTM E-83, class B1. Scan rates of 100 Hz with 2 scan averaging were used during testing.

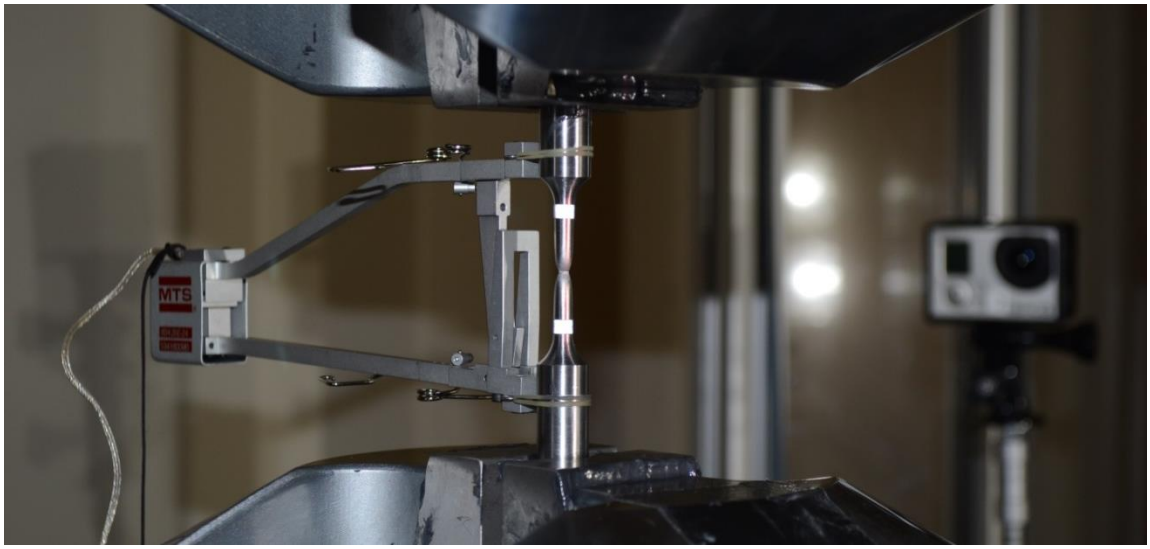

Figure 88. 2-in. Axial Extensometer and Retro-Reflective Laser Extensometer Tape on Specimen

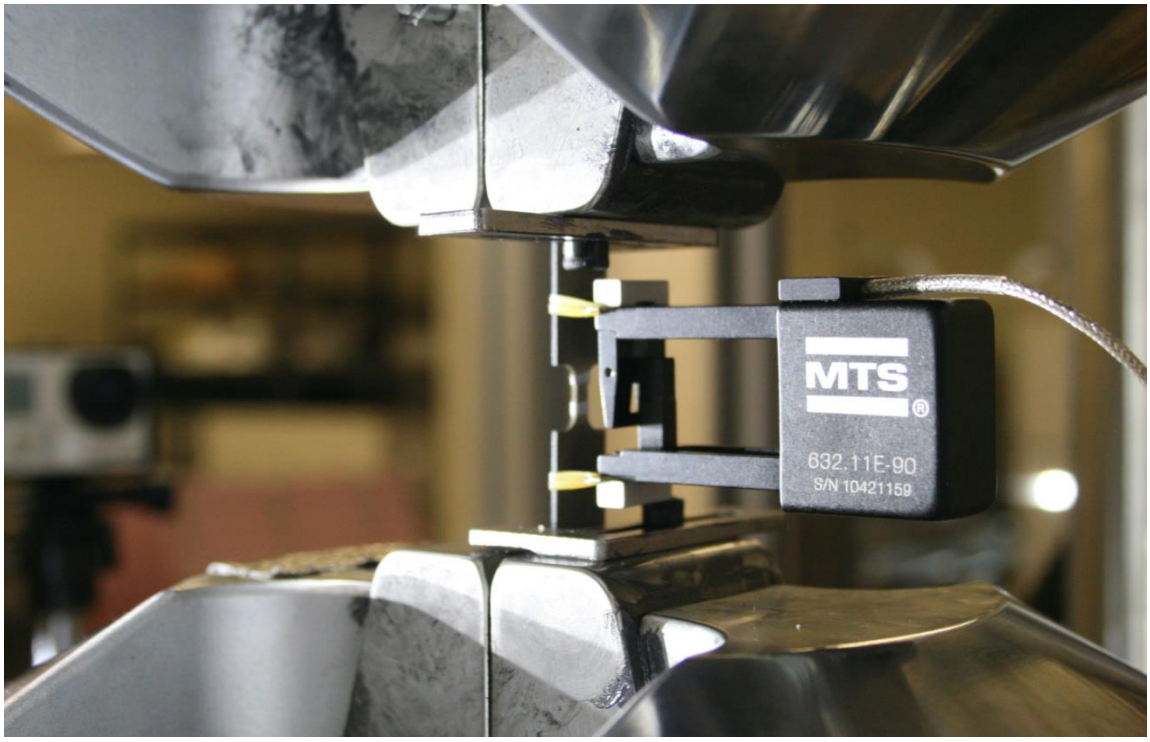

Figure 89. 1-in. Extensometer Attached to Specimen

Figure 90. Laser Extensometer on Mount with 1-in. Axial Extensometer Attached to Specimen

5.4.2.2 Load Cells

Three load cells were used during testing. The 220-kip Criterion Load Frame used a load cell model LPF.106 with a maximum capacity of 220 kip (1,000 kN). The 22-kip Landmark load Frame was mounted with two load cells during testing. The thin specimens, test nos. SEFT-14 through SEFT-25, which did not utilize the digital image correlation (DIC) measurement equipment, were evaluated using a 2.2-kip (10-kN) load cell, model no. 661.19F-02. The 2.2-kip load cell was installed inline, as seen in Figure 91, and was removed before performing the remaining tests. The remaining specimens utilized a 22-kip (100-kN) load cell, model no. 661.20H-03.

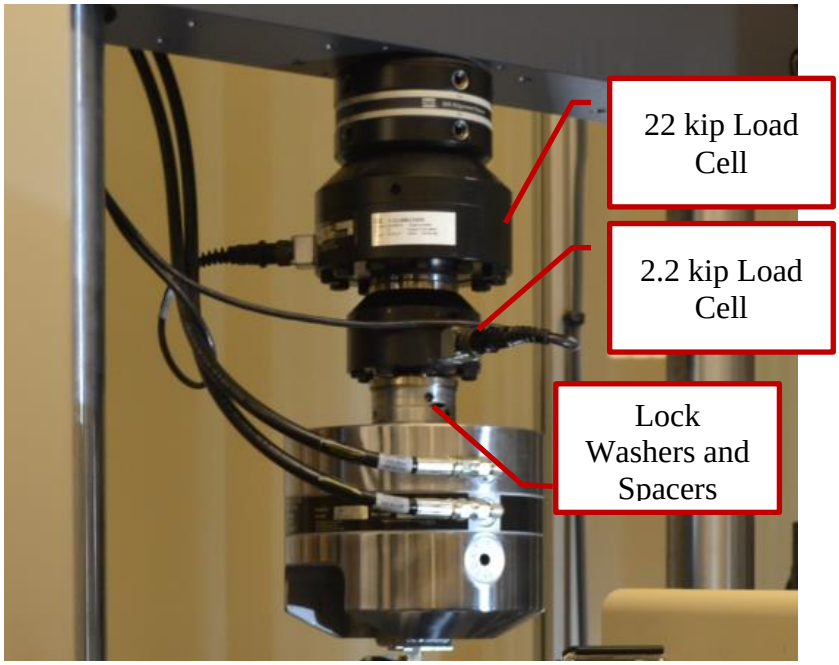

Figure 91. Inline 22-kip and 2.2-kip Load Cells on Landmark 22-kip Load Frame

5.4.2.3 Aramis DIC

A 3-D ARAMIS 2M Digital Image Correlation (DIC) system was utilized to record surface displacements and strains for a portion of the testing matrix. A number of viewing sizes ranging from 1.38 x 1.10 in. (35 x 28 mm) to 0.39 x 0.31 in. (10 x 8 mm)

were used depending on the critical gauge length and width of the testing specimen. A stereoscopic camera mount with two FWX20, 12 Hz, CCD sensor, cameras with Schneider Kreuznack Componon-S 50-mm lens were used to record images during testing. The aperture value was set to a constant f/16 during use. Numerous lights were used to illuminate the specimen to maintain an appropriately short shutter time. The selection of lights depended on the specimen size and shape. Bright directional lights could be used to illuminate flat specimen as long as they were positioned in a way that the main reflection was not aimed at the cameras. However, many lights from multiple angles using umbrella diffusers were required for axial-symmetric specimens, because direct light reflections would have been seen by the cameras regardless of light placement. Alternatively, lights were bounced off the back wall to diffuse the light and minimize direct reflections.

Due to limits of the buffer size, typically, the first 4 seconds recorded 10 frames per second before reducing to 2 frames per second for the remainder of the test. This selection allowed greater resolution during the elastic portion of the test without the need to alter the displacement rate of the actuator. Due to the length of testing expected on the compression cylinder, the recording rate was reduced to 1 frame per second. A digital output was configured on the FlexTest controller and "TestSuite TW Elite" software to be used as an input trigger on the ARAMIS trigger box.

Post-processing was achieved using the ARAMIS v6 software. Depending on the shape of the specimen, either rectangular or quadrangle facets were used to track the pattern. Quadrangle-shaped patterns were preferred to track curved surfaces, such as those found on the notched specimens. A facet-size ratio of 3H:2V was used on the

tension specimens so that the specimen would maintain an aspect ratio closer to 1 during deformation. Conversely, an aspect ratio of 2H:3V was used on the compression specimen. The history of the effective engineering strain at the location of maximum effective engineering strain was exported, including a plot containing the effective engineering strain on the surface of the specimens. Due to the nature of the element calculation, the reported strain is the engineering strain. Also, displacement data from two points on either side of the notch was exported. As the points were outside the notched length, the displacement data is in agreement with the physical extensometers.

A number of techniques were explored to achieve a stochastic pattern of appropriate size, thickness, and contrast, while also adhering to the metal surface through failure initiation. Since some specimens were machined to a reflective polish, it was important to utilize a technique that would prevent reflection of the material or stochastic pattern from the lights into the cameras. A sample of the experimentation can be seen in Figure 92. The left most specimen utilized a flat white primer spray paint and a very fine flat black spray paint speckle pattern applied one-half an hour before testing. The speckle pattern was found to be too small, and the paint separated from the metal surface in the necking region. The second specimen was the same as the first, except a high-heat formulation of flat white paint was used with a slightly larger black speckle size. The paint did not adhere to the metal in the necking region. The third specimen was prepared identical to the first specimen, except a slightly larger speckle size was used and the paint was allowed to dry for a number of days before testing. The paint did not adhere to the metal in the necking region. The fourth specimen was prepared with a white wet chalk marker. After a short period to allow for partial drying, excess chalk was blotted away to

minimize the thickness. Flat black paint was used for the speckle pattern. The chalk was unable to flow with the material. As a result, flacking of the chalk occurred, which prevented the ARAMIS software from tracking the surface. The fifth specimen was prepared with black Sharpie Marker as the base layer with a flat white primer used for the speckle pattern. The contrast was not ideal between the white and black, and too few white speckles were used. A thicker white ink was considered for the speckle pattern. However, the sharpie ink was found to have separated from the base material in the region directly around the failure surface. Thus, the idea was not pursued. The sixth specimen was prepared using an extremely thin layer of wet chalk to reduce the reflection of the base metal. A flat black primer was then used to create a relatively larger speckle size. The contrast created with this method was not ideal, and the thin layer of wet chalk separated slightly in the necking region. Unfortunately, this method was impractical for the highly-reflective, axial-symmetric specimens as it failed to reduce reflection off of the base material.

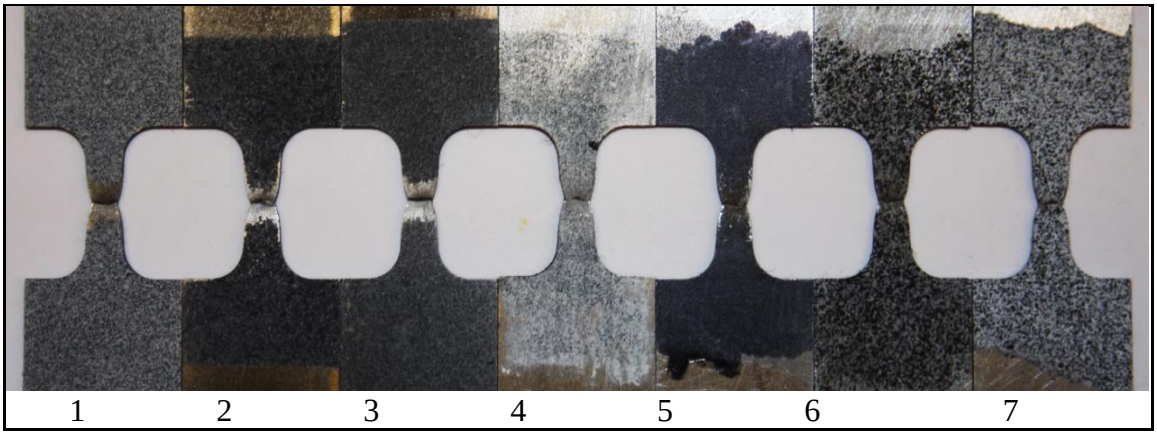

Figure 92. Stochastic Patterns Applied to Specimens Using Various Techniques

The seventh, or final, specimen utilized a unique white spray paint that adhered to and flowed with the metal surface. “The Rust-Oleum Universal Advanced Formula Satin Paint and Primer in One” spray paint was found to create a superior bond to the metal,

while also maintaining a thin paint layer. Furthermore, it was found that the white paint would adhere better as a uniform layer if the paint was applied with the paint nozzle no more than 6 in. (150 mm) away from the specimen in two or three consecutive passes. The resulting layer would appear wet and thick, but the paint would dry to a thickness less than 0.0006 in. (0.015 mm) thick. Once the white paint dried so that it was just slightly tacky, the black speckle pattern was applied. The black speckle pattern was achieved using inexpensive flat black spray paint. With the spray nozzle positioned 24 in (610 mm) away from the specimen, the paint was applied in casual sweeping motions. A more uniform speckle size was achieved if the paint was allowed to fall onto the specimen, as opposed to spraying directly onto the specimen. Care was also taken to begin spraying while pointed away from the specimen until a regular flow was achieved. This method prevented any irregular droplets from landing on the specimen. Spraying could take up to a minute or more to achieve a 50 percent coverage between white and black paint. An example of the preparation results from process no. 7 can be seen in the post-test image provided in Figure 93. The specimens were tested within 30 minutes of painting.

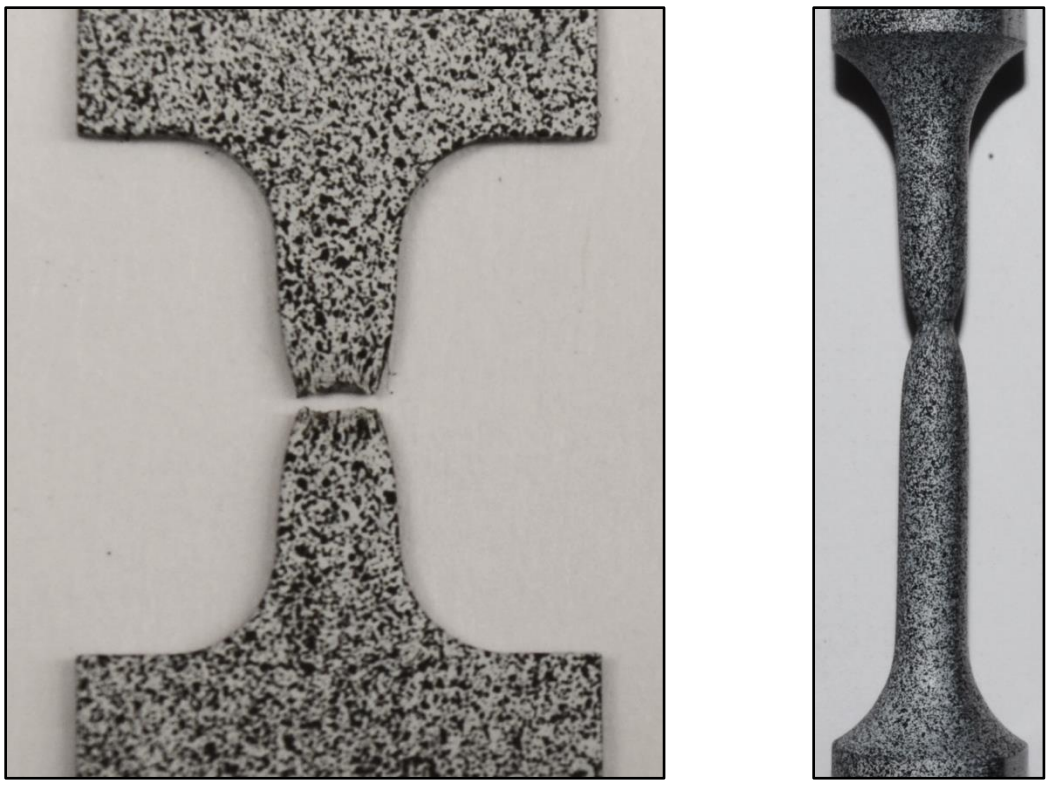

Figure 93. Specimens Prepared with Advanced Formula White Paint and Black Speckle Pattern

5.4.2.4 Digital Photography

Two GoPro digital video cameras operating at a frame rate of 120 frames per second were used to document the testing. A Nikon D5100 digital camera with an 18 to 55-mm lens was also used to document pre- and post-test conditions for all the tests.

5.4.3 Data Processing

The "TestSuite TW Elite" software recorded the actuator displacement, load cell force, extensometer strain, and laser extensometer length at a rate of 100 Hz. The data was then exported into a comma delimited text file. The unfiltered data was then brought into an Excel spreadsheet to create force vs. displacement curves. When applicable, further processing was performed to produce pertinent material property data. This processing is detailed in Section 6.1.

6 MATERIAL TESTING RESULTS – STEEL SPECIMENS

6.1 Material Properties Determined from Testing

Various material properties can be determined from processing test data. In order to process the data, numerous relationships and definitions were used. This subsection contains the equations and techniques that were used.

The exported data file contained the recorded data including time, primary and secondary load cell forces, actuator displacement, axial extensometer strain, and laser extensometer separation length. The displacement and engineering strain from the laser extensometer were calculated with Equations 6.28 through 6.29. Note that the engineering strain can only be measured when extensometers are placed within a uniform critical gauge length. Thus, only the Axial-Symmetric Round Smooth Specimen and the Flat Dog Bone Specimen allowed engineering strain to be measured directly. Therefore, the displacement, rather than the strain, was reported for the remaining specimens.

$$d_{Laser} = L - L_i \tag{6.28}$$

where

$d_{Laser} =$ Extensometer Displacement
$L =$ Curent Length Measurement
$L_i =$ Initial Length Measurement

and

$$\varepsilon_{Laser} = d_{Laser}/L_i \tag{6.29}$$

where

$\varepsilon_{Laser} =$ Laser Extensometer Engineering Strain
$d_{Laser} =$ Laser Extensometer Displacement
$L_i =$ Initial Length Measurement

Alternatively, the axial extensometer was utilized to measure the engineering strain. Thus the displacement was calculated with the following equations:

$$d_{Extensometer} = \varepsilon_{Extensometer} L_i \tag{6.30}$$

where

$d_{Extensometer}$ = Axial Extensometer displacement
$\varepsilon_{Extensometer}$ = Current Engineering Strain Measured
L_i = Initial Length of Axial Extensometer

If either extensometer is placed within the critical length of the testing specimen, the true strain can also be calculated. The true strain is calculated as seen in Equation 6.31, where the engineering strain is either acquired from the axial extensometer or laser extensometer. Note, this equation is only valid until the initiation of diffuse necking.

$$\varepsilon_T = \ln(1 + \varepsilon) \tag{6.31}$$

where

ε_T = True Strain
ε = Engineering Strain

After the initiation of diffuse necking, a linear interpolation is assumed between the last true strain prior to diffuse necking and the true strain at failure. The true strain at failure is calculated using the adjustment method used by Bridgman, as seen in Equation 6.32 [21].

$$\varepsilon_f = \ln\left(\frac{A_i}{A_f}\right) \tag{6.32}$$

where

ε_f = True Strain at Failure
A_i = Initial Measured Cross Sectional Area
A_f = Final Measured Cross Sectional Area

Also, the reduction in area is given as a percent as seen in Equation 6.33.

$$\text{Cross Sectional Percent Area at Failure} = \frac{A_i - A_f}{A_i} \tag{6.33}$$

where

A_i = Initial Measured Cross Sectional Area
A_f = Final Measured Cross Sectional Area

The initiation of diffuse necking is given by Considère's criterion [87]. Considère's criterion states that the plastic instability of necking begins at the point when

the increase in stress due to the decrease in the cross-sectional area is equal to the increase in load bearing capacity of the specimen due to work hardening [21,87-88]. As the stress continues to increase with decreased cross-sectional area, the instability continues. Utilizing Equation 6.34, the point of necking initiation can be determined.

$$\text{Diffuse Necking Occurs when: } \frac{d\sigma_T}{d\varepsilon_T} = \sigma_T \tag{6.34}$$

where

$\sigma_T = \text{True Stress}$

$\frac{d\sigma_T}{d\varepsilon_T} = \text{Slope of True Stress vs. True Strain Curve}$

The Offset Method was used to determine yield values of the specimens with uniform cross sections along their gauge lengths. This method applies an offset to a line with a slope equal to the elastic modulus. The intersection of this line and the stress vs. strain curve gives the quantitative yield strain and stress of the specimen. A 0.2 percent offset was utilized in this report. The Offset Method process is further described in the ASTM publication, "Standard Test Methods and Definitions for Mechanical Testing of Steel Products [89]."

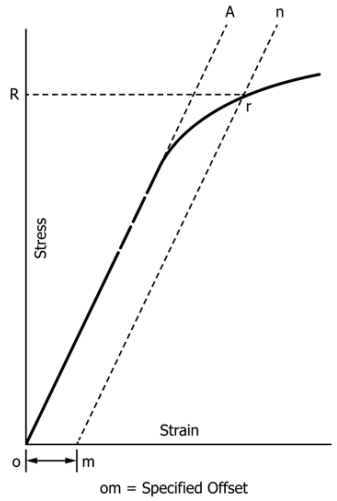

Figure 94. Offset Method to define Quantitative Yield Values [89]

While the method previously described to determine yield provides adequate results for uniform cross section specimens, the method is not adequate for specimens with non-uniform cross sections. If the offset method was used to determine the yield for non-uniform cross sections, a bias would occur due to the difference in notch lengths. In order to determine quantitative yield values for the non-uniform cross section specimens, a ratio method was utilized. First, the ratio between the calculated elastic modulus and slope of the stress vs. strain curve at the 0.2 percent offset yield point was determined for the uniform cross section specimens. These values were then averaged. This process gave a ratio of elastic modulus to slope at yield of 6. The yield point was then defined for the non-uniform cross section specimens at the point in which the ratio of elastic modulus to the slope of the stress vs. strain curve to be equal to the value of 6. This process allowed for unbiased quantitative yield values to be determined for all tension specimens.

It should be noted that in order to obtain the stress vs. strain slope data, the data was filtered using the SAE Class 60 Butterworth filter conforming to SAE J211/a specifications [90]. However, the filtered data was only used to determine the elastic modulus and slope values at yield.

The true plastic strain is often calculated using slightly varying techniques. Under the simplest of conditions, the elastic region can be simplified to the 0.2 percent offset yield strain value. This simplification results in the equation seen in Equation 6.35. However, this equation does not account for two aspects. First, if the elastic region varies from the 0.2 percent offset yield assumption, the equation is no longer valid. Second, the equation does not account for strain hardening effects. A more generalized alternate approach can be used, which accounts for strain hardening effects, as seen in Equation

6.36. The second term accounts for the growing elastic portion of the strain as strain hardening occurs. In general, the two approaches produce results that are typically similar enough for most purposes, so the simplified true plastic strain, as shown in Equation 6.35 was used in this report.

$$\varepsilon_P = \varepsilon_T - \varepsilon_y \tag{6.35}$$

Where

$\varepsilon_p = \text{Plastic Strain}$
$\varepsilon_T = \text{Total Strain}$
$\varepsilon_y = \text{Yield Strain}$

and

$$\varepsilon_P = \varepsilon_T - \frac{\sigma_T}{E} \tag{6.36}$$

where

$\varepsilon_p = \text{Plastic Strain}$
$\varepsilon_T = \text{Total Strain}$
$\sigma_T = \text{True Stress}$
$E = \text{Young's Modulus}$

The engineering stress was calculated using Equation 6.37.

$$\sigma = \frac{P}{A_i} \tag{6.37}$$

where

$\sigma = \text{Engineering Stress}$
$P = \text{Load}$
$A_i = \text{Initial Measured Cross Sectional Area}$

The true stress was calculated as seen in the Equation 6.38.

$$\sigma_T = \sigma(1 + \varepsilon) \tag{6.38}$$

where

$\sigma_T = \text{True Stress}$
$\varepsilon = \text{Engineering Strain}$

Similar to the true strain, Equation 6.38 is only valid until the initiation of diffuse necking, as defined by Considère's criterion. After the initiation of diffuse necking, a linear interpolation is assumed between the last point prior to diffuse necking and the true

strain at failure. The true stress at failure is calculated using the adjustment method used by Bridgman, as seen in Equation 6.39 [21].

$$\sigma_f = \frac{P_f}{A_f} \tag{6.39}$$

where

$\sigma_f = \text{True Stress at Failure}$
$P_f = \text{Load at Failure}$
$A_f = \text{Final Measured Cross Sectional Area}$

The elastic modulus was calculated using a tangent method, as see in Equation 6.40. However, it should be noted that this method involves judgment as to the value of the proportional limit, and as a result, it is not a very well-defined property [16].

$$E = \frac{\sigma_{pl}}{\varepsilon_{pl}} \tag{6.40}$$

where

$\sigma_{pl} = \text{Stress at Proportional Limit}$
$\varepsilon_{\text{pl}} = \text{Strain at Proportional Limit}$

Failure initiation in this report was defined as the point in which a sharp drop in the measured force occurred. However, further analysis of the DIC data may provide more detailed information on the crack propagation and initiation. Furthermore, when applicable, the ASTM definition of failure is also reported. ASTM defines failure when the measured force exhibits a 10 percent drop from the maximum force [89].

The ultimate strength was calculated using Equation 6.41.

$$\sigma_u = \frac{P_{max}}{A_i} \tag{6.41}$$

where

σ_u = Ultimate Strength
P_{max} = Maximum Load
A_i = Initial Measured Cross Sectional Area

6.2 Material Testing Results

The results of the component testing program are summarized within this section. Material properties calculated from the test data is also presented. Detailed test results can be found in Appendix F.

6.2.1 Flat Standard Dog Bone Specimen Test Results

The Flat Standard Dog Bone Specimen was tested extensively as part of the material testing program. In addition to determining material properties, the specimen was used to verify test procedures and equipment performance, as well as determine the optimum DIC stochastic pattern. As such, the specimen was tested numerous times.

Test nos. SEFT-01 through SEFT-13 were used to adjust the testing procedure to ensure that no pre-load was applied to the specimen during installation. A risk of applying a pre-load to the specimen was observed during installation, specifically while gripping the specimen. The force originated when applying pressure with the grips. During this process a slight displacement could be exerted on the specimen, and as a result, a pre-load force could be imparted into the specimen. This finding was remedied by setting the load frame into force control and allowing the actuator to move during installation to maintain a minimal pre-loading on the specimen. However, due to the small size of the specimens, the inherent noise in the load cell, and the limited response from the actuator, the load frame could still potentially pre-load the specimen. To limit the amount of loading on the specimen, it was determined that actuator response was

greatly improved if the hydraulic pump was allowed to run for an hour in advance of testing. It is assumed that the warmer hydraulic fluid allowed superior performance from the actuator valves. Lastly, these tests highlighted the importance of not zeroing the load cell measurement immediately prior to the test. For the remainder of the testing program, the specimen was secured with the top grip, the load cell was zeroed, and then the bottom grip was secured. If any pre-load was recorded at this time, it would be seen in the recorded data. Due to the prevalence of pre-loading and not measuring the pre-load magnitude during test nos. SEFT-01 through SEFT-13, the load recorded could not be taken as a reliable measurement. As such, the data has been archived but is not shown within this report.

Test nos. SEFT-14 through SEFT-16 and SEFT-69 evaluated the Flat Dog Bone Specimens using the new reliable testing procedure which greatly limited the risk of pre-loading the specimens. Two strips of retro-reflective tape, cut to a width of $^{1}/_{16}$ in. (1.6 mm), were placed within the critical gauge length of the specimens, and a 1-in. (25.4-mm) axial extensometer was placed on the specimen outside the gauge length. The laser extensometer was the primary measurement for these tests, because the placement of the retro-reflective tape allowed the engineering strain to be measured directly. The engineering stress vs. engineering strain curves using the laser extensometer produced similar results up to the initiation of necking, as seen in Figure 95. After necking initiation, some variations in the engineering strain measurement occurred. This variation can be attributed to slight differences in the placement of the retro reflective tape relative to the region of diffuse necking.

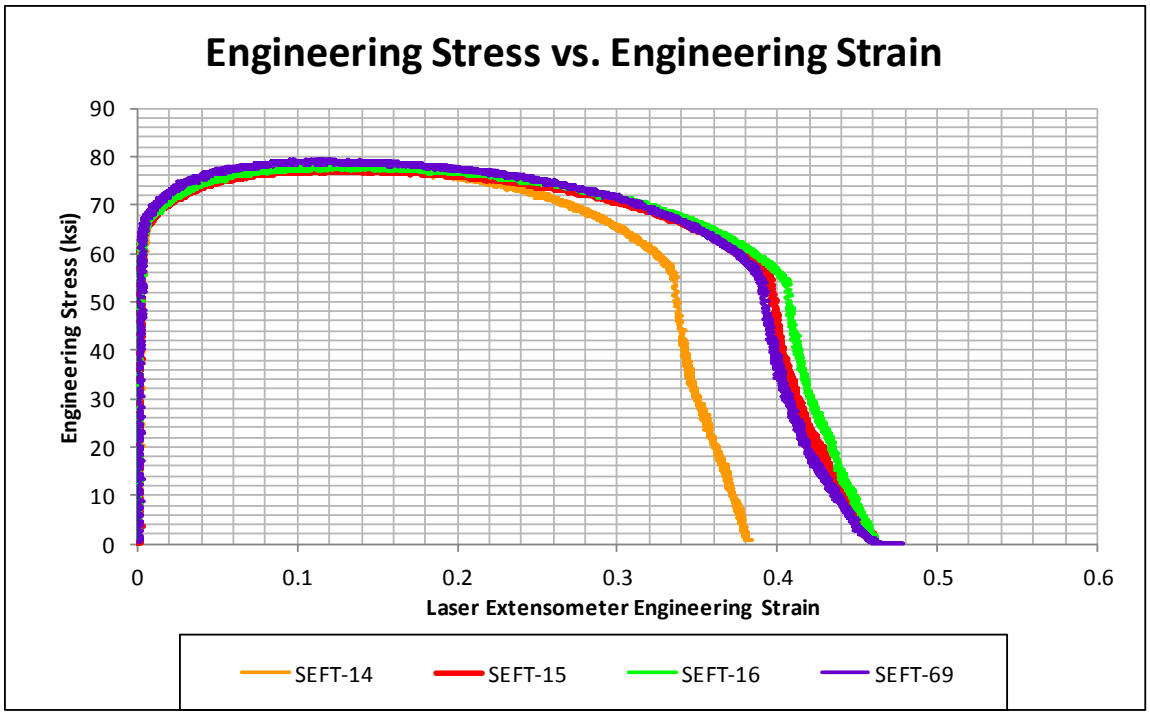

Figure 95. Flat Standard Dog Bone Specimen: Engineering Stress vs. Engineering Strain from Critical Gauge Length Measurements

The 1-in. (25.4-mm) axial extensometer was utilized to measure the displacement of two points located 1 in. apart on the specimen. The extra measurement was taken to aid in FEM modeling by providing a consistent length measurement for each test. As seen in Figure 96, the four tests have closely-grouped engineering stress vs. displacement curves with an average displacement at failure of 0.0711 in. (1.806 mm). Furthermore, the true stress vs. true strain curves for the four tests, calculated with the laser extensometer and post-test cross-sectional area measurements, are also closely grouped, as seen in Figure 97. The average true strain at failure and true stress at failure were 0.6806 and 139.5 ksi (962 MPa), respectively. These similar results suggest that the material is relatively uniform throughout the specimens. A macro image of the typical failure zone can be seen in Figure 98.

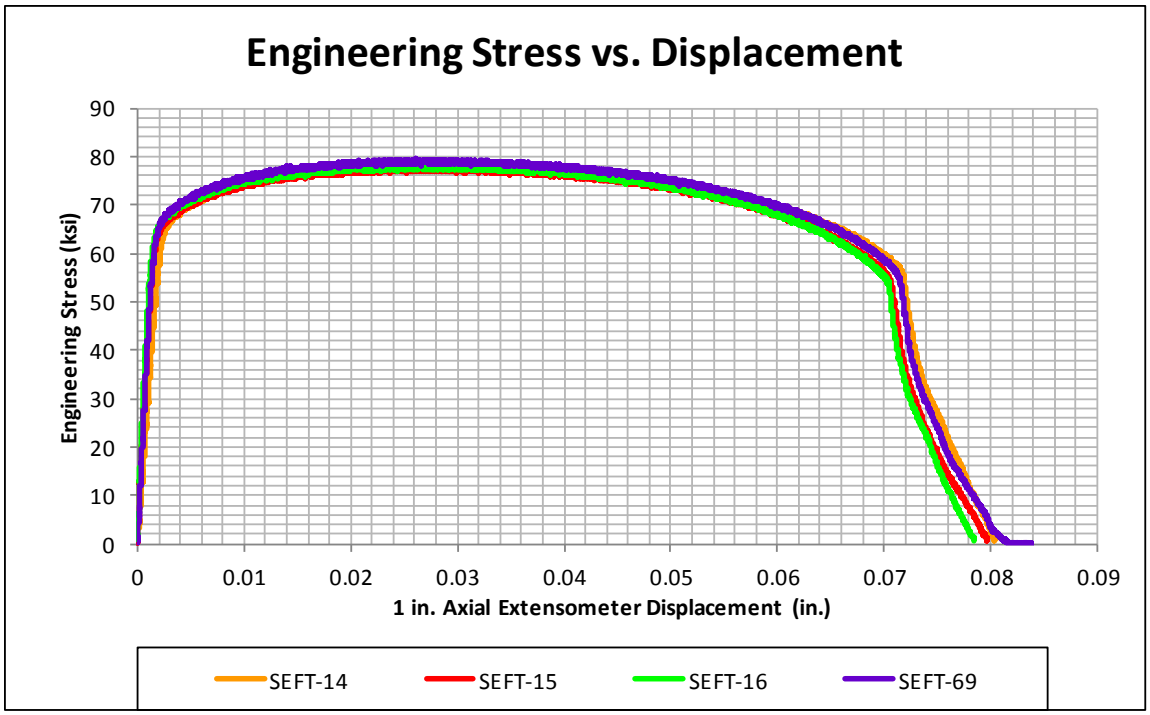

Figure 96. Flat Standard Dog Bone Specimen: Engineering Stress vs. Displacement from 1-in. (25.4-mm) Gauge Length Measurements, Test Nos. SEFT-14 through SEFT-16 and SEFT-69

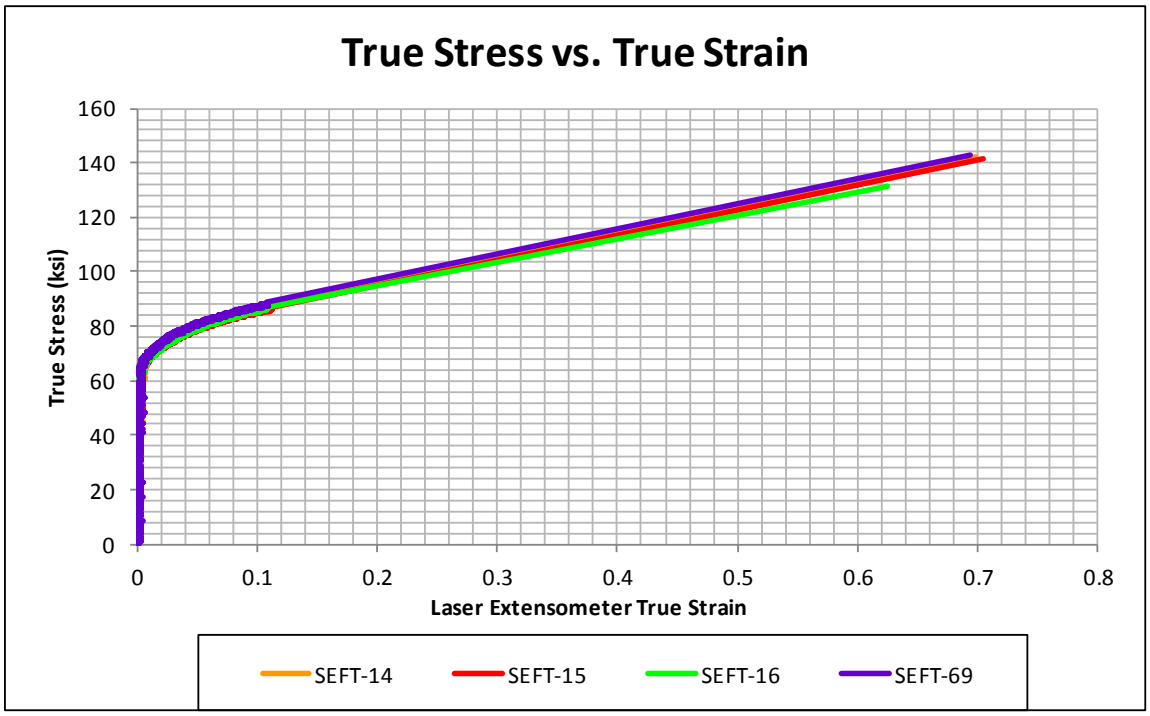

Figure 97. Flat Standard Dog Bone Specimen: True Stress vs. True Strain from Critical Gauge Length Measurements, Test Nos. SEFT-14 through SEFT-16 and SEFT-69

Figure 98. Flat Standard Dog Bone Specimen: Macro View of Typical Failure Zone

Test nos. SEFT-70 through SEFT-72, SEFT-74, SEFT-76, SEFT-77, and SEFT-79 were used to determine the optimum DIC pattern, as previously described in Section 5.4. A 1-in. (25.4-mm) axial extensometer was also used to measure the displacement of the specimens. As seen in Figure 99, the engineering stress vs. the 1-in. (25.4-mm) axial extensometer displacement curves were also closely grouped and were similar to the previous tests. This comparison suggests that the paint applied for the stochastic pattern had a negligible effect on the results. The average displacement of failure of all of the noted tests was nearly identical to the average of the first four tests at a displacement of 0.0709 in. (1.800 mm). Material properties compiled from all of the tested Flat Standard Dog Bone Specimens can be found in Table 10.

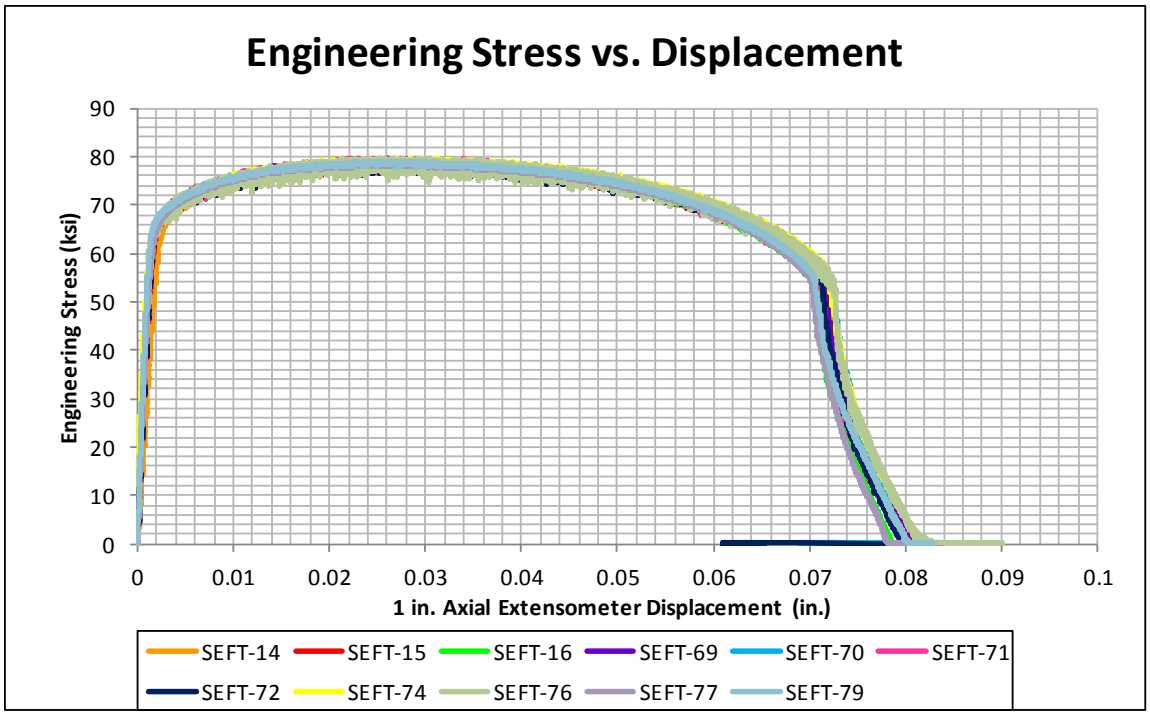

Figure 99. Flat Standard Dog Bone Specimen: Engineering Stress vs. Displacement from 1-in. (25.4-mm) Gauge Length Measurements

Table 10. Flat Standard Dog Bone Specimen: Summary of Results

Average Young's Modulus (Laser Extensometer)	29,917 ksi (206,270 MPa)
Average Yield Stress (0.2% Offset) (Laser Extensometer and 1-in. Axial Extensometer)	64.3 ksi (444 MPa)
Average Ultimate Strength	79.3 ksi (547 MPa)
Engineering Stress at Failure	56.3 ksi (388 MPa)
Average Displacement at Failure (1-in. Axial Extensometer)	0.0710 in. (1.803 mm)
Average Cross-Sectional Area Reduction	49.1%
Average True Strain at Failure	0.6760
Average True Stress at Failure	139.8 ksi (964 MPa)
Maximum Effective Engineering Strain (DIC Analysis)	0.82

While DIC data results were collected for all seven tests, only DIC data for test no. SEFT-79 is presented herein as the stochastic pattern gave superior results through the entire test duration up to failure initiation.

A 0.98-in. x 0.79-in. (25-mm x 20-mm) viewing size was used to capture the DIC data on test no. SEFT-79. A pattern using the standard technique was utilized to prepare the specimen, as seen in Figure 100(a). The pattern allowed reliable displacement and strain data to be computed from the recorded images. During loading, the specimen failed when a crack formed starting in the center of the specimen, as seen in Figure 100(b). Prior to failure occurring, the DIC analysis recorded a maximum effective engineering strain of 0.82, as shown in Figure 101. The effective engineering strain plot at the state of maximum recorded strain can be found in Figure 100(c). The majority of the diffuse necking region was captured in the DIC analysis. After the crack formed, the DIC analysis was unable to accurately continue tracking the stochastic pattern around the crack region, and as a result, the recorded maximum effective engineering strain decreased due to the analysis's inability to track strain in the area of the newly formed crack.

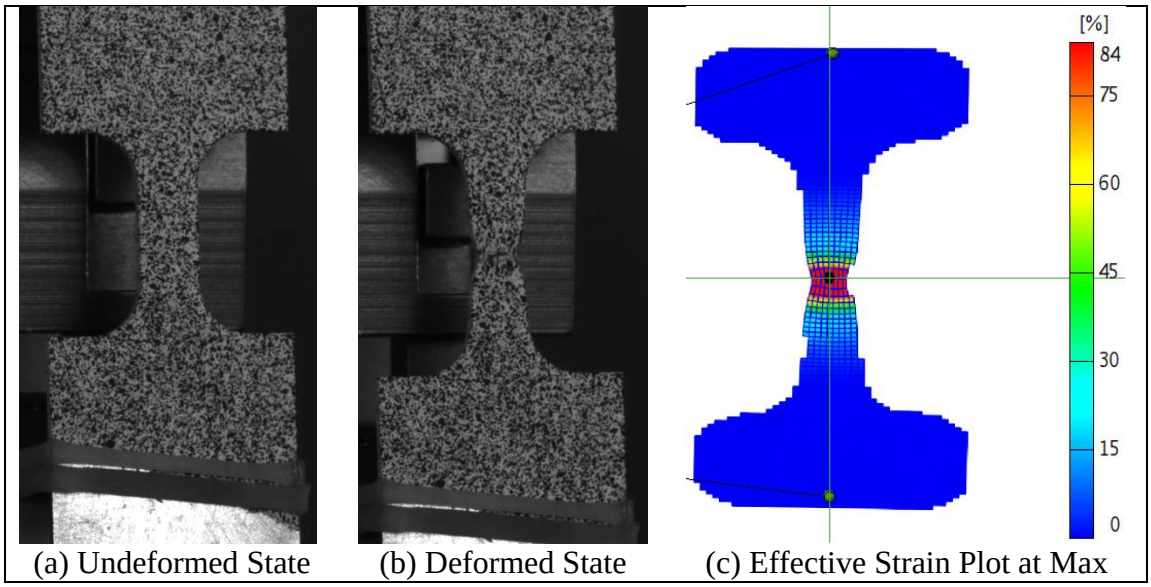

(a) Undeformed State (b) Deformed State (c) Effective Strain Plot at Max

Figure 100. Flat Standard Dog Bone Specimen: DIC Analysis, Test No. SEFT-79

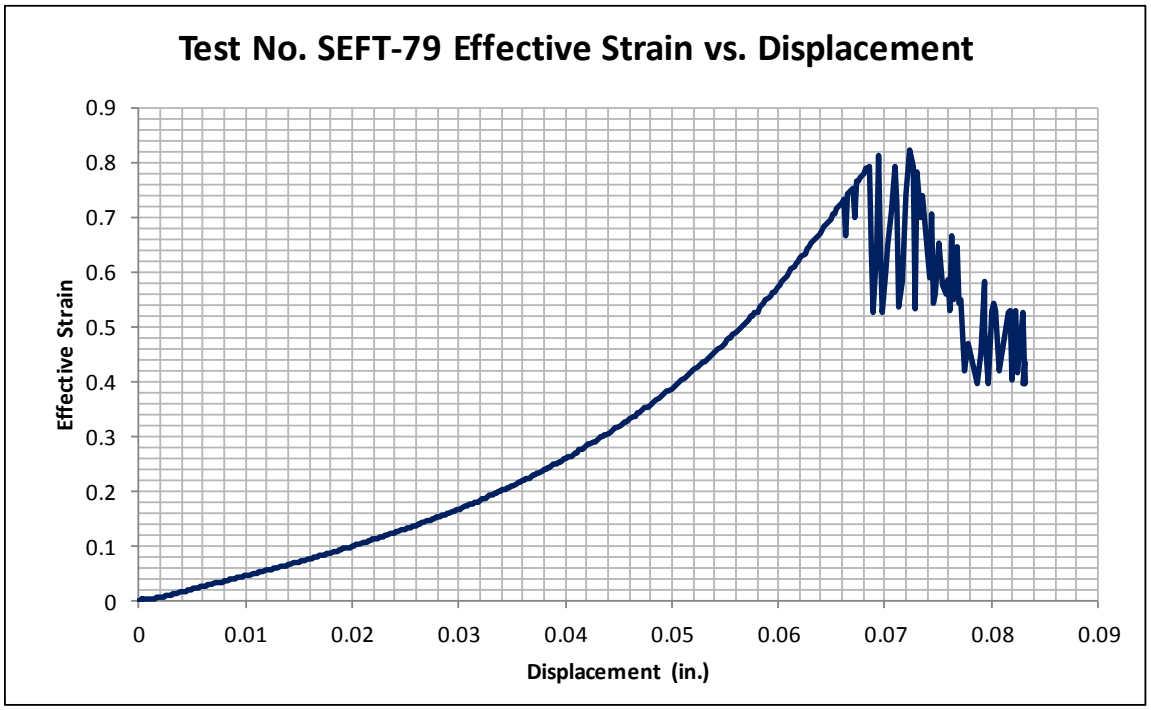

Figure 101. Flat Standard Dog Bone Specimen: Effective Engineering Strain vs. Displacement Data from DIC Analysis, Test No. SEFT-79

6.2.2 Large Notched Flat Specimen Test Results

Test nos. SEFT-17 through SEFT-19, SEFT-73, and SEFT-75 evaluated the Large Notched Flat Specimens. Test nos. SEFT-17 through SEFT-19 were tested with two

strips of retro-reflective tape, cut to a width of $^{1}/_{8}$ in. (3.2 mm), placed immediately outside the notched length of the specimens. All of the Large Notched Flat Specimen tests utilized a 1-in. (25.4-mm) axial extensometer placed on the specimen outside the notched length. The 1-in. (25.4-mm) axial extensometer was the primary measurement for all of the noted tests. However, the differences between the laser extensometer displacements and axial extensometer displacements were minimal, because the plastic deformation was localized to the region within the critical gauge length.

The specimens produced closely-grouped engineering stress vs. displacement curves, as shown in Figure 102. The average yield stress was 70.6 ksi (487 MPa). The average stress and displacement at failure was 59.5 ksi (410 MPa) and 0.0353 in. (0.897 mm), respectively. Also, the average reduction in cross section was 42.8 percent. A macro image of the typical failure zone can be seen in Figure 103.

DIC was utilized for test nos. SEFT-73 and SEFT-75. However, only DIC results for test no. SEFT-75 is presented herein, as the selected stochastic pattern provided superior results through the entire test duration up to failure initiation.

A 0.98-in. x 0.79-in. (25-mm x 20-mm) viewing size was used to capture the DIC data on test no. SEFT-75. A pattern used to prepare the specimen can be as seen in Figure 104(a). The pattern allowed fairly reliable displacement and strain data to be computed from the recorded images. During loading, the specimen failed when a crack formed starting in the center of the specimen, as seen in Figure 104(b). Prior to failure occurring, the DIC analysis recorded a maximum effective engineering strain of 0.63, as shown in Figure 105. The effective engineering strain plot at the state of maximum recorded strain can be found in Figure 104(c). The majority of the diffuse necking region was captured in

the DIC analysis. Around the time the crack formed, the DIC analysis was unable to accurately continue tracking the stochastic pattern around the crack region, and as a result, the recorded maximum effective engineering strain decreased due to the analysis's inability to track strain in the area of the newly formed crack. A summary of results is provided in Table 11.

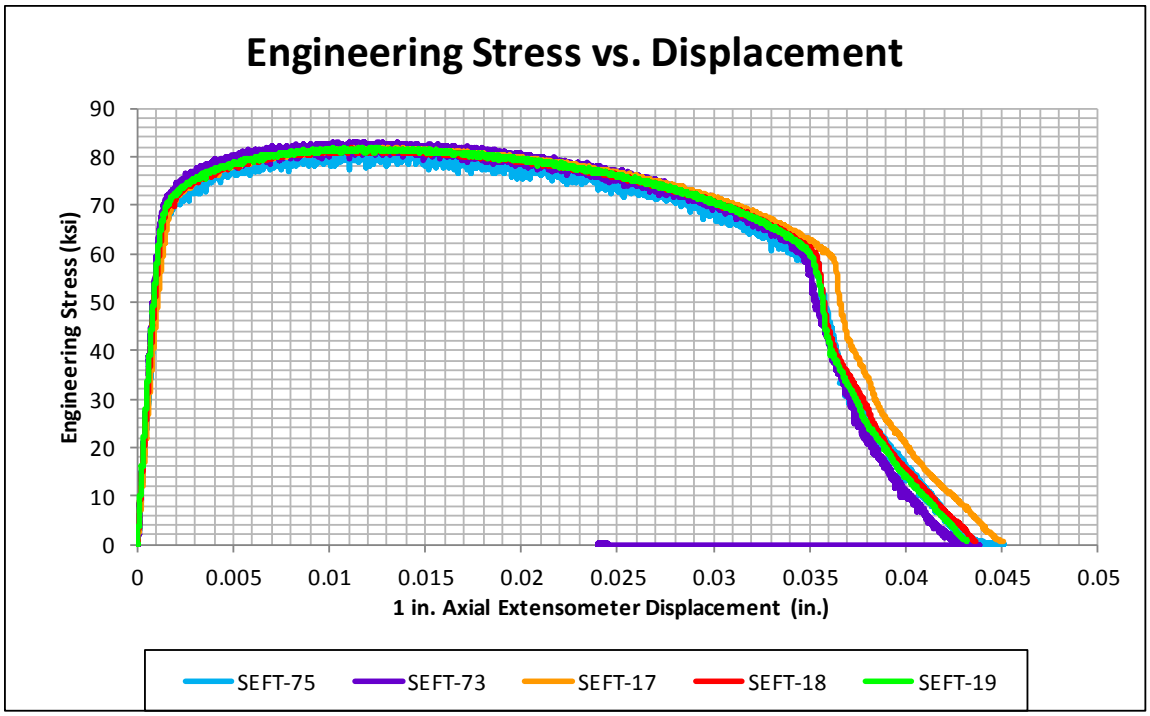

Figure 102. Flat Large Notch Specimen: Engineering Stress vs. Displacement from 1-in. (25.4-mm) Gauge Length Measurements

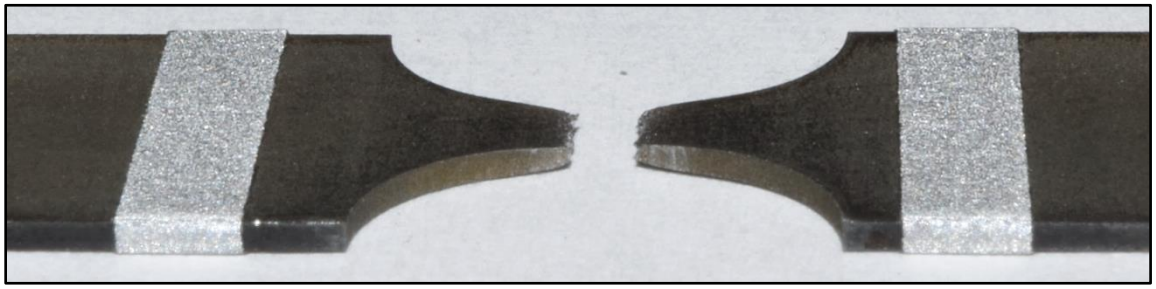

Figure 103. Large Notched Flat Specimen: Macro View of Typical Failure Zone

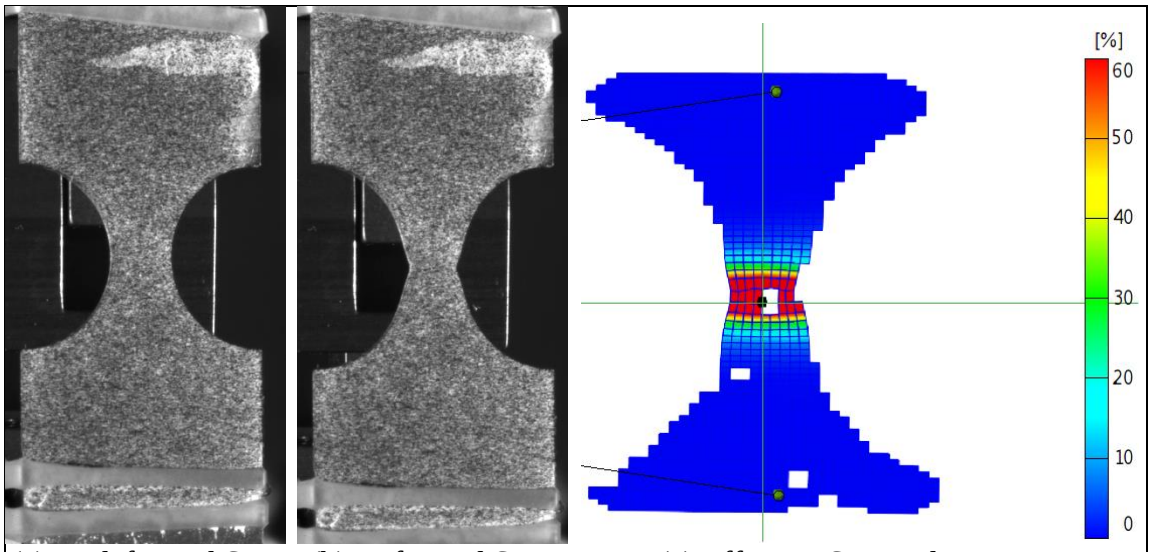

(a) Undeformed State (b) Deformed State (c) Effective Strain Plot at Max

Figure 104. Large Notched Flat Specimen: DIC Analysis, Test No. SEFT-75

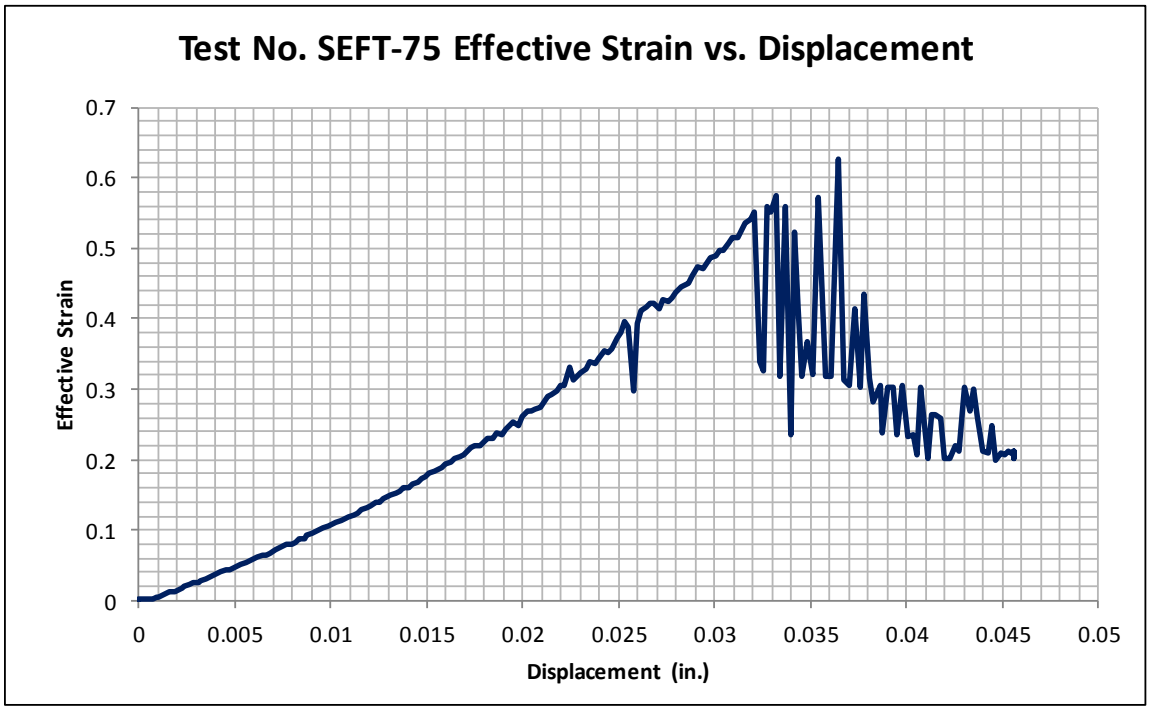

Figure 105. Large Notched Flat Specimen: Effective Engineering Strain vs. Displacement Data from DIC Analysis, Test No. SEFT-75

Table 11. Large Notched Flat Specimen:: Summary of Results

Average Yield Stress (0.2% Offset) (1-in. Axial Extensometer)	70.7 ksi (488 MPa)
Average Ultimate Strength	82.2 ksi (567 MPa)
Engineering Stress at Failure	59.5 ksi (410 MPa)
Average Displacement at Failure (1-in. Axial Extensometer)	0.0353 in. (0.897 mm)
Average Cross-Sectional Area Reduction	42.8%
Maximum Effective Engineering Strain (DIC Analysis)	0.63

6.2.3 Small Notched Flat Specimen Test Results

Test nos. SEFT-20 through SEFT-22, and SEFT-83 evaluated the Small Notched Flat Specimens. Test nos. SEFT-20 through SEFT-22 were tested with two strips of retro-reflective tape, cut to a width of $^{1}/_{8}$ in. (3.2 mm), placed immediately outside the notched length of the specimen. All of the Small Notched Flat Specimen tests utilized a 1 in. axial extensometer placed on the specimen outside the notched length. The 1-in. (25.4-mm) axial extensometer was the primary measurement for all of the noted tests. However, the differences between the laser extensometer displacements and axial extensometer displacements were minimal, because the plastic deformation was localized to the region within the critical gauge length.

The specimens produced closely-grouped engineering stress vs. displacement curves, as shown in Figure 106. The average yield stress was 72.4 ksi (499 MPa). The average stress and displacement at failure was 58.7 ksi (404 MPa) and 0.0276 in. (0.701 mm), respectively. Also, the average reduction in cross section was 38.2 percent. A macro image of the typical failure zone can be seen in Figure 107.

DIC was also utilized to track the strain and displacements of the specimen tested during test no. SEFT-83. A 0.59-in. x 0.47-in. (15-mm x 12-mm) viewing size was used to capture the DIC data on test no. SEFT-83. A pattern using the standard technique was utilized to prepare the specimen, as seen in Figure 108(a). The pattern allowed reliable displacement and strain data to be computed from the recorded images. During loading, the specimen failed when a crack formed starting in the center of the specimen, as seen in Figure 108(b). Prior to failure occurring, the DIC analysis recorded a maximum effective engineering strain of 0.76, as shown in Figure 109. The effective engineering strain plot at the state of maximum recorded strain can be found in Figure 108(c). The majority of the diffuse necking region was captured in the DIC analysis. Around the time the crack formed, the DIC analysis was unable to accurately continue tracking the stochastic pattern around the crack region, and as a result, the recorded maximum effective engineering strain decreased due to the analysis's inability to track strain in the area of the newly formed crack. A summary of results is provided in Table 12.

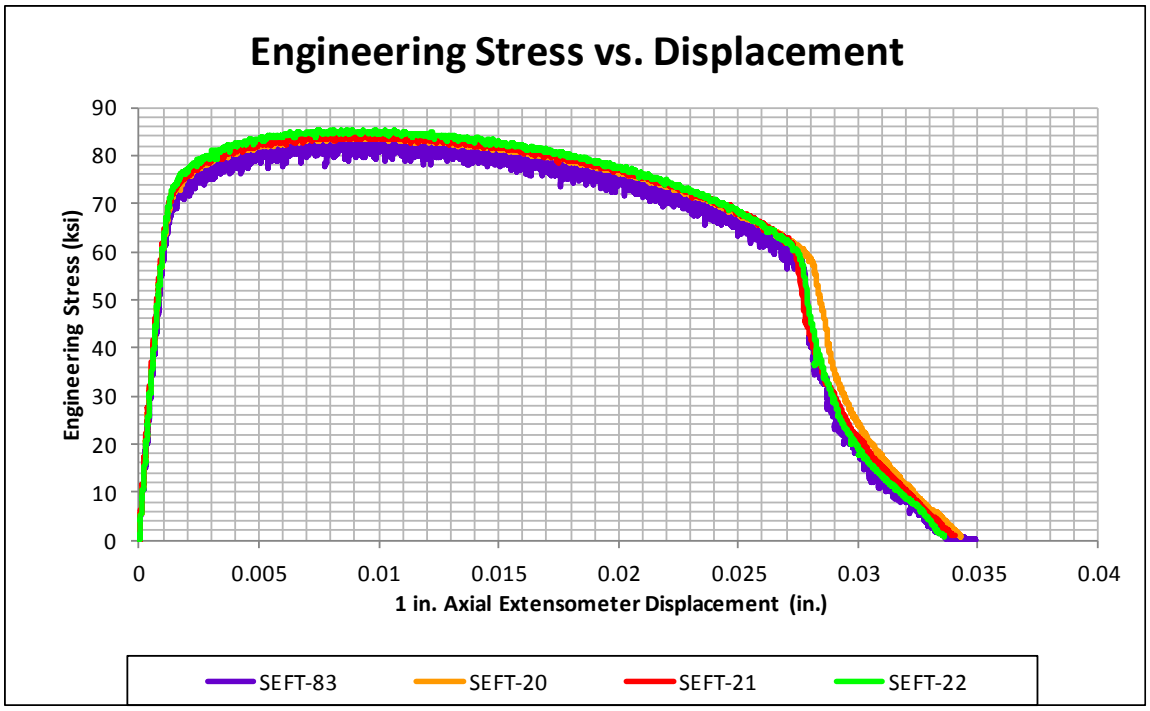

Figure 106. Flat Small Notch Specimen: Engineering Stress vs. Displacement from 1-in. (25.4-mm) Gauge Length Measurements

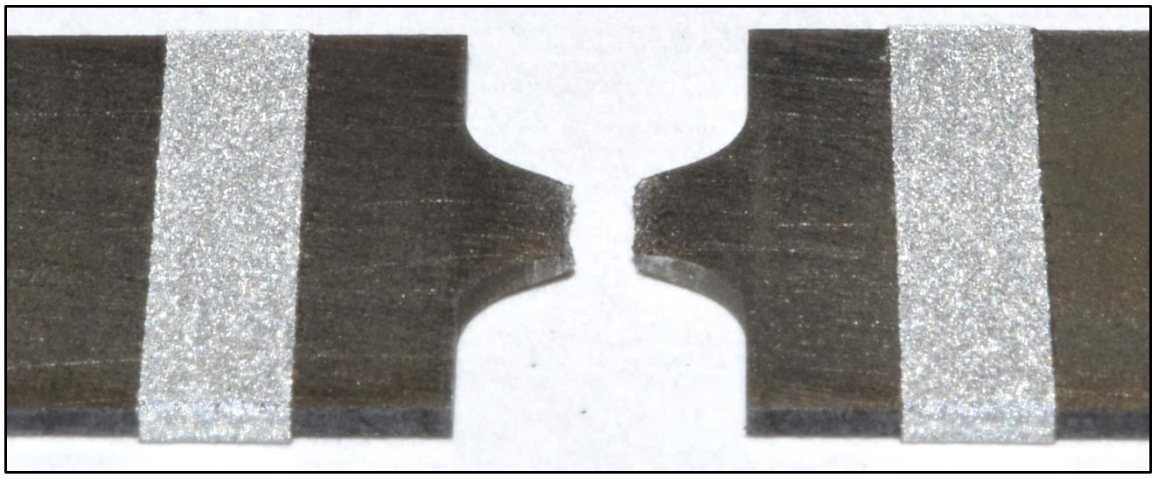

Figure 107. Small Notched Flat Specimen: Macro View of Typical Failure Zone

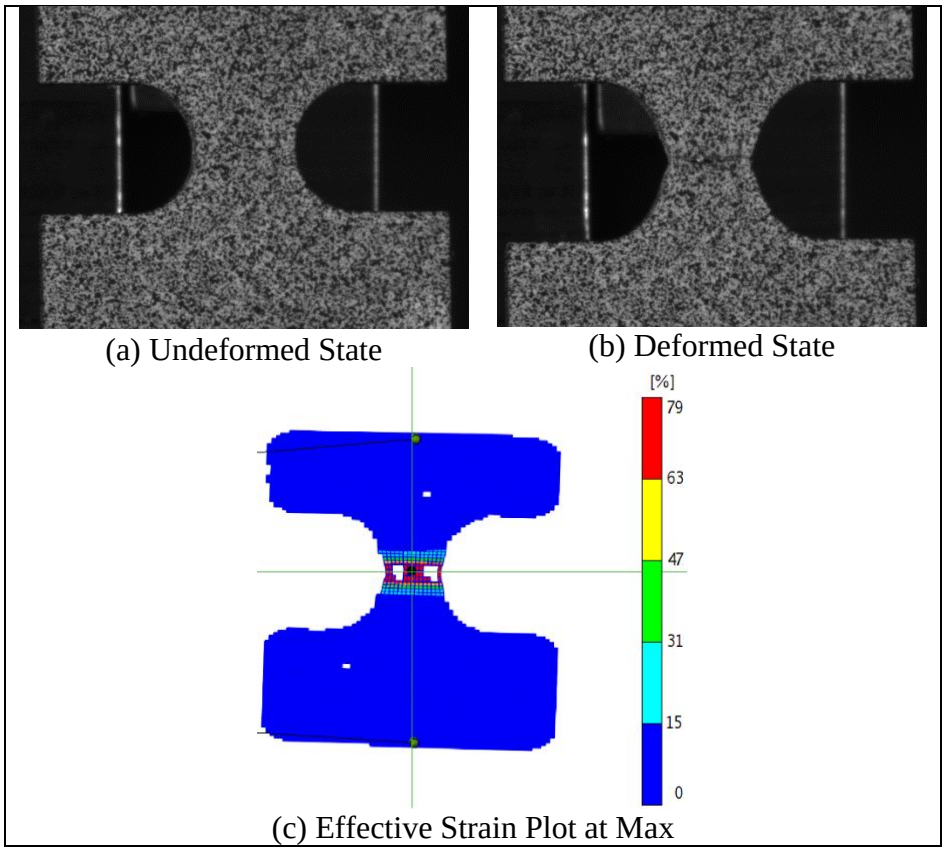

Figure 108. Small Notched Flat Specimen: DIC Analysis, Test No. SEFT-83

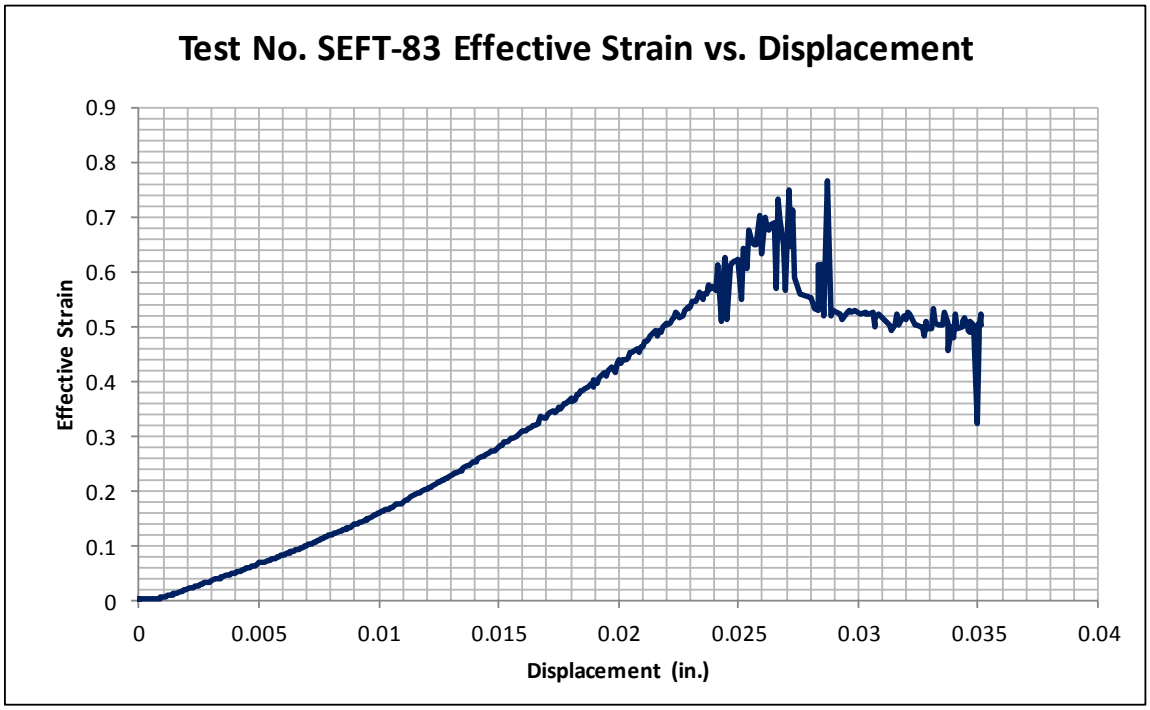

Figure 109. Flat Small Notched Specimen: Effective Engineering Strain vs. Displacement Data from DIC Analysis, Test No. SEFT-83

Table 12. Flat Small Notched Specimen: Summary of Results

Average Yield Stress (0.2% Offset) (1-in. Axial Extensometer)	72.4 ksi (499 MPa)
Average Ultimate Strength	84.5 ksi (405 MPa)
Engineering Stress at Failure	58.7 ksi (583 MPa)
Average Displacement at Failure (1-in. Axial Extensometer)	0.0276 in. (0.701 mm)
Average Cross-Sectional Area Reduction	38.2%
Maximum Effective Engineering Strain (DIC Analysis)	0.76

6.2.4 Sharp Notched Flat Specimen Test Results

Test nos. SEFT-66 through SEFT-68, SEFT-88, and SEFT-89 evaluated the Sharp Notched Flat Specimens. Test nos. SEFT-23 through SEFT-25 were tested with two strips of retro-reflective tape, cut to a width of $^{1}/_{8}$ in. (3.2 mm), placed immediately outside the notched length of the specimens. All of the Sharp Notched Flat Specimen tests utilized a 1-in. (25.4-mm) axial extensometer placed on the specimen outside the notched length. The 1-in. (25.4-mm) axial extensometer was the primary measurement for all of the noted tests. However, the difference between the laser extensometer displacements and axial extensometer displacements was minimal, because the plastic deformation was localized to the region within the critical gauge length.

The specimens produced closely-grouped engineering stress vs. displacement curves, as shown in Figure 110. The average yield stress was 77.3 ksi (533 MPa). The average stress and displacement at failure was 59.9 ksi (413 MPa) and 0.0204 in. (0.518 mm), respectively. Also, the average reduction in cross section was 41.0 percent. A macro image of the typical failure zone can be seen in Figure 111.

DIC was also utilized to track the strain and displacements of the specimen tested during test no. SEFT-84. A 0.31-in. x 0.39-in. (10-mm x 8-mm) viewing size was used to capture the DIC data on test no. SEFT-84. A pattern using the standard technique was utilized to prepare the specimen, as seen in Figure 112(a). The pattern allowed reliable displacement and strain data to be computed from the recorded images. During loading, the specimen failed when cracks initiating at the notch edge on either side of the specimen, as seen in Figure 112(b). Prior to failure occurring, the DIC analysis recorded a maximum effective engineering strain of 0.54, as shown in Figure 113. The effective engineering strain plot at the state of maximum recorded strain can be found in Figure 112(c). The majority of the diffuse necking region was captured in the DIC analysis. Around the time the crack formed, the DIC analysis was unable to accurately continue tracking the stochastic pattern around the crack region, and as a result, the recorded maximum effective engineering strain decreased due to the analysis's inability to track strain in the area of the newly formed crack. A summary of results is provided in Table 13.

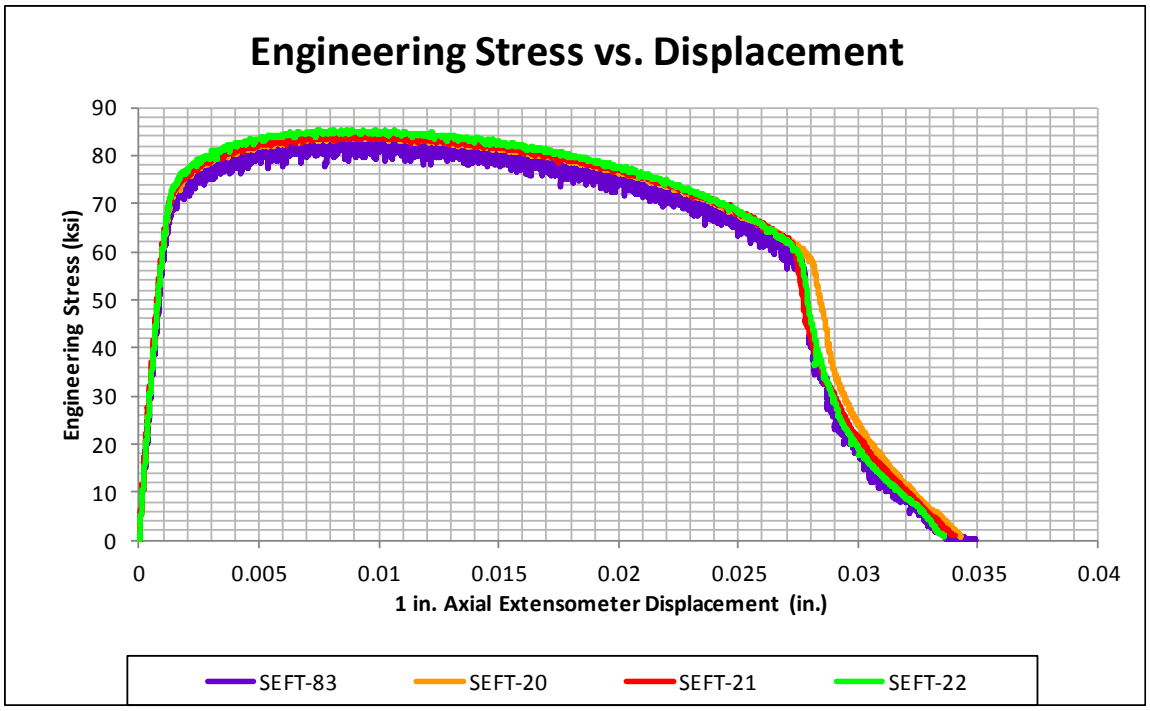

Figure 110. Flat Sharp Notch Specimen: Engineering Stress vs. Displacement from 1-in. (25.4-mm) Gauge Length Measurements

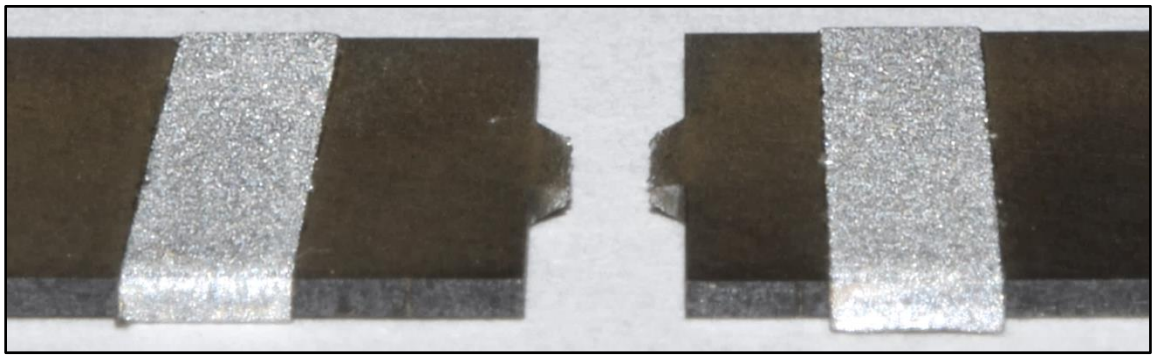

Figure 111. Small Notched Flat Specimen: Macro View of Typical Failure Zone

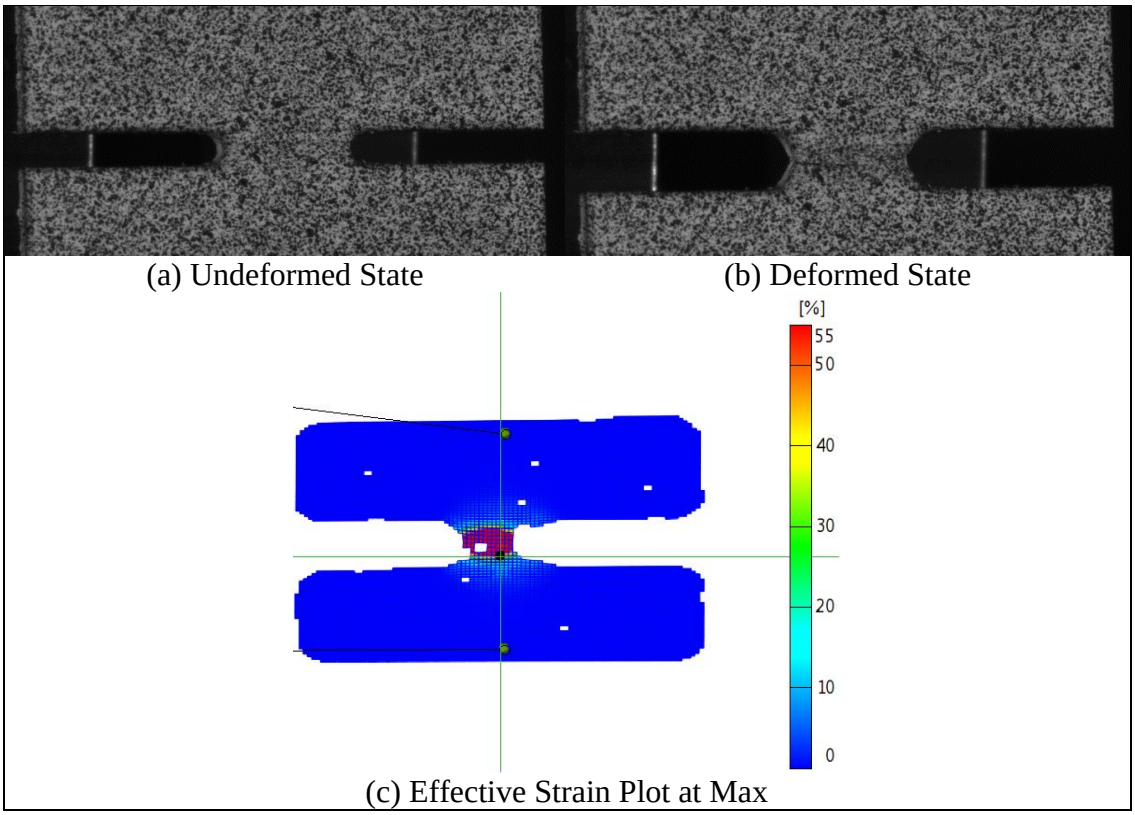

Figure 112. Sharp Notched Flat Specimen: DIC Analysis, SEFT-84

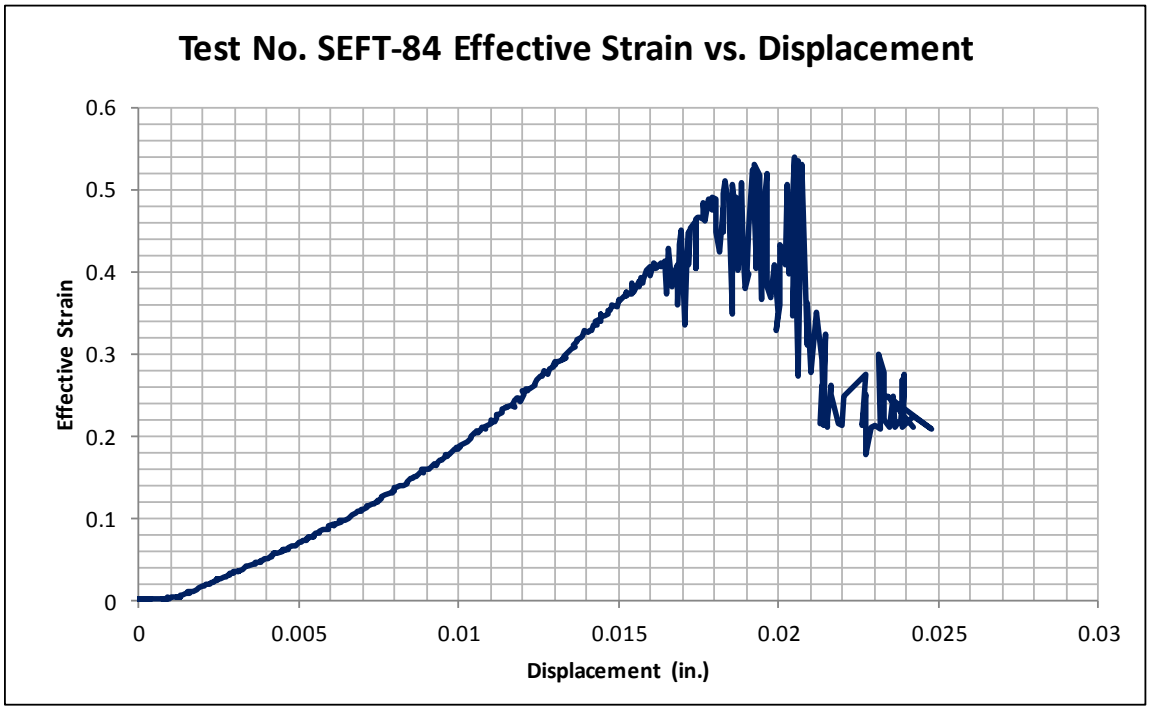

Figure 113. Flat Sharp Notched Specimen: Effective Engineering Strain vs. Displacement Data from DIC Analysis, SEFT-84

Table 13. Flat Sharp Notched Specimen: Summary of Results

Average Yield Stress (0.2% Offset) (1-in. Axial Extensometer)	77.3 ksi (533 MPa)
Average Ultimate Strength	89.2 ksi (615 MPa)
Engineering Stress at Failure	59.9 ksi (413 MPa)
Average Displacement at Failure (1-in. Axial Extensometer)	0.0204 in. (0.518 mm)
Average Cross-Sectional Area Reduction	41.0%
Maximum Effective Engineering Strain (DIC Analysis)	0.54

6.2.5 Axial-Symmetric Round Smooth Specimen Test Results

Test nos. SEFT-66 through SEFT-68 and SEFT-88 through SEFT-89 evaluated the Axial-Symmetric Round Smooth Specimen. Test nos. SEFT-66 through SEFT-68 were tested with two strips of retro-reflective tape, cut to a width of $^1/_8$ in. (3.2 mm), placed within the critical gauge length of the specimens. The laser extensometer was the primary measurement device for test nos. SEFT-66 through SEFT-68 as the retro-reflective tape placement allowed direct strain measurements of the specimen within the critical gauge length. A 2-in. (50.8-mm) axial extensometer was utilized on all of the noted tests and was placed outside the gauge length. The extra measurement device was utilized to aid in FEM modeling by providing a consistent length measurement for each test.

The engineering stress vs. engineering strain curves, as measured with the laser extensometer, produced similar results up to the initiation of necking, as seen in Figure 114. However, after necking initiation, some variations in the engineering strain measurement occurred. This variation can also be seen in the engineering stress vs. displacement curves measured with the 2-in. (50.8-mm) axial extensometer, as seen in

Figure 115. These differences can possibly be attributed to some variations in the post-necking initiation, material behavior of the test specimens.

Material properties calculated from the various measurements can be found in Table 14. Furthermore, a macro image of the typical failure zone can be seen in Figure 116. Typical cup and cone ductile failure behavior was exhibited in the failure region.

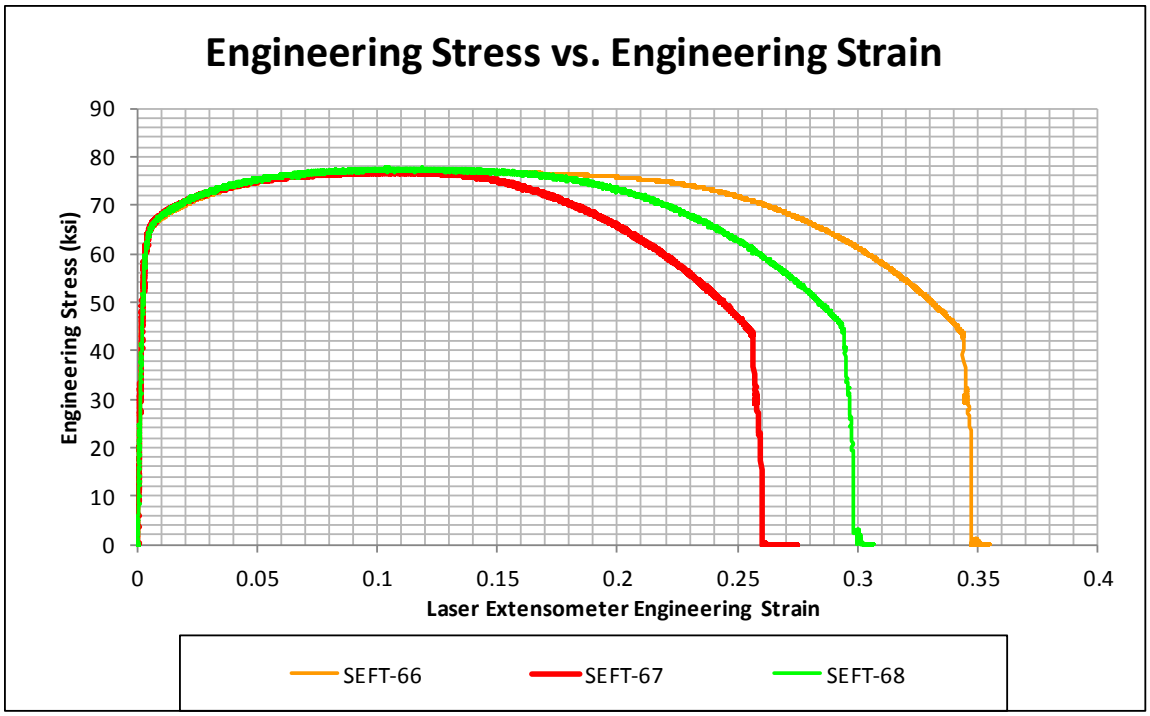

Figure 114. Axial-Symmetric Round Smooth Specimen: Engineering Stress vs. Engineering Strain from Critical Gauge Length Measurements, Test Nos. SEFT-66 through SEFT-68

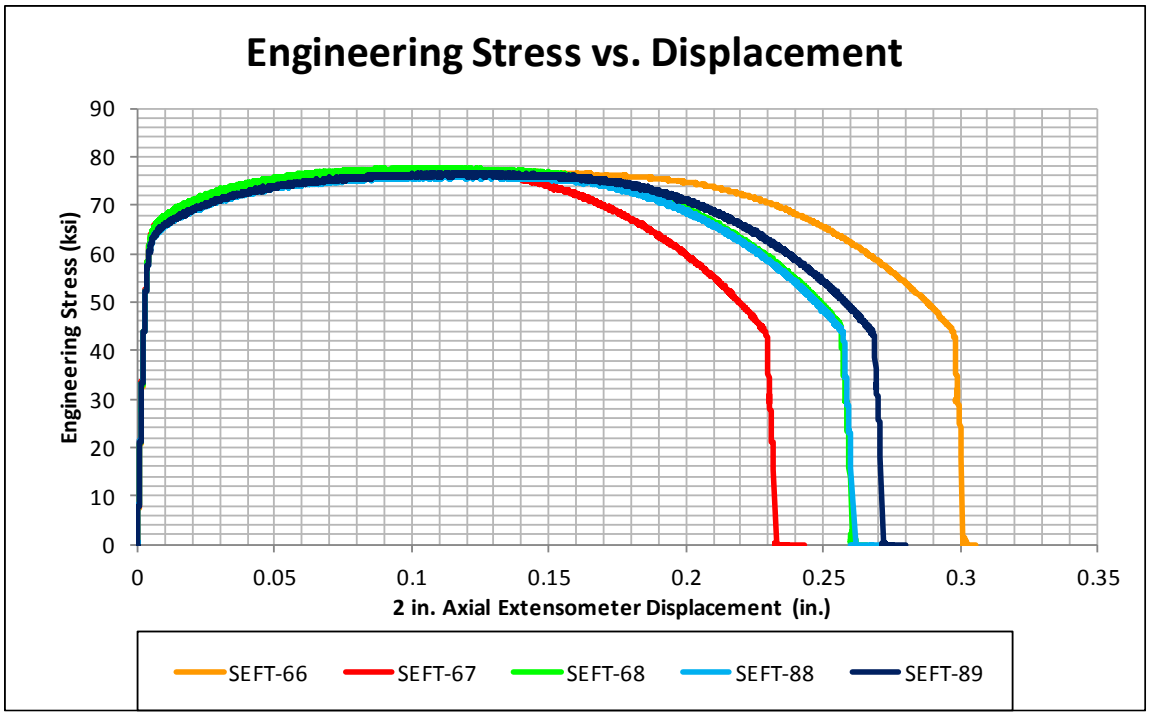

Figure 115. Axial-Symmetric Round Smooth Specimen: Engineering Stress vs. Displacement from 2-in. (50.8-mm) Axial Extensometer Measurements

Table 14. Axial-Symmetric Round Smooth Specimen: Summary of Material Properties

Average Young's Modulus (Laser Extensometer)	24,370 ksi (168,025 MPa)
Average Yield Stress (0.2% Offset) (Laser Extensometer and 2-in. Axial Extensometer)	62.7 ksi (432 MPa)
Average Ultimate Strength	76.4 ksi (527 MPa)
Engineering Stress at Failure	43.4 ksi (299 MPa)
Average Displacement at Failure (2-in. Axial Extensometer)	0.2619 in. (6.651 mm)
Average Cross-Sectional Area Reduction at Failure	73.1%
Average True Stress at Failure	241.3 ksi (1,664 MPa)
Average True Strain at Failure	1.2439
Maximum Effective Engineering Strain (DIC Analysis)	1.45

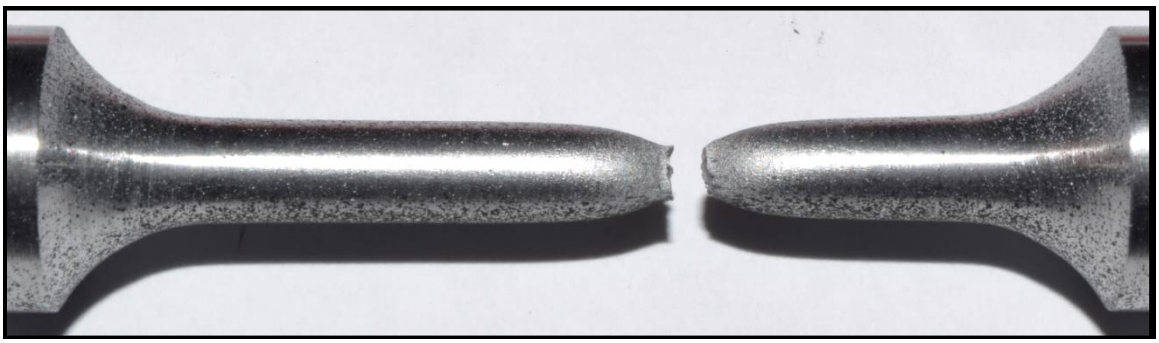

Figure 116. Axial-Symmetric Round Smooth Specimen, Typical Macro View of Failure Zone

DIC was utilized for test nos. SEFT-88 and SEFT-89. However, SEFT-89 provided superior results as diffuse necking and failure occurred in a more centralized region of the viewing area. As such, only the data for SEFT-89 is contained herein. A 1.34-in. x 1.10-in. (35-mm x 28-mm) viewing size was used to capture the DIC data on test no. SEFT-89. This viewing size did not allow any region outside the critical gauge length to be captured, as such the displacements measured with the DIC analysis cannot be directly compared to the physical extensometer measurements. However, the chosen viewing size was necessary to achieve an acceptable minimum resolution in the horizontal direction for the relatively-thin specimen. A pattern using the standard technique was utilized to prepare the specimen, as seen in Figure 117(a). The pattern allowed reliable displacement and strain data to be computed from the recorded images. During loading, the specimen failed when a crack formed, as seen in Figure 117(b). Prior to failure occurring, the DIC analysis recorded a maximum effective engineering strain of 1.45, as shown in Figure 118. The effective engineering strain plot at the state of maximum recorded strain can be found in Figure 117(c). The majority of the diffuse necking region was captured in the DIC analysis. Prior to the crack forming, the DIC analysis was unable to accurately continue tracking the stochastic pattern around the

crack region, and as a result, the recorded maximum effective engineering strain decreased or completely failed to measure strain due to the analysis's inability to track the pattern immediately prior to when the crack formed.

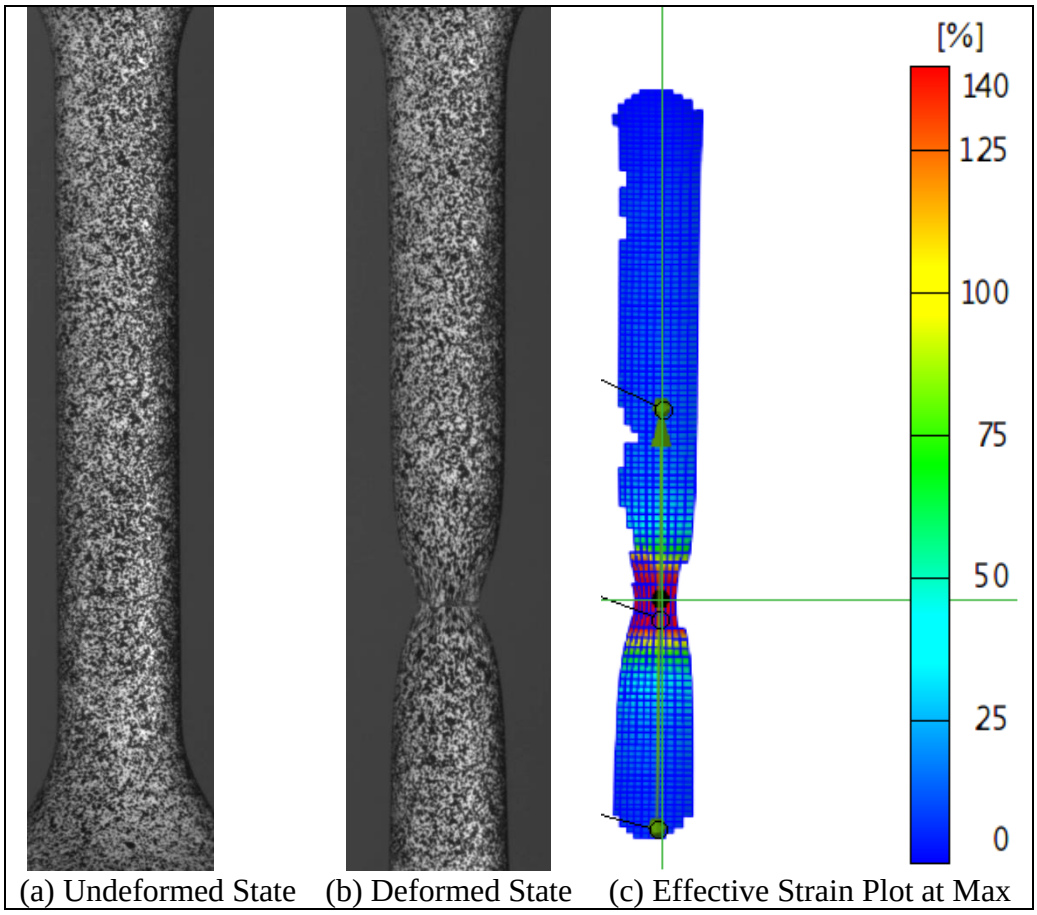

(a) Undeformed State (b) Deformed State (c) Effective Strain Plot at Max

Figure 117. Axial-Symmetric Round Smooth Specimen: DIC Analysis, Test No. SEFT-89

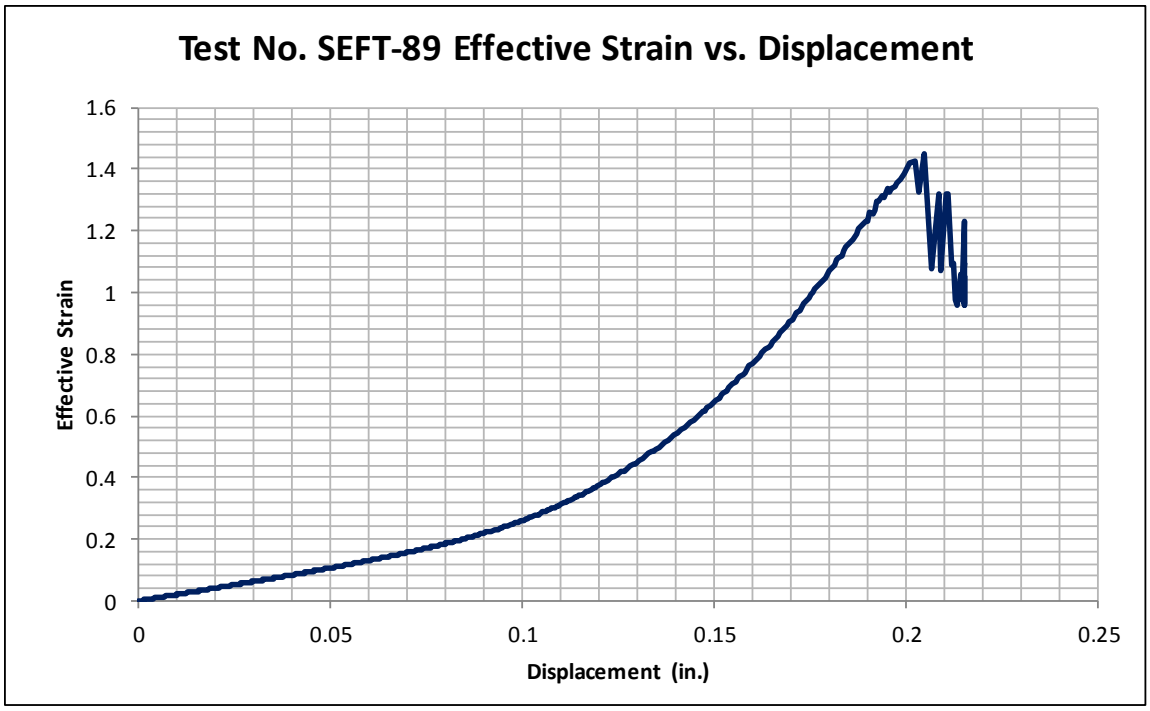

Figure 118. Axial-Symmetric Round Smooth Specimen: Effective Engineering Strain vs. Displacement Data from DIC Analysis, Test No. SEFT-89

6.2.6 Notched Round Specimen No. 1 Test Results

Test nos. SEFT-27 through SEFT-29, and SEFT-86 evaluated the Notched Round Specimen No. 1. Test nos. SEFT-27 through SEFT-29 were tested with two strips of retro-reflective tape, cut to a width of $^{1}/_{8}$ in. (3.2 mm), placed immediately outside the notched length of the specimen. All of the Notched Round Specimen No. 1 tests utilized a 2-in. (50.8-mm) axial extensometer placed on the specimen outside the notched length. The 2 in. axial extensometer was the primary measurement for all of the noted tests. However, the difference between the laser extensometer displacements and axial extensometer displacements was minimal, because the plastic deformation was localized to the region within the critical gauge length.

The specimens produced closely-grouped engineering stress vs. displacement curves, as shown in Figure 119. The average yield stress was 70.9 ksi (489 MPa). The

average stress and displacement at failure was 49.1 ksi (338 MPa) and 0.1057 in. (2.685 mm), respectively. Also, the average reduction in cross section was 68.8 percent. A macro image of the typical failure zone can be seen in Figure 120.

DIC was also utilized to track the strain and displacements of the specimen tested during test no. SEFT-86. A 1.34-in. x 1.10-in. (35-mm x 28-mm) viewing size was used to capture the DIC data on test no. SEFT-86. A pattern using the standard technique was utilized to prepare the specimen, as seen in Figure 121(a). The pattern allowed reliable displacement and strain data to be computed from the recorded images. During loading, the specimen failed when a crack formed initiating in the center of the specimen, as seen in Figure 121(b). Prior to failure occurring, the DIC analysis recorded a maximum effective engineering strain of 1.22, as shown in Figure 122. The effective engineering strain plot at the state of maximum recorded strain can be found in Figure 121(c). The majority of the diffuse necking region was captured in the DIC analysis. Prior to crack forming, the DIC analysis was unable to accurately continue tracking the stochastic pattern around the crack region, and as a result, the recorded maximum effective engineering strain decreased a large amount due to the analysis's inability to track strain immediately prior to when the crack formed. A summary of results is provided in Table 15.

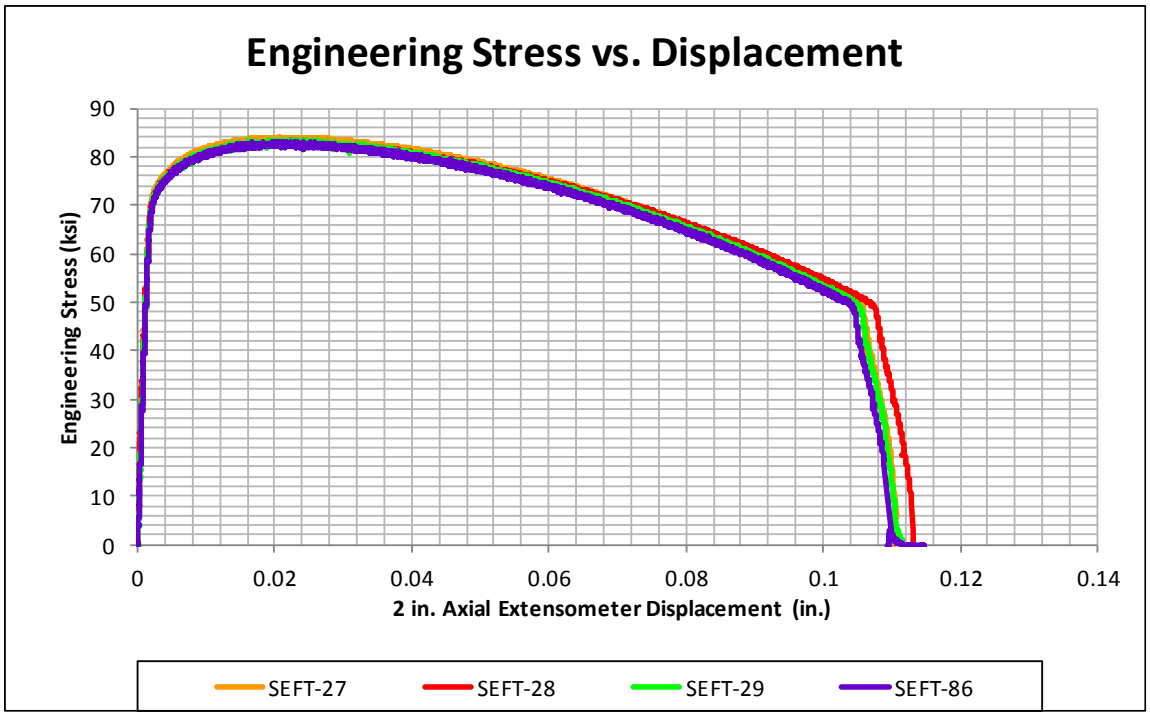

Figure 119. Notched Round Specimen No. 1: Engineering Stress vs. Displacement from 2-in. (50.8-mm) Gauge Length Measurements

Figure 120. Notched Round Specimen No. 1: Macro View of Typical Failure Zone

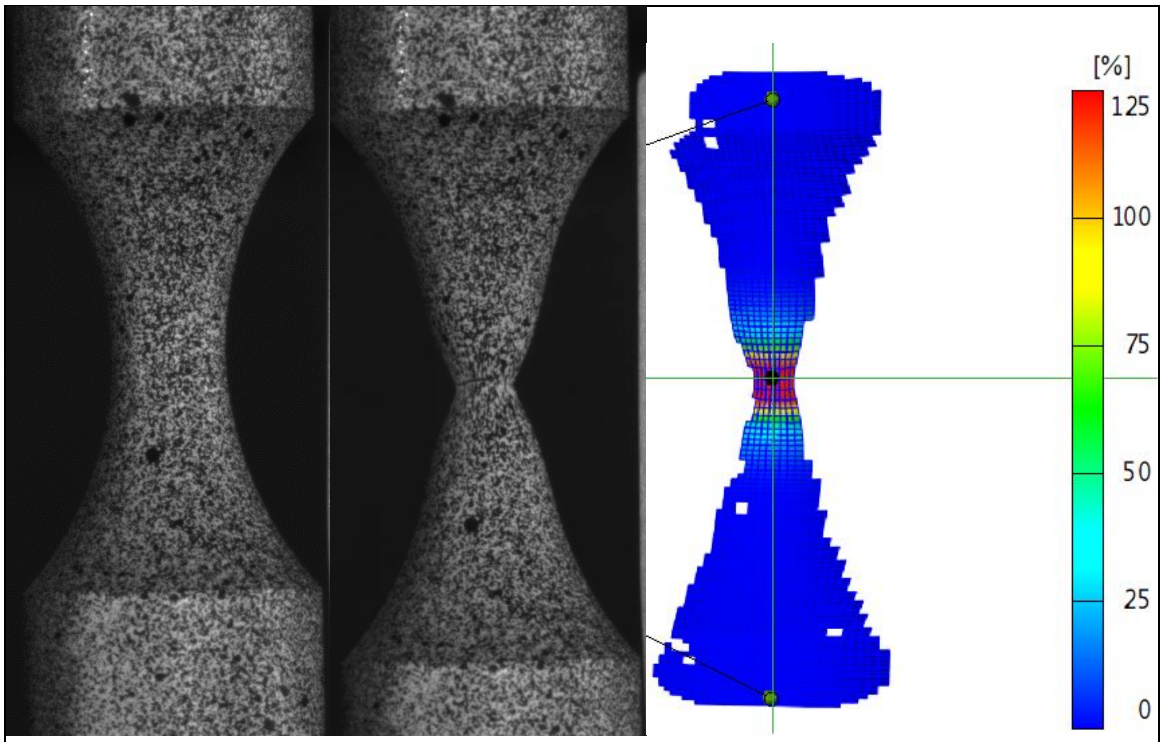

(a) Undeformed State (b) Deformed State (c) Effective Strain Plot at Max

Figure 121. Notched Round Specimen No.: DIC Analysis, Test No. SEFT-86

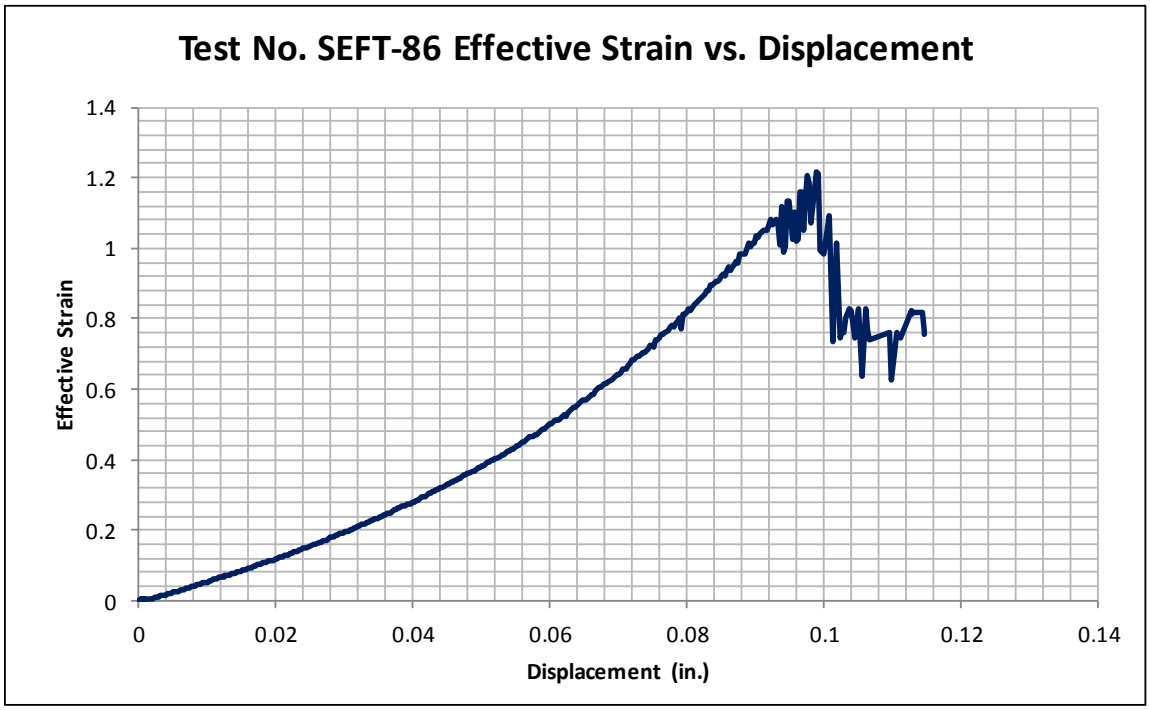

Figure 122. Notched Round Specimen No. 1: Effective Engineering Strain vs. Displacement Data from DIC Analysis, Test No. SEFT-86

Table 15. Notched Round Specimen No. 1: Summary of Results

Average Yield Stress (0.2% Offset) (2-in. Axial Extensometer)	70.9 ksi (489 MPa)
Average Ultimate Strength	83.5 ksi (576 MPa)
Engineering Stress at Failure	49.1 ksi (339 MPa)
Average Displacement at Failure (2-in. Axial Extensometer)	0.1057 in. (2.685 mm)
Average Cross-Sectional Area Reduction	68.8%
Maximum Effective Engineering Strain (DIC Analysis)	1.22

6.2.7 Notched Round Specimen No. 2 Test Results

Test nos. SEFT-30 through SEFT-32, and SEFT-87 evaluated the Notched Round Specimen No. 2. Test nos. SEFT-30 through SEFT-32 were tested with two strips of retro-reflective tape, cut to a width of $^{1}/_{8}$ in. (3.2 mm), placed immediately outside the notched length of the specimen. All of the Notched Round Specimen No. 2 tests utilized a 2-in. (50.8-mm) axial extensometer placed on the specimen outside the notched length. The 2-in. (50.8-mm) axial extensometer was the primary measurement for all of the noted tests. However, the difference between the laser extensometer displacements and axial extensometer displacements was minimal, because the plastic deformation was localized to the region within the critical gauge length.

The specimens produced closely-grouped engineering stress vs. displacement curves, as shown in Figure 123. The average yield stress was 72.3 ksi (498 MPa). The average stress and displacement at failure was 51.9 ksi (258 MPa) and 0.0932 in. (2.367 mm), respectively. Also, the average reduction in cross section was 68.3 percent. A macro image of the typical failure zone can be seen in Figure 124.

DIC was also utilized to track the strain and displacements of the specimen during test no. SEFT-87. A 1.34-in. x 1.10-in. (35-mm x 28-mm) viewing size was used to capture the DIC data on test no. SEFT-87. A pattern using the standard technique was utilized to prepare the specimen, as seen in Figure 125(a). The pattern allowed reliable displacement and strain data to be computed from the recorded images. During loading, the specimen failed when a crack formed initiating in the center of the specimen, as seen in Figure 125(b). Prior to failure occurring, the DIC analysis recorded a maximum effective engineering strain of 1.13, as shown in Figure 126. The effective engineering strain plot at the state of maximum recorded strain can be found in Figure 125(c). The majority of the diffuse necking region was captured in the DIC analysis. Prior to crack forming, the DIC analysis was unable to accurately continue tracking the stochastic pattern around the crack region, and as a result, the recorded maximum effective engineering strain decreased and became noisy due to the analysis's inability to accurately track strain in the area where the crack formed. A summary of results is provided in Table 16.

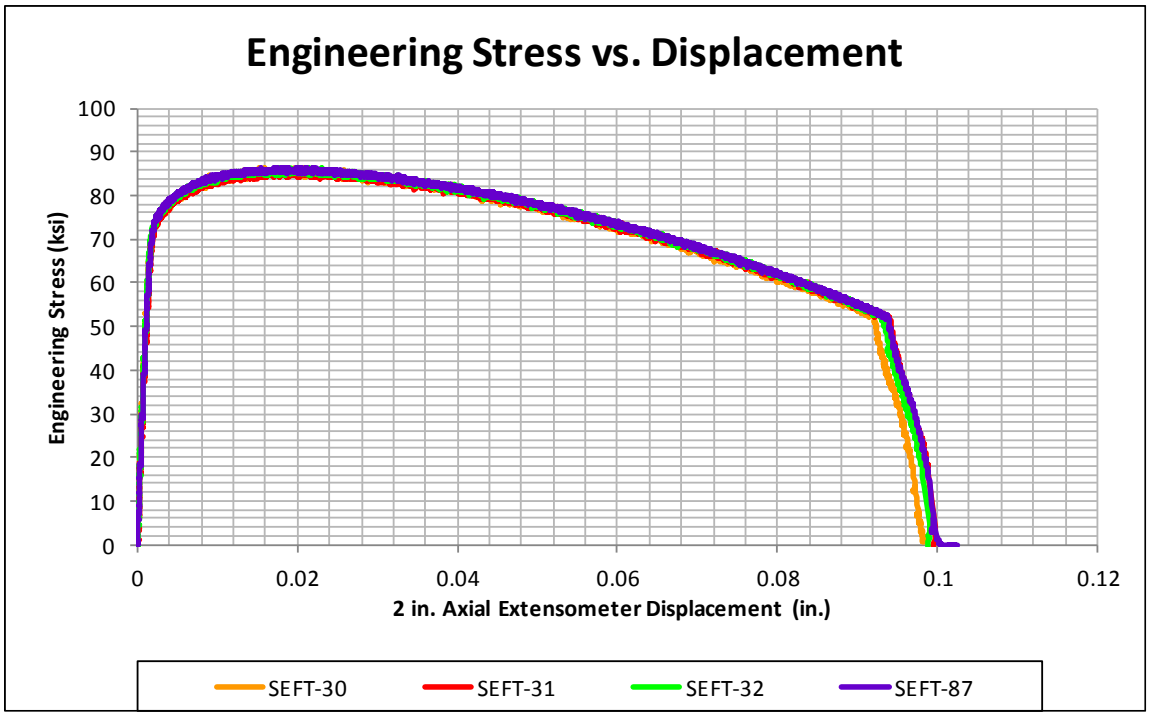

Figure 123. Notched Round Specimen No. 2: Engineering Stress vs. Displacement from 2 in. (50.8 mm) Gauge Length Measurements

Figure 124. Notched Round Specimen No. 2: Macro View of Typical Failure Zone

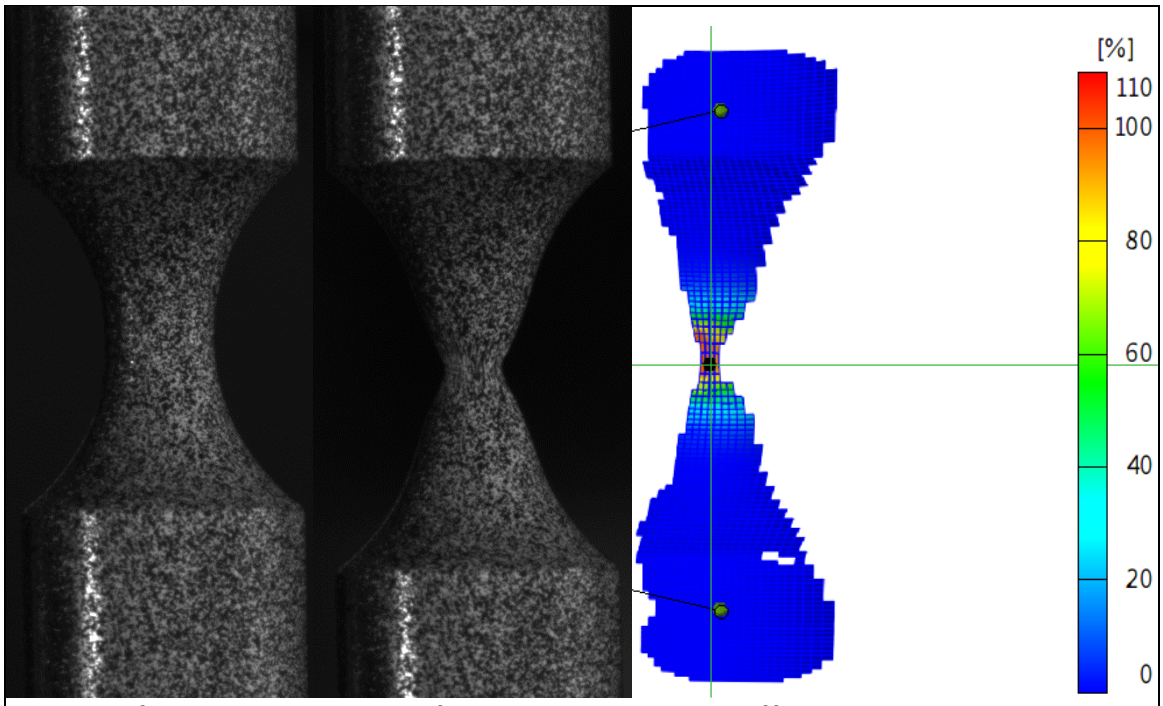

(a) Undeformed State (b) Deformed State (c) Effective Strain Plot at Max

Figure 125. Notched Round Specimen No. 2: DIC Analysis, Test No. SEFT-87

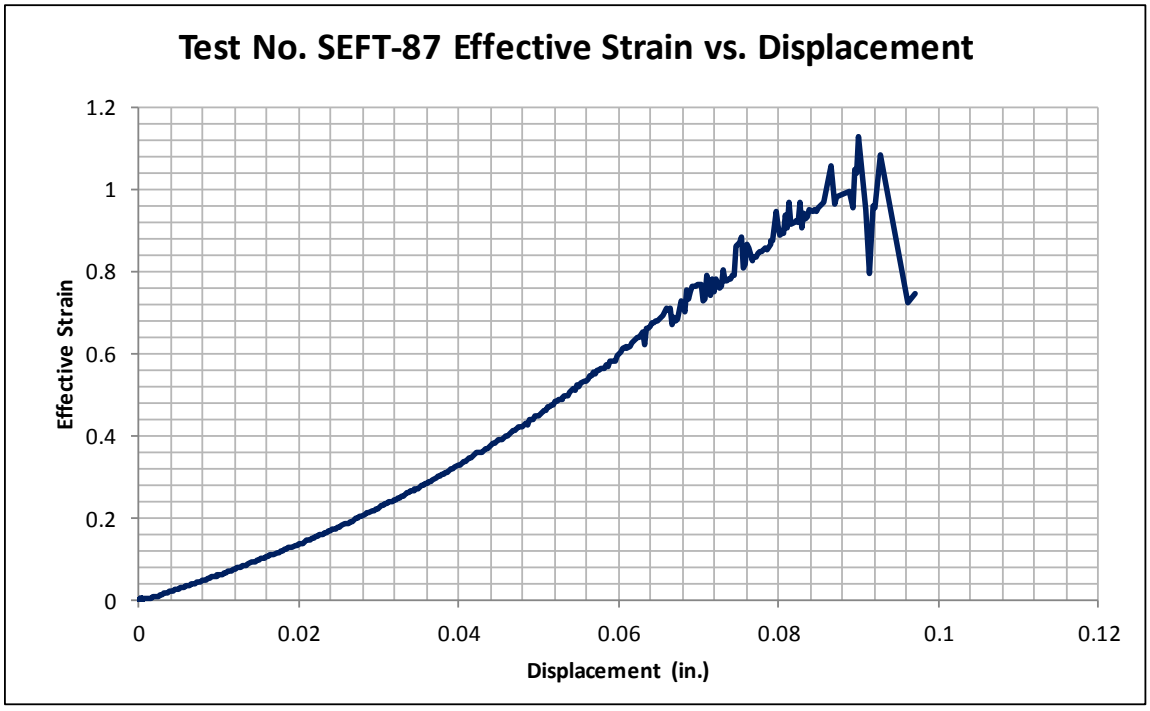

Figure 126. Notched Round Specimen No. 2: Effective Engineering Strain vs. Displacement Data from DIC Analysis, Test No. SEFT-87

Table 16. Notched Round Specimen No. 2: Summary of Results

Average Yield Stress (0.2% Offset) (2-in. Axial Extensometer)	72.3 ksi (498 MPa)
Average Ultimate Strength	86.3 ksi (595 MPa)
Engineering Stress at Failure	51.9 ksi (358 MPa)
Average Displacement at Failure (2-in. Axial Extensometer)	0.0932 in. (2.367 mm)
Average Cross-Sectional Area Reduction	68.3%
Maximum Effective Engineering Strain (DIC Analysis)	1.13

6.2.8 Notched Round Specimen No. 3 Test Results

Test nos. SEFT-33 through SEFT-35, and SEFT-80 evaluated the Notched Round Specimen No. 3. Test nos. SEFT-33 through SEFT-35 were tested with two strips of retro-reflective tape, cut to a width of $^{1}/_{8}$ in. (3.2 mm), placed immediately outside the notched length of the specimen. All of the Notched Round Specimen No. 3 tests utilized a 2-in. (50.8-mm) axial extensometer placed on the specimen outside the notched length. The 2-in. (50.8-mm) axial extensometer was the primary measurement for all of the noted tests. However, the difference between the laser extensometer displacements and axial extensometer displacements was minimal, because the plastic deformation was localized to the region within the critical gauge length.

The specimens produced-closely grouped engineering stress vs. displacement curves, as shown in Figure 127. The average yield stress was 76.9 ksi (530 MPa). The average stress and displacement at failure was 56.2 ksi (389 MPa) and 0.0806 in. (2.047 mm), respectively. Also, the average reduction in cross section was 65.7 percent. A macro image of the typical failure zone can be seen in Figure 128.

DIC was also utilized to track the strain and displacements of the specimen tested during test no. SEFT-80. A 0.98-in. x 0.79-in. (25-mm x 20-mm) viewing size was used to capture the DIC data on test no. SEFT-80. A pattern using the standard technique was utilized to prepare the specimen, as seen in Figure 129(a). The pattern allowed reliable displacement and strain data to be computed from the recorded images. During loading, the specimen failed when a crack formed initiating in the center of the specimen, as seen in Figure 129(b). Prior to failure occurring, the DIC analysis recorded a maximum effective engineering strain of 1.23, as shown in Figure 130. The effective engineering strain plot at the state of maximum recorded strain can be found in Figure 129(c). The majority of the diffuse necking region was captured in the DIC analysis. Prior to crack forming, the DIC analysis was able to continue tracking the stochastic pattern around the crack region. However, immediately prior to the crack forming, the effective engineering strain calculations decrease and become noisy. The reliability of the later measurements is questionable. A summary of results is provided in Table 17.

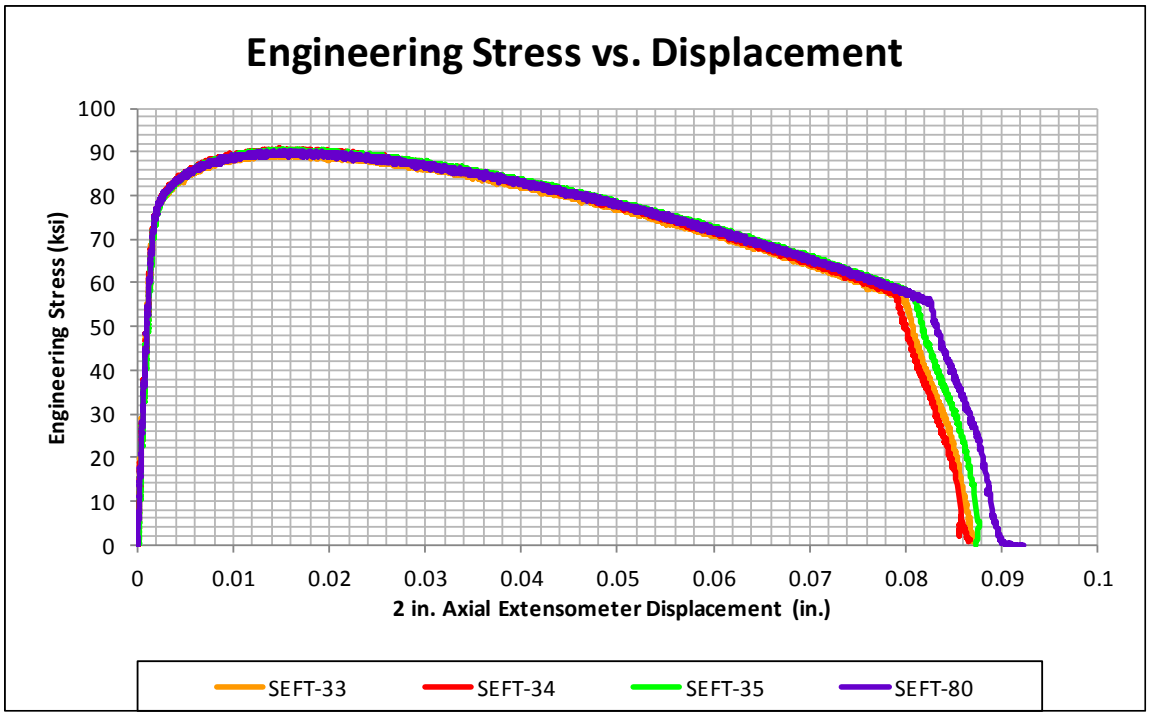

Figure 127. Notched Round Specimen No. 3: Engineering Stress vs. Displacement from 2-in. (50.8-mm) Gauge Length Measurements

Figure 128. Notched Round Specimen No. 3: Macro View of Typical Failure Zone

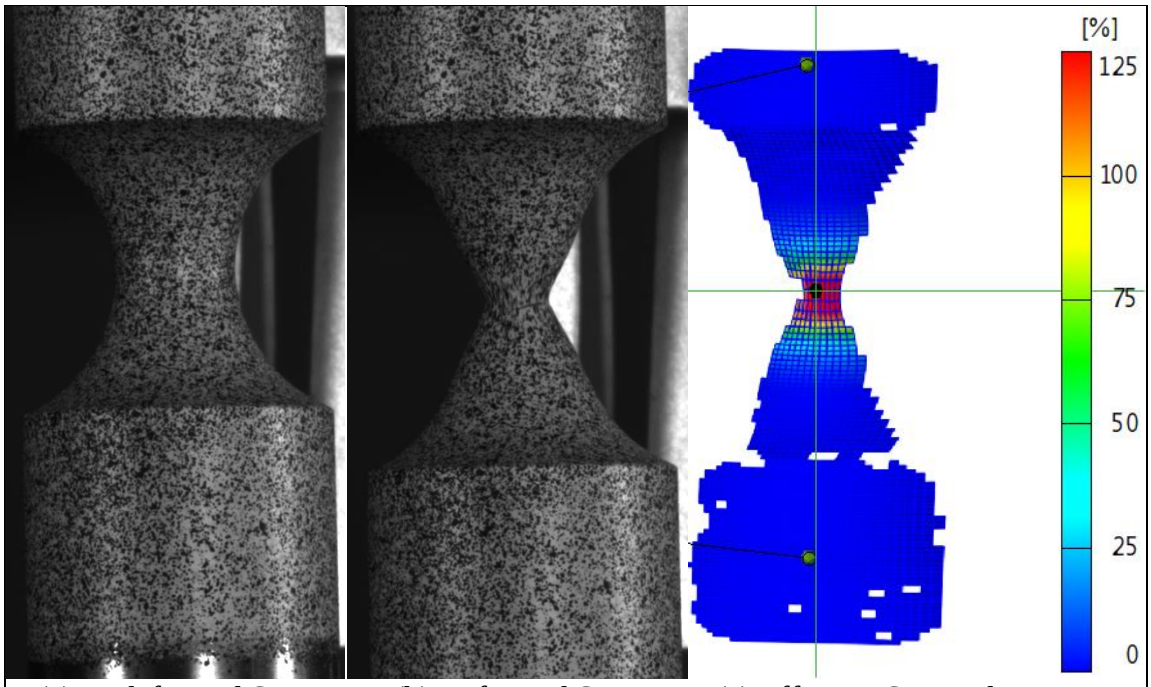

(a) Undeformed State (b) Deformed State (c) Effective Strain Plot at Max

Figure 129. Notched Round Specimen No. 3: DIC Analysis, Test No. SEFT-80

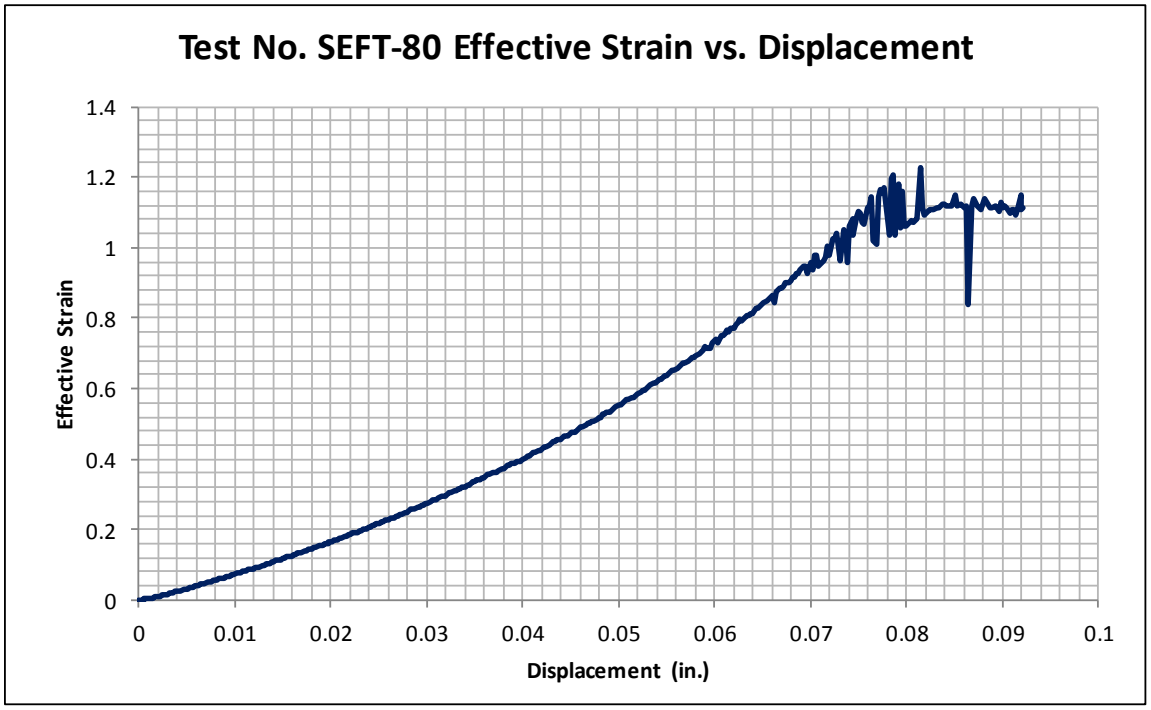

Figure 130. Notched Round Specimen No. 3: Effective Engineering Strain vs. Displacement Data from DIC Analysis, Test No. SEFT-80

Table 17. Notched Round Specimen No. 3: Summary of Results

Average Yield Stress (0.2% Offset) (2-in. Axial Extensometer)	76.9 ksi (530 MPa)
Average Ultimate Strength	90.5 ksi (624 MPa)
Engineering Stress at Failure	56.4 ksi (389 MPa)
Average Displacement at Failure (2-in. Axial Extensometer)	0.0806 in. (2.047 mm)
Average Cross-Sectional Area Reduction	65.7%
Maximum Effective Engineering Strain (DIC Analysis)	1.23

6.2.9 Notched Round Specimen No. 4 Test Results

Test nos. SEFT-36 through SEFT-38, and SEFT-78 evaluated the Notched Round Specimen No. 4. Test nos. SEFT-36 through SEFT-38 were tested with two strips of retro-reflective tape, cut to a width of $^{1}/_{8}$ in. (3.2 mm), placed immediately outside the notched length of the specimen. All of the Notched Round Specimen No. 4 tests utilized a 2-in. (50.8-mm) axial extensometer placed on the specimen outside the notched length. The 2-in. (50.8-mm) axial extensometer was the primary measurement for all of the noted tests. However, the difference between the laser extensometer displacements and axial extensometer displacements was minimal, because the plastic deformation was localized to the region within the critical gauge length.

The specimens produced closely-grouped engineering stress vs. displacement curves, as shown in Figure 131. The average yield stress was 79.2 ksi (546 MPa). The average stress and displacement at failure was 60.1 ksi (414 MPa) and 0.0720 in. (1.829 mm), respectively. Also, the average reduction in cross section was 63.3 percent. A macro image of the typical failure zone can be seen in Figure 132.

DIC was also utilized to track the strain and displacements of the specimen tested during test no. SEFT-78. A 0.98-in. x 0.79-in. (25-mm x 20-mm) viewing size was used to capture the DIC data on test no. SEFT-78. A pattern using the standard technique was utilized to prepare the specimen, as seen in Figure 133(a). The pattern allowed reliable displacement and strain data to be computed from the recorded images. During loading, the specimen failed when a crack formed initiating in the center of the specimen, as seen in Figure 133(b). Prior to failure occurring, the DIC analysis recorded a maximum effective engineering strain of 0.82 at a displacement of 0.0615 in. (1.562 mm), as shown in Figure 134. The effective engineering strain plot at the state of maximum recorded strain can be found in Figure 133(c). An adequate portion of the diffuse necking region was captured in the DIC analysis. However, prior to the crack forming, the DIC analysis was unable to accurately continue tracking the stochastic pattern around the crack region, and as a result, a portion of the strain measurement prior to the crack forming was unable to be measured. A summary of results is provided in Table 18.

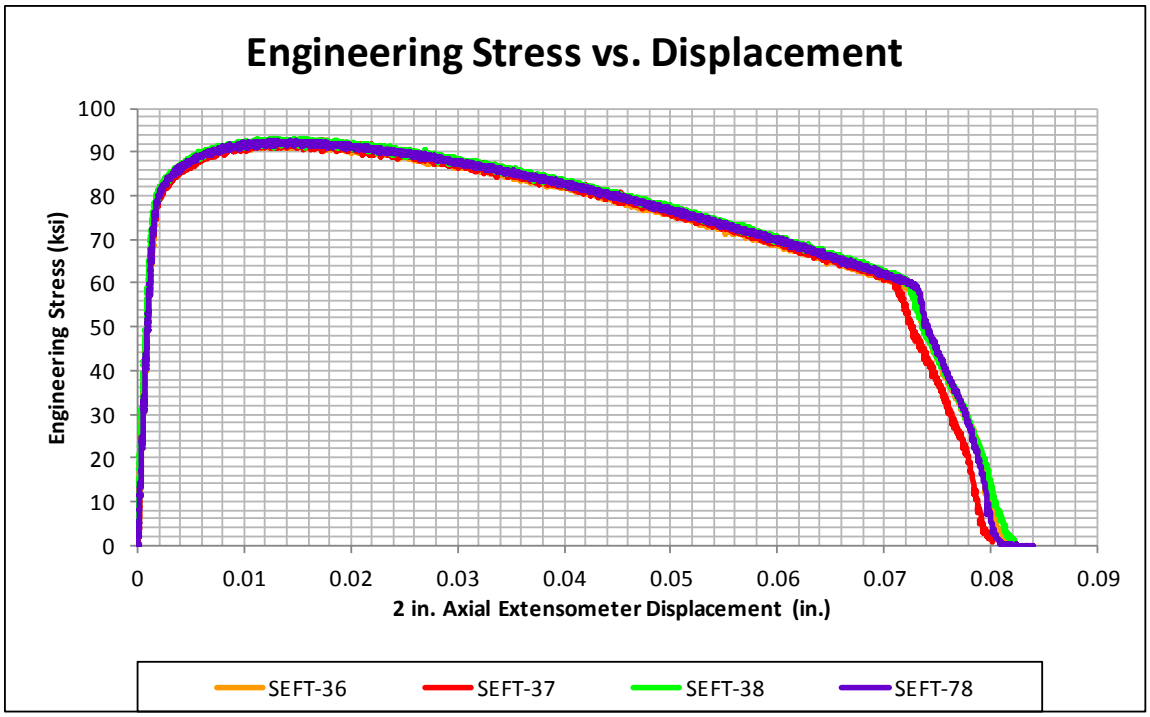

Figure 131. Notched Round Specimen No. 4: Engineering Stress vs. Displacement from 2-in. (50.8-mm) Gauge Length Measurements

Figure 132. Notched Round Specimen No. 4: Macro View of Typical Failure Zone

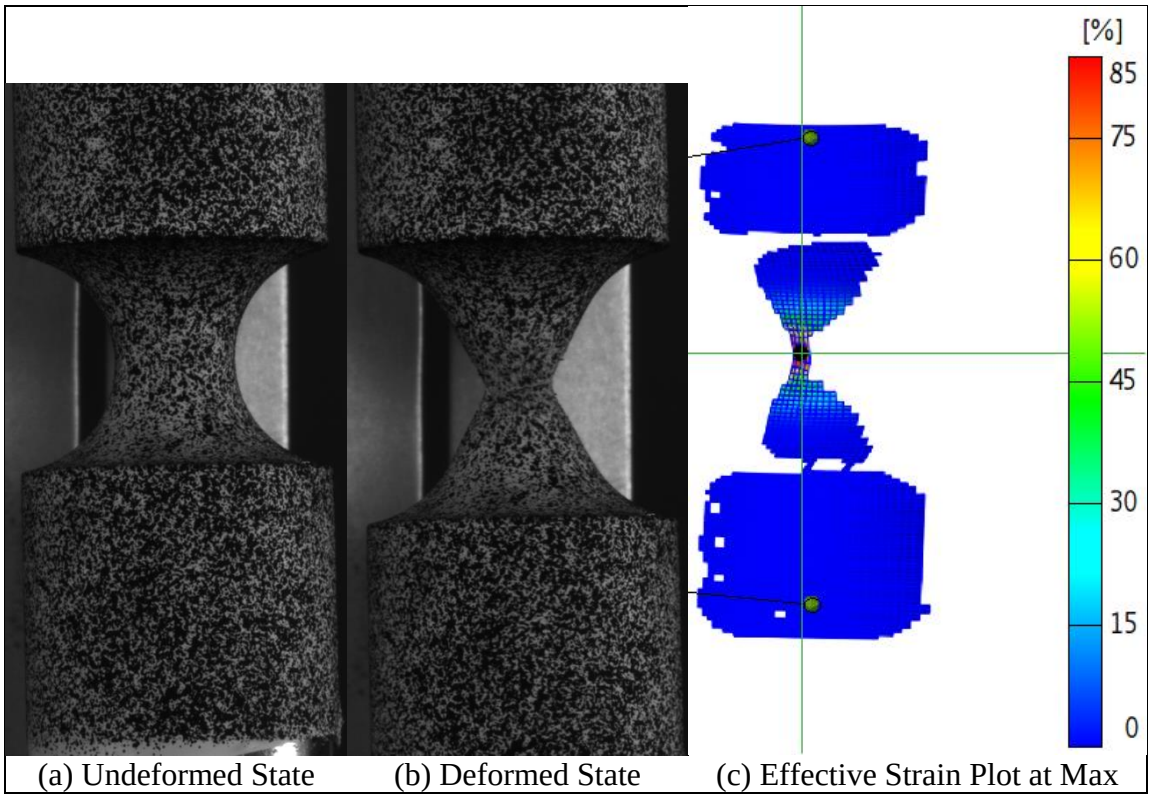

(a) Undeformed State (b) Deformed State (c) Effective Strain Plot at Max

Figure 133. Notched Round Specimen No. 4: DIC Analysis, Test No. SEFT-78

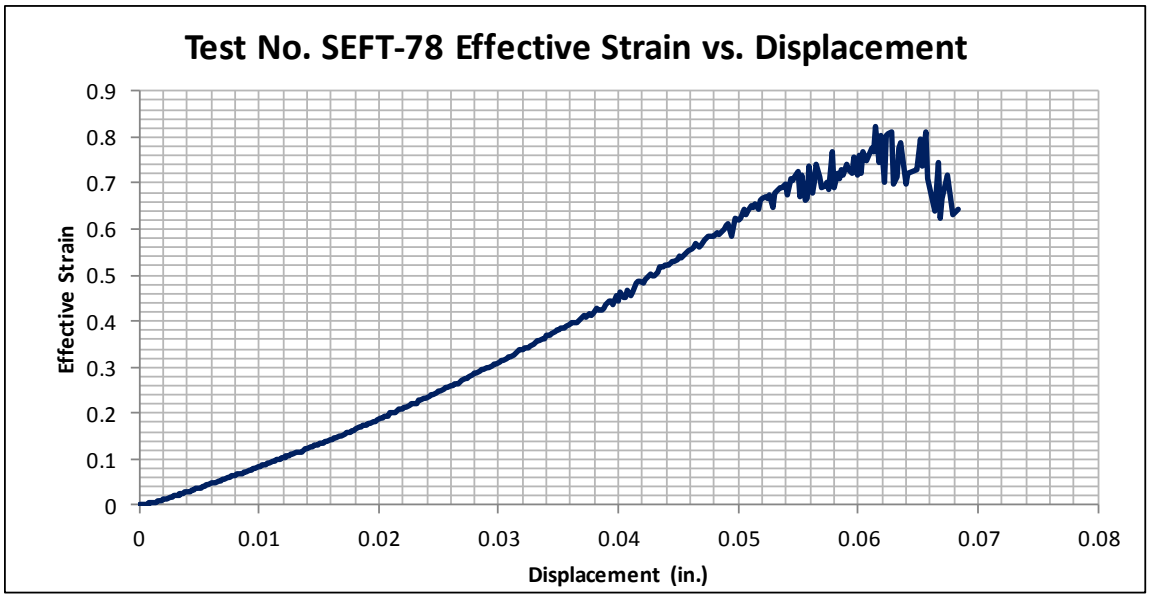

Figure 134. Notched Round Specimen No. 4: Effective Engineering Strain vs. Displacement Data from DIC Analysis, Test No. SEFT-78

Table 18. Notched Round Specimen No. 4: Summary of Results

Average Yield Stress (0.2% Offset) (2-in. Axial Extensometer)	79.2 ksi (546 MPa)
Average Ultimate Strength	92.8 ksi (640 MPa)
Engineering Stress at Failure	60.1 ksi (414 MPa)
Average Displacement at Failure (2-in. Axial Extensometer)	0.0720 in. (1.829 mm)
Average Cross-Sectional Area Reduction	63.3%
Maximum Effective Engineering Strain (DIC Analysis)	0.82

6.2.10 Notched Round Specimen No. 5 Test Results

Test nos. SEFT-39 through SEFT-41, and SEFT-82 evaluated the Notched Round Specimen No. 5. Test nos. SEFT-39 through SEFT-41 were tested with two strips of retro-reflective tape, cut to a width of $^{1}/_{8}$ in. (3.2 mm), placed immediately outside the notched length of the specimen. All of the Notched Round Specimen No. 5 tests utilized a 2-in. (50.8-mm) axial extensometer placed on the specimen outside the notched length. The 2-in. (50.8-mm) axial extensometer was the primary measurement for all of the noted tests. However, the difference between the laser extensometer displacements and axial extensometer displacements was minimal, because the plastic deformation was localized to the region within the critical gauge length.

The specimens produced closely-grouped engineering stress vs. displacement curves, as shown in Figure 135. The average yield stress was 85.1 ksi (587 MPa). The average stress and displacement at failure was 66.1 ksi (455 MPa) and 0.0602 in. (1.529 mm), respectively. Also, the average reduction in cross section was 60.9 percent. A macro image of the typical failure zone can be seen in Figure 136.

DIC was also utilized to track the strain and displacements of the specimen during test no. SEFT-82. A 0.59-in. x 0.47-in. (15-mm x 12-mm) viewing size was used to capture the DIC data on test no. SEFT-80. A pattern using the standard technique was utilized to prepare the specimen, as seen in Figure 137(a). The pattern allowed reliable displacement and strain data to be computed from the recorded images. During loading, the specimen failed when a crack formed initiating in the center of the specimen, as seen in Figure 137(b). Prior to failure occurring, the DIC analysis recorded a maximum effective engineering strain of 1.40, as shown in Figure 138. The effective engineering strain plot at the state of maximum recorded strain can be found in Figure 137(c). The majority of the diffuse necking region was captured in the DIC analysis. Prior to crack forming, the DIC analysis was able to accurately continue tracking the stochastic pattern around the crack region, and as a result, the calculated effective engineering strain became noisy due to errors. A summary of results is provided in Table 19.

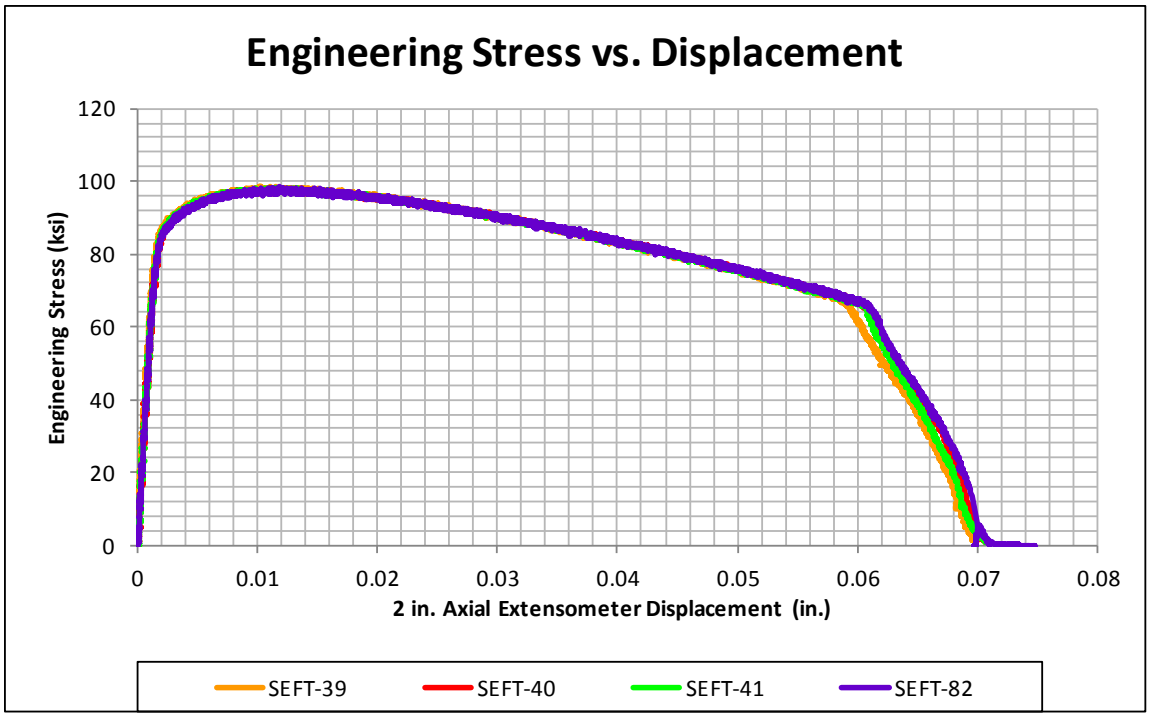

Figure 135. Notched Round Specimen No. 5: Engineering Stress vs. Displacement from 2-in. (50.8-mm) Gauge Length Measurements

Figure 136. Notched Round Specimen No. 5: Macro View of Typical Failure Zone

(a) Undeformed State (b) Deformed State

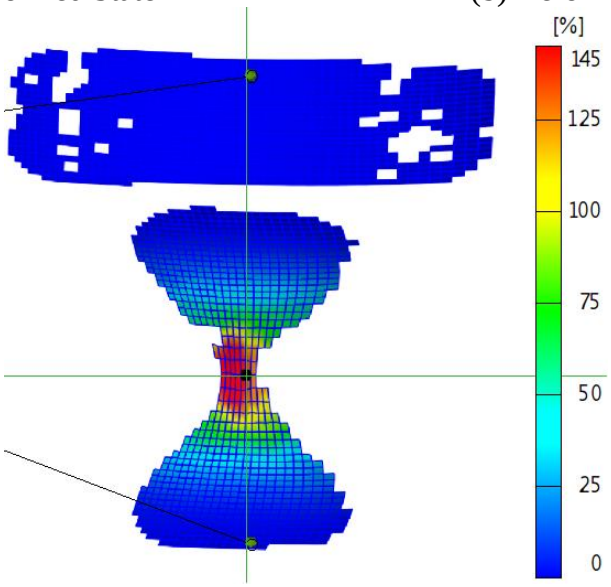

(c) Effective Strain Plot at Max

Figure 137. Notched Round Specimen No. 5: DIC Analysis, Test No. SEFT-82

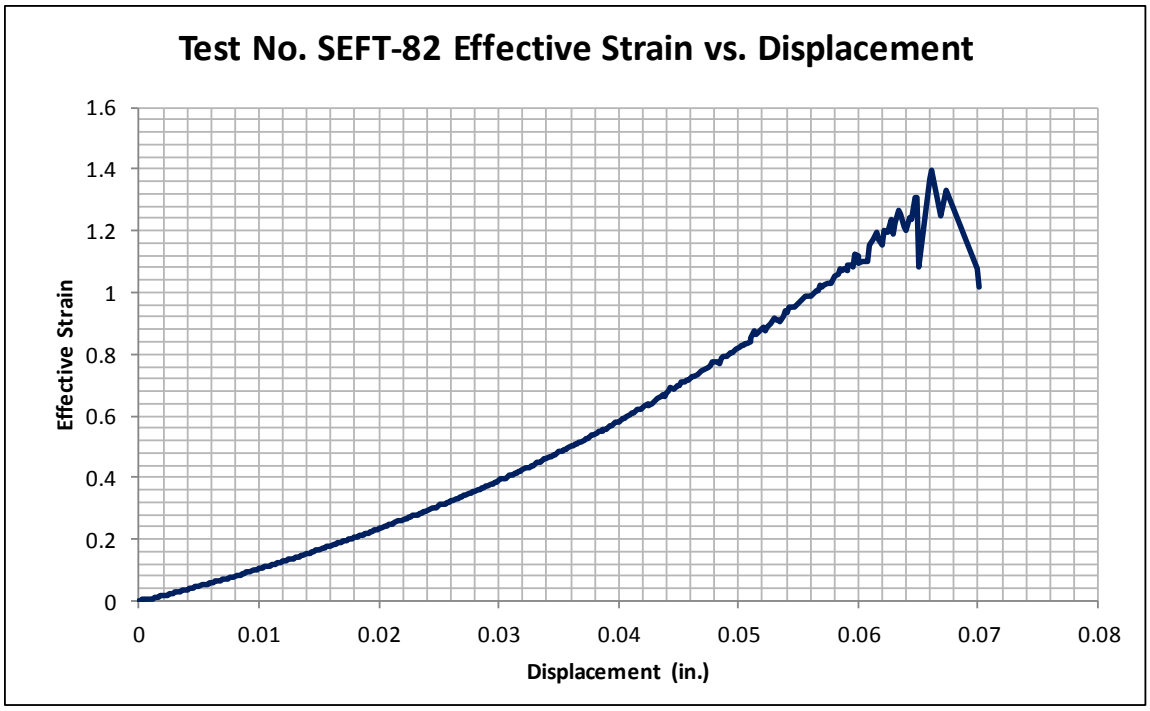

Figure 138. Notched Round Specimen No. 5: Effective Engineering Strain vs. Displacement Data from DIC Analysis, Test No. SEFT-82

Table 19. Notched Round Specimen No. 5: Summary of Results

Average Yield Stress (0.2% Offset) (2-in. Axial Extensometer)	85.1 ksi (587 MPa)
Average Ultimate Strength	98.3 ksi (678 MPa)
Engineering Stress at Failure	66.0 ksi (455 MPa)
Average Displacement at Failure (2-in. Axial Extensometer)	0.0602 in. (1.529 mm)
Average Cross-Sectional Area Reduction	60.9%
Maximum Effective Engineering Strain (DIC Analysis)	1.40

6.2.11 Thick Dog Bone Specimen Test Results

Test nos. SEFT-42 through SEFT-44, and SEFT-81 evaluated the Thick Dog Bone Specimens. Test nos. SEFT-42 through SEFT-44 were tested with two strips of retro-reflective tape, cut to a width of $^1/_8$ in. (3.2 mm), placed immediately outside the gauge length of the specimen. All of the Thick Dog Bone Specimens tests utilized a 2-in.

(50.8-mm) axial extensometer placed on the specimen outside the gauge length. The 2-in. (50.8-mm) axial extensometer was the primary measurement for all of the noted tests. However, the difference between the laser extensometer displacements and axial extensometer displacements was minimal, because the plastic deformation was localized to the region within the critical gauge length.

The specimen failed starting from the center of the critical cross section, as seen in Figure 139. The crack then extended outward until the specimen was completely separated, as seen in Figure 140.

The specimens produced closely-grouped engineering stress vs. displacement curves, as shown in Figure 141. The average yield stress was 64.6 ksi (446 MPa). The average stress and displacement at failure was 67.6 ksi (466 MPa) and 0.0727 in. (1.847 mm), respectively. Also, the average reduction in cross section was 41.3 percent. A macro image of the typical failure zone can be seen in Figure 140.

DIC was also utilized to track the strain and displacements of the specimen tested during test no. SEFT-81. A 0.98-in. x 0.79-in. (25-mm x 20-mm) viewing size was used to capture the DIC data on test no. SEFT-81. A pattern using the standard technique was utilized to prepare the specimen, as seen in Figure 142(a). The pattern allowed reliable displacement and strain data to be computed from the recorded images. During loading, the specimen failed when a crack quickly initiating in the center of the specimen, as seen in Figure 142(b). Prior to failure occurring, the DIC analysis recorded a maximum effective engineering strain of 1.04, as shown in Figure 143. The effective engineering strain plot immediately before failure had occurred can be found in Figure 142(c). The majority of the diffuse necking region was captured in the DIC analysis. The analysis was

able to continue tracking the pattern up to when the crack formed. After this point, the recorded maximum effective engineering strain decreased due to the analysis's inability to track strain in immediately adjacent to the newly formed crack. A summary of results is provided in Table 20.

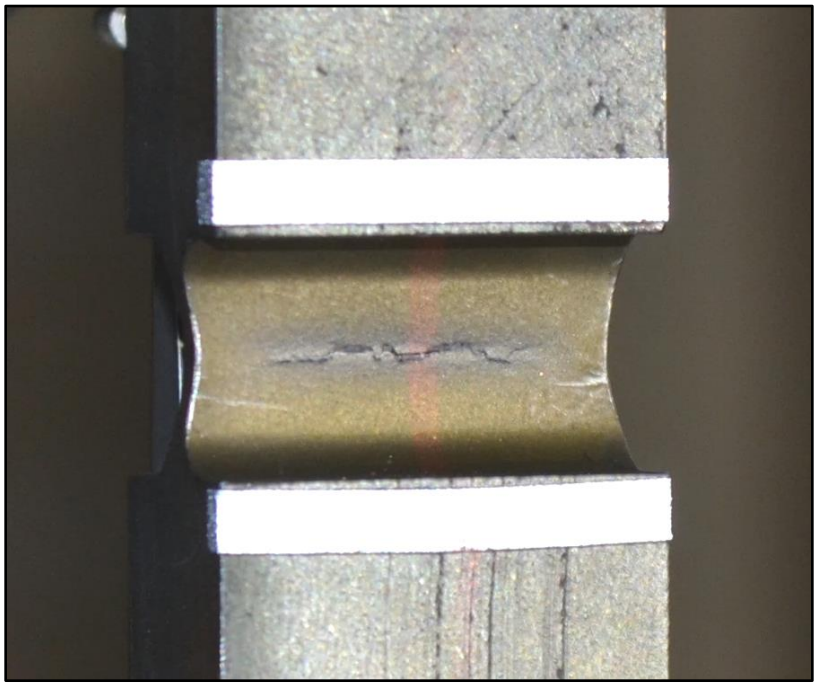

Figure 139. Thick Dog Bone Specimen: Macro View of Typical Partial Failure

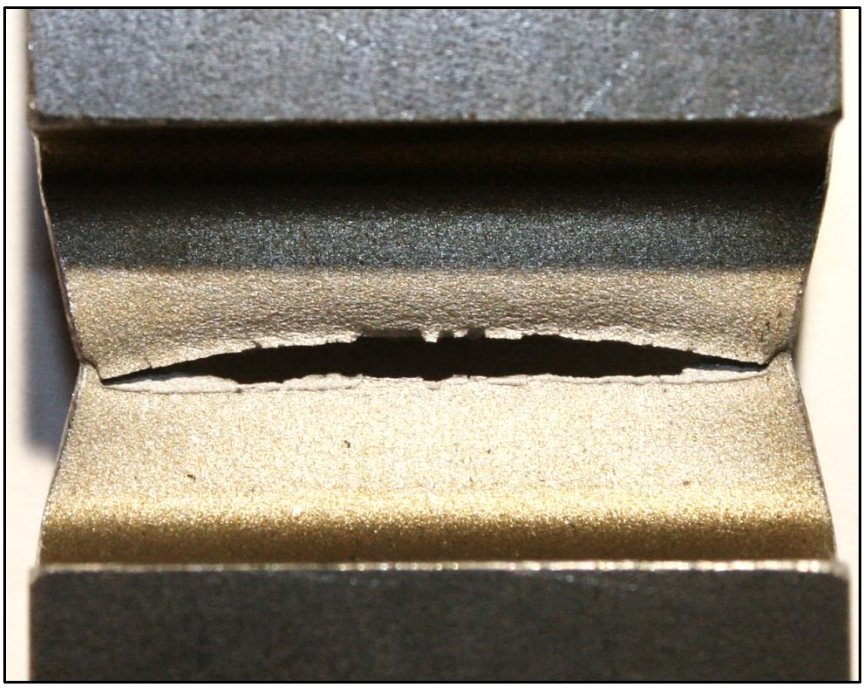

Figure 140. Thick Dog Bone Specimen: Macro View of Typical Complete Failure

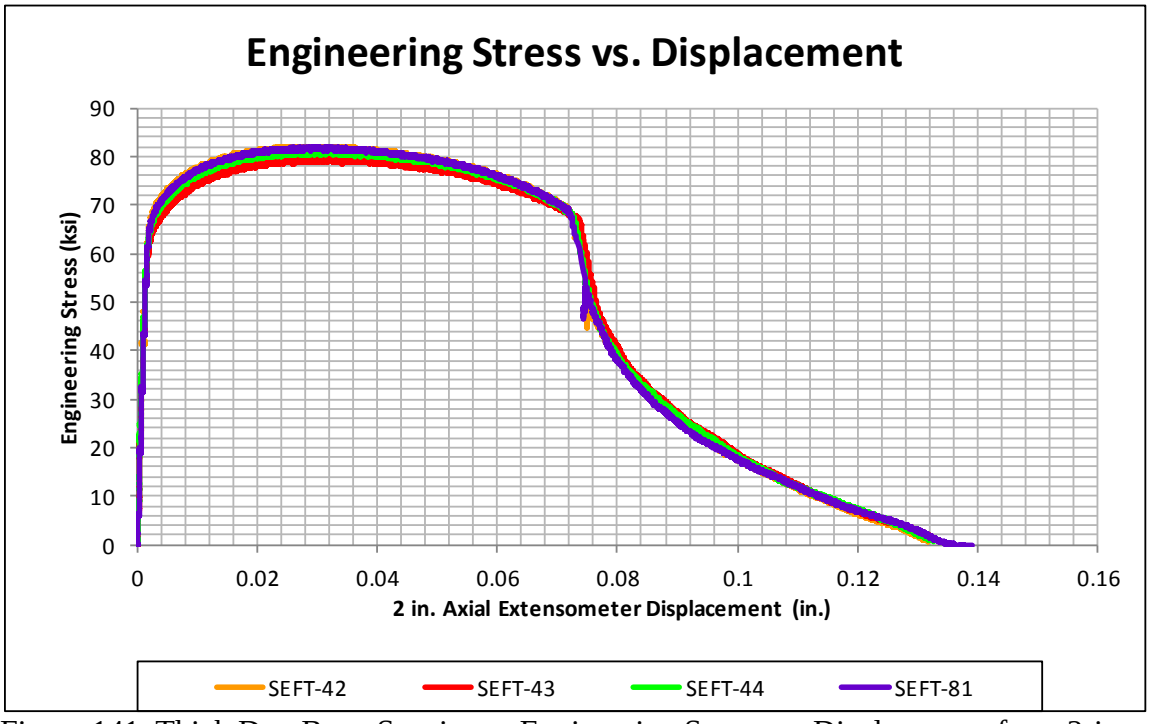

Figure 141. Thick Dog Bone Specimen: Engineering Stress vs. Displacement from 2-in. (50.8-mm) Gauge Length Measurements

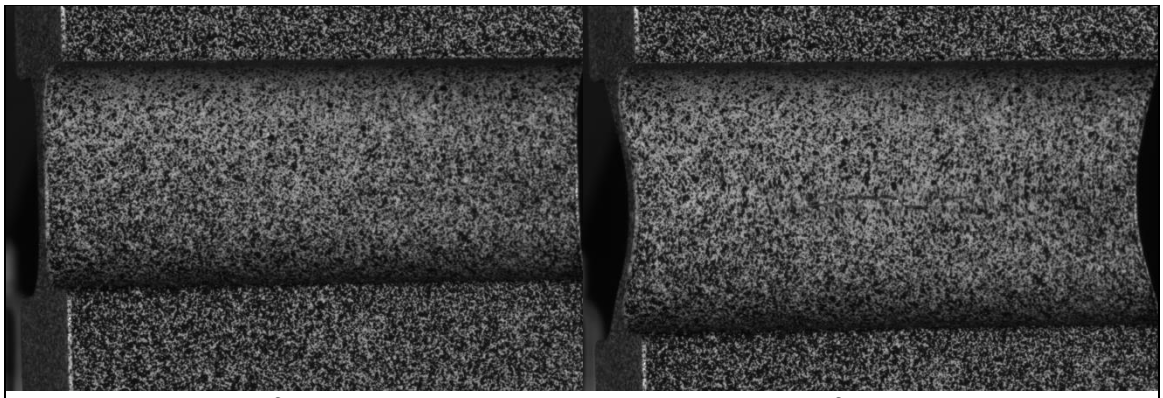

(a) Undeformed State (b) Deformed State

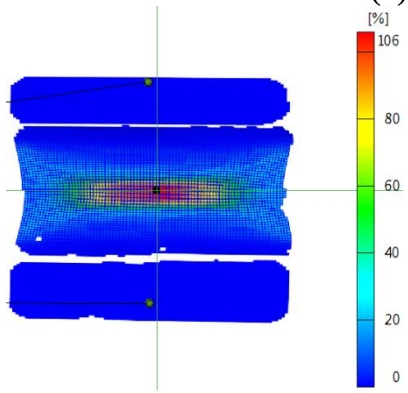

(c) Effective Strain Plot at Max

Figure 142. Thick Dog Bone Specimen: DIC Analysis, Test No. SEFT-81

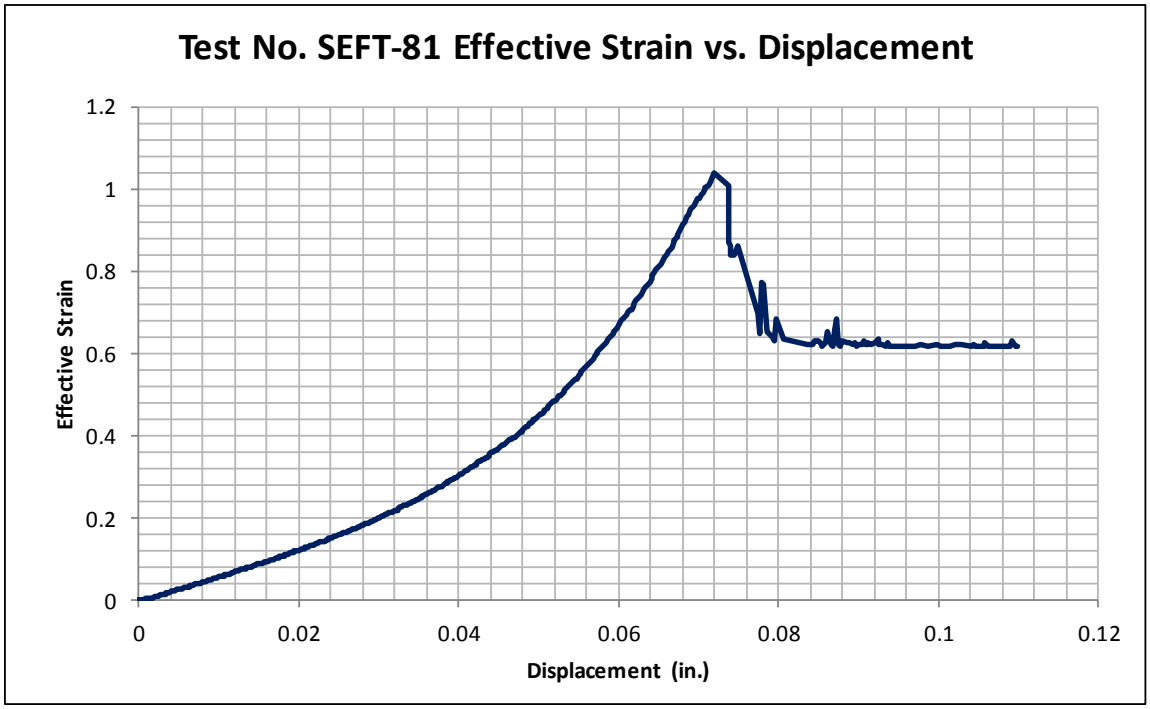

Figure 143. Thick Dog Bone Specimen: Effective Engineering Strain vs. Displacement Data from DIC Analysis, Test No. SEFT-81

Table 20. Thick Dog Bone Specimen: Summary of Results

Average Yield Stress (0.2% Offset) (2-in. Axial Extensometer)	64.6 ksi (445 MPa)
Average Ultimate Strength	81.3 ksi (561 MPa)
Engineering Stress at Failure	67.6 ksi (466 MPa)
Average Displacement at Failure (2-in. Axial Extensometer)	0.0727 in. (1.847 mm)
Average Cross-Sectional Area Reduction	41.3%
Maximum Effective Engineering Strain (DIC Analysis)	1.04

6.2.12 Thick Large Notched Specimen Test Results

Test nos. SEFT-45 through SEFT-47, and SEFT-85 evaluated the Thick Large Notched Specimens. Test nos. SEFT-45 through SEFT-47 were tested with two strips of retro-reflective tape, cut to a width of $^{1}/_{8}$ in. (3.2 mm), placed immediately outside the notched length of the specimen. All of the Thick Large Notched Specimens tests utilized a 2-in. (50.8-mm) axial extensometer placed on the specimen outside the notched length. The 2-in. (50.8-mm) axial extensometer was the primary measurement for all of the noted tests. However, the difference between the laser extensometer displacements and axial extensometer displacements was minimal, because the plastic deformation was localized to the region within the critical gauge length.

The specimens failed by quickly separating in the center of the critical cross section, while the far edges remained connected. As the actuator continued to displace, the specimen was reloaded, and the remaining material then plastically deformed and failed. Note, the test procedure for test nos. SEFT-45 and SEFT-47 were stopped prior to complete separation. The partial separation at the center of the thickness can be seen in Figure 144, while the complete separation can be seen in Figure 145.

The specimens produced closely-grouped engineering stress vs. displacement curves, as shown in Figure 146. The average yield stress was 73.0 ksi (503 MPa). The average stress and displacement at failure was 69. ksi (476 MPa) and 0.0516 in. (1.311 mm), respectively. Also, the average reduction in cross section was 39.2 percent.

DIC was also utilized to track the strain and displacements of the specimen tested during test no. SEFT-85. A 1.34-in. x 1.10-in. (35-mm x 28-mm) viewing size was used to capture the DIC data on test no. SEFT-85. A pattern using the standard technique was utilized to prepare the specimen, as seen in Figure 147(a). The pattern allowed reliable displacement and strain data to be computed from the recorded images. During loading, the specimen failed when a crack quickly initiated in the center of the specimen, as seen in Figure 147(b). Prior to failure occurring, the DIC analysis recorded a maximum effective engineering strain of 0.98, as shown in Figure 148. The effective engineering strain plot immediately before failure had occurred can be found in Figure 147(c). The majority of the diffuse necking region was captured in the DIC analysis. The analysis was able to continue tracking the pattern up to when the crack formed. After this point, the recorded maximum effective engineering strain decreased due to the analysis's inability to track strain in immediately adjacent to the newly formed crack. A summary of results is provided in Table 21.

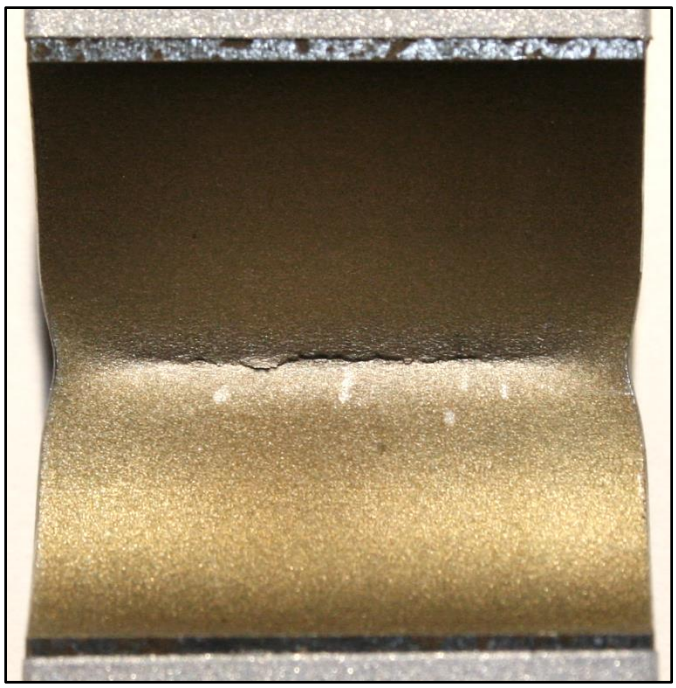

Figure 144. Thick Large Notched Specimen: Macro View of Typical Partial Failure

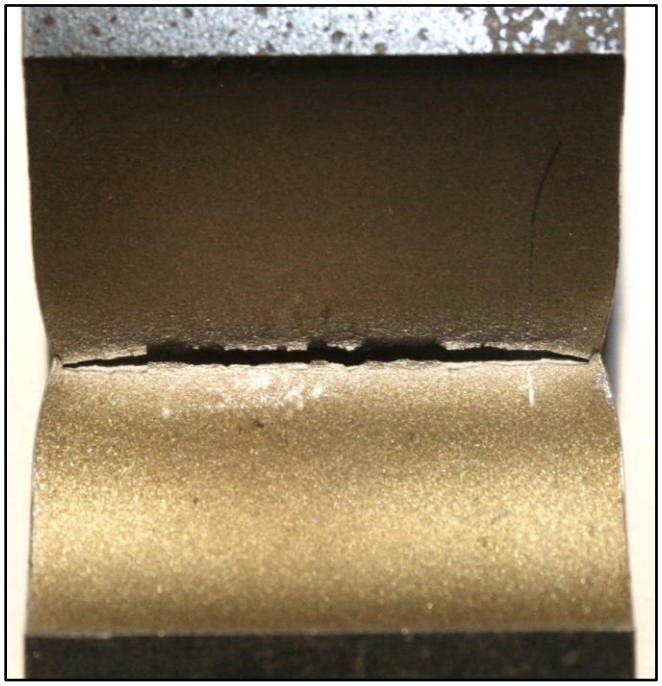

Figure 145. Thick Large Notched Specimen: Macro View of Typical Complete Failure

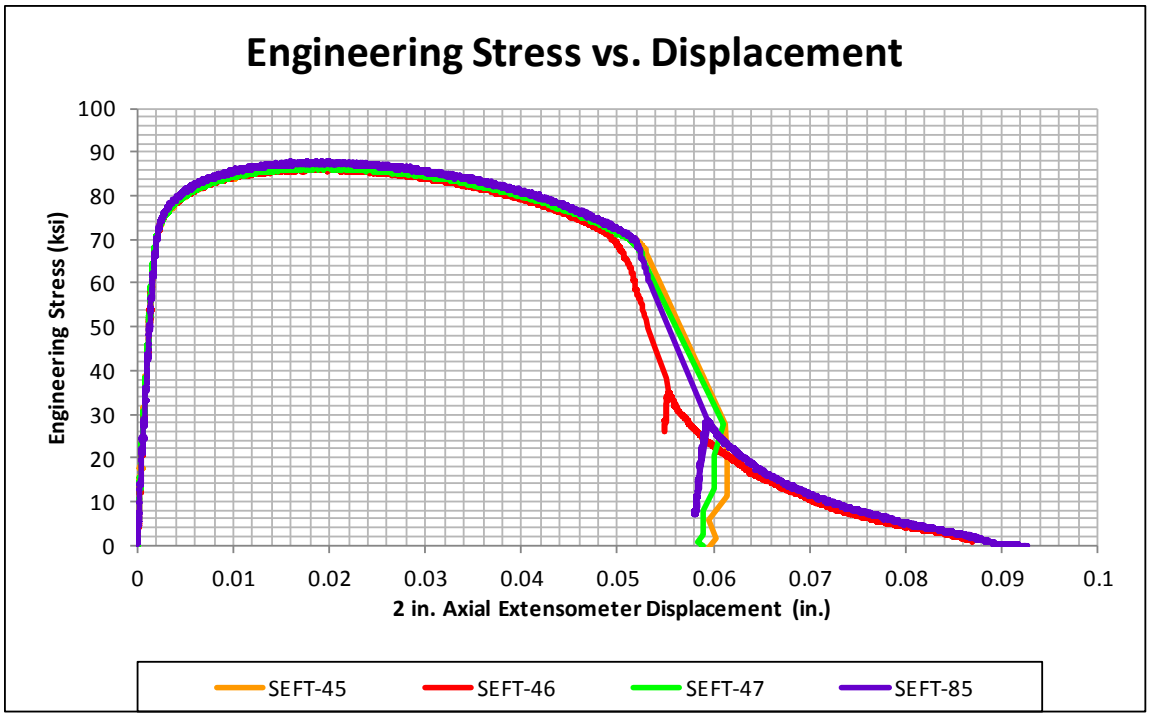

Figure 146. Thick Large Notched Specimen: Engineering Stress vs. Displacement from 2-in. (50.8-mm) Gauge Length Measurements

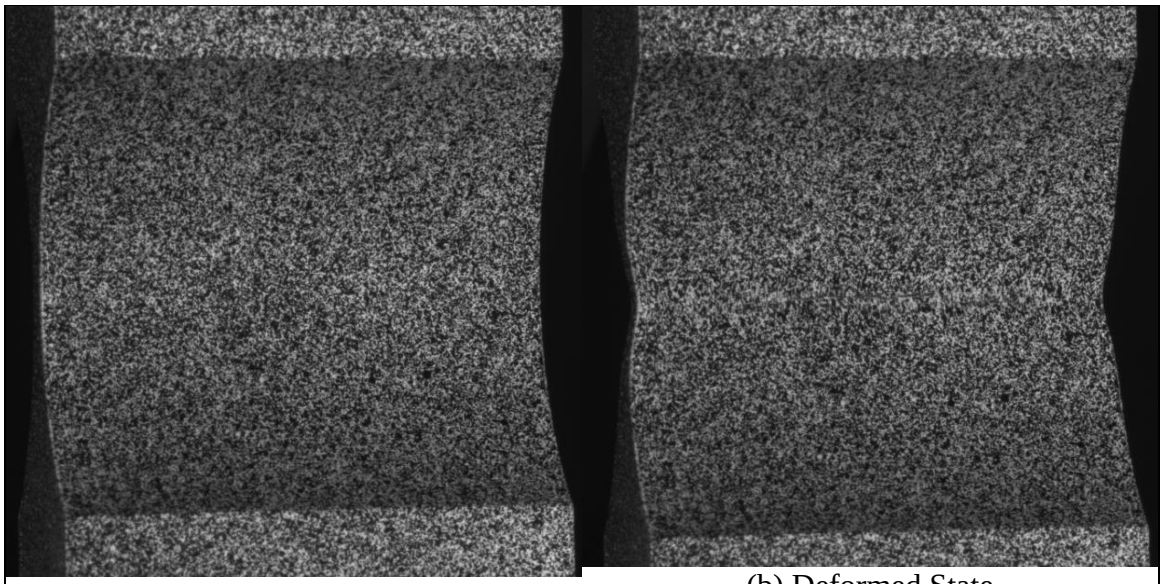

(a) Undeformed State (b) Deformed State

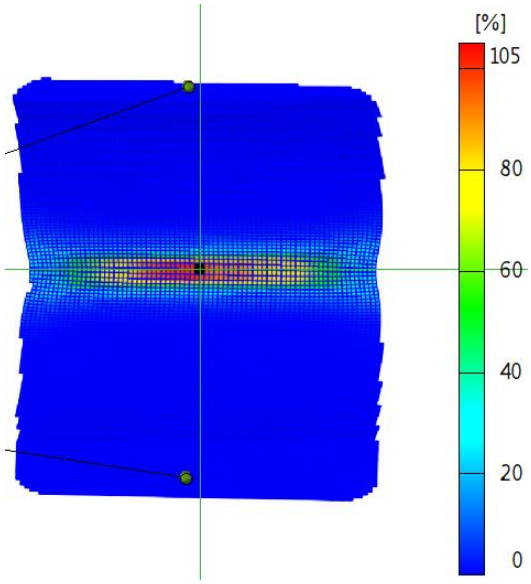

(c) Effective Strain Plot at Max

Figure 147. Large Notched Thick Specimen: DIC Analysis, Test No. SEFT-85

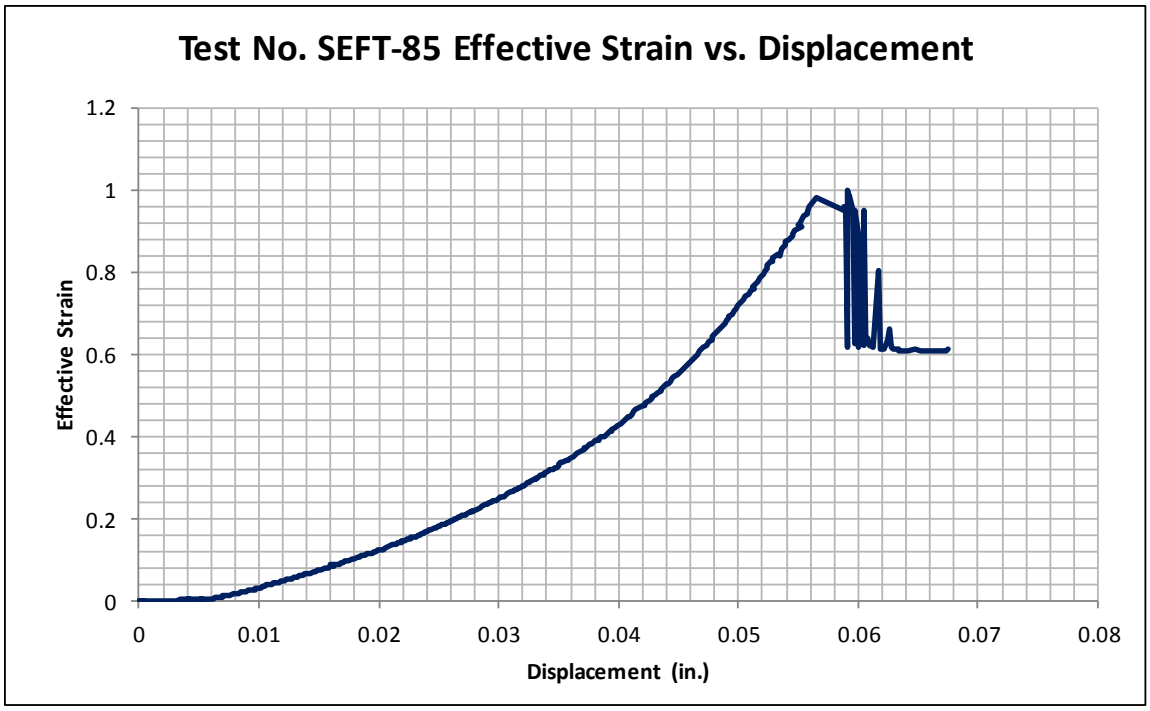

Figure 148. Thick Large Notched Specimen: Effective Engineering Strain vs. Displacement Data from DIC Analysis, Test No. SEFT-85

Table 21. Thick Large Notched Specimen: Summary of Results

Average Yield Stress (0.2% Offset) (2-in. Axial Extensometer)	73.0 ksi (503 MPa)
Average Ultimate Strength	86.9 ksi (599 MPa)
Engineering Stress at Failure	69.0 ksi (476 MPa)
Average Displacement at Failure (2-in. Axial Extensometer)	0.0516 in. (1.311 mm)
Average Cross-Sectional Area Reduction	39.2%
Maximum Effective Engineering Strain (DIC Analysis)	0.98

6.2.13 Thick Small Notched Specimen Test Results

Test nos. SEFT-48 through SEFT-50, and SEFT-101 evaluated the Thick Dog Bone Specimen. Test nos. SEFT-48 through SEFT-50 were tested with two strips of retro-reflective tape, cut to a width of $^1/_8$ in. (3.2 mm), placed immediately outside the notched length of the specimen. All of the Thick Small Notched Specimens tests utilized

a 2-in. (50.8-mm) axial extensometer placed on the specimen outside the notched length. The 2-in. (50.8-mm) axial extensometer was the primary measurement for all of the noted tests. However, the difference between the laser extensometer displacements and axial extensometer displacements was minimal, because the plastic deformation was localized to the region within the critical gauge length.

The specimens failed by quickly separating in the center of the critical cross section, while the far edges remained connected. As the actuator continued to displace, the specimen was reloaded and the remaining material then plastically deformed and failed. Note the test procedure for test no. SEFT-48 was stopped prior to complete separation. The partial separation can be seen in Figure 149, while the complete separation can be seen in Figure 150.

The specimens produced closely-grouped engineering stress vs. displacement curves, as shown in Figure 151. The average yield stress was 78.0 ksi (538 MPa). The average stress and displacement at failure was 70.6 ksi (487 MPa) and 0.0398 in. (1.011 mm), respectively. Also, the average reduction in cross section was 36.0 percent.

DIC was also utilized to track the strain and displacements of the specimen during test no. SEFT-101. A 0.98-in. x 0.79-in. (25-mm x 20-mm) viewing size was used to capture the DIC data on test no. SEFT-101. A pattern using the standard technique was utilized to prepare the specimen, as seen in Figure 152(a). The pattern allowed reliable displacement and strain data to be computed from the recorded images. During loading, the specimen failed when a crack quickly initiated in the center of the specimen, as seen in Figure 152(b). Prior to failure occurring, the DIC analysis recorded a maximum effective engineering strain of 0.57, as shown in Figure 153. The effective engineering

strain plot at immediately before failure had occurred can be found in Figure 152(c). The majority of the diffuse necking region was captured in the DIC analysis. The analysis was able to continue tracking the pattern up to when the crack formed. After this point, the recorded maximum effective engineering strain decreased due to the analysis's inability to track strain in immediately adjacent to the newly formed crack. A summary of results is provided in Table 22.

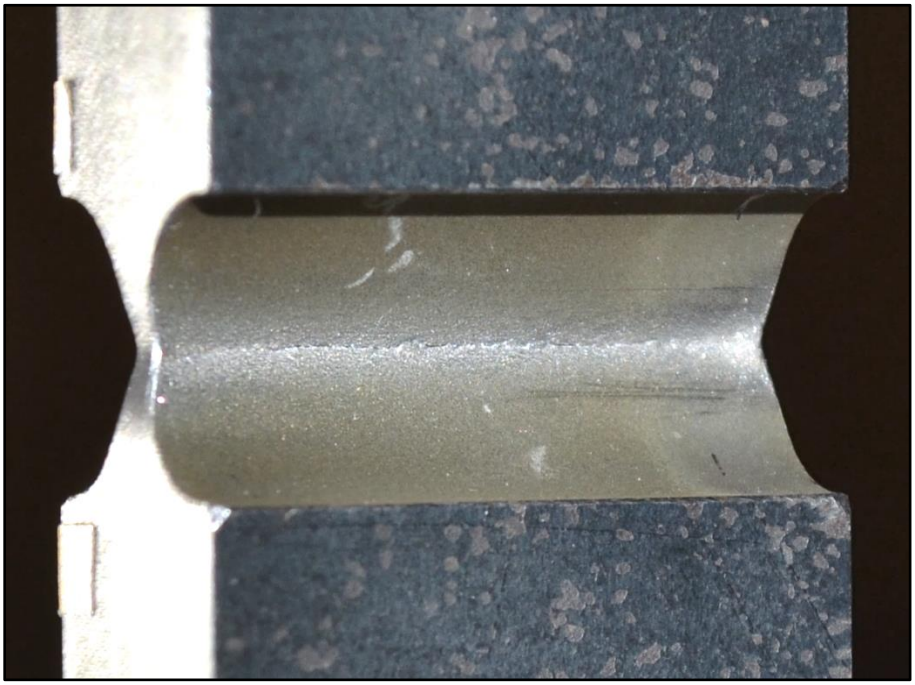

Figure 149. Thick Small Notched Specimen: Macro View of Typical Partial Failure

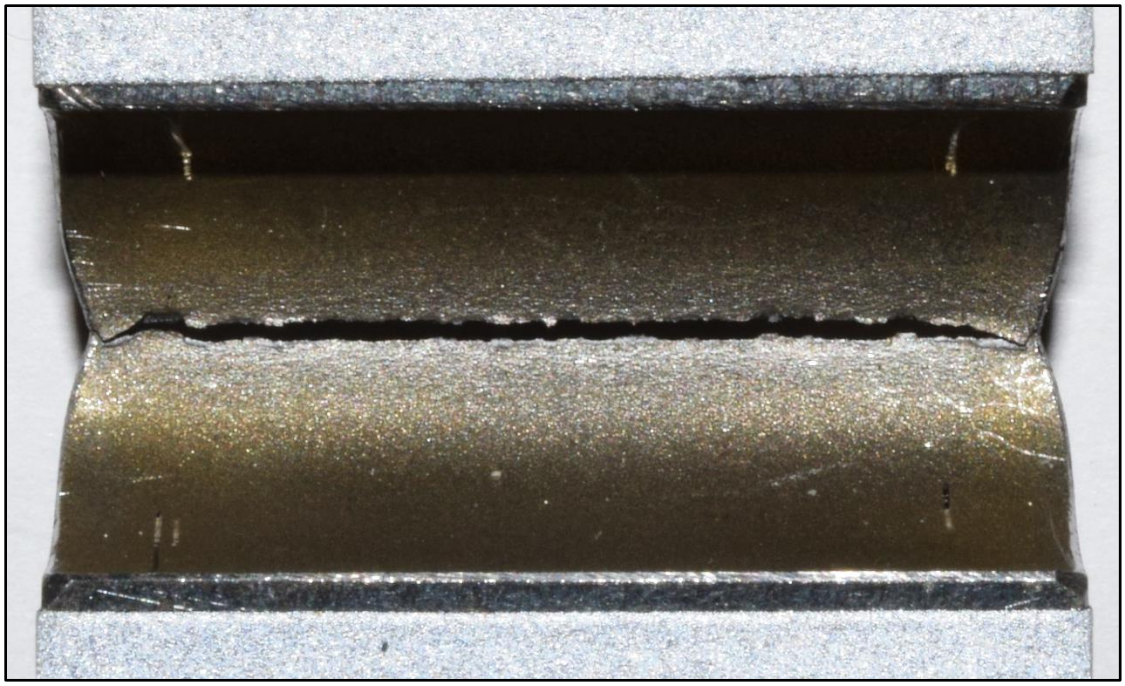

Figure 150. Thick Small Notched Specimen: Macro View of Typical Complete Failure

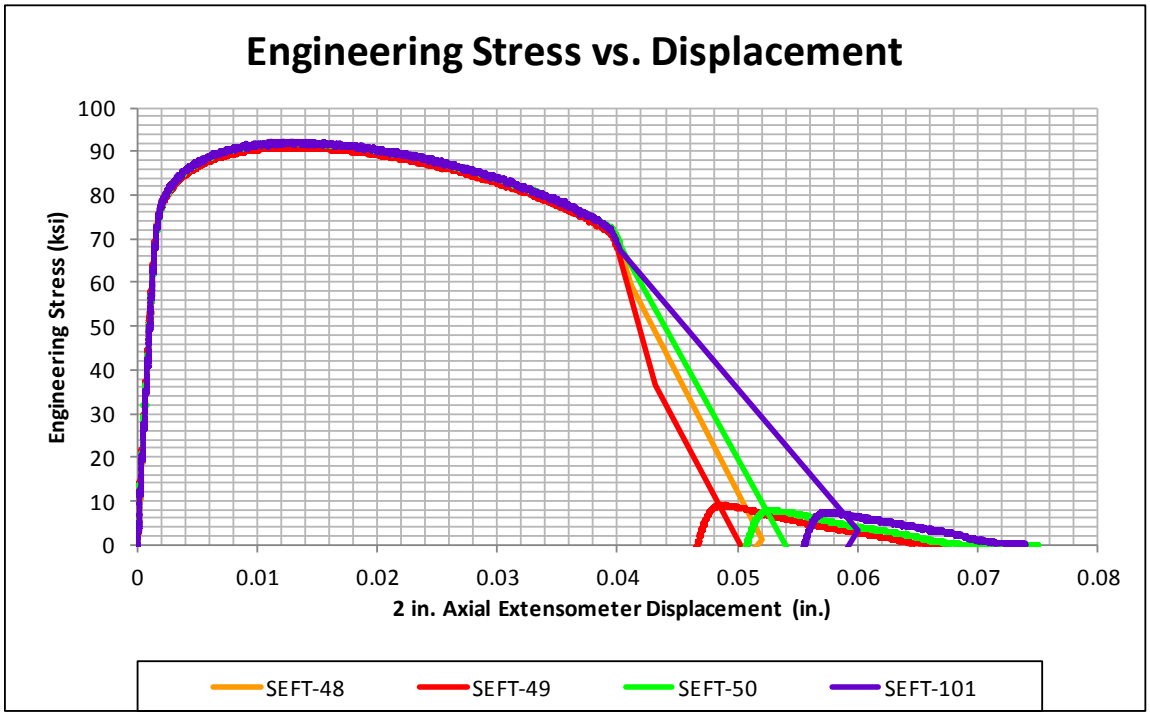

Figure 151. Thick Small Notched Specimen: Engineering Stress vs. Displacement from 2-in. (50.8-mm) Gauge Length Measurements

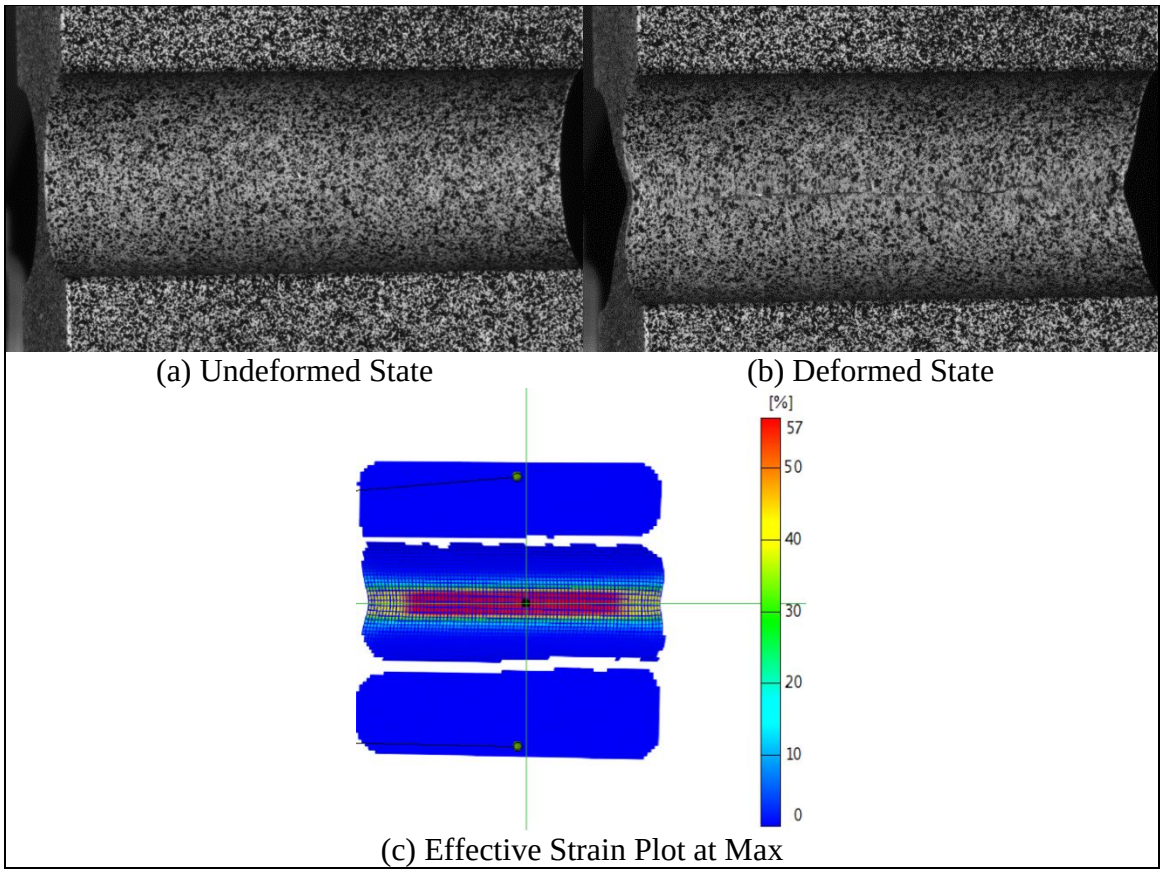

Figure 152. Thick Small Notched Specimen: DIC Analysis, Test No. SEFT-101

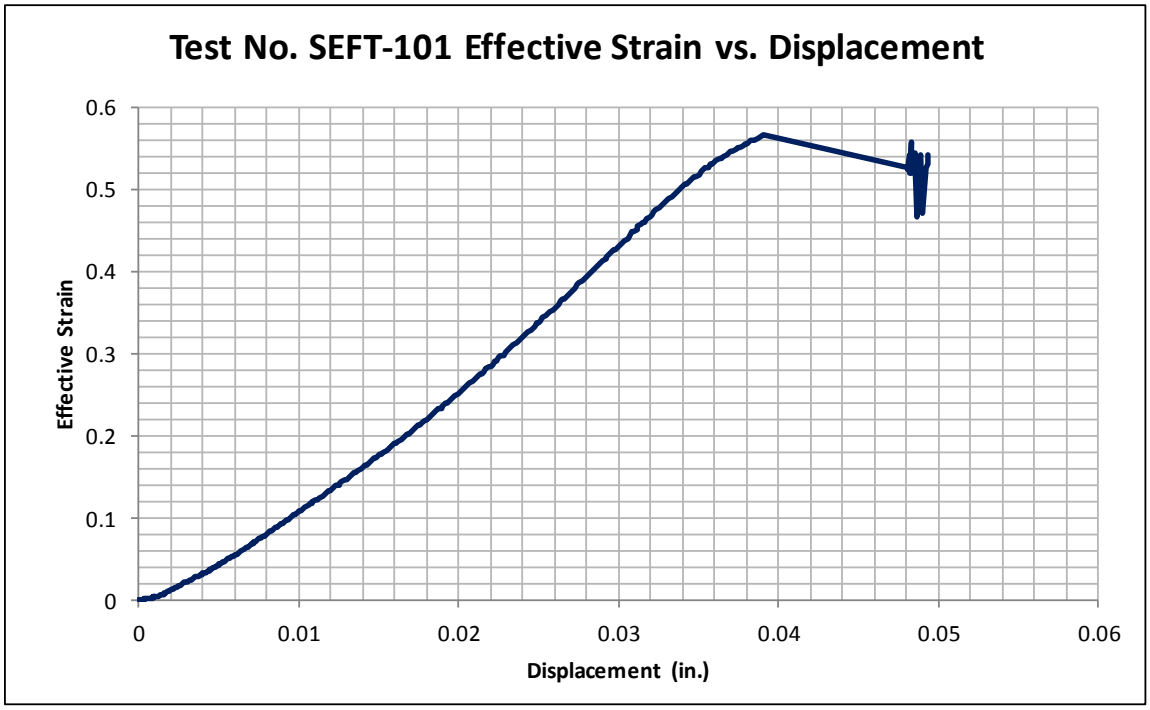

Figure 153. Thick Small Notched Specimen: Effective Engineering Strain vs. Displacement Data from DIC Analysis, Test No. SEFT-101

Table 22. Thick Small Notched Specimen: Summary of Results

Average Yield Stress (0.2% Offset) (2-in. Axial Extensometer)	78.0 ksi (538 MPa)
Average Ultimate Strength	91.8 ksi (633 MPa)
Engineering Stress at Failure	70.6 ksi (487 MPa)
Average Displacement at Failure (2-in. Axial Extensometer)	0.0398 in. (1.011 mm)
Average Cross-Sectional Area Reduction	36.0%
Maximum Effective Engineering Strain (DIC Analysis)	0.57

6.2.14 Cylinder Upsetting Specimen Test Results

Test nos. SEFT-51, SEFT-59 through SEFT-61, and SEFT-99 evaluated the Cylinder Upsetting Specimens. Due to the size of the specimen, no measurement device could be placed directly onto the upsetting cylinder. However, strips of retro-reflective tape, cut to a width of $^{1}/_{8}$ in. (3.2 mm), were placed on the edge of the compression platens to measure the distance between the two platens.

Test no. SEFT-51 was tested with the Landmark 22-kip Load Frame and was compressed to the load frame's capacity. However, the self-aligning compression platen tilted during loading. As a result, an angled load was applied to the specimen. This behavior resulted in uneven deformation of the specimen, with a maximum difference in height of 0.006 in. (0.15 mm). Fortunately, the 2-in. (50.8-mm) axial extensometer and the laser extensometer were placed on opposite sides, as seen in Figure 154. This setup allowed the two measurement devices to be averaged to produce a displacement at the center of the specimen.

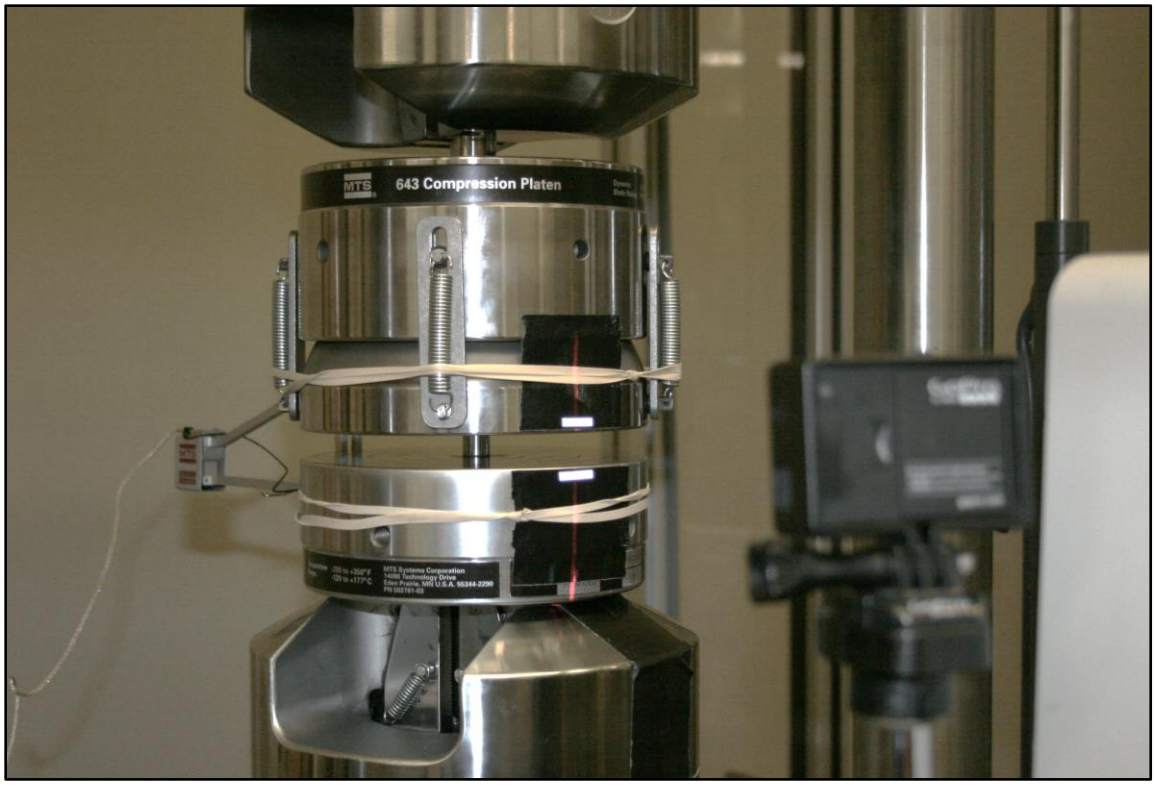

Figure 154. Test No. SEFT-51 Test Setup on Landmark 20-kip Load Frame

Test nos. SEFT-59 through SEFT-61 were tested on the Criterion 220-kip Load Frame with a setup provided in Figure 155. However, due to the magnitude of the expected deformation, only the laser extensometer could be used. All three of tests exhibited some small compression platen tilt during the initial loading of the specimen. This behavior prevented accurate elastic and yield measurements from being collected. However, the amount of movement was not expected to affect the specimen during plastic deformation. Test nos. SEFT-59 through SEFT-61 were loaded up to 49.5 kip (220 kN), 56.3 (250 kN), and 165.3 kip (735 kN), respectively. No macro-scale failure could be seen during these tests. Test no. SEFT-61 was compressed from its original height of 0.49 in. (12.4 mm) down to 0.10 in. (2.5 mm), and the specimen plastically compressed without failing, as seen in Figure 156. The engineering stress vs. displacement curves can be seen in Figure 157.

Test no. SEFT-99 was performed with a similar setup to those used for test nos. SEFT-59 through SEFT-61, with the addition of the ARAMIS 2M DIC system. However, due to failure of the load frame controller, the specimen could only be loaded up to 12.9 kips (57.3 kN). Fortunately, the compression platen movement was not detected and reasonable elastic and yield measurements could be collected. The maximum load for each test, final cross-sectional area increase, and other material properties are given in Table 23.

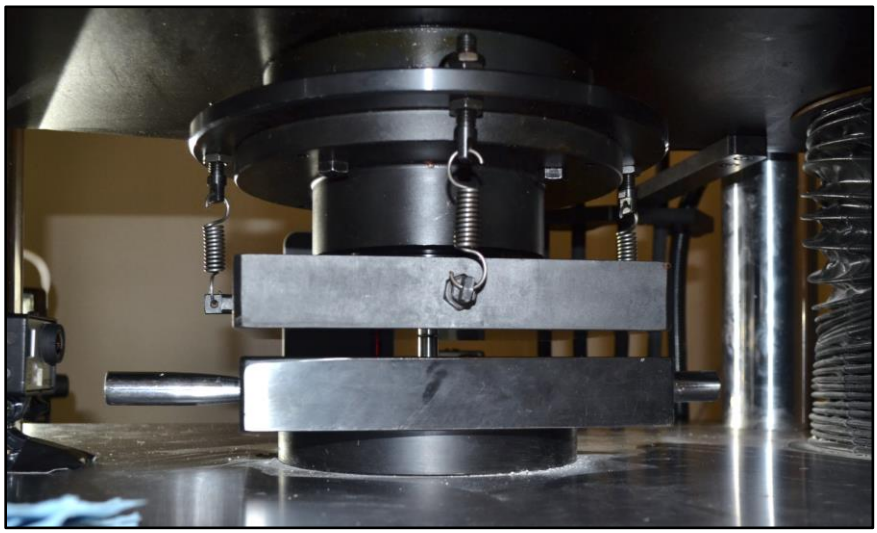

Figure 155. Test Nos. SEFT-59 through SEFT-61 Test Setup on Criterion 200-kip Load Frame

Figure 156. Cylinder Upsetting Specimen: Test No. SEFT-61 Specimen Without Failure

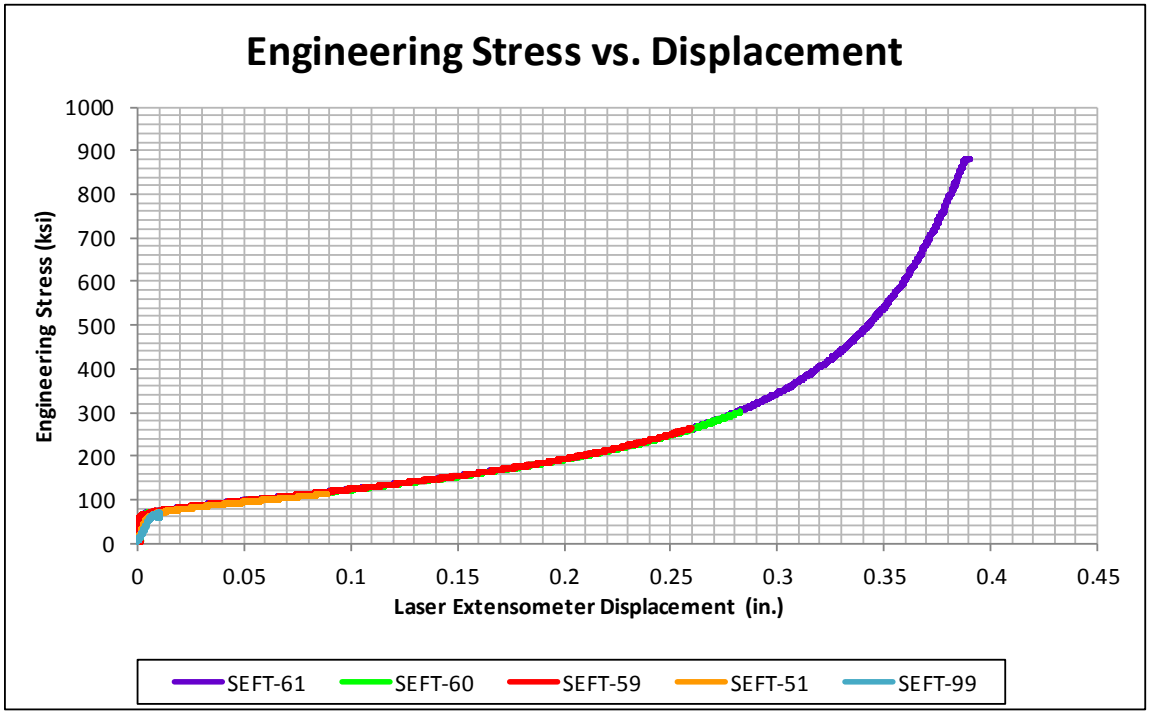

Figure 157. Cylinders Upsetting Specimen: Engineering Stress vs. Displacement

Table 23. Cylinder Upsetting Specimen: Summary of Results

Test No.	Maximum Load	Maximum Displacement	Cross-Sectional Area Increase	Young's Modulus	Yield Stress (0.2% Offset)
SEFT-51	21.2 kip (146 kN)	0.0891 in. (2.262 mm)	21.2%	5,881 kip (26,160 kN)	65.6 ksi (452 MPa)
SEFT-59	49.5 kip (220 kN)	0.2595 in. (6.592 mm)	120.6%	-	-
SEFT-60	56.3 kip (250 kN)	0.2820 in. (7.164 mm)	141.4%	-	-
SEFT-61	165.3 kip (735 kN)	0.3893 in (9.888 mm)	363.4%	-	-
SEFT-99	12.9 kip (88.9 kN)	0.0098 in. (0.250 mm)	0.9%	5,061 kip (22,512 kN)	62.4 ksi (430 MPa)

Test nos. SEFT-51 and SEFT-99 exhibited Young's Moduli of 5,881 kip (26,160 kN) and 5,061 kip (22,512 kN), respectively. The yield strength, calculated with the 0.2 percent offset method with the measured Young's Moduli, were 65.6 ksi (452 MPa) and 62.4 ksi (430 MPa), respectively. The engineering stress vs. engineering strain for these two tests can be found in Figure 158.

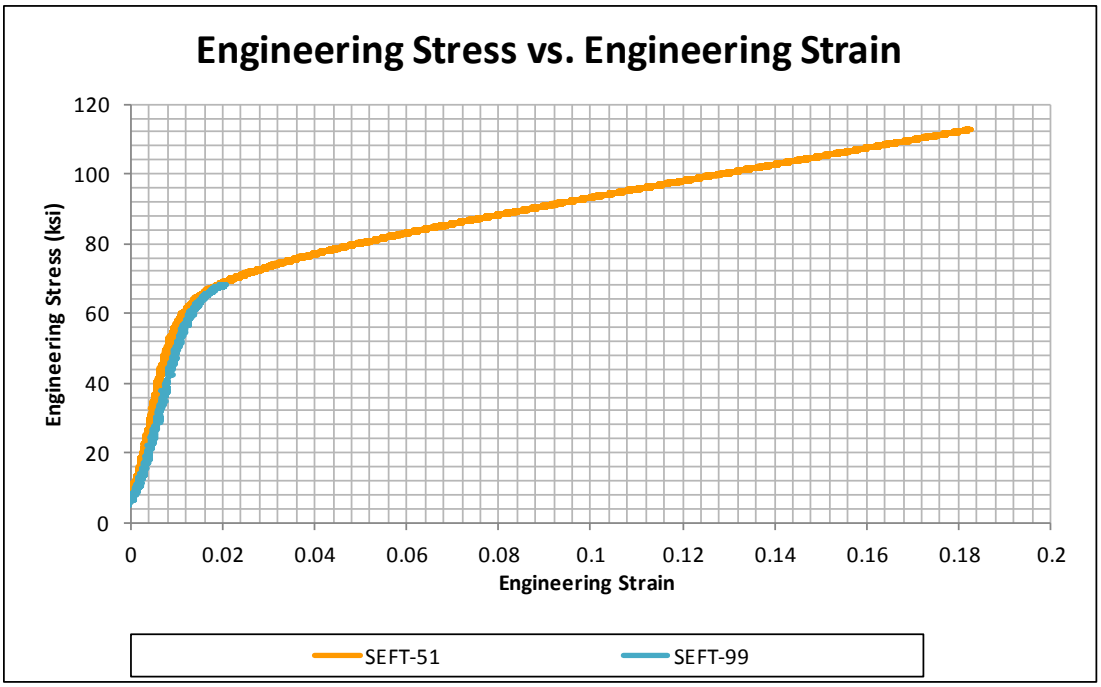

Figure 158. Cylinder Upsetting Specimen: Engineering Stress vs. Engineering Strain, Test Nos. SEFT-51 and SEFT-99

DIC was also utilized to track the strain and displacements of the specimen tested during test no. SEFT-99. A 0.59-in. x 0.47-in. (15-mm x 12-mm) viewing size was used to capture the DIC data, and a pattern using the standard technique was utilized to prepare the specimen, as seen in Figure 159(a). Unfortunately, only a relatively small load was applied to the specimen. Thus, a small amount of deformation occurred unevenly throughout the specimen. As seen in Figure 160, a maximum effective engineering strain of 0.011 was recorded on the right side of the specimen. Furthermore, the uneven loading can be seen in the effective engineering strain plot found in Figure 159 (b). Interestingly, the points near the top and bottom of the specimen were tracked at a maximum displacement of 0.0033 in. (0.0826 mm). However, the displacement of the compression platens using the laser extensometer gave a maximum displacement of 0.0101 in. (0.256 mm). The difference could potentially be caused by either additional displacement along the top and bottom faces of the specimen that was not captured by the DIC analysis, or deflection of the compression platens causing skewed laser extensometer displacement data.

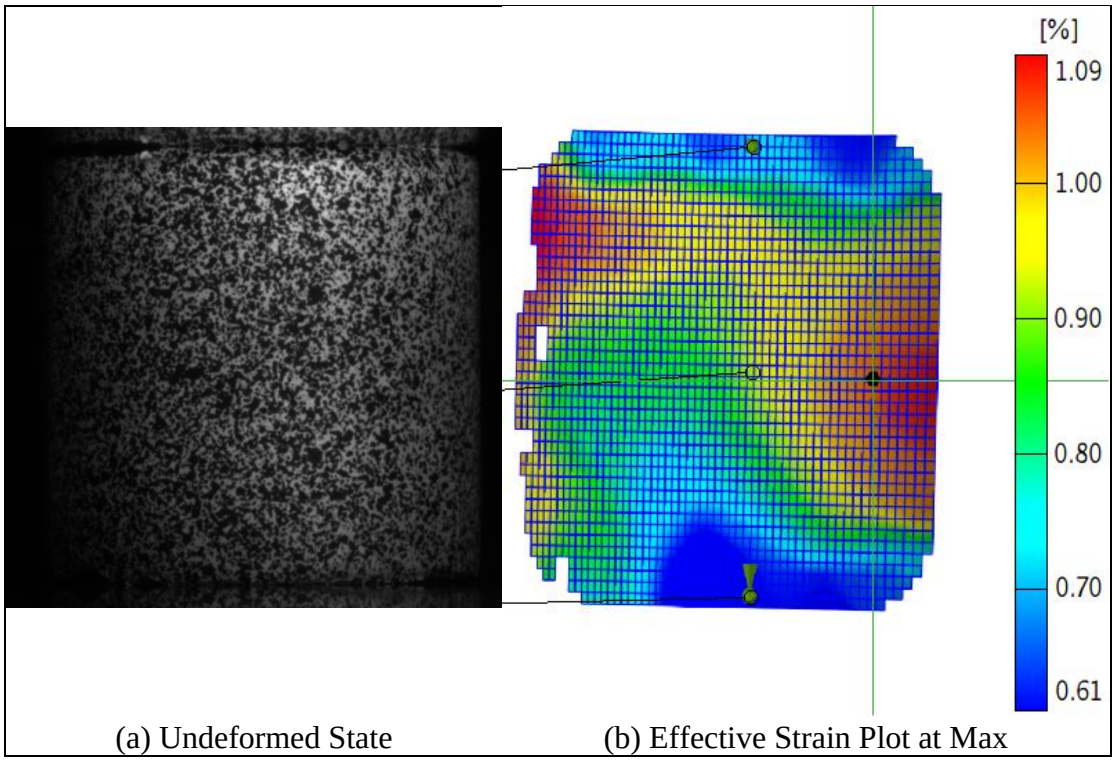

(a) Undeformed State (b) Effective Strain Plot at Max

Figure 159. Cylinder Upsetting Specimen: DIC Analysis, Test No. SEFT-99

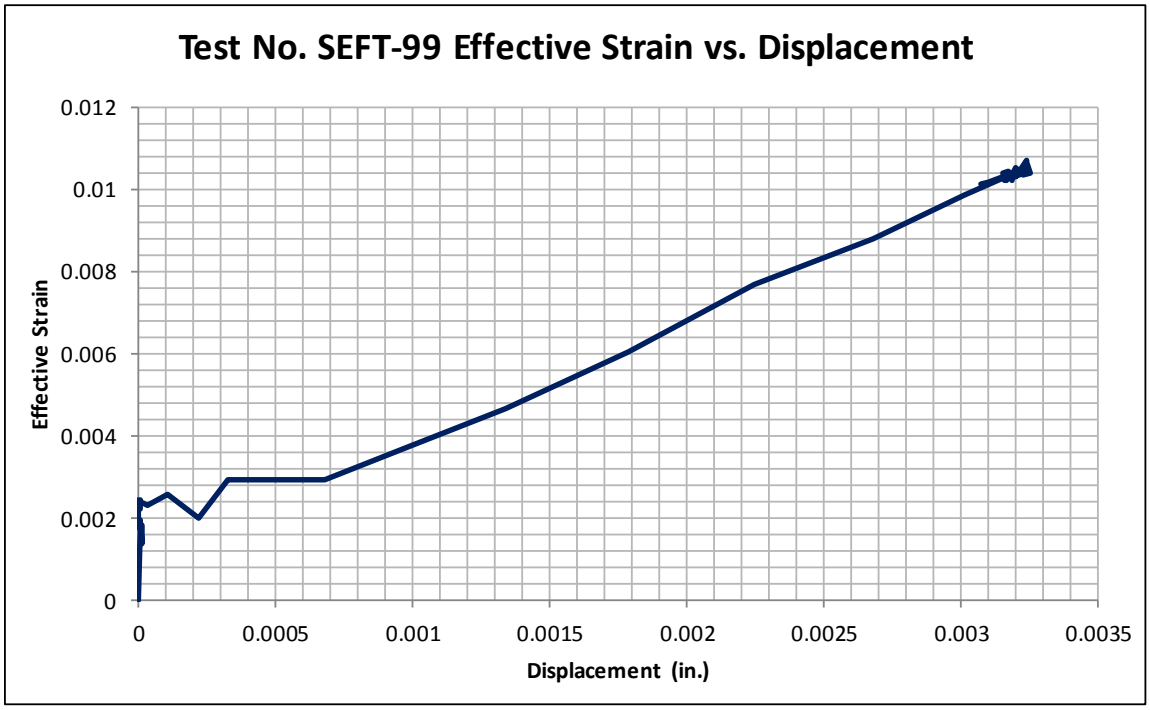

Figure 160. Cylinder Upsetting Specimen: Effective Engineering Strain vs. Displacement Data from DIC Analysis, Test No. SEFT-99

6.2.15 Standard Punch Rod Specimen Test Results

Test nos. SEFT-52 through SEFT-56 evaluated the disk specimens in a punch fixture with the Standard Punch Rod. The laser extensometer was utilized to measure the displacement between the punch rod and punch fixture for all of the noted tests. Test nos. SEFT-52 through SEFT-54 were programmed to stop at a displacement that was less than that required to cause failure in the specimen. As a result, no failure was exhibited during the three tests. Test nos. SEFT-55 and SEFT-56 were stopped after failure in the specimen had occurred. However, as seen in Figure 161, the specimen did not fail in the expected bi-axial tension near the center of the specimen. Instead, the specimen failed in a shearing manner near the inner radius of the recessed edge. Upon closer examination, it was believed that this behavior was due to interference of the punch head and fixture. To accommodate the specimen being drawn farther down without shear failure occurring, a smaller diameter punch rod was designed.

The maximum forces recorded during test nos. SEFT-55 and SEFT-56 were 3.95 kip (27.2 kN) and 4.01 kip (27.6 kN), respectively. The specimens failed at displacements of 0.2407 in. (6.11 mm) and 0.2490 in. (6.32 mm), respectively. A tabulated summary of the tests can be found in Table 24. The compiled force vs. displacement curves can be found in Figure 166. Furthermore, the 1-in. (25.4-mm) axial extensometer was utilized to measure the movement between the top and center fixture sections on test nos. SEFT-57. The displacements between the two pieces of the fixture during the maximum load was 0.0051 in. (0.129 mm).

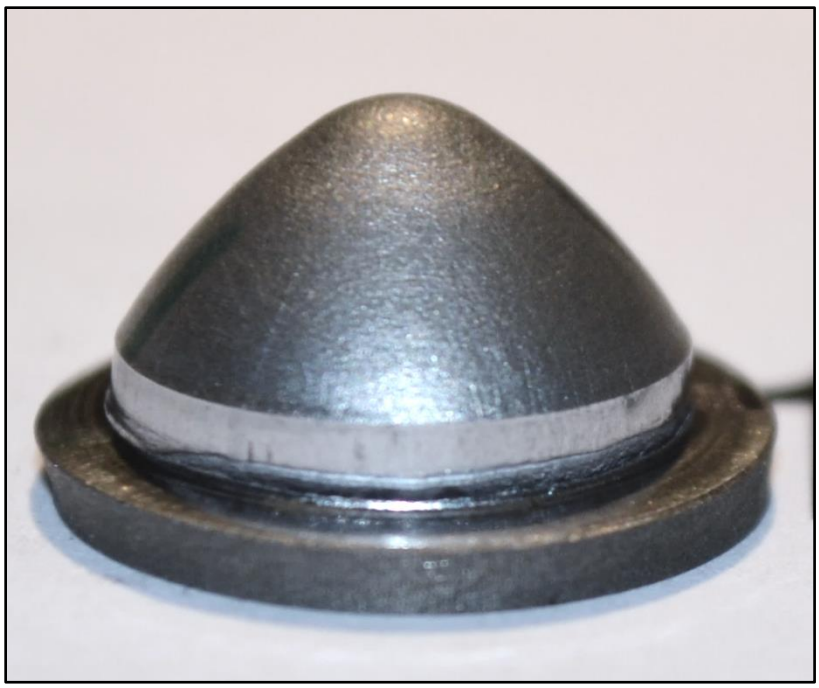

Figure 161. Standard Punch Rod Specimen: Macro View of Typical Shear Failure

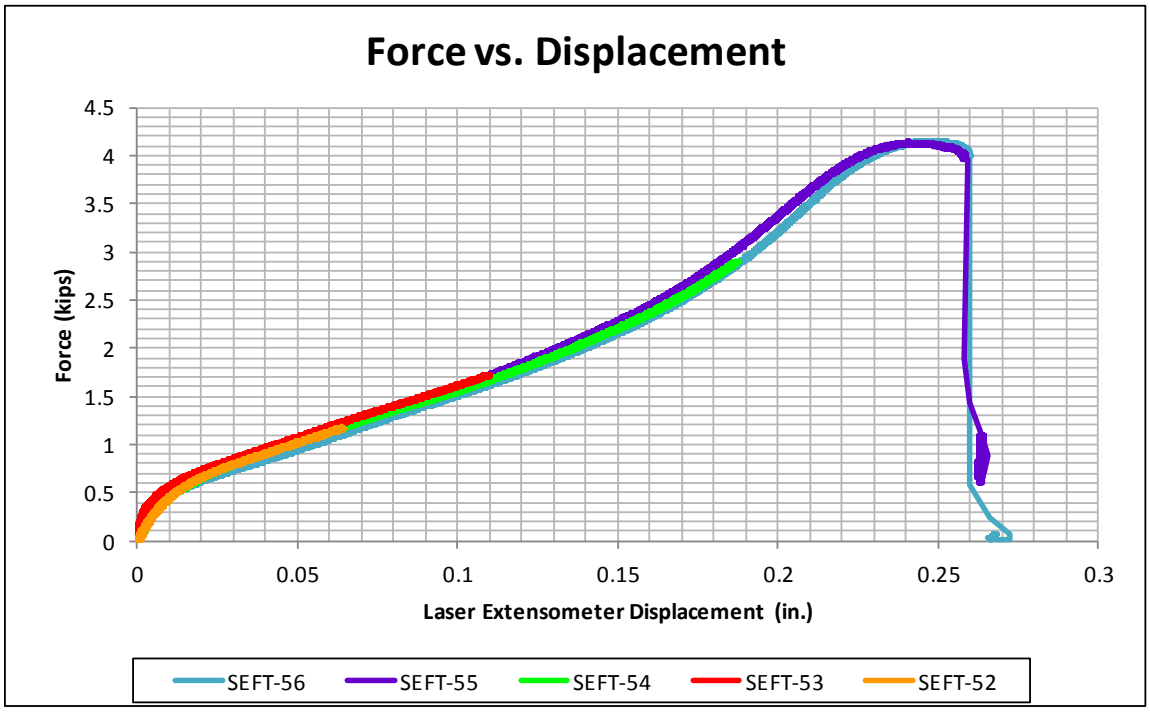

Figure 162. Standard Punch Rod Specimens: Force vs. Displacement

The Revised Standard Punch Rods were used in test nos. SEFT-90 through SEFT-92. A similar test setup to that used in the previous punch tests was utilized. However, it

was necessary to ensure that the revised punch rods would be centered. Thus, a new top fixture part was designed so that the punch rod hole diameter was oversized just enough to allow a tight fit between the hole and punch rod. This design proved to be superior in that the punch rod was guaranteed to load each specimen near its center. This change allowed greater consistency during testing.

Test nos. SEFT-90 through SEFT-92 were stopped after failure in the specimen had occurred. Fortunately, as seen in Figure 163, the specimens failed near the tension region that was expected to be present around the center. The average maximum forces recorded during test nos. SEFT-90 through SEFT-92 was 3.24 kip (22.3 kN). The specimens failed at an average displacement of 0.2186 in. (5.55 mm) and an average force of 2.95 kip (13.1 kN). As seen in the compiled force vs. displacement curves found in Figure 164, the tests behaved similarly. A tabulated summary of the tests can be found in Table 24. Furthermore, the 1-in. (25.4-mm) axial extensometer was utilized to measure the movement between the top and center fixture sections. The average displacement between the two pieces of the fixture during the maximum load of the noted tests was 0.0014 in. (0.035 mm).

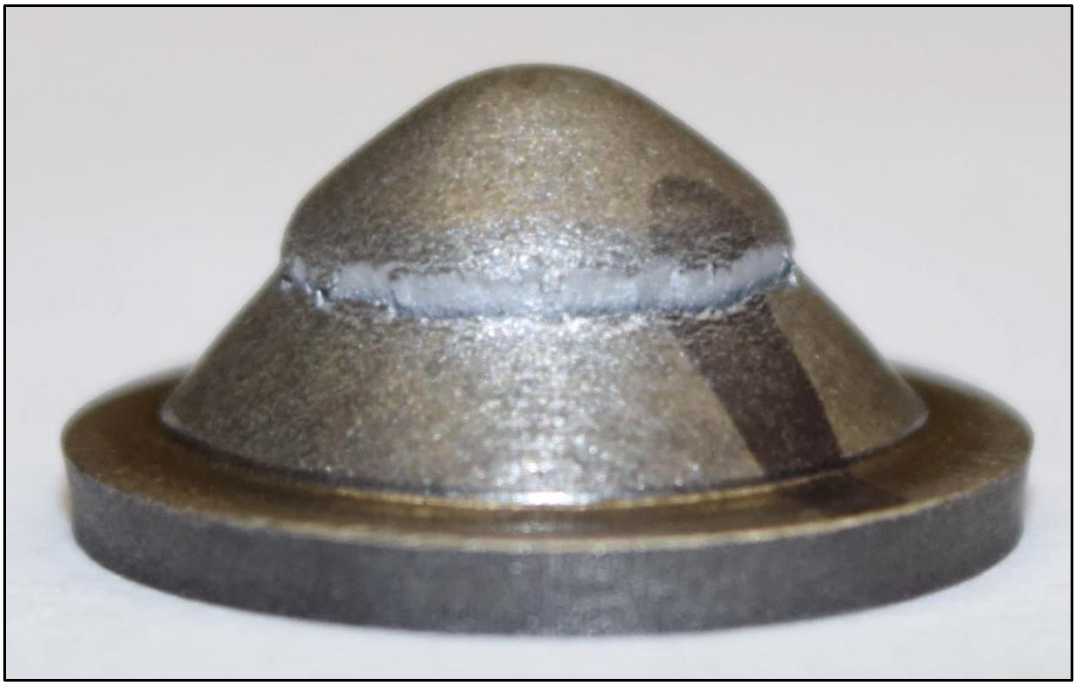

Figure 163. Standard Punch Head R1 Specimen: Macro View of Typical Failure

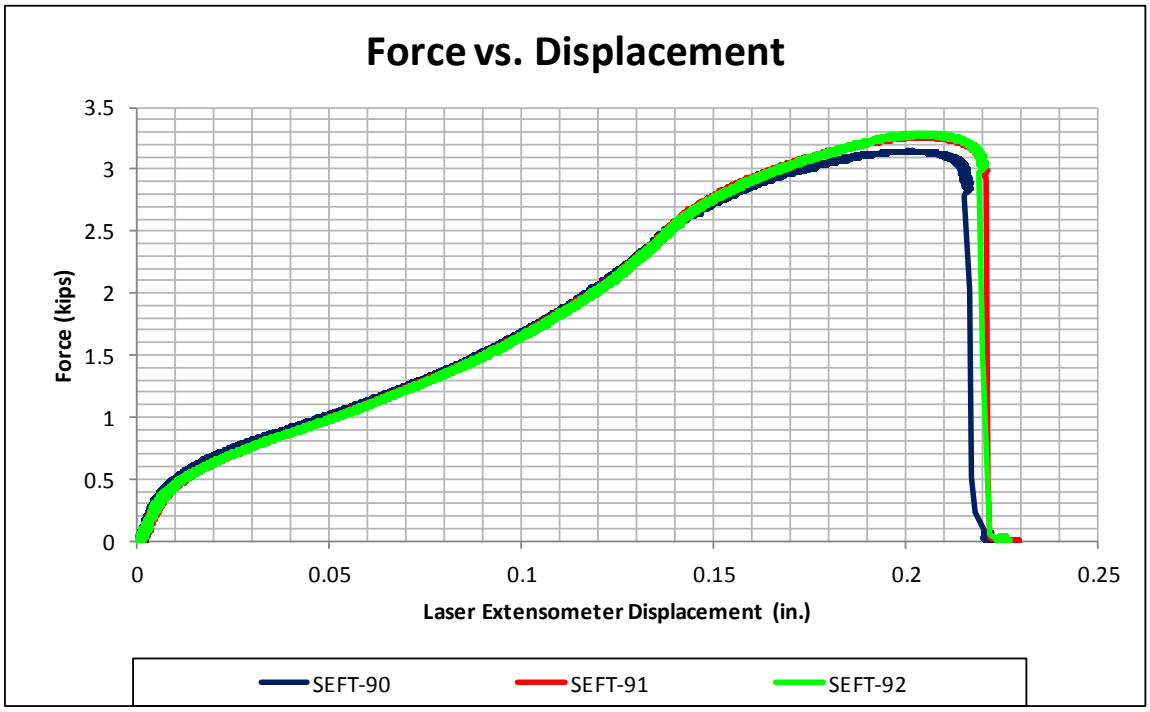

Figure 164. Standard Punch Rod R1 Specimen: Force vs. Displacement

Table 24. Original and Revised Standard Punch Rod Specimen: Summary of Results

	Original Standard Punch Rod	Revised Standard Punch Rod
Average Maximum Load	4.2 kips (18.7 kN)	3.2 kip (13.3 kN)
Average Displacement at Maximum Load	0.2449 in. (6.330 mm)	0.2024 in. (5.552 mm)
Average Load at Failure	4.0 kips (17.8 kN)	3.0 kip (13.3 kN)
Average Displacement at Failure	0.2595 in. (6.591 mm)	0.2186 in. (5.552 mm)

6.2.16 Round Punch Rod Specimen Test Results

Test nos. SEFT-57 and SEFT-58 evaluated the disk specimens in a punch fixture with the Round Punch Rod. The laser extensometer was utilized to measure the displacement between the punch rod and punch fixture for both of the noted tests. Failure occurred in both tests and the tests were stopped after failure had occurred. However, as seen in Figure 165, the specimen did not fail in the expected bi-axial tension near the center of the specimen. Instead, the specimen failed in a shearing manner near the inner radius of the recessed edge. Upon closer examination, it was believed that this was due to interference of the punch head and fixture. To accommodate the specimen being drawn farther down without shear failure occurring, a smaller diameter punch rod was designed.

The maximum forces recorded during test nos. SEFT-57 and SEFT-58 were 4.09 kip (28.2 kN) and 3.63 kip (25.0 kN), respectively. The specimens failed at displacements of 0.2091 in. (5.31 mm) and 0.1474 in. (3.74 mm), respectively. It should also be noted that the punch rod in test no. SEFT-58 was not centered. As a result, failure occurred at a lower displacement. However, similar shearing around the inner radius was seen. The compiled force vs. displacement curves can be found in Figure 166. A tabulated summary of the test no SEFT-57 can be found in Table 25. Furthermore, the 1-in. (25.4-mm) axial

extensometer was utilized to measure the movement between the top and center fixture sections. The displacements between the two pieces of the fixture during the maximum load of test nos. SEFT-57 and SEFT-58 were 0.0022 in. (0.057 mm) and 0.0034 in. (0.087 mm), respectively.

Figure 165. Macro View of Shear Failure on Standard Punch Rod Specimen

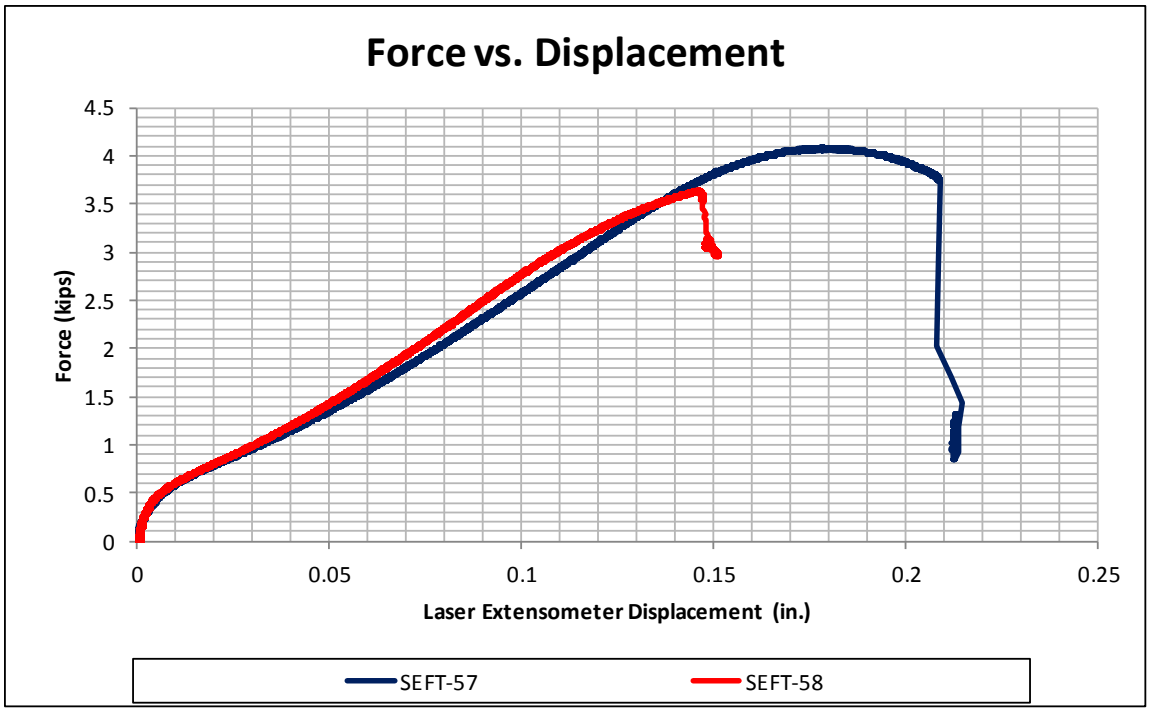

Figure 166. Round Punch Rod Specimen: Force vs. Displacement

Table 25. Original Standard Punch Rod Specimen: Summary of Results, Test No. SEFT-57

Maximum Load	4.1 kips (18.2 kN)
Displacement at Maximum Load	0.1786 in. (4.536 mm)
Load at Failure	3.7 kips (16.5 kN)
Displacement at Failure	0.2091 in. (5.311 mm)

The Revised Round Punch Rods were used in test nos. SEFT-93 through SEFT-95. A similar test setup to that used in the previous punch tests was utilized. However, it was necessary to ensure that the punch rods would be centered. Thus, a new top fixture part was designed so that the punch rod hole diameter was oversized just enough to allow a tight fit between the hole and punch rod. This design proved to be superior in that the punch rod was guaranteed to load each specimen near its center. This change allowed greater consistency during testing.

Test nos. SEFT-93 through SEFT-95 were stopped after failure in the specimen had occurred. Fortunately, as seen in Figure 167, the specimens failed near the tension region that was expected to be present around the center. The average maximum force recorded during test nos. SEFT-93 through SEFT-95 was 3.13 kip (13.9 kN). The specimens failed at an average displacement of 0.2477 in. (6.29 mm) and an average force of 2.61 kip (11.6 kN). As seen in the compiled force vs. displacement curves found in Figure 168, the tests behaved similarly. A tabulated summary of the tests can be found in Table 26. Furthermore, the 1-in. (25.4-mm) axial extensometer was utilized to measure the movement between the top and center fixture sections. The average displacement between the two pieces of the fixture during the maximum load of the noted tests was 0.0012 in. (0.031 mm).

Figure 167. Round Punch Head R1 Specimen: Macro View of Typical Failure

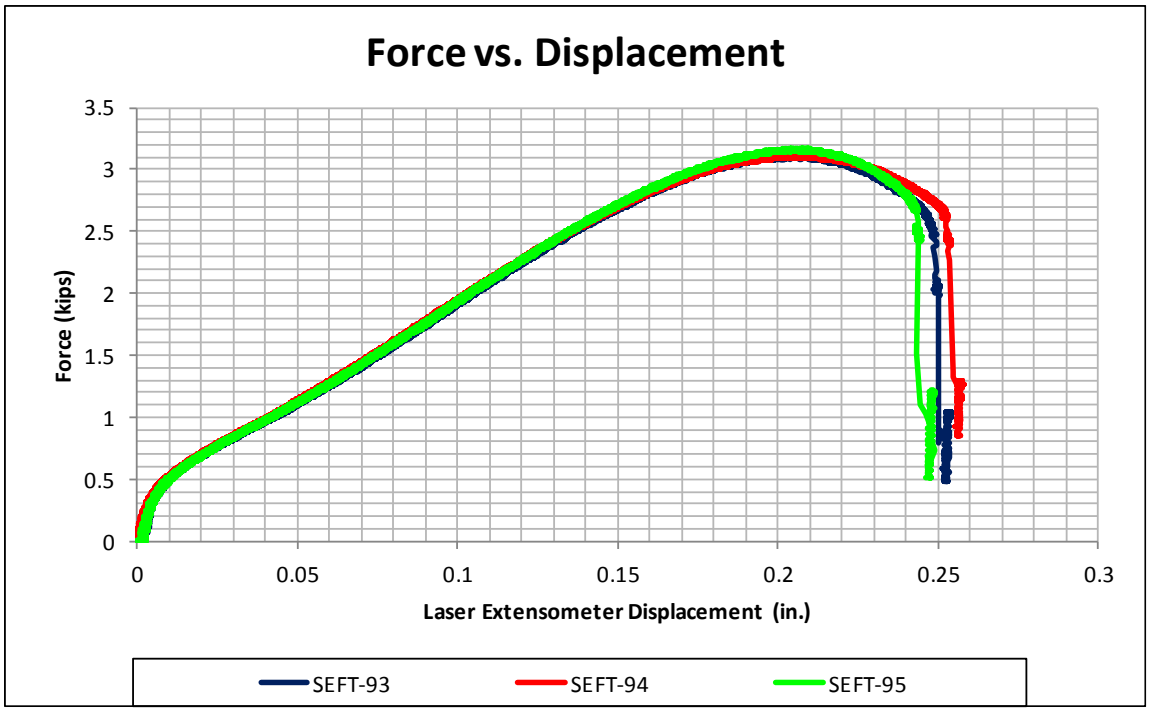

Figure 168. Round Punch Rod R1 Specimen: Force vs. Displacement

Table 26. Revised Standard Punch Rod Specimen: Summary of Results

Average Maximum Load	3.1 kip (13.8 kN)
Average Displacement at Maximum Load	0.2066 in. (5.248 mm)
Average Load at Failure	2.6 kip (11.6 kN)
Average Displacement at Failure	0.2477 in. (6.292 mm)

6.2.17 Sharp Punch Rod Specimen Test Results

Test nos. SEFT-96 and SEFT-98 evaluated the disk specimens in a punch fixture with the Sharp Punch Rod. The laser extensometer was utilized to measure the displacement of the punch rod and punch fixture for all of the noted tests. Failure occurred in all of the tests, and the tests were stopped after failure had occurred. Furthermore, as seen in Figure 169, the specimen did fail in the expected shearing fashion near the inner radius of the recessed edge.

The average maximum force that was recorded during test nos. SEFT-96 through SEFT-98 was 4.09 kip (18.2 kN). The specimens failed at an average displacement of 0.0851 in. (2.162 mm) and an average force of 3.70 kip (16.5 kN). As seen in the compiled force vs. displacement curves found in Figure 170, the tests behaved similarly. A tabulated summary of the tests can be found in Table 27. Furthermore, the 1-in. (25.4-mm) axial extensometer was utilized to measure the movement between the top and center fixture sections. The average displacement between the two pieces of the fixture during the maximum load of the noted tests was 0.0006 in. (0.016 mm).

Figure 169. Sharp Punch Rod Specimen: Macro View of Shear Failure

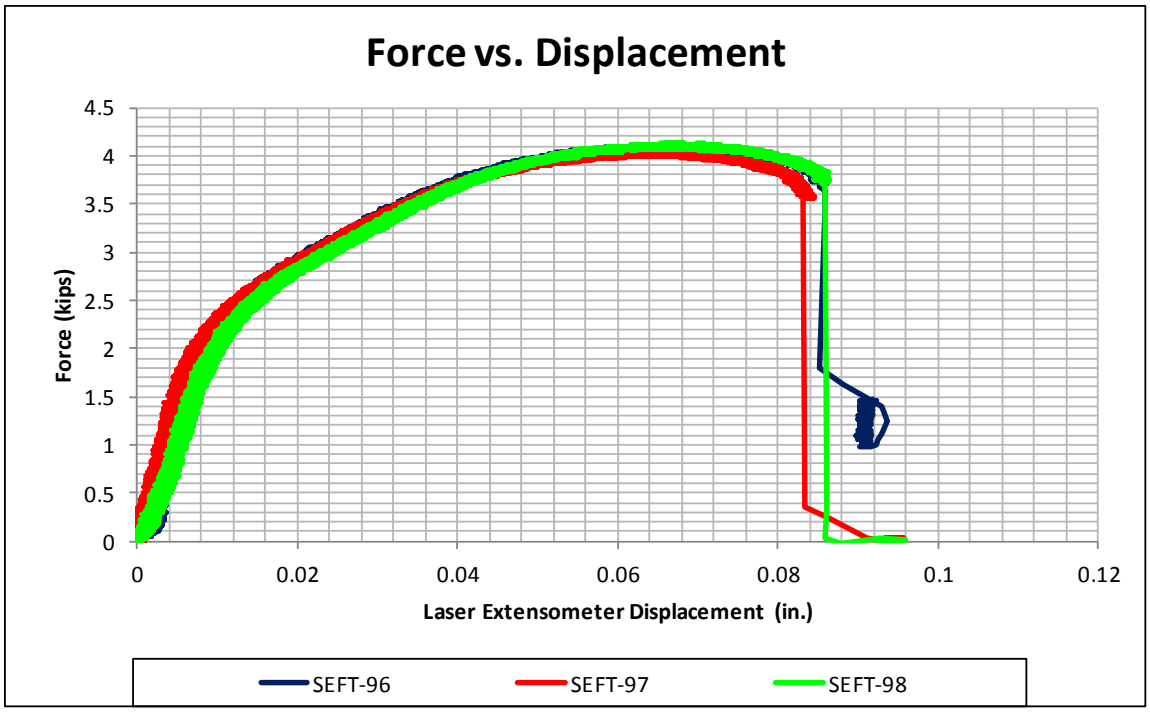

Figure 170. Sharp Punch Rod Specimen: Force vs. Displacement

Table 27. Sharp Punch Rod Specimen: Summary of Results

Average Maximum Load	4.1 kip (18.2 kN)
Average Displacement at Maximum Load	0.0656 in. (1.666 mm)
Average Load at Failure	3.7 kip (16.5 kN)
Average Displacement at Failure	0.0851 in. (2.162 mm)

6.2.18 Dual-Point Shear Specimen Test Results

Test nos. SEFT-62 and SEFT-65 evaluated the rod specimens in a Dual-Point Shear Fixture using the Criterion 200-kip Load Frame. The laser extensometer was utilized to measure the displacement between the upper mount and fixture base for all of the noted tests with the retro-reflective tape placed on the upper mount and fixture base, as seen in Figure 171. The specimen was loaded until it reached a maximum load, and then it gradually declined, as seen in Figure 172. Due to the lack of a sharp drop off, it

was not possible to determine when failure initiated. Test nos. SEFT-62 through SEFT-64 were run until the specimen was severed completely. However, test no. SEFT-65 was stopped prematurely to determine if any failure had occurred. Unfortunately, the clearances between the fixture parts were too small to observe the specimen failure region. The fixture was reinstalled and run to complete separation. As seen in Figures 173 and 174, the specimen failed in a shearing mode at the fixture interfaces.

The average maximum force recorded during test nos. SEFT-62 through SEFT-65 was 13.58 kip (60.4 kN) at an average displacement of 0.0539 in. (1.369 mm). The load then gradually declined until complete separation occurred. As seen in the compiled force vs. displacement curves, the tests all behaved similarly.

Figure 171. Test nos. SEFT-62 and SEFT-65 Test Setup on Criterion 200-kip Load Frame

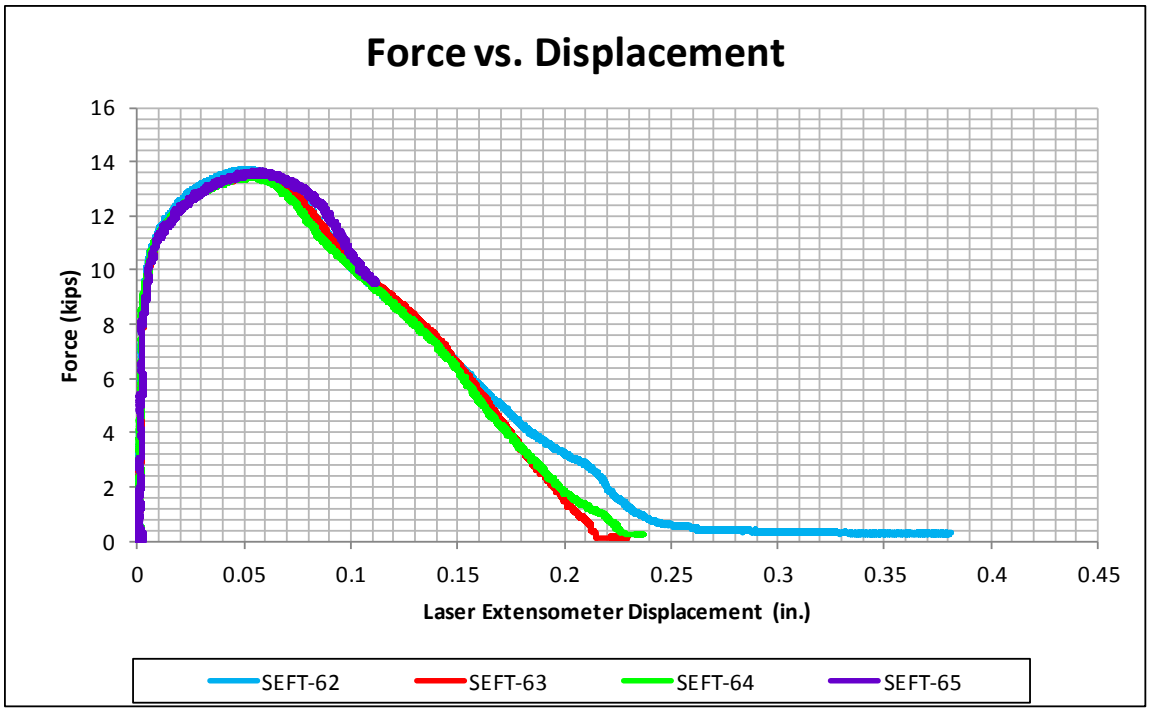

Figure 172. Dual-Point Shear Specimen: Force vs. Displacement

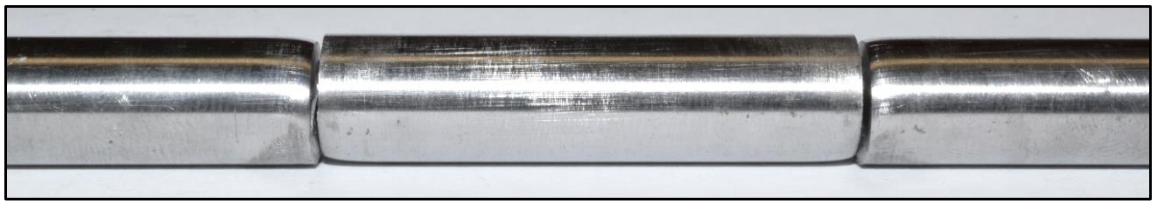

Figure 173. Dual-Point Shear Specimen: Macro View of Shear Failure

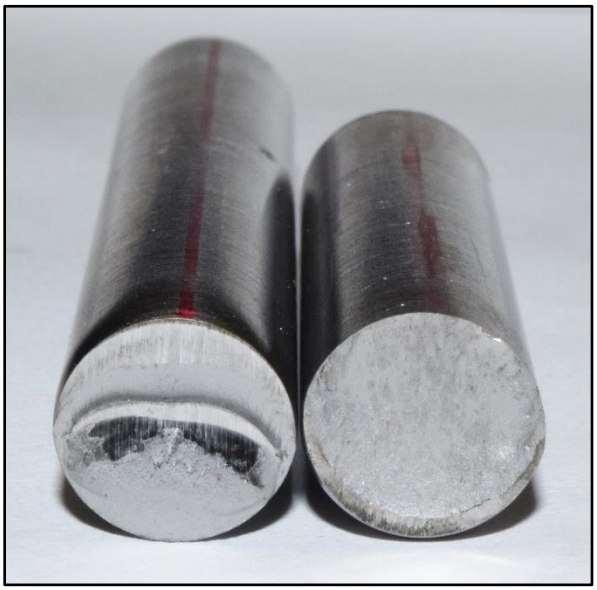

Figure 174. Dual-Point Shear Specimen: Macro View of Failure Surface

6.2.19 Torsion Specimen Test Results

Test nos. SEFT-102 through SEFT-104 evaluated the torsion specimens using the Tinius Olsen & Company Torsion Frame. Angle vs. torque measurements were collected for test nos. SEFT-103 and SEFT-104. However, the equipment calibration could not be verified. As such, the data was archived but is not presented herein.

The three test specimens failed in similar fashions. Unfortunately, pure torsion was not achieved as the rotating grip heads allowed some radial translation as well as some angle divergence from the axial centerline. As a result, the specimens partially buckled before shearing, as seen in Figure 175. The specimens in test nos. SEFT-102 through SEFT-104, had failed at angular rotations of 170, 160, and 170 degrees, respectively. Further testing of the specimen may be warranted with more a more precise torsion loading frame.

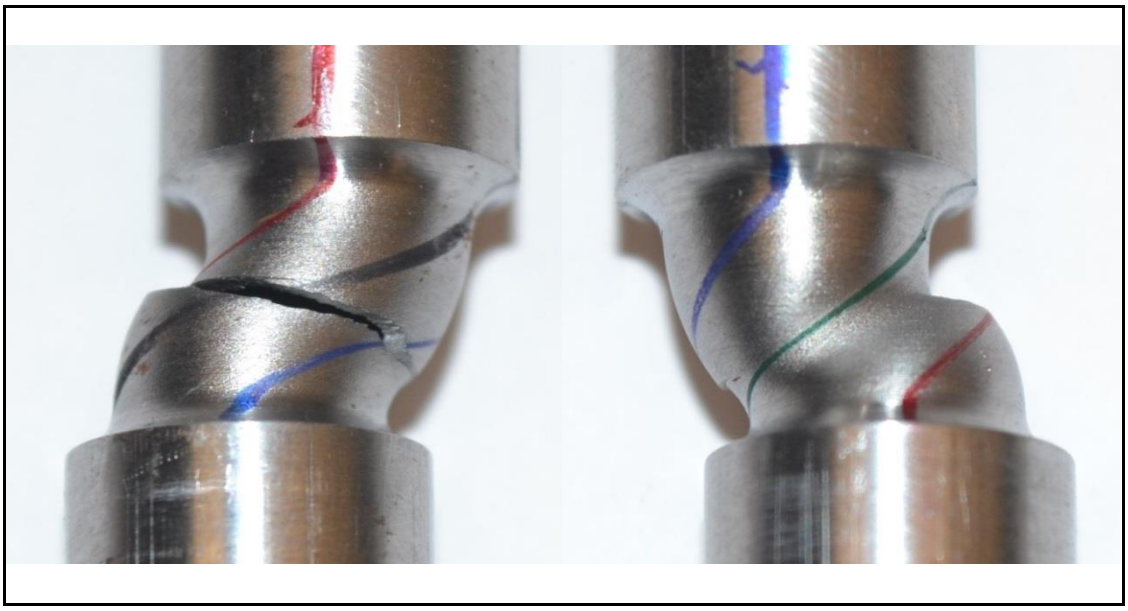

Figure 175. Torsion Specimen: Macro Views of Typical Failure Zone

6.3 Material Testing Discussion

A total of 21 different specimen configurations were tested and evaluated as part of the material testing program. Based on the recorded and calculated data presented herein, a FEM material model can be calibrated. Furthermore, the test data can be used to aid in the development of a state of stress dependent failure surface. Unfortunately, due to the limitations in directly correlating the effective plastic strain in FEM models to the recorded physical measurements and calculations, further modeling and analysis efforts are required.

6.3.1 Flat Specimens Discussion

Four unique flat specimen types were evaluated in this testing program: the Flat Standard Dog Bone Specimen, the Flat Large Notch Specimen, the Flat Small Notch Specimen, and the Flat Sharp Notch Specimen. All four of the specimens are plane stress specimens with varying degrees of triaxiality in the critical cross section. The expectation of exhibiting different triaxialities is reinforced by examining the engineering stress vs. displacement data, as seen in Figure 176. As the notch radius decreased, it is expected that the triaxiality in the critical cross section will increase. Furthermore, as the triaxiality increased, the yield stress and ultimate strength measured from the uniaxial load cell increased. This behavior can be explained with the von Mises Yield Criteria. As the notch radius decreased, the second and third principal stresses increased relative to the stress in the axial direction (the first principal stress). As a result, the von Mises stress decreased relative to the axial stress. Due to this relative shift between the first principal and von Mises stress, a larger axial force was exerted to cause yielding in the specimen. A

tabulated summary of the flat specimen yield and ultimate stresses can be found in Table 28.

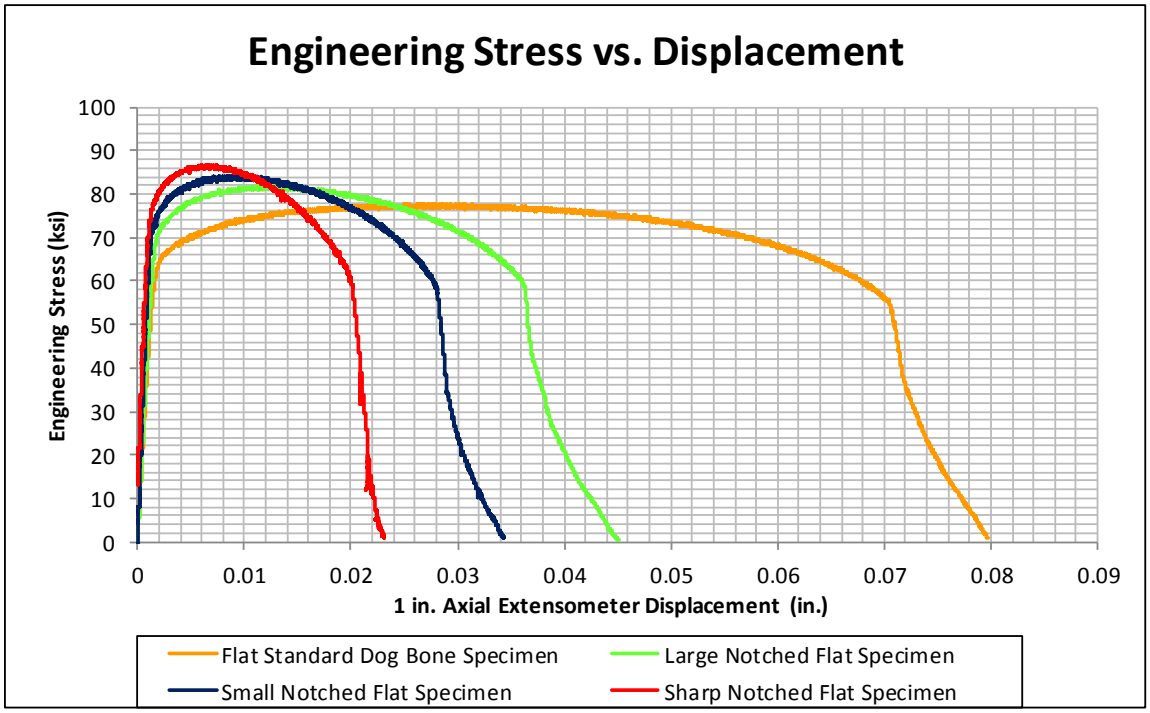

Figure 176. Flat Specimens: Engineering Stress vs. Displacement

Table 28. Flat Specimens: Summary of Yield and Ultimate Stresses

Specimen Type	Yield Stress (0.2% Offset)	Ultimate Strength
Flat Standard Dog Bone Specimen	64.3 ksi (444 MPa)	79.3 ksi (547 MPa)
Flat Large Notch Specimen	70.7 ksi (488 MPa)	82.2 ksi (567 MPa)
Flat Small Notch Specimen	72.4 ksi (499 MPa)	84.5 ksi (405 MPa)
Flat Sharp Notch Specimen	77.3 ksi (533 MPa)	89.2 ksi (615 MPa)

Interestingly, the cross-sectional reduction in area decreased as triaxiality increased, excluding the Flat Sharp Notch Specimen. This trend can be seen in Figure 177. Tabulated results are also summarized in Table 29. This trend may suggest that failure is triaxiality dependent. However, further analysis is needed to determine the respective effective plastic strains at failure for FEM modeling.

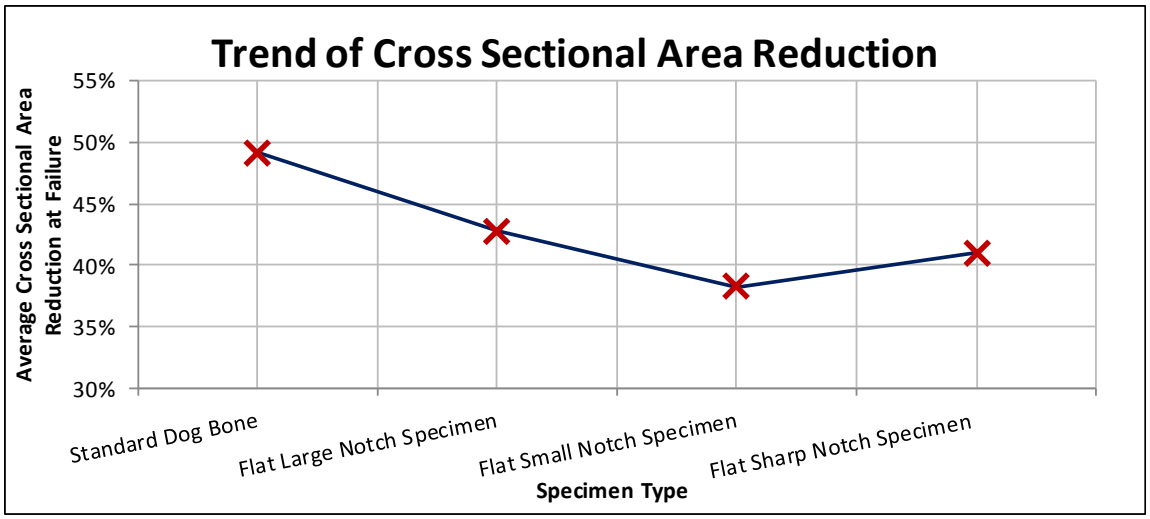

Figure 177. Flat Specimens: Summary of Average Cross-Sectional Area Reduction at Failure

Table 29. Flat Specimens: Summary of Average Cross-Sectional Area Reduction at Failure

Specimen Type	Cross-Sectional Area Reduction
Flat Standard Dog Bone Specimen	49.1%
Flat Large Notch Specimen	42.8%
Flat Small Notch Specimen	38.2%
Flat Sharp Notch Specimen	41.0%

6.3.2 Round Specimens Discussion

Six unique round specimen types were evaluated in this testing program. These configurations included one smooth specimen and five notched specimens with varying notch radii. Similar to the flat specimens, as the radii decreased, it is expected that the triaxiality in the critical cross section will increase. This expectation is reinforced by examining the engineering stress vs. displacement data of six specimens, as seen in Figure 178. As the notch radius decreased, the second and third principal stresses increased relative to the stress in the axial direction (the first principal stress). As a result, the von Mises stress decreased relative to the axial stress. Due to this relative shift between the first principal and von Mises stress, a larger axial force was exerted to cause yielding in the specimen. A tabulated summary of the flat specimen yield and ultimate

stresses can be found in Table 30. This shift in the stress state, as shown by the shifting ratio between the first principal stress and the von Mises stress, suggests that the triaxiality also shifted.

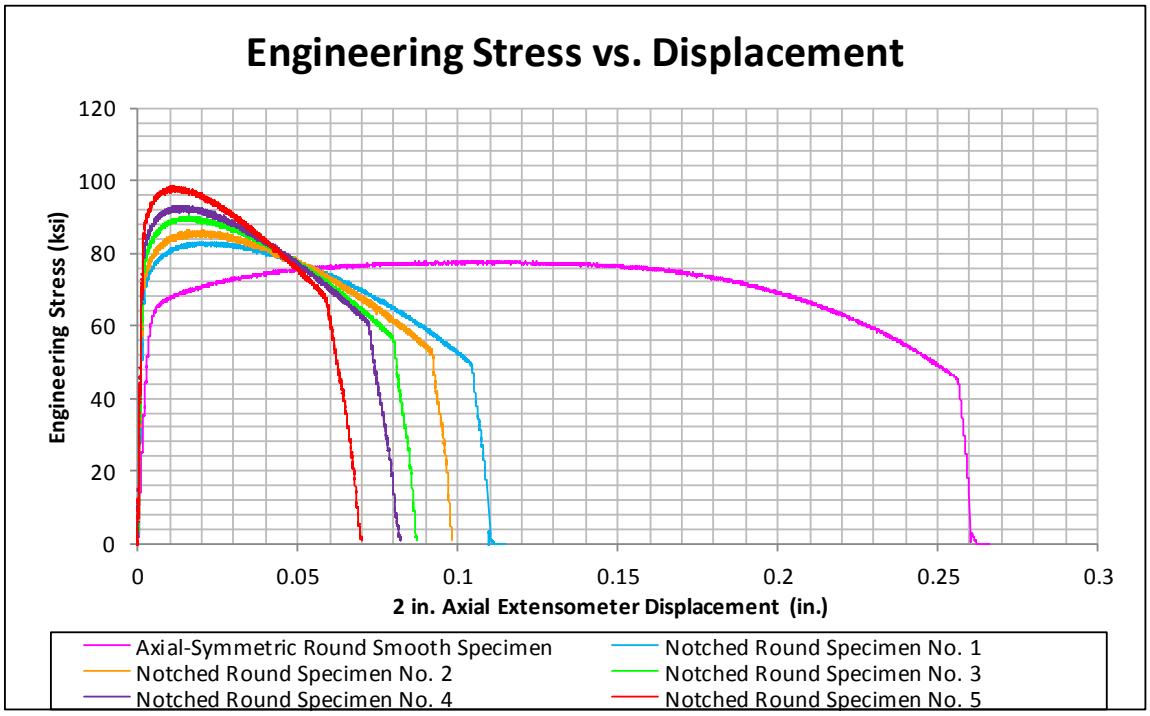

Figure 178. Round Specimens: Engineering Stress vs. Displacement

Table 30. Round Specimens: Summary of Yield and Ultimate Stresses

Specimen Type	Yield Stress (0.2% Offset)	Ultimate Strength
Axial-Symmetric Round Smooth Specimen	62.7 ksi (432 MPa)	76.4 ksi (527 MPa)
Notched Round Specimen No. 1	70.9 ksi (489 MPa)	83.5 ksi (576 MPa)
Notched Round Specimen No. 2	72.3 ksi (498 MPa)	86.3 ksi (595 MPa)
Notched Round Specimen No. 3	76.9 ksi (530 MPa)	90.5 ksi (624 MPa)
Notched Round Specimen No. 4	79.2 ksi (546 MPa)	92.8 ksi (640 MPa)
Notched Round Specimen No. 5	85.1 ksi (587 MPa)	98.3 ksi (678 MPa)

Similarly exhibited in the flat specimens, the cross-sectional reduction in area decreased as triaxiality increased. This trend can be seen in Figure 179. Tabulated results are also summarized in Table 31. This trend may suggest that failure is triaxiality dependent. However, further analysis is needed to determine the respective effective plastic strains at failure for FEM modeling.

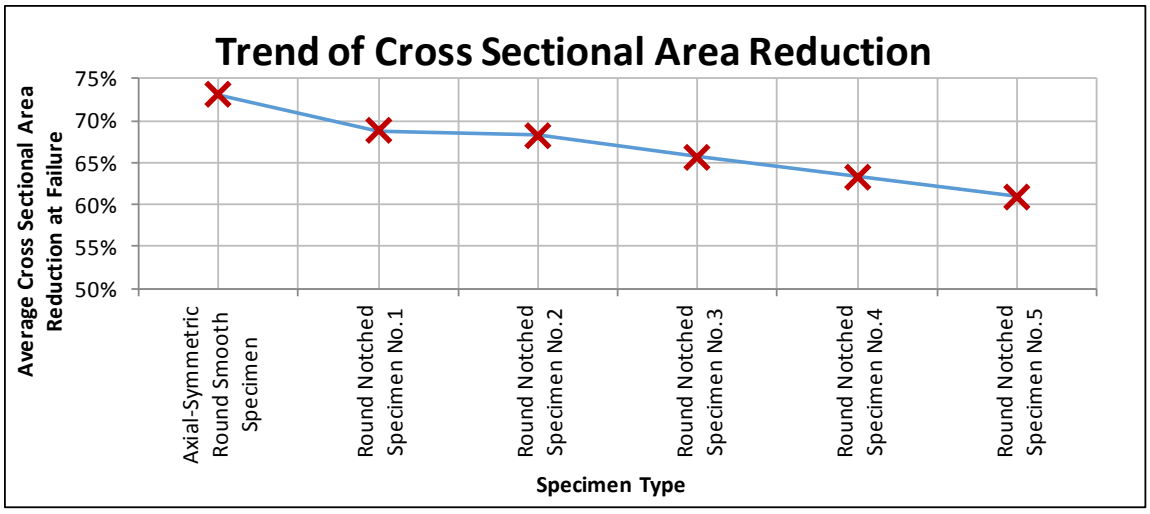

Figure 179. Round Specimens: Summary of Average Cross-Sectional Area Reduction at Failure

Table 31. Round Specimens: Summary of Average Cross-Sectional Area Reduction at Failure

Specimen Type	Cross-Sectional Area Reduction
Axial-Symmetric Round Smooth Specimen	73.1%
Notched Round Specimen No. 1	68.8%
Notched Round Specimen No. 2	68.3%
Notched Round Specimen No. 3	65.7%
Notched Round Specimen No. 4	63.3%
Notched Round Specimen No. 5	60.9%

Critical material properties were calculated from the recorded data from the Flat Standard Dog Bone and Axial-Symmetric Round Smooth Specimens. These material properties are provided and compared in Table 32. Interestingly, the yield stress, and ultimate stress exhibited some small variation. However, the Young's modulus, cross-

sectional area reduction, true strain at failure, and true stress at failure varied widely between the two specimens.

Table 32. Summary of Critical Material Properties

Material Parameter	Flat Standard Dog Bone Specimen	Axial-Symmetric Round Smooth Specimen
Average Young's Modulus	29,917 ksi (206,270 MPa)	24,370 ksi (168,025 MPa)
Average Yield Stress (0.2% Offset)	64.3 ksi (444 MPa)	62.7 ksi (432 MPa)
Average Ultimate Strength	79.3 ksi (547 MPa)	76.4 ksi (527 MPa)
Average Cross-Sectional Area Reduction	49.1%	73.1%
Average True Strain at Failure	0.6760	1.2439
Average True Stress at Failure	139.8 ksi (964 MPa)	241.3 ksi (1,664 MPa)

6.3.3 Thick Specimen Discussion

Three unique thick specimen types were evaluated in this testing program. These included the Thick Dog Bone Specimen and two notched specimens with different notch radii. Similar to the flat and round specimens, as the radii decreased, it is expected that the triaxiality in the critical cross section will increase. This expectation is reinforced by examining the engineering stress vs. displacement data of three specimens, as seen in Figure 180. As the notch radius decreased, the second and third principal stresses increased relative to the stress in the axial direction (the first principal stress). As a result, the von Mises stress decreased relative to the axial stress. Due to this relative shift between the first principal and von Mises stress, a larger axial force was exerted to cause yielding in the specimen. A tabulated summary of the flat specimen yield and ultimate stresses can be found in Table 33. This shift in the stress state, as shown by the shifting

ratio between the first principal stress and the von Mises stress, suggests that the triaxiality also shifted.

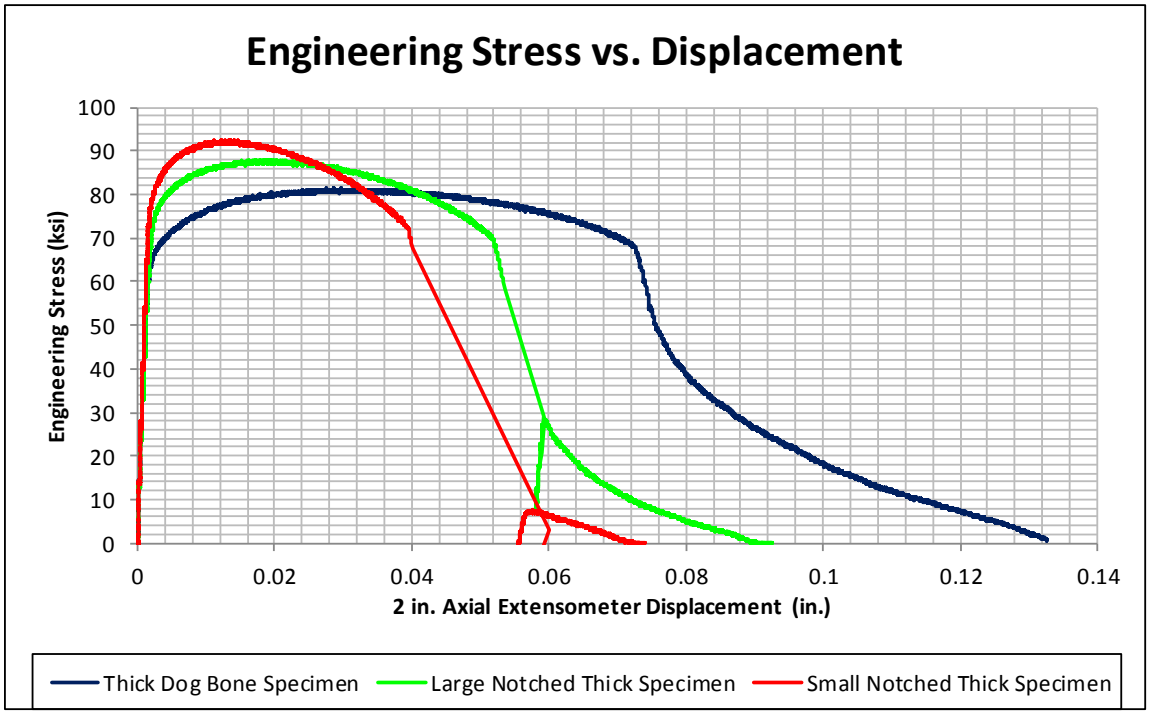

Figure 180. Thick Specimens: Engineering Stress vs. Displacement

Table 33. Thick Specimens: Summary of Yield and Ultimate Stresses

Specimen Type	Yield Stress (0.2% Offset)	Ultimate Strength
Thick Dog Bone Specimen	64.6 ksi (445 MPa)	81.3 ksi (561 MPa)
Thick Large Notch Specimen	73.0 ksi (503 MPa)	86.9 ksi (599 MPa)
Thick Small Notch Specimen	78.0 ksi (538 MPa)	91.8 ksi (633 MPa)

As seen in the round and flat specimens, the cross-sectional reduction in area decreased as triaxiality increased. This trend can clearly be seen in Figure 81. Tabulated results are also summarized in Table 34. This trend may suggest that failure is triaxiality dependent. However, further analysis is needed to determine the respective effective plastic strains at failure for FEM modeling.

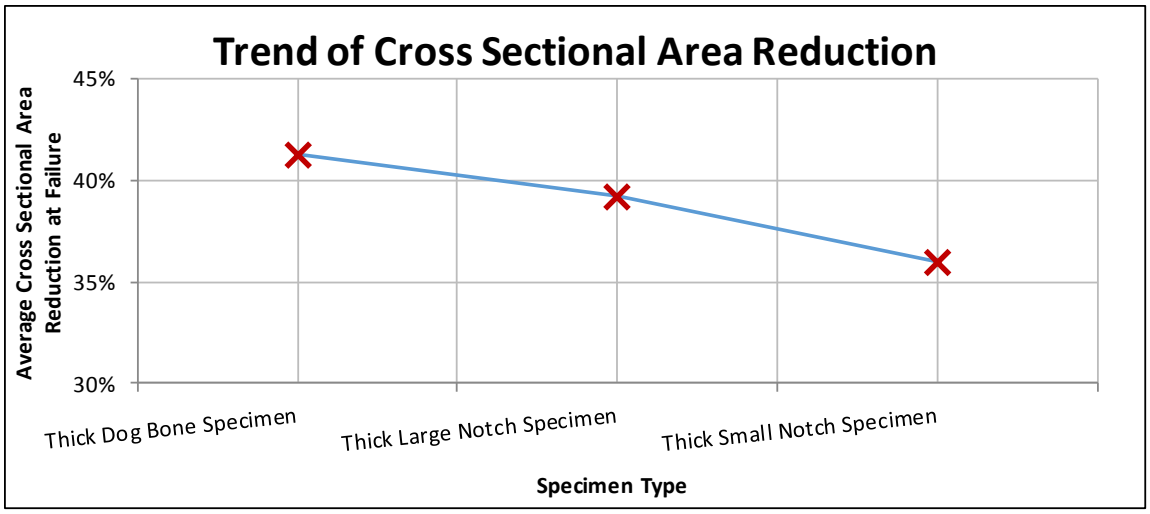

Figure 181. Thick Specimens: Summary of Average Cross-Sectional Area Reduction at Failure

Table 34. Thick Specimens: Summary of Average Cross-Sectional Area Reduction at Failure

Specimen Type	Cross-Sectional Area Reduction
Thick Dog Bone Specimen	41.3%
Thick Large Notch Specimen	39.2%
Thick Small Notch Specimen	36.0%

7 BASELINE FEM MODELING OF TESTING SPECIMENS

7.1 Simulation Procedure

In order to calibrate and validate the material model for guardrail steel fracture, finite element models for each of the proposed test specimens will be required. These models will serve several purposes:

1) confirm the stress state, as represented by triaxiality and Lode parameter, for each of the proposed tests;
2) determine effective plastic strain at failure for test specimen configurations; and
3) aid in calibration of the material model's effective plastic strain at failure vs. stress state surface.

Preliminary simulations were conducted to aid in the creation of consistent LS-DYNA Version R7.1 models for all specimen configurations. These efforts included an examination of the effects of hourglass controls, mesh size, simulation duration, element formulations, and data processing techniques for the various specimen geometries and loading conditions. The models were created prior to component testing but were used throughout evaluation of the material models. The material properties that were used in this preliminary analysis were taken from the default MAT_24 – Piecewise Linear Plasticity material, which has been previously used by MwRSF to model steel guardrail beams in research and development efforts [74]. The effective plastic strain at failure was arbitrarily set to a value of 0.4 in order to investigate model parameters and specimen failure. Note that the material model that was used in this preliminary analysis is not the

proposed baseline material model, as provided in Section 7.6, in which parameters were developed from the steel material testing found in Chapter 6.

As part of the investigation for the preliminary simulation models, the effects of different hourglass controls and element formulations were examined. Next, a mesh-size study was performed to explore an appropriate mesh size that may capture the necking and failure behavior in all specimens. Also, the effects of varied simulation durations were examined. Next, an element investigation and analysis was performed to examine the difference in results between shell and solid elements, as guardrail sections are commonly modeled with shell elements. Consistent guidelines were required so that each specimen could be modeled using similar parameters, which reduced the possibility of imposing a bias on any one model over others. Consistent units were also used and are shown in Table 35. Furthermore, all simulations were conducted on the University of Nebraska Lincoln supercomputer, Crane, with Intel Xeon E5-2670 2.6GHz processors utilizing 32 cores per simulation.

Table 35. Consistent Units for LS-DYNA Simulations

Mass	**Length**	**Time**	**Force**	**Stress**	**Energy**	**Density**	**Young's Modulus**
kg	mm	ms	kN	GPa	kN-mm	kg/mm^3	GPa

It should be noted that the “critical element” was defined as the element that failed first in the stable simulations. The critical element was typically the center most element in the critical cross-section and was found by using a custom MATLAB program to search through all of the LS-DYNA message files to determine which element failed first. The critical element was utilized to provide the stress state and effective plastic strain history.

7.2 Hourglass Control Analysis

Early modeling showed that some models exhibited the propensity to show visible hourglassing. While the energy histories exhibited minimal hourglass energies, it was necessary to impose a consistent hourglass control that would prevent visible hourglassing for all of the models. As part of the hourglass control analysis, various hourglass controls (HGC) were tried, including both the viscous and stiffness formulations [2]. In the following subsections, hourglass control instabilities and deficiencies are presented for selected specimen configurations. Based on this analysis, a preferred hourglass control was then provided. The keyword Control_Hourglass was utilized to impose the hourglass control to the specimen in the models.

It was found that the various initial specimen models reacted differently depending on their basic shape when different hourglass controls were used. For example, the axial-symmetric specimens produced results that were generally more consistent when different hourglass control types and element formulations were tried. Conversely, the Flat Sharp Notched Specimen produced results that varied greater when different hourglass control types and element formulations were tried. Due to the propensity of some specimen models to produce unstable simulations, specimens representing each general shape were selected to reduce the size of the model parameter investigation into a manageable size. These specimens included the following:

- Specimen Geometry No. 1: Flat Standard Dog Bone;
- Specimen Geometry No. 4: Sharp Notched Flat;
- Specimen Geometry No. 5: Axial-Symmetric Round Smooth;
- Specimen Geometry No. 11: Thick Dog Bone;

- Specimen Geometry No. 15: Standard Punch; and
- Specimen Geometry No. 18: Dual-Point Shear.

7.2.1 Analysis of Viscous Hourglass Controls, Types 1, 2, and 3

The viscous hourglass control formulations (HGC=1, 2, and 3) were attempted in selected specimen configurations. While the viscous formulations appeared to produce fair results for the various tensile specimens, the viscous formulations were unstable for the punch specimen models, as seen in Figure 182. A large amount of hourglassing can be seen in final plot state for hourglass controls type 2 and type 3 with coefficient values of 0.05 in Figure 182(a) and (b). Also, a simulation with no visible hourglassing is also shown for reference in Figure 182(c). Details on the punch models are provided in Section 7.6. Due to their inability to provide reliable hourglass control for the punch simulations, the viscous formulations were excluded from further analysis.

(a)

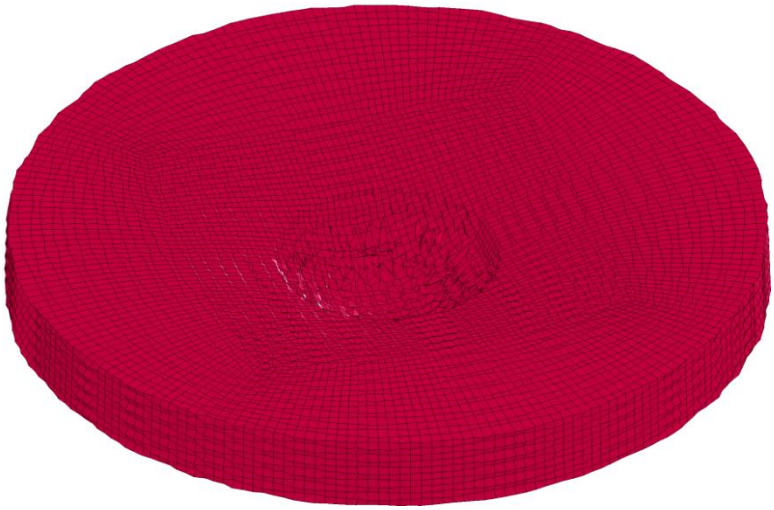

HGC=2, Coef.=0.05

(b)

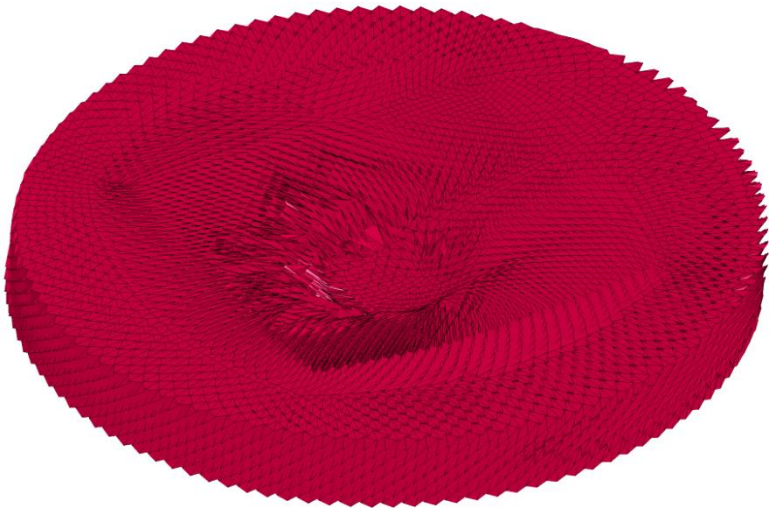

HGC=3, Coef.=0.05

(c)

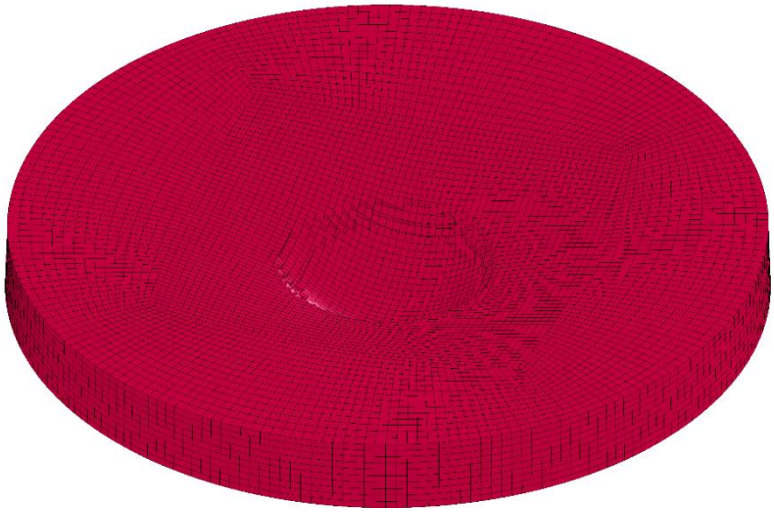

Stable Simulation (HGC=6, Coef.=0.01)

Figure 182. Hourglass Effects with Viscous Hourglass Control on Standard Punch Specimen

7.2.2 Analysis of Stiffness Hourglass Controls, Types 4, 5, 6, 7, and 9

The stiffness-based hourglass controls of type 4, 5, and 6 (HGC=4, 5, 6) were also investigated [2]. They all provided reasonable results and prevented visible hourglass effects in the specimen models. Furthermore, they produced results that are similar to each other and the fully-integrated element formulation, as shown in Table 36. Therefore, utilizing either type 4 or type 5 hourglass controls for the models would have been adequate. However, type 6 was preferred as it tended to show less artificial stiffness, particularly in the post-necking initiation region and the region immediately prior to failure, in the Flat Standard Dog Bone and Flat Sharp Notched Specimen, as seen in Figures 183 and 184, respectively. However, the behavior is better illustrated in the Flat Sharp Notched Specimen. Also, as shown in Table 36, type 6 hourglass control allowed the largest cross-sectional area reduction, which implies less artificial stiffness was imposed due to the hourglass control. It was assumed that the less stiff behavior was preferred as that meant less artificial stiffness was being imposed by the hourglass control. Due to propensity to impose a greater artificial stiffness, the type 4 and 5 hourglass control formulations were excluded from further analysis.

Table 36. Stress State (Triaxiality and Lode Parameter) and Cross-Sectional Area Reduction Values for Stiffness-Based Hourglass Control, Flat Sharp Notched Specimen

Hourglass Control Type and Coefficient Value	Average Triaxiality through Plastic Strain	Average Lode Parameter through Plastic Strain	Cross-Sectional Area Reduction
Default HGC	0.60	0.01	21.2%
Fully Integrated	0.61	0.04	20.1%
Type 4, 0.01	0.62	-0.02	23.9%
Type 5, 0.01	0.61	-0.00	22.6%
Type 6, 0.01	0.62	-0.04	24.7%

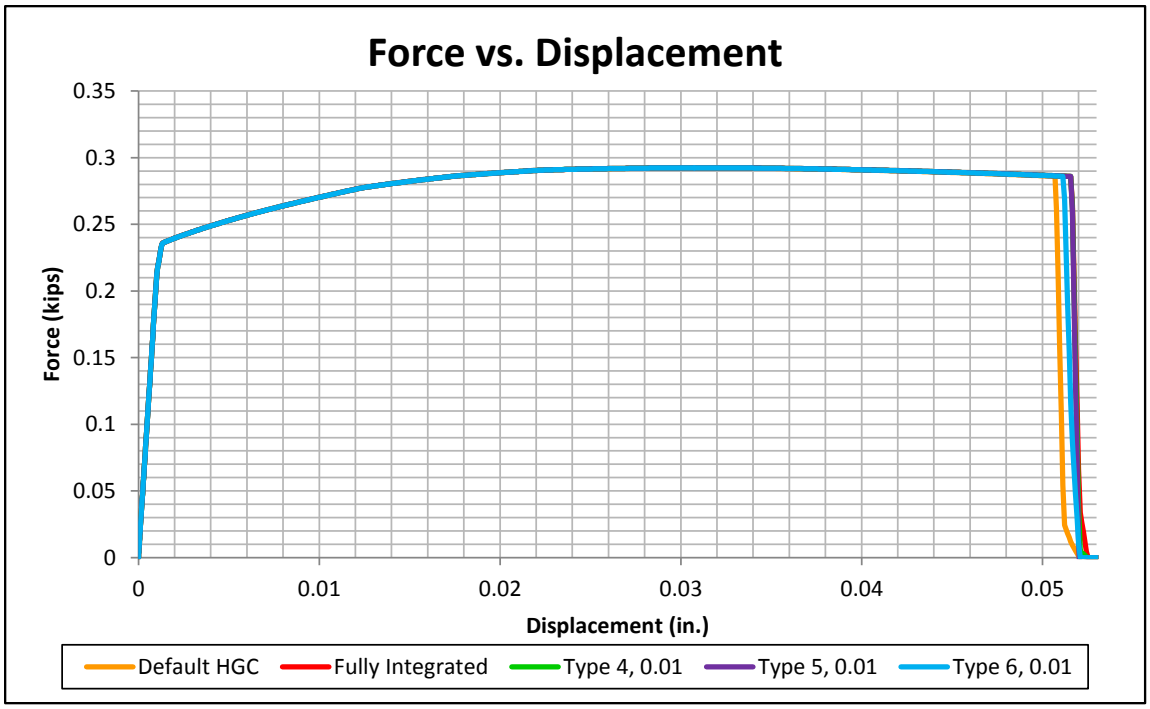

Figure 183. Stiffness-Based Hourglass Control Effects on Force vs. Displacement, Flat Standard Dog Bone Specimen

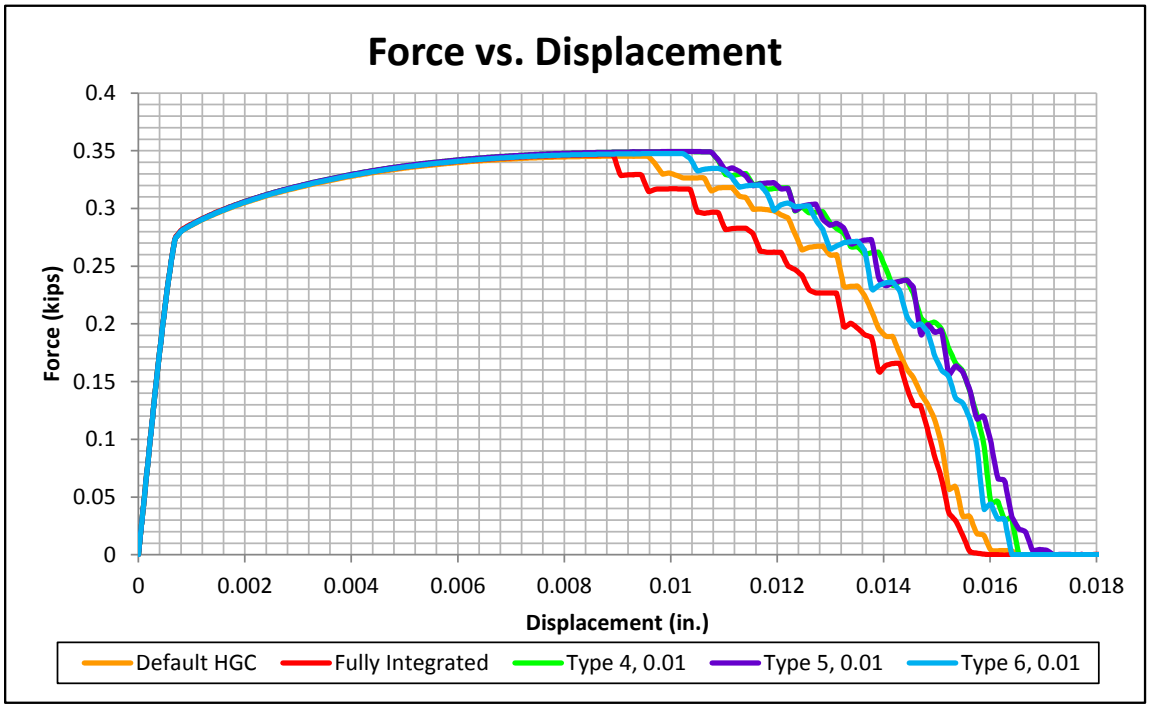

Figure 184. Stiffness-Based Hourglass Control Effects on Force vs. Displacement, Flat Sharp Notched Specimen

Type 6 and type 7 hourglass controls (HGC=6, 7) are both assumed-strain, co-rotational stiffness formulations [2]. However, type 6 is an incremental approach, while type 7 is a total hourglass approach so that it is not path dependent. The implementation of type 7 hourglass control resulted in an increase of computation time by approximately 10 to 20 percent over type 6. Both hourglass controls produced similar results in the experimental models. As a result, type 6 was preferred over type 7.

The type 9 hourglass control (HGC=9) developed by Puso is an enhanced assumed-strain method similar to type 6 hourglass control [2]. The formulation provided reasonable results for the Flat Standard Dog Bone Specimen, the Flat Sharp Notched Specimen, and the Axial-Symmetric Smooth Specimen when a coefficient of -1.00 was used. However, the formulation was unable to prevent hourglassing and inconsistent failure in the thick dog bone specimen, as seen in Figure 185(a) and (b). A stable simulation with no visible hourglassing is also provided in Figure 185(c) for comparison. Negative coefficients were utilized so that the current material properties, as opposed to the initial, would be used when calculating the hourglass control forces. Type 9 hourglass control was eliminated from consideration due to its instability.

(a)

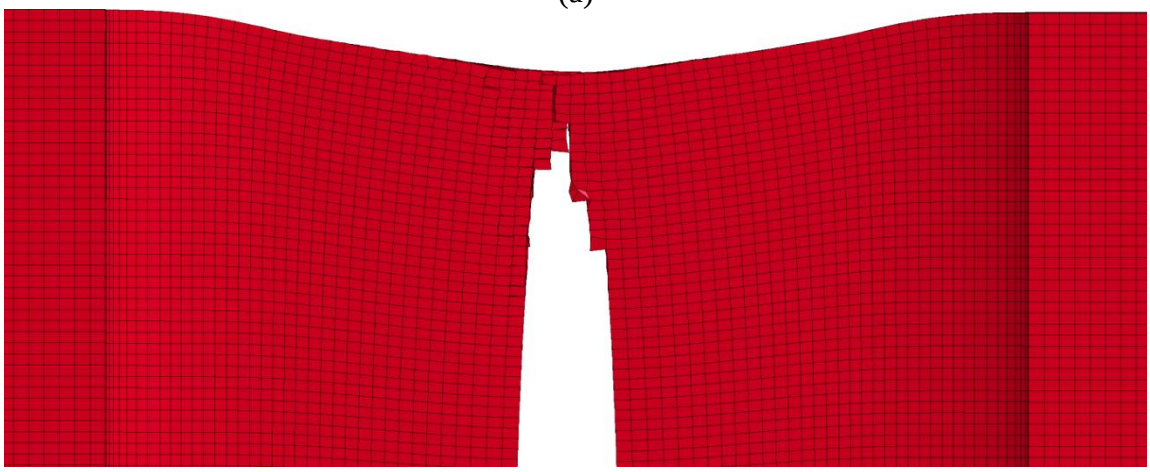

HGC=9, Coef.=-0.05

(b)

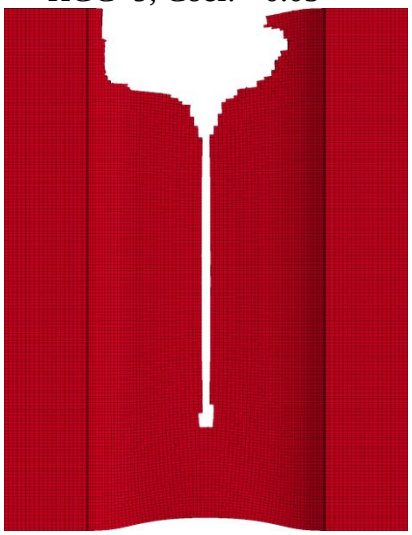

HGC=9, Coef.=-1.00

(c)

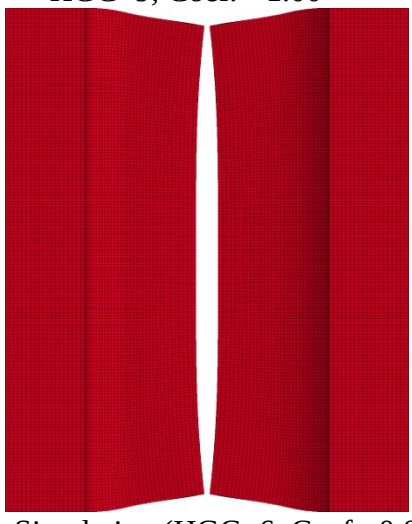

Stable Simulation (HGC=6, Coef.=0.01)

Figure 185. Hourglass Effects with Type 9 Hourglass Control on Thick Dog Bone Specimen

7.2.3 Analysis of Hourglass Control Coefficient

A range of coefficient values for hourglass control type 6, developed by Belytschko and Bindeman, were investigated, and the effects on the model behavior and results were observed. For plasticity material models, small hourglass control coefficients, such as 0.05, have been recommended to limit the artificial stiffness imposed by the hourglass control. Hourglass control coefficients ranging from 0.001 to 1 were attempted and the force vs. displacement behavior for the Flat Sharp Notched Specimen are shown in Figure 186. The Flat Sharp Notched Specimen was chosen for analysis as it showed a higher sensitivity to hourglass control effects, as shown by comparing Figures 183 and 184. Higher hourglass control coefficients created substantial artificial stiffness in the FEM model, which increased both the displacement and force at failure. Furthermore, the state of stress in the critical element was affected as well. As shown in Figures 187 through 190, the greater the coefficient, the farther away the critical element was from the targeted state of stress. The targeted state of stress is given by Buyuk [70] as around $\eta = 0.58$ and $\xi = 0$. However, the average triaxiality through the plastic strain regime trended away from the targeted value with increasing hourglass control coefficients. A similar trend can be seen in the Lode parameter vs. effective plastic strain at failure curves. However, the average values are consistent until the model becomes unstable with excessively-high hourglass control coefficients of 0.5 and 1.0. With these factors in mind, a coefficient of 0.01 was preferred as it eliminated visible hourglass effects on the other specimen models, while also limiting the effects on the force vs. displacement curve and the state of stress.

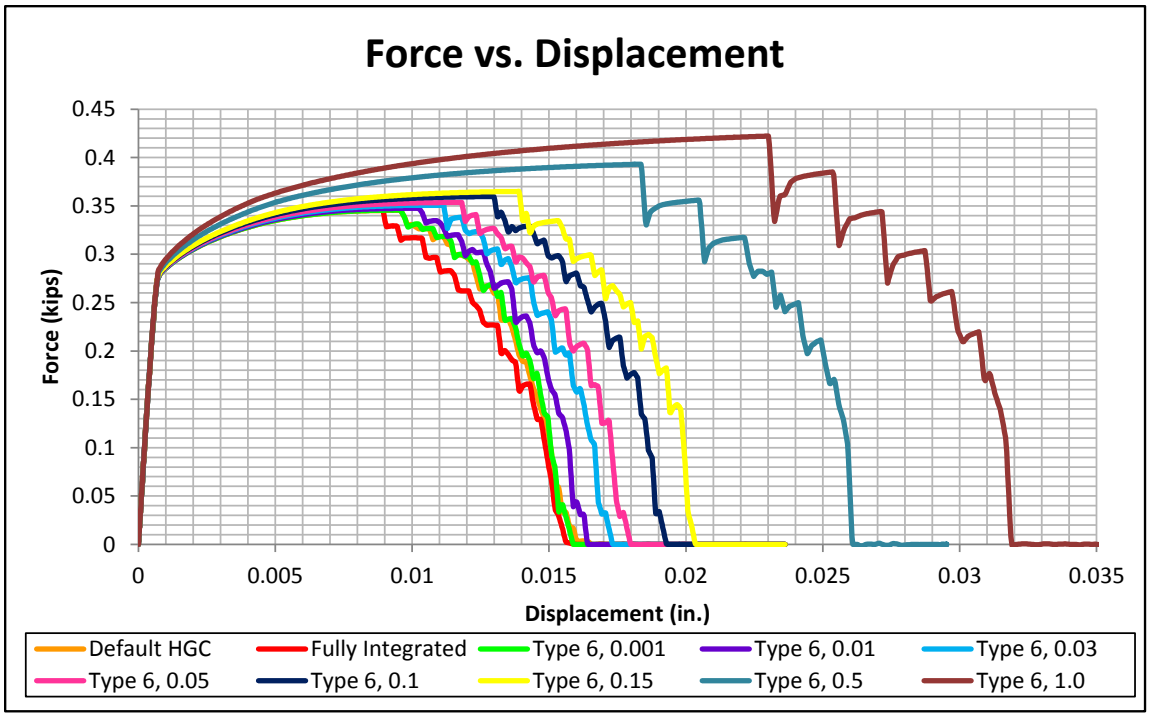

Figure 186. Effects of Type 6 Hourglass Control Coefficient on Force vs. Displacement, Flat Sharp Notched Specimen

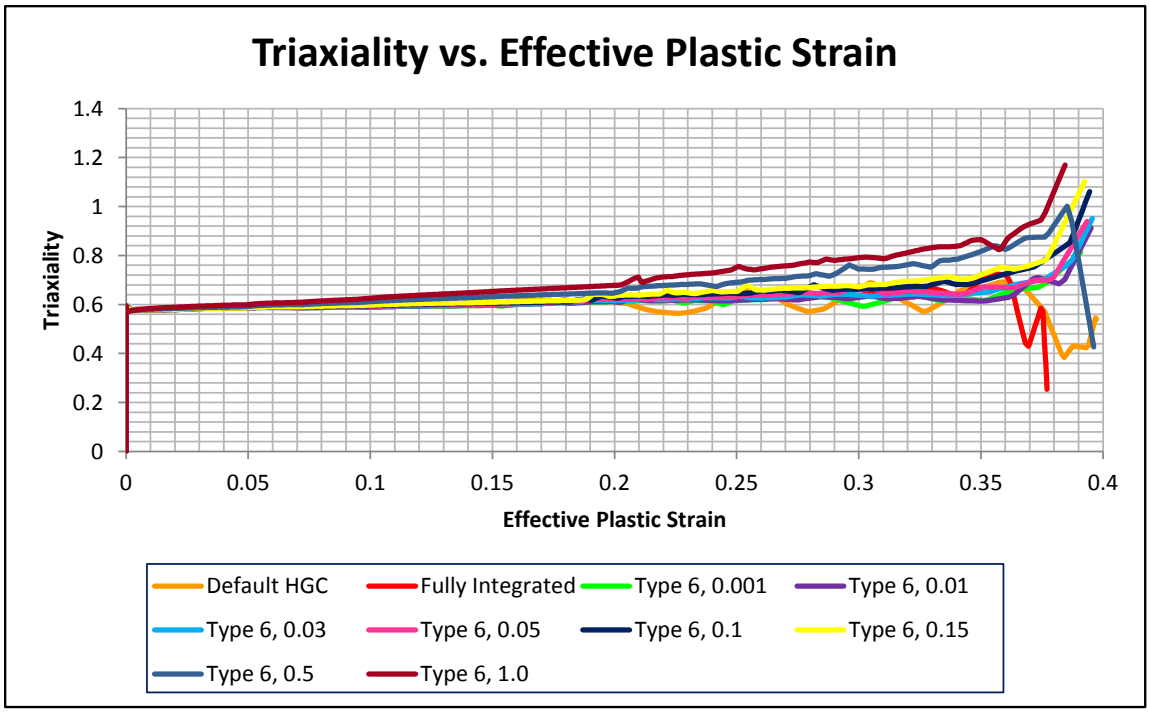

Figure 187. Effects of Type 6 Hourglass Control Coefficient on Triaxiality, Flat Sharp Notched Specimen

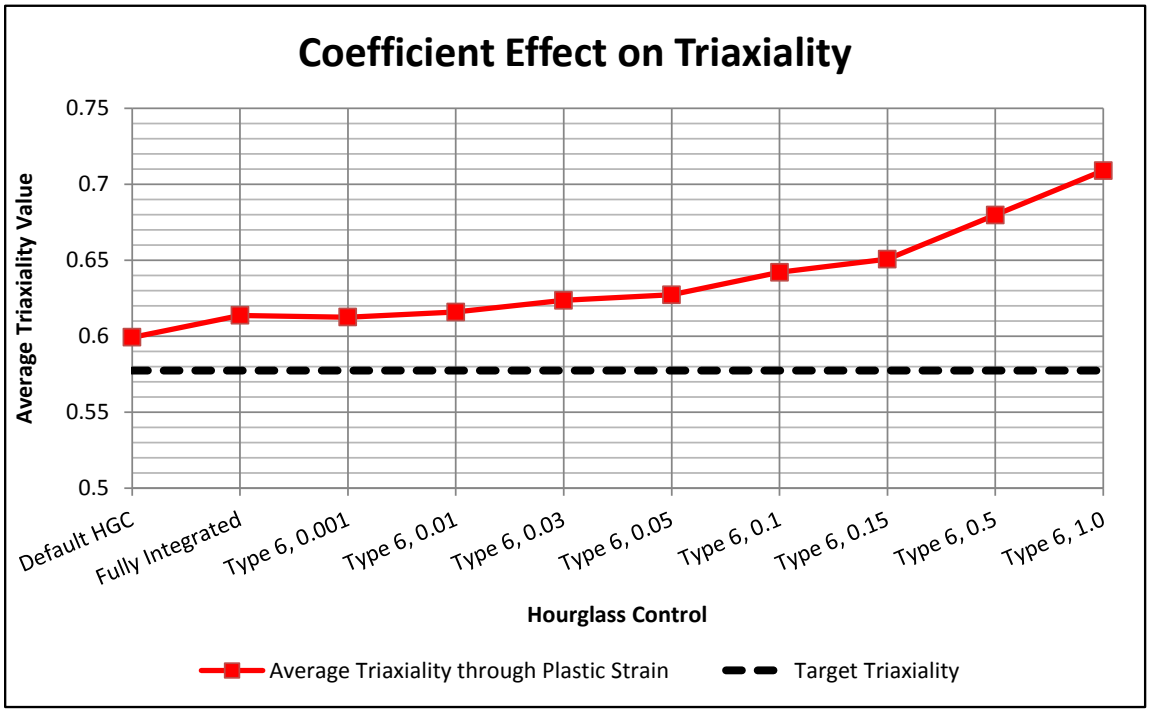

Figure 188. Effects of Type 6 Hourglass Control Coefficient on Average Triaxiality, Flat Sharp Notched Specimen

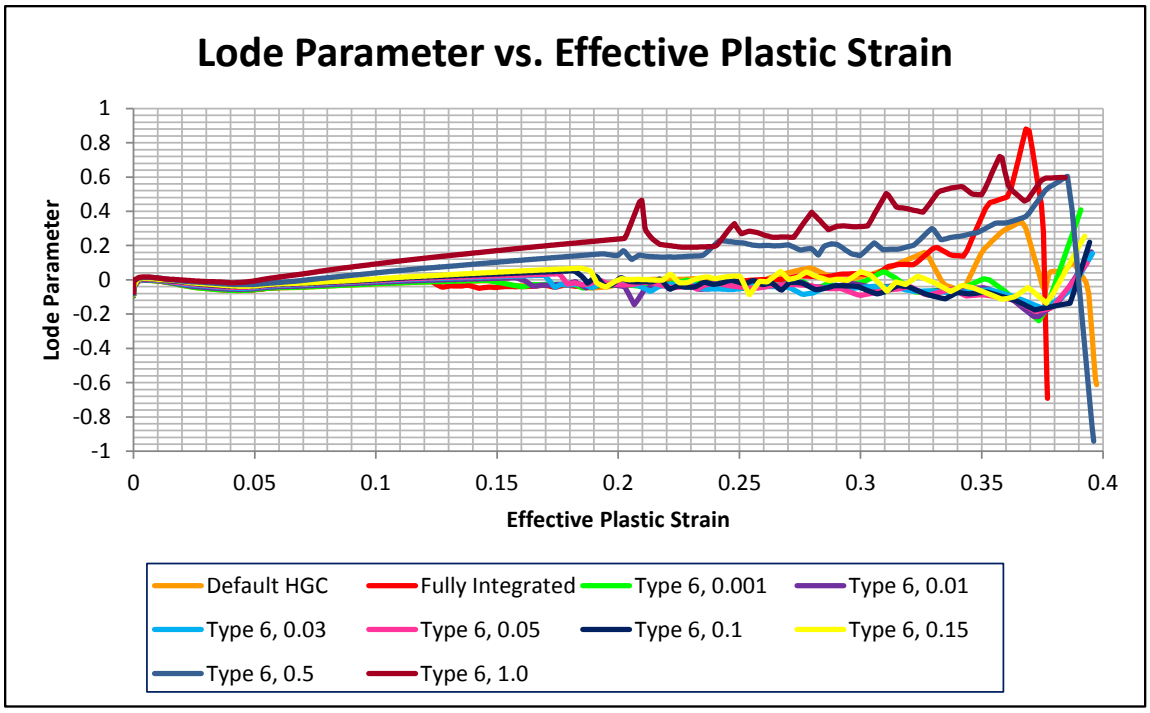

Figure 189. Effects of Type 6 Hourglass Control Coefficient on Lode Parameter, Flat Sharp Notched Specimen

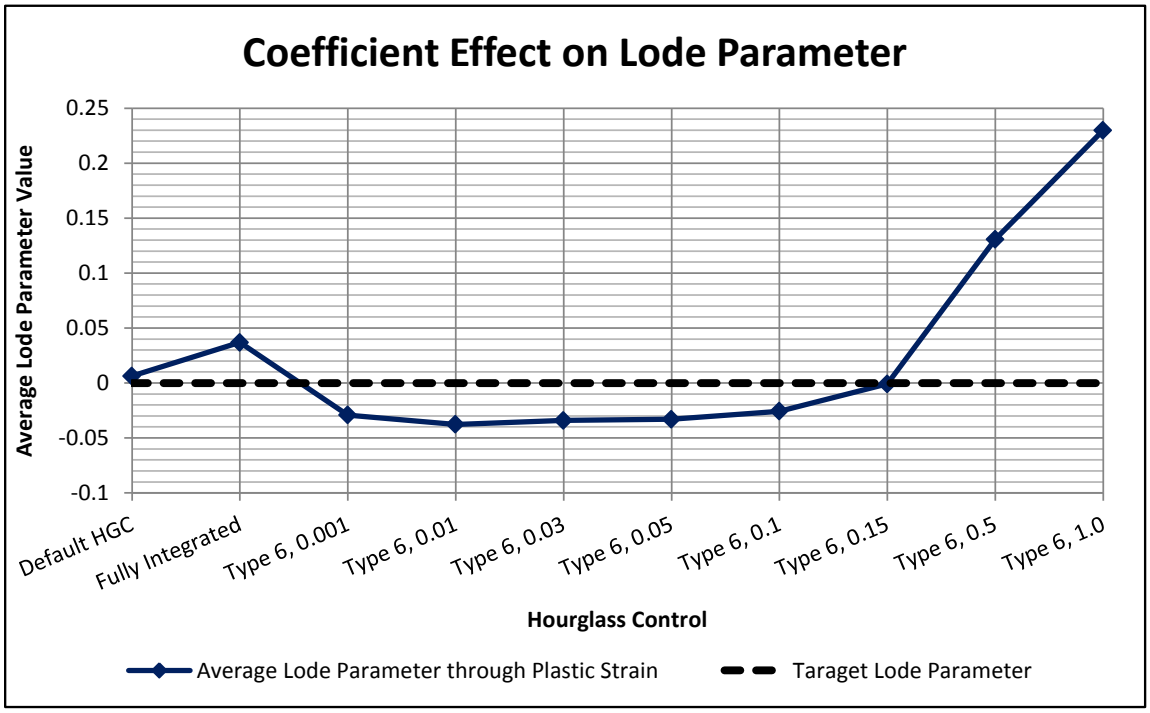

Figure 190. Effects of Type 6 Hourglass Control Coefficient on Average Lode Parameter, Flat Sharp Notched Specimen

7.2.4 Summary of Hourglass Control Analysis

As part of this analysis, various hourglass control methods were implemented on various specimen models. The viscous hourglass controls, types 1, 2, and 3, failed to prevent hourglassing in the Standard Punch Specimen model, as shown in Figure 182. Thus, they were not chosen for further analysis. Hourglass control types 4 and 5 provided similar hourglass control performance as type 6. However, types 4 and 5 imposed a greater artificial stiffness to the model. Furthermore, hourglass control type 7 produced similar hourglass control abilities as type 6, but at additional computation cost. Due to the superior performance of the hourglass control type 6, the hourglass control type 4, 5, and 7 were eliminated from further analysis. Lastly, hourglass control type 9 resulted in model instabilities in the Thick Dog Bone Specimen model, and thus was eliminated from further analysis.

The hourglass control type 6 generally produced superior results over the other hourglass control types, and was chosen to be used for further analysis. As depicted in Figures 186 through 190, a minimal coefficient value is preferred to reduce the effect of the artificial stiffness imposed by the hourglass control. A coefficient value of 0.01 was chosen for further analysis as an appropriate balance between preventing hourglassing and minimizing the artificial stiffness.

7.3 Mesh Size Determination

A consistent mesh size was necessary throughout all specimen FEM models to reduce any mesh-size effects. Thus, a mesh-size sensitivity study was conducted. Two specimens were critical in examining mesh size effects due to their unique geometry. The Flat Dog Bone Specimen and the Flat Sharp Notched Specimen were meshed with various mesh sizes to study the effects on the models. The elements were meshed so that the width, thickness, and height of the elements in the critical cross section were nearly equal. The force vs. displacement curves, stress states through plastic strain, and the cross-sectional areas at failure were compared. Further details on the models are provided in Section 7.6.

The Flat Dog Bone Specimen was chosen due to its simple shape, uniform stress state, and prevalence in material characterization studies. Seven mesh sizes were selected and created, as seen in Figure 191. As the mesh size decreased, convergence in the post-necking behavior was exhibited, as seen in the force vs. displacement curves in Figure 192. The larger element size models exhibited higher forces in the post-necking initiation region as well as increased displacements at failure. Furthermore, the stress states converged as well. The triaxiality values were similar regardless of element size, as seen in Table 37 and Figure 193(a) and (c), and the Lode parameter values were consistent at three elements through the thickness as seen in Table 37 and Figure 193(b) and (d). Also, the percent of reduced cross-sectional area at failure only varies by 1 percent through the simulations, as provided in Table 37.

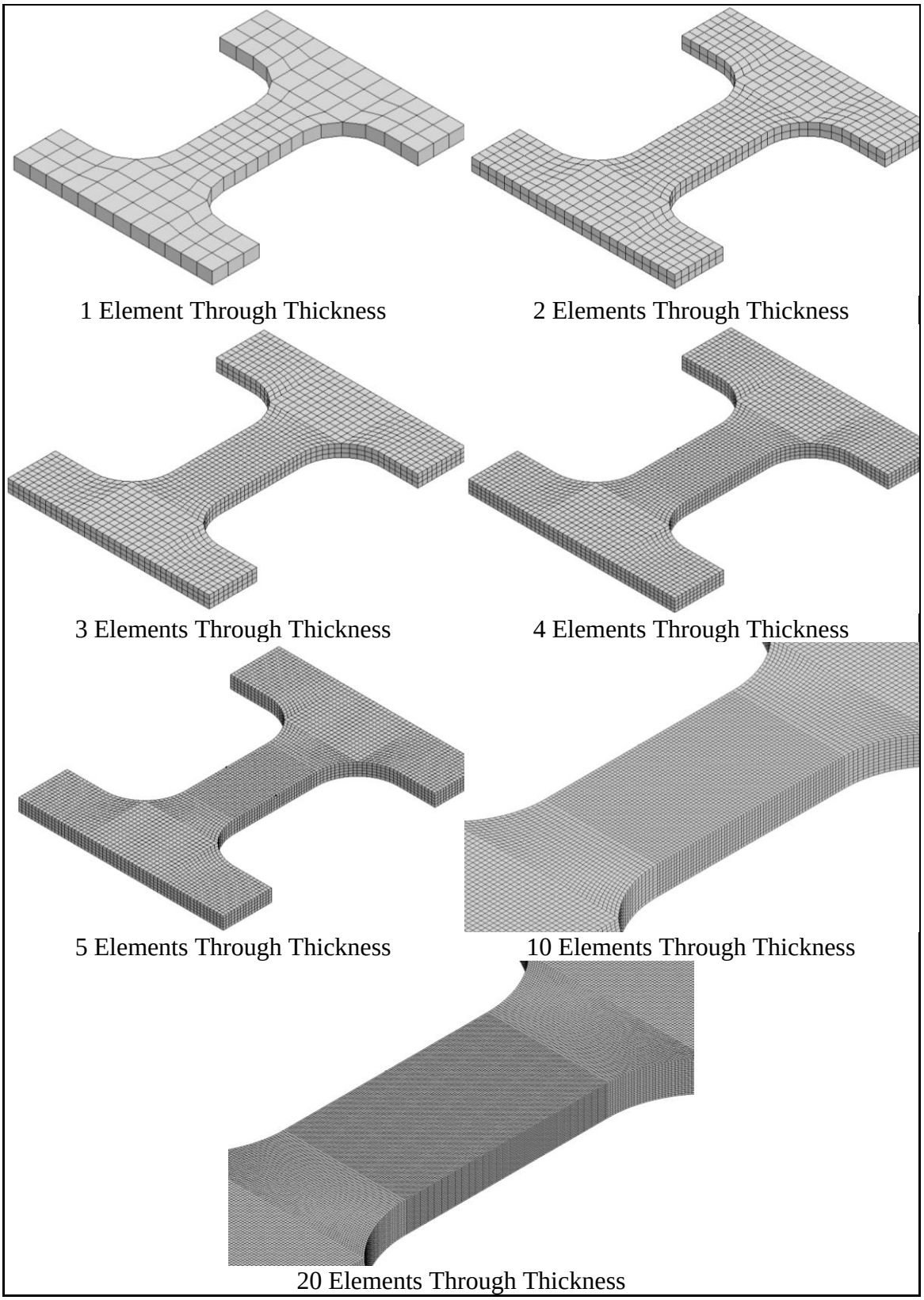

Figure 191. Models of Flat Standard Dog Bone Specimen for Mesh-Size Dependency Study

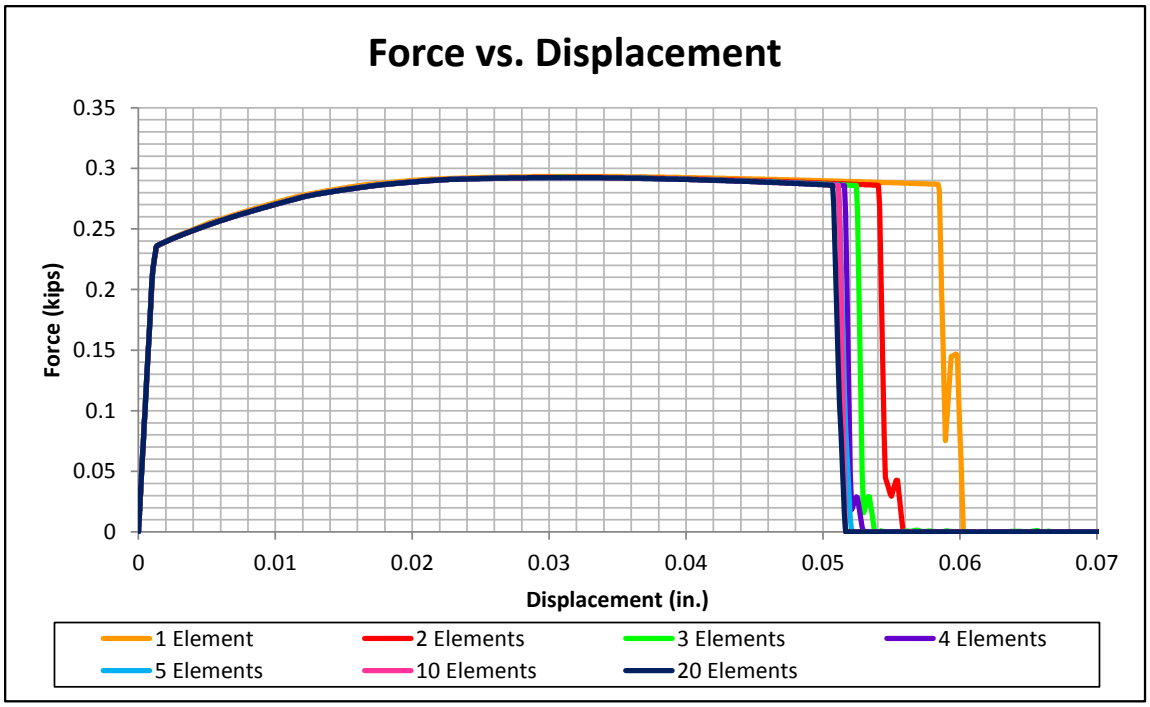

Figure 192. Force vs. Displacement for Various Mesh Sizes (Through Thickness), Flat Standard Dog Bone Specimen

Table 37. Modeling Results with Various Mesh Sizes, Flat Standard Dog Bone Specimen

Number of Elements Through Thickness	Element Size in. (mm)	Average Triaxiality through Plastic Strain	Average Lode Parameter through Plastic Strain	Final Cross-Sectional Area Reduction
1 Element	0.3000 (0.762)	0.349	0.965	32.9%
2 Elements	0.0150 (0.381)	0.349	0.950	32.6%
3 Elements	0.0100 (0.254)	0.352	0.935	33.0%
4 Elements	0.0075 (0.191)	0.352	0.934	32.6%
5 Elements	0.0060 (0.152)	0.353	0.931	32.4%
10 Elements	0.0030 (0.076)	0.353	0.928	32.6%
20 Elements	0.0015 (0.038)	0.353	0.929	-

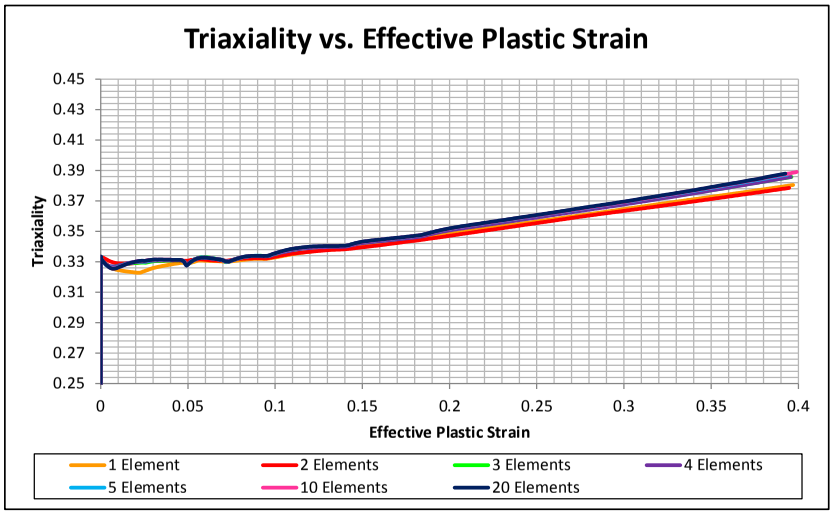

(a)

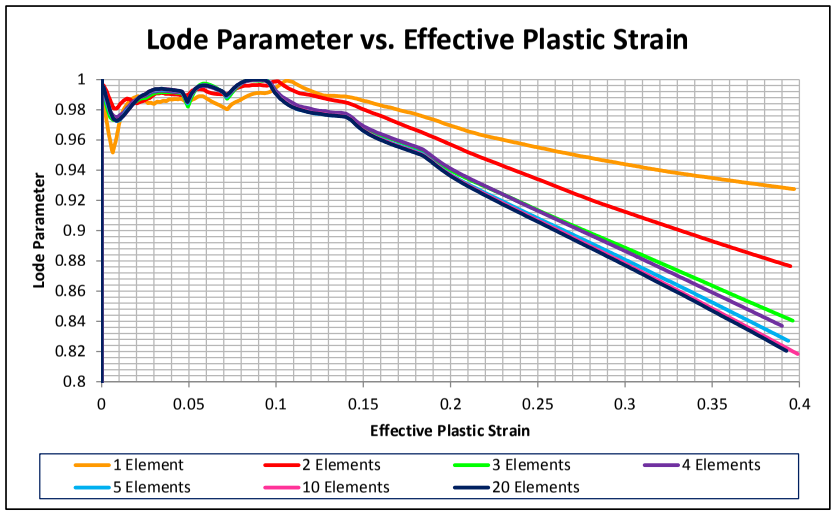

(b)

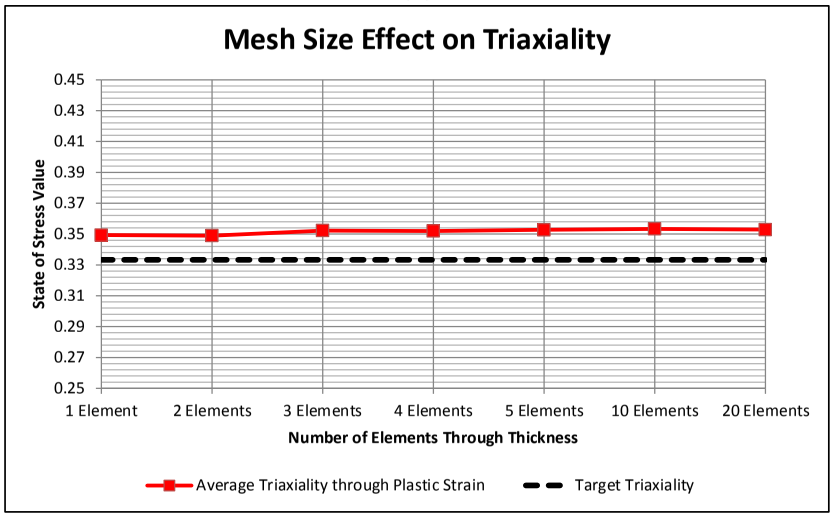

(c)

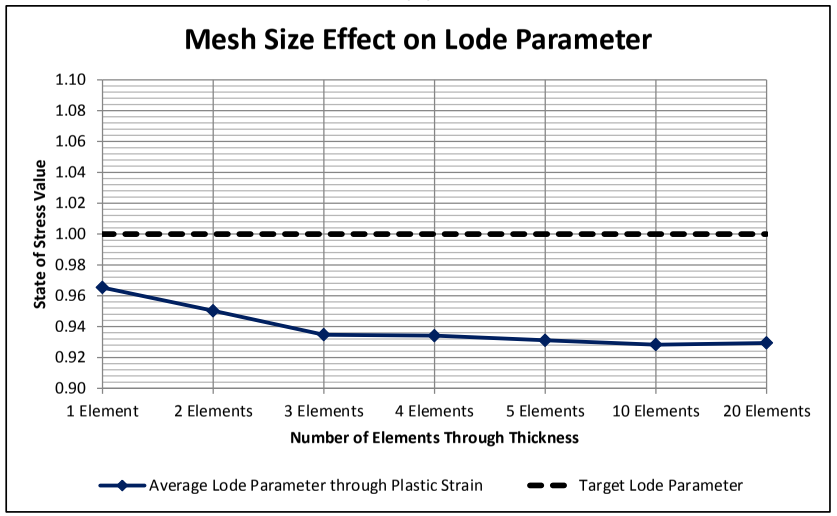

(d)

Figure 193. Stress State vs. Effective Plastic Strain for Various Mesh Sizes, Flat Standard Dog Bone Specimen

The Flat Standard Dog Bone Specimen model produced relatively consistent results, starting with a model with three elements through the thickness. However, the results were much more mesh-dependent with more complex shapes. To illustrate this finding, a similar mesh-size study was performed on the Flat Sharp Notched Specimen. Five mesh sizes were selected and created, as seen in Figure 194. As the mesh size decreased, the yield force, ultimate force, force at failure, and displacement at failure all decreased, as seen in the force vs. displacement curves in Figure 195. This behavior can be attributed to two factors. First, if too large of a mesh size is selected to represent the geometry around the notch, the differences in the model's geometry in the notched length may not allow for an accurate representation of the physical model. This selection can affect the model during the entire range of elongation. However, as the mesh size decreases, the model's geometry will converge. Second, if a sufficiently small mesh size is not selected, the model may not accurately capture the diffuse necking behavior. After diffuse necking initiation, the stresses within a region began to localize. As necking continued, the mesh must be sufficiently small enough to allow this necking to be captured. Model behavior after diffuse necking initiation and particularly immediately prior to failure can be affected.

Furthermore, the stress states show convergence as mesh size decreases. The triaxiality values are similar, excluding the two elements through the thickness mesh, as seen in Figure 196 (a) and (c). However, the Lode parameter shows less convergence with values still varying slightly between the ten and twenty elements through the thickness meshes, as seen in Figure 196 (b) and (d).

It was believed that the Flat Sharp Notched Specimen would exhibit the greatest mesh-size effects due to its shape. The small gauge section, where the majority of the deformation occurred, had the least number of finite elements in all of the models, which limited the model's ability to predict the necking and plastic behavior of the material in this section. Furthermore, the sharp notches created large stress concentrations at the radii of the notches. As a result of these concentrators, large plastic deformations occurred in relatively small areas. If a fine mesh was not used, these deformations were not accurately modeled as the point of high stress was distributed over a larger element. This scenario created a model with an increased strength and displacement at failure, as opposed to a model that captured the higher degree of plastic deformation at the stress concentrator.

Based on the results of these two studies, it was determined that a mesh size equal to five elements through the thickness of the flat specimens, or an element length equal to 0.0060 in. (0.152 mm), would provide adequate results, while limiting the number of elements required for mesh each specimen. A reasonable convergence was found in the model's geometry, state of stress, and the necking behavior with this element size. A finer mesh size could be used, but with the increased simulation time required for finer meshes, particularly with the thick specimens, it was determined to be unnecessary. However, further evaluation may be necessary with each specimen type.

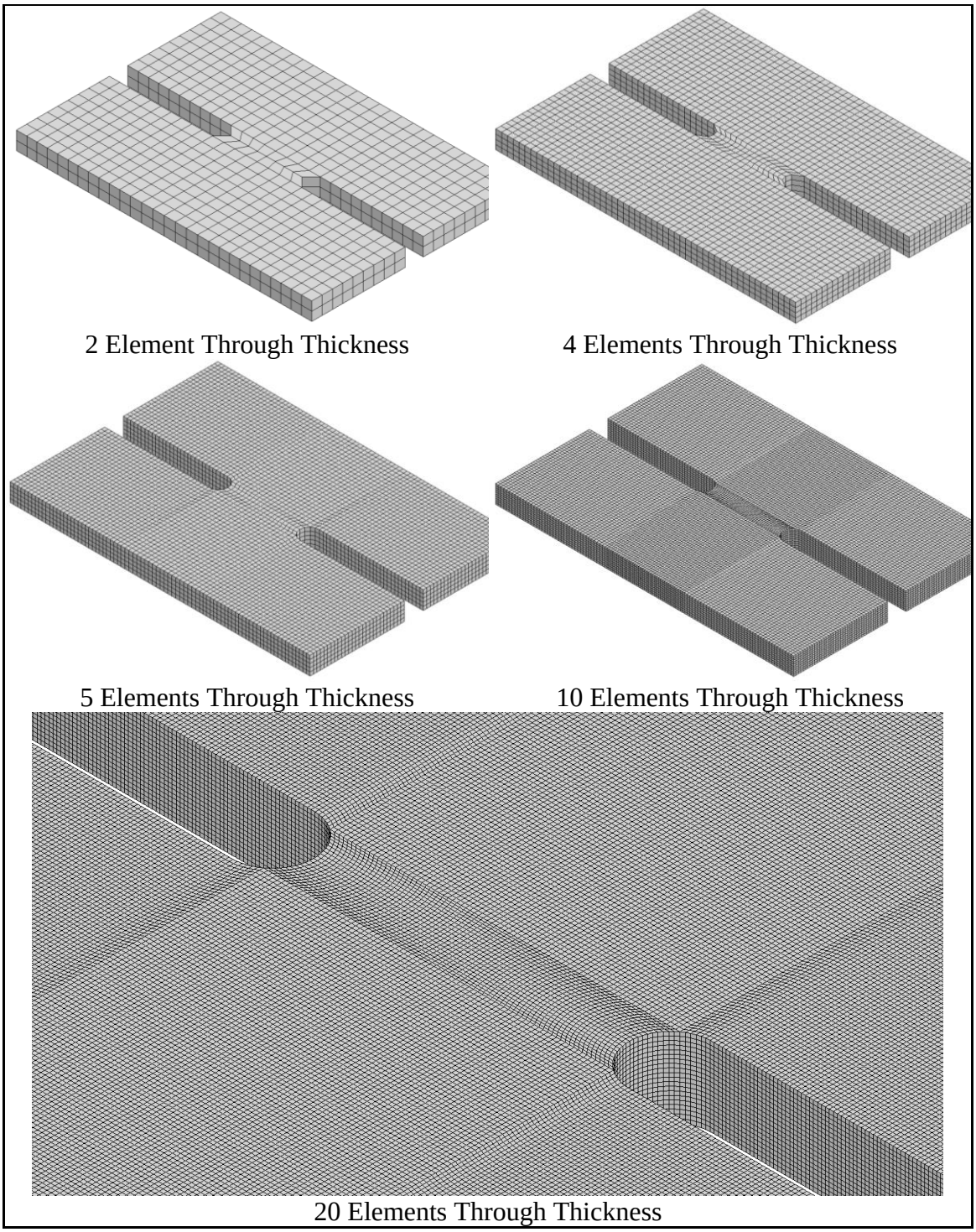

Figure 194. Models of Flat Sharp Notched Specimen for Mesh-Size Dependency Study

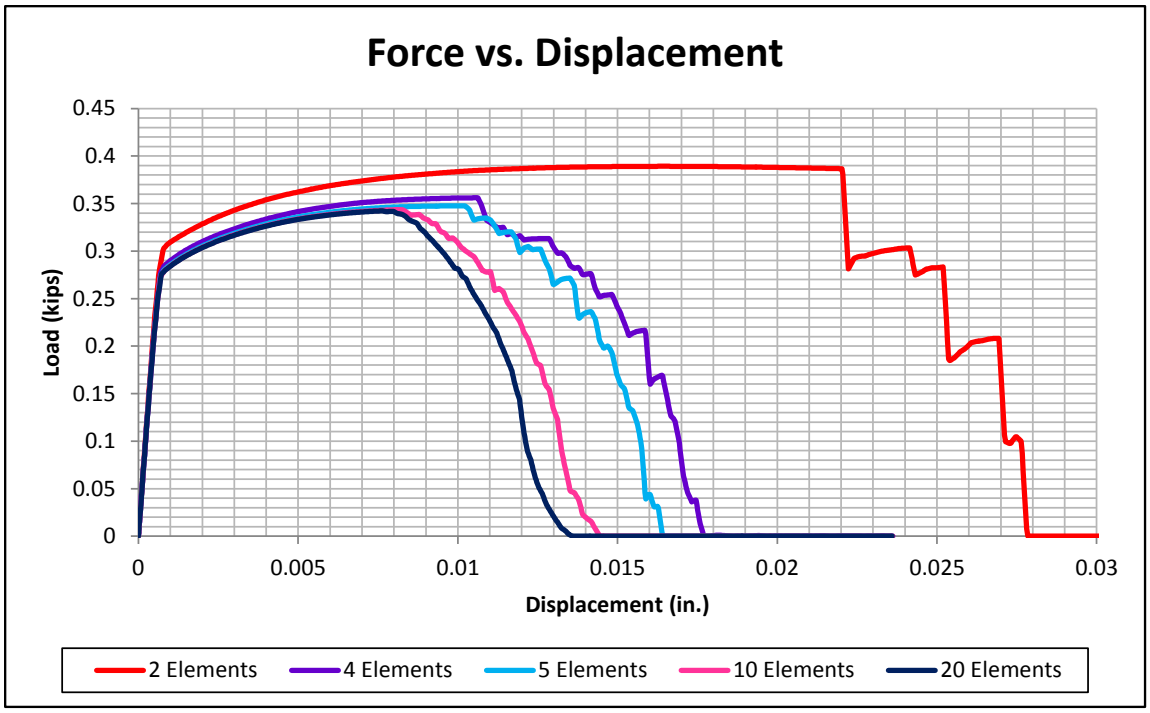

Figure 195. Force vs. Displacement for Various Mesh Sizes, Flat Sharp Notched Specimen

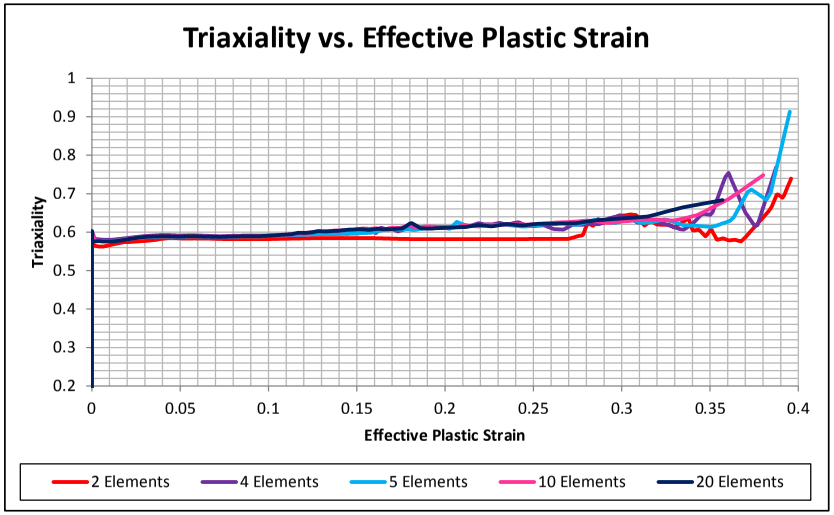

(a)

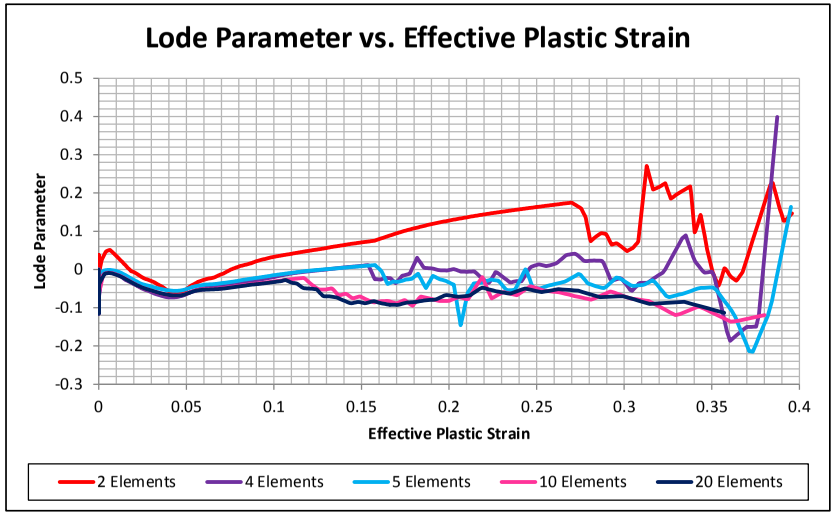

(b)

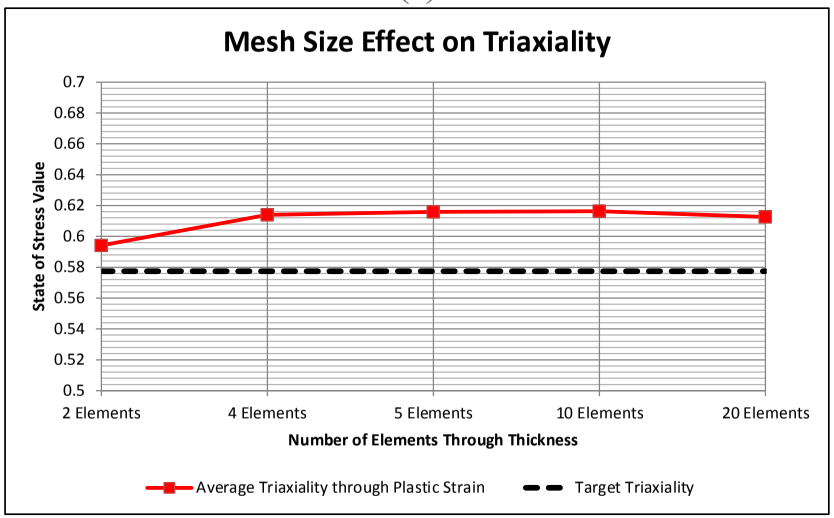

(c)

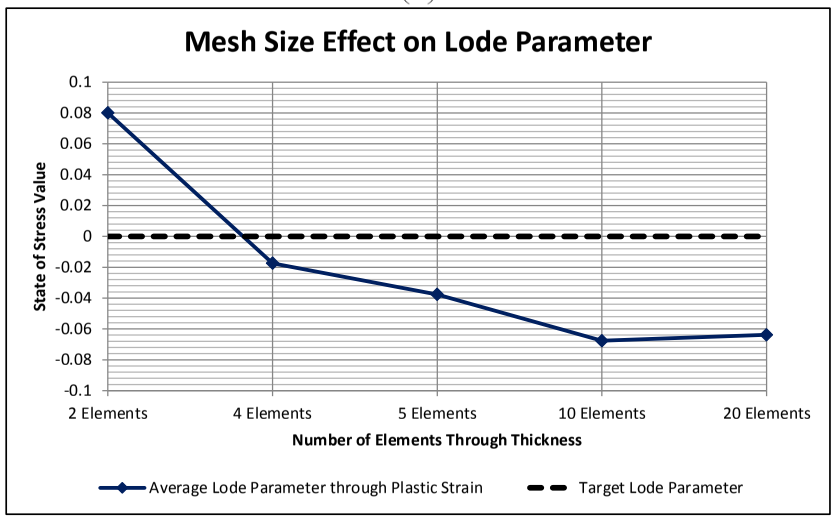

(d)

Figure 196. Stress State vs. Effective Plastic Strain for Various Mesh Sizes, Flat Sharp Notched Specimen

7.4 Simulation Duration Effects

In order to model the specimens, it was necessary to shorten the simulation times to be representations of the physical tests. Using an explicit time integration model, such as that used in LS-DYNA, to simulate a static test for 200 seconds is infeasible due to the time required for the calculations as well as the instabilities that would likely form. To avoid these problems, it was required to shorten the simulation time by increasing loading rates. However, if too short of a simulation duration was selected, the increased loading rate could cause inertial effects to become evident and skew the results. To determine the ideal simulation durations, a number of simulations were performed on the Flat Standard Dog Bone Specimen with various simulation durations. Note that strain rate effects were not utilized in the material model. The loading curves and database output intervals were scaled with the termination time so that one edge of the specimen was displaced 0.0787 in. (2.000 mm) by the end of each simulation. Further details on the models are provided in Section 7.6.

A simulation time of 10 ms was determined to be an appropriate simulation time. As seen in Figure 197, the force vs. displacement behavior converges very well. The simulation time of 0.1 ms exhibited inertial effects, as seen by the wave in the plastic region between 0.0014 and 0.0244 in. (0.036 and 0.620 mm). The 1, 10, and 100 ms duration simulations were nearly identical with only small variations in the displacement at failure. Furthermore, the effect of simulation duration on the state of stress, as represented by triaxiality and Lode parameter, was examined. The triaxiality and Lode parameter behaviors for the various simulation durations can be found in Figures 198 and 199, respectively. The 0.1 and 1 ms simulation durations show a higher degree of

variation through the plastic regime. The 10 and 100 ms simulations converge to similar curves. For these reasons, a 10 ms simulation duration was considered to provide the most accurate representation of the actual testing while limited the cpu wall time required for the calculations. However, further evaluation may be necessary in future simulation efforts.

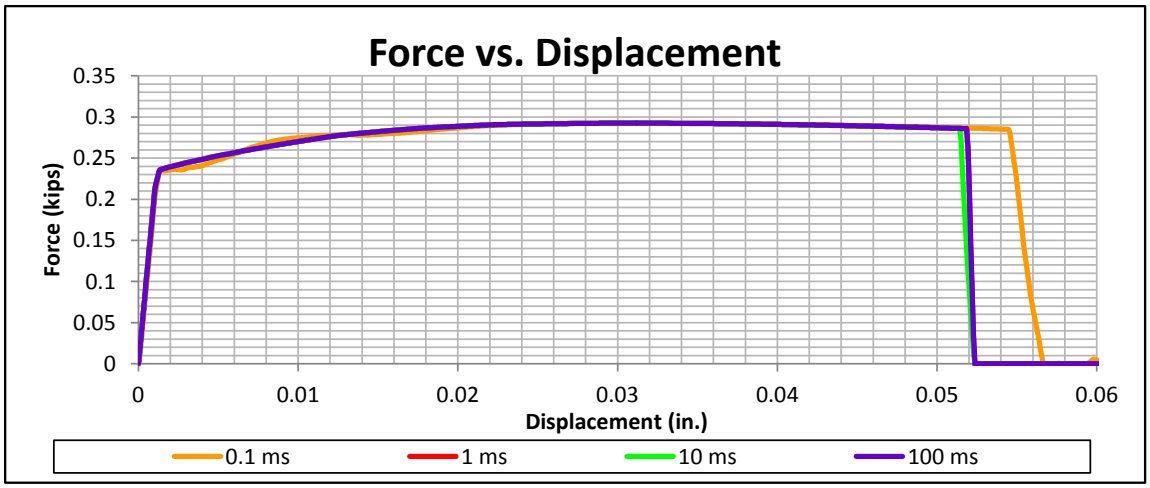

Figure 197. Force vs. Displacement for Various Simulation Durations

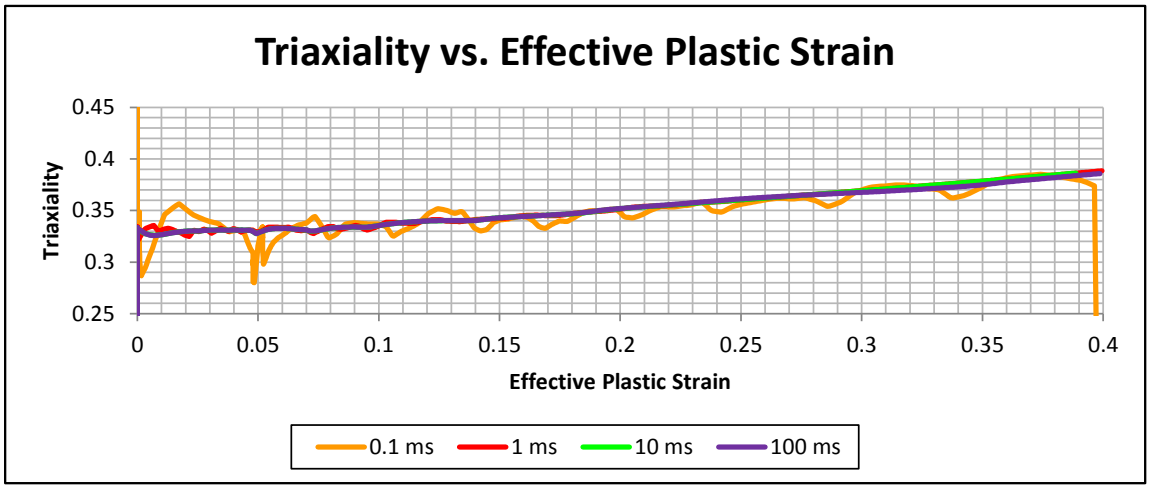

Figure 198. Triaxiality vs. Effective Plastic Strain for Various Simulation Durations

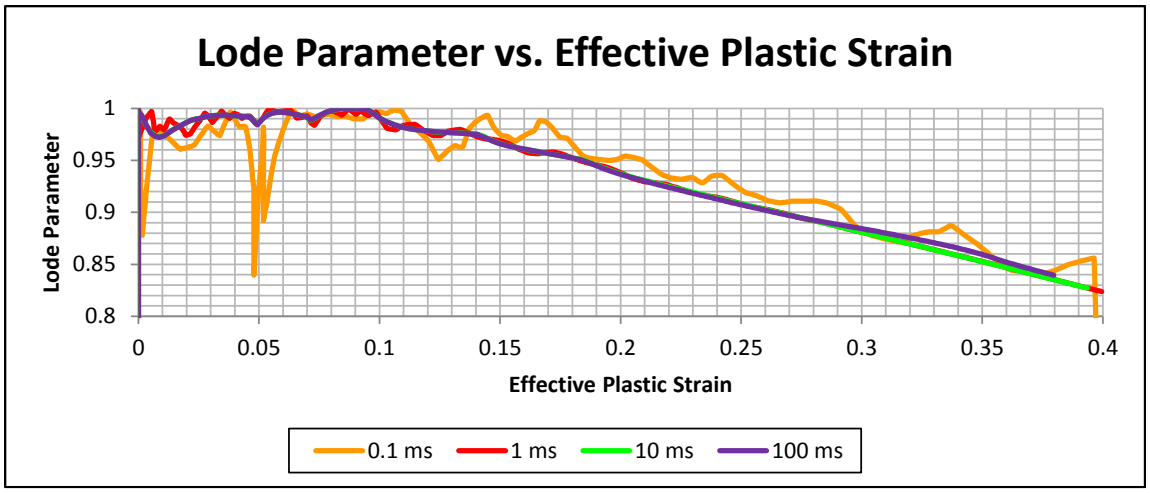

Figure 199. Lode Parameter vs. Effective Plastic Strain for Various Simulation Durations

7.5 Solid vs. Shell Analysis

Shell elements are typically used to model rail sections within guardrail systems. Thus, it is important to investigate whether shell and solid element models produce similar results. To analyze the performance of shell elements when compared to solid elements, a number of simulations were performed to model the flat specimens. Specimen strength, failure behavior, and critical element stress states were of particular interest in this analysis.

Due to the limitations of shell elements, only the flat plane stress specimens were modeled with shell elements and compared to their equivalent solid element models. Identical 0.0060-in. (0.152-mm) element size meshes were used for the shell and solid element meshes with identical constraints and loading conditions. Type 2 Belytschko-Tsay (ELFORM=2) and Type 16 fully integrated Bathe-Dvorkin (ELFORM=16) shell element formulations were investigated [2]. The shell elements were modeled with 5 through thickness integration points. Further details on the models are provided in Section 7.6. Also, the thickness update option (ISTUPD) was examined to evaluate the effects of the optional shell membrane thinning. Three thickness update options were

attempted as part of the analysis. The membrane thickness options included types 0, 1, and 4 (ISTUPD=0, 1, and 4). The effects from these values are described in Table 38 [2]. Five through-thickness integration points were utilized, and the central integration point was used to track effective plastic strain and the state of stress.

Table 38. ISTUPD Flag Value Effects on Shell Thickness Update Method [2]

ISTUPD Flag Value	Effect
0	No thickness change
1	Membrane straining causes thickness change in shell elements
4	Similar to option 1, but the elastic strains are neglected from the thickness update to provide more stable simulations

7.5.1 Flat Standard Dog Bone Specimen

When the thickness update options ISTUPD=1 and 4 were utilized, the Flat Standard Dog Bone Specimen model produced similar force vs. displacement curves to the solid element model. However, when the thickness update option was equal to ISTUPD=0, the model overestimated the displacement at failure by nearly double and over predicted the specimen strength throughout elongation when compared to the results corresponding to the solid element baseline model, as seen in Figure 200. This over-prediction was likely the result of the thickness update option ISTUPD=0, which did not allow the specimen to thin and neck normal to the plane of the element. This thinning and necking was observed in the solid element model as well as the shell element model with thickness update options ISTUPD=1 and 4.

Similar trends were seen in the triaxiality and Lode parameter vs. effective plastic strain curves. As the specimen elongated and necked, the state of stress shifted away from their initial values for the solid element model and the ISTUPD=1 and 4 thickness update models, as seen in Figures 201 and 202. While some variation existed in the state of

stress through elongation, the values were generally similar. However, in the ISTUPD=0 thickness update models, the lack of membrane thinning caused the drift away from the initial state of stress through elongation to be small. This resulted in a substantial difference in stress states in the later part of elongation when compared to the solid element model. In summary, the type 2 Belytschko-Tsay and type 16 Bathe-Dvorkin shell element formulations adequately reproduced results obtained from the solid element baseline model for the Flat Standard Dog Bone Specimen model when the thickness update option was equal to ISTUPD=1 and 4. However, the ISTUPD=0 thickness update option does not provide similar results.

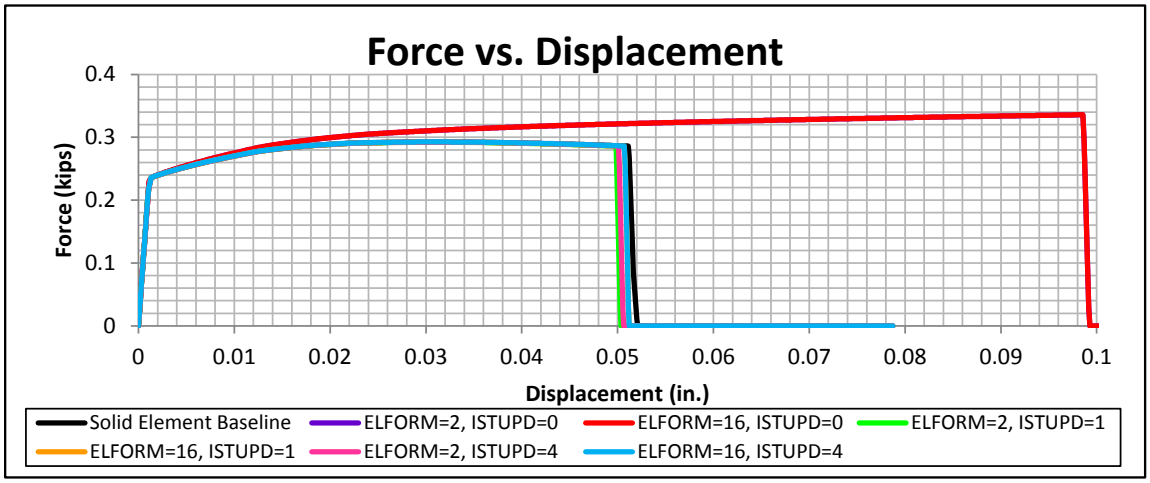

Figure 200. Force vs. Displacement for Solid vs. Shell Analysis, Flat Standard Dog Bone Specimen

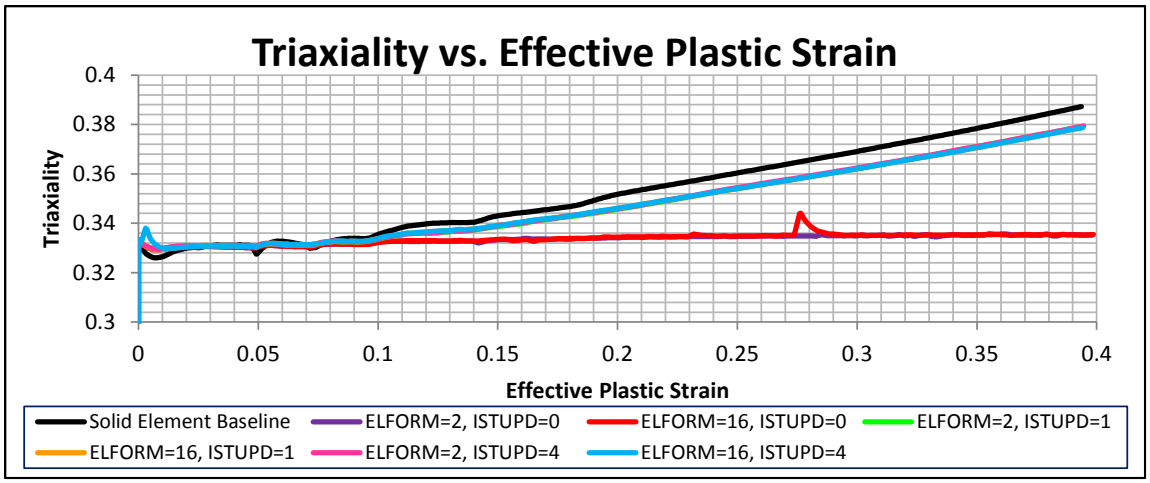

Figure 201. Triaxiality vs. Effective Plastic Strain for Solid vs. Shell Analysis, Flat Standard Dog Bone Specimen

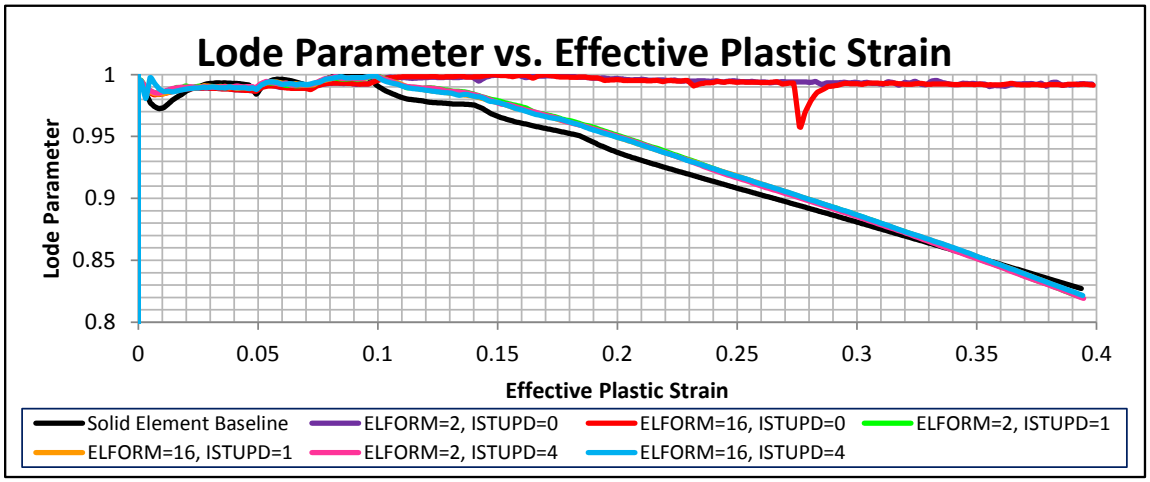

Figure 202. Lode Parameter vs. Effective Plastic Strain for Solid vs. Shell Analysis, Flat Standard Dog Bone Specimen

7.5.2 Flat Large Notched Specimen

The Flat Large Notched Specimen produced similar force vs. displacement curves to the solid element model prior to failure initiation when the ISTUPD=1 and 4 thickness update options were used, as shown in Figure 203. However, the displacement at failure initiation was underestimated when compared to the results corresponding to the solid element model. Contrariwise, when the thickness update option was set to ISTUPD=0,

the models overestimated the displacement at failure as well as specimen strength throughout elongation when compared to the solid element baseline models.

As the specimen elongated and necked, the state of stress in the models when the ISTUPD=1 and 4 thickness update options were used shifted roughly following the solid element model, as depicted in Figures 204 and 205. However, in the thickness update option ISTUPD=0 models, the drift was substantially different from the solid element model.

Interestingly, when the thickness update option was equal to ISTUPD=0 the outside elements failed first. The tear then moved inward to the center, as opposed to the inside-out failure method observed with the other simulations. This outside-in tearing produced a shift in the triaxiality and Lode parameter in the center element immediately prior to complete separation. This shift in the state of stress can be explained by deletion of the surrounding elements, which were providing a partial confinement stress. Note for this analysis the center element remained the critical element for the thickness update option ISTUPD=0 models even though it was not the first element to fail.

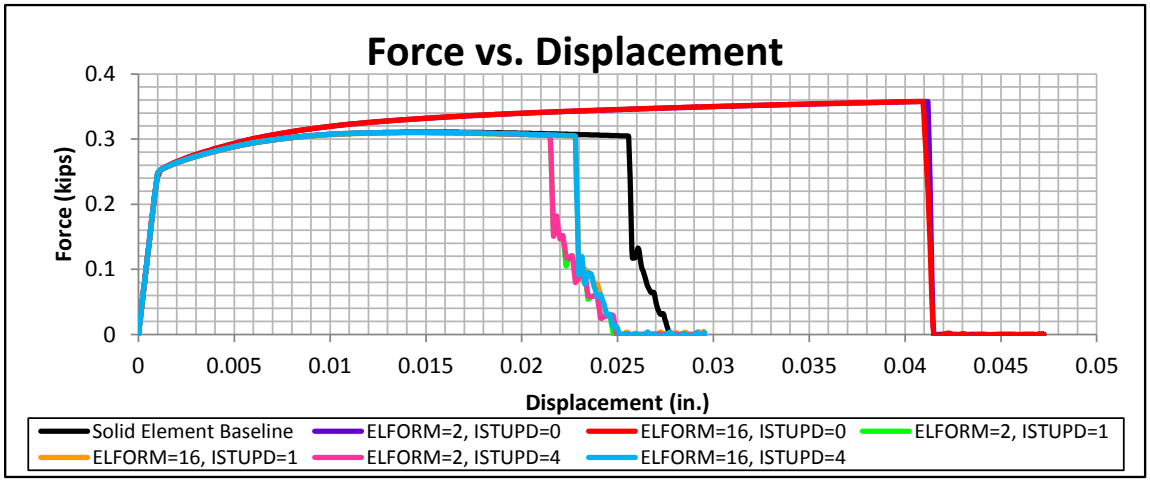

Figure 203. Force vs. Displacement for Solid vs. Shell Analysis, Flat Large Notched Specimen

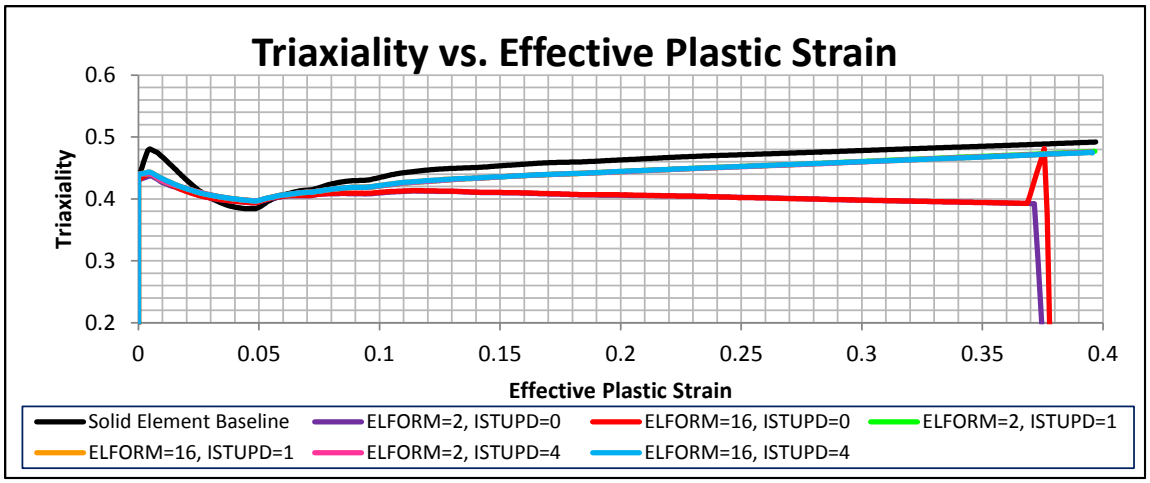

Figure 204. Triaxiality vs. Effective Plastic Strain for Solid vs. Shell Analysis, Flat Large Notched Specimen

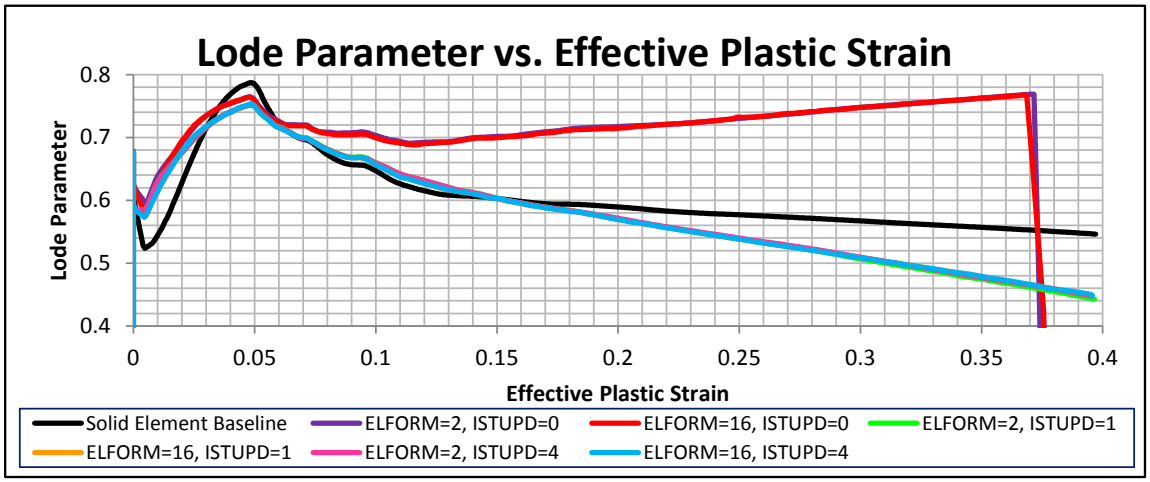

Figure 205. Lode Parameter vs. Effective Plastic Strain for Solid vs. Shell Analysis, Flat Large Notched Specimen

7.5.3 Flat Small Notched Specimen

The Flat Small Notched Specimen produced similar force vs. displacement curves to the solid element model prior to failure initiation when the thickness update options ISTUPD=1 and 4 were used, as seen in Figure 206. Again, the displacement at failure initiation was underestimated when compared to the results corresponding to the solid element model. Furthermore, when the thickness update option was set to ISTUPD=0, the

models overestimated the displacement at failure as well as specimen strength throughout elongation when compared to the solid element baseline model.

Similar to the Flat Large Notched Specimen, the thickness update option ISTUPD=0 models failed starting with the outside elements. The tear then moved inward to the center, as opposed to the inside-out failure method seen with the other simulations, as shown in Figure 207. This outside-in tearing produced a shift in the triaxiality and Lode parameter in the center element immediately prior to complete separation. This shift in the state of stress can be explained by the deletion of surrounding elements, which were providing a partial confinement stress. As the elements were deleted, the confinement of the critical element reduced until it was the only remaining element. A large shift in the state of stress immediately prior to failure is the result.

As the specimen elongated and necked, the triaxiality in the models with the thickness update options equal to ISTUPD=1 and 4 shifted roughly following the solid element model, as shown in Figure 208. However, in the thickness update option ISTUPD=0 models, the triaxiality drifted substantially lower from the solid element model. Interestingly, all of the shell element models produced Lode parameter behavior that drifted away from the solid element baseline model, as seen in Figure 209. The models with thickness update options equal to ISTUPD=1 and 4 underestimated the Lode parameter value, while the models with the thickness update option equal to ISTUPD=0 overestimated the Lode parameter value before the outside-in tearing caused the state of stress to change rapidly immediately before complete separation.

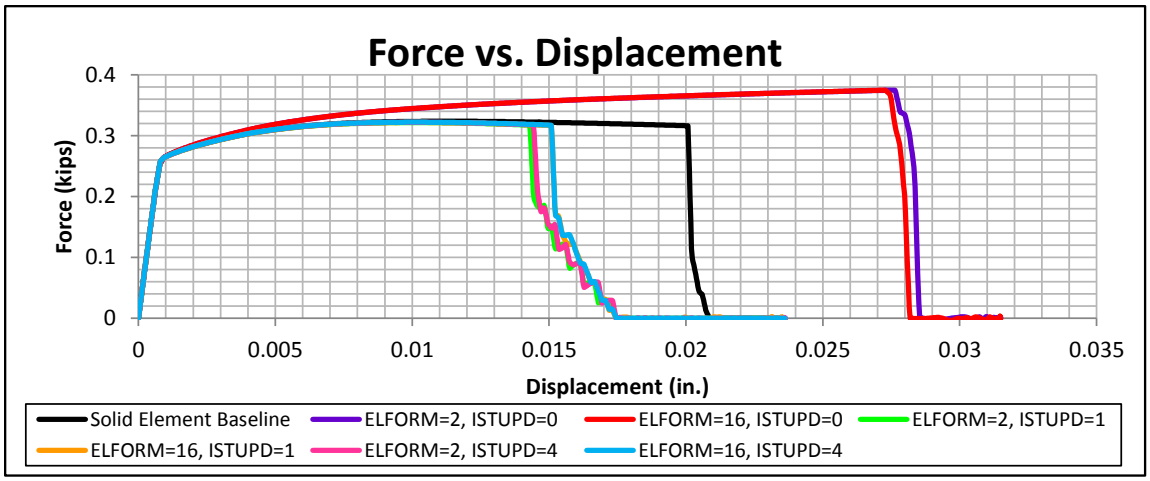

Figure 206. Force vs. Displacement for Solid vs. Shell Analysis, Flat Small Notched Specimen

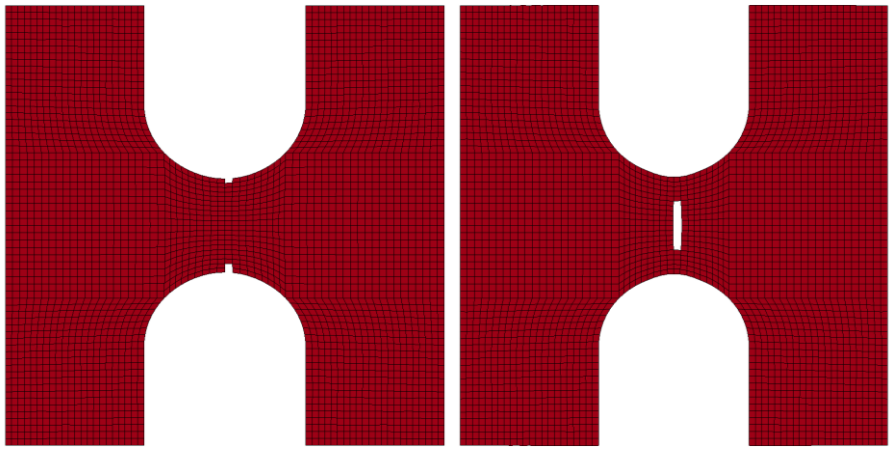

Figure 207. Type 0 (Left) and Solid Element, Type 1, and Type 4 (Right) Thickness Update Methods at Failure Initiation, Flat Small Notched Specimen

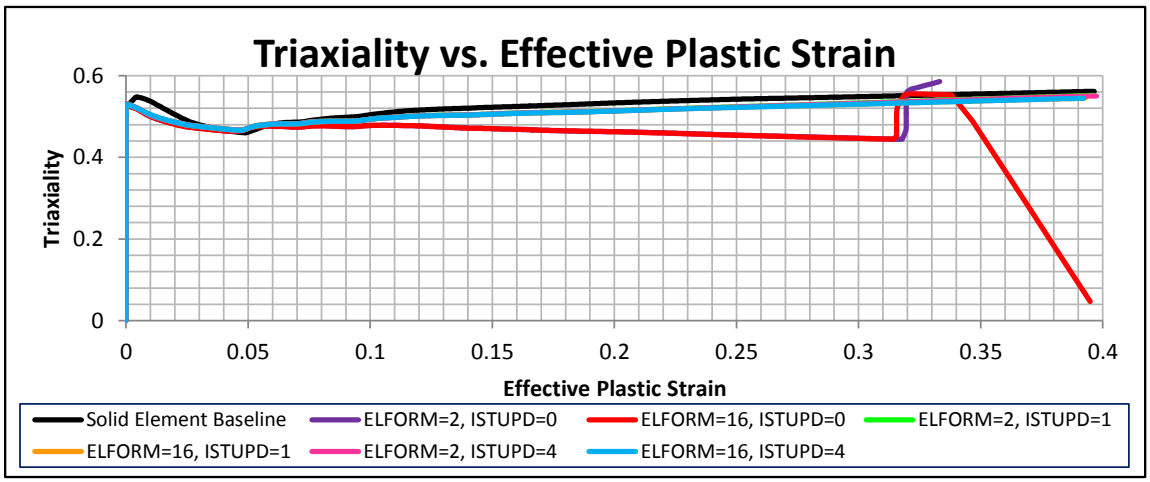

Figure 208. Triaxiality vs. Effective Plastic Strain for Solid vs. Shell Analysis, Flat Small Notched Specimen

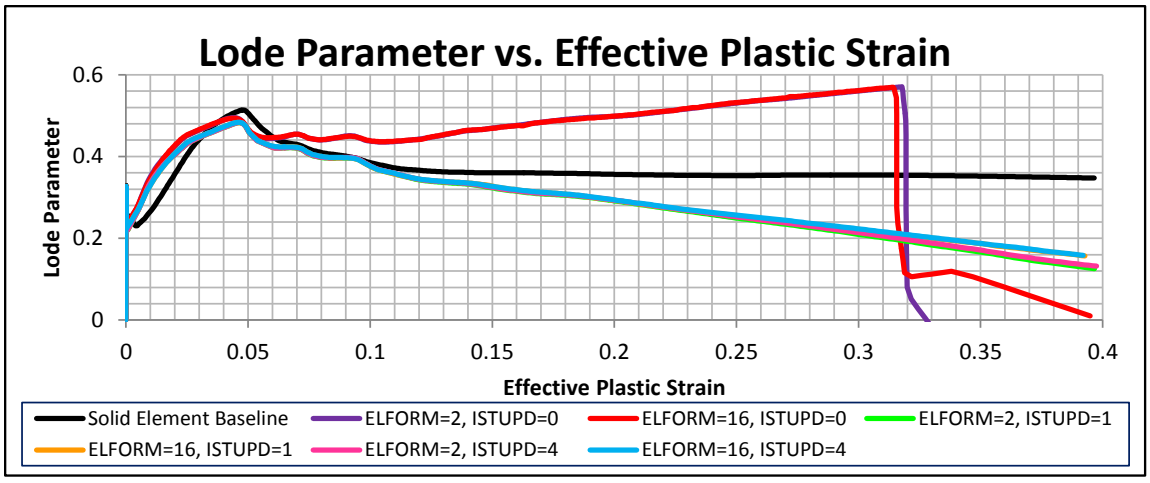

Figure 209. Lode Parameter vs. Effective Plastic Strain for Solid vs. Shell Analysis, Flat Small Notched Specimen

7.5.4 Flat Sharp Notched Specimen

The Flat Sharp Notched Specimen produced similar force vs. displacement curves to the solid element model when the thickness update options ISTUPD=1 and 4 were used, as seen in Figure 210. However, the displacement at failure initiation was underestimated when compared to the results corresponding to the solid element model. Also, the ultimate strength of the material was slightly lower than the solid element results. Conversely, when the thickness update option ISTUPD=0 was used, the model overestimated the displacement at failure and over predicted the material strength when compared to the solid element baseline model.

As the specimen elongated and necked, the state of stress for the models with the thickness update options equal to ISTUPD=1 and 4 roughly followed the stress state exhibited in the solid element model, as seen in Figures 211 and 212. However, in the models in which the thickness update option was set equal to ISTUPD=0, the triaxiality and Lode parameters drifted away substantially from the solid element baseline model during the later stages of elongation. Note, all of the models exhibited an outside-in

tearing method where the outside elements fail first. However, the critical element was selected as the center element.

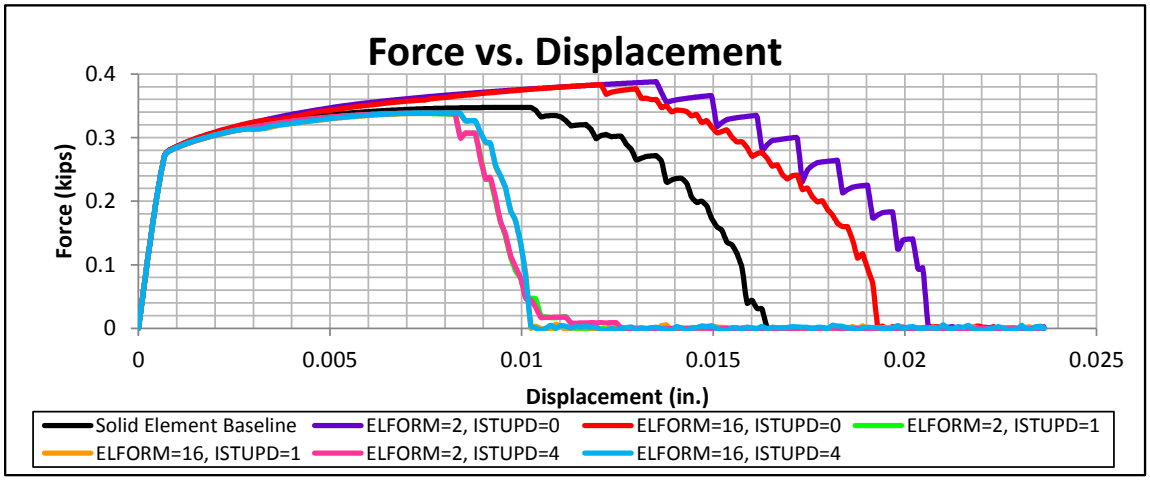

Figure 210. Force vs. Displacement for Solid vs. Shell Analysis, Flat Sharp Notched Specimen

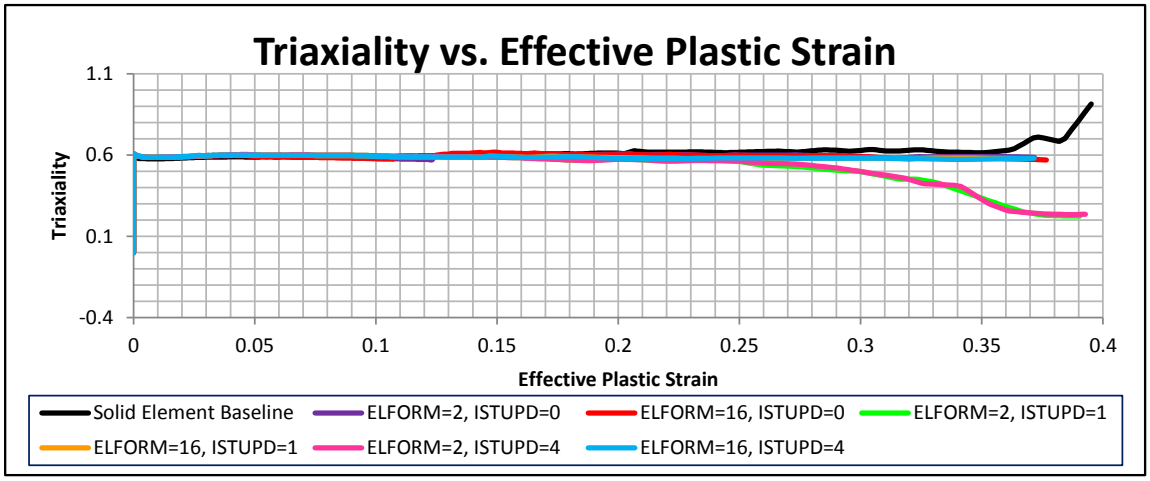

Figure 211. Triaxiality vs. Effective Plastic Strain for Solid vs. Shell Analysis, Flat Sharp Notched Specimen

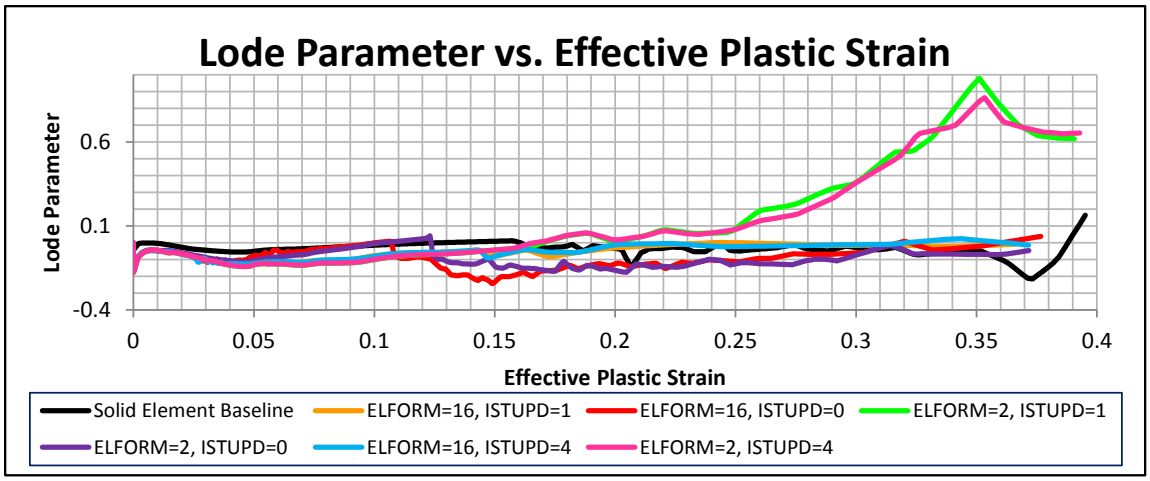

Figure 212. Lode Parameter vs. Effective Plastic Strain for Solid vs. Shell Analysis, Flat Sharp Notched Specimen

7.5.5 Conclusions of Solid vs. Shell Analysis

Based on the shell vs. solid element analysis performed, a number of conclusions could be made. First, it is clear that the shell element models utilizing the thickness update option ISTUPD=0 do not adequately reproduce the solid element model results. The lack of membrane thinning did not allow thinning and necking behavior to occur. As a result, the models strengths and displacements at failure were over predicted. Furthermore, the lack of membrane thinning caused the shell elements to generally not be an accurate prediction of the state of stress of the solid element models. This finding was likely caused by the limited stress modeling capabilities due to the lack of membrane thinning. Also, the outside-in element failure behavior exhibited in the thickness update option ISTUPD=0 shifted the state of stress in the critical element immediately prior to the critical element failure.

Second, the shell elements with the thickness update options set equal to ISTUPD=1 and 4 did not produce identical results to the solid element model results. This result is exhibited by three aspects: the model strength; the failure initiation

displacement; and the state of stress throughout elongation. First, the shell element models had varying degrees of strength when compared to the solid element baseline models. Under a uniaxial load of the Standard Dog Bone Specimen, the shell and solid element models had nearly identical force vs. displacement behavior. However, as the notch size decreased and the targeted triaxiality shifted positively away from simple tension, the strength of the shell models decreased slightly in relation to the solid element models. Furthermore, the ratio of displacement at failure initiation of shell element to solid element models decreased substantially as the notch size decreased and the targeted triaxiality shifted positively away from simple tension. As a result of these differences, if shell elements were used, different material model parameters would need to be defined compared to the material model parameters calibrated with solid element models. Particularly, the effective plastic strain at failure would need to be recalibrated for the higher triaxiality stress states. Lastly, the shell element models produced relatively similar state of stress results as the solid element models, as seen in Table 39. As the size of the notch decreased, the difference between the average triaxiality and Lode parameter in the shell and solid element models generally increased. However, the differences remain smaller than 0.1 and are not expected to be a major concern.

Table 39. Average State of Stress Values for Solid and Shell Element Formulations

Specimen Type	Element Type	Average Triaxiality Through Plastic Strain	Average Lode Parameter Through Plastic Strain
Flat Standard Dog Bone	Solid Element Baseline	0.35	0.93
	Shell Element Average, ISTUPD=1	0.35	0.94
	Shell Element Average, ISTUPD=4	0.35	0.94
Flat Large Notched Specimen	Solid Element Baseline	0.46	0.61
	Shell Element Average, ISTUPD=1	0.44	0.58
	Shell Element Average, ISTUPD=4	0.44	0.58
Flat Small Notched Specimen	Solid Element Baseline	0.53	0.37
	Shell Element Average, ISTUPD=1	0.51	0.29
	Shell Element Average, ISTUPD=4	0.51	0.29
Flat Sharp Notched Specimen	Solid Element Baseline	0.62	-0.04
	Shell Element Average, ISTUPD=1	0.56	0.05
	Shell Element Average, ISTUPD=4	0.55	0.05

7.6 FEM Baseline Modeling of Testing Specimen

The baseline material model, MAT_24 - Isotropic Piecewise Linear Plasticity, was used to model each testing specimen. To calibrate the material model, a number of material properties were required. Assumed values were used for the density, elastic modulus, and Poisson ratio. Values calculated from testing were used for the yield stress, true stress vs. effective plastic strain curve, and effective plastic strain at failure. The yield stress and initial true stress vs. effective plastic strain curve were taken from the Axial-Symmetric Smooth test specimen data. However, the true stress vs. effective

plastic strain curve and effective plastic strain at failure were adjusted iteratively such that the FEM model matched the test data.

As shown in previous papers, the post necking initiation behavior of the model is highly dependent on the mesh size [91-92]. As a result, an adjusted, or artificial, true stress vs. effective plastic strain curve was used to define the material model. A comparison of the true and artificial curve can be found in Figure 213. The curves are identical up to the point of diffuse necking, as defined by Considère's criterion, which states that the plastic instability of necking begins at the point when the increase in stress due to the decrease in the cross-sectional area is equal to the increase in load bearing capacity of the specimen due to work hardening [21,87-88]. As the stress continues to increase with decreased cross-sectional area, the instability continues. Utilizing Equation 7.42, the point of necking initiation can be determined.

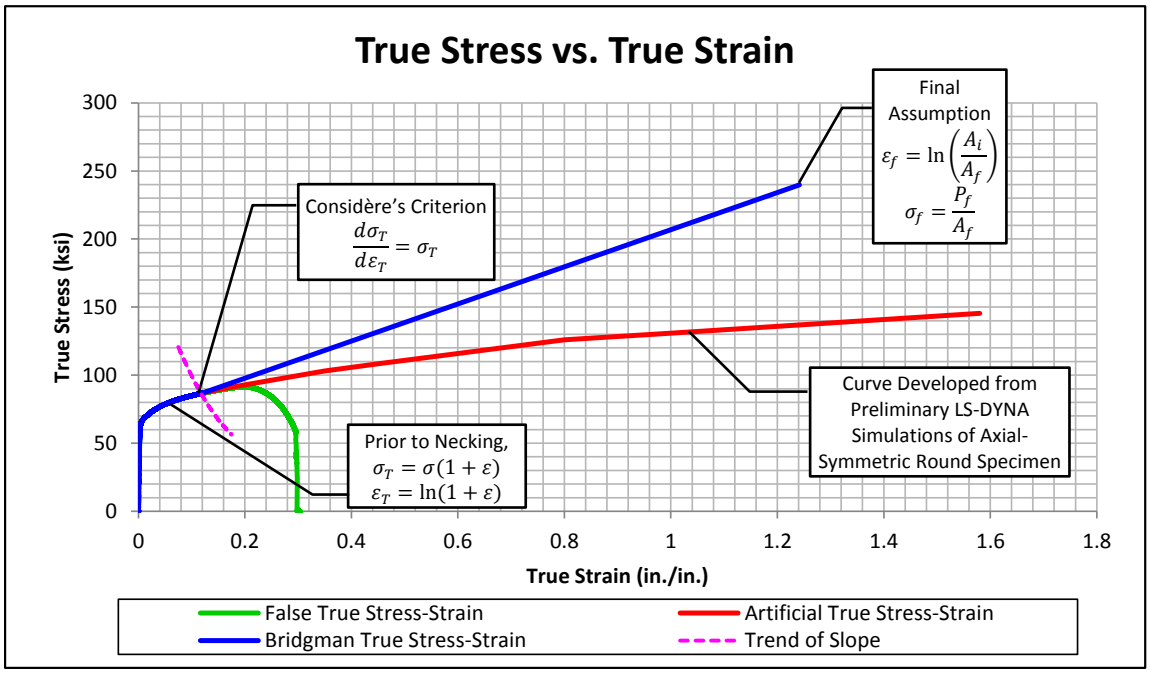

Figure 213. Comparison of True Stress and True Strain between Physical Test Data and Computer Simulation

$$\frac{d\sigma_T}{d\varepsilon_T} = \sigma_T \tag{7.42}$$

where

$\sigma_T = \text{True Stress}$

$\frac{d\sigma_T}{d\varepsilon_T} = \text{Slope of True Stress vs. True Strain Curve}$

The as-tested true stress vs. effective plastic strain curve was developed using a linear interpolation between the point of necking initiation and the point at failure. The stress and strain at failure are calculated using the adjustment method used by Bridgman, as seen in Equations 7.43 and 7.44 [21].

$$\sigma_f = \frac{\mathrm{P_f}}{A_f} \tag{7.43}$$

where

$\sigma_f = \text{True Stress at Failure}$

$P_f = \text{Load at Failure}$

$A_f = \text{Final Measured Cross Sectional Area}$

and

$$\varepsilon_f = \ln\left(\frac{A_i}{A_f}\right) \tag{7.44}$$

where

$\varepsilon_f = \text{True Strain at Failure}$

$A_i = \text{Initial Measured Cross Sectional Area}$

$A_f = \text{Final Measured Cross Sectional Area}$

To describe the post-necking-initiation portion of the adjusted curve, a C_0 continuous linear piecewise curve was used. A series of iterative simulations were run until the force vs. displacement and cross section area at failure matched the test data. An alternative option is to define the curve utilizing a power law relationship. However, it was found that using a linear piecewise curve in the simulation accurately reproduced physical test results while requiring less iterations to match the data.

The comparison between the force vs. displacement data for the five Axial-Symmetric Round Smooth Specimen tests and the proposed baseline material model can

be found in Figure 214. The material performed well in modeling the force vs. displacement behavior exhibited in physical tests through necking and failure initiation. However, the model exhibited a cross section area reduction of 77.8 percent, while the average cross section area reduction exhibited in physical testing was 73.1 percent. This 4.7 percent difference may possibly be reduced with further adjustment.

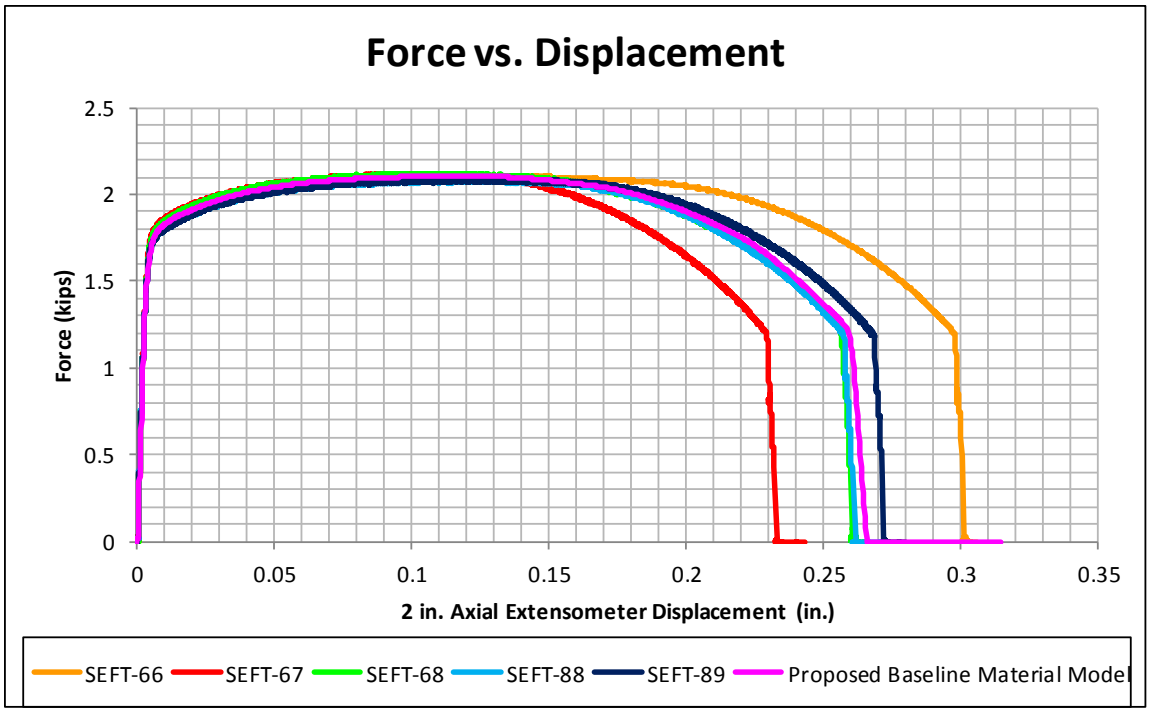

Figure 214. Axial-Symmetric Round Smooth Specimen: Comparison Between Physical Test Results and Proposed Baseline FEM Model

The proposed baseline material card and defined plastic curve is given below:

```
*MAT_PIECEWISE_LINEAR_PLASTICITY
$#     mid        ro         e        pr      sigy      etan      fail      tdel
         1 7.8600E-6 176.87801  0.280000  0.337334           1.540000
$#       c         p      lcss      lcsr        vp
                           333
*DEFINE_CURVE
$#    lcid      sidr       sfa       sfo      offa      offo    dattyp
       333            1.000000  1.000000
$#               a1                  o1
            0.000000           0.3373343
```

0.000942	0.4074389
0.001844	0.4346554
0.002924	0.4469487
0.004947	0.4592113
0.010646	0.4769367
0.019434	0.4960417
0.028153	0.5132857
0.039070	0.5305526
0.056177	0.5512854
0.073278	0.566997
0.090497	0.580201
0.116759	0.5973568
0.158000	0.6215262
0.348000	0.7112614
0.448000	0.7471142
0.798000	0.8677724
0.998000	0.9022462
1.578000	1.0022202

7.6.1 FEM Model of Flat Standard Dog Bone Specimen

A FEM model was created to simulate the tensile tests performed on the Flat Standard Dog Bone Specimen. A mesh was created using 5 elements through the thickness of the specimen. Therefore, the mesh was created to use elements approximately 0.0060 in. (0.152 mm) in each direction in the critical gauge region, as determined previously. The mesh created to model this specimen can be seen in Figure 215. The total length of the model was 1.0 in. (25.4 mm), so that the extensometer length could be compared directly if substantial deformation outside the critical gauge length occurred. Non-reflecting boundary conditions were applied on one end of the specimen that prevented displacement in the longitudinal direction only. Therefore, the nodes were allowed to displace in the transverse directions at this boundary. A prescribed motion was applied to the opposite side. Transverse displacements of the nodes were also allowed at

the moving boundary. A smooth curve with a rise time equal to $^{1}/_{10}$ of the simulation time was utilized to reduce effects from suddenly loading the specimen. Type 6 hourglass control with a coefficient value of 0.01 and a simulation time of 10 ms was utilized, as determined in previous sections. Cross sections, node histories, and solid element histories were collected to aid in post-processing.

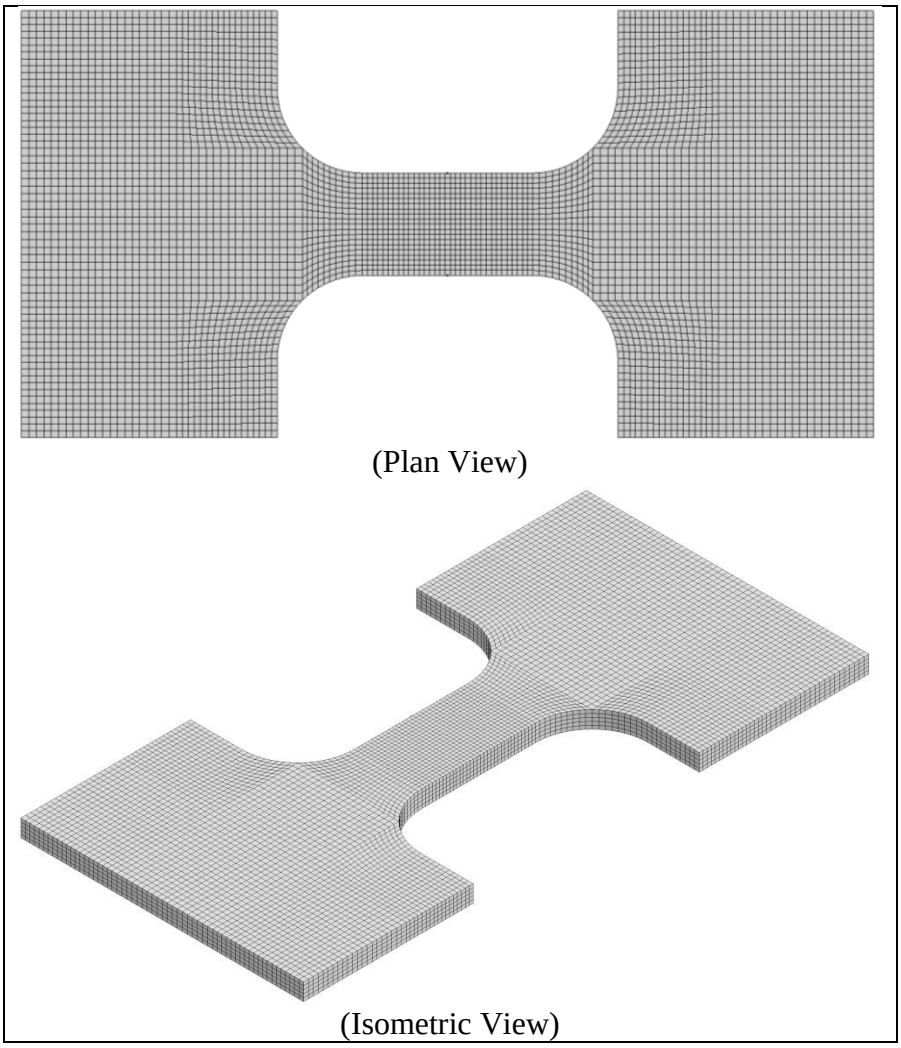

Figure 215. Plan and Isometric View of Flat Standard Dog Bone FEM Model

7.6.2 FEM Model of Large Notched Flat Specimen

A FEM model was created to simulate the tensile tests performed on the Large Notched Flat Specimen. A mesh was created with 5 elements through the thickness of the

specimen. Therefore, the mesh was created to use elements approximately 0.0060 in. (0.152 mm) in each direction in the critical gauge region. The mesh created to model this specimen can be seen in Figure 216. The total length of the model was 1.0 in. (25.4 mm), so that the extensometer length could be compared directly if substantial deformation outside the notched length occurred. Non-reflecting boundary conditions were applied on one end of the specimen that prevented displacement in the longitudinal direction only. Therefore, the nodes were allowed to displace in the transverse directions at this boundary. A prescribed motion was applied to the opposite side. Transverse displacements of the nodes were also allowed at the moving boundary. A smooth curve with a rise time equal to $^{1}/_{10}$ of the simulation time was utilized to reduce effects from suddenly loading the specimen. Type 6 hourglass control with a coefficient value of 0.01, and a simulation time of 10 ms was utilized, as determined in previous sections. Cross sections, node histories, and solid element histories were collected to aid in post-processing.

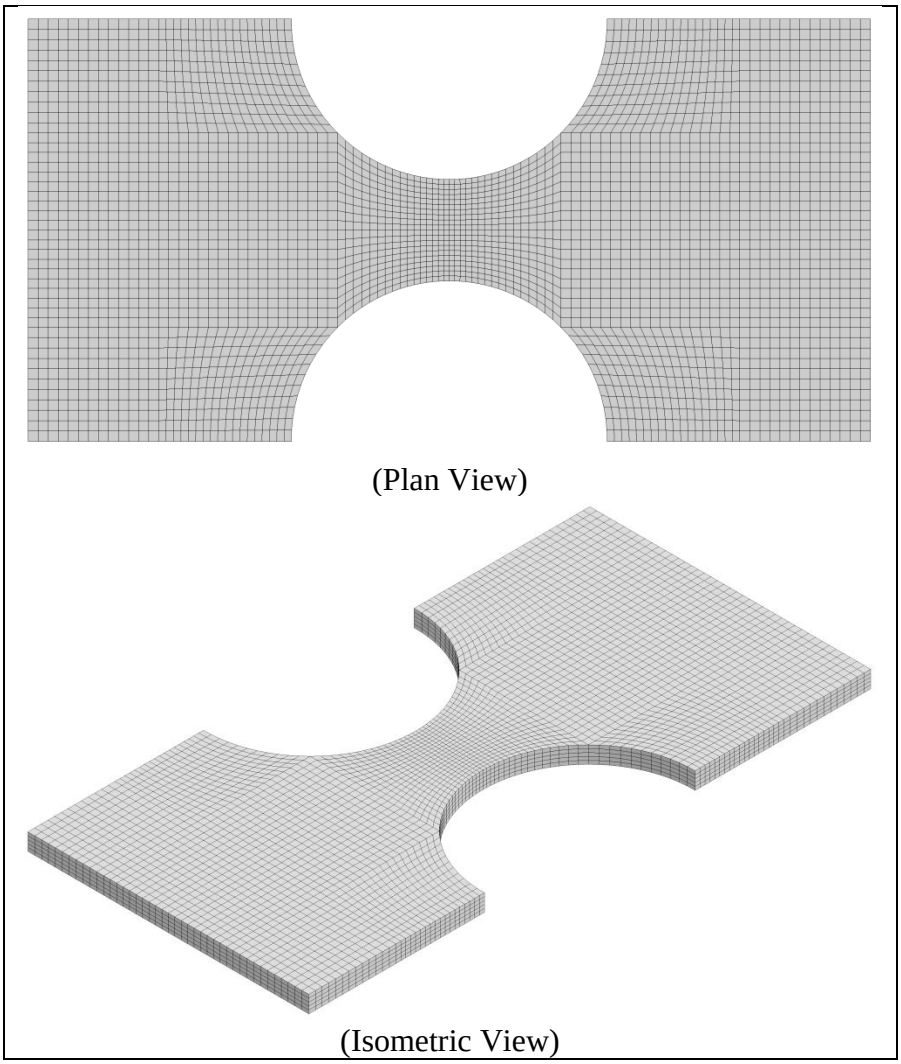

Figure 216. Plan and Isometric View of Flat Large Notched FEM Model

7.6.3 FEM Model of Small Notched Flat Specimen

A FEM model was created to simulate the tensile tests performed on the Small Notched Flat Specimen. A mesh was created with 5 elements through the thickness of the specimen. Therefore, the mesh was created to use elements approximately 0.0060 in. (0.152 mm) in each direction in the critical gauge region. The mesh created to model this specimen can be seen in Figure 217. The total length of the model was 1.0 in. (25.4 mm), so that the extensometer length could be compared directly if substantial deformation outside the notched length occurred. Non-reflecting boundary conditions were applied on

one end of the specimen that prevented displacement in the longitudinal direction only. Therefore, the nodes were allowed to displace in the transverse directions at this boundary. A prescribed motion was applied to the opposite side. Transverse displacements of the nodes were also allowed at the moving boundary. A smooth curve with a rise time equal to $^{1}/_{10}$ of the simulation time was utilized to reduce effects from suddenly loading the specimen. Type 6 hourglass control with a coefficient value of 0.01, and a simulation time of 10 ms was utilized, as determined in previous sections. Cross sections, node histories, and solid element histories were collected to aid in post-processing.

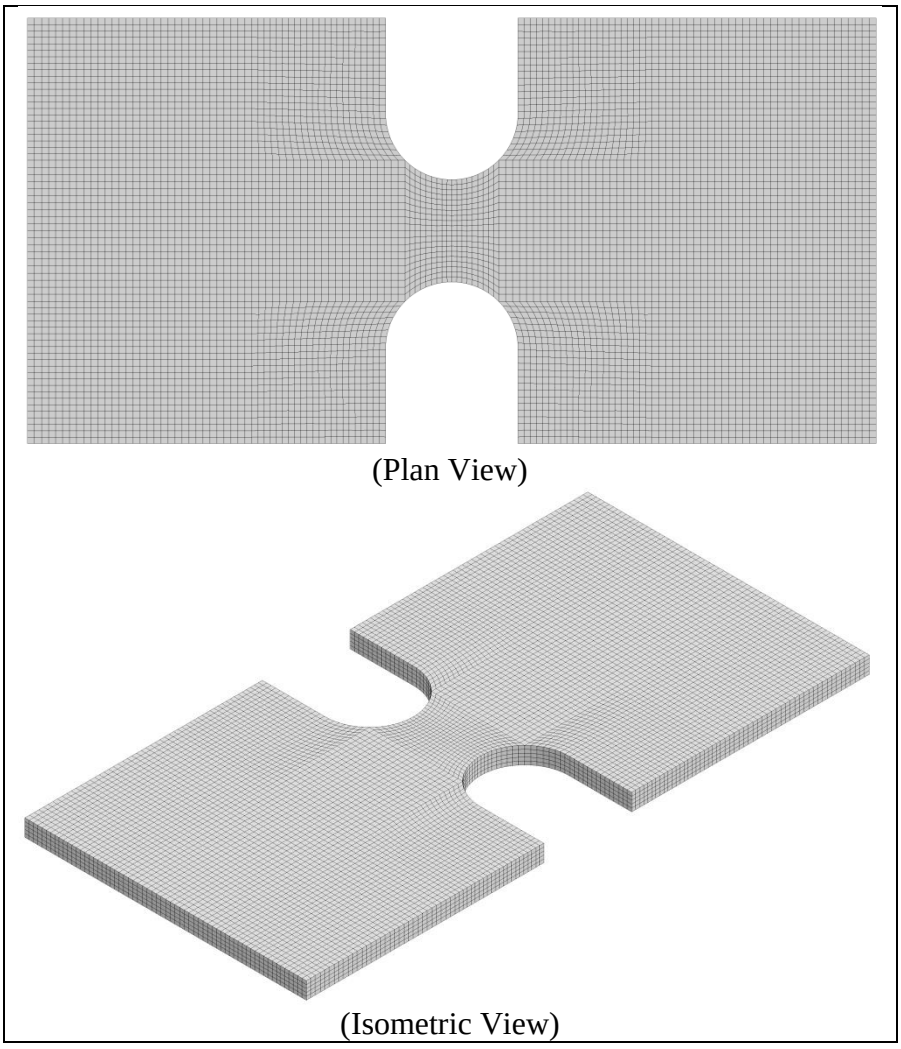

Figure 217. Plan and Isometric View of Flat Small Notched FEM Model

7.6.4 FEM Model of Sharp Notched Flat Specimen

A FEM model was created to simulate the tensile tests performed on the Sharp Notched Flat Specimen. A mesh was created with 5 elements through the thickness of the specimen. Therefore, the mesh was created to use elements approximately 0.0060 in. (0.152 mm) in each direction in the critical gauge region. The total length of the model was 1.0 in. (25.4 mm), so that the extensometer length could be compared directly if substantial deformation outside the notched length occurred. The mesh created to model this specimen can be seen in Figure 218. Non-reflecting boundary conditions were

applied on one end of the specimen that prevented displacement in the longitudinal direction only. Therefore, the nodes were allowed to displace in the transverse directions at this boundary. A prescribed motion was applied to the opposite side. Transverse displacements of the nodes were also allowed at the moving boundary. A smooth curve with a rise time equal to $^{1}/_{10}$ of the simulation time was utilized to reduce effects from suddenly loading the specimen. Type 6 hourglass control with a coefficient value of 0.01, and a simulation time of 10 ms was utilized, as determined in previous sections. Cross sections, node histories, and solid element histories were collected to aid in post-processing.

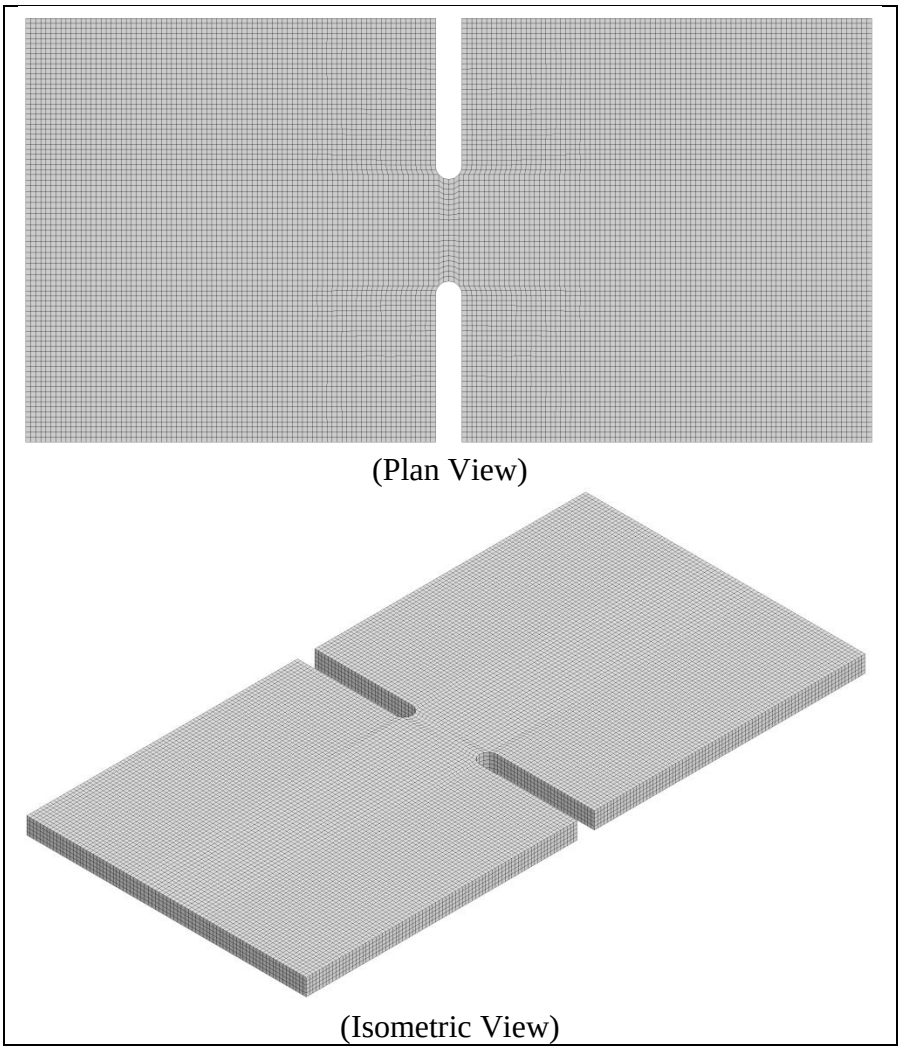

Figure 218. Plan and Isometric View of Flat Sharp Notched FEM Model

7.6.5 FEM Model of Axial-Symmetric Round Smooth Specimen

A FEM model was created to simulate the tensile tests performed on the Axial-Symmetric Round Smooth Specimen. A mesh was created using an element size equal to the previous models. Therefore, the elements were meshed to have lengths of approximately 0.0060 in. (0.152 mm) in each direction in the critical gauge region. The mesh created to model this specimen can be seen in Figure 219. The total length of the model was 2.0 in. (50.8 mm), so that the extensometer length could be compared directly if substantial deformation outside the critical gauge length occurred. Non-reflecting

boundary conditions were applied on one end of the specimen that prevented displacement in the longitudinal direction only. Therefore, the nodes were allowed to displace in the transverse directions at this boundary. A prescribed motion was applied to the opposite side. Transverse displacements of the nodes were also allowed at the moving boundary. A smooth curve with a rise time equal to $^{1}/_{10}$ of the simulation time was utilized to reduce effects from suddenly loading the specimen. Type 6 hourglass control with a coefficient value of 0.01, and a simulation time of 10 ms was utilized, as determined in previous sections. Cross sections, node histories, and solid element histories were collected to aid in post-processing.

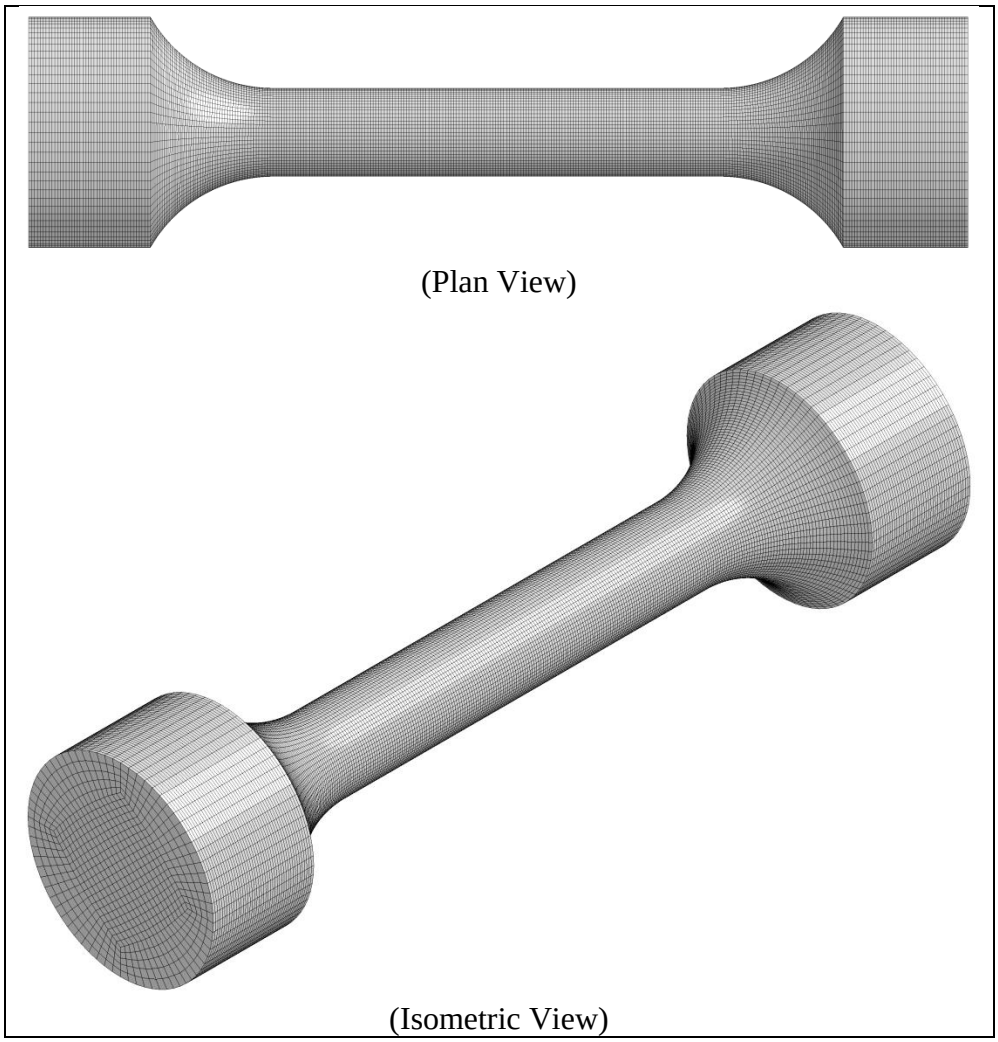

Figure 219. Plan and Isometric View Axial Symmetric Round Smooth FEM Model

7.6.6 FEM Model of Notched Round Specimen No. 1

A FEM model was created to simulate the tensile tests performed on the Notched Round Specimen No. 1. A mesh was created using an element size equal to the previous models. Therefore, the elements were meshed to have lengths of approximately 0.0060 in. (0.152 mm) in each direction in the critical gauge region. The mesh created to model this specimen can be seen in Figure 220. The total length of the model was 2.0 in. (50.8 mm), so that the extensometer length could be compared directly if substantial deformation outside the notched length occurred. Non-reflecting boundary conditions

were applied on one end of the specimen that prevented displacement in the longitudinal direction only. Therefore, the nodes were allowed to displace in the transverse directions at this boundary. A prescribed motion was applied to the opposite side. Transverse displacements of the nodes were also allowed at the moving boundary. A smooth curve with a rise time equal to $^{1}/_{10}$ of the simulation time was utilized to reduce effects from suddenly loading the specimen. Type 6 hourglass control with a coefficient value of 0.01, and a simulation time of 10 ms was utilized, as determined in previous sections. Cross sections, node histories, and solid element histories were collected to aid in post-processing.

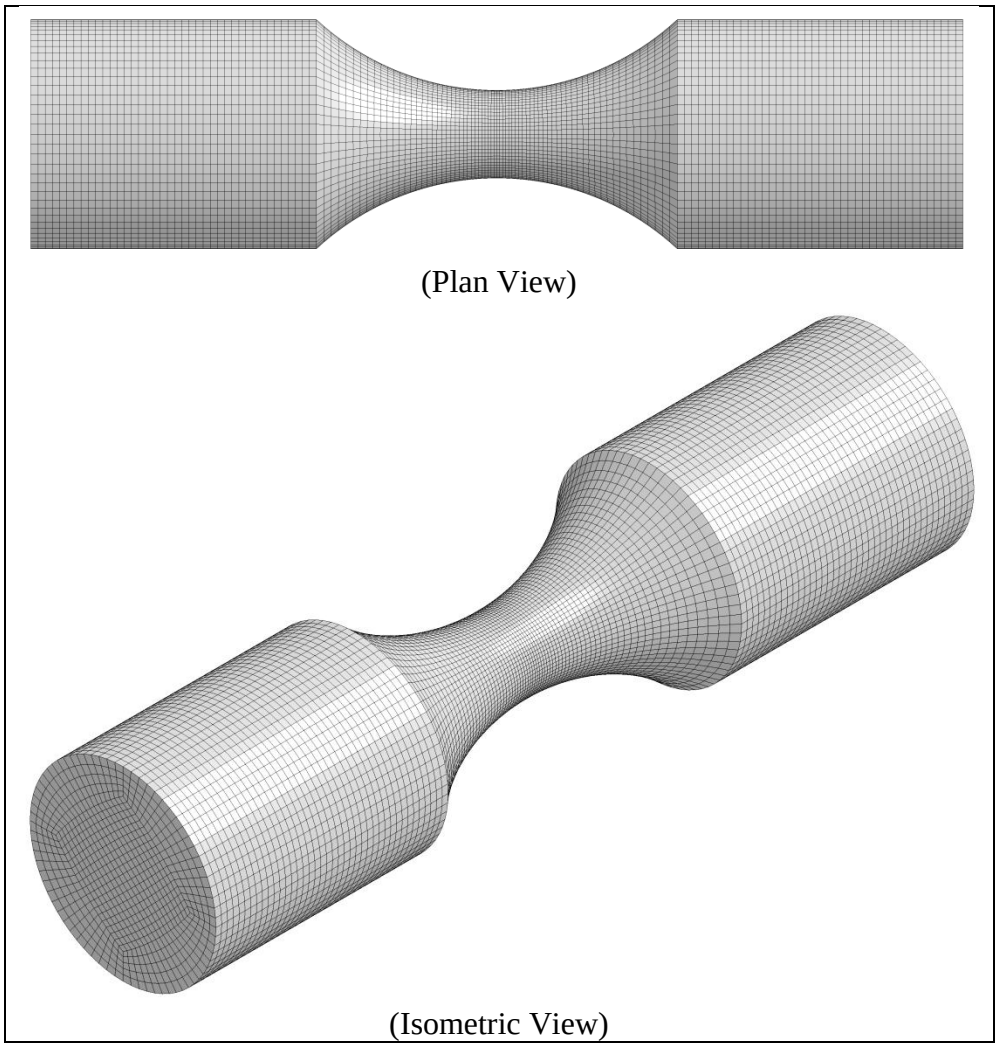

Figure 220. Plan and Isometric View of Notched Round Specimen No. 1 FEM Model

7.6.7 FEM Model of Notched Round Specimen No. 2

A FEM model was created to simulate the tensile tests performed on the Notched Round Specimen No. 2. A mesh was created using an element size equal to the previous models. Therefore, the elements were meshed to have lengths of approximately 0.0060 in. (0.152 mm) in each direction in the critical gauge region. The mesh created to model this specimen can be seen in Figure 221. The total length of the model was 2.0 in. (50.8 mm), so that the extensometer length could be compared directly if substantial deformation outside the notched length occurred. Non-reflecting boundary conditions

were applied on one end of the specimen that prevented displacement in the longitudinal direction only. Therefore, the nodes were allowed to displace in the transverse directions at this boundary. A prescribed motion was applied to the opposite side. Transverse displacements of the nodes were also allowed at the moving boundary. A smooth curve with a rise time equal to $^{1}/_{10}$ of the simulation time was utilized to reduce effects from suddenly loading the specimen. Type 6 hourglass control with a coefficient value of 0.01, and a simulation time of 10 ms was utilized, as determined in previous sections. Cross sections, node histories, and solid element histories were collected to aid in post-processing.

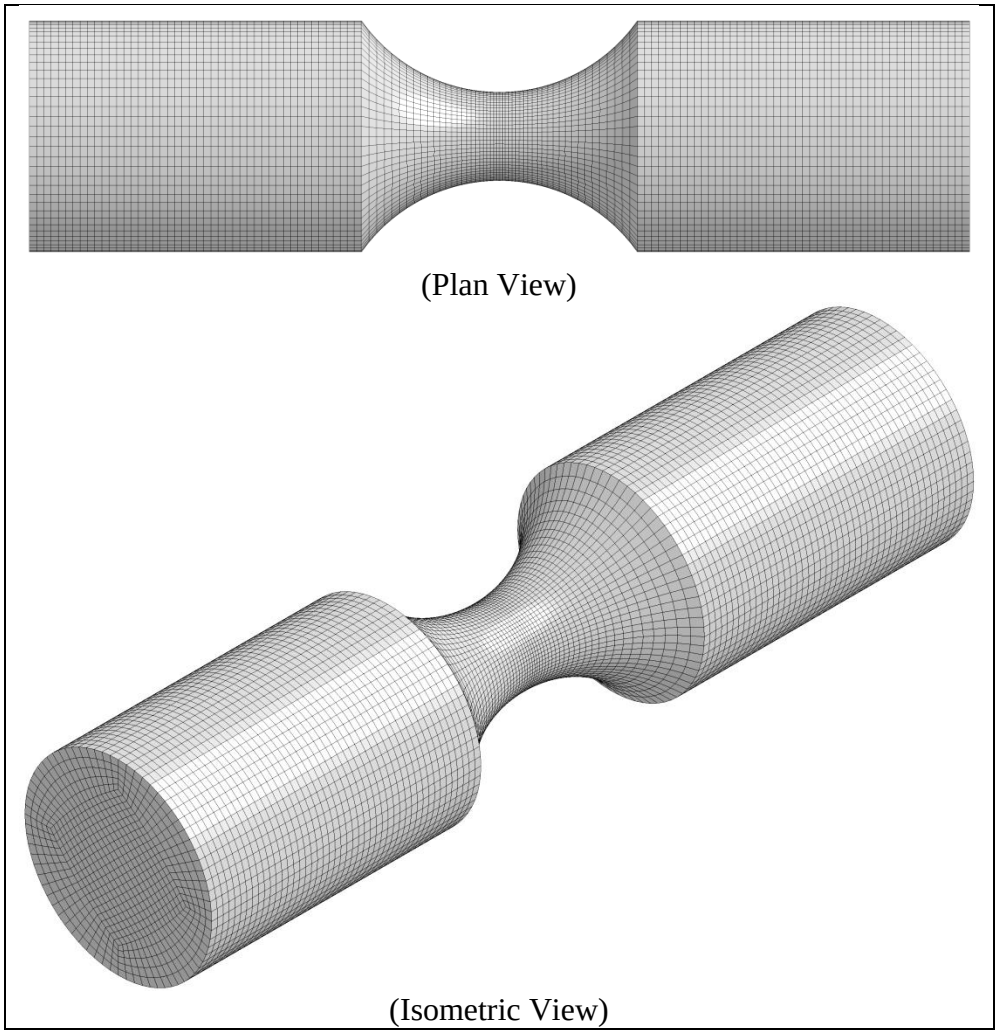

Figure 221. Plan and Isometric View of Notched Round Specimen No. 2 FEM Model

7.6.8 FEM Model of Notched Round Specimen No. 3

A FEM model was created to simulate the tensile tests performed on the Notched Round Specimen No. 3. A mesh was created using an element size equal to the previous models. Therefore, the elements were meshed to have lengths of approximately 0.0060 in. (0.152 mm) in each direction in the critical gauge region. The mesh created to model this specimen can be seen in Figure 222. The total length of the model was 2.0 in. (50.8 mm), so that the extensometer length could be compared directly if substantial deformation outside the notched length occurred. Non-reflecting boundary conditions were applied on one end of the specimen that prevented displacement in the longitudinal direction only. Therefore, the nodes were allowed to displace in the transverse directions at this boundary. A prescribed motion was applied to the opposite side. Transverse displacements of the nodes were also allowed at the moving boundary. A smooth curve with a rise time equal to $^{1}/_{10}$ of the simulation time was utilized to reduce effects from suddenly loading the specimen. Type 6 hourglass control with a coefficient value of 0.01, and a simulation time of 10 ms was utilized, as determined in previous sections. Cross sections, node histories, and solid element histories were collected to aid in post-processing.

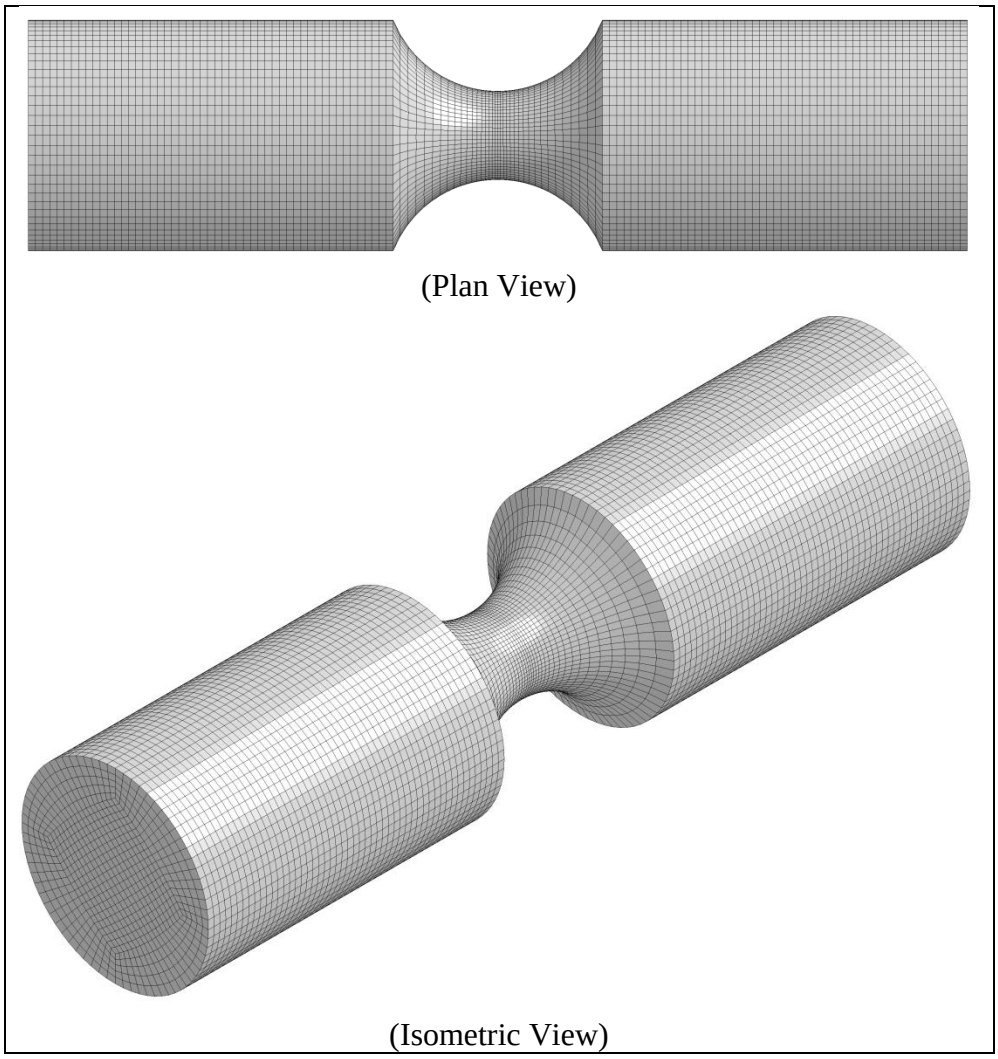

Figure 222. Plan and Isometric View of Notched Round Specimen No. 3 FEM Model

7.6.9 FEM Model of Notched Round Specimen No. 4

A FEM model was created to simulate the tensile tests performed on the Notched Round Specimen No. 4. A mesh was created using an element size equal to the previous models. Therefore, the elements were meshed to have lengths of approximately 0.0060 in. (0.152 mm) in each direction in the critical gauge region. The mesh created to model this specimen can be seen in Figure 223. The total length of the model was 2.0 in. (50.8 mm), so that the extensometer length could be compared directly if substantial deformation outside the notched length occurred. Non-reflecting boundary conditions

were applied on one end of the specimen that prevented displacement in the longitudinal direction only. Therefore, the nodes were allowed to displace in the transverse directions at this boundary. A prescribed motion was applied to the opposite side. Transverse displacements of the nodes were also allowed at the moving boundary. A smooth curve with a rise time equal to $^{1}/_{10}$ of the simulation time was utilized to reduce effects from suddenly loading the specimen. Type 6 hourglass control with a coefficient value of 0.01, and a simulation time of 10 ms was utilized, as determined in previous sections. Cross sections, node histories, and solid element histories were collected to aid in post-processing.

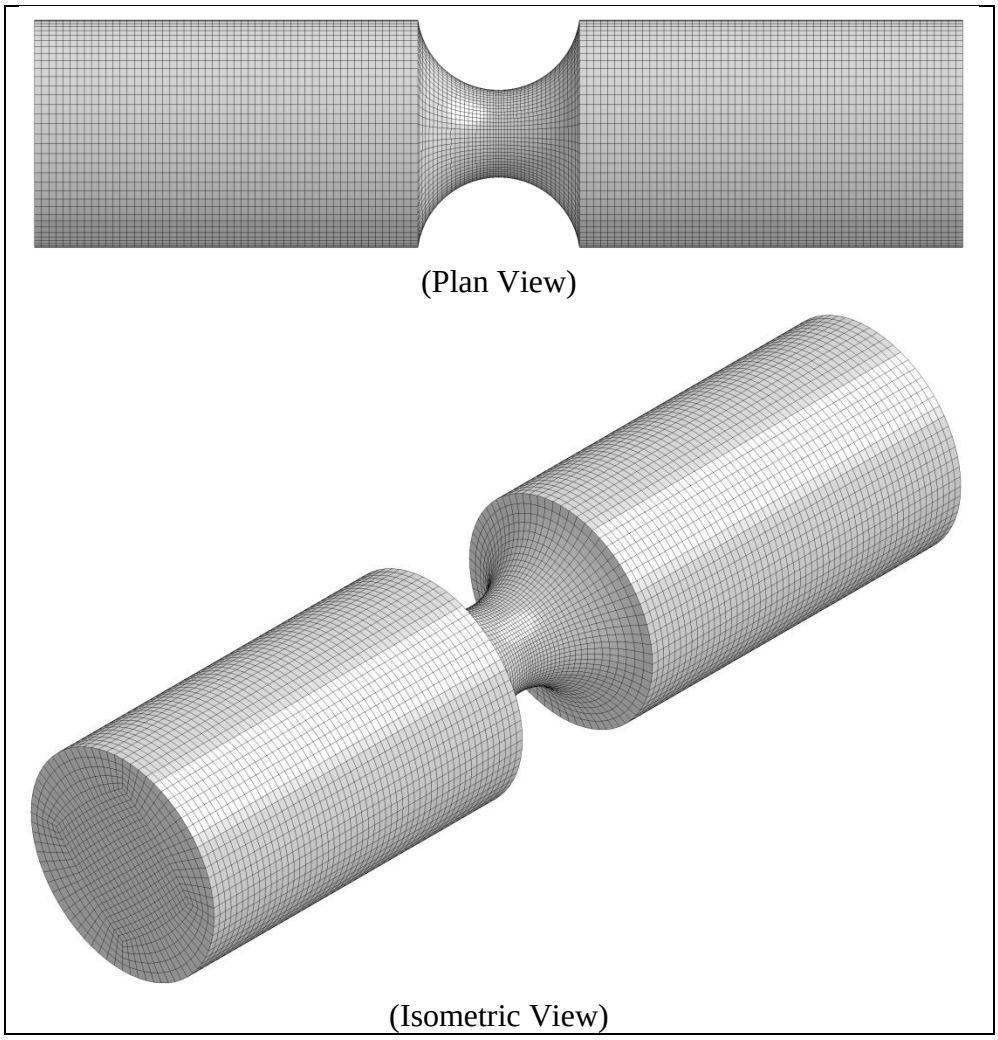

Figure 223. Plan and Isometric View of Notched Round Specimen No.4 FEM Model

7.6.10 FEM Model of Notched Round Specimen No. 5

A FEM model was created to simulate the tensile tests performed on the Notched Round Specimen No. 5. A mesh was created using an element size equal to the previous models. Therefore, the elements were meshed to have lengths of approximately 0.0060 in. (0.152 mm) in each direction in the critical gauge region. The mesh created to model this specimen can be seen in Figure 224. The total length of the model was 2.0 in. (50.8 mm), so that the extensometer length could be compared directly if substantial deformation outside the notched length occurred. Non-reflecting boundary conditions

were applied on one end of the specimen that prevented displacement in the longitudinal direction only. Therefore, the nodes were allowed to displace in the transverse directions at this boundary. A prescribed motion was applied to the opposite side. Transverse displacements of the nodes were also allowed at the moving boundary. A smooth curve with a rise time equal to $^{1}/_{10}$ of the simulation time was utilized to reduce effects from suddenly loading the specimen. Type 6 hourglass control with a coefficient value of 0.01, and a simulation time of 10 ms was utilized, as determined in previous sections. Cross sections, node histories, and solid element histories were collected to aid in post-processing.

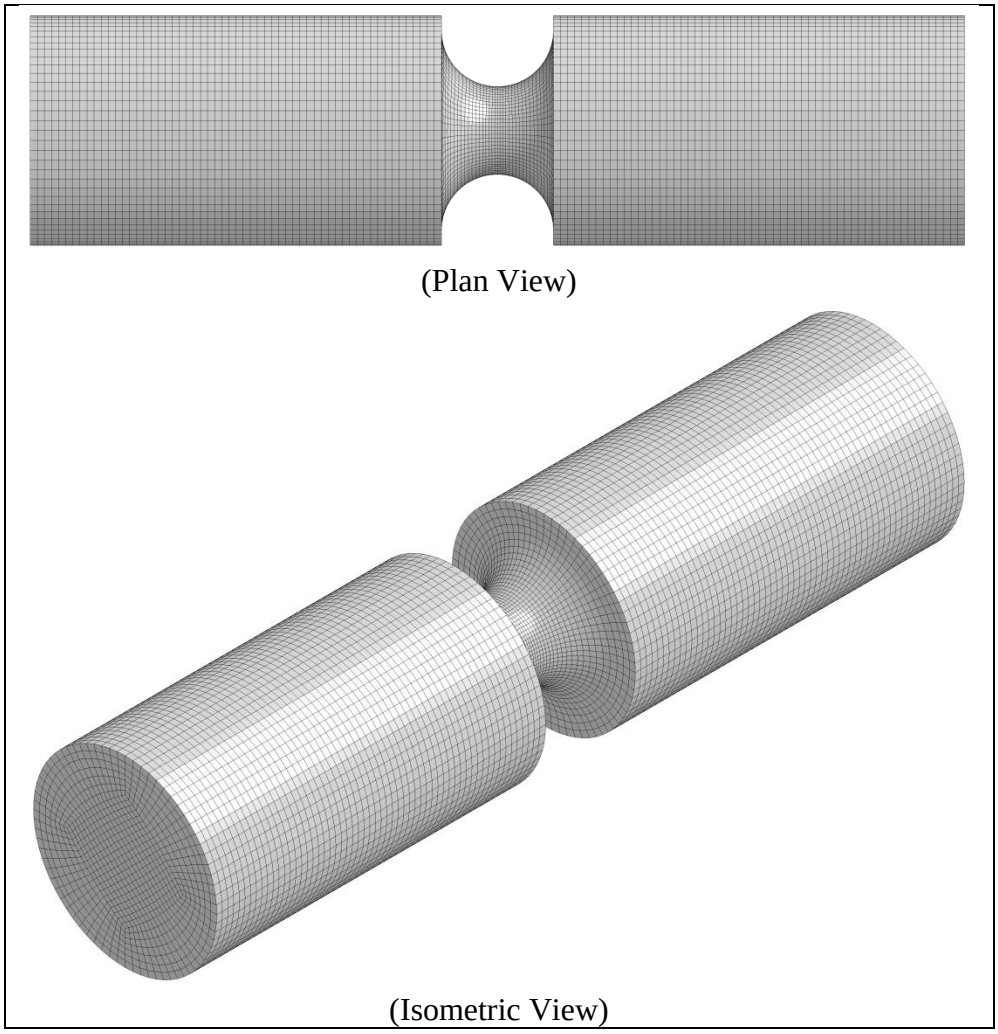

Figure 224. Plan and Isometric View of Notched Round Specimen No.5 FEM Model

7.6.11 FEM Model of Thick Dog Bone Specimen

A FEM model was created to simulate the tensile tests performed on the Thick Dog Bone Specimen. A mesh was created using an element size equal to the previous models. Therefore, the elements were meshed to have lengths of approximately 0.0060 in. (0.152 mm) in each direction in the critical gauge region. The mesh created to model this specimen can be seen in Figure 225. The total length of the model was 2.0 in. (50.8 mm), so that the extensometer length could be compared directly if substantial deformation outside the notched length occurred. Non-reflecting boundary conditions were applied on one end of the specimen that prevented displacement in the longitudinal direction only. Therefore, the nodes were allowed to displace in the transverse directions at this boundary. A prescribed motion was applied to the opposite side. Transverse displacements of the nodes were also allowed at the moving boundary. A smooth curve with a rise time equal to $^{1}/_{10}$ of the simulation time was utilized to reduce effects from suddenly loading the specimen. Type 6 hourglass control with a coefficient value of 0.01, and a simulation time of 10 ms was utilized, as determined in previous sections. Cross sections, node histories, and solid element histories were collected to aid in post-processing.

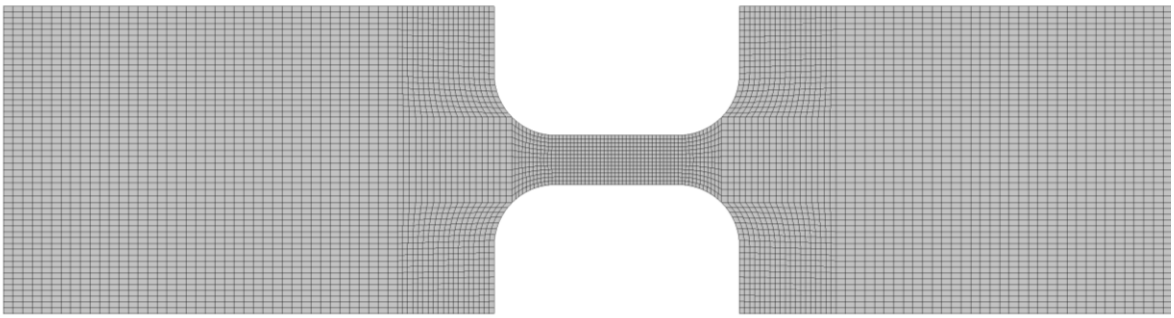

(Plan View)

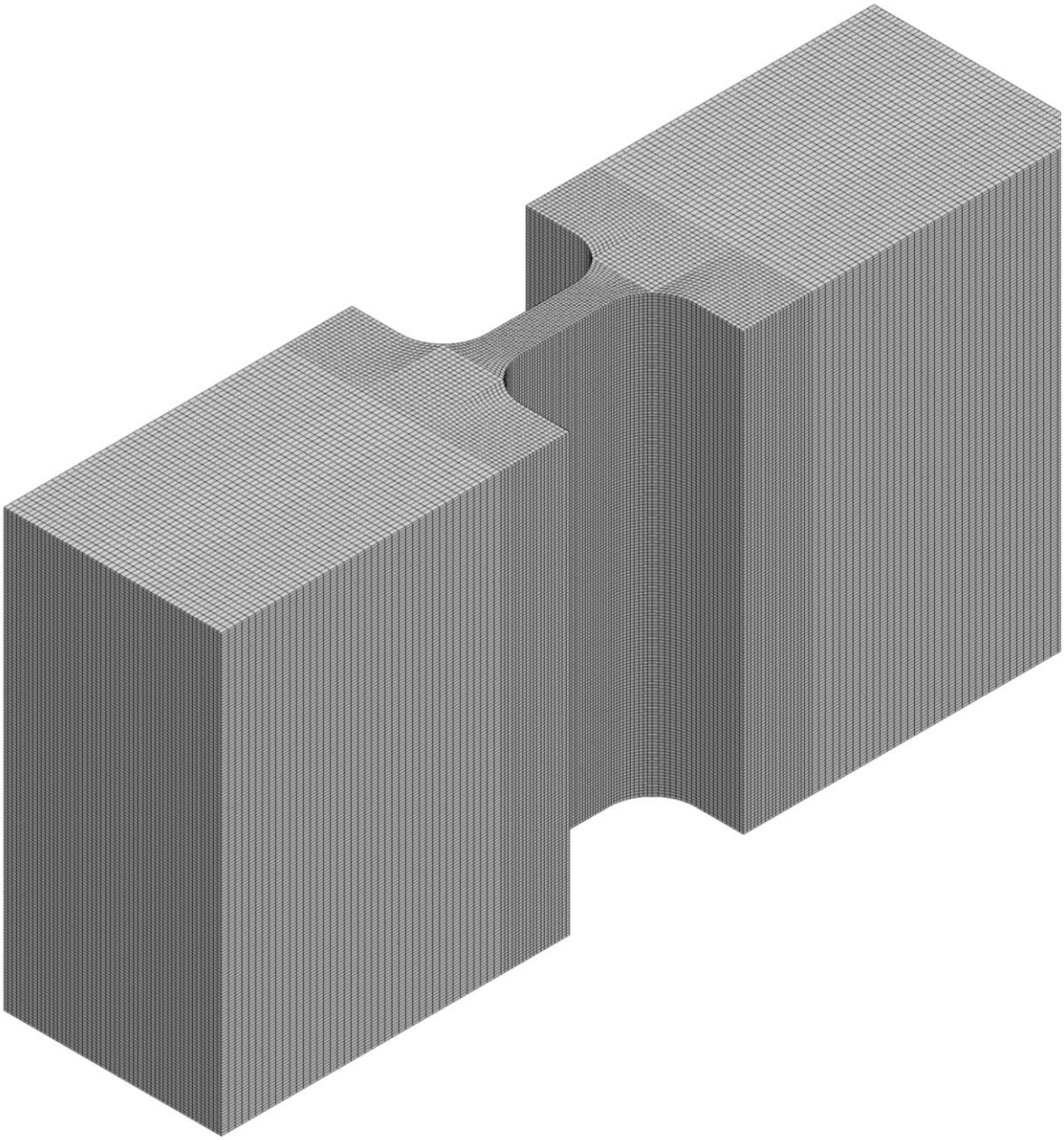

(Isometric View)

Figure 225. Plan and Isometric View of Thick Dog FEM Model

7.6.12 FEM Model of Thick Large Notched Specimen

A FEM model was created to simulate the tensile tests performed on the Thick Large Notched Specimen. A mesh was created using an element size equal to the previous models. Therefore, the elements were meshed to have lengths of approximately 0.0060 in. (0.152 mm) in each direction in the critical gauge region. The mesh created to model this specimen can be seen in Figure 226. The total length of the model was 2.0 in. (50.8 mm), so that the extensometer length could be compared directly if substantial deformation outside the notched length occurred. Non-reflecting boundary conditions were applied on one end of the specimen that prevented displacement in the longitudinal direction only. Therefore, the nodes were allowed to displace in the transverse directions at this boundary. A prescribed motion was applied to the opposite side. Transverse displacements of the nodes were also allowed at the moving boundary. A smooth curve with a rise time equal to $^{1}/_{10}$ of the simulation time was utilized to reduce effects from suddenly loading the specimen. Type 6 hourglass control with a coefficient value of 0.01, and a simulation time of 10 ms was utilized, as determined in previous sections. Cross sections, node histories, and solid element histories were collected to aid in post-processing.

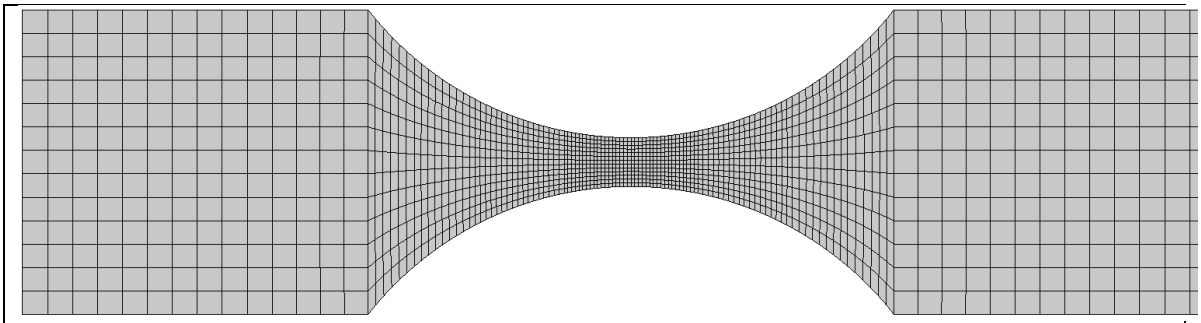

(Plan View)

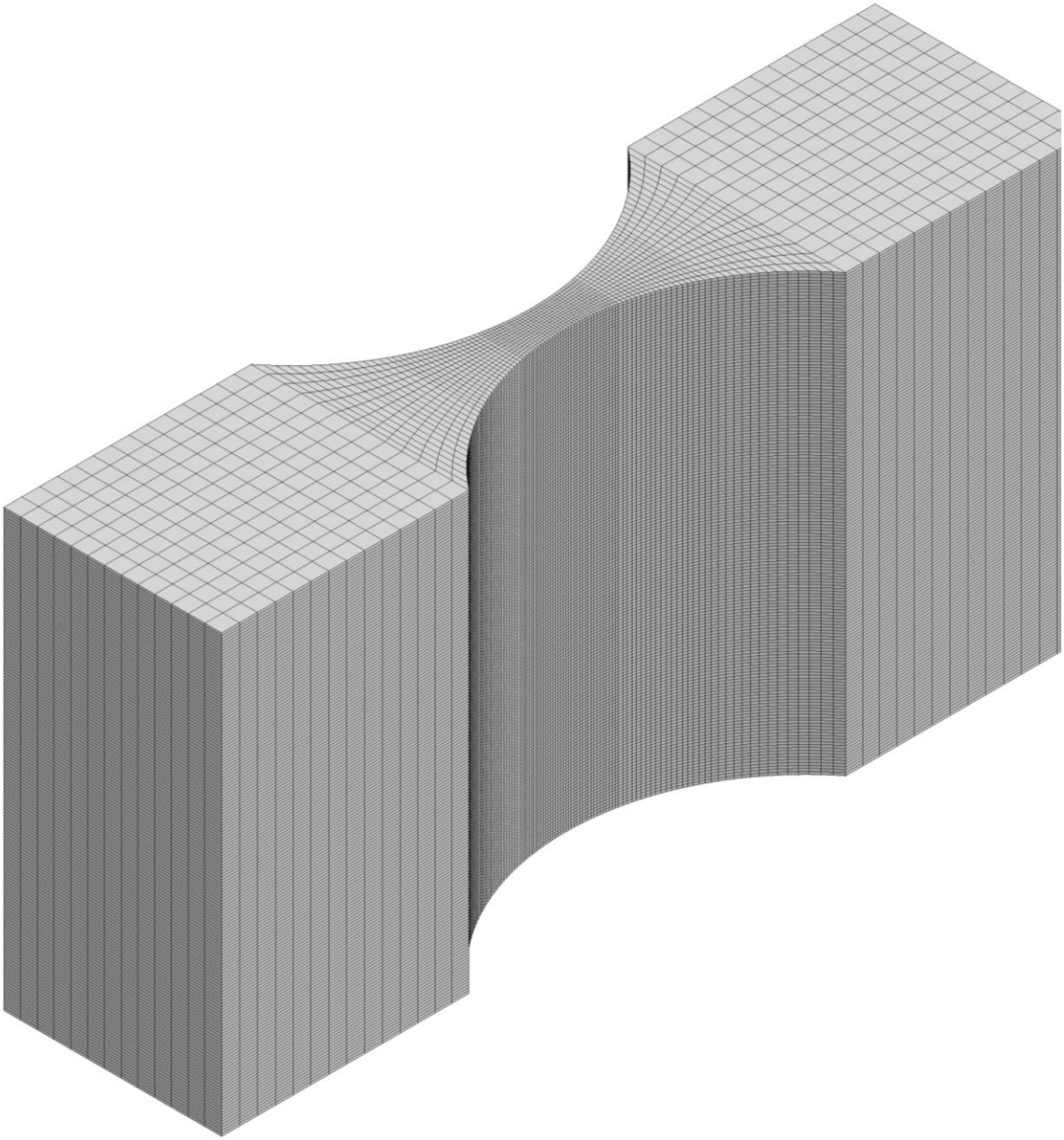

(Isometric View)

Figure 226. Plan and Isometric View of Thick Large Notched FEM Model

7.6.13 FEM Model of Thick Small Notched Specimen

A FEM model was created to simulate the tensile tests performed on the Thick Small Notched Specimen. A mesh was created using an element size equal to the previous models. Therefore, the elements were meshed to have lengths of approximately 0.0060 in. (0.152 mm) in each direction in the critical gauge region. The mesh created to model this specimen can be seen in Figure 227. The total length of the model was 2.0 in. (50.8 mm), so that the extensometer length could be compared directly if substantial deformation outside the notched length occurred. Non-reflecting boundary conditions were applied on one end of the specimen that prevented displacement in the longitudinal direction only. Therefore, the nodes were allowed to displace in the transverse directions at this boundary. A prescribed motion was applied to the opposite side. Transverse displacements of the nodes were also allowed at the moving boundary. A smooth curve with a rise time equal to $^{1}/_{10}$ of the simulation time was utilized to reduce effects from suddenly loading the specimen. Type 6 hourglass control with a coefficient value of 0.01, and a simulation time of 10 ms was utilized, as determined in previous sections. Cross sections, node histories, and solid element histories were collected to aid in post-processing.

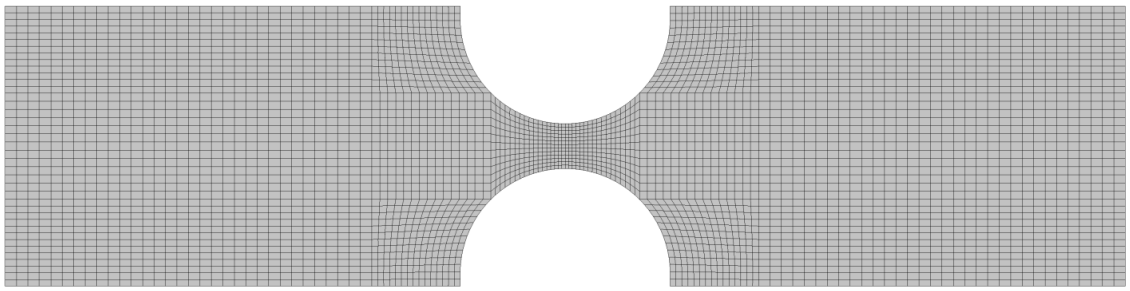

(Plan View)

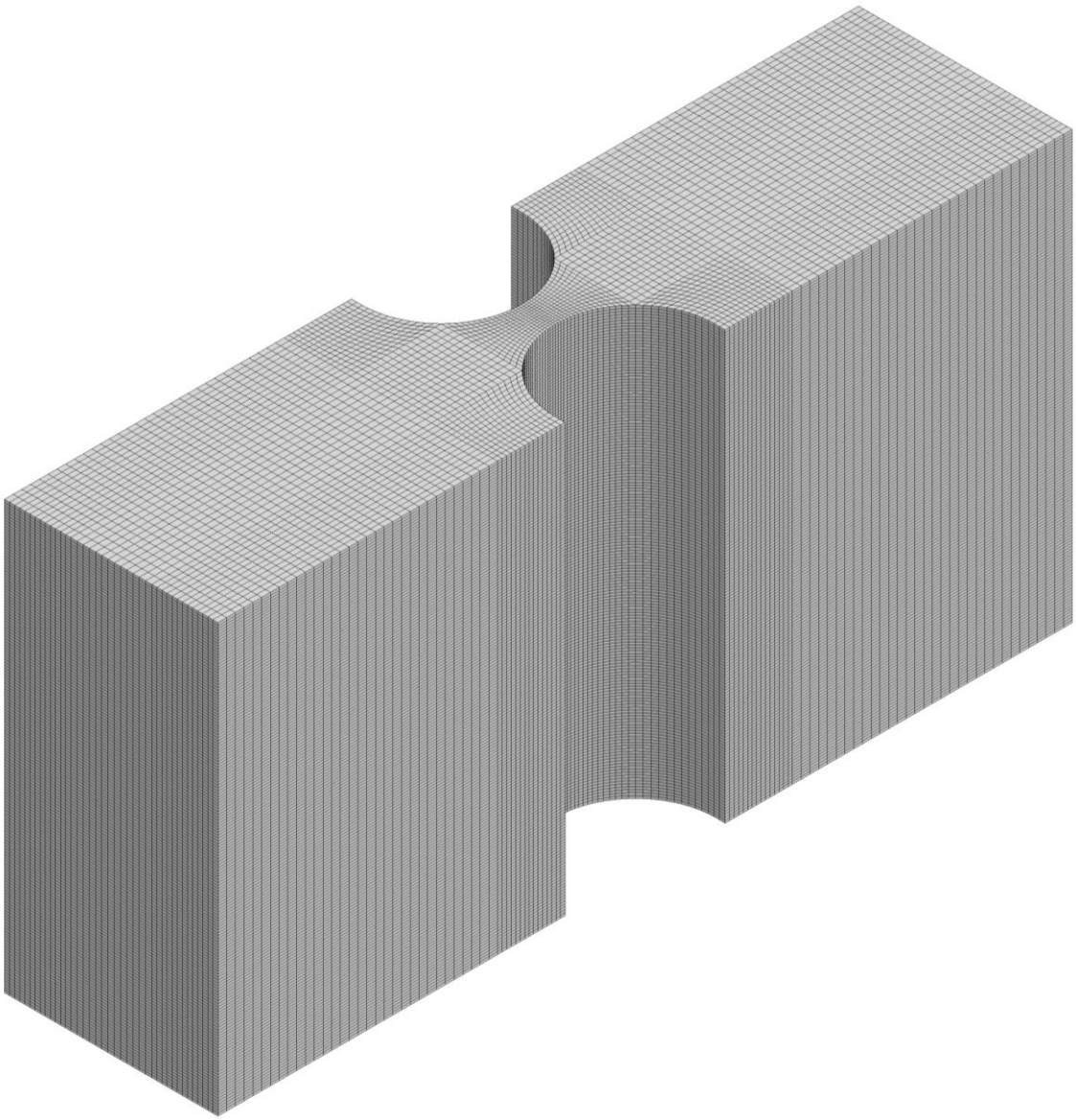

(Isometric View)

Figure 227. Plan and Isometric View of Thick Small Notched FEM Model

7.6.14 FEM Model of Cylinder Upsetting Specimen

A FEM model was created to simulate the compression tests performed on the Cylinder Upsetting Specimen. A mesh was created using an element size equal to the previous models. Therefore, the elements were meshed to have lengths of approximately 0.0060 in. (0.152 mm) in each direction in the critical gauge region. The mesh created to model this specimen can be seen in Figure 228. A planar rigid wall was placed on the bottom side of the specimen to act as one compression platen. A planar rigid wall with a prescribed motion curve was placed on the top of the specimen to act as the moving compression platen. A smooth curve with a rise time equal to $^1/_5$ of the simulation time was utilized to reduce effects from suddenly loading the specimen. Type 6 hourglass control with a coefficient value of 0.01, and a simulation time of 10 ms was utilized, as determined in previous sections. Cross sections, node histories, and solid element histories were collected to aid in post-processing.

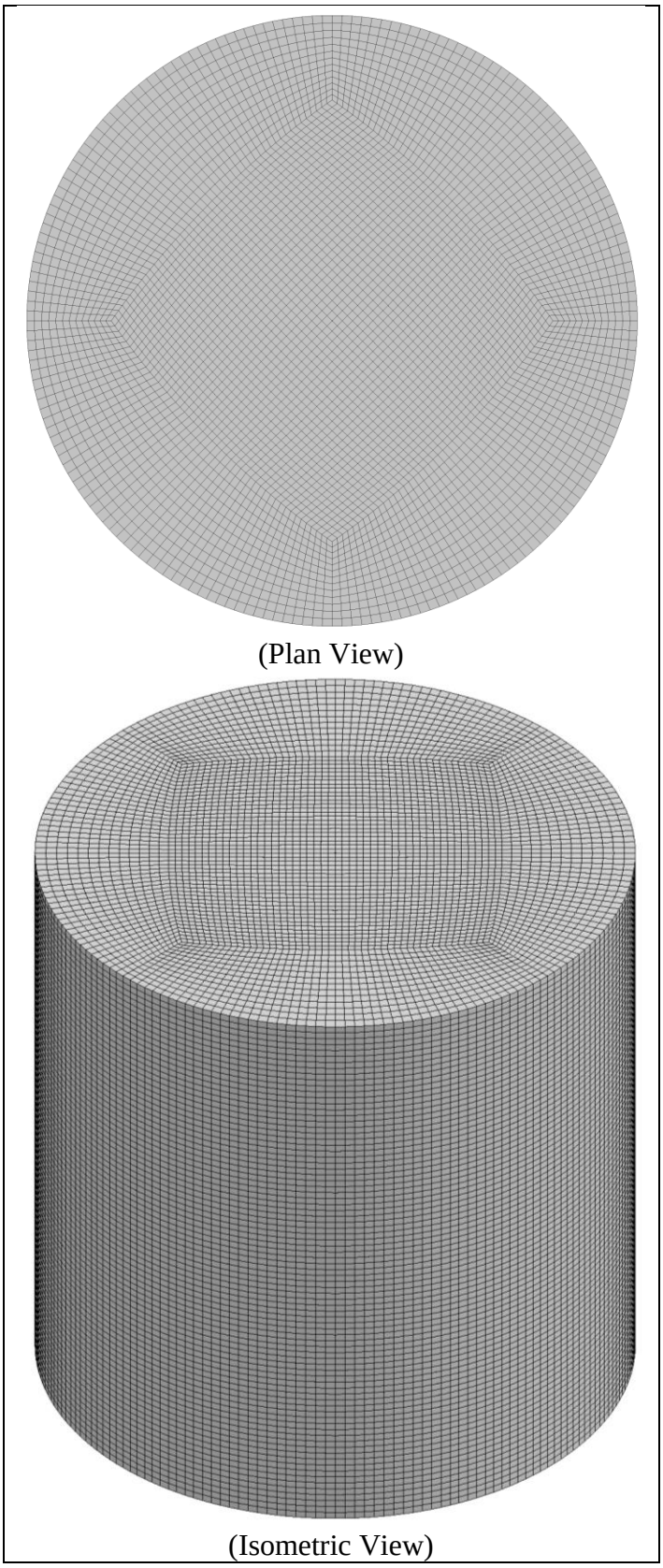

(Plan View)

(Isometric View)

Figure 228. Plan and Isometric View of Cylinder Upsetting FEM Model

7.6.15 FEM Model of Standard Punch Specimen

A FEM model was created to simulate the standard punch tests performed. The fixture was modeled as three parts, as shown in Figure 223. Two parts modeled the recessed area; one as the lower face and the other as the outer lip. These two parts were modeled as rigid bodies in which no movement was allowed. The third part modeled the lower face of the top of the fixture, also referred to as the binder, as a rigid body. The pre-load applied from tightening the bolts was modeled by applying a prescribed motion to the binder prior to the punch head movement. This prescribed motion was defined using a smoothed curve lasting 2 ms for a total distance of 0.00013 in. (0.0033 mm) with a 0.1 ms rise time. This distance was determined to give a pre-loading to the specimen comparable to the pre-load applied during physical testing. However, the binder was not allowed to move after the pre-loading prescribed motion was finished. This setup is unlike the physical testing in which the upper and middle fixture separate during loading as a result of the moment applied on the specimen from the punch head. However, as part of this modeling effort, the difference in behavior was assumed to be negligible. The parts modeling the punch fixture were all modeled as rigid shells with a thickness of 0.0079 in. (0.2 mm).

The punch head was modeled as a rigid body in which a prescribed motion defined by a smooth curve was applied. The smooth curve was programed with a 2 ms rise time with an end equal to the simulation termination time. Similar to the fixture parts, the punch head was modeled as rigid shells with a thickness of 0.0079 in. (0.2 mm). The original and revised punch heads can be seen in Figures 230 and 231, respectively. The geometry was offset 0.1 mm to account for the shell thickness. The mesh of the specimen

was created using solid elements with a size of approximately 0.0060 in. (0.152 mm) in each direction, as seen in Figure 232.

Surface to surface contact definitions were applied between the specimen and lower face, and specimen and binder. An eroding surface to surface contact definition was applied between the punch head and specimen. No contact definition was required for the outer lip, however, the part was left as a visual reference. A viscous damping coefficient of 20 was utlized with a SOFT=2 segment-based contact option for all of the contact definitions. All contacts were assumed to be frictionless. Similar to previous simulations type 6 hourglass control with a coefficient value of 0.01 was used. However, the simulation time was increased to 30 ms to potentially allow for a more stable simulation. Cross sections, node histories, solid element histories, and contact forces histories were collected to aid in post-processing.

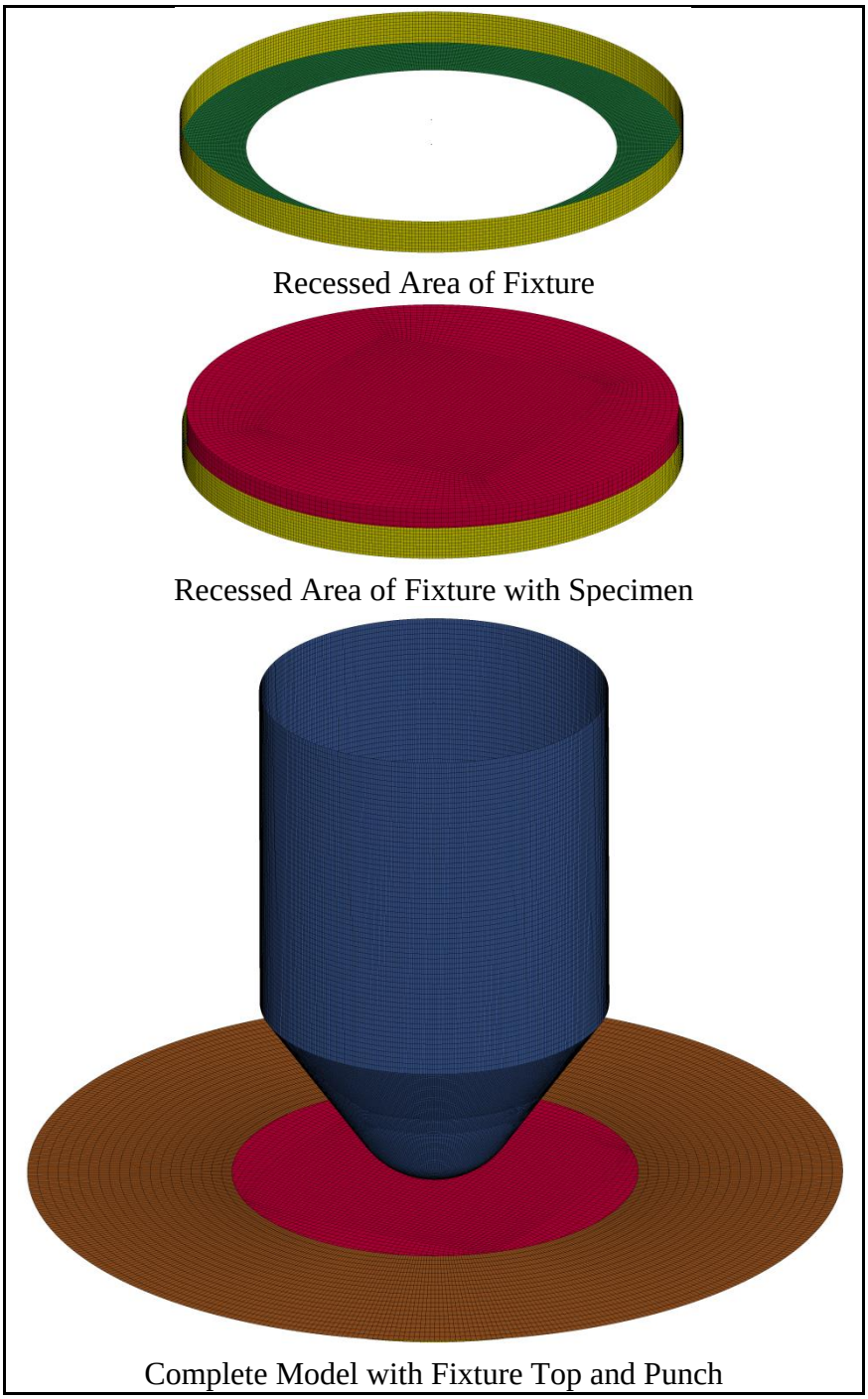

Figure 229. Punch Fixture, Specimen, and Punch Head FEM Model

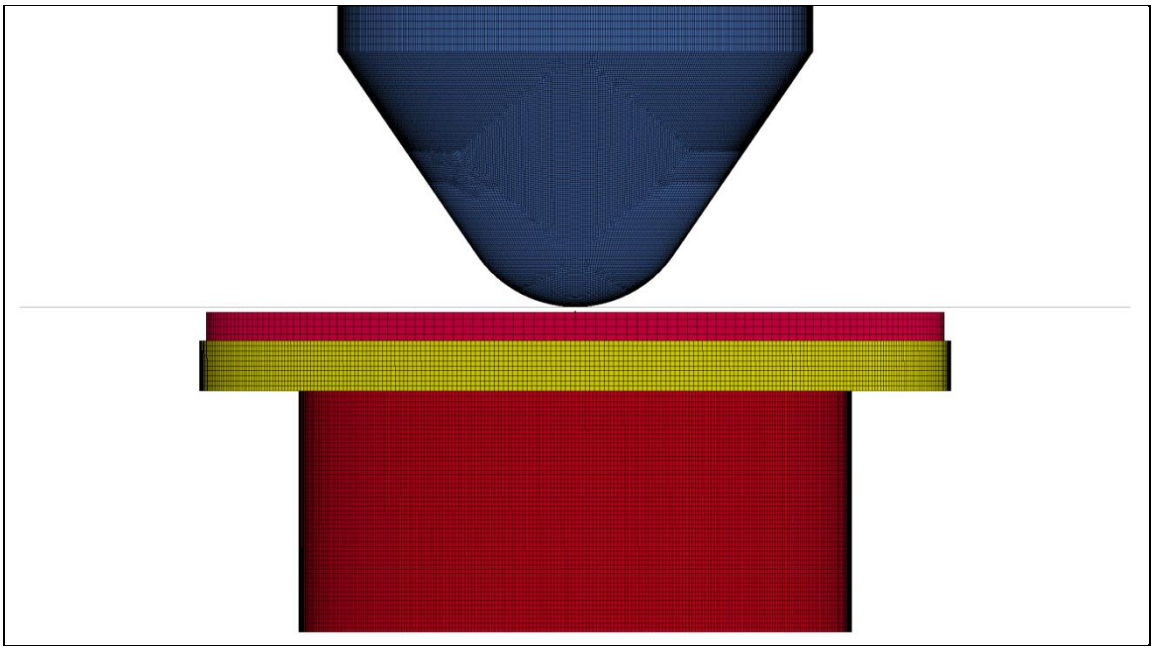

Figure 230. Original Standard Punch Head, Fixture, and Specimen FEM Model

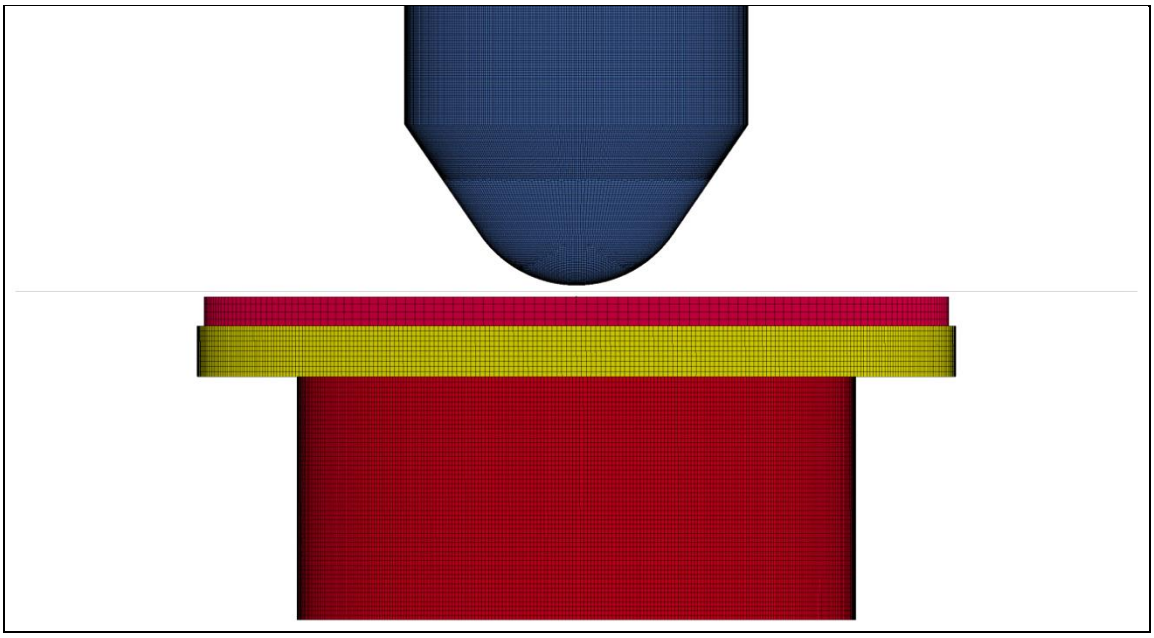

Figure 231. Revised Standard Punch Head, Fixture, and Specimen FEM Model

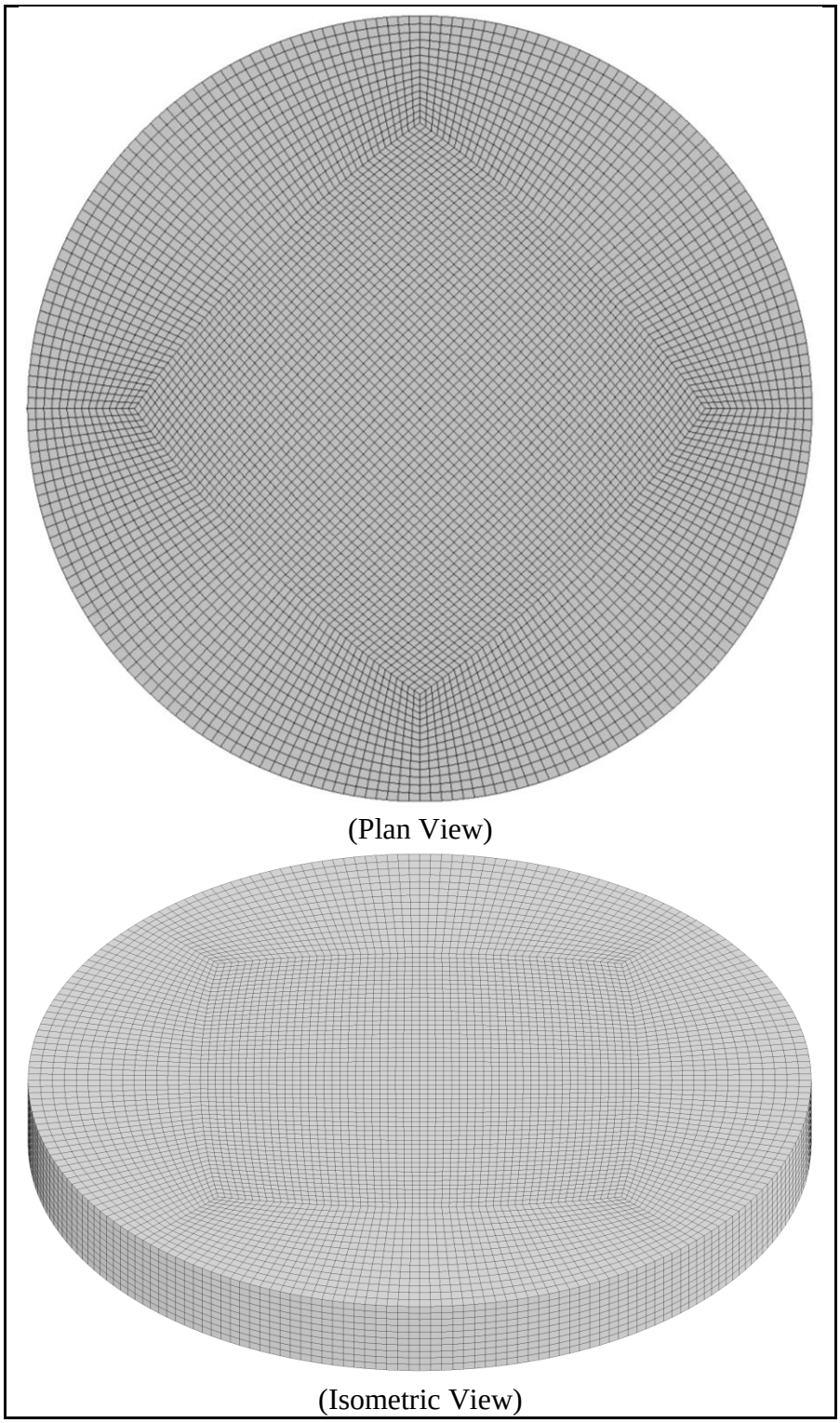

Figure 232. Plan and Isometric View of Punch Specimen FEM Model

7.6.16 FEM Model of Round Punch Specimen

The punch fixture and specimen were modeled identically to the fixture utilized in the Standard Punch Specimen FEM model. Furthermore, the round punch heads were developed in identical fashions. The resulting models with the original and revised round punch heads can be seen in Figures 233 and 234, respectively.

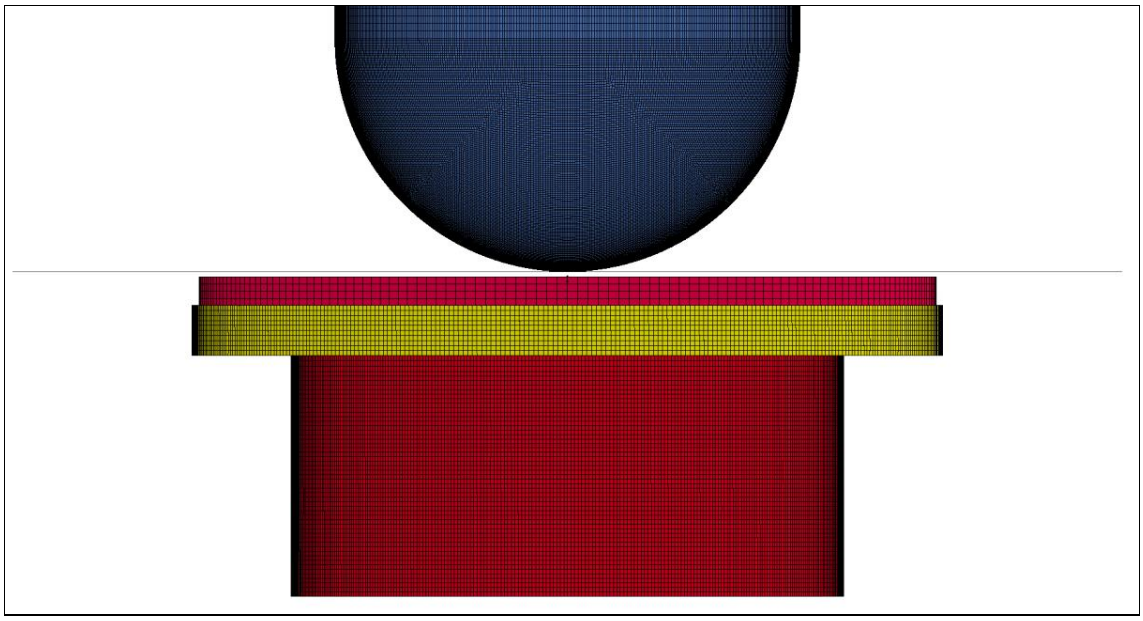

Figure 233. Original Round Punch Head, Fixture, and Specimen FEM Model

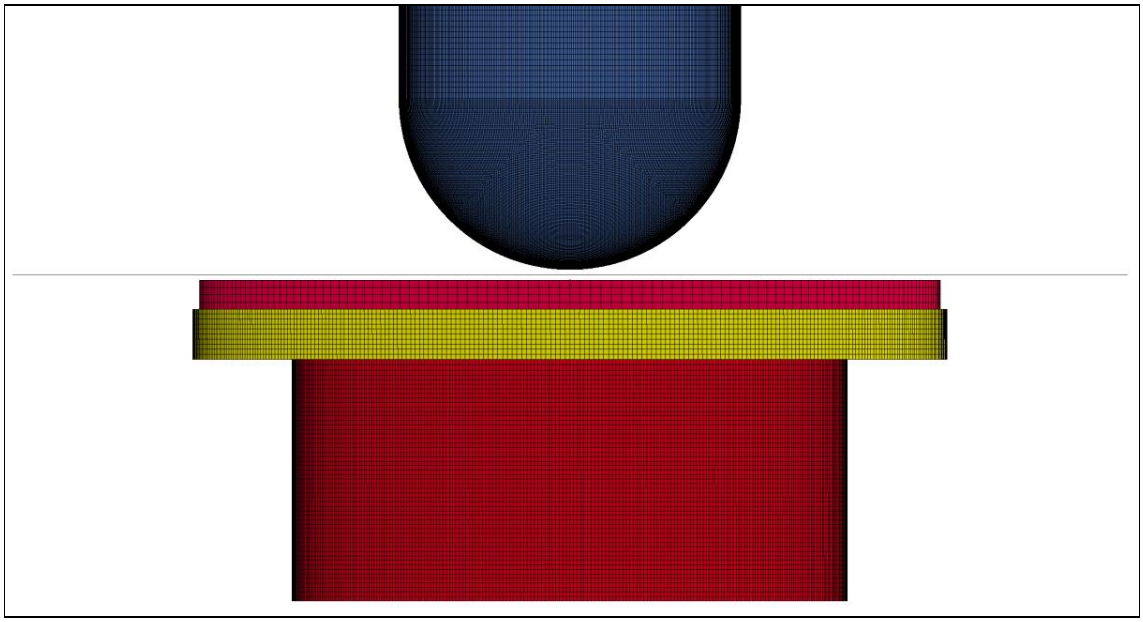

Figure 234. Revised Round Punch Head, Fixture, and Specimen FEM Model

7.6.17 FEM Model of Sharp Punch Specimen

The punch fixture, and specimen were modeled identically to the fixture utilized in the previous punch FEM models. Furthermore, the sharp punch head was developed in an identical fashion. The resulting models with the sharp punch heads can be seen in Figure 235.

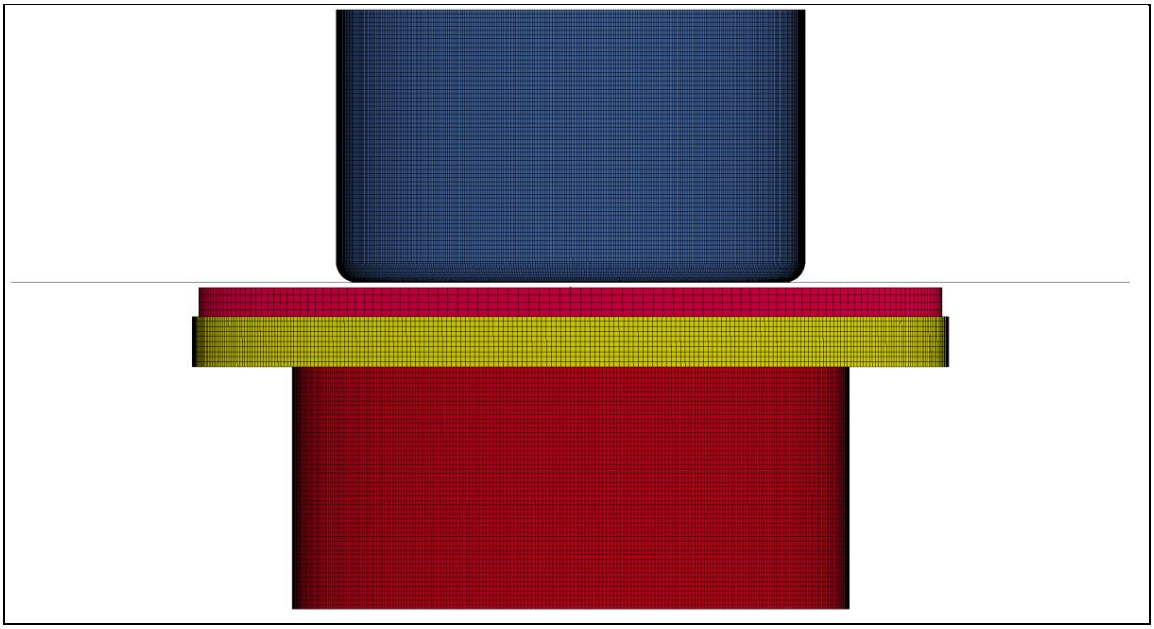

Figure 235. Sharp Punch Head, Fixture, and Specimen FEM Model

7.6.18 FEM Model of Dual-Point Shear

The dual punch shear fixture was modeled using three rigid shell element parts meshed as seen in Figure 236. The blue and yellow parts acted as the portion of the fixture base that holds the specimen. The inner green part modeled the inner cylinder that displaced relative to the fixture base. The three parts were created with shells with a thickness of 0.0079 in. (0.2 mm). Therefore, the diameter of the cylinders were oversized by 0.0079 in. (0.2 mm). The outer fixture parts were fully constrained while the inner part was constrained in all degrees of freedom, except linear movement in one direction perpendicular to the specimen. The dual-point shear specimen was meshed, as seen in

Figure 236. A mesh size of approximately 0.0060 in. (0.152 mm) in each direction was utilized in the shear region of the specimen. However, a larger mesh was utilized outside of the shear region to reduce computation time. A smooth curve with a rise time equal to $^{1}/_{10}$ of the simulation time was utilized to define the prescribed motion in order to reduce the effects from suddenly loading the specimen. Type 6 hourglass control with a coefficient value of 0.01, and a simulation time of 10 ms was utilized. Cross sections, node histories, and solid element histories were collected to aid in post-processing.

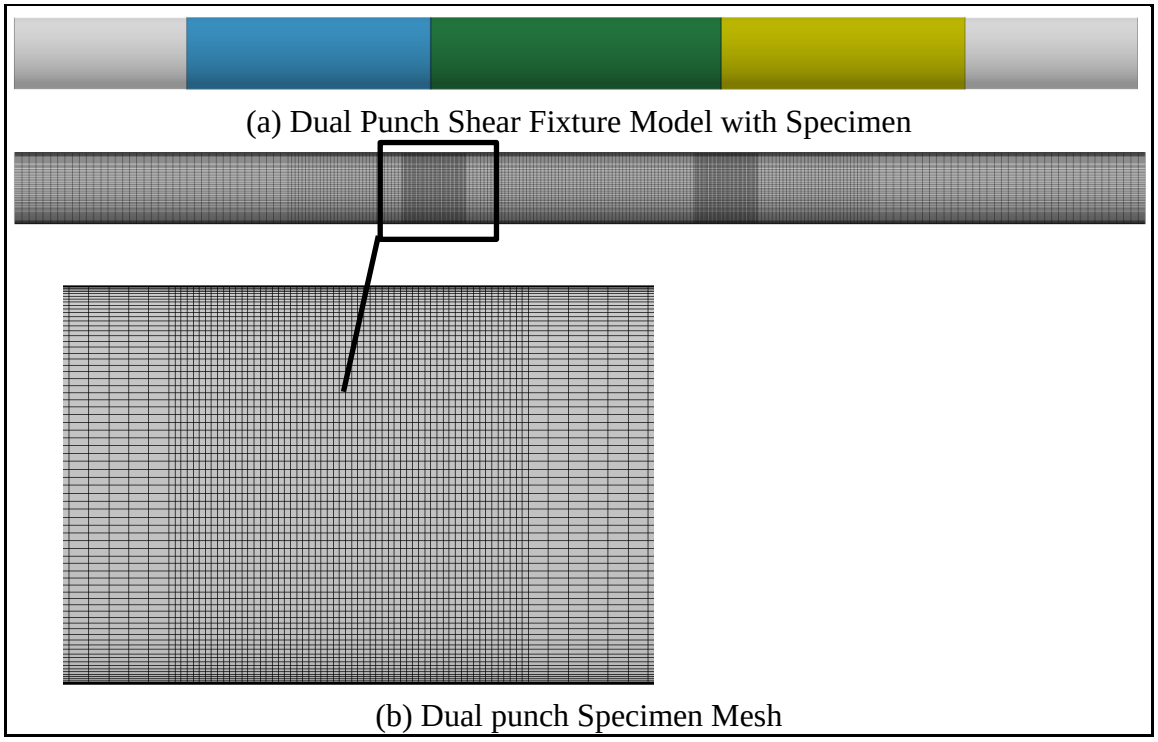

(a) Dual Punch Shear Fixture Model with Specimen

(b) Dual punch Specimen Mesh

Figure 236. Dual Punch Specimen and Fixture FEM Model

7.6.19 FEM Model of Torsion Specimen

The torsion specimen was modeled using the mesh seen in Figure 237. One end of the specimen was constrained only in the transverse direction so that the nodes at the boundary were not allowed to rotate. However, the nodes at the end were allowed to

freely displace in the axial direction. The other end used a layer of rigid elements with shared nodes to the specimen that imparted the rotational displacement of the specimen. Unfortunately the use of this method may not accurately model the degrees of freedom seen in the physical testing. The physical testing allowed relatively large transverse displacement in the non-rotating end and a small angular deflection from the axial centerline, on either end. As a result of the disparity of constraints used in the model compared to what was seen in the physical testing, it is unlikely that similar failure behavior will be exhibited. Further model refinement may be necessary. A smooth curve with a rise time equal to $^{1}/_{10}$ of the simulation time was utilized to define the prescribed rotation in order to reduce the effects from suddenly loading the specimen. Type 6 hourglass control with a coefficient value of 0.01, and a simulation time of 10 ms was utilized. Cross sections, node histories, and solid element histories were collected to aid in post-processing.

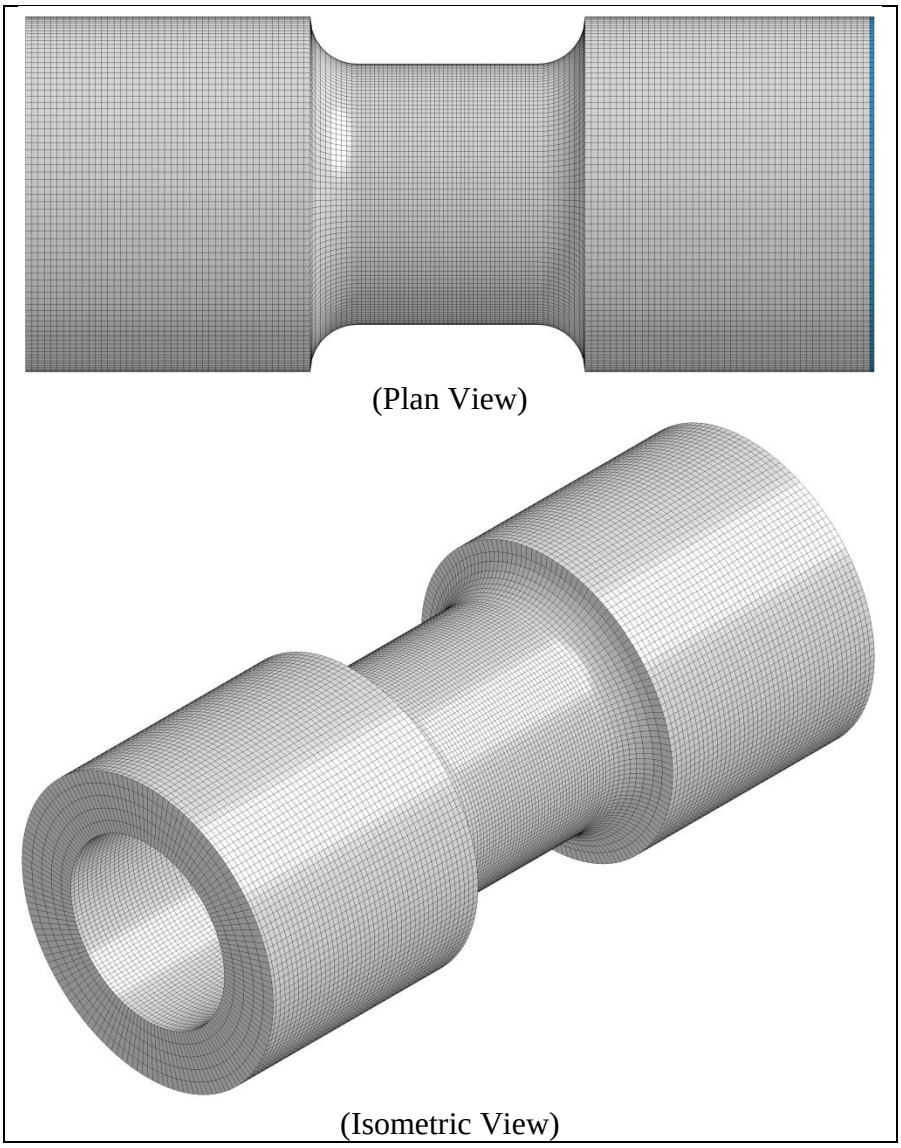

Figure 237. Plan and Isometric Views of Torsion Specimen FEM Model

8 SUMMARY, CONCLUSIONS, AND RECOMMENDATIONS

8.1 Summary and Conclusions

The objectives of the research study were to advance the knowledge and understanding of failure in AASHTO Specification M-180 guardrail steel. More specifically, it was desired to contribute to the development of an improved steel material model with material failure criteria, which can be used in common computer simulation programs, such as LS-DYNA, to predict guardrail failure in vehicle to barrier impact events. The objective of this project was accomplished over six tasks.

First, a literature review was conducted to provide a general overview of historical and modern strength and failure methods for ductile steel materials. This review effort can be found in Chapter 2. Triaxiality and Lode parameter dependent failure criteria were introduced and discussed as a method to potentially predict the failure behavior of ductile steel. Previous research efforts have proposed that these two parameters are capable of defining complex loading conditions so that failure criteria dependent on triaxiality and Lode parameter can be implemented to produce more accurate predictions. Also, prior research efforts on strain rate effects were examined and summarized.

Next, a review was conducted to better understand the material models that are available in LS-DYNA for simulating ductile material through failure. Through a series of progressive material model reviews and eliminations, it was determined that three material models justified further analysis. The examination of the various material models can be found in Chapter 3. The chosen material models included the MAT_24 – Isotropic Piecewise-Linear Plasticity and MAT_224 – Tabulated Johnson Cook, as well

as the optional additional failure criteria, MAT_ADD_EROSION – GISSMO. MAT_24 – Isotropic Piecewise-Linear Plasticity was chosen due to its popularity and widespread use in crash simulations. MAT_ADD_EROSION – GISSMO, and MAT_224 – Tabulated Johnson Cook were chosen due to their diverse modeling options with tabulated inputs and their ability to define failure as a function on triaxiality and Lode parameter.

In order to define the necessary test matrix to calibrate a material model for FEM analysis, a study was then conducted to review and analyze existing state-of-stress dependent failure surface methods. This effort included a review of four failure surface methods including the Xue and Wierzbicki, Bai Symmetric, Bai Asymmetric, and the Buyuk methods, as detailed in Section 4.2. Next, in order to better understand the performance of each method, data from previously-published physical testing programs was used to calibrate surfaces that were configured with each failure surface method. Also, partial data sets were selected from the full data sets to determine if a data set containing a fewer number of tests could reproduce the failure surface calibrated with the full data set. This effort can be found in Sections 4.3 through 4.4. Comparisons were made between the surfaces, and it was determined that more flexible failure surface methods may be required to accurately represent test data, as explained in Section 4.6. To accommodate this requirement, a failure surface method was proposed utilizing a Smoothed, Thin-Plate Spline. Section 4.5 details how this method can create a surface that can easily be adjusted to balance the potential bias and variance witnessed with the existing failure surface methods. Furthermore, it was determined that a data set with numerous specimen geometries over a wide range of stress states would provide vastly superior results over reduced data sets under complex loading conditions.

Based on the analysis performed on calibrating failure surfaces with various data sets, a test matrix was developed and presented in Chapter 5. A total of 103 tests were then conducted on 21 unique test configurations. Based on the test data, material properties were determined, and the critical information to aid in FEM modeling and validation was summarized. The test results were summarized in Chapter 6, while detailed test data was archived in Appendix F.

A FEM modeling effort was also performed, as detailed in Chapter 7, to aid in developing baseline modeling parameters. Various modeling parameters were examined, and preferred parameters were given. The use of consistent parameters would reduce concerns for bias being imposed on any specimen model. To determine the optimum modeling parameters, various parameters were examined, such as element formulation, hourglass control, mesh size, and simulation duration. Through a series of preliminary simulations, as summarized in Section 7.2, it was determined that solid, type 1, constant-stress, elements with type 6, Belytschko-Binderman, assumed co-rotational stiffness, hourglass control with a coefficient of 0.01 produced adequate results. This formulation prevented visual hourglass effects and imposed minimal artificial stiffness and strength to the specimen models. Furthermore, a mesh-size sensitivity study was performed, as presented in Section 7.3. This study determined that an element size of 0.0060 in. (0.152 mm) provided reasonable performance in modeling each specimen. Also, a baseline simulation time of 10 ms was determined to produce results in which inertial effects were negligible, while also maintaining short cpu wall times and stable simulations, as shown in Section 7.4. Lastly, an analysis was conducted to compare the behavior of specimen geometries modeled with solid and shell elements as shown in Section 7.5. It was found

that shell element models with thickness update options equal to ISTUPD=1 and 4 produced results more similar to the solid element models than the thickness update option equal to ISTUPD=0. However, the difference between the shell element models became more prominent as the notch radii increased. It was determined that if shell elements were used in lieu of solid elements, the material model would need to be recalibrated with updated parameters. Particularly, the effective plastic strain at failure would need to be recalibrated for the higher triaxiality stress states.

Based on the noted parameters, FEM models were developed and presented in Section 7.6 for the 21 test configurations. A baseline material model using the MAT_24 – Isotropic Piecewise-Linear Plasticity model was also created and iteratively calibrated to the Axial-Symmetric Round Smooth Specimen using the respective test data.

8.2 Recommendations

A number of steps remain before a validated material model can successfully predict and model failure in AASHTO M-180 steel guardrail sections. The recommended steps are included below:

1) First, this research effort was unable to fully examine the performance of the calibrated MAT_24 – Isotropic Piecewise-Linear Plasticity material model under the various testing configurations. Thus, a number of unknowns still exist. Particularly, it is unknown if the steel material tested herein exhibits stress-state dependent failure. In order to examine this further, all test configurations should be simulated using the specimen models and baseline material model presented in Section 7.6. A review of the performance of the material model, particularly the simplified failure criteria, can then be

performed. Based on these results, it should be clear if the material exhibits stress-state dependent failure.

2) If the as-tested steel material shows stress-state dependent failure, the baseline material model likely will not accurately predict failure for the specimen models that are not under uniaxial tension (i.e., specimens other than the Flat Standard Dog Bone Specimen and the Axial-Symmetric Round Smooth Specimen). However, the effective plastic strain at failure can be iteratively adjusted for each model until the model accurately predicts failure initiation. This effort will provide an effective plastic strain at failure for each specimen. Therefore, a data set with the state of stress, as represented by triaxiality and Lode parameter vs. the effective plastic strain at failure, will be produced.
3) Now that a stress-state dependent data set is available, a failure surface can be produced utilizing one of the existing or proposed failure surfaces contained within this report. This surface can then be inputted into either MAT_ADD_EROSION – GISSMO or the MAT_224 – Tabulated Johnson Cook. The performance of these material models with stress-state dependent failure criteria can then be evaluated. Also, non-local options can be evaluated to reduce mesh-size effects, or coupled damage criteria can be implemented to allow the specimens to fail gradually before eroding completely from the simulation.
4) Lastly, an evaluation could be performed to examine the failure behavior of formed and unformed AASHTO M-180 guardrail sections with material properties similar to the material used in this phase of research. First, this

analysis would verify that the failure behavior exhibited in the unformed AASHTO M-180 guardrail section is similar to the failure behavior exhibited in the material tested in this phase of research. Plane stress (flat) specimens with notches similar to those used in this testing program could be machined from the unformed guardrail section to compare the failure behavior. If the failure behavior shows a variation in the state of stress failure surface, the failure surface may need to be calibrated so that the material model's failure surface accurately represents failure behavior of AASHTO M-180 guardrail steel. Second, strain history effects and residual stress effects can be examined. By conducting parallel testing and modeling on the unformed and formed sections, as well as modeling the forming process of guardrail sections, insight into modeling vehicle to barrier impact events with accurate failure prediction can be gained.

Numerous other factors remain to be studied that could potentially increase the accuracy of modeling AASHTO M-180 guardrail steel. A non-inclusive list of those other factors may include strain-history effects from the forming process, temperature effects, and strain rate effects.

9 REFERENCES

1. Winkelbauer, B.J., Putjenter, J.G., Rosenbaugh, S.K., Lechtenberg, K.A., Bielenberg, R.W., and Faller, R.K., *Dynamic Evaluation of MGS Stiffness Transition with Curb,* Final Report to the Midwest States' Regional Pooled Fund Program, MwRSF Research Report No. TRP-03-291-14, Project No. TRP-5(193) Supplement #58 and 63, Project Code: RPFP-13-AGT-1 and RPFP-14-AGT-1 - Years 23 and 24, Midwest Roadside Safety Facility, University of Nebraska-Lincoln, Lincoln, Nebraska, June 30, 2014.

2. Livermore Software Technology Corporation, *LS-DYNA Keyword User's Manual R7.1 (Revision 5442),* Livermore, May 2014.

3. American Association of State Highway Officials (AASHTO), *Standard Specification for Corrugated Sheet Steel Beams of Highway Gaurdrail,* AASHTO Designation: M 180-12, 2012.

4. Yu, M.-h., *Advances in Strength Theories for Materials Under Complex Stress State in the 20th Century,* ASME Applied Mechanics Review, vol. 55, no. 3, pp. 169-218, 2002.

5. Ray, M.H., Engstrand, K., Plaxico, C.A., and McGinnis, R.G., *Improvements to the Weak-Post W-Beam Guardrail,* Transportation Research Record No. 1743, pp. 88-96, 2001.

6. Bielenberg, R.W., *Finite Element Simulations of a Bulnose Median Barrier System,* A Thesis Presented to the Faculty of The Graduate College at the University of Nebraska in Partial Fullfillment of Requirements for the Degree of Master of Science in Mechanical Engineering, 1999.

7. Bielenberg, B.W., Faller, R.K., Reid, J.D., Rohde, J.R., Sicking, D.L., and Keller, E.A., *Concept Development of a Bullnose Guardrail System for Median Applications,* Final Report to the Midwest States' Regional Pooled Fund Program, MwRSF Research Report No. TRP-03-73-98, Project No. SPR-3(017), Midwest Roadside Safety Facility, University of Nebraska-Lincoln, Lincoln, Nebraska, May 22, 1998.

8. Bielenberg, B.W., Reid, J.D., Faller, R.K., Rohde, J.R., Sicking, D.L., and Keller, E.A., *Phase II Development of a Bullnose Guardroil System for Median Applications,* Final Report to the Midwest States' Regional Pooled Fund Program, MwRSF Research Report No. TRP-03-78-98, Project No. SPR-3(017), Midwest Roadside Safety Facility, University of Nebraska-Lincoln, Lincoln, Nebraska, December 18, 1998.

9. Bielenberg, B.W., Reid, J.D., and Faller, R.K., *NCHRP Report No. 350 Compliance Testing of a Bullnose Median Barrier System,* Transportation Research Record, no. 1743, pp. 60-70, January 2001.

10. Bielenberg, B.W., Reid, J.D., Faller, R.K., Rohde, J.R., Sicking, D.L., Keller, E.A., Holloway, J.C., and Supencheck, L., *Phase III Development of Bulllnose Guardrail System for Median Applications,* Final Report to the Midwest States' Regional Pooled Fund Program, MwRSF Research Report No. TRP-03-95-00, Project No. SPR-3(017), Midwest Roadside Safety Facility, University of Nebraska-Lincoln, Lincoln, Nebraska, June 1, 2000.

11. Coulomb, C.A., *Essai sur une application des regles de maximis et minimis a quelques problemes de statique, relatifs a,* Memoires de Mathematique et de Physique, presentes a l' Academie, Royale des Sciences par divers Savans, et lus dans ses Assemblees, vol. 7, pp. 343-382, 1773.

12. Rankine, W. J., *Manual of Applied Mechanics,* 1921.

13. Mariotto, E., *Traite du mouvement des eaux, (posthumously), de la Hire M ed; English transl by Desvaguliers JT,* 1718.

14. Tresca, H., *Sur I'ecoulement des corps solids soumis a de fortes pression,* Comptes Rendus hebdomadaires des Seances de l'Academie des Sciences, vol. 59, pp. 754-758, 1864.

15. Timoshenko, S. P., *History of Strength of Materials, with a Brief Account of the History of Theory of Elasticity and Theory of Structures,* New York: McGraw-Hill, 1953.

16. Dowling, N. E., *Mechanical Behavior of Materials: Engineering Methods for Deformations, Fracture, and Fatigue,* Boston: Pearson, 2013.

17. Curran, D.R., Seaman, L., and Shockey, D.A., *Dynamic Failure in Solids,* Physics Today, vol. 30, no. 1, pp. 46-55, 1977.

18. Tvergaard, V. and Hutchinson, J.W., *Two Mechanisms of Ductile Fracture: Void by Void Growth versus Mutiple Void Interaction,* International Journal of Solids and Structures, vol. 39, pp. 3581-3597, 2002.

19. Thomason, P. F., *Ductile Fracture of Metals,* Oxford: Pergamon Press, 1990.

20. Garrison Jr, W.M. and Moody, N.R., *Ductile Fracture,* Journal of Physics and Chemistry of Solids, vol. 48, no. 11, pp. 1035-1074, 198.

21. Bridgman, P., *Studies in Large Plastic Flow and Fracture with Special Emphasis on the Effects of hydrostatic Pressure,* New York: McGraw-Hill Book Company, 1952.

22. Bridgman, P.W., *The Effect of Hydrostatic Pressure on the Fracture of Brittle Substances,* Journal of Applied Physics, vol. 18, no. 2, pp. 246-258, 1947.

23. Hancock, J.W. and Mackenzie, A.C., *On the Mechanisms of Ductile Failure in High-Strength Steels Subjected to Multi-Axial Stress-State,* Journal of Mechanics and Physics of Solids, vol. 24, no. 2-3, pp. 147-160, June 1976.

24. Rice, J.R. and Tracey, D.M., *On The Ductile Enlargement of Voids in Triaxial Stress Fields,* Journal of Mechanics and Physics of Solids, vol. 3, no. 2, pp. 201-217, June 1969.

25. Gurson, A.L., *Plastic Flow and Fracture Behavior of Ductile Materials Incorporating Void Nucleation, Growth, and Interaction,* A Thesis Submitted in partial Fulfillment of the Requirements for the Degree of Doctor of Philosophy in the Division of Engineering at Brown University, 1975.

26. Gurson, A.L., *Continuum Theory of Ductile Rupture by Void Nucleation and Growth,* Journal of Engineering Materials and Technology, vol. 99, no. 1, pp. 2-15, 1977.

27. Tvergaard, V., *Influence of Voids on Shear Band Instabilities Under Plane Strain Conditions,* International Journal of Fracture, vol. 17, no. 4, pp. 389-407, 1981.

28. Norris, D.M., Reaugh, J.E., Okimoto, K., and Quiñones, D.F., *A Plastic-Strain, Mean-Stress Criterion for Ductile Fracture,* Journal of Engineering Materials and Technology, vol. 100, no. 3, pp. 249-286, July 1978.

29. Oyane, M., Sato, T., Okimoto, K., and Shima, S., *Criteria for Ductile Fracture and their Applications,* Journal of Mechanical Working Technology, vol. 4, no. 1, pp. 65-81, April 1980.

30. Lemaître, J. *A, Course on Damage Mechanics,* Springer-Verlag, 1992.

31. La Rosa, G., Mirone, G., and Risitano, A., *Effects of Stress Triaxiality Corrected Plastic Flow on Ductile Damage Evolution in the Frameworls of Continuum Damage Mechanics,* Engineering Fracture Mechanics, vol. 68, no. 4, pp. 417-434, March 2001.

32. Johnson, G.R. and Cook, W.H., *A Constitutive Model and Data for Metals Subjected to Large Strains, High Strain Rates and High Tempuratures,* Proceedings of the 7th International Symposium on Ballistics, vol. 21, pp. 541-547, 1983.

33. Johnson, G.R. and Cook, W.H., *Fracture Characteristics of Three Metals Subjected to Various Strains, Strain Rates, Tempuratures, and Pressures,* Engineering Fracture Mechanics, vol. 2, no. 1, pp. 31-48, 1985.

34. Lewandowski, J.J. and Lowhaphandu, P., *Effects of Hydrostatic Pressure on Mechanical Behavior and Deformation Processing of Materials,* International Materials Reviews, vol. 43, no. 4, pp. 145-187, 1998.

35. Bai, Y., Teng, X., and Wierzbicki, T., *On the Application of Stress Triaxiality Formula for Plane Strain Fracture Testing,* Journal of Engineering Materials and Technology, vol. 131, pp. 1-10, 2009.

36. Chinzei, S., Naito, J., and Saito, K., *The Simulation of Fracture Prediction by the Damage Model GISSMO in Various Materials of Sheet Metal,* in LS-DYNA Forum, Bamberg, 2014.

37. Wierzbicki, T., Bao, Y., and Lee, Y.-W., *Calibration and Evaluation of Seven Fracture Models,* International Journal of Mechanical Sciences, vol. 47, no. 4-5, pp. 719-743, 2005.

38. Buyuk, M., *Development of a New Metal Material Model in LS-DYNA, Part 2: Development of a Tabulated Thermo-Viscoplastic Material Model with Regularized Failure for Dynamic Ductile Failure Prediction of Structures Under Impact Loading,* Federal Aviation Administration, U.S. Department of Transportation, July 2014.

39. Bai, Y. and Wierzbicki, T., *A New Model of Metal Plasticity and Fracture with Pressure and Lode Dependence,* International Journal of Plasticity, vol. 24, pp. 1071-1096, 2008.

40. Bao, Y. and Wierzbicki, T., *A Comparitive Study on Various Ductile Crack Formation Criteria,* Journal of Engineering Materials and Technology, vol. 126, no. 3, pp. 314-324, July 2004.

41. Gao, X., Zhang, G., and Roe, C., *A Study on the Effect of the Stress State on Ductile Fracture,* International Journal of Damage Mechanics, vol. 00, pp. 1-20, 2009.

42. Emmerling, W., Altobelli, D., Carney, K., and Pereira, M., *Development of a New Metal Material Model in LS-DYNA Part:1: FAA, NASA, and Industry Collaboration Background,* Federal Aviation Administration, U.S. Department of Transportation, April 2014.

43. Seidt, J.D., *Development of a New Metal Material Model in LS-DYNA, Part 3: Plastic Deformation and Ductile Fracture of 2024 Aluminum Under Various Loading Conditions,* Federal Aviation Administration, U.S. Department of Transportation, April 2014.

44. Soyarslan, C., Richter, H., and Bargmann, S., *Lode Parameter Dependence and Quasi-Unilateral Effects in Continuum Damage Mechanics: Models and Applications in Metal Forming,* Key Engineering Materials, Vols. 651-653, pp. 187-192, 2015.

45. Danas, K., and Ponte Castañeda, P., *Influence of the Lode Parameter and the Stress Triaxiality on the Failure of Elasto-Plastic Porous Materials,* International Journal of Solids and Structures, vol. 49, pp. 1325-1342, 2012.

46. Bao, Y., *Prediction of Ductile Crack Formation in Uncracked Bodies,* A Dissertation Submitted to the Department of Ocean Engineering in partial fulfillment of the requirements for the degree of Doctor of Philosophy in Applied Mechanics at the Massachusetts Institute of Technology, 2003.

47. Carney, K.S., DuBois, P.A., Buyuk, M., and Kan, S., *A Generalized, Three Dimensional Definition, Description and Derived Limits of the Triaxiality Failure Metals,* Earth & Space 2008: Engineering, Science, Construction, and Operations in Challenging Environments, Long Beach, 2008.

48. Kiran, R. and Khandelwal, K., *Experimental Studies and Models for Ductile Fracture in ASTM A992 Steels at High Triaxiality,* Journal of Structural Engineering, vol. 140, no. 2, 2014.

49. Wright, A.E. and Ray, M.H., *Characterizing Guardrail Steel for LS-DYNA3d Simulations,* Transportation Research Record, vol. 1528, pp. 138-145, 1996.

50. Jones, N., *Structural Impact,* Cambridge: Cambridge University Press, 1989.

51. Du Bois, P.A., Kolling, S., Feucht, M., and Haufe, A., *A Comparative Review of Damage and Failure Models and a Tabulated Generalization,* in 6th European LS-DYNA Conference, Gothenburg, 2007.

52. Livermore Software Technology Corporation, *LS-DYNA Theory Manual (Revision 5514),* Livermore, May 2015.

53. Bammann, D.J., *Modeling Temperature and Strain Rate Dependent Large Deformations of Metals,* Applied Mechanics Reviews, vol. 43, no. 5, pp. S312-S319, 1990.

54. Bammann, D.J., Chiesa, M.L., Horstemeyer, M.F., and Weingarten, L.I., *Failure in Ductile Materials Using Finite Element Methods,* in Third International Symposium on Structural Crashworthiness, Liverpool, 1993.

55. Duó, P. and Nowell, D., *Predictive Numerical Modeling of Foreign Object Damage,* in 9th International LS-DYNA Conference, Detroit, 2004.

56. Abed, F.H. and Voyiadjis, G.Z., *A Consistent modified Zerilli-Armstrong Flow Stress Model for BCC and FCC Metals for Elevated Temperatures,* Acta Mechanica, vol. 175, pp. 1-18, 2005.

57. Liang, R. and Khan, A.S., *A Critical Review of Experimental Results and Constituitve Models for BCC and FCC Metals Over a Wide Range of Strain Rates and Temperatures,* International Journal of Plasticity, vol. 15, pp. 963-980, 1999.

58. Aretz, H., *Applications of a New Plane Stress Yield Function to Orthotropic Steel and Aluminum Sheet Metals,* Modelling and Simulation in Materials Science and ENgineering, vol. 12, pp. 491-509, 2004.

59. Barlat, F. and Lian, K., *Plastic Behavior and Stretchability of Sheet Metals. Part I: A Yield Function for Orthotropic Sheets Under Plane Stress,* International Journal of Plasticity, vol. 5, no. 1, pp. 51-66, 1989.

60. Marin, E.B., Bammann, D.J., Regueiro, R.A., and Johnson, G.C., *On the Formulation, Paramter Identification and Numerical Integration of the EMMI Model: Plasticity and Isotropic Damage,* Sandia National Laboratories, Albuquerque, New Mexico, 2006.

61. Huang, Y. and Mahin, S., *A Cyclic Damage Plasticity Model: Implentation and Application,* in 10th International LS-DYNA Conference, Detroit, 2008.

62. Feucht, M., Sun, D.-Z., Erhart, T., and Frank, T., *Recnet Development and Applications of the Gurson Model,* in 2006 German LS-DYNA Forum, Ulm, 2006.

63. Haufe, A., Neukamm, F., Feucht, M., and DuBois, P., *A Comparison of Recent Damage and Failure Models for Steel Materials in Crashworthiness Application in LS-DYNA,* in 11th International LS-DYNA Confernce, Detroit, 2010.

64. Wilkins, M.L., Streit, R.D., and Reaugh, J.E., *Cumulative-Strain_Damage Model of Ductile Fracture: Simulation and Prediction of Engineering Fracture Tests,* Lawrence Livermore National Laboratory, Livermore, CA, 1980.

65. Norris, D.M., Wilkins, M.L., Reaugh, J.E., Moran, B., Scudder, J.K., Quinoñes, D.F., and Prado, M.E., *Fundamental Study of Crack Initiation and Propagation Annual Progress Report,* Lawrence Livermore Laboratory, Livermore, CA, 1977.

66. Nahshon, K. and Hutchinson, J.W., *Modification of the Gurson Model for Shear Failure,* European Journal of Mechanics and Solids, vol. 27, pp. 1-17, 2008.

67. Cockcroft, M.G. and Latham, D.J., *Ductility and the Workability of Metals,* Journal of the Institute of Metals, vol. 96, pp. 33-39, 1968.

68. Wierzbicki, T. and Xue, L., *On the Effect of the Third Invariant of the Stress Deviator on Ductile Fracture.*, Impact and Crashworthiness Lab, Massachusetts Institute of Technology, Cambridge, 2005.

69. Bai, Y., *Effect of Loading History on Necking and Fracture,* A Dissertation submitted to the Department of Mechanical Engineering in partial fulfillment of the requirments for the degree of Doctor of Philosophy in Applied Mechanics at the Massachsetts Institute of Technology, 2008.

70. Buyuk, M., *Development of a Tabulated Thermo-Viscoplastic Material Model with Regularized Failure for Dynamic Ductile Failure Prediction of Structures under Impact Loading,* A Dissertation submitted to the Faculty of Engineering and Applied Science of The George Washington University in partial fulfillment of the requirements for the degree of Doctor of Philosophy, 2013.

71. MathWorks, "MATLAB Product Page: Revision 2014b," [Online]. Available: http://www.mathworks.com/products/matlab. [Accessed 15 September 2014].

72. Xue, L., *Ductile Fracture Modeling - Theory, Experimental Investigation and Numerical Verification,* A Dissertation Submitted to the Department of Mechanical Engineering in partial fulfillment of the requirements for the degree of Doctor of Philosophy in Mechanical Engineering at the Massachusetts Institute of Technology, June 2007.

73. MathWorks, "MATLAB Thin-Plate Smoothing Spline Documentation," [Online]. Available: http://www.mathworks.com/help/curvefit/tpaps.html. [Accessed 3 May 2015].

74. Schmidt, J.D., Reid, J.D., Bielenberg, R.W., and Faller, R.K., *Numerical Investigation on the Performance of Steel Guardrail Systems With Varied Mechanical Properties,* Final Report to the Mid-America Transportation Center (MATC), Transportation Research Report No. TRP-03-290-13, July 25, 2013.

75. Schrum, K.D., Sicking, D.L., Faller, R.K., and Reid, J.D., *Predicting the Dynamic Fracture of Steel Via a Non-Local Strain Energy Density Failure Criterion,* Final Report to the Mid-America Transportation Research Center (MATC), Transportation Research Report No. TRP-03-311-14, June 23, 2014.

76. Schrum, K.D., *Predicting the Dynamic Fracture of Steel Via a Non-Local Strain Energy Density Failure Criterion,* A Disertation Presented to the Faculty of The Graduate College at the University of Nebraska In Partial Fullfillment of Requirements For the Degree of Doctor of Philosophy, Decemeber, 2013.

77. ASTM International, *Standard Specification for High-Strength Low-Alloy Columbium-Vanadium Structural Steel,* A572/572M-13a, 2013.

78. Mirone, G., *Role of Stress Triaxiality in Elastoplastic Characterization and Ductile Failure Prediction,* Engineering Fracture Mechanics, vol. 74, pp. 1203-1221, 2007.

79. Ebelsheiser, H., Feucht, M., and Neukamm, F., *On Calibrating Advanced Damage Models Using Sheet Metal Coupon Tests,* German LS-DYNA Forum, Bamberg, 2008.

80. Clausing, D.P., *Effect of Plastic Strani State on Ductility and Toughness,* International Journal of Fracture Mechanics, vol. 6, no. 1, pp. 71-85, 1969.

81. Bao, Y. and Wierzbicki, T., *On Fracture Locus in the Equivalent Strain and Stress Triaxiality Space,* International Journal of Mechanical Sciences, vol. 46, pp. 81-98, 2004.

82. Seidt, J.D., *Plastic Deformation and Ductile Fracture of 2024-T351 Aluminum under Various Loading Conditions,* A Dissertation Presented in Partial Fulfillment of the Requirements for the Degree Doctor of Philosophy in the Graduate School of the Ohio State University, 2010.

83. Lee, Y.-W., Woertz, J.C., and Wierzbicki, T., *Fracture Prediction of Thin Plates under Hemi-Spherical Punch with Calibration and Experimetal Verification,* International Journal of Mechanical Sciences, vol. 46, pp. 751-781, 2004.

84. Grytten, F., Borvik, T., and Hopperstad, O.S., *Quasi-Static Perforation of Thin Aluminum Plates,* International Journal of Impact Engineering, vol. 36, pp. 486-497, 2009.

85. Walters, C.L., *Dyanamic Bulging Technique for Testing Fracture in Intermediate Strain Rates,* Proceedings of the SEM Annual Conference & Exposition on Experimental & Applied Mechanics, 2009.

86. National Aerospace Standards Committee, *Fastener Test Methods: Method 13 Double Shear Test*, NASM1312, 1997.

87. Considère, A.G., *Memoire sur l'Emploi du Fer et de l'Acier dans les Constructions,* Annales des Ponts et Chaussées, vol. 9, no. 6, pp. 574-775, 1885.

88. Havner, K.S., *On the Onset of Necking in the Tensile Test,* International Journal of Plasticity, vol. 20, no. 4-5, pp. 965-978, 2004.

89. ASTM International, *Standard Test Methods and Definitions for Mechanical Testing of Steel Products,* A370-14, 2014.

90. Society of Automotive Engineers (SAE), *Instrumentation for Impact Test - Part 1 - Electronic Instrumentation,* in SAE J211/1 MAR95, New York, NY, July, 2007.

91. Hill, R. *The Mathematical Theory of Plasticity,* Oxford: The University Press, 1998.

92. Ling, Y., *Uniaxial True Stress-Strain after Necking,* AMP Journal of Technology, vol. 5, pp. 37-48, 1996.

10 APPENDICES

Appendix A. Xue-Wierzbicki Failure Surface Fitting MATLAB Code

```
function XueSurface(TestData,DisplayData)


%% Xue Failure Surface Equation

% Assume n=(1/6)
%% Xue Symmetrical Equation
%epsilonfailXue=C1*exp(-C2*eta)-(C1*exp(-C2.*eta)-C3*exp(-C4*eta))*(1-
(abs(xi)).^(1/(1/6))).^(1/6);

%% The data is split into 3 vectors for curve/surface fitting app
dataxi=(TestData.AverageLodeAngle);
dataeta=(TestData.AverageTriaxiality);
datafail=(TestData.EffectivePlasticStrainatFailure);

if istable(DisplayData) == 1
    displaydataxi=(DisplayData.AverageLodeAngle);
    displaydataeta=(DisplayData.AverageTriaxiality);
    displaydatafail=(DisplayData.EffectivePlasticStrainatFailure);
    j=1;
    for i=1:length(displaydataeta)
        if DisplayData.IsPlaneStress(i)==1
            displaydataxiPS(j)=DisplayData.AverageLodeAngle(i);
            displaydataetaPS(j)=DisplayData.AverageTriaxiality(i);

displaydatafailPS(j)=DisplayData.EffectivePlasticStrainatFailure(i);
            j=j+1;
        end
    end
else
    j=1;
    for i=1:length(dataeta)
        if TestData.IsPlaneStress(i)==1
            displaydataxiPS(j)=TestData.AverageLodeAngle(i);
            displaydataetaPS(j)=TestData.AverageTriaxiality(i);

displaydatafailPS(j)=TestData.EffectivePlasticStrainatFailure(i);
            j=j+1;
        end
    end
end

%% Perform Curve Fit
[fitresult, gof, coefs] = XueFit1(dataxi, dataeta, datafail);

display(coefs);
C1=coefs(1);
C2=coefs(2);
C3=coefs(3);
C4=coefs(4);
```

```
%% Define density of surface etc.
density=50;
%density=253 is the largest density available to plot surface in excel
without array reduction
eta=linspace(-1/3,1,density);
xi=linspace(-1,1,density);

%% Compute failure surface
failure=zeros(density,density);
for xicount=1:density
   for etacount=1:density
       failure(etacount,xicount) = xuecalc(xi(xicount),eta(etacount));
   end
end

%Check for imaginary numbers in surfrace
for etacount=1:density
%    display(eta(etacount))
   for xicount=1:density
%       display(xicount)
       if isreal(failure(xicount,etacount))
       else
           display(etacount);
           display(xicount);
           display('error');
       end
   end
end

%% Compute Plane Stress Curve etc.

%Plane Stress Curve
densityfactor=1000;
xips=zeros(1,round(density*2/3*densityfactor));
pscount=0;
etaps=linspace(-1/3,1,density*densityfactor);
while min(xips)>-1.0000000001
    pscount=pscount+1;
    xips(pscount)=-27/2.*etaps(pscount).*(etaps(pscount).^2-1/3);
    %display(pscount)
end

etaps2=linspace(-1/3,2/3,density*densityfactor);
xips2=-27./2.*etaps2.*(etaps2.^2-1./3);

%Make 3D curve using Plane Stress relationship
failureps=zeros(length(xips2),1);
for pscount2=1:length(xips2)
        %failureps(pscount2)=xuepscalc(C1,C2,C3,C4,etaps(pscount2));
        %failureps(pscount2)=xuepscalc(etaps(pscount2));

failureps(pscount2)=fitresult(xips2(pscount2),etaps2(pscount2));
        %display(pscount2)
```

```
end

failurepsUpper=zeros(length(etaps),1);
failurepsLower=zeros(length(etaps),1);
failureps2DXue=zeros(length(etaps),1);
for pscount4=1:length(etaps)
        %failurepsUpper(pscount4)=xueupper(etaps(pscount4));
        %failurepsLower(pscount4)=xuelower(etaps(pscount4));
        failurepsUpper(pscount4)=fitresult(-1,etaps(pscount4));
        failurepsLower(pscount4)=fitresult(0,etaps(pscount4));

failureps2DXue(pscount4)=fitresult(xips2(pscount4),etaps2(pscount4));
        %display(pscount4)
end


%% Plane Stress 2D Plot
    failureps2DXueUpper=failurepsUpper;
    failureps2DXueLower=failurepsLower;
%Compute 2D Curve for Failure Strain vs. Triax.

%2D Plane Stress Plot Bai Data
fig2d=figure;
hold on
cc=hsv(3);
h(1)=plot(etaps2,failureps2DXue,'color',cc(1,:),'LineWidth',2);
h(2)=plot(etaps,failureps2DXueLower,'color',cc(2,:),'LineWidth',2);
h(3)=plot(etaps,failureps2DXueUpper,'color',cc(3,:),'LineWidth',2);
h(4)=scatter(dataeta, datafail);
set(h(4),'SizeData',50);
set(h(4),'LineWidth',1.5);
% if max(dataeta)>1
%     axis([-0.333,1.1,0,ceil(max(failureps2DBaiUpper))])
% elseif max(dataeta)>0.6
%     axis([-0.333,1.0,0,ceil(max(failureps2DBaiUpper))])
% else
%     axis([-0.333,0.666,0,ceil(max(failureps2DBaiUpper))])
% end
if ceil(max(failureps2DXueUpper))>5
    maxz=3;
else

maxz=ceil(2*max([max(failureps2DXue),max(failureps2DXueUpper),1]))/2;
end

if max(dataeta)>1
    etaaxis=1.05;
else
    etaaxis=1;
end

axis([-0.333,etaaxis,0,maxz])
grid on
title(char(sprintf('2-Dimensional Plot of\nXue and Wierzbicki Method
Using %s for Calibration',char(TestData.Name(1)))))
xlabel('Triaxiality')
```

```
ylabel('Eff. Plastic Strain at Failure')
h(5)=scatter(displaydataetaPS,displaydatafailPS,'*','k','LineWidth',0.7
5,'SizeData',40);
legendnames{1}='Plain Stress Curve';
legendnames{2}='Plane Strain-Lower Bound';
legendnames{3}='Axial Symmetry-Upper Bound';
legendnames{4}=sprintf('Calibration Tests: %s',char(TestData.Name(1)));
legendnames{5}='Plane Stress Tests';
legend(h,legendnames{1},legendnames{2},legendnames{3},legendnames{4},le
gendnames{5});

hold off

%% 3D Surface Plot Surface previously computed

%3D Plot
fig3d=figure;
hold on
k(1)=surface(xi,eta,failure,'FaceAlpha',0.8','EdgeColor','k','LineWidth
',1,'EdgeAlpha',0.4,'facecolor','interp');
cview=[140,40];
view(cview)
xlabel('Lode Parameter')
ylabel('Triaxiality')
zlabel('Eff. Plastic Strain at Failure')
xhandle=get(gca,'xlabel');
set(xhandle,'fontsize',8)
yhandle=get(gca,'ylabel');
set(yhandle,'fontsize',8)
zhandle=get(gca,'zlabel');
set(zhandle,'fontsize',8)
caxis([min(min(failure)),min(maxz,max(max(failure)))]);
%shading interp
colorbar('Location','EastOutside','AxisLocation','in','FontSize',8)
%colorbar EastOutside
grid on

xyzrange=[-1,1,-1/3,etaaxis,0,maxz];
axis(xyzrange)
t1=title(char(sprintf('3-Dimensional Plot of\nXue and Wierzbicki Method
Using %s for Calibration',char(TestData.Name(1)))));
set(t1,'FontSize',8)
tiPos=get(t1,'position');
set(t1,'position',tiPos+[0 0 0.1*(xyzrange(6)-xyzrange(5))]);
%set(gca, 'CameraPosition',[20 10 10])
set(gca,'Position',[.1,.275,.75,.620])
g(1)=plot3(xips2,etaps2,failureps,'color',cc(1,:),'LineWidth',2);
g(2)=plot3(zeros(1,length(etaps)),etaps,failurepsLower,'color',cc(2,:),
'LineWidth',2);
g(3)=plot3((zeros(1,length(etaps))+1),etaps,failurepsUpper,'color','k',
'LineWidth',2);
g(4)=plot3((zeros(1,length(etaps))-
1),etaps,failurepsUpper,'color','k','LineWidth',2);
%Plot calibration tests as scatter
g(5)=scatter3(dataxi,dataeta,datafail,'LineWidth',1,'MarkerEdgeColor','
k','MarkerFaceColor','r');
```

```
if istable(DisplayData) == 1
    %Plot all tests if partial tests used for calibration

g(6)=scatter3(displaydataxi,displaydataeta,displaydatafail,'*','k');
    legendnames{5}='All Tests';
    gleg=legend(g([1,2,4,5,6]),legendnames{[1:5]});
    set(gleg,'FontSize',8);
    set(gleg,'Position',[0.33,0.075,0.33,0.1]);
else
    gleg=legend(g([1,2,4,5]),legendnames{[1:4]});
    set(gleg,'FontSize',8);
    set(gleg,'Position',[0.33,0.05,0.33,0.1]);
end
set(gcf, 'PaperPositionMode', 'auto');

%% Contour Plot
figcont=figure;
hold on
grid on
density=199;
%density=253 is the largest density available to plot surface in excel
without array reduction
eta=linspace(-1/3,1,density);
xi=linspace(-1,1,density);
[X,Y] = meshgrid(xi,eta);
Z=zeros(length(eta),length(xi));
for indexxi=1:length(xi)
    for indexeta=1:length(eta)
        Z(indexeta,indexxi)=xuecalc(xi(indexxi),eta(indexeta));
    end
end
%[C_cont,h_cont]=contour(X,Y,Z,'LineWidth',2);
%[C_cont,h_cont]=contour(X,Y,Z,linspace(min(min(Z)),maxz,20),'LineWidth
',2);
%[C_cont,h_cont]=contour(X,Y,Z,linspace(0,1,21),'LineWidth',2);
[C_cont,h_cont]=contour(X,Y,Z,linspace(0,2,41),'LineWidth',2);
%clabel(C_cont,h_cont,'LabelSpacing',1000,'FontSize',8);
%ch=clabel(C_cont,h_cont,'manual');
%set(ch,'margin',2,'backgroundcolor','w')
clabel(C_cont,h_cont);
[Loweta,Lowxi] = find(Z == min(min(Z)));
[Higheta,Highxi] = find(Z == max(max(Z)));
xlabel('Lode Parameter')
ylabel('Triaxiality')
title(char(sprintf('Calibration Tests: %s Using Xue and Wierzbicki
Method\nContour Plot',char(TestData.Name(1)))))
title(char(sprintf('Contour Plot of\nXue and Wierzbicki Method Using %s
for Calibration',char(TestData.Name(1)))))

% Plot and annotate the Max and Min
color=jet(255);
for index=1:length(Lowxi);


plot(xi(Lowxi(index)),eta(Loweta(index)),'x','MarkerEdgeColor',color(1,
:),'LineWidth',2,'MarkerSize',10)
```

```
    minvalue{index}=sprintf('Min at
%0.4f',Z(Loweta(index),Lowxi(index)));
    if xi(Lowxi(index))<0
        text(xi(Lowxi(index)),eta(Loweta(index)),['
','\leftarrow',char(minvalue(index))]);
    else

text(xi(Lowxi(index)),eta(Loweta(index)),[char(minvalue(index)),'\right
arrow',' '],'HorizontalAlignment','Right')
    end;
end
for index=1:length(Highxi);

plot(xi(Highxi(index)),eta(Higheta(index)),'x','MarkerEdgeColor',color(
255,:),'LineWidth',2,'MarkerSize',10)
    maxvalue{index}=sprintf('Max at
%0.4f',Z(Higheta(index),Highxi(index)));
    if xi(Highxi(index))<0
        text(xi(Highxi(index)),eta(Higheta(index)),['
','\leftarrow',char(maxvalue(index))])
    else

text(xi(Highxi(index)),eta(Higheta(index)),[char(maxvalue(index)),'\rig
htarrow',' '],'HorizontalAlignment','Right')
    end
end
alphable = findobj(h_cont, '-property', 'EdgeAlpha');
set(alphable, 'EdgeAlpha', 0.8);

%% Plot Residual Analysis
figresid=figure;
plot(fitresult,[dataxi,dataeta],datafail,'Style','Residuals');
axis([-1,1,-1/3,etaaxis])
title(char(sprintf('Residuals Plot of\nXue and Wierzbicki Method Using
%s for Calibration\nRSquare= %0.5f\nSSE=
%0.5f',char(TestData.Name(1)),gof.rsquare,gof.sse)))
view(cview)
xlabel('Lode Parameter')
ylabel('Triaxiality')
zlabel('Residual')

figpred=figure;
plot(fitresult,[dataxi,dataeta],datafail,'Style','predfunc')
title(char(sprintf('95 Percent Confidence Interval Plot of\nXue and
Wierzbicki Method Using %s for Calibration',char(TestData.Name(1)))))
view(cview)
xlabel('Lode Parameter')
ylabel('Triaxiality')
zlabel('Eff. Plastic Strain at Failure')

%% Output Script
OutputMessage=msgbox({'Saving Figures' 'Please Wait'});
method='Xue_Surf';
outputfolder=sprintf('output_%s\\',method);
nn=1;
plotname{nn}='2d-Plot';
```

```
nn=nn+1;
plotname{nn}='3d-Plot';
nn=nn+1;
plotname{nn}='Cont-Plot';
nn=nn+1;
plotname{nn}='Resid-Plot';
nn=nn+1;
%plotname{nn}='Pred-Plot';

nn=1;
figurenames(nn)=fig2d;
nn=nn+1;
figurenames(nn)=fig3d;
nn=nn+1;
figurenames(nn)=figcont;
nn=nn+1;
figurenames(nn)=figresid;
nn=nn+1;
%figurenames(nn)=figpred;

if(exist(outputfolder) ~= 7)
    mkdir(outputfolder);
    fileattrib(outputfolder,'+w')
end
for i=1:length(figurenames);

pathname=sprintf('%s%s_%s_w_%s',outputfolder,plotname{i},char(TestData.
Name(1)),method);
    delete(sprintf('%s.eps',pathname));
    delete(sprintf('%s.png',pathname));
    print(figurenames(i),pathname,'-dpng','-r600');
    %print(figurenames(i),pathname,'-depsc2','-r300', '-opengl');
end
delete(OutputMessage);

%% Function to calculate failure strain
function failurevalue = xuecalc(xifun,etafun)
%failurevalue=C1*exp(-C2*eta)-(C1*exp(-C2.*eta)-C3*exp(-C4*eta))*(1-
(abs(xi)).^(1/(1/6))).^(1/6);
failurevalue=fitresult(xifun,etafun);
end

%% Function to calculate failure strain at PS conditions
function failurevalue= xuepscalc(etafun)
%failurevalue=C1*exp(-C2*eta)-(C1*exp(-C2.*eta)-C3*exp(-C4*eta))*(1-
(abs((-27/2.*eta.*(eta.^2-1/3)))).^(1/(1/6))).^(1/6);
xifun=-27/2.*etafun.*(etafun.^2-1/3);
failurevalue=fitresult(xifun,etafun);
end

%% Function to calculate the upper bound

function failurevalue = xueupper(etafun)
        %failurevalue=(C1*exp(-C2*eta));
        failurevalue=fitresult(1,etafun);
end
```

```
%% Function to calculate the lower bound

function failurevalue = xuelower(etafun)
        %failurevalue=(C3*exp(-C4*eta));
        failurevalue=fitresult(0,etafun);
end


%%
function [fitresultfun, gof, coefs] = XueFit1(dataXuexi, dataXueeta,
dataXuefail)
%CREATEFIT2(dataXueXI,dataXueETA,dataXueFAIL)
%  Create a fit.
%
%  Data for 'untitled fit 1' fit:
%      X Input : dataXuexi
%      Y Input : dataXueeta
%      Z Output: dataXuefail
%  Output:
%      fitresult : a fit object representing the fit.
%      gof : structure with goodness-of fit info.
%
%  See also FIT, CFIT, SFIT.

%  Auto-generated by MATLAB on 18-Sep-2014 18:37:44


% Fit: 'Xue Wierzbicki Fit'.

[xData, yData, zData] = prepareSurfaceData( dataXuexi, dataXueeta,
dataXuefail );

% Set up fittype and options.
ft = fittype( 'C1*exp(-C2*y)-(C1*exp(-C2.*y)-C3*exp(-C4*y))*(1-
(abs(x)).^(1/(1/6))).^(1/6)', 'independent', {'x', 'y'}, 'dependent',
'z' );
opts = fitoptions( 'Method', 'NonlinearLeastSquares' );
opts.Display = 'Off';
opts.MaxFunEvals = 6000;
opts.MaxIter = 4000;
opts.StartPoint = [0.416799467930787 0.656859890973707
0.627973359190104 0.291984079961715];
opts.TolFun = 1e-09;
opts.TolX = 1e-09;

% Fit model to data.
[fitresultfun, gof, output] = fit( [xData, yData], zData, ft, opts );

coefs = coeffvalues(fitresultfun);

end

end
```

Appendix B. Bai (Symmetrical) Failure Surface Fitting MATLAB Code

```
function BaiSurface(TestData,DisplayData)


%% Bai Failure Surface Equation

%% Bai Symmetrical Equation
%epsilonfailBai=(DB1*exp(-DB2*eta)-DB3*exp(-DB4*eta))*xi^2+DB3*exp(-
DB4*eta);

%% The data is split into 3 vectors for curve/surface fitting app
dataxi=(TestData.AverageLodeAngle);
dataeta=(TestData.AverageTriaxiality);
datafail=(TestData.EffectivePlasticStrainatFailure);

if istable(DisplayData) == 1
    displaydataxi=(DisplayData.AverageLodeAngle);
    displaydataeta=(DisplayData.AverageTriaxiality);
    displaydatafail=(DisplayData.EffectivePlasticStrainatFailure);
    j=1;
    for i=1:length(displaydataeta)
        if DisplayData.IsPlaneStress(i)==1
            displaydataxiPS(j)=DisplayData.AverageLodeAngle(i);
            displaydataetaPS(j)=DisplayData.AverageTriaxiality(i);

displaydatafailPS(j)=DisplayData.EffectivePlasticStrainatFailure(i);
            j=j+1;
        end
    end
else
    j=1;
    for i=1:length(dataeta)
        if TestData.IsPlaneStress(i)==1
            displaydataxiPS(j)=TestData.AverageLodeAngle(i);
            displaydataetaPS(j)=TestData.AverageTriaxiality(i);

displaydatafailPS(j)=TestData.EffectivePlasticStrainatFailure(i);
            j=j+1;
        end
    end
end

%% Perform Curve Fit
[fitresult, gof, coefs] = createFit1(dataxi, dataeta, datafail);

display(coefs);
DB1=coefs(1);
DB2=coefs(2);
DB3=coefs(3);
DB4=coefs(4);
```

```
%% Define density of surface etc.
density=50;
eta=linspace(-1/3,1,density);
xi=linspace(-1,1,density);

%% Compute failure surface
failure=zeros(density,density);
for xicount=1:density
   for etacount=1:density
       failure(etacount,xicount) =
baicalc(DB1,DB2,DB3,DB4,xi(xicount),eta(etacount));
   end
end

%Check for imaginary numbers in surfrace
for etacount=1:density
%    display(eta(etacount))
   for xicount=1:density
%       display(xicount)
       if isreal(failure(xicount,etacount))
       else
           display(etacount);
           display(xicount);
           display('error');
       end
   end
end

%% Compute Plane Stress Curve etc.

%Plane Stress Curve
densityfactor=3000;
xips=zeros(1,round(density*2/3*densityfactor));
pscount=0;
etaps=linspace(-1/3,1,density*densityfactor);
while min(xips)>-1.0001
    pscount=pscount+1;
    xips(pscount)=-27/2.*etaps(pscount).*(etaps(pscount).^2-1/3);
end

%Make 3D curve using Plane Stress relationship
failureps=zeros(length(xips),1);
for pscount2=1:length(xips)
        failureps(pscount2)=baipscalc(DB1,DB2,DB3,DB4,etaps(pscount2));
end

failurepsUpper=zeros(length(etaps),1);
for pscount4=1:length(etaps)
        failurepsUpper(pscount4)=baiupper(DB1,DB2,etaps(pscount4));
end

failurepsLower=zeros(length(etaps),1);
for pscount4=1:length(etaps)
        failurepsLower(pscount4)=bailower(DB3,DB4,etaps(pscount4));
end
```

```
%% Plane Stress 2D Plot

%Compute 2D Curve for Failure Strain vs. Triax.
failureps2DBai=zeros(length(etaps),1);
for pscount3=1:length(etaps)

failureps2DBai(pscount3)=baipscalc(DB1,DB2,DB3,DB4,etaps(pscount3));
end

failureps2DBaiUpper=zeros(length(etaps),1);
for pscount3=1:length(etaps)
    failureps2DBaiUpper(pscount3)=baiupper(DB1,DB2,etaps(pscount3));
end

failureps2DBaiLower=zeros(length(etaps),1);
for pscount3=1:length(etaps)
    failureps2DBaiLower(pscount3)=bailower(DB3,DB4,etaps(pscount3));
end



%2D Plane Stress Plot Bai Data
fig2d=figure;
hold on
cc=hsv(3);
h(1)=plot(etaps(1:pscount-1),failureps2DBai(1:pscount-
1),'color',cc(1,:),'LineWidth',2);
h(2)=plot(etaps,failureps2DBaiLower,'color',cc(2,:),'LineWidth',2);
h(3)=plot(etaps,failureps2DBaiUpper,'color',cc(3,:),'LineWidth',2);
h(4)=scatter(dataeta, datafail);
set(h(4),'SizeData',50);
set(h(4),'LineWidth',1.5);
% if max(dataeta)>1
%     axis([-0.333,1.1,0,ceil(max(failureps2DBaiUpper))])
% elseif max(dataeta)>0.6
%     axis([-0.333,1.0,0,ceil(max(failureps2DBaiUpper))])
% else
%     axis([-0.333,0.666,0,ceil(max(failureps2DBaiUpper))])
% end
if ceil(max(failureps2DBaiUpper))>5
    maxz=3;
else
    maxz=ceil(5*max(failureps2DBaiUpper))/5;
end

if max(dataeta)>1
    etaaxis=1.05;
else
    etaaxis=1;
end

axis([-0.333,etaaxis,0,maxz])
grid on
```

```
title(char(sprintf('2-Dimensional Plot of\nBai Method Using %s for
Calibration',char(TestData.Name(1)))))
xlabel('Triaxiality')
ylabel('Eff. Plastic Strain at Failure')
h(5)=scatter(displaydataetaPS,displaydatafailPS,'*','k','LineWidth',0.7
5,'SizeData',40);
legendnames{1}='Plain Stress Curve';
legendnames{2}='Plane Strain-Lower Bound';
legendnames{3}='Axial Symmetry-Upper Bound';
legendnames{4}=sprintf('Calibration Tests: %s',char(TestData.Name(1)));
legendnames{5}='Plane Stress Tests';
legend(h,legendnames{1},legendnames{2},legendnames{3},legendnames{4},le
gendnames{5});

hold off


%% 3D Surface Plot Surface previously computed

%3D Plot
fig3d=figure;
hold on
k(1)=surface(xi,eta,failure,'FaceAlpha',0.8','EdgeColor','k','LineWidth
',1,'EdgeAlpha',0.4,'facecolor','interp');
xlabel('Lode Parameter')
ylabel('Triaxiality')
zlabel('Eff. Plastic Strain at Failure')
caxis([min(min(failure)),min(maxz,max(max(failure)))]);
%shading interp
colorbar('Location','EastOutside','AxisLocation','in','FontSize',8)
%colorbar EastOutside
grid on

axis([-1,1,-1/3,etaaxis,0,maxz])
t1=title(char(sprintf('3-Dimensional Plot of\nBai Method Using %s for
Calibration',char(TestData.Name(1))))));
set(t1,'FontSize',9)
cview=[140,40];
view(cview)
%set(gca, 'CameraPosition',[20 10 10])
set(gca,'Position',[.1,.275,.75,.620])
g(1)=plot3(xips,etaps(1:length(xips)),failureps,'color',cc(1,:),'LineWi
dth',2);
g(2)=plot3(zeros(1,length(etaps)),etaps,failurepsLower,'color',cc(2,:),
'LineWidth',2);
g(3)=plot3((zeros(1,length(etaps))+1),etaps,failurepsUpper,'color','k',
'LineWidth',2);
g(4)=plot3((zeros(1,length(etaps))-
1),etaps,failurepsUpper,'color','k','LineWidth',2);
%Plot calibration tests as scatter
g(5)=scatter3(dataxi,dataeta,datafail,'LineWidth',1,'MarkerEdgeColor','
k','MarkerFaceColor','r');
if istable(DisplayData) == 1
    %Plot all tests if partial tests used for calibration

g(6)=scatter3(displaydataxi,displaydataeta,displaydatafail,'*','k');
```

```
    legendnames{5}='All Tests';
    gleg=legend(g([1,2,4,5,6]),legendnames{[1:5]});
    set(gleg,'FontSize',8);
    set(gleg,'Position',[0.33,0.075,0.33,0.1]);
else
    gleg=legend(g([1,2,4,5]),legendnames{[1:4]});
    set(gleg,'FontSize',8);
    set(gleg,'Position',[0.33,0.05,0.33,0.1]);
end
set(gcf, 'PaperPositionMode', 'auto');

%% Contour Plot
figcont=figure;
hold on
grid on
density=199;
eta=linspace(-1/3,1,density);
xi=linspace(-1,1,density);
[X,Y] = meshgrid(xi,eta);
Z=zeros(length(eta),length(xi));
for indexxi=1:length(xi)
    for indexeta=1:length(eta)

Z(indexeta,indexxi)=baicalc(DB1,DB2,DB3,DB4,xi(indexxi),eta(indexeta));
    end
end
%[C_cont,h_cont]=contour(X,Y,Z,linspace(min(min(Z)),min(1.5,max(max(Z))
),20),'LineWidth',2);
%[C_cont,h_cont]=contour(X,Y,Z,'LineWidth',2);
%[C_cont,h_cont]=contour(X,Y,Z,linspace(min(min(Z)),maxz,20),'LineWidth
',2);
%[C_cont,h_cont]=contour(X,Y,Z,linspace(0,1,21),'LineWidth',2);
[C_cont,h_cont]=contour(X,Y,Z,linspace(0,2,41),'LineWidth',2);
%clabel(C_cont,h_cont,'LabelSpacing',1000,'FontSize',8);
%clabel(C_cont,h_cont,'manual');
clabel(C_cont,h_cont);
[Loweta,Lowxi] = find(Z == min(min(Z)));
[Higheta,Highxi] = find(Z == max(max(Z)));
xlabel('Lode Parameter')
ylabel('Triaxiality')
title(char(sprintf('Contour Plot of\nBai Method Using %s for
Calibration',char(TestData.Name(1)))))
% Plot and annotate the Max and Min
color=jet(255);
for index=1:length(Lowxi);

plot(xi(Lowxi(index)),eta(Loweta(index)),'x','MarkerEdgeColor',color(1,
:),'LineWidth',2,'MarkerSize',10)
    minvalue{index}=sprintf('Min at
%0.4f',Z(Loweta(index),Lowxi(index)));
    if xi(Lowxi(index))<0
        text(xi(Lowxi(index)),eta(Loweta(index)),['
',\leftarrow',char(minvalue(index))]);
    else

text(xi(Lowxi(index)),eta(Loweta(index)),[char(minvalue(index)),'\right
arrow',' '],'HorizontalAlignment','Right')
```

```
    end;
end
for index=1:length(Highxi);

plot(xi(Highxi(index)),eta(Higheta(index)),'x','MarkerEdgeColor',color(
255,:),'LineWidth',2,'MarkerSize',10)
    maxvalue{index}=sprintf('Max at
%0.4f',Z(Higheta(index),Highxi(index)));
    if xi(Highxi(index))<0
        text(xi(Highxi(index)),eta(Higheta(index)),['
','\leftarrow',char(maxvalue(index))])
    else

text(xi(Highxi(index)),eta(Higheta(index)),[char(maxvalue(index)),'\rig
htarrow',' '],'HorizontalAlignment','Right')
    end
end
alphable = findobj(h_cont, '-property', 'EdgeAlpha');
set(alphable, 'EdgeAlpha', 0.8);



%% Plot Residual Analysis
figresid=figure;
plot(fitresult,[dataxi,dataeta],datafail,'Style','Residuals')
axis([-1,1,-1/3,etaaxis])
title(char(sprintf('Residuals Plot of\nBai Method Using %s for
Calibration\nRSquare= %0.5f\nSSE=
%0.5f',char(TestData.Name(1)),gof.rsquare,gof.sse)))
view(cview)
xlabel('Lode Parameter')
ylabel('Triaxiality')
zlabel('Residual')

figpred=figure;
plot(fitresult,[dataxi,dataeta],datafail,'Style','predfunc')
title(char(sprintf('95 Percent Confidence Interval Plot of\nBai Method
Using %s for Calibration',char(TestData.Name(1)))))
view(cview)
xlabel('Lode Parameter')
ylabel('Triaxiality')
zlabel('Eff. Plastic Strain at Failure')

%% Output Script
OutputMessage=msgbox({'Saving Figures' 'Please Wait'});
method='Bai_Surf';
outputfolder=sprintf('output_%s\\',method);
nn=1;
plotname{nn}='2d-Plot';
nn=nn+1;
plotname{nn}='3d-Plot';
nn=nn+1;
plotname{nn}='Cont-Plot';
nn=nn+1;
plotname{nn}='Resid-Plot';
nn=nn+1;
```

```
%plotname{nn}='Pred-Plot';

nn=1;
figurenames(nn)=fig2d;
nn=nn+1;
figurenames(nn)=fig3d;
nn=nn+1;
figurenames(nn)=figcont;
nn=nn+1;
figurenames(nn)=figresid;
nn=nn+1;
%figurenames(nn)=figpred;

if(exist(outputfolder) ~= 7)
    mkdir(outputfolder);
    fileattrib(outputfolder,'+w')
end
for i=1:length(figurenames);

pathname=sprintf('%s%s_%s_w_%s',outputfolder,plotname{i},char(TestData.
Name(1)),method);
    delete(sprintf('%s.eps',pathname));
    delete(sprintf('%s.png',pathname));
    print(figurenames(i),pathname,'-dpng','-r600');
    %print(figurenames(i),pathname,'-depsc2','-r300', '-opengl');
end
delete(OutputMessage);

%% Function to calculate failure strain
function failurevalue = baicalc(DB1,DB2,DB3,DB4,xi,eta)
failurevalue=(DB1*exp(-DB2*eta)-DB3*exp(-DB4*eta))*xi^2+DB3*exp(-
DB4*eta);
end

%% Function to calculate failure strain at PS conditions
function failurevalue= baipscalc(DB1,DB2,DB3,DB4,eta)
failurevalue=(DB1*exp(-DB2*eta)-DB3*exp(-DB4*eta))*(-
27/2.*eta.*(eta.^2-1/3))^2+DB3*exp(-DB4*eta);
%xi=-27/2.*etaps.*(etaps.^2-1/3)
end

%% Function to calculate the upper bound

function failurevalue = baiupper(DB1,DB2,eta)
        failurevalue=(DB1*exp(-DB2*eta));
end

%% Function to calculate the lower bound

function failurevalue = bailower(DB3,DB4,eta)
        failurevalue=(DB3*exp(-DB4*eta));
end


%%
```

```
function [fitresult, gof, coefs] = createFit1(dataxi, dataeta,
datafail)
%CREATEFIT1(DATABAIXI,DATABAIETA,DATABAIFAIL)
%  Create a fit.
%
%  Data for 'createFit1' fit:
%      X Input : dataxi
%      Y Input : dataeta
%      Z Output: datafail
%  Output:
%      fitresult : a fit object representing the fit.
%      gof : structure with goodness-of fit info.
%
%  See also FIT, CFIT, SFIT.

%  Auto-generated by MATLAB on 18-Sep-2014 18:37:44


% Fit: 'Bai Wierzbicki Fit'.

[xData, yData, zData] = prepareSurfaceData( dataxi, dataeta, datafail
);

% Set up fittype and options.
ft = fittype( '(DB1*exp(-DB2*y)-DB3*exp(-DB4*y))*x^2+DB3*exp(-DB4*y)',
'independent', {'x', 'y'}, 'dependent', 'z' );
opts = fitoptions( 'Method', 'NonlinearLeastSquares' );
opts.Display = 'Off';
opts.MaxFunEvals = 6000;
opts.MaxIter = 4000;
opts.StartPoint = [0.416799467930787 0.656859890973707
0.627973359190104 0.291984079961715];
opts.TolFun = 1e-09;
opts.TolX = 1e-09;

% Fit model to data.
[fitresult, gof, output] = fit( [xData, yData], zData, ft, opts );

coefs = coeffvalues(fitresult);

end

end
```

Appendix C. Bai (Asymmetrical) Failure Surface Fitting MATLAB Code

```
function BaiSurfaceAsym(TestData,DisplayData)


%% Bai Failure Surface Equation

%% Bai Asymmetrical Equation
%epsilonfailBai=(0.5*(DB1*exp(-DB2*eta)-DB5*exp(-
DB6*eta)))*xi^2+0.5*(DB1*exp(-DB2*eta)-DB5*exp(-DB6*eta))*xi+DB3*exp(-
DB4*eta);

%% The data is split into 3 vectors for curve/surface fitting app
dataxi=(TestData.AverageLodeAngle);
dataeta=(TestData.AverageTriaxiality);
datafail=(TestData.EffectivePlasticStrainatFailure);

if istable(DisplayData) == 1
    displaydataxi=(DisplayData.AverageLodeAngle);
    displaydataeta=(DisplayData.AverageTriaxiality);
    displaydatafail=(DisplayData.EffectivePlasticStrainatFailure);
    j=1;
    for i=1:length(displaydataeta)
        if DisplayData.IsPlaneStress(i)==1
            displaydataxiPS(j)=DisplayData.AverageLodeAngle(i);
            displaydataetaPS(j)=DisplayData.AverageTriaxiality(i);

displaydatafailPS(j)=DisplayData.EffectivePlasticStrainatFailure(i);
            j=j+1;
        end
    end
else
    j=1;
    for i=1:length(dataeta)
        if TestData.IsPlaneStress(i)==1
            displaydataxiPS(j)=TestData.AverageLodeAngle(i);
            displaydataetaPS(j)=TestData.AverageTriaxiality(i);

displaydatafailPS(j)=TestData.EffectivePlasticStrainatFailure(i);
            j=j+1;
        end
    end
end

%% Perform Curve Fit
[fitresult, gof, coefs] = createFit1(dataxi, dataeta, datafail);

display(coefs);
DB1=coefs(1);
DB2=coefs(2);
DB3=coefs(3);
DB4=coefs(4);
```

```
DB5=coefs(5);
DB6=coefs(6);


%% Define density of surface etc.
density=50;
%density=253 is the largest density available to plot surface in excel
without array reduction
eta=linspace(-1/3,1,density);
xi=linspace(-1,1,density);

%% Compute failure surface
failure=zeros(density,density);
for xicount=1:density
   for etacount=1:density
       failure(etacount,xicount) =
baicalc(DB1,DB2,DB3,DB4,DB5,DB6,xi(xicount),eta(etacount));
   end
end

%Check for imaginary numbers in surfrace
for etacount=1:density
%    display(eta(etacount))
   for xicount=1:density
%       display(xicount)
       if isreal(failure(xicount,etacount))
       else
           display(etacount);
           display(xicount);
           display('error');
       end
   end
end

%% Compute Plane Stress Curve etc.

%Plane Stress Curve
densityfactor=3000;
xips=zeros(1,round(density*2/3*densityfactor));
pscount=0;
etaps=linspace(-1/3,1,density*densityfactor);
while min(xips)>-1.0001
    pscount=pscount+1;
    xips(pscount)=-27/2.*etaps(pscount).*(etaps(pscount).^2-1/3);
end

%Make 3D curve using Plane Stress relationship
failureps=zeros(length(xips),1);
for pscount2=1:length(xips)

failureps(pscount2)=baipscalc(DB1,DB2,DB3,DB4,DB5,DB6,etaps(pscount2));
end

failurepsUpper=zeros(length(etaps),1);
for pscount4=1:length(etaps)
```

```
        failurepsUpper(pscount4)=baiupper(DB1,DB2,etaps(pscount4));
end

failurepsUpperOther=zeros(length(etaps),1);
for pscount4=1:length(etaps)

failurepsUpperOther(pscount4)=bailupperother(DB5,DB6,etaps(pscount4));
end

failurepsLower=zeros(length(etaps),1);
for pscount4=1:length(etaps)
        failurepsLower(pscount4)=bailower(DB3,DB4,etaps(pscount4));
end


%% Plane Stress 2D Plot

%Compute 2D Curve for Failure Strain vs. Triax.
failureps2DBai=zeros(length(etaps),1);
for pscount3=1:length(etaps)

failureps2DBai(pscount3)=baipscalc(DB1,DB2,DB3,DB4,DB5,DB6,etaps(pscoun
t3));
end

failureps2DBaiUpper=zeros(length(etaps),1);
for pscount3=1:length(etaps)
    failureps2DBaiUpper(pscount3)=baiupper(DB1,DB2,etaps(pscount3));
end

failureps2DBaiLower=zeros(length(etaps),1);
for pscount3=1:length(etaps)
    failureps2DBaiLower(pscount3)=bailower(DB3,DB4,etaps(pscount3));
end

failureps2DBaiUpperOther=zeros(length(etaps),1);
for pscount3=1:length(etaps)

failureps2DBaiUpperOther(pscount3)=bailupperother(DB5,DB6,etaps(pscount
3));
end


%2D Plane Stress Plot Bai Data
fig2d=figure;
hold on
cc=hsv(3);
colors=get(gca,'ColorOrder');
markercolor=colors(4,:);
h(1)=plot(etaps(1:pscount-1),failureps2DBai(1:pscount-
1),'color',cc(1,:),'LineWidth',2);
h(2)=plot(etaps,failureps2DBaiLower,'color',cc(2,:),'LineWidth',2);
h(3)=plot(etaps,failureps2DBaiUpper,'color',cc(3,:),'LineStyle','--
','LineWidth',2);
```

```
h(4)=plot(etaps,failureps2DBaiUpperOther,'color',cc(3,:),'LineStyle','-
.','LineWidth',2);
h(5)=scatter(dataeta, datafail,'MarkerEdgeColor',markercolor);
set(h(5),'SizeData',60);
set(h(5),'LineWidth',1.5);
% if max(dataeta)>1
%     axis([-0.333,1.1,0,ceil(max(failureps2DBaiUpper))])
% elseif max(dataeta)>0.6
%     axis([-0.333,1.0,0,ceil(max(failureps2DBaiUpper))])
% else
%     axis([-0.333,0.666,0,ceil(max(failureps2DBaiUpper))])
% end
if ceil(max(failureps2DBaiUpper))>5
    maxz=3;
else

maxz=ceil(2*max([round(max(failureps2DBaiUpper),2),round(max(failureps2
DBaiUpperOther),2),1]))/2;
end

if max(dataeta)>1
    etaaxis=1.05;
else
    etaaxis=1;
end

axis([-0.333,etaaxis,0,maxz])
grid on
title(char(sprintf('2-Dimensional Plot of\nBai (Asymmetric) Method
Using %s for Calibration',char(TestData.Name(1)))));
xlabel('Triaxiality')
ylabel('Eff. Plastic Strain at Failure')
h(6)=scatter(displaydataetaPS,displaydatafailPS,'*','k','LineWidth',0.7
5,'SizeData',25);
legendnames{1}='Plain Stress Curve';
legendnames{2}='Plane Strain-Lower Bound';
legendnames{3}='Axial Symmetry-Upper Bound, Lode= +1';
legendnames{4}='Axial Symmetry-Upper Bound, Lode= -1';
legendnames{5}=sprintf('Calibration Tests: %s',char(TestData.Name(1)));
legendnames{6}='Plane Stress Tests';
legend(h,legendnames{1},legendnames{2},legendnames{3},legendnames{4},le
gendnames{5},legendnames{6});

hold off


%% 3D Surface Plot Surface previously computed

%3D Plot
fig3d=figure;
hold on
k(1)=surface(xi,eta,failure,'FaceAlpha',0.8','EdgeColor','k','LineWidth
',1,'EdgeAlpha',0.4,'facecolor','interp');
cview=[140,40];
view(cview)
xhandle=xlabel('Lode Parameter');
```

```
yhandle=ylabel('Triaxiality');
zhandle=zlabel('Eff. Plastic Strain at Failure');
set(xhandle,'fontsize',8)
yhandle=get(gca,'ylabel');
set(yhandle,'fontsize',8)
zhandle=get(gca,'zlabel');
set(zhandle,'fontsize',8)
caxis([min(min(failure)),min(maxz,max(max(failure)))]);
%shading interp
colorbar('Location','EastOutside','AxisLocation','in','FontSize',8)
%colorbar EastOutside
grid on

xyzrange=[-1,1,-1/3,etaaxis,0,maxz];
axis(xyzrange)
t1=title(char(sprintf('3-Dimensional Plot of\nBai (Asymmetric) Method
Using %s for Calibration',char(TestData.Name(1)))));
set(t1,'FontSize',8.0)
tiPos=get(t1,'position');
set(t1,'position',tiPos+[0 0 0.1*(xyzrange(6)-xyzrange(5))]);
%set(gca, 'CameraPosition',[20 10 10])
set(gca,'Position',[.1,.275,.75,.620])
g(1)=plot3(xips,etaps(1:length(xips)),failureps,'color',cc(1,:),'LineWi
dth',2);
g(2)=plot3(zeros(1,length(etaps)),etaps,failurepsLower,'color',cc(2,:),
'LineWidth',2);
g(3)=plot3((zeros(1,length(etaps))+1),etaps,failurepsUpper,'color','k',
'LineStyle','--','LineWidth',2);
g(4)=plot3((zeros(1,length(etaps))-
1),etaps,failurepsUpperOther,'color','k','LineStyle','-
.','LineWidth',2);
%Plot calibration tests as scatter
g(5)=scatter3(dataxi,dataeta,datafail,'LineWidth',1,'MarkerEdgeColor','
k','MarkerFaceColor','r');
if istable(DisplayData) == 1
    %Plot all tests if partial tests used for calibration

g(6)=scatter3(displaydataxi,displaydataeta,displaydatafail,'*','k');
    legendnames{6}='All Tests';
    gleg=legend(g([1,2,3,4,5,6]),legendnames{[1:6]});
    set(gleg,'FontSize',8);
    set(gleg,'Position',[0.33,0.075,0.33,0.1]);
else
    gleg=legend(g([1,2,3,4,5]),legendnames{[1:5]});
    set(gleg,'FontSize',8);
    set(gleg,'Position',[0.33,0.05,0.33,0.1]);
end
set(gcf, 'PaperPositionMode', 'auto');

%% Contour Plot
figcont=figure;
hold on
grid on
density=199;
eta=linspace(-1/3,1,density);
xi=linspace(-1,1,density);
```

```
[X,Y] = meshgrid(xi,eta);
Z=zeros(length(eta),length(xi));
for indexxi=1:length(xi)
    for indexeta=1:length(eta)

Z(indexeta,indexxi)=baicalc(DB1,DB2,DB3,DB4,DB5,DB6,xi(indexxi),eta(ind
exeta));
    end
end
%[C_cont,h_cont]=contour(X,Y,Z,linspace(min(min(Z)),min(1.5,max(max(Z))
),20),'LineWidth',2);
%[C_cont,h_cont]=contour(X,Y,Z,'LineWidth',2);
%[C_cont,h_cont]=contour(X,Y,Z,linspace(min(min(Z)),maxz,20),'LineWidth
',2);
%[C_cont,h_cont]=contour(X,Y,Z,linspace(0,2,21),'LineWidth',2);
[C_cont,h_cont]=contour(X,Y,Z,linspace(0,2,41),'LineWidth',2);
%clabel(C_cont,h_cont,'LabelSpacing',1000,'FontSize',8);
%clabel(C_cont,h_cont,'manual');
clabel(C_cont,h_cont);

[Loweta,Lowxi] = find(Z == min(min(Z)));
[Higheta,Highxi] = find(Z == max(max(Z)));
xlabel('Lode Parameter')
ylabel('Triaxiality')
title(char(sprintf('Contour Plot of\nBai (Asymmetric) Method Using %s
for Calibration',char(TestData.Name(1)))))
% Plot and annotate the Max and Min
color=jet(255);
for index=1:length(Lowxi);


plot(xi(Lowxi(index)),eta(Loweta(index)),'x','MarkerEdgeColor',color(1,
:),'LineWidth',2,'MarkerSize',10)
    minvalue{index}=sprintf('Min at
%0.4f',Z(Loweta(index),Lowxi(index)));
    if xi(Lowxi(index))<0
        text(xi(Lowxi(index)),eta(Loweta(index)),['
','\leftarrow',char(minvalue(index))]);
    else

text(xi(Lowxi(index)),eta(Loweta(index)),[char(minvalue(index)),'\right
arrow',' '],'HorizontalAlignment','Right')
    end;
end
for index=1:length(Highxi);

plot(xi(Highxi(index)),eta(Higheta(index)),'x','MarkerEdgeColor',color(
255,:),'LineWidth',2,'MarkerSize',10)
    maxvalue{index}=sprintf('Max at
%0.4f',Z(Higheta(index),Highxi(index)));
    if xi(Highxi(index))<0
        text(xi(Highxi(index)),eta(Higheta(index)),['
','\leftarrow',char(maxvalue(index))])
    else
```

```
text(xi(Highxi(index)),eta(Higheta(index)),[char(maxvalue(index)),'\rig
htarrow',' '],'HorizontalAlignment','Right')
    end
end
alphable = findobj(h_cont, '-property', 'EdgeAlpha');
set(alphable, 'EdgeAlpha', 0.8);

%% Residual Analysis
figresid=figure;
plot(fitresult,[dataxi,dataeta],datafail,'Style','Residuals')
axis([-1,1,-1/3,etaaxis])
title(char(sprintf('Residuals Plot of\nBai (Asymmetric) Method Using %s
for Calibration\nRSquare= %0.5f\nSSE=
%0.5f',char(TestData.Name(1)),gof.rsquare,gof.sse)))
view(cview)
xlabel('Lode Parameter')
ylabel('Triaxiality')
zlabel('Residual')

figpred=figure;
plot(fitresult,[dataxi,dataeta],datafail,'Style','predfunc')
title(char(sprintf('95 Percent Confidence Interval Plot of\nBai
(Asymmetric) Method Using %s for Calibration',char(TestData.Name(1)))))
view(cview)
xlabel('Lode Parameter')
ylabel('Triaxiality')
zlabel('Eff. Plastic Strain at Failure')

%% Output Script
OutputMessage=msgbox({'Saving Figures' 'Please Wait'});
method='Bai_Asym_Surf';
outputfolder=sprintf('output_%s\\',method);
nn=1;
plotname{nn}='2d-Plot';
nn=nn+1;
plotname{nn}='3d-Plot';
nn=nn+1;
plotname{nn}='Cont-Plot';
nn=nn+1;
plotname{nn}='Resid-Plot';
nn=nn+1;
%plotname{nn}='Pred-Plot';

nn=1;
figurenames(nn)=fig2d;
nn=nn+1;
figurenames(nn)=fig3d;
nn=nn+1;
figurenames(nn)=figcont;
nn=nn+1;
figurenames(nn)=figresid;
nn=nn+1;
%figurenames(nn)=figpred;

if(exist(outputfolder) ~= 7)
```

```
    mkdir(outputfolder);
    fileattrib(outputfolder,'+w')
end
for i=1:length(figurenames);

pathname=sprintf('%s%s_%s_w_%s',outputfolder,plotname{i},char(TestData.
Name(1)),method);
    delete(sprintf('%s.eps',pathname));
    delete(sprintf('%s.png',pathname));
    print(figurenames(i),pathname,'-dpng','-r600');
    %print(figurenames(i),pathname,'-depsc2','-r300', '-opengl');
end
delete(OutputMessage);

%% Function to calculate failure strain
function failurevalue = baicalc(DB1,DB2,DB3,DB4,DB5,DB6,xi,eta)
failurevalue=(0.5*(DB1*exp(-DB2*eta)+DB5*exp(-DB6*eta))-DB3*exp(-
DB4*eta))*xi^2+0.5*(DB1*exp(-DB2*eta)-DB5*exp(-DB6*eta))*xi+DB3*exp(-
DB4*eta);
end

%% Function to calculate failure strain at PS conditions
function failurevalue= baipscalc(DB1,DB2,DB3,DB4,DB5,DB6,eta)
failurevalue=(0.5*(DB1*exp(-DB2*eta)+DB5*exp(-DB6*eta))-(DB3*exp(-
DB4*eta)))*(-27/2.*eta.*(eta.^2-1/3))^2+0.5*(DB1*exp(-DB2*eta)-
DB5*exp(-DB6*eta))*(-27/2.*eta.*(eta.^2-1/3))+DB3*exp(-DB4*eta);
%xi=-27/2.*etaps.*(etaps.^2-1/3)
end

%% Function to calculate the upper bound

function failurevalue = baiupper(DB1,DB2,eta)
        failurevalue=(DB1*exp(-DB2*eta));
end
%% Function to calculate the lower upper bound

function failurevalue = bailupperother(DB5,DB6,eta)
        failurevalue=(DB5*exp(-DB6*eta));
end
%% Function to calculate the lower bound

function failurevalue = bailower(DB3,DB4,eta)
        failurevalue=(DB3*exp(-DB4*eta));
end



%%
function [fitresult, gof, coefs] = createFit1(dataBaixi, dataBaieta,
dataBaifail)
%CREATEFIT1(DATABAIXI,DATABAIETA,DATABAIFAIL)
%  Create a fit.
%
%  Data for 'untitled fit 1' fit:
%      X Input : dataBaixi
%      Y Input : dataBaieta
```

```
%       Z Output: dataBaifail
%  Output:
%       fitresult : a fit object representing the fit.
%       gof : structure with goodness-of fit info.
%
%  See also FIT, CFIT, SFIT.

%  Auto-generated by MATLAB on 18-Sep-2014 18:37:44

%Use this equation to normalize the Lode Angle Parameter (as seen in
Bai
%report only)
%dataBaixi=1-2./pi().*acos(dataBaixi);

% Fit: 'untitled fit 1'.
[xData, yData, zData] = prepareSurfaceData( dataBaixi, dataBaieta,
dataBaifail );

% Set up fittype and options.
ft = fittype( '(0.5*(DB1*exp(-DB2*y)+DB5*exp(-DB6*y))-DB3*exp(-
DB4*y))*x.^2+0.5*(DB1*exp(-DB2*y)-DB5*exp(-DB6*y))*x+DB3*exp(-DB4*y)',
'independent', {'x', 'y'}, 'dependent', 'z' );
opts = fitoptions( 'Method', 'NonlinearLeastSquares' );
opts.Display = 'Off';
opts.Lower = [0 0 0 0 0 0];
opts.StartPoint = [0.141886338627215 0.421761282626275
0.915735525189067 0.792207329559554 0.959492426392903
0.655740699156587];

% Fit model to data.
[fitresult, gof] = fit( [xData, yData], zData, ft, opts );
coeffnames(fitresult);
coefs = coeffvalues(fitresult);

end

end
```

Appendix D. Proposed TPS Failure Surface Fitting MATLAB Code

```
function TPSSurface(TestData,DisplayData)


%% The data is split into 3 vectors for curve/surface fitting app
dataxi=(TestData.AverageLodeAngle);
dataeta=(TestData.AverageTriaxiality);
datafail=(TestData.EffectivePlasticStrainatFailure);

if istable(DisplayData) == 1
    displaydataxi=(DisplayData.AverageLodeAngle);
    displaydataeta=(DisplayData.AverageTriaxiality);
    displaydatafail=(DisplayData.EffectivePlasticStrainatFailure);
    j=1;
    for i=1:length(displaydataeta)
        if DisplayData.IsPlaneStress(i)==1
            displaydataxiPS(j)=DisplayData.AverageLodeAngle(i);
            displaydataetaPS(j)=DisplayData.AverageTriaxiality(i);

displaydatafailPS(j)=DisplayData.EffectivePlasticStrainatFailure(i);
            j=j+1;
        end
    end
else
    j=1;
    for i=1:length(dataeta)
        if TestData.IsPlaneStress(i)==1
            displaydataxiPS(j)=TestData.AverageLodeAngle(i);
            displaydataetaPS(j)=TestData.AverageTriaxiality(i);

displaydatafailPS(j)=TestData.EffectivePlasticStrainatFailure(i);
            j=j+1;
        end
    end
end

%% Perform Curve Fit
xy=[dataxi.';dataeta.'];
%thin plate smoothing spline
%p=smoothing value - if p=1 -no smoothing (interpolative)
p=0.9990;
% p=0;
% p=.7;
% st=tpaps(xy,datafail.');
st=tpaps(xy,datafail.',p);


%% Define density of surface etc.
density=50;
eta=linspace(-1/3,1,density);
xi=linspace(-1,1,density);
```

```
%% Compute failure surface
failure=zeros(density,density);
for xicount=1:density
   for etacount=1:density
       failure(etacount,xicount) =
fnval(st,[xi(xicount),eta(etacount)]');
   end
end

%Check for imaginary numbers in surfrace

%% Compute Plane Stress Curve etc.

%Plane Stress Curve
densityfactor=1000;
xips=zeros(1,round(density*2/3*densityfactor));
pscount=0;
etaps=linspace(-1/3,1,density*densityfactor);
while min(xips)>-1.0000000001
    pscount=pscount+1;
    xips(pscount)=-27/2.*etaps(pscount).*(etaps(pscount).^2-1/3);
    %display(pscount)
end

etaps2=linspace(-1/3,2/3,density*densityfactor);
xips2=-27./2.*etaps2.*(etaps2.^2-1./3);


%Make 3D curve using Plane Stress relationship
failureps=zeros(length(xips2),1);
for pscount2=1:length(xips2)

failureps(pscount2)=fnval(st,[xips2(pscount2),etaps2(pscount2)]');
        %display(pscount2)
end

failurepsUpper=zeros(length(etaps),1);
failurepsLower=zeros(length(etaps),1);
failureps2DTPS=zeros(length(etaps),1);
for pscount4=1:length(etaps)
    failurepsUpper(pscount4)=fnval(st,[1,etaps(pscount4)]');
    failurepsUpperOther(pscount4)=fnval(st,[-1,etaps(pscount4)]');
    failurepsLower(pscount4)=fnval(st,[0,etaps(pscount4)]');

failureps2DTPS(pscount4)=fnval(st,[xips2(pscount4),etaps2(pscount4)]');
    %display(pscount4)
end


%% Plane Stress 2D Plot
    failureps2DTPSUpper=failurepsUpper;
    failureps2DTPSUpperOther=failurepsUpperOther;
    failureps2DTPSLower=failurepsLower;
%Compute 2D Curve for Failure Strain vs. Triax.
```

```
%2D Plane Stress Plot Bai Data
fig2d=figure;
hold on
cc=hsv(3);
colors=get(gca,'ColorOrder');
markercolor=colors(4,:);
h(1)=plot(etaps2,failureps2DTPS,'color',cc(1,:),'LineWidth',2);
h(2)=plot(etaps,failureps2DTPSLower,'color',cc(2,:),'LineWidth',2);
h(3)=plot(etaps,failureps2DTPSUpper,'color',cc(3,:),'LineStyle','--
','LineWidth',2);
h(4)=plot(etaps,failureps2DTPSUpperOther,'color',cc(3,:),'LineStyle','-
.','LineWidth',2);
h(5)=scatter(dataeta, datafail,'MarkerEdgeColor',markercolor);
set(h(5),'SizeData',50);
set(h(5),'LineWidth',1.5);
% if max(dataeta)>1
%     axis([-0.333,1.1,0,ceil(max(failureps2DBaiUpper))])
% elseif max(dataeta)>0.6
%     axis([-0.333,1.0,0,ceil(max(failureps2DBaiUpper))])
% else
%     axis([-0.333,0.666,0,ceil(max(failureps2DBaiUpper))])
% end
if ceil(max(failureps2DTPSUpper))>5
    maxz=3;
else

maxz=ceil(2*max([max(failureps2DTPS),max(failureps2DTPSUpper),1]))/2;
end
maxz=1;

if max(dataeta)>1
    etaaxis=1.05;
else
    etaaxis=1;
end

axis([-0.333,etaaxis,0,maxz])
grid on
title(char(sprintf('2-Dimensional Plot of\nThin Plate Spline Method
Using %s for Calibration',char(TestData.Name(1)))))
xlabel('Triaxiality')
ylabel('Eff. Plastic Strain at Failure')
h(6)=scatter(displaydataetaPS,displaydatafailPS,'*','k','LineWidth',0.7
5,'SizeData',25);
legendnames{1}='Plain Stress Curve';
legendnames{2}='Plane Strain-Lower Bound';
legendnames{3}='Axial Symmetry-Upper Bound, Lode= +1';
legendnames{4}='Axial Symmetry-Upper Bound, Lode= -1';
legendnames{5}=sprintf('Calibration Tests: %s',char(TestData.Name(1)));
legendnames{6}='Plane Stress Tests';
legend(h,legendnames{1},legendnames{2},legendnames{3},legendnames{4},le
gendnames{5},legendnames{6});

hold off
```

```
%% 3D Surface Plot Surface previously computed

%3D Plot
fig3d=figure;
hold on
k(1)=surface(xi,eta,failure,'FaceAlpha',0.8','EdgeColor','k','LineWidth
',1,'EdgeAlpha',0.4,'facecolor','interp');
cview=[140,40];
view(cview)
xlabel('Lode Parameter')
ylabel('Triaxiality')
zlabel('Eff. Plastic Strain at Failure')
xhandle=get(gca,'xlabel');
set(xhandle,'fontsize',8)
yhandle=get(gca,'ylabel');
set(yhandle,'fontsize',8)
zhandle=get(gca,'zlabel');
set(zhandle,'fontsize',8)
caxis([min(min(failure)),min(maxz,max(max(failure)))]);
%shading interp
colorbar('Location','EastOutside','AxisLocation','in','FontSize',8)
%colorbar EastOutside
grid on

xyzrange=[-1,1,-1/3,etaaxis,0,maxz];
axis(xyzrange)
t1=title(char(sprintf('3-Dimensional Plot of\nThin Plate Spline Method
Using %s for Calibration',char(TestData.Name(1)))));
set(t1,'FontSize',8)
tiPos=get(t1,'position');
set(t1,'position',tiPos+[0 0 0.1*(xyzrange(6)-xyzrange(5))]);
%set(gca, 'CameraPosition',[20 10 10])
set(gca,'Position',[.1,.275,.75,.620])
g(1)=plot3(xips2,etaps2,failureps,'color',cc(1,:),'LineWidth',2);
g(2)=plot3(zeros(1,length(etaps)),etaps,failurepsLower,'color',cc(2,:),
'LineWidth',2);
g(3)=plot3((zeros(1,length(etaps))+1),etaps,failurepsUpper,'color','k',
'LineStyle','--','LineWidth',2);
g(4)=plot3((zeros(1,length(etaps))-
1),etaps,failurepsUpperOther,'color','k','LineStyle','-
.','LineWidth',2);
%Plot calibration tests as scatter
g(5)=scatter3(dataxi,dataeta,datafail,'LineWidth',1,'MarkerEdgeColor','
k','MarkerFaceColor','r');
if istable(DisplayData) == 1
    %Plot all tests if partial tests used for calibration

g(6)=scatter3(displaydataxi,displaydataeta,displaydatafail,'*','k');
    legendnames{6}='All Tests';
    gleg=legend(g([1,2,3,4,5,6]),legendnames{[1:6]});
    set(gleg,'FontSize',8);
    set(gleg,'Position',[0.33,0.075,0.33,0.1]);
else
    gleg=legend(g([1,2,3,4,5]),legendnames{[1:5]});
    set(gleg,'FontSize',8);
    set(gleg,'Position',[0.33,0.05,0.33,0.1]);
```

```
end
set(gcf, 'PaperPositionMode', 'auto');

%% Contour Plot
figcont=figure;
hold on
grid on
density=199;
%density=253 is the largest density available to plot surface in excel
without array reduction
eta=linspace(-1/3,1,density);
xi=linspace(-1,1,density);
[X,Y] = meshgrid(xi,eta);
Z=zeros(length(eta),length(xi));
for indexxi=1:length(xi)
    for indexeta=1:length(eta)
        Z(indexeta,indexxi)=fnval(st,[xi(indexxi),eta(indexeta)]');
    end
end
%[C_cont,h_cont]=contour(X,Y,Z,'LineWidth',2);
%[C_cont,h_cont]=contour(X,Y,Z,linspace(min(min(Z)),maxz,20),'LineWidth
',2);
%[C_cont,h_cont]=contour(X,Y,Z,linspace(0,1,21),'LineWidth',2);
[C_cont,h_cont]=contour(X,Y,Z,linspace(0,2,41),'LineWidth',2);
%clabel(C_cont,h_cont,'LabelSpacing',1000,'FontSize',8);
%ch=clabel(C_cont,h_cont,'manual');
%set(ch,'margin',2,'backgroundcolor','w')
clabel(C_cont,h_cont);
[Loweta,Lowxi] = find(Z == min(min(Z)));
[Higheta,Highxi] = find(Z == max(max(Z)));
xlabel('Lode Parameter')
ylabel('Triaxiality')
title(char(sprintf('Calibration Tests: %s Using Thin Plate Spline
Method\nContour Plot',char(TestData.Name(1)))))
title(char(sprintf('Contour Plot of\nThin Plate Spline Method Using %s
for Calibration',char(TestData.Name(1)))))

% Plot and annotate the Max and Min
color=jet(255);
for index=1:length(Lowxi);


plot(xi(Lowxi(index)),eta(Loweta(index)),'x','MarkerEdgeColor',color(1,
:),'LineWidth',2,'MarkerSize',10)
    minvalue{index}=sprintf('Min at
%0.4f',Z(Loweta(index),Lowxi(index)));
    if xi(Lowxi(index))<0
        text(xi(Lowxi(index)),eta(Loweta(index)),['
','\leftarrow',char(minvalue(index))]);
    else

text(xi(Lowxi(index)),eta(Loweta(index)),[char(minvalue(index)),'\right
arrow',' '],'HorizontalAlignment','Right')
    end;
end
for index=1:length(Highxi);
```

```
plot(xi(Highxi(index)),eta(Higheta(index)),'x','MarkerEdgeColor',color(
255,:),'LineWidth',2,'MarkerSize',10)
    maxvalue{index}=sprintf('Max at
%0.4f',Z(Higheta(index),Highxi(index)));
    if xi(Highxi(index))<0
        text(xi(Highxi(index)),eta(Higheta(index)),['
','\leftarrow',char(maxvalue(index))])
    else

text(xi(Highxi(index)),eta(Higheta(index)),[char(maxvalue(index)),'\rig
htarrow',' '],'HorizontalAlignment','Right')
    end
end
alphable = findobj(h_cont, '-property', 'EdgeAlpha');
set(alphable, 'EdgeAlpha', 0.8);

%% Output Script
OutputMessage=msgbox({'Saving Figures' 'Please Wait'});
method='TPS_Surf';
outputfolder=sprintf('output_%s\\',method);
nn=1;
plotname{nn}='2d-Plot';
nn=nn+1;
plotname{nn}='3d-Plot';
nn=nn+1;
plotname{nn}='Cont-Plot';
%nn=nn+1;
%plotname{nn}='Resid-Plot';
%nn=nn+1;
%plotname{nn}='Pred-Plot';

nn=1;
figurenames(nn)=fig2d;
nn=nn+1;
figurenames(nn)=fig3d;
nn=nn+1;
figurenames(nn)=figcont;
nn=nn+1;
%figurenames(nn)=figresid;
%nn=nn+1;
%figurenames(nn)=figpred;

if(exist(outputfolder) ~= 7)
    mkdir(outputfolder);
    fileattrib(outputfolder,'+w')
end
for i=1:length(figurenames);

pathname=sprintf('%s%s_%s_w_%s',outputfolder,plotname{i},char(TestData.
Name(1)),method);
    delete(sprintf('%s.eps',pathname));
    delete(sprintf('%s.png',pathname));
    print(figurenames(i),pathname,'-dpng','-r600');
    %print(figurenames(i),pathname,'-depsc2','-r300', '-opengl');
end
```

```
delete(OutputMessage);

end
```

Appendix E. Material Certificates

SSAB

St. Paul, MN 55164-0303

Test Certificate

Form TC1: Revision 1: Date 31 Oct 2000

Customer: RYERSON INC. ACCOUNTS PAYABLE DEPT. PO BOX 91601 LUBBOCK TX 79490-1601	**Customer P.O. No.:** 4500570681	**Mill Order No.:** 41-370663-01	**Shipping Manifest :** PT089976
	Product Description: ASTM A572-50/M345(07)/A709-50/M345(11)	**Ship Date:** 27 Aug 13 **Cert Date:** 27 Aug 13	**Cert No:** 041162950 (Page 1 of 1)
	Size: 0.500 X 60.00 X 120.0 (IN)		

Tested Pieces				Tensiles						Charpy Impact Tests						
Heat Id	Piece Id	Tested Thickness	Tst Loc	YS (KSI)	UTS (KSI)	%RA	Elong % 2in 8in	Tst Dir	Hardness	Abs. Energy(FTLB) 1 2 3 Avg	% Shear 1 2 3 Avg	Tst Tmp	Tst Dir	Tst Siz (mm)	BDWTT Tmp %Shr
R1622	5053280	0.500 (T.L.C)	L C	66 64	74 74		33 28	T T							

Heat Id	Chemical Analysis C	Mn	P	S	Si	Tot Al	Cu	Ni	Cr	Mo	Cb	V	Ti	ORGN
R1622	.06	.91	.010	.010	.02	.032	.13	.06	.05	.02	.003	.082	.001	USA

MATERIAL MARKED WITH AN ASTERISK IS PRODUCED FROM COIL
PRODUCTS SHIPPED:
* R1622 5053280 PCES: 43, WGT: 43903

(U) Cust Part # : 160004889

WE HEREBY CERTIFY THAT THIS MATERIAL WAS TESTED IN ACCORDANCE WITH, AND MEETS THE REQUIREMENTS OF, THE APPROPRIATE SPECIFICATION

Chad Falteysek
CHECKED BY

Figure E-1. Testing Specimens Material

Appendix F. Test Results Summaries

MIDWEST ROADSIDE SAFETY FACILITY

Tension Test Summary

Test Information

Test No.	SEFT-14
Specimen Description:	Flat Standard Dog Bone
Specimen Geometry No.:	1
Specimen ID:	014
Test Date:	9/25/2015
Results Folder:	Test Run 65

Testing Procedure

Testing Frame:	Landmark 20 kip
Loading Type:	Tension
Load Rate:	0.0004 in./sec
Grips:	0-0.30 in. Surfalloy
Grip Pressure:	1000 psi
Fixture:	N/A
Measurement Equipment:	1 in. Axial Extensometer Laser Extensometer 22 kip Load Cell 2.2 kip Load Cell
Primary Extensometer:	Laser Extensometer

Initial Measurements

Average Width:	0.120	in.
Average Thickness:	0.029	in.
Initial Area:	0.0035	sq. in.
Initial Gauge Length	0.1912	in.

Final Measurements

Average Width:	0.082	in.
Average Thickness:	0.022	in.
Final Area:	0.0018	sq. in.
Reduction in Area:	50.3	%
Gauge Length at Failure Initiation:	0.2552	in.

Test Results Summary

Yield Load (0.2% Offset):	0.218	kip
Peak Load:	0.278	kip
Failure Initiation Load:	0.197	kip
Failure Load (ASTM):	0.250	kip
Yield Strength (0.2% Offset):	61.58	ksi
Ultimate Tensile Strength:	78.64	ksi
Engineering Stress at Failure Initiation:	55.61	ksi
Engineering Strain at Failure Initiation:	0.3349	in./in.
Engineering Stress at Failure (ASTM):	70.78	ksi
Engineering Strain at Failure (ASTM):	0.2638	in./in.
True Stress at Failure Initiation:	111.80	ksi
True Strain at Failure Initiation:	0.6983	in./in.
Effective Plastic Strain at Failure:	0.6942	in./in.
Young's Modulus:	25,270	ksi

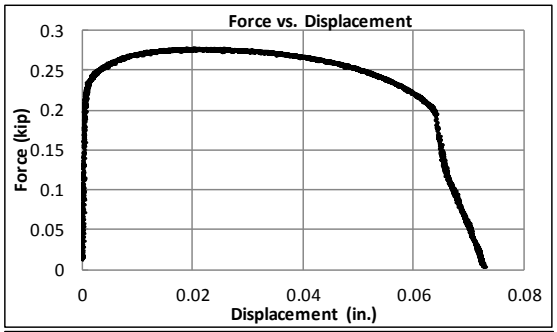

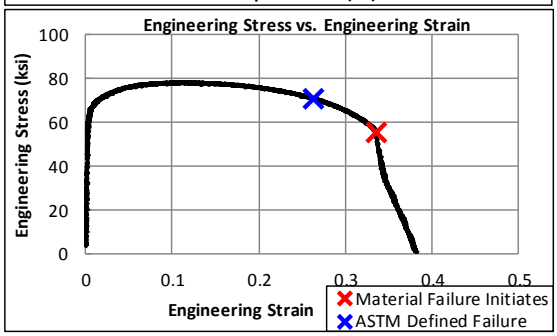

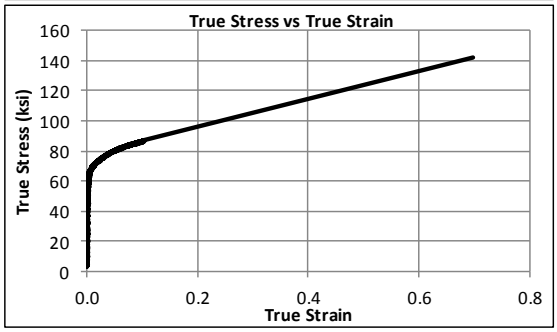

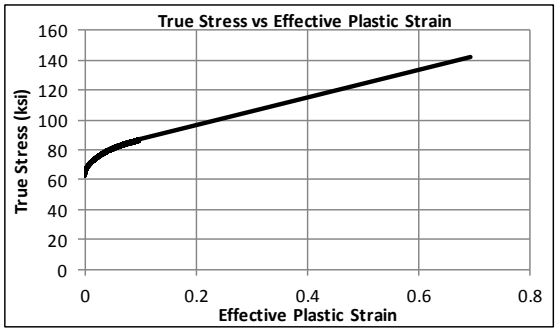

Figure F-1. Test No. SEFT-14 Test Results Summary

MIDWEST ROADSIDE SAFETY FACILITY

Tension Test Summary

Test Information

Test No.	SEFT-15
Specimen Description:	Flat Standard Dog Bone
Specimen Geometry No.:	1
Specimen ID:	015
Test Date:	9/25/2015
Results Folder:	Test Run 66

Testing Procedure

Testing Frame:	Landmark 20 kip
Loading Type:	Tension
Load Rate:	0.0004 in./sec
Grips:	0-0.30 in. Surfalloy
Grip Pressure:	1000 psi
Fixture:	N/A
Measurement Equipment:	1 in. Axial Extensometer Laser Extensometer 22 kip Load Cell 2.2 kip Load Cell
Primary Extensometer:	Laser Extensometer

Initial Measurements

Average Width:	0.120	in.
Average Thickness:	0.030	in.
Initial Area:	0.0036	sq. in.
Initial Gauge Length	0.1592	in.

Final Measurements

Average Width:	0.082	in.
Average Thickness:	0.022	in.
Final Area:	0.0018	sq. in.
Reduction in Area:	50.6	%
Gauge Length at Failure Initiation:	0.2219	in.

Test Results Summary

Yield Load (0.2% Offset):	0.229	kip
Peak Load:	0.276	kip
Failure Initiation Load:	0.192	kip
Failure Load (ASTM):	0.249	kip
Yield Strength (0.2% Offset):	64.45	ksi
Ultimate Tensile Strength:	77.71	ksi
Engineering Stress at Failure Initiation:	53.92	ksi
Engineering Strain at Failure Initiation:	0.3934	in./in.
Engineering Stress at Failure (ASTM):	69.94	ksi
Engineering Strain at Failure (ASTM):	0.3090	in./in.
True Stress at Failure Initiation:	109.05	ksi
True Strain at Failure Initiation:	0.7044	in./in.
Effective Plastic Strain at Failure:	0.7002	in./in.
Young's Modulus:	34,189	ksi

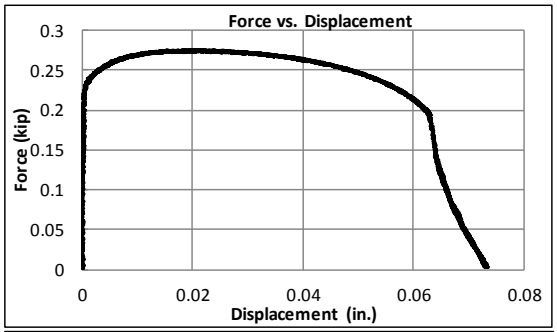

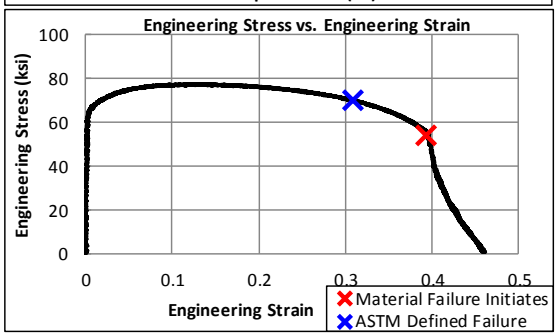

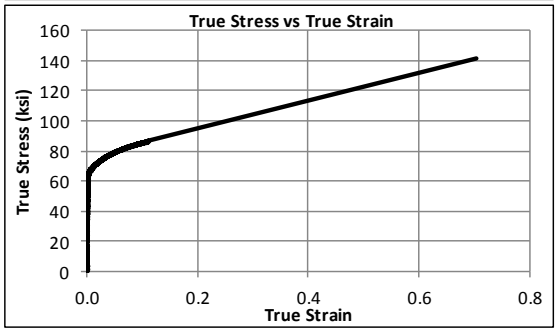

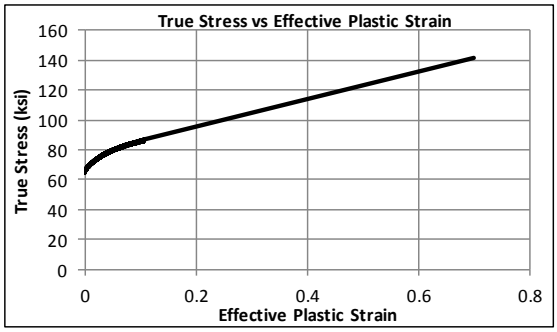

Figure F-2. Test No. SEFT-15 Test Results Summary

MIDWEST ROADSIDE SAFETY FACILITY

Tension Test Summary

Test Information

Test No.	SEFT-16
Specimen Description:	Flat Standard Dog Bone
Specimen Geometry No.:	1
Specimen ID:	016
Test Date:	9/25/2015
Results Folder:	Test Run 67

Testing Procedure

Testing Frame:	Landmark 20 kip
Loading Type:	Tension
Load Rate:	0.0004 in./sec
Grips:	0-0.30 in. Surfalloy
Grip Pressure:	1000 psi
Fixture:	N/A
Measurement Equipment:	1 in. Axial Extensometer Laser Extensometer 22 kip Load Cell 2.2 kip Load Cell
Primary Extensometer:	Laser Extensometer

Initial Measurements

Average Width:	0.120	in.
Average Thickness:	0.029	in.
Initial Area:	0.0035	sq. in.
Initial Gauge Length	0.1533	in.

Final Measurements

Average Width:	0.083	in.
Average Thickness:	0.023	in.
Final Area:	0.0019	sq. in.
Reduction in Area:	46.5	%
Gauge Length at Failure Initiation:	0.2156	in.

Test Results Summary

Yield Load (0.2% Offset):	0.224	kip
Peak Load:	0.276	kip
Failure Initiation Load:	0.186	kip
Failure Load (ASTM):	0.248	kip
Yield Strength (0.2% Offset):	63.53	ksi
Ultimate Tensile Strength:	78.19	ksi
Engineering Stress at Failure Initiation:	52.76	ksi
Engineering Strain at Failure Initiation:	0.4065	in./in.
Engineering Stress at Failure (ASTM):	70.38	ksi
Engineering Strain at Failure (ASTM):	0.3141	in./in.
True Stress at Failure Initiation:	98.65	ksi
True Strain at Failure Initiation:	0.6257	in./in.
Effective Plastic Strain at Failure:	0.6215	in./in.
Young's Modulus:	31,936	ksi

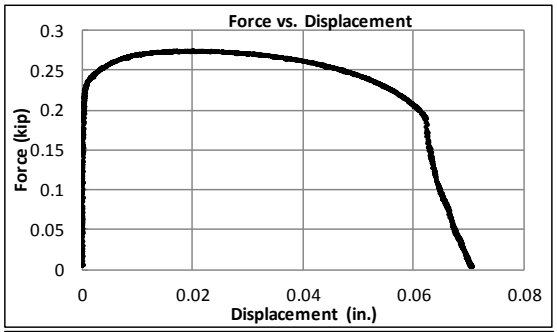

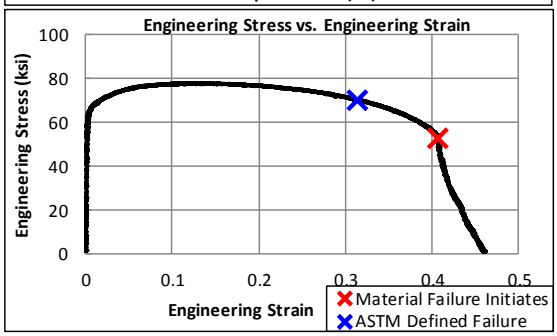

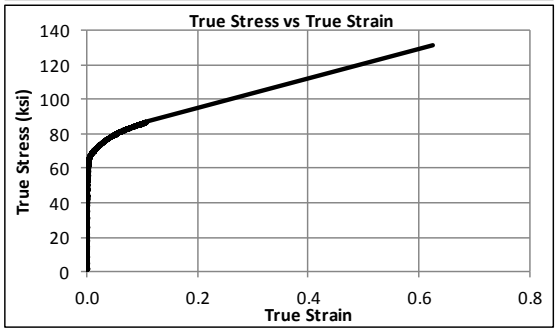

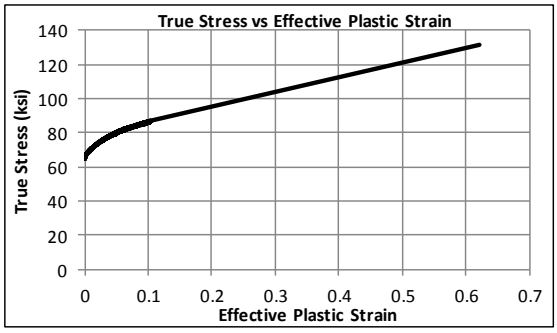

Figure F-3. Test No. SEFT-16 Test Results Summary

MIDWEST ROADSIDE SAFETY FACILITY

Tension Test Summary

Test Information	
Test No.	SEFT-17
Specimen Description:	Flat Large Notch
Specimen Geometry No.:	2
Specimen ID:	041
Test Date:	9/25/2015
Results Folder:	Test Run 68

Testing Procedure	
Testing Frame:	Landmark 20 kip
Loading Type:	Tension
Load Rate:	0.0004 in./sec
Grips:	0-0.30 in. Surfalloy
Grip Pressure:	1000 psi
Fixture:	N/A
Measurement Equipment:	1 in. Axial Extensometer
	Laser Extensometer
	22 kip Load Cell
	2.2 kip Load Cell
Primary Extensometer:	1 in. Axial Extensometer

Initial Measurements		
Average Width:	0.121	in.
Average Thickness:	0.030	in.
Initial Area:	0.0036	sq. in.
Initial Gauge Length	1.0000	in.

Final Measurements		
Average Width:	0.096	in.
Average Thickness:	0.022	in.
Final Area:	0.0021	sq. in.
Reduction in Area:	41.8	%
Gauge Length at Failure Initiation:	1.0363	in.

Test Results Summary		
Yield Load:	0.257	kip
Peak Load:	0.298	kip
Failure Initiation Load:	0.212	kip
Failure Load (ASTM):	0.268	kip
Displacement at Peak:	0.0131	in.
Displacement at Failure Initiation:	0.0363	in.
Displacement at Failure Load (ASTM):	0.0282	in.
Yield Strength:	70.57	ksi
Ultimate Tensile Strength:	81.76	ksi
Engineering Stress at Failure Initiation:	58.14	ksi
Engineering Stress at Failure (ASTM):	73.58	ksi

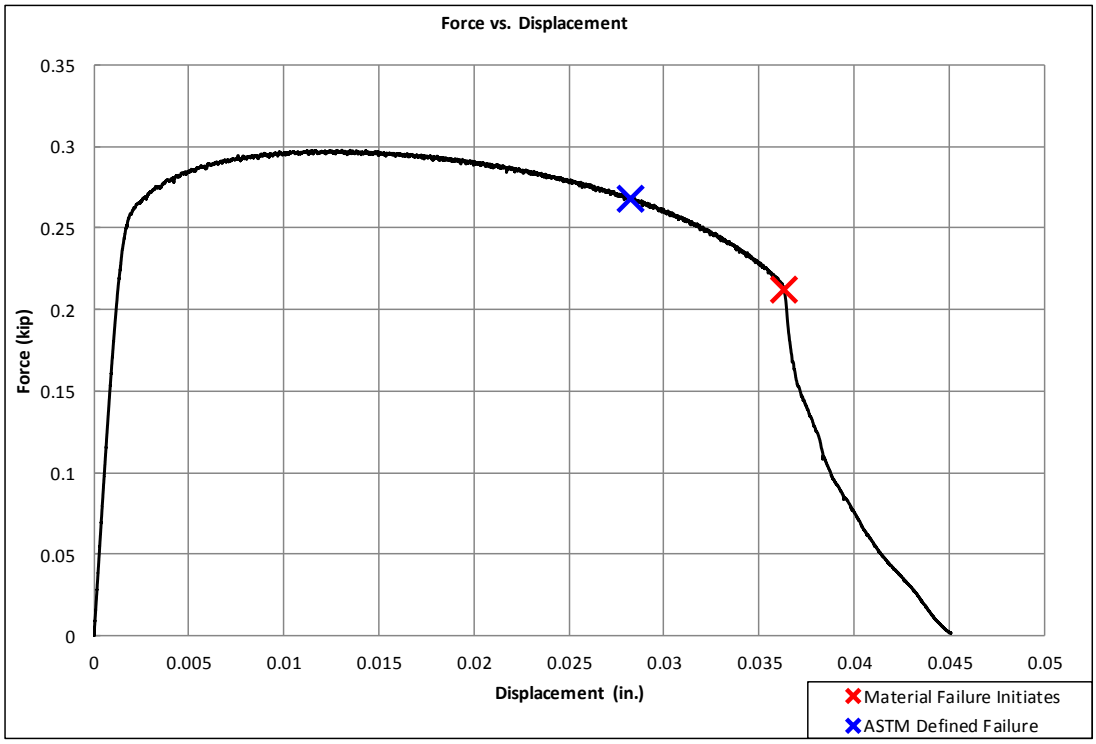

Figure F-4. Test No. SEFT-17 Test Results Summary

MIDWEST ROADSIDE SAFETY FACILITY

Tension Test Summary

Test Information	
Test No.	SEFT-18
Specimen Description:	Flat Large Notch
Specimen Geometry No.:	2
Specimen ID:	042
Test Date:	9/25/2015
Results Folder:	Test Run 69

Testing Procedure	
Testing Frame:	Landmark 20 kip
Loading Type:	Tension
Load Rate:	0.00025 in./sec
Grips:	0-0.30 in. Surfalloy
Grip Pressure:	1000 psi
Fixture:	N/A
Measurement Equipment:	1 in. Axial Extensometer
	Laser Extensometer
	22 kip Load Cell
	2.2 kip Load Cell
Primary Extensometer:	1 in. Axial Extensometer

Initial Measurements		
Average Width:	0.121	in.
Average Thickness:	0.030	in.
Initial Area:	0.0036	sq. in.
Initial Gauge Length	1.0000	in.

Final Measurements		
Average Width:	0.096	in.
Average Thickness:	0.022	in.
Final Area:	0.0022	sq. in.
Reduction in Area:	40.5	%
Gauge Length at Failure Initiation:	1.0354	in.

Test Results Summary		
Yield Load:	0.258	kip
Peak Load:	0.297	kip
Failure Initiation Load:	0.214	kip
Failure Load (ASTM):	0.267	kip
Displacement at Peak:	0.0111	in.
Displacement at Failure Initiation:	0.0354	in.
Displacement at Failure Load (ASTM):	0.0276	in.
Yield Strength:	71.02	ksi
Ultimate Tensile Strength:	81.69	ksi
Engineering Stress at Failure Initiation:	58.83	ksi
Engineering Stress at Failure (ASTM):	73.53	ksi

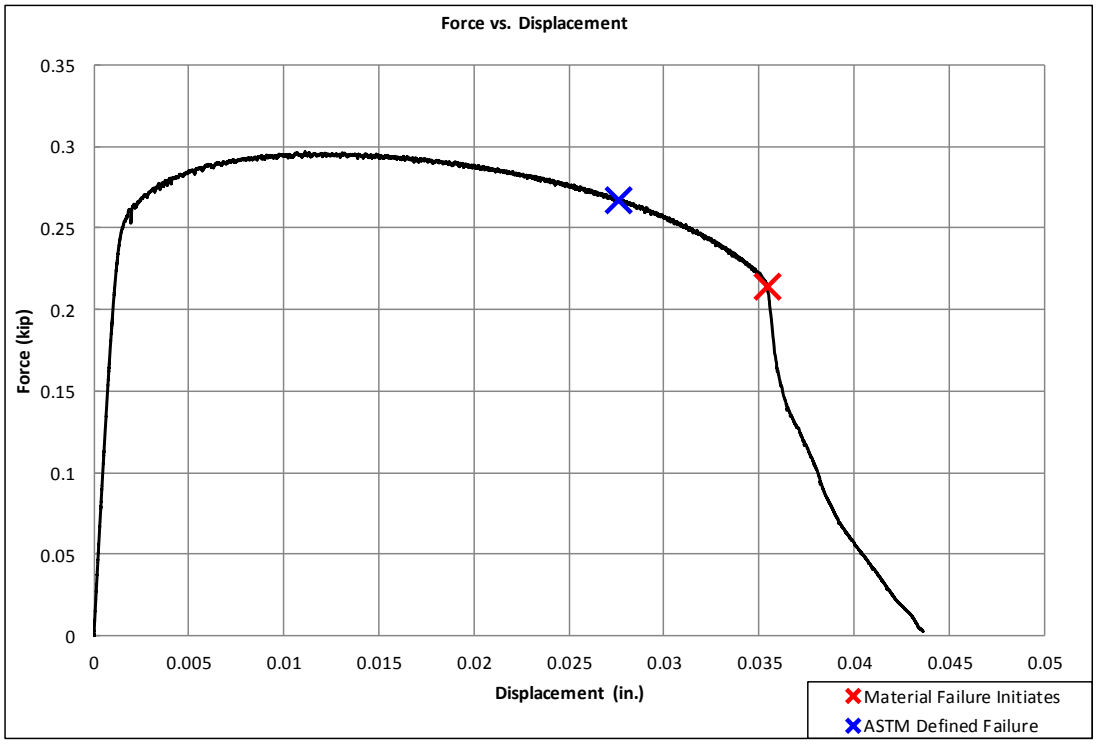

Figure F-5. Test No. SEFT-18 Test Results Summary

MIDWEST ROADSIDE SAFETY FACILITY

Tension Test Summary

Test Information	
Test No.	SEFT-19
Specimen Description:	Flat Large Notch
Specimen Geometry No.:	2
Specimen ID:	043
Test Date:	9/25/2015
Results Folder:	Test Run 70

Testing Procedure	
Testing Frame:	Landmark 20 kip
Loading Type:	Tension
Load Rate:	0.00025 in./sec
Grips:	0-0.30 in. Surfalloy
Grip Pressure:	1000 psi
Fixture:	N/A
Measurement Equipment:	1 in. Axial Extensometer
	Laser Extensometer
	22 kip Load Cell
	2.2 kip Load Cell
Primary Extensometer:	1 in. Axial Extensometer

Initial Measurements		
Average Width:	0.121	in.
Average Thickness:	0.030	in.
Initial Area:	0.0036	sq. in.
Initial Gauge Length	1.0000	in.

Final Measurements		
Average Width:	0.096	in.
Average Thickness:	0.022	in.
Final Area:	0.0021	sq. in.
Reduction in Area:	42.7	%
Gauge Length at Failure Initiation:	1.0351	in.

Test Results Summary		
Yield Load:	0.255	kip
Peak Load:	0.296	kip
Failure Initiation Load:	0.214	kip
Failure Load (ASTM):	0.266	kip
Displacement at Peak:	0.0115	in.
Displacement at Failure Initiation:	0.0351	in.
Displacement at Failure Load (ASTM):	0.0275	in.
Yield Strength:	70.54	ksi
Ultimate Tensile Strength:	81.95	ksi
Engineering Stress at Failure Initiation:	59.33	ksi
Engineering Stress at Failure (ASTM):	73.76	ksi

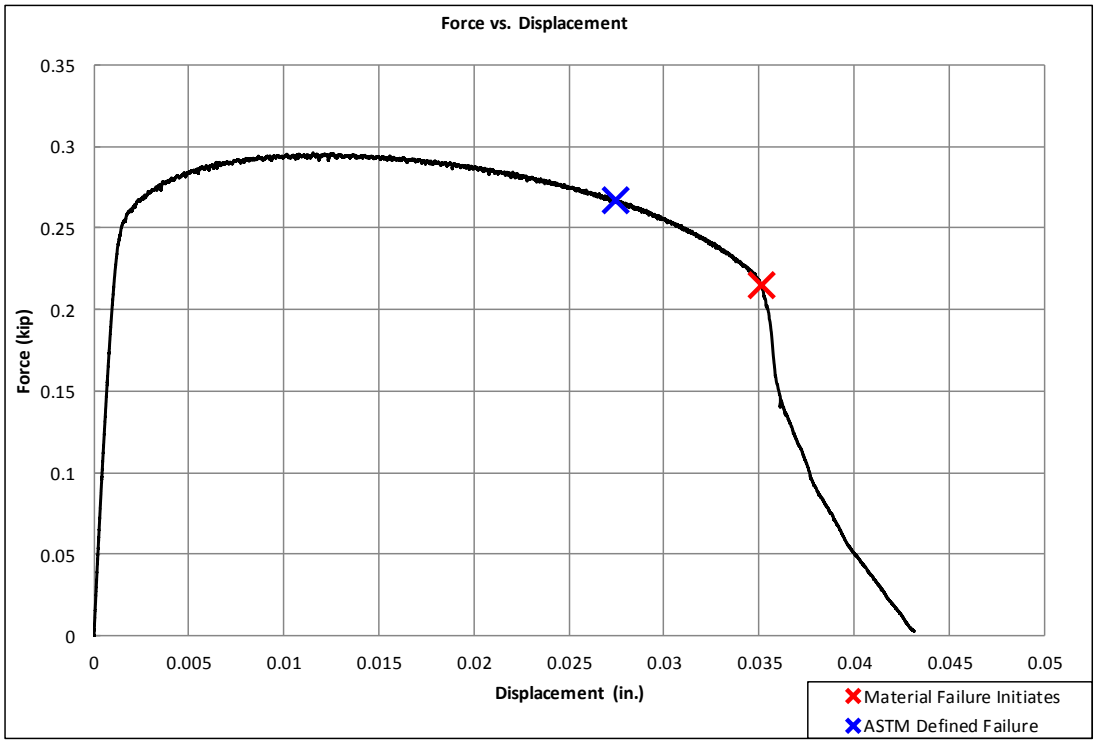

Figure F-6. Test No. SEFT-19 Test Results Summary

MIDWEST ROADSIDE SAFETY FACILITY

Tension Test Summary

Test Information	
Test No.	SEFT-20
Specimen Description:	Flat Small Notch
Specimen Geometry No.:	3
Specimen ID:	047
Test Date:	9/25/2015
Results Folder:	Test Run 71

Testing Procedure	
Testing Frame:	Landmark 20 kip
Loading Type:	Tension
Load Rate:	0.0001 in./sec
Grips:	0-0.30 in. Surfalloy
Grip Pressure:	1000 psi
Fixture:	N/A
Measurement Equipment:	1 in. Axial Extensometer
	Laser Extensometer
	22 kip Load Cell
	2.2 kip Load Cell
Primary Extensometer:	1 in. Axial Extensometer

Initial Measurments		
Average Width:	0.121	in.
Average Thickness:	0.030	in.
Initial Area:	0.0036	sq. in.
Initial Gauge Length	1.0000	in.

Final Measurments		
Average Width:	0.101	in.
Average Thickness:	0.022	in.
Final Area:	0.0023	sq. in.
Reduction in Area:	37.7	%
Gauge Length at Failure Initiation:	1.0281	in.

Test Results Summary		
Yield Load:	0.263	kip
Peak Load:	0.307	kip
Failure Initiation Load:	0.208	kip
Failure Load (ASTM):	0.276	kip
Displacement at Peak:	0.0093	in.
Displacement at Failure Initiation:	0.0281	in.
Displacement at Failure Load (ASTM):	0.0207	in.
Yield Strength:	72.23	ksi
Ultimate Tensile Strength:	84.21	ksi
Engineering Stress at Failure Initiation:	57.17	ksi
Engineering Stress at Failure (ASTM):	75.79	ksi

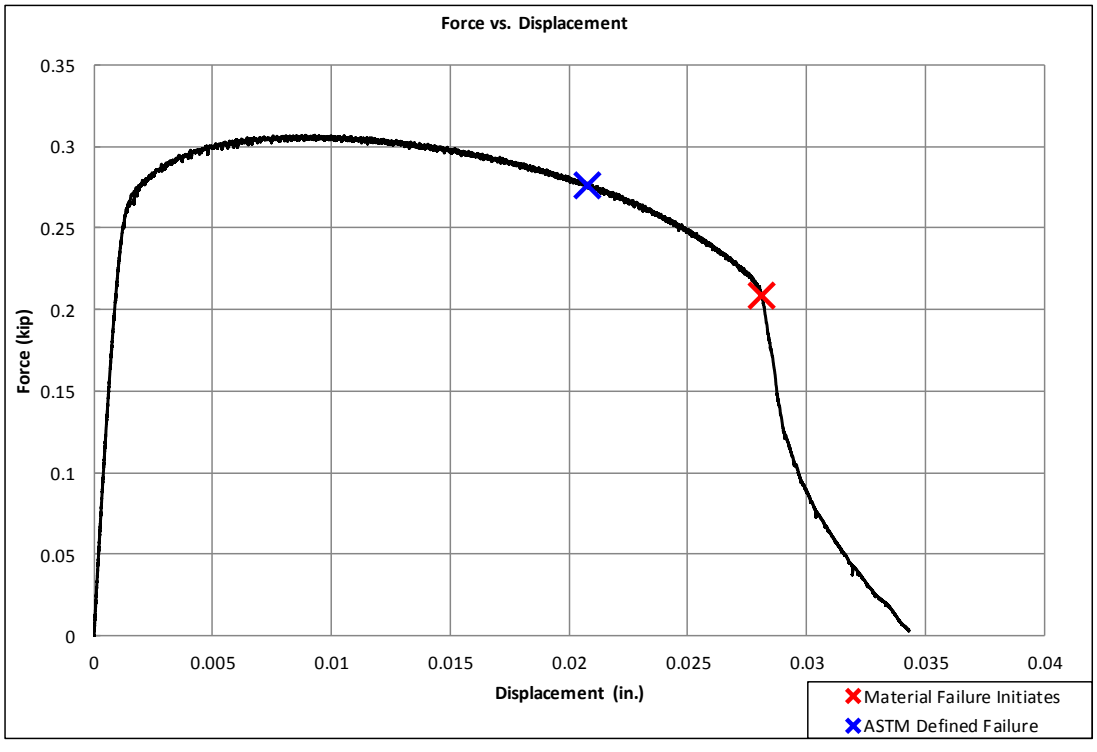

Figure F-7. Test No. SEFT-20 Test Results Summary

MIDWEST ROADSIDE SAFETY FACILITY

Tension Test Summary

Test Information	
Test No.	SEFT-21
Specimen Description:	Flat Small Notch
Specimen Geometry No.:	3
Specimen ID:	048
Test Date:	9/25/2015
Results Folder:	Test Run 72

Testing Procedure	
Testing Frame:	Landmark 20 kip
Loading Type:	Tension
Load Rate:	0.00017 in./sec
Grips:	0-0.30 in. Surfalloy
Grip Pressure:	1000 psi
Fixture:	N/A
Measurement Equipment:	1 in. Axial Extensometer
	Laser Extensometer
	22 kip Load Cell
	2.2 kip Load Cell
Primary Extensometer:	1 in. Axial Extensometer

Initial Measurements		
Average Width:	0.122	in.
Average Thickness:	0.030	in.
Initial Area:	0.0036	sq. in.
Initial Gauge Length	1.0000	in.

Final Measurements		
Average Width:	0.102	in.
Average Thickness:	0.023	in.
Final Area:	0.0023	sq. in.
Reduction in Area:	36.5	%
Gauge Length at Failure Initiation:	1.0273	in.

Test Results Summary		
Yield Load:	0.264	kip
Peak Load:	0.306	kip
Failure Initiation Load:	0.220	kip
Failure Load (ASTM):	0.275	kip
Displacement at Peak:	0.0083	in.
Displacement at Failure Initiation:	0.0273	in.
Displacement at Failure Load (ASTM):	0.0208	in.
Yield Strength:	72.58	ksi
Ultimate Tensile Strength:	84.21	ksi
Engineering Stress at Failure Initiation:	60.57	ksi
Engineering Stress at Failure (ASTM):	75.79	ksi

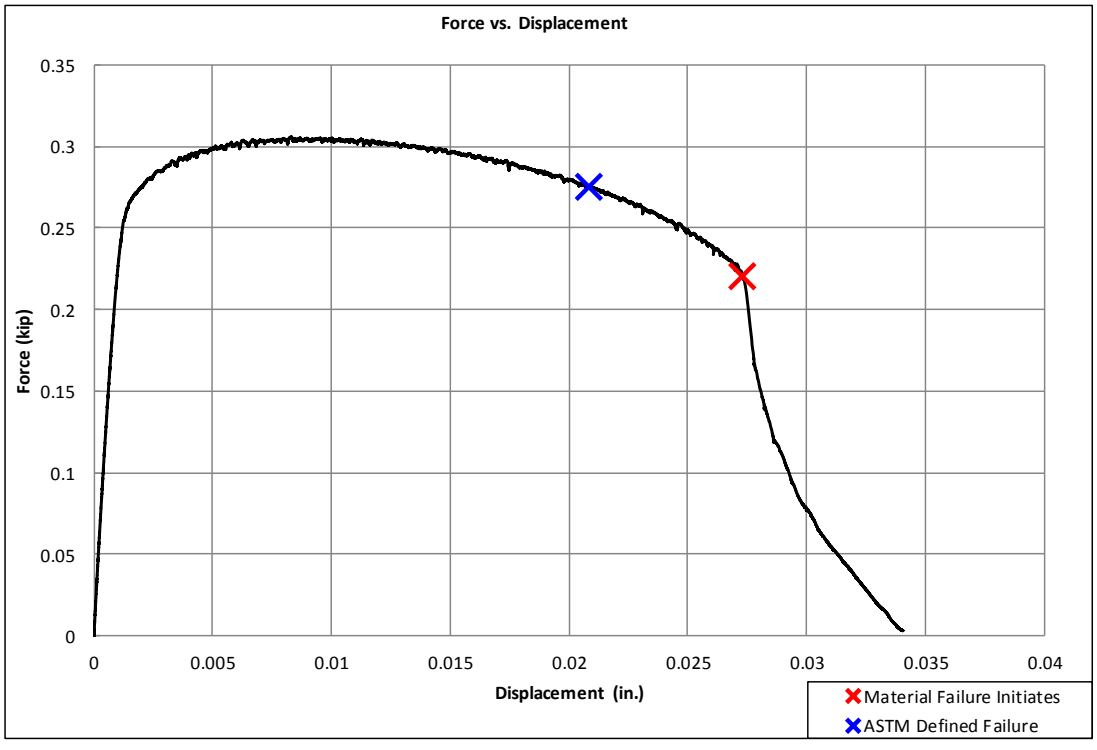

Figure F-8. Test No. SEFT-21 Test Results Summary

MIDWEST ROADSIDE SAFETY FACILITY

Tension Test Summary

Test Information	
Test No.	SEFT-22
Specimen Description:	Flat Small Notch
Specimen Geometry No.:	3
Specimen ID:	049
Test Date:	9/25/2015
Results Folder:	Test Run 73

Testing Procedure	
Testing Frame:	Landmark 20 kip
Loading Type:	Tension
Load Rate:	0.00017 in./sec
Grips:	0-0.30 in. Surfalloy
Grip Pressure:	1000 psi
Fixture:	N/A
Measurement Equipment:	1 in. Axial Extensometer
	Laser Extensometer
	22 kip Load Cell
	2.2 kip Load Cell
Primary Extensometer:	1 in. Axial Extensometer

Initial Measurements		
Average Width:	0.121	in.
Average Thickness:	0.030	in.
Initial Area:	0.0036	sq. in.
Initial Gauge Length	1.0000	in.

Final Measurements		
Average Width:	0.102	in.
Average Thickness:	0.022	in.
Final Area:	0.0022	sq. in.
Reduction in Area:	37.6	%
Gauge Length at Failure Initiation:	1.0275	in.

Test Results Summary		
Yield Load:	0.267	kip
Peak Load:	0.307	kip
Failure Initiation Load:	0.213	kip
Failure Load (ASTM):	0.277	kip
Displacement at Peak:	0.0087	in.
Displacement at Failure Initiation:	0.0275	in.
Displacement at Failure Load (ASTM):	0.0204	in.
Yield Strength:	74.17	ksi
Ultimate Tensile Strength:	85.39	ksi
Engineering Stress at Failure Initiation:	59.04	ksi
Engineering Stress at Failure (ASTM):	76.85	ksi

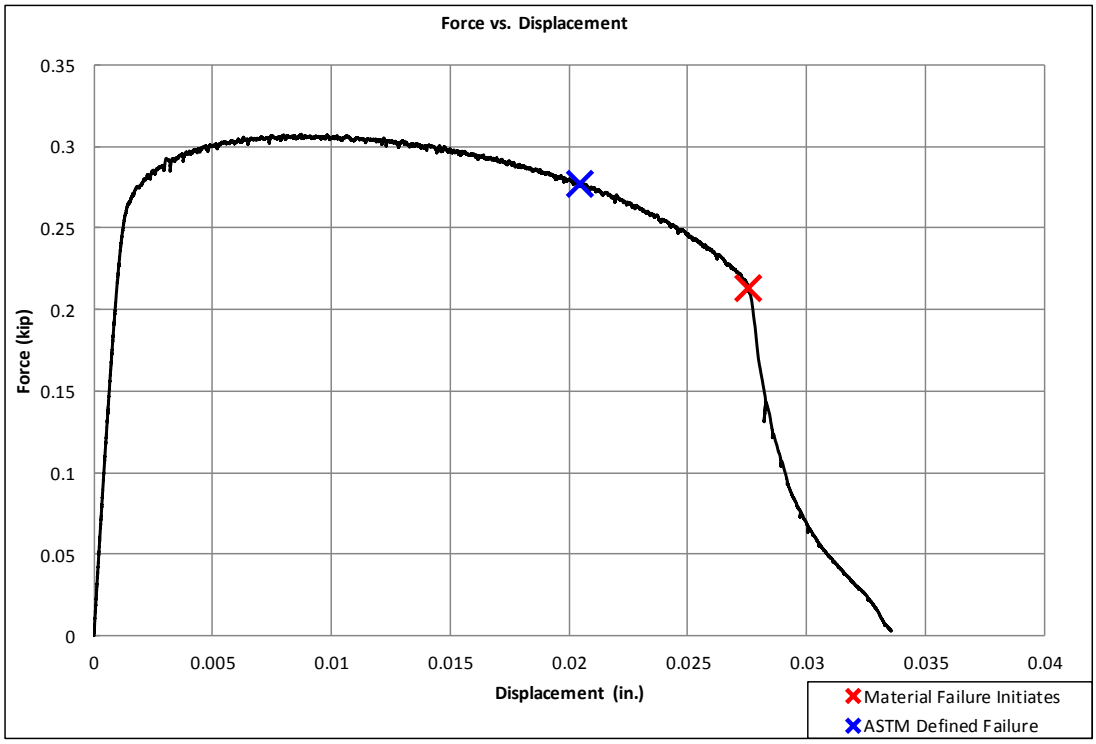

Figure F-9. Test No. SEFT-22 Test Results Summary

MIDWEST ROADSIDE SAFETY FACILITY

Tension Test Summary

Test Information

Test No.	SEFT-23
Specimen Description:	Flat Sharp Notch
Specimen Geometry No.:	4
Specimen ID:	053
Test Date:	10/2/2015
Results Folder:	Test Run 74

Testing Procedure

Testing Frame:	Landmark 20 kip
Loading Type:	Tension
Load Rate:	0.000034 in./sec
Grips:	0-0.30 in. Surfalloy
Grip Pressure:	1000 psi
Fixture:	N/A
Measurement Equipment:	1 in. Axial Extensometer
	Laser Extensometer
	22 kip Load Cell
	2.2 kip Load Cell
Primary Extensometer:	1 in. Axial Extensometer

Initial Measurements

Average Width:	0.120	in.
Average Thickness:	0.030	in.
Initial Area:	0.0036	sq. in.
Initial Gauge Length	1.0000	in.

Final Measurements

Average Width:	0.120	in.
Average Thickness:	0.016	in.
Final Area:	0.0019	sq. in.
Reduction in Area:	46.9	%
Gauge Length at Failure Initiation:	1.0201	in.

Test Results Summary

Yield Load:	0.271	kip
Peak Load:	0.310	kip
Failure Initiation Load:	0.210	kip
Failure Load (ASTM):	0.279	kip
Displacement at Peak:	0.0070	in.
Displacement at Failure Initiation:	0.0201	in.
Displacement at Failure Load (ASTM):	0.0145	in.
Yield Strength:	75.64	ksi
Ultimate Tensile Strength:	86.61	ksi
Engineering Stress at Failure Initiation:	58.76	ksi
Engineering Stress at Failure (ASTM):	77.95	ksi

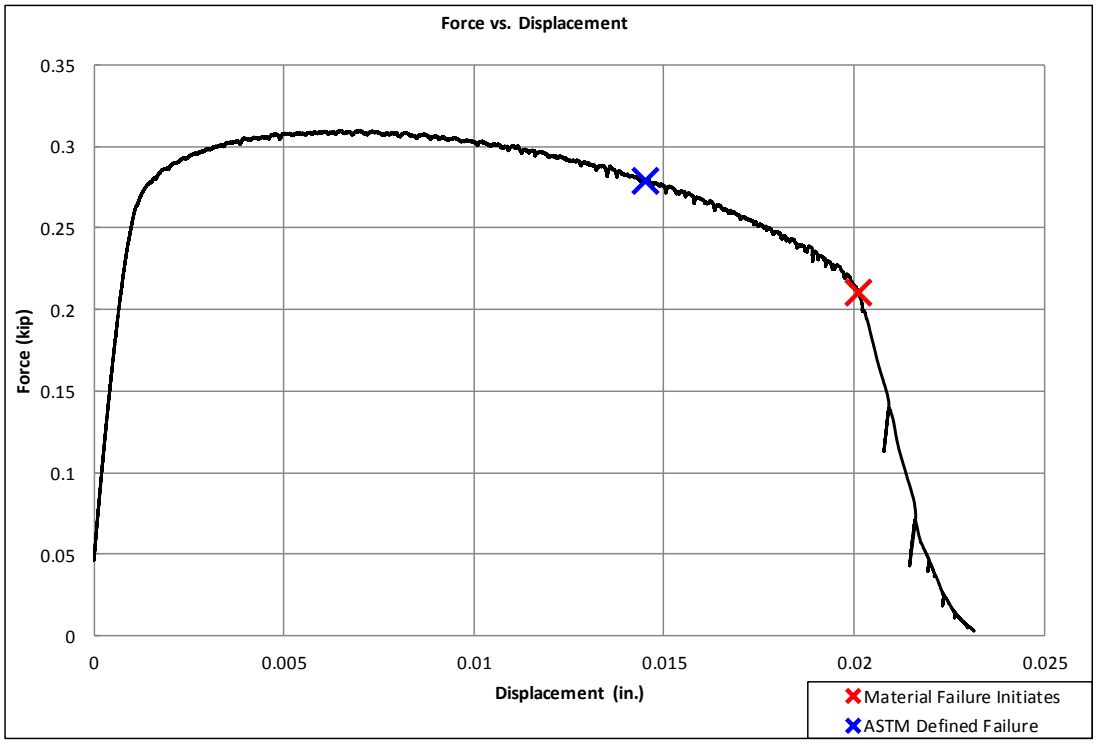

Figure F-10. Test No. SEFT-23 Test Results Summary

MIDWEST ROADSIDE SAFETY FACILITY

Tension Test Summary

Test Information	
Test No.	SEFT-24
Specimen Description:	Flat Sharp Notch
Specimen Geometry No.:	4
Specimen ID:	054
Test Date:	10/2/2015
Results Folder:	Test Run 75

Testing Procedure	
Testing Frame:	Landmark 20 kip
Loading Type:	Tension
Load Rate:	0.000108 in./sec
Grips:	0-0.30 in. Surfalloy
Grip Pressure:	1000 psi
Fixture:	N/A
Measurement Equipment:	1 in. Axial Extensometer
	Laser Extensometer
	22 kip Load Cell
	2.2 kip Load Cell
Primary Extensometer:	1 in. Axial Extensometer

Initial Measurements		
Average Width:	0.120	in.
Average Thickness:	0.029	in.
Initial Area:	0.0035	sq. in.
Initial Gauge Length	1.0000	in.

Final Measurements		
Average Width:	0.111	in.
Average Thickness:	0.018	in.
Final Area:	0.0020	sq. in.
Reduction in Area:	44.0	%
Gauge Length at Failure Initiation:	1.0209	in.

Test Results Summary		
Yield Load:	0.273	kip
Peak Load:	0.315	kip
Failure Initiation Load:	0.210	kip
Failure Load (ASTM):	0.283	kip
Displacement at Peak:	0.0064	in.
Displacement at Failure Initiation:	0.0209	in.
Displacement at Failure Load (ASTM):	0.0145	in.
Yield Strength:	77.58	ksi
Ultimate Tensile Strength:	89.57	ksi
Engineering Stress at Failure Initiation:	59.90	ksi
Engineering Stress at Failure (ASTM):	80.61	ksi

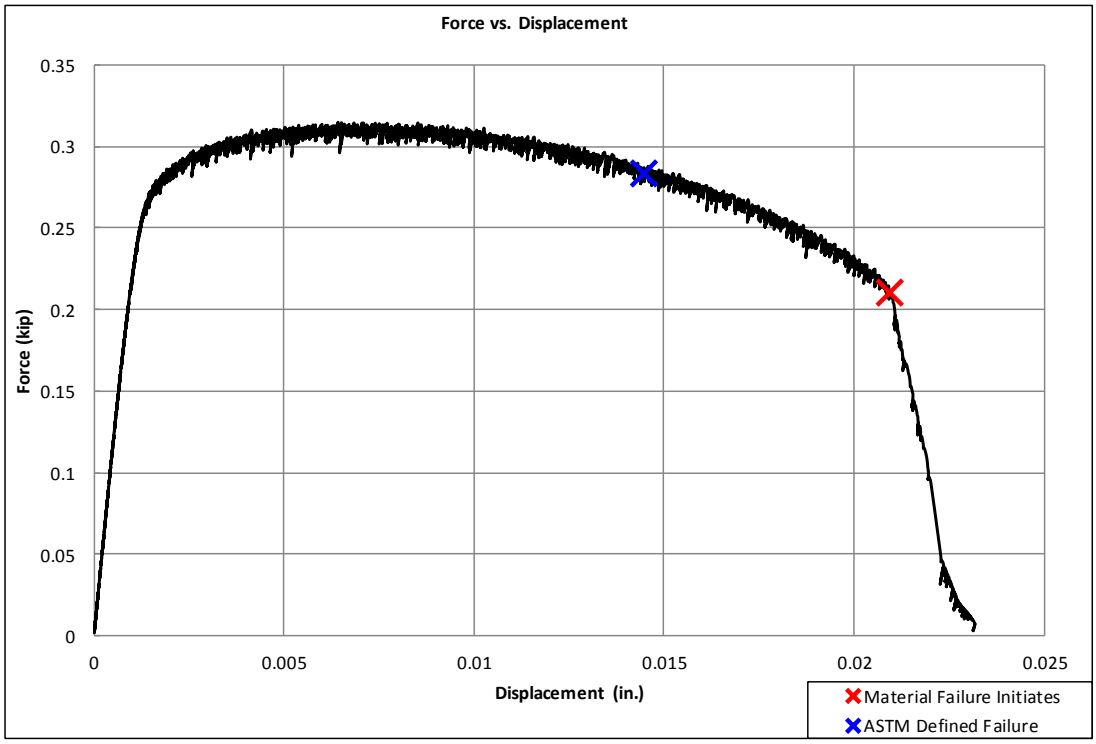

Figure F-11. Test No. SEFT-24 Test Results Summary

MIDWEST ROADSIDE SAFETY FACILITY

Tension Test Summary

Test Information	
Test No.	SEFT-25
Specimen Description:	Flat Sharp Notch
Specimen Geometry No.:	4
Specimen ID:	055
Test Date:	10/2/2015
Results Folder:	Test Run 76

Testing Procedure	
Testing Frame:	Landmark 20 kip
Loading Type:	Tension
Load Rate:	0.000108 in./sec
Grips:	0-0.30 in. Surfalloy
Grip Pressure:	1000 psi
Fixture:	N/A
Measurement Equipment:	1 in. Axial Extensometer
	Laser Extensometer
	22 kip Load Cell
	2.2 kip Load Cell
Primary Extensometer:	1 in. Axial Extensometer

Initial Measurements		
Average Width:	0.120	in.
Average Thickness:	0.029	in.
Initial Area:	0.0035	sq. in.
Initial Gauge Length	1.0000	in.

Final Measurements		
Average Width:	0.115	in.
Average Thickness:	0.019	in.
Final Area:	0.0022	sq. in.
Reduction in Area:	36.7	%
Gauge Length at Failure Initiation:	1.0207	in.

Test Results Summary		
Yield Load:	0.272	kip
Peak Load:	0.317	kip
Failure Initiation Load:	0.210	kip
Failure Load (ASTM):	0.285	kip
Displacement at Peak:	0.0060	in.
Displacement at Failure Initiation:	0.0207	in.
Displacement at Failure Load (ASTM):	0.0141	in.
Yield Strength:	77.83	ksi
Ultimate Tensile Strength:	90.55	ksi
Engineering Stress at Failure Initiation:	60.12	ksi
Engineering Stress at Failure (ASTM):	81.49	ksi

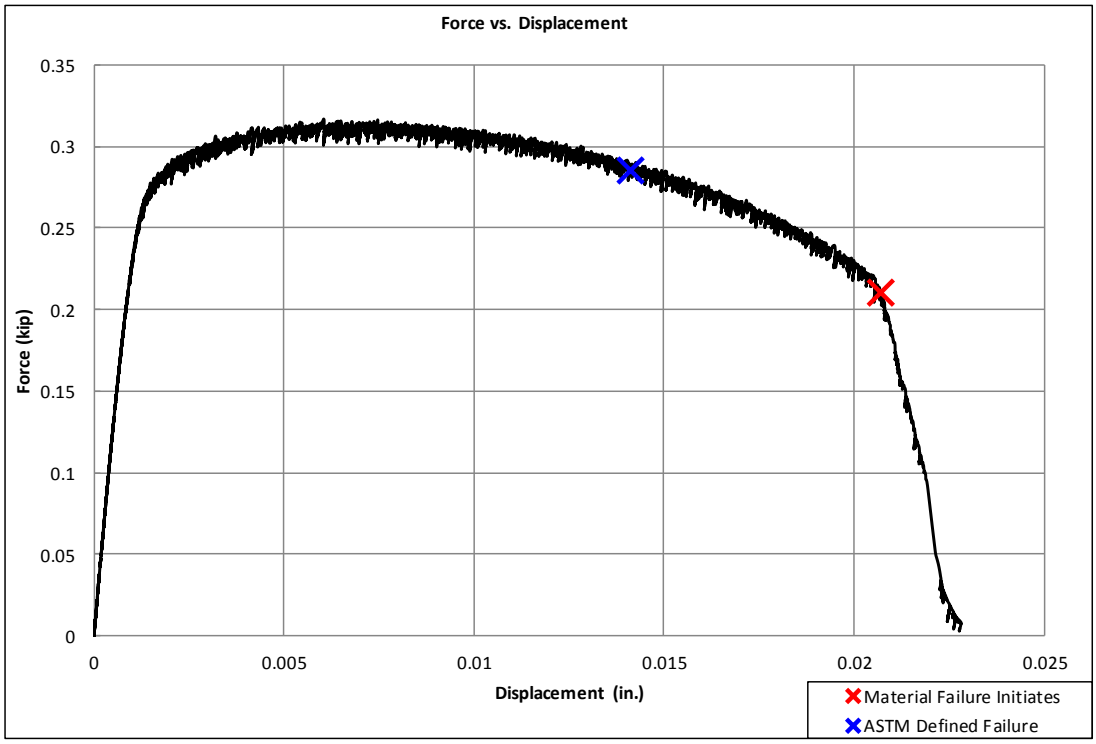

Figure F-12. Test No. SEFT-25 Test Results Summary

MIDWEST ROADSIDE SAFETY FACILITY

Tension Test Summary

Test Information

Test No.	SEFT-27
Specimen Description:	Notched Round Specimen #1
Specimen Geometry No.:	6
Specimen ID:	65
Test Date:	10/9/2015
Results Folder:	Test Run 78

Testing Procedure

Testing Frame:	Landmark 20 kip
Loading Type:	Tension
Load Rate:	0.000564 in./sec
Grips:	0.43-0.65 in. Serrated Vee
Grip Pressure:	1000 psi
Fixture:	N/A
Measurement Equipment:	2 in. Axial Extensometer
	Laser Extensometer
	22 kip Load Cell
Primary Extensometer:	2 in. Axial Extensometer

Initial Measurements

Average Diameter:	0.189	in.
Initial Area:	0.0280	sq. in.
Initial Gauge Length	2.0000	in.

Final Measurements

Average Diameter:	0.104	in.
Final Area:	0.0086	sq. in.
Reduction in Area:	69.4	%
Gauge Length at Failure Initiation:	2.1058	in.

Test Results Summary

Yield Load:	1.998	kip
Peak Load:	2.349	kip
Failure Initiation Load:	1.386	kip
Failure Load (ASTM):	2.114	kip
Displacement at Peak:	0.0207	in.
Displacement at Failure Initiation:	0.1058	in.
Displacement at Failure Load (ASTM):	0.0596	in.
Yield Strength:	71.43	ksi
Ultimate Tensile Strength:	83.97	ksi
Engineering Stress at Failure Initiation:	49.55	ksi
Engineering Stress at Failure (ASTM):	75.57	ksi

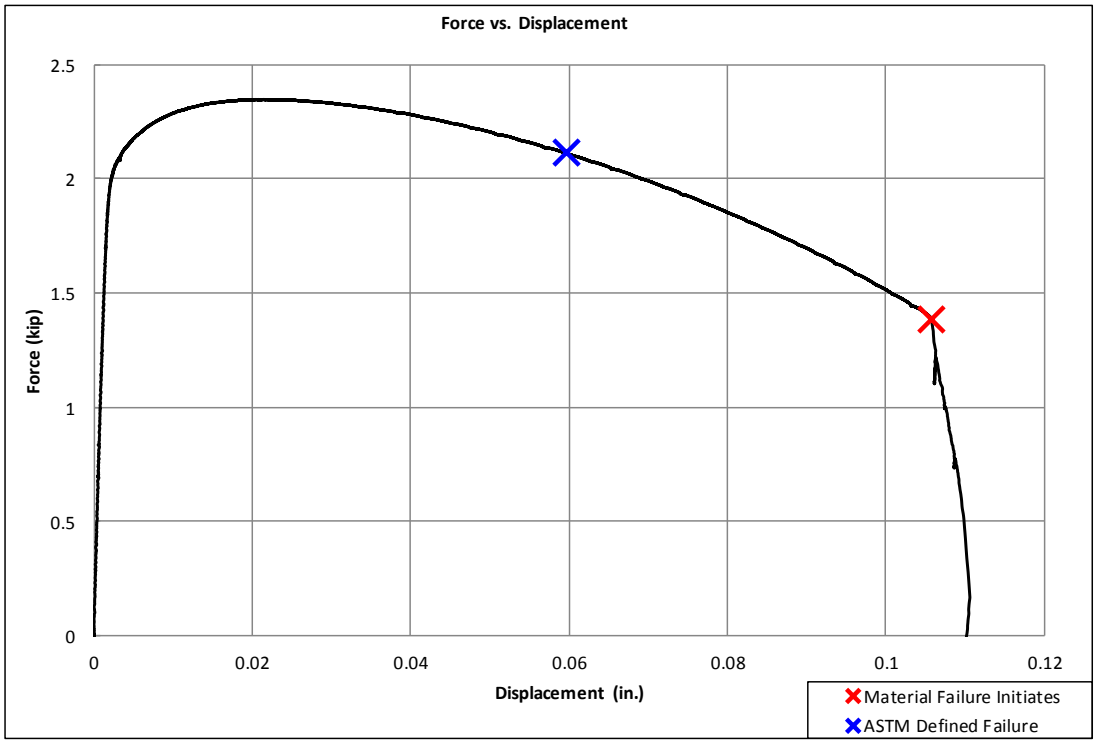

Figure F-13. Test No. SEFT-27 Test Results Summary

MIDWEST ROADSIDE SAFETY FACILITY

Tension Test Summary

Test Information	
Test No.	SEFT-28
Specimen Description:	Notched Round Specimen #1
Specimen Geometry No.:	6
Specimen ID:	66
Test Date:	10/9/2015
Results Folder:	Test Run 79
Testing Procedure	
Testing Frame:	Landmark 20 kip
Loading Type:	Tension
Load Rate:	0.000564 in./sec
Grips:	0.43-0.65 in. Serrated Vee
Grip Pressure:	1000 psi
Fixture:	N/A
Measurement Equipment:	2 in. Axial Extensometer
	Laser Extensometer
	22 kip Load Cell
Primary Extensometer:	2 in. Axial Extensometer

Initial Measurements		
Average Diameter:	0.188	in.
Initial Area:	0.0279	sq. in.
Initial Gauge Length	2.0000	in.
Final Measurements		
Average Diameter:	0.106	in.
Final Area:	0.0088	sq. in.
Reduction in Area:	68.5	%
Gauge Length at Failure Initiation:	2.1075	in.
Test Results Summary		
Yield Load:	1.968	kip
Peak Load:	2.320	kip
Failure Initiation Load:	1.363	kip
Failure Load (ASTM):	2.088	kip
Displacement at Peak:	0.0229	in.
Displacement at Failure Initiation:	0.1075	in.
Displacement at Failure Load (ASTM):	0.0600	in.
Yield Strength:	70.66	ksi
Ultimate Tensile Strength:	83.29	ksi
Engineering Stress at Failure Initiation:	48.94	ksi
Engineering Stress at Failure (ASTM):	74.96	ksi

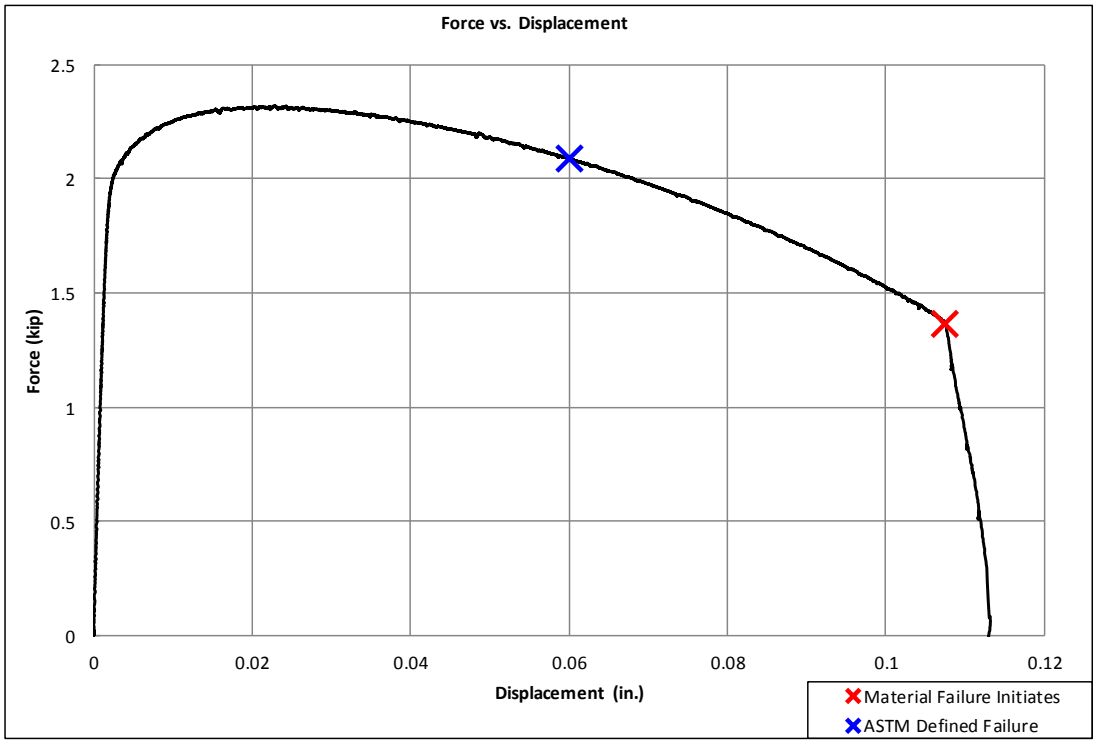

Figure F-14. Test No. SEFT-28 Test Results Summary

MIDWEST ROADSIDE SAFETY FACILITY

Tension Coupon Test Summary

Test Information	
Test No.	SEFT-29
Specimen Description:	Notched Round Specimen #1
Specimen Geometry No.:	1
Specimen ID:	067
Test Date:	10/9/2015
Results Folder:	Test Run #80

Testing Procedure	
Testing Frame:	Landmark 22kip
Loading Type:	Tension
Load Rate:	.000564 in/sec
Grips:	0.43-0.65 in. Serrated Vee
Grip Pressure:	7500 psi
Fixture:	None
Measurement Equipment:	1 in. Axial Extensometer
	Laser Extensometer
	2.2 kip Load Cell
	22 kip Load Cell
Primary Extensometer:	1 in. Axial Extensometer

Initial Measurements		
Average Diameter:	0.187	in.
Initial Area:	0.697	sq. in.
Initial Gauge Length	2.000	in.

Final Measurements		
Average Diameter:	0.105	in.
Final Area:	0.219	sq. in.
Reduction in Area:	68.6	%
Gauge Length at Failure Initiation:	2.105	in.

Test Results Summary		
Yield Load:	1.689	kip
Peak Load:	2.290	kip
Failure Initiation Load:	1.337	kip
Failure Load (ASTM):	2.061	kip
Displacement at Yield:	0.0016	in.
Displacement at Peak:	0.0199	in.
Displacement at Failure Initiation:	0.1053	in.
Displacement at Failure Load (ASTM):	0.0563	in.
Yield Strength:	61.57	ksi
Ultimate Tensile Strength:	83.48	ksi
Engineering Stress at Failure Initiation:	48.75	ksi
Engineering Stress at Failure (ASTM):	75.13	ksi

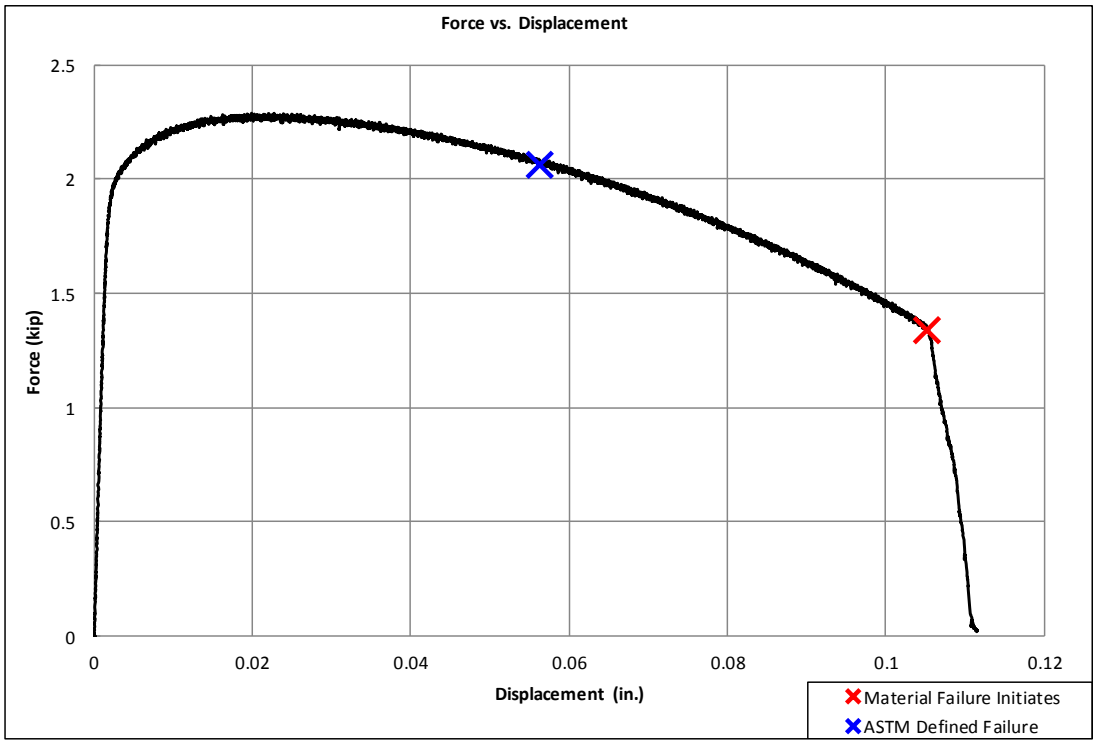

Figure F-15. Test No. SEFT-29 Test Results Summary

MIDWEST ROADSIDE SAFETY FACILITY

Tension Test Summary

Test Information	
Test No.	SEFT-30
Specimen Description:	Notched Round Specimen #2
Specimen Geometry No.:	7
Specimen ID:	71
Test Date:	10/9/2015
Results Folder:	Test Run 81

Testing Procedure	
Testing Frame:	Landmark 20 kip
Loading Type:	Tension
Load Rate:	0.000426 in./sec
Grips:	0.43-0.65 in. Serrated Vee
Grip Pressure:	1000 psi
Fixture:	N/A
Measurement Equipment:	2 in. Axial Extensometer
	Laser Extensometer
	22 kip Load Cell
Primary Extensometer:	2 in. Axial Extensometer

Initial Measurements		
Average Diameter:	0.186	in.
Initial Area:	0.0272	sq. in.
Initial Gauge Length	2.0000	in.

Final Measurements		
Average Diameter:	0.104	in.
Final Area:	0.0084	sq. in.
Reduction in Area:	69.0	%
Gauge Length at Failure Initiation:	2.0921	in.

Test Results Summary		
Yield Load:	1.955	kip
Peak Load:	2.348	kip
Failure Initiation Load:	1.420	kip
Failure Load (ASTM):	2.113	kip
Displacement at Peak:	0.0158	in.
Displacement at Failure Initiation:	0.0921	in.
Displacement at Failure Load (ASTM):	0.0496	in.
Yield Strength:	71.76	ksi
Ultimate Tensile Strength:	86.22	ksi
Engineering Stress at Failure Initiation:	52.14	ksi
Engineering Stress at Failure (ASTM):	77.60	ksi

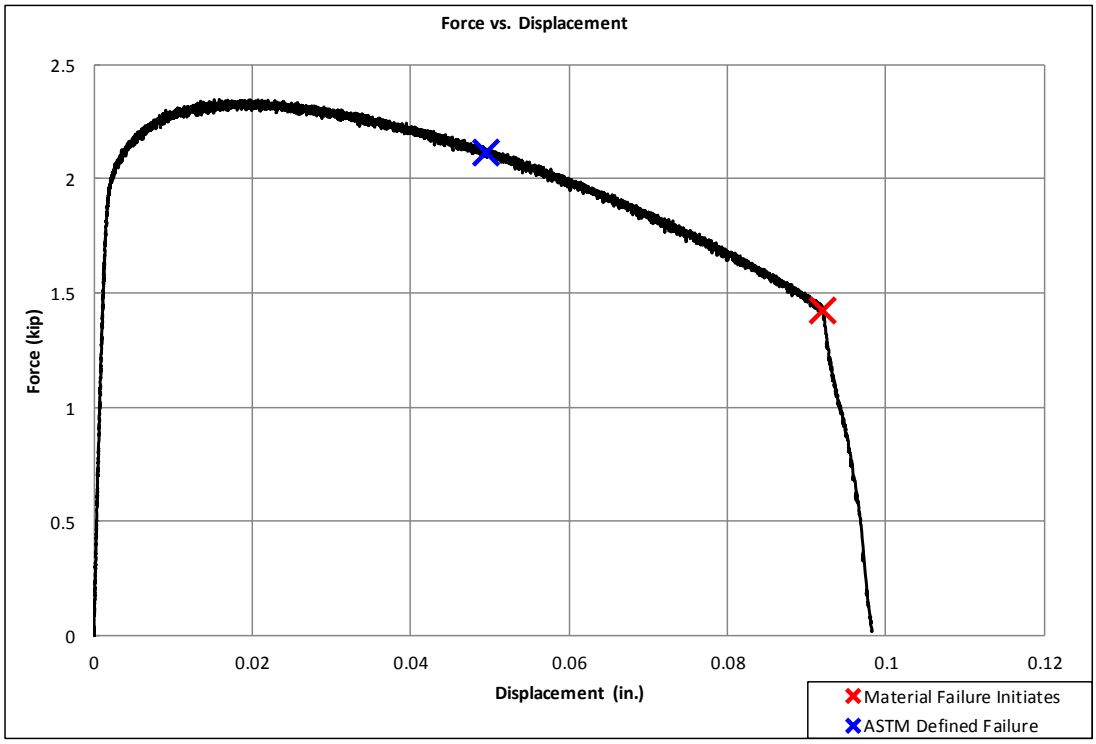

Figure F-16. Test No. SEFT-30 Test Results Summary

MIDWEST ROADSIDE SAFETY FACILITY

Tension Test Summary

Test Information	
Test No.	SEFT-31
Specimen Description:	Notched Round Specimen #2
Specimen Geometry No.:	7
Specimen ID:	72
Test Date:	10/9/2015
Results Folder:	Test Run 82

Testing Procedure	
Testing Frame:	Landmark 20 kip
Loading Type:	Tension
Load Rate:	0.000496 in./sec
Grips:	0.43-0.65 in. Serrated Vee
Grip Pressure:	1000 psi
Fixture:	N/A
Measurement Equipment:	2 in. Axial Extensometer Laser Extensometer 22 kip Load Cell
Primary Extensometer:	2 in. Axial Extensometer

Initial Measurements		
Average Diameter:	0.187	in.
Initial Area:	0.0276	sq. in.
Initial Gauge Length	2.0000	in.

Final Measurements		
Average Diameter:	0.105	in.
Final Area:	0.0087	sq. in.
Reduction in Area:	68.4	%
Gauge Length at Failure Initiation:	2.0940	in.

Test Results Summary		
Yield Load:	1.988	kip
Peak Load:	2.369	kip
Failure Initiation Load:	1.418	kip
Failure Load (ASTM):	2.132	kip
Displacement at Peak:	0.0189	in.
Displacement at Failure Initiation:	0.0940	in.
Displacement at Failure Load (ASTM):	0.0505	in.
Yield Strength:	72.09	ksi
Ultimate Tensile Strength:	85.88	ksi
Engineering Stress at Failure Initiation:	51.41	ksi
Engineering Stress at Failure (ASTM):	77.29	ksi

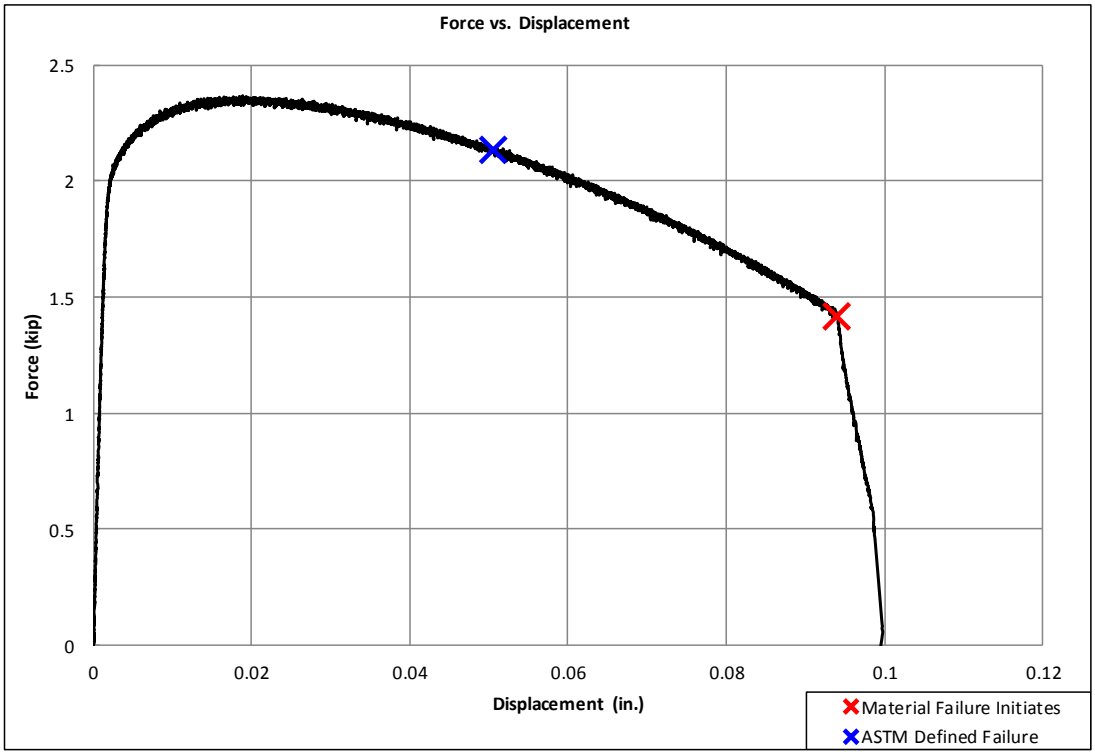

Figure F-17. Test No. SEFT-31 Test Results Summary

MIDWEST ROADSIDE SAFETY FACILITY

Tension Test Summary

Test Information	
Test No.	SEFT-32
Specimen Description:	Notched Round Specimen #2
Specimen Geometry No.:	7
Specimen ID:	73
Test Date:	10/9/2015
Results Folder:	Test Run 83
Testing Procedure	
Testing Frame:	Landmark 20 kip
Loading Type:	Tension
Load Rate:	0.000496 in./sec
Grips:	0.43-0.65 in. Serrated Vee
Grip Pressure:	1000 psi
Fixture:	N/A
Measurement Equipment:	2 in. Axial Extensometer
	Laser Extensometer
	22 kip Load Cell
Primary Extensometer:	2 in. Axial Extensometer

Initial Measurements		
Average Diameter:	0.188	in.
Initial Area:	0.0277	sq. in.
Initial Gauge Length	2.0000	in.
Final Measurements		
Average Diameter:	0.105	in.
Final Area:	0.0086	sq. in.
Reduction in Area:	68.8	%
Gauge Length at Failure Initiation:	2.0933	in.
Test Results Summary		
Yield Load:	2.003	kip
Peak Load:	2.392	kip
Failure Initiation Load:	1.433	kip
Failure Load (ASTM):	2.152	kip
Displacement at Peak:	0.0176	in.
Displacement at Failure Initiation:	0.0933	in.
Displacement at Failure Load (ASTM):	0.0499	in.
Yield Strength:	72.41	ksi
Ultimate Tensile Strength:	86.46	ksi
Engineering Stress at Failure Initiation:	51.82	ksi
Engineering Stress at Failure (ASTM):	77.82	ksi

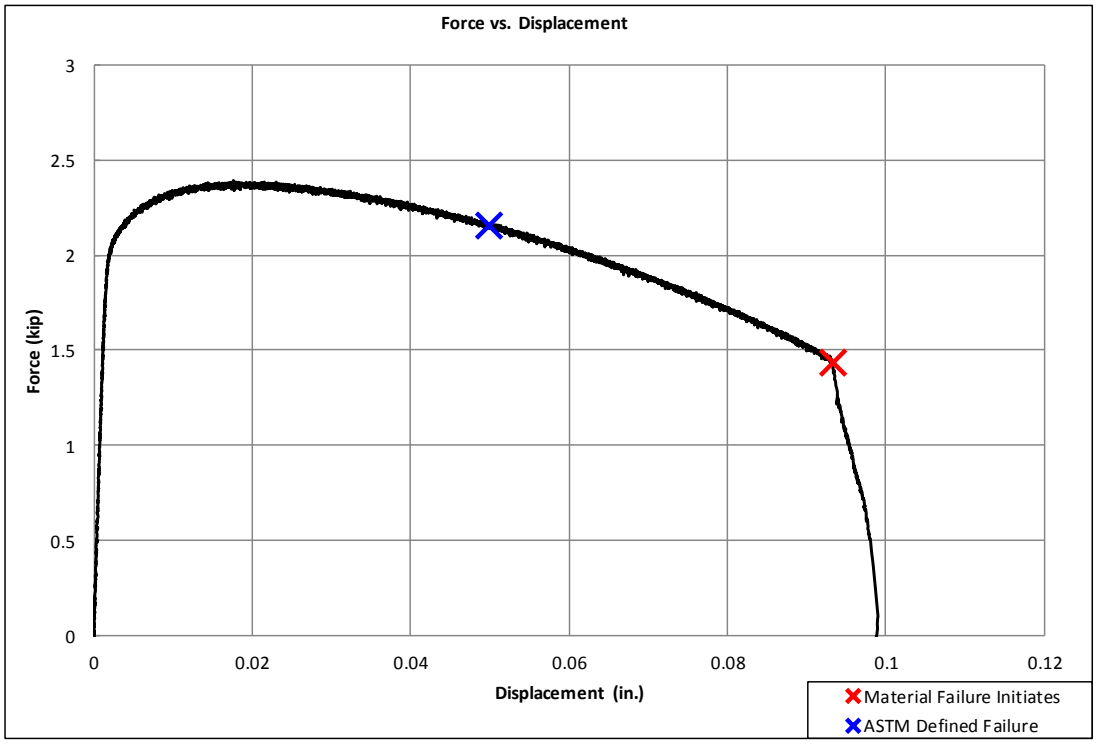

Figure F-18. Test No. SEFT-32 Test Results Summary

MIDWEST ROADSIDE SAFETY FACILITY

Tension Test Summary

Test Information	
Test No.	SEFT-33
Specimen Description:	Notched Round Specimen #3
Specimen Geometry No.:	8
Specimen ID:	77
Test Date:	10/9/2015
Results Folder:	Test Run 84
Testing Procedure	
Testing Frame:	Landmark 20 kip
Loading Type:	Tension
Load Rate:	0.000366 in./sec
Grips:	0.43-0.65 in. Serrated Vee
Grip Pressure:	1000 psi
Fixture:	N/A
Measurement Equipment:	2 in. Axial Extensometer
	Laser Extensometer
	22 kip Load Cell
Primary Extensometer:	2 in. Axial Extensometer

Initial Measurements		
Average Diameter:	0.186	in.
Initial Area:	0.0273	sq. in.
Initial Gauge Length	2.0000	in.
Final Measurements		
Average Diameter:	0.110	in.
Final Area:	0.0095	sq. in.
Reduction in Area:	65.1	%
Gauge Length at Failure Initiation:	2.0800	in.
Test Results Summary		
Yield Load:	2.086	kip
Peak Load:	2.464	kip
Failure Initiation Load:	1.529	kip
Failure Load (ASTM):	2.218	kip
Displacement at Peak:	0.0157	in.
Displacement at Failure Initiation:	0.0800	in.
Displacement at Failure Load (ASTM):	0.0423	in.
Yield Strength:	76.38	ksi
Ultimate Tensile Strength:	90.23	ksi
Engineering Stress at Failure Initiation:	55.98	ksi
Engineering Stress at Failure (ASTM):	81.21	ksi

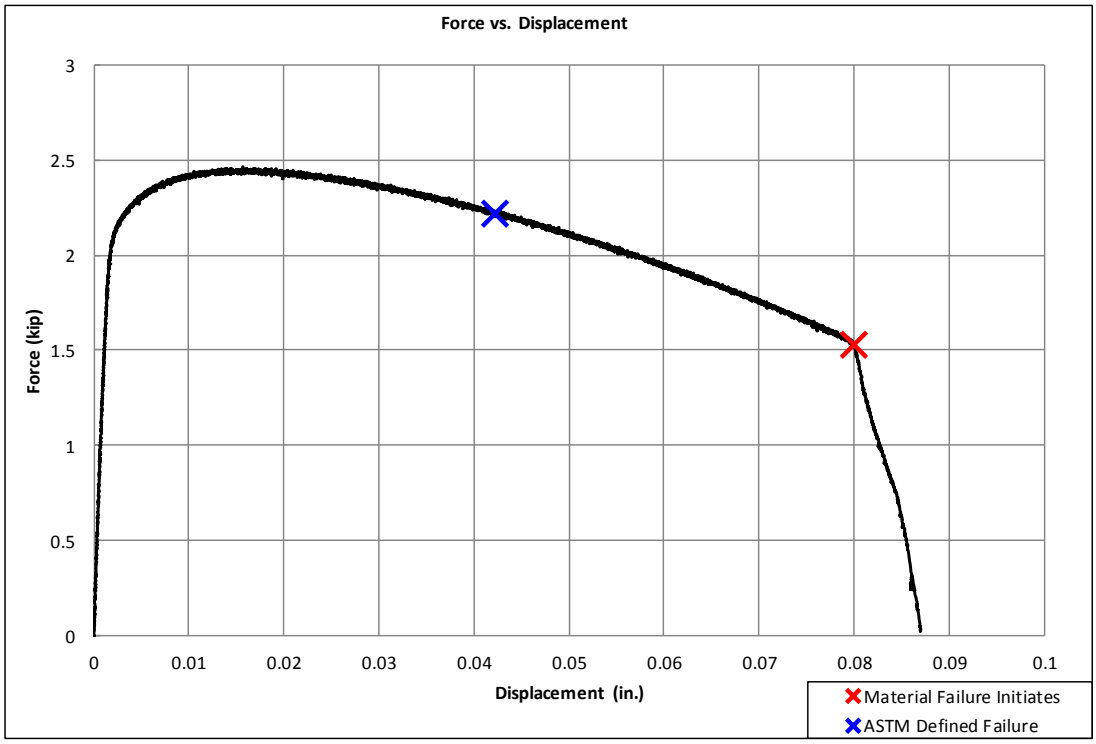

Figure F-19. Test No. SEFT-33 Test Results Summary

MIDWEST ROADSIDE SAFETY FACILITY

Tension Test Summary

Test Information

Test No.	SEFT-34
Specimen Description:	Notched Round Specimen #3
Specimen Geometry No.:	8
Specimen ID:	78
Test Date:	10/9/2015
Results Folder:	Test Run 85

Testing Procedure

Testing Frame:	Landmark 20 kip
Loading Type:	Tension
Load Rate:	0.000447 in./sec
Grips:	0.43-0.65 in. Serrated Vee
Grip Pressure:	1000 psi
Fixture:	N/A
Measurement Equipment:	2 in. Axial Extensometer
	Laser Extensometer
	22 kip Load Cell
Primary Extensometer:	2 in. Axial Extensometer

Initial Measurements

Average Diameter:	0.187	in.
Initial Area:	0.0274	sq. in.
Initial Gauge Length	2.0000	in.

Final Measurements

Average Diameter:	0.112	in.
Final Area:	0.0098	sq. in.
Reduction in Area:	64.0	%
Gauge Length at Failure Initiation:	2.0791	in.

Test Results Summary

Yield Load:	2.108	kip
Peak Load:	2.483	kip
Failure Initiation Load:	1.559	kip
Failure Load (ASTM):	2.235	kip
Displacement at Peak:	0.0148	in.
Displacement at Failure Initiation:	0.0791	in.
Displacement at Failure Load (ASTM):	0.0427	in.
Yield Strength:	77.08	ksi
Ultimate Tensile Strength:	90.78	ksi
Engineering Stress at Failure Initiation:	57.00	ksi
Engineering Stress at Failure (ASTM):	81.70	ksi

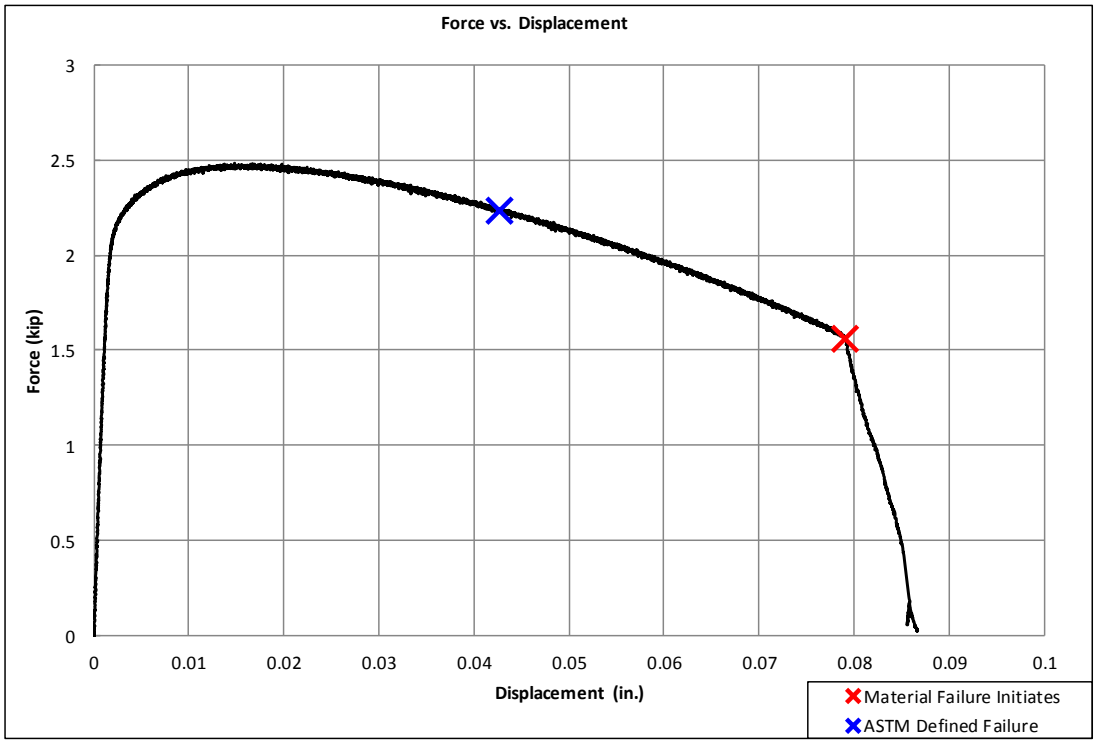

Figure F-20. Test No. SEFT-34 Test Results Summary

MIDWEST ROADSIDE SAFETY FACILITY

Tension Test Summary

Test Information	
Test No.	SEFT-35
Specimen Description:	Notched Round Specimen #3
Specimen Geometry No.:	8
Specimen ID:	79
Test Date:	10/9/2015
Results Folder:	Test Run 86

Testing Procedure	
Testing Frame:	Landmark 20 kip
Loading Type:	Tension
Load Rate:	0.000447 in./sec
Grips:	0.43-0.65 in. Serrated Vee
Grip Pressure:	1000 psi
Fixture:	N/A
Measurement Equipment:	2 in. Axial Extensometer Laser Extensometer 22 kip Load Cell
Primary Extensometer:	2 in. Axial Extensometer

Initial Measurements		
Average Diameter:	0.188	in.
Initial Area:	0.0278	sq. in.
Initial Gauge Length	2.0000	in.

Final Measurements		
Average Diameter:	0.108	in.
Final Area:	0.0091	sq. in.
Reduction in Area:	67.3	%
Gauge Length at Failure Initiation:	2.0810	in.

Test Results Summary		
Yield Load:	2.139	kip
Peak Load:	2.515	kip
Failure Initiation Load:	1.570	kip
Failure Load (ASTM):	2.264	kip
Displacement at Peak	0.0151	in.
Displacement at Failure Initiation:	0.0810	in.
Displacement at Failure Load (ASTM):	0.0439	in.
Yield Strength:	77.01	ksi
Ultimate Tensile Strength:	77.01	ksi
Engineering Stress at Failure Initiation:	56.53	ksi
Engineering Stress at Failure (ASTM):	81.49	ksi

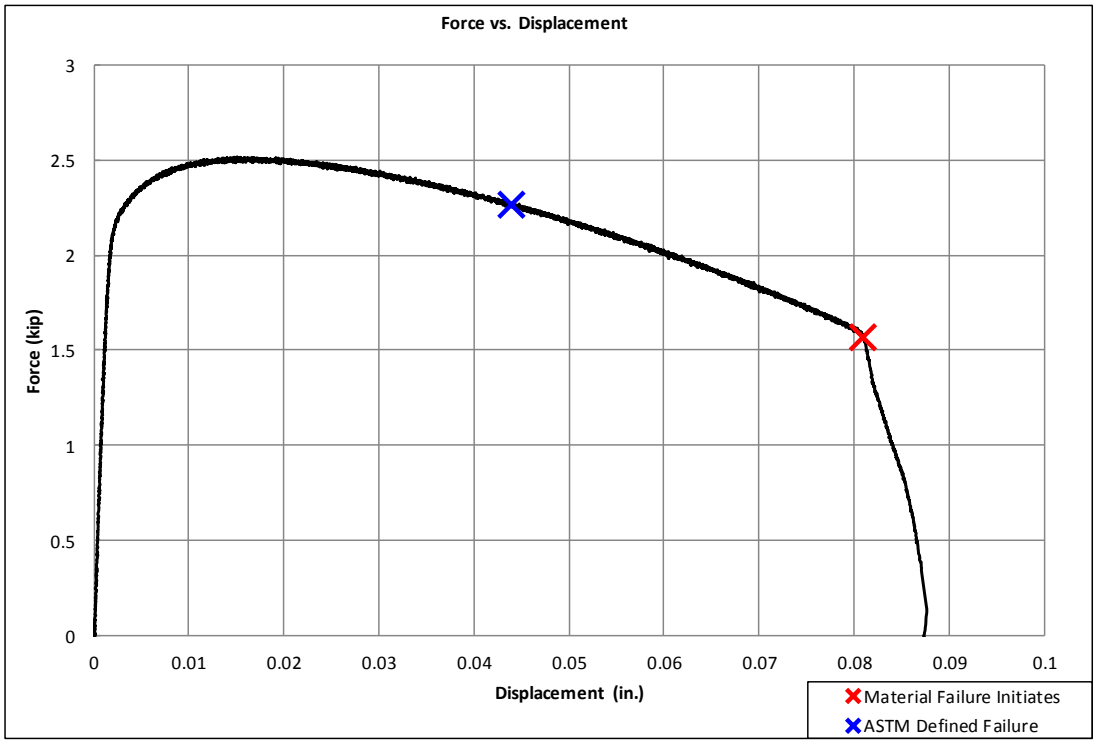

Figure F-21. Test No. SEFT-35 Test Results Summary

MIDWEST ROADSIDE SAFETY FACILITY

Tension Test Summary

Test Information	
Test No.	SEFT-36
Specimen Description:	Notched Round Specimen #4
Specimen Geometry No.:	9
Specimen ID:	083
Test Date:	10/12/2015
Results Folder:	Test Run 87
Testing Procedure	
Testing Frame:	Landmark 20 kip
Loading Type:	Tension
Load Rate:	0.000177 in./sec
Grips:	0.43-0.65 in. Serrated Vee
Grip Pressure:	1000 psi
Fixture:	N/A
Measurement Equipment:	2 in. Axial Extensometer
	Laser Extensometer
	22 kip Load Cell
Primary Extensometer:	2 in. Axial Extensometer

Initial Measurements		
Average Diameter:	0.188	in.
Initial Area:	0.0277	sq. in.
Initial Gauge Length	2.0000	in.
Final Measurements		
Average Diameter:	0.115	in.
Final Area:	0.0104	sq. in.
Reduction in Area:	62.5	%
Gauge Length at Failure Initiation:	2.0724	in.
Test Results Summary		
Yield Load:	2.208	kip
Peak Load:	2.565	kip
Failure Initiation Load:	1.652	kip
Failure Load (ASTM):	2.308	kip
Displacement at Peak:	0.0149	in.
Displacement at Failure Initiation:	0.0724	in.
Displacement at Failure Load (ASTM):	0.0381	in.
Yield Strength:	79.62	ksi
Ultimate Tensile Strength:	92.47	ksi
Engineering Stress at Failure Initiation:	59.55	ksi
Engineering Stress at Failure (ASTM):	83.22	ksi

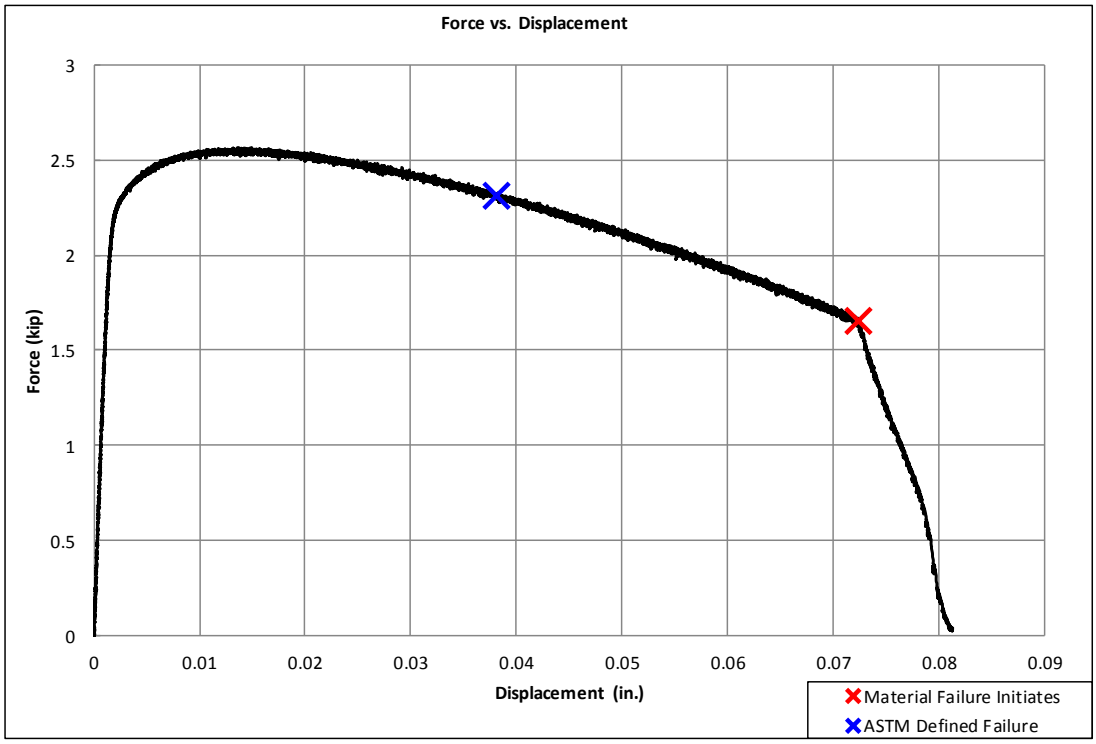

Figure F-22. Test No. SEFT-36 Test Results Summary

MIDWEST ROADSIDE SAFETY FACILITY

Tension Test Summary

Test Information	
Test No.	SEFT-37
Specimen Description:	Notched Round Specimen #4
Specimen Geometry No.:	9
Specimen ID:	084
Test Date:	10/12/2015
Results Folder:	Test Run 88

Testing Procedure	
Testing Frame:	Landmark 20 kip
Loading Type:	Tension
Load Rate:	0.000404 in./sec
Grips:	0.43-0.65 in. Serrated Vee
Grip Pressure:	1000 psi
Fixture:	N/A
Measurement Equipment:	2 in. Axial Extensometer
	Laser Extensometer
	22 kip Load Cell
Primary Extensometer:	2 in. Axial Extensometer

Initial Measurements		
Average Diameter:	0.186	in.
Initial Area:	0.0273	sq. in.
Initial Gauge Length	2.0000	in.

Final Measurements		
Average Diameter:	0.114	in.
Final Area:	0.0103	sq. in.
Reduction in Area:	62.3	%
Gauge Length at Failure Initiation:	2.0709	in.

Test Results Summary		
Yield Load:	2.137	kip
Peak Load:	2.537	kip
Failure Initiation Load:	1.658	kip
Failure Load (ASTM):	2.283	kip
Displacement at Peak:	0.0130	in.
Displacement at Failure Initiation:	0.0709	in.
Displacement at Failure Load (ASTM):	0.0381	in.
Yield Strength:	78.23	ksi
Ultimate Tensile Strength:	92.89	ksi
Engineering Stress at Failure Initiation:	60.71	ksi
Engineering Stress at Failure (ASTM):	83.60	ksi

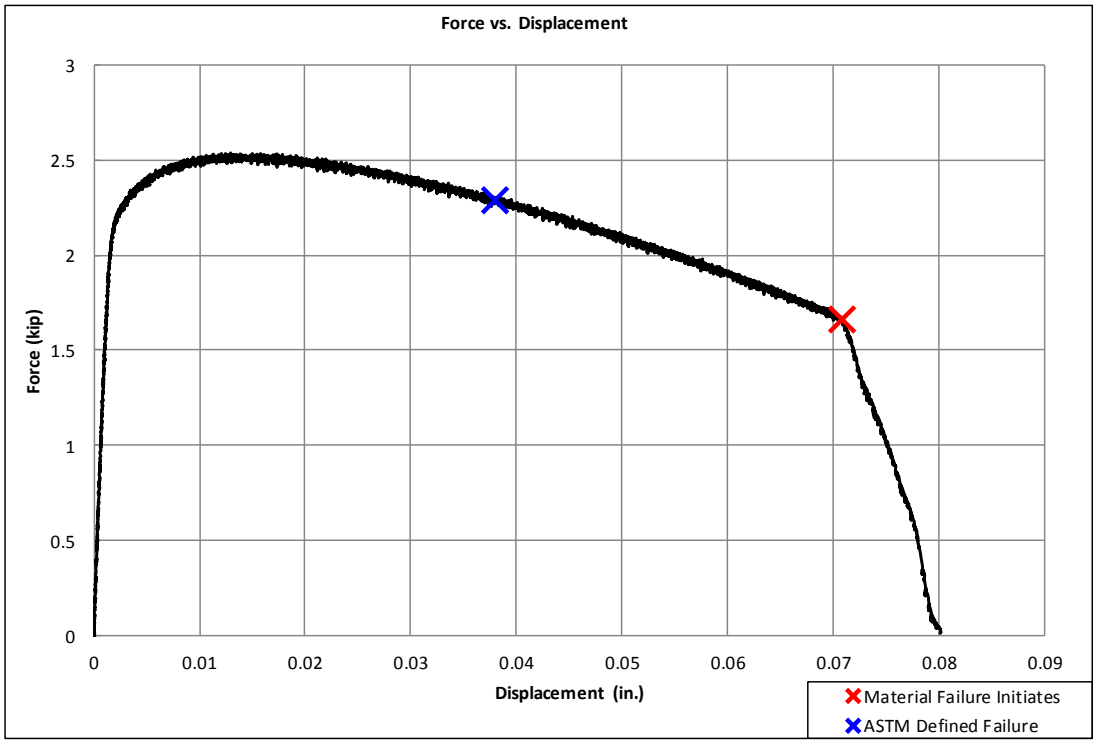

Figure F-23. Test No. SEFT-37 Test Results Summary

MIDWEST ROADSIDE SAFETY FACILITY

Tension Test Summary

Test Information	
Test No.	SEFT-38
Specimen Description:	Notched Round Specimen #4
Specimen Geometry No.:	9
Specimen ID:	085
Test Date:	10/12/2015
Results Folder:	Test Run 89

Testing Procedure	
Testing Frame:	Landmark 20 kip
Loading Type:	Tension
Load Rate:	0.000404 in./sec
Grips:	0.43-0.65 in. Serrated Vee
Grip Pressure:	1000 psi
Fixture:	N/A
Measurement Equipment:	2 in. Axial Extensometer
	Laser Extensometer
	22 kip Load Cell
Primary Extensometer:	2 in. Axial Extensometer

Initial Measurements		
Average Diameter:	0.188	in.
Initial Area:	0.0278	sq. in.
Initial Gauge Length	2.0000	in.

Final Measurements		
Average Diameter:	0.113	in.
Final Area:	0.0100	sq. in.
Reduction in Area:	64.1	%
Gauge Length at Failure Initiation:	2.0723	in.

Test Results Summary		
Yield Load:	2.205	kip
Peak Load:	2.592	kip
Failure Initiation Load:	1.672	kip
Failure Load (ASTM):	2.333	kip
Displacement at Peak:	0.0128	in.
Displacement at Failure Initiation:	0.0723	in.
Displacement at Failure Load (ASTM):	0.0384	in.
Yield Strength:	79.28	ksi
Ultimate Tensile Strength:	93.18	ksi
Engineering Stress at Failure Initiation:	60.12	ksi
Engineering Stress at Failure (ASTM):	83.86	ksi

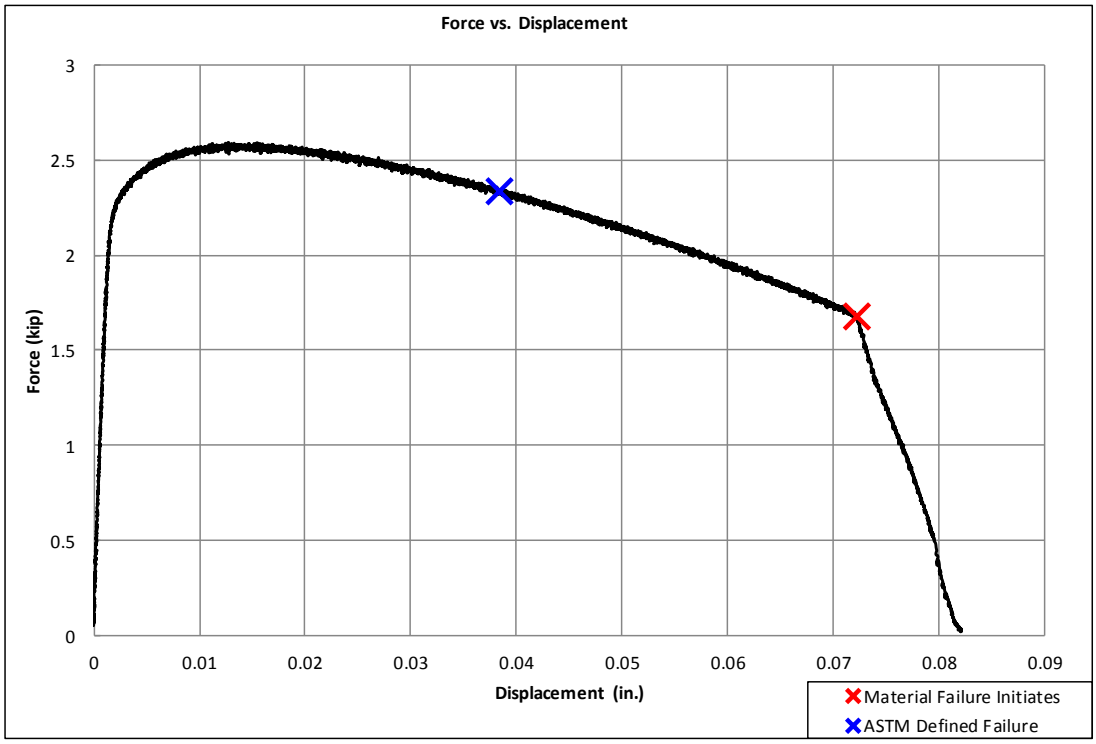

Figure F-24. Test No. SEFT-38 Test Results Summary

MIDWEST ROADSIDE SAFETY FACILITY

Tension Test Summary

Test Information	
Test No.	SEFT-39
Specimen Description:	Notched Round Specimen #5
Specimen Geometry No.:	10
Specimen ID:	089
Test Date:	10/12/2015
Results Folder:	Test Run 90
Testing Procedure	
Testing Frame:	Landmark 20 kip
Loading Type:	Tension
Load Rate:	0.000324 in./sec
Grips:	0.43-0.65 in. Serrated Vee
Grip Pressure:	1000 psi
Fixture:	N/A
Measurement Equipment:	2 in. Axial Extensometer
	Laser Extensometer
	22 kip Load Cell
Primary Extensometer:	2 in. Axial Extensometer

Initial Measurements		
Average Diameter:	0.188	in.
Initial Area:	0.0278	sq. in.
Initial Gauge Length	2.0000	in.
Final Measurements		
Average Diameter:	0.118	in.
Final Area:	0.0110	sq. in.
Reduction in Area:	60.5	%
Gauge Length at Failure Initiation:	2.0589	in.
Test Results Summary		
Yield Load:	2.358	kip
Peak Load:	2.736	kip
Failure Initiation Load:	1.858	kip
Failure Load (ASTM):	2.462	kip
Displacement at Peak:	0.0110	in.
Displacement at Failure Initiation:	0.0589	in.
Displacement at Failure Load (ASTM):	0.0324	in.
Yield Strength:	84.89	ksi
Ultimate Tensile Strength:	98.48	ksi
Engineering Stress at Failure Initiation:	66.88	ksi
Engineering Stress at Failure (ASTM):	88.64	ksi

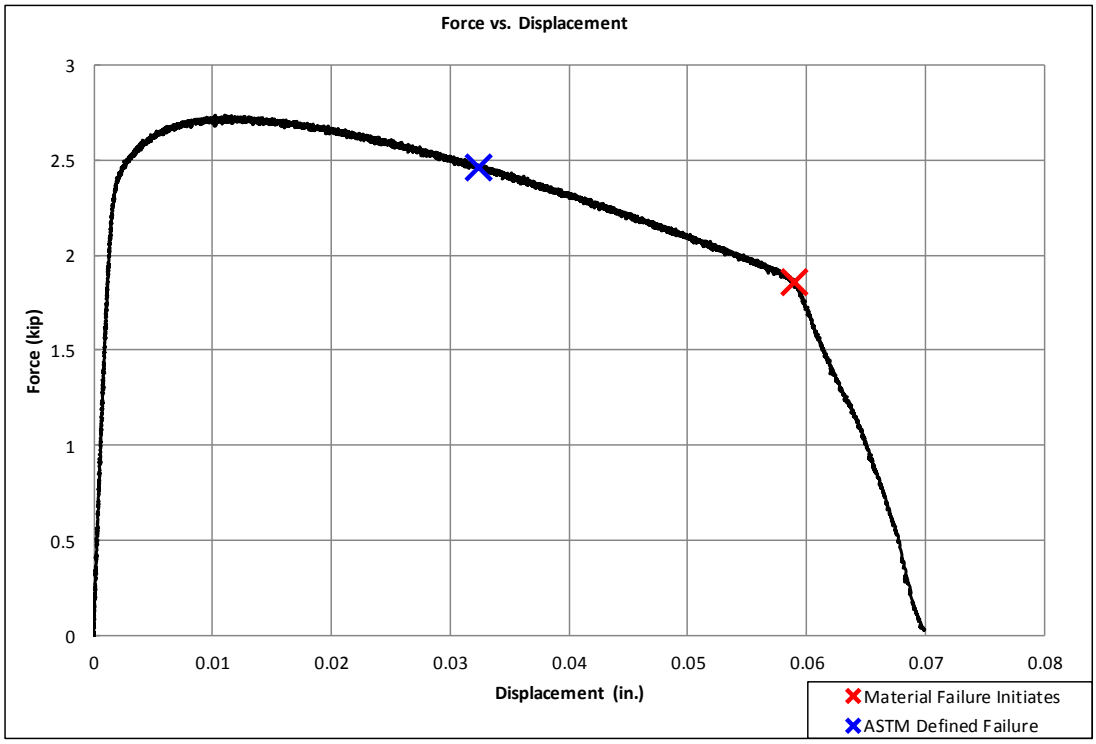

Figure F-25. Test No. SEFT-39 Test Results Summary

MIDWEST ROADSIDE SAFETY FACILITY

Tension Test Summary

Test Information	
Test No.	SEFT-40
Specimen Description:	Notched Round Specimen #5
Specimen Geometry No.:	10
Specimen ID:	090
Test Date:	10/12/2015
Results Folder:	Test Run 91
Testing Procedure	
Testing Frame:	Landmark 20 kip
Loading Type:	Tension
Load Rate:	0.000353 in./sec
Grips:	0.43-0.65 in. Serrated Vee
Grip Pressure:	1000 psi
Fixture:	N/A
Measurement Equipment:	2 in. Axial Extensometer
	Laser Extensometer
	22 kip Load Cell
Primary Extensometer:	2 in. Axial Extensometer

Initial Measurements		
Average Diameter:	0.188	in.
Initial Area:	0.0279	sq. in.
Initial Gauge Length	2.0000	in.
Final Measurements		
Average Diameter:	0.117	in.
Final Area:	0.0107	sq. in.
Reduction in Area:	61.6	%
Gauge Length at Failure Initiation:	2.0605	in.
Test Results Summary		
Yield Load:	2.387	kip
Peak Load:	2.733	kip
Failure Initiation Load:	1.837	kip
Failure Load (ASTM):	2.460	kip
Displacement at Peak:	0.0119	in.
Displacement at Failure Initiation:	0.0605	in.
Displacement at Failure Load (ASTM):	0.0331	in.
Yield Strength:	85.68	ksi
Ultimate Tensile Strength:	98.13	ksi
Engineering Stress at Failure Initiation:	65.94	ksi
Engineering Stress at Failure (ASTM):	88.31	ksi

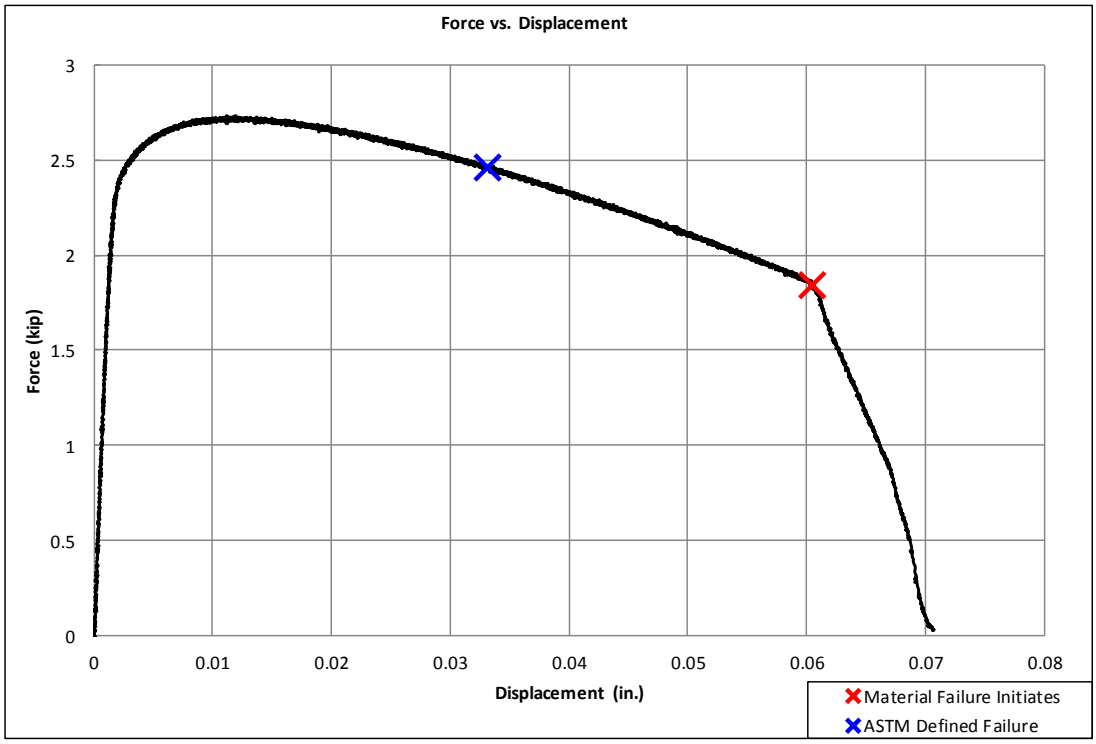

Figure F-26. Test No. SEFT-40 Test Results Summary

MIDWEST ROADSIDE SAFETY FACILITY

Tension Test Summary

Test Information	
Test No.	SEFT-41
Specimen Description:	Notched Round Specimen #5
Specimen Geometry No.:	10
Specimen ID:	091
Test Date:	10/12/2015
Results Folder:	Test Run 92
Testing Procedure	
Testing Frame:	Landmark 20 kip
Loading Type:	Tension
Load Rate:	0.000353 in./sec
Grips:	0.43-0.65 in. Serrated Vee
Grip Pressure:	1000 psi
Fixture:	N/A
Measurement Equipment:	2 in. Axial Extensometer
	Laser Extensometer
	22 kip Load Cell
Primary Extensometer:	2 in. Axial Extensometer

Initial Measurements		
Average Diameter:	0.188	in.
Initial Area:	0.0279	sq. in.
Initial Gauge Length	2.0000	in.
Final Measurements		
Average Diameter:	0.119	in.
Final Area:	0.0112	sq. in.
Reduction in Area:	59.8	%
Gauge Length at Failure Initiation:	2.0606	in.
Test Results Summary		
Yield Load:	2.398	kip
Peak Load:	2.737	kip
Failure Initiation Load:	1.821	kip
Failure Load (ASTM):	2.463	kip
Displacement at Peak:	0.0106	in.
Displacement at Failure Initiation:	0.0606	in.
Displacement at Failure Load (ASTM):	0.0327	in.
Yield Strength:	85.96	ksi
Ultimate Tensile Strength:	98.13	ksi
Engineering Stress at Failure Initiation:	65.28	ksi
Engineering Stress at Failure (ASTM):	88.32	ksi

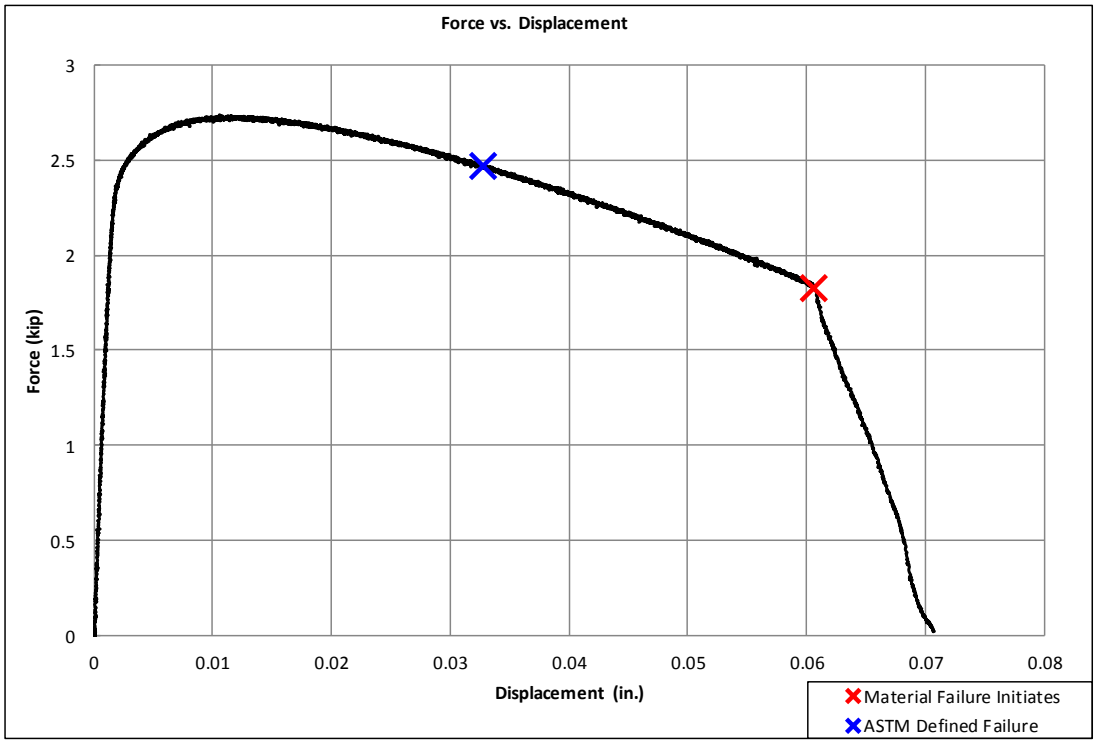

Figure F-27. Test No. SEFT-41 Test Results Summary

MIDWEST ROADSIDE SAFETY FACILITY

Tension Test Summary

Test Information	
Test No.	SEFT-42
Specimen Description:	Thick Dog Bone
Specimen Geometry No.:	11
Specimen ID:	095
Test Date:	10/23/2015
Results Folder:	Test Run 93

Testing Procedure	
Testing Frame:	Landmark 20 kip
Loading Type:	Tension
Load Rate:	0.0004 in./sec
Grips:	0.28-0.56 in. Flat Diamond Wedge
Grip Pressure:	1000 psi
Fixture:	N/A
Measurement Equipment:	2 in. Axial Extensometer
	Laser Extensometer
	22 kip Load Cell
Primary Extensometer:	2 in. Axial Extensometer

Initial Measurements		
Average Width:	0.080	in.
Average Thickness:	1.001	in.
Initial Area:	0.0804	sq. in.
Initial Gauge Length	2.0000	in.

Final Measurements		
Average Width:	0.052	in.
Average Thickness:	0.905	in.
Final Area:	0.0473	sq. in.
Reduction in Area:	41.2	%
Gauge Length at Failure Initiation:	2.0725	in.

Test Results Summary		
Yield Load:	5.366	kip
Peak Load:	6.593	kip
Failure Initiation Load:	5.448	kip
Failure Load (ASTM):	5.934	kip
Displacement at Peak:	0.0295	in.
Displacement at Failure Initiation:	0.0725	in.
Displacement at Failure Load (ASTM):	0.0651	in.
Yield Strength:	66.76	ksi
Ultimate Tensile Strength:	82.02	ksi
Engineering Stress at Failure Initiation:	67.77	ksi
Engineering Stress at Failure (ASTM):	73.82	ksi

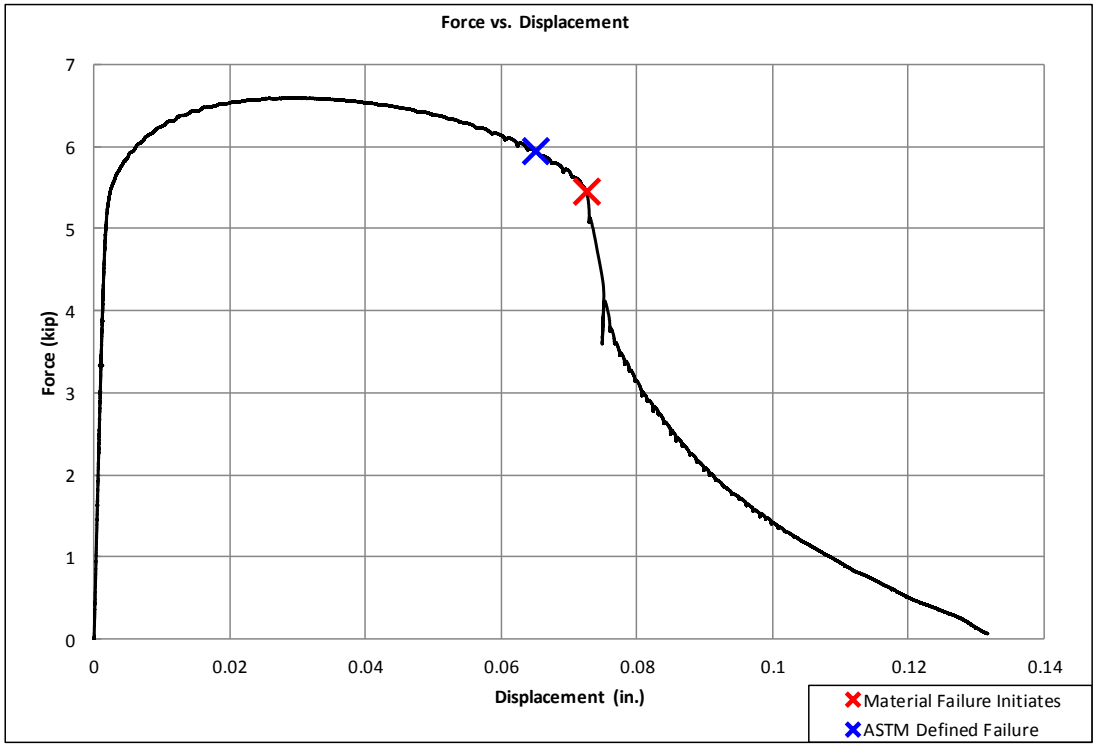

Figure F-28. Test No. SEFT-42 Test Results Summary

MIDWEST ROADSIDE SAFETY FACILITY

Tension Test Summary

Test Information	
Test No.	SEFT-43
Specimen Description:	Thick Dog Bone
Specimen Geometry No.:	11
Specimen ID:	096
Test Date:	10/23/2015
Results Folder:	Test Run 94

Testing Procedure	
Testing Frame:	Landmark 20 kip
Loading Type:	Tension
Load Rate:	0.0004 in./sec
Grips:	0.28-0.56 in. Flat Diamond Wedge
Grip Pressure:	1000 psi
Fixture:	N/A
Measurement Equipment:	2 in. Axial Extensometer
	Laser Extensometer
	22 kip Load Cell
Primary Extensometer:	2 in. Axial Extensometer

Initial Measurements		
Average Width:	0.081	in.
Average Thickness:	1.000	in.
Initial Area:	0.0810	sq. in.
Initial Gauge Length	2.0000	in.

Final Measurements		
Average Width:	0.053	in.
Average Thickness:	0.902	in.
Final Area:	0.0475	sq. in.
Reduction in Area:	41.3	%
Gauge Length at Failure Initiation:	2.0736	in.

Test Results Summary		
Yield Load:	5.016	kip
Peak Load:	6.463	kip
Failure Initiation Load:	5.383	kip
Failure Load (ASTM):	5.816	kip
Displacement at Peak:	0.0294	in.
Displacement at Failure Initiation:	0.0736	in.
Displacement at Failure Load (ASTM):	0.0661	in.
Yield Strength:	61.95	ksi
Ultimate Tensile Strength:	79.81	ksi
Engineering Stress at Failure Initiation:	66.48	ksi
Engineering Stress at Failure (ASTM):	71.83	ksi

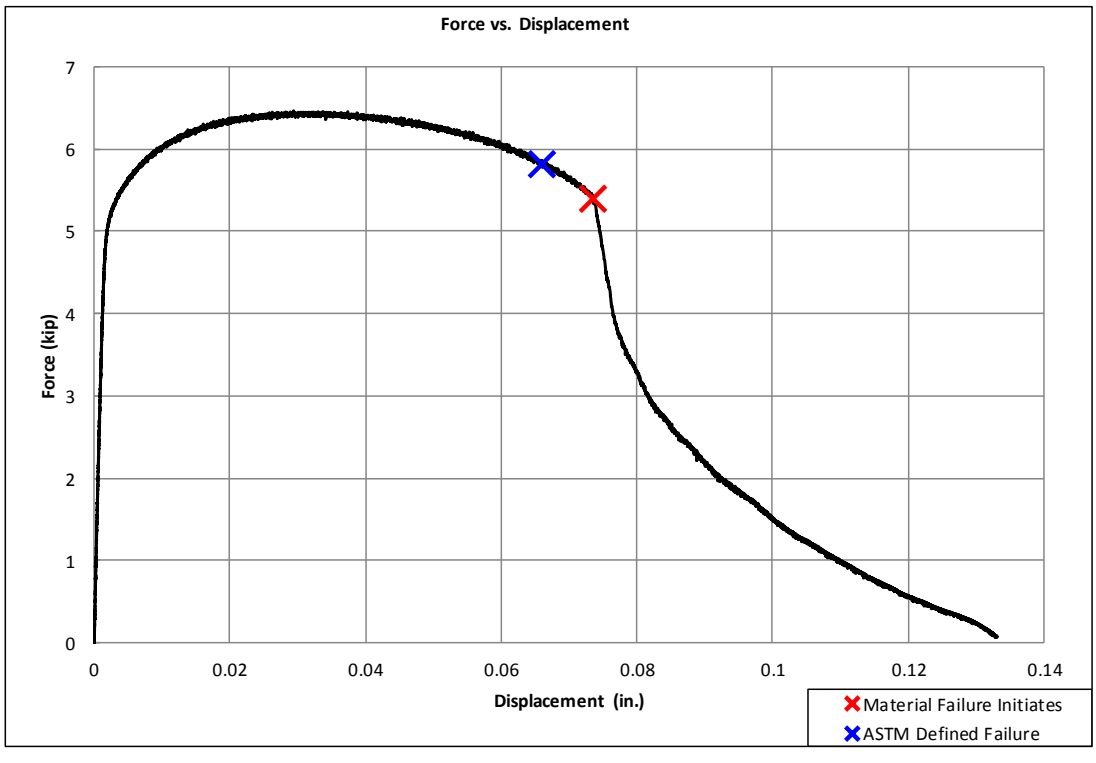

Figure F-29. Test No. SEFT-43 Test Results Summary

MIDWEST ROADSIDE SAFETY FACILITY

Tension Test Summary

Test Information	
Test No.	SEFT-44
Specimen Description:	Thick Dog Bone
Specimen Geometry No.:	11
Specimen ID:	097
Test Date:	10/23/2015
Results Folder:	Test Run 95

Testing Procedure	
Testing Frame:	Landmark 20 kip
Loading Type:	Tension
Load Rate:	0.0004 in./sec
Grips:	0.28-0.56 in. Flat Diamond Wedge
Grip Pressure:	1000 psi
Fixture:	N/A
Measurement Equipment:	2 in. Axial Extensometer
	Laser Extensometer
	22 kip Load Cell
Primary Extensometer:	2 in. Axial Extensometer

Initial Measurements		
Average Width:	0.080	in.
Average Thickness:	1.000	in.
Initial Area:	0.0799	sq. in.
Initial Gauge Length	2.0000	in.

Final Measurements		
Average Width:	0.054	in.
Average Thickness:	0.903	in.
Final Area:	0.0489	sq. in.
Reduction in Area:	38.8	%
Gauge Length at Failure Initiation:	2.0726	in.

Test Results Summary		
Yield Load:	5.121	kip
Peak Load:	6.505	kip
Failure Initiation Load:	5.392	kip
Failure Load (ASTM):	5.854	kip
Displacement at Peak:	0.0298	in.
Displacement at Failure Initiation:	0.0726	in.
Displacement at Failure Load (ASTM):	0.0651	in.
Yield Strength:	64.06	ksi
Ultimate Tensile Strength:	81.37	ksi
Engineering Stress at Failure Initiation:	67.45	ksi
Engineering Stress at Failure (ASTM):	73.23	ksi

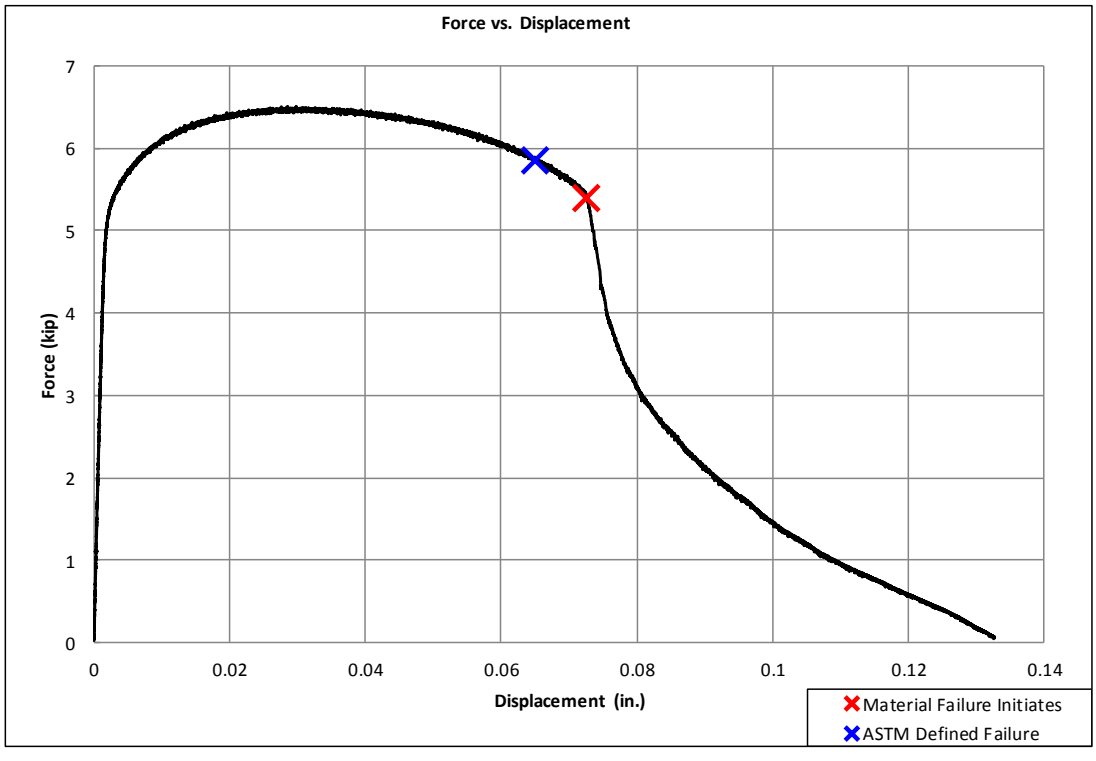

Figure F-30. Test No. SEFT-44 Test Results Summary

MIDWEST ROADSIDE SAFETY FACILITY

Tension Test Summary

Test Information

Test No.	SEFT-45
Specimen Description:	Thick Large Notch
Specimen Geometry No.:	13
Specimen ID:	101
Test Date:	10/23/2015
Results Folder:	Test Run 96

Testing Procedure

Testing Frame:	Landmark 20 kip
Loading Type:	Tension
Load Rate:	0.00052 in./sec
Grips:	0.28-0.56 in. Flat Diamond Wedge
Grip Pressure:	1000 psi
Fixture:	N/A
Measurement Equipment:	2 in. Axial Extensometer Laser Extensometer 22 kip Load Cell
Primary Extensometer:	2 in. Axial Extensometer

Note: The specimen did not completely separate before the test was stopped.

Initial Measurements

Average Width:	0.081 in.
Average Thickness:	1.000 in.
Initial Area:	0.0814 sq. in.
Initial Gauge Length	2.0000 in.

Final Measurements

Average Width:	0.053 in.
Average Thickness:	0.935 in.
Final Area:	0.0495 sq. in.
Reduction in Area:	39.2 %
Gauge Length at Failure Initiation:	2.0528 in.

Test Results Summary

Yield Load:	5.918 kip
Peak Load:	7.064 kip
Failure Initiation Load:	5.549 kip
Failure Load (ASTM):	6.357 kip
Displacement at Peak:	0.0203 in.
Displacement at Failure Initiation:	0.0528 in.
Displacement at Failure Load (ASTM):	0.0433 in.
Yield Strength:	72.72 ksi
Ultimate Tensile Strength:	86.80 ksi
Engineering Stress at Failure Initiation:	68.19 ksi
Engineering Stress at Failure (ASTM):	78.12 ksi

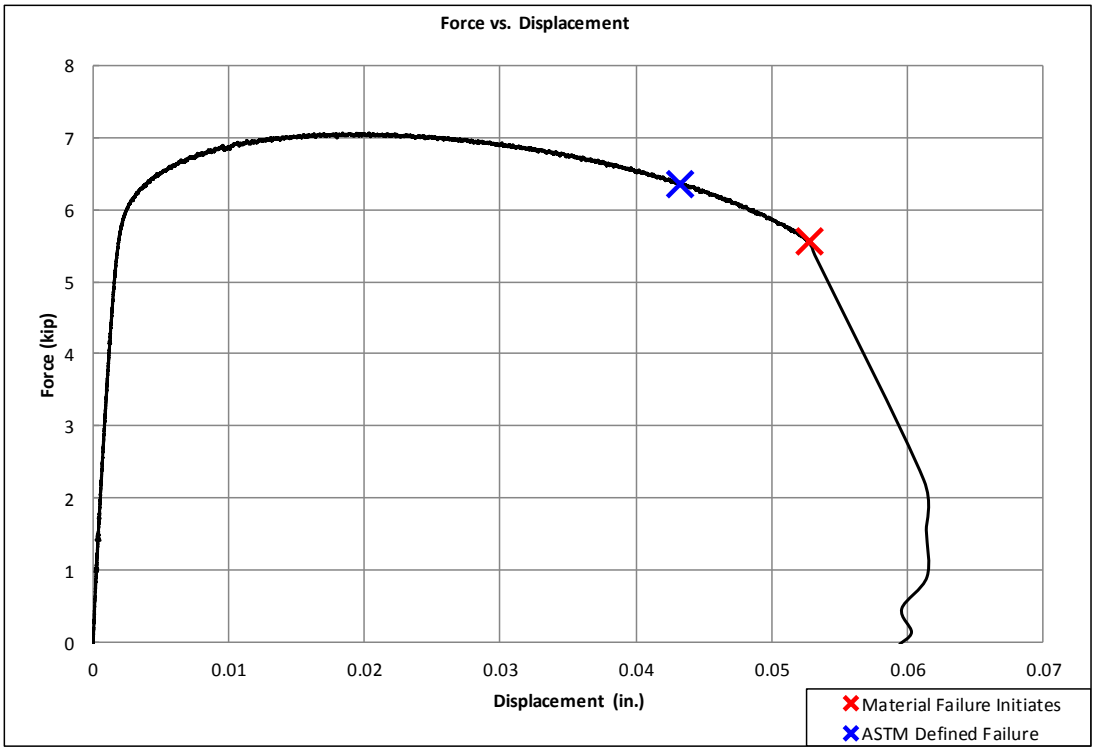

Figure F-31. Test No. SEFT-45 Test Results Summary

MIDWEST ROADSIDE SAFETY FACILITY

Tension Test Summary

Test Information	
Test No.	SEFT-46
Specimen Description:	Thick Large Notch
Specimen Geometry No.:	13
Specimen ID:	102
Test Date:	10/23/2015
Results Folder:	Test Run 97

Testing Procedure	
Testing Frame:	Landmark 20 kip
Loading Type:	Tension
Load Rate:	0.000312 in./sec
Grips:	0.28-0.56 in. Flat Diamond Wedge
Grip Pressure:	1000 psi
Fixture:	N/A
Measurement Equipment:	2 in. Axial Extensometer
	Laser Extensometer
	22 kip Load Cell
Primary Extensometer:	2 in. Axial Extensometer

Initial Measurements		
Average Width:	0.081	in.
Average Thickness:	0.999	in.
Initial Area:	0.0812	sq. in.
Initial Gauge Length	2.0000	in.

Final Measurements		
Average Width:	0.053	in.
Average Thickness:	0.934	in.
Final Area:	0.0499	sq. in.
Reduction in Area:	38.5	%
Gauge Length at Failure Initiation:	2.0494	in.

Test Results Summary		
Yield Load:	5.943	kip
Peak Load:	6.997	kip
Failure Initiation Load:	5.725	kip
Failure Load (ASTM):	6.297	kip
Displacement at Peak:	0.0175	in.
Displacement at Failure Initiation:	0.0494	in.
Displacement at Failure Load (ASTM):	0.0424	in.
Yield Strength:	73.21	ksi
Ultimate Tensile Strength:	86.19	ksi
Engineering Stress at Failure Initiation:	70.53	ksi
Engineering Stress at Failure (ASTM):	77.57	ksi

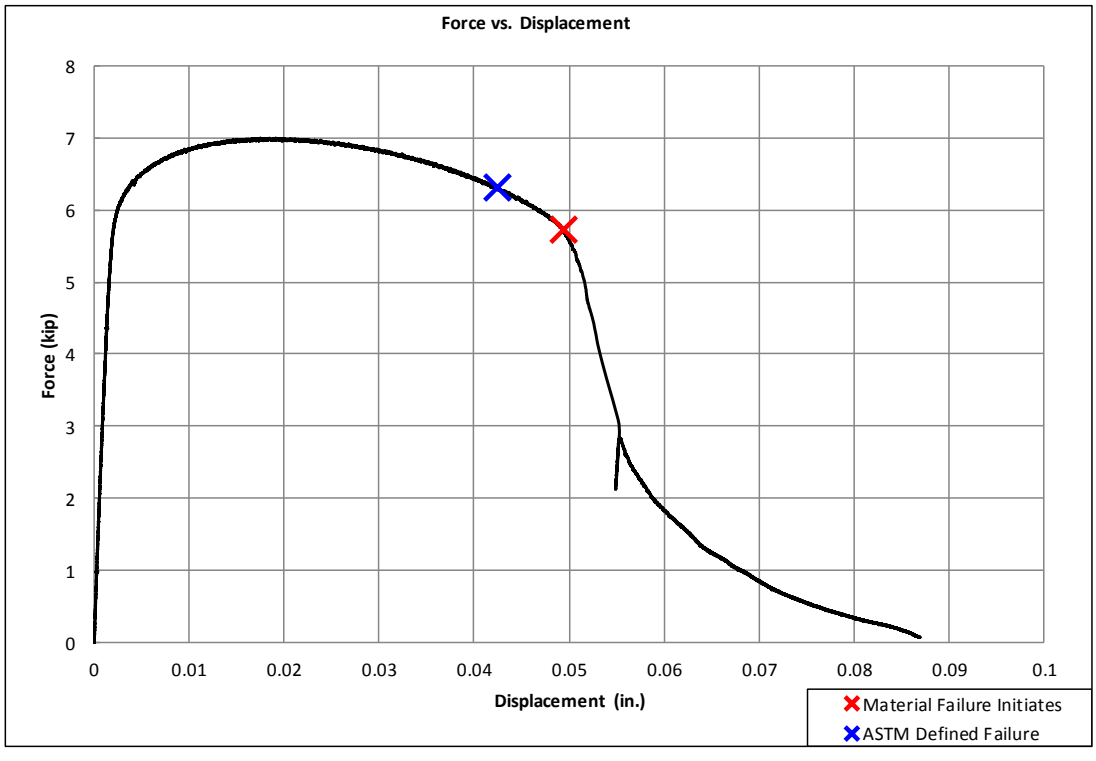

Figure F-32. Test No. SEFT-46 Test Results Summary

MIDWEST ROADSIDE SAFETY FACILITY

Tension Test Summary

Test Information	
Test No.	SEFT-47
Specimen Description:	Thick Large Notch
Specimen Geometry No.:	13
Specimen ID:	103
Test Date:	10/23/2015
Results Folder:	Test Run 98

Testing Procedure	
Testing Frame:	Landmark 20 kip
Loading Type:	Tension
Load Rate:	0.000312 in./sec
Grips:	0.28-0.56 in. Flat Diamond Wedge
Grip Pressure:	1000 psi
Fixture:	N/A
Measurement Equipment:	2 in. Axial Extensometer
	Laser Extensometer
	22 kip Load Cell
Primary Extensometer:	2 in. Axial Extensometer

Note: The specimen did not completely separate before the test was stopped.

Initial Measurements		
Average Width:	0.081	in.
Average Thickness:	1.000	in.
Initial Area:	0.0807	sq. in.
Initial Gauge Length	2.0000	in.

Final Measurements		
Average Width:	0.053	in.
Average Thickness:	0.935	in.
Final Area:	0.0499	sq. in.
Reduction in Area:	38.2	%
Gauge Length at Failure Initiation:	2.0524	in.

Test Results Summary		
Yield Load:	5.878	kip
Peak Load:	6.983	kip
Failure Initiation Load:	5.453	kip
Failure Load (ASTM):	6.285	kip
Displacement at Peak:	0.0183	in.
Displacement at Failure Initiation:	0.0524	in.
Displacement at Failure Load (ASTM):	0.0431	in.
Yield Strength:	72.86	ksi
Ultimate Tensile Strength:	86.56	ksi
Engineering Stress at Failure Initiation:	67.59	ksi
Engineering Stress at Failure (ASTM):	77.90	ksi

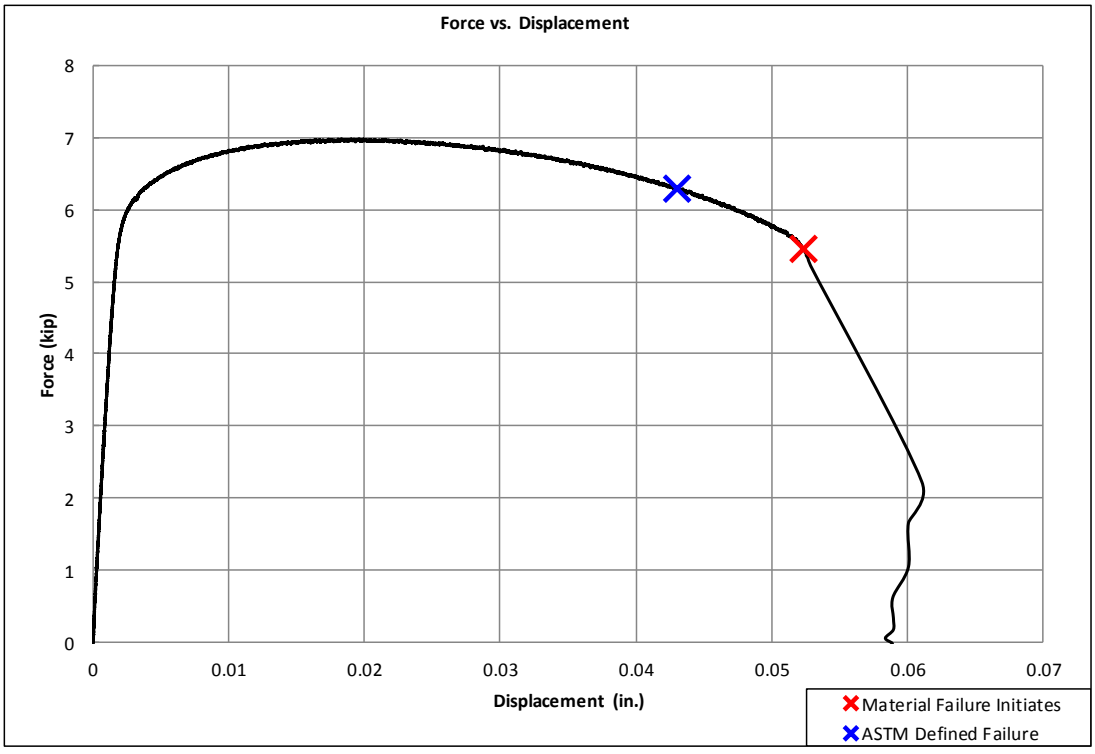

Figure F-33. Test No. SEFT-47 Test Results Summary

MIDWEST ROADSIDE SAFETY FACILITY

Tension Test Summary

Test Information

Test No.	SEFT-48
Specimen Description:	Thick Small Notch
Specimen Geometry No.:	12
Specimen ID:	107
Test Date:	10/23/2015
Results Folder:	Test Run 99

Testing Procedure

Testing Frame:	Landmark 20 kip
Loading Type:	Tension
Load Rate:	0.000156 in./sec
Grips:	0.28-0.56 in. Flat Diamond Wedge
Grip Pressure:	1000 psi
Fixture:	N/A
Measurement Equipment:	2 in. Axial Extensometer Laser Extensometer 22 kip Load Cell
Primary Extensometer:	2 in. Axial Extensometer

Note: The specimen did not completely separate before the test was stopped.

Initial Measurements

Average Width:	0.081 in.
Average Thickness:	1.000 in.
Initial Area:	0.0809 sq. in.
Initial Gauge Length	2.0000 in.

Final Measurements

Average Width:	0.055 in.
Average Thickness:	0.951 in.
Final Area:	0.0519 sq. in.
Reduction in Area:	35.9 %
Gauge Length at Failure Initiation:	2.0402 in.

Test Results Summary

Yield Load:	6.337 kip
Peak Load:	7.433 kip
Failure Initiation Load:	5.604 kip
Failure Load (ASTM):	6.690 kip
Displacement at Peak:	0.0138 in.
Displacement at Failure Initiation:	0.0402 in.
Displacement at Failure Load (ASTM):	0.0307 in.
Yield Strength:	78.28 ksi
Ultimate Tensile Strength:	91.82 ksi
Engineering Stress at Failure Initiation:	69.22 ksi
Engineering Stress at Failure (ASTM):	82.64 ksi

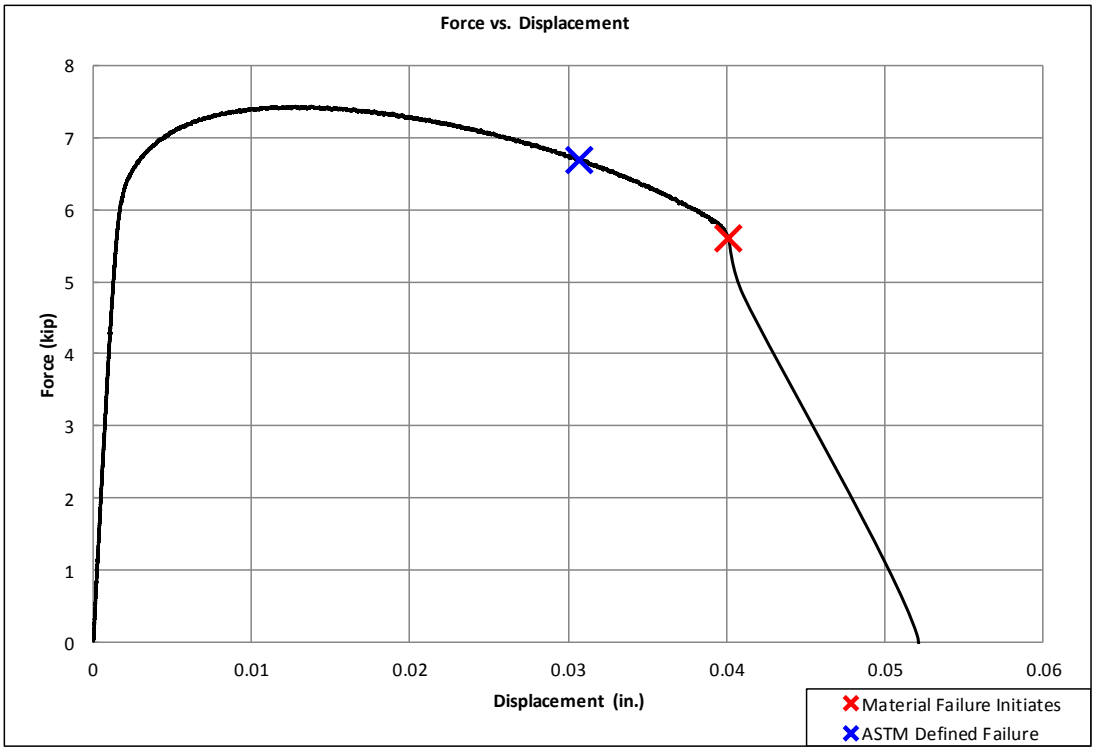

Figure F-34. Test No. SEFT-48 Test Results Summary

MIDWEST ROADSIDE SAFETY FACILITY

Tension Test Summary

Test Information	
Test No.	SEFT-49
Specimen Description:	Thick Small Notch
Specimen Geometry No.:	12
Specimen ID:	108
Test Date:	10/23/2015
Results Folder:	Test Run 100

Testing Procedure	
Testing Frame:	Landmark 20 kip
Loading Type:	Tension
Load Rate:	0.00025 in./sec
Grips:	0.28-0.56 in. Flat Diamond Wedge
Grip Pressure:	1000 psi
Fixture:	N/A
Measurement Equipment:	2 in. Axial Extensometer
	Laser Extensometer
	22 kip Load Cell
Primary Extensometer:	2 in. Axial Extensometer

Initial Measurements		
Average Width:	0.082	in.
Average Thickness:	0.999	in.
Initial Area:	0.0816	sq. in.
Initial Gauge Length	2.0000	in.

Final Measurements		
Average Width:	0.055	in.
Average Thickness:	0.949	in.
Final Area:	0.0525	sq. in.
Reduction in Area:	35.6	%
Gauge Length at Failure Initiation:	2.0396	in.

Test Results Summary		
Yield Load:	6.337	kip
Peak Load:	7.420	kip
Failure Initiation Load:	5.753	kip
Failure Load (ASTM):	6.678	kip
Displacement at Peak:	0.0128	in.
Displacement at Failure Initiation:	0.0396	in.
Displacement at Failure Load (ASTM):	0.0309	in.
Yield Strength:	77.67	ksi
Ultimate Tensile Strength:	90.95	ksi
Engineering Stress at Failure Initiation:	70.52	ksi
Engineering Stress at Failure (ASTM):	81.85	ksi

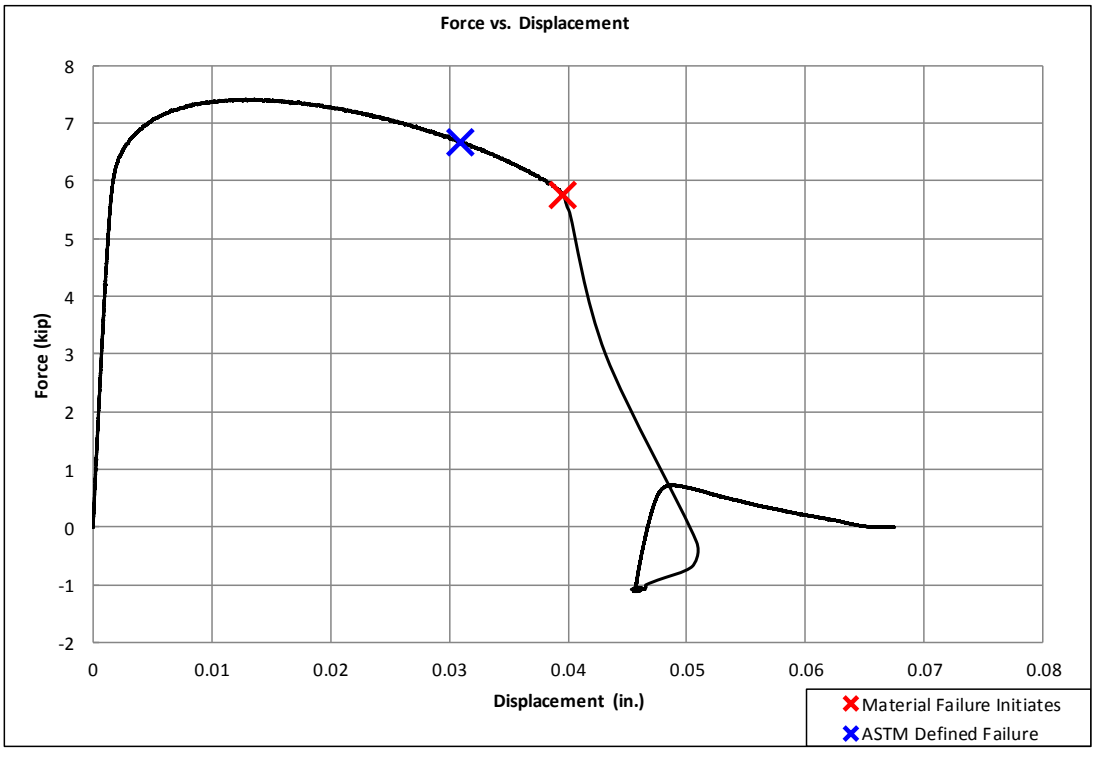

Figure F-35. Test No. SEFT-49 Test Results Summary

MIDWEST ROADSIDE SAFETY FACILITY

Tension Test Summary

Test Information	
Test No.	SEFT-50
Specimen Description:	Thick Small Notch
Specimen Geometry No.:	12
Specimen ID:	109
Test Date:	10/23/2015
Results Folder:	Test Run 101

Testing Procedure	
Testing Frame:	Landmark 20 kip
Loading Type:	Tension
Load Rate:	0.00025 in./sec
Grips:	0.28-0.56 in. Flat Diamond Wedge
Grip Pressure:	1000 psi
Fixture:	N/A
Measurement Equipment:	2 in. Axial Extensometer
	Laser Extensometer
	22 kip Load Cell
Primary Extensometer:	2 in. Axial Extensometer

Initial Measurements		
Average Width:	0.082	in.
Average Thickness:	1.000	in.
Initial Area:	0.0820	sq. in.
Initial Gauge Length	2.0000	in.

Final Measurements		
Average Width:	0.057	in.
Average Thickness:	0.950	in.
Final Area:	0.0544	sq. in.
Reduction in Area:	33.6	%
Gauge Length at Failure Initiation:	2.0399	in.

Test Results Summary		
Yield Load:	6.404	kip
Peak Load:	7.550	kip
Failure Initiation Load:	5.813	kip
Failure Load (ASTM):	6.795	kip
Displacement at Peak:	0.0125	in.
Displacement at Failure Initiation:	0.0399	in.
Displacement at Failure Load (ASTM):	0.0311	in.
Yield Strength:	78.08	ksi
Ultimate Tensile Strength:	92.05	ksi
Engineering Stress at Failure Initiation:	70.88	ksi
Engineering Stress at Failure (ASTM):	82.85	ksi

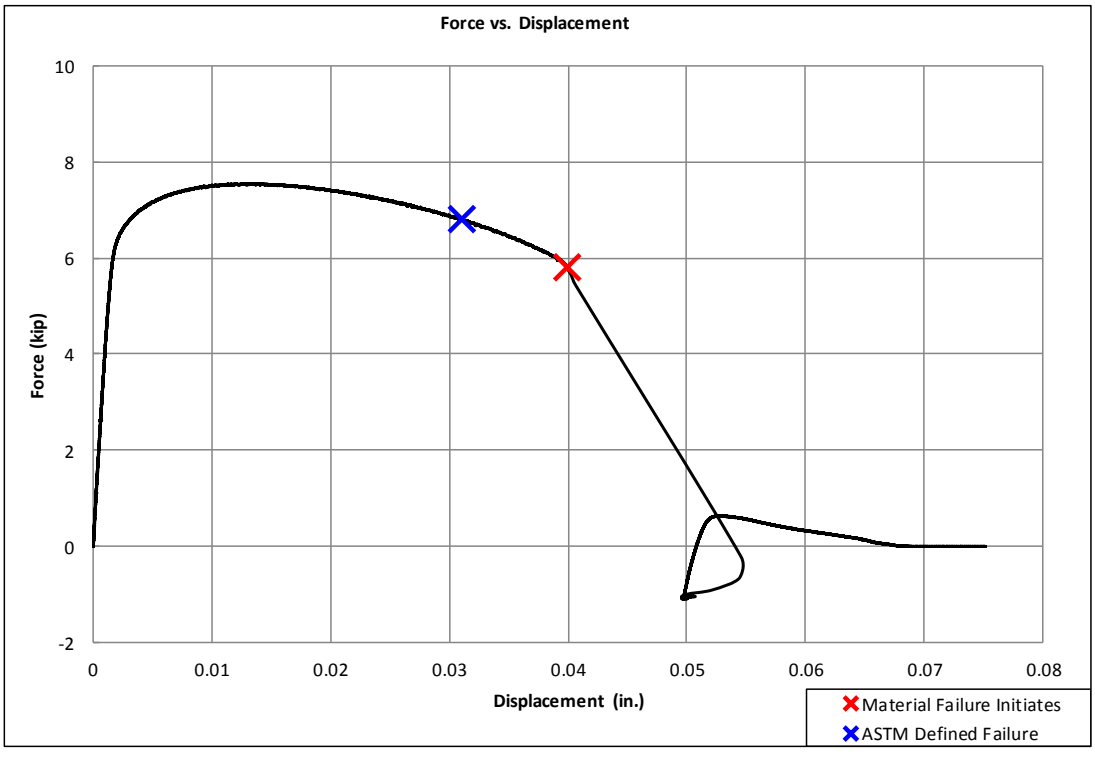

Figure F-36. Test No. SEFT-50 Test Results Summary

MIDWEST ROADSIDE SAFETY FACILITY

Compression Test Summary

Test Information

Test No.	SEFT-51
Specimen Description:	Compression Cylinder
Specimen Geometry No.:	14
Specimen ID:	113
Test Date:	10/23/2015
Results Folder:	Test Run 102

Testing Procedure

Testing Frame:	Landmark 20 kip
Loading Type:	Compression
Load Rate:	0.0004 in./sec
Grips:	N/A
Grip Pressure:	1000 psi
Fixture:	Compression Platen
Measurement Equipment:	Laser Extensometer
	2 in. Axial Extensometer
	22 kip Load Cell
Primary Extensometer:	See Note

*Note: The self-aligning compression platen tilted during loading with the laser extensometer on the low side and the 2 in. axial extensometer on the high side. The two devices were averaged to produce the displacements shown.

Initial Measurements

Average Diameter:	0.489	in.
Initial Area:	0.1880	sq. in.
Initial Gauge Length:	0.49	in.

Final Measurements

Average Diameter:	0.539	in.
Final Area:	0.2279	sq. in.
Increase in Area:	21.2	%

Test Results Summary

Yield Load (0.2% Offset):	11.577	kip
Peak Load:	21.174	kip
Displacement at Peak:	0.0891	in.
Yield Strength:	61.59	ksi
True Strain at Final:	-0.1927	in./in.
Young's Modulus:	5,881	ksi

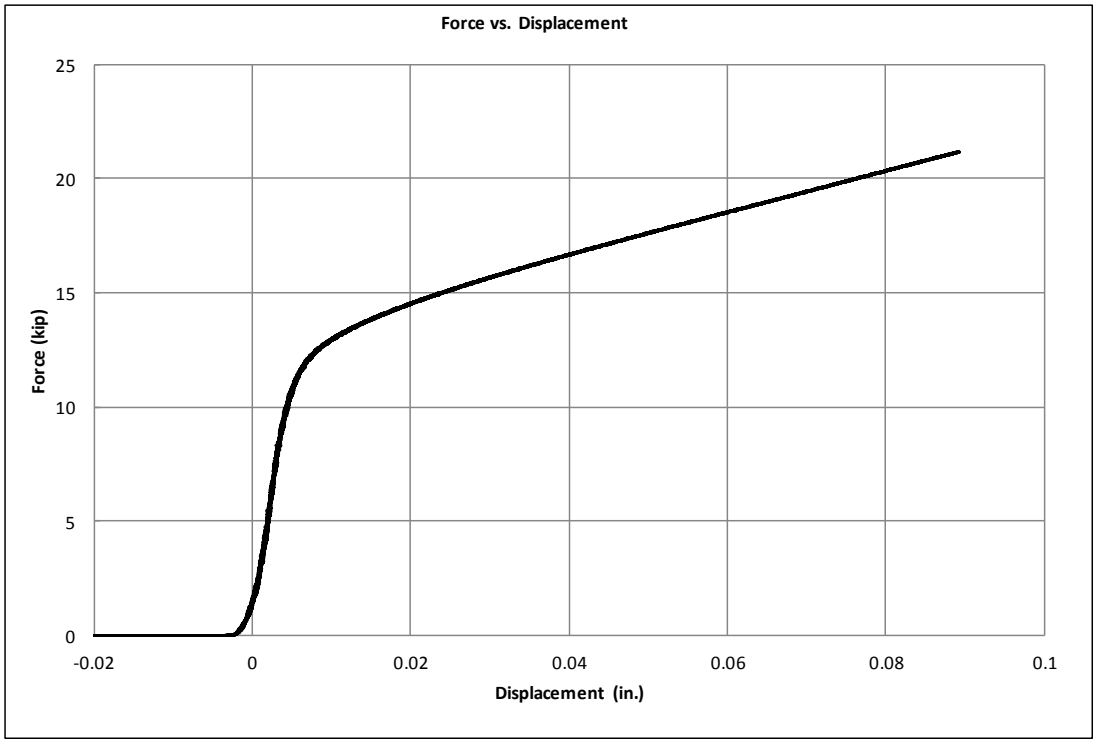

Figure F-37. Test No. SEFT-51 Test Results Summary

MIDWEST ROADSIDE SAFETY FACILITY

Punch Test Summary

Test Information

Test No.	SEFT-52
Specimen Description:	Standard Punch
Specimen Geometry No.:	15
Specimen ID:	119
Test Date:	10/26/2015
Results Folder:	Test Run 103

Testing Procedure

Testing Frame:	Landmark 20 kip
Loading Type:	Punch
Load Rate:	0.0003 in./sec
Grips:	N/A
Grip Pressure:	1000 psi
Fixture:	Compression Platen with Punch Fixture 1 and Punch Head B
Measurement Equipment:	Laser Extensometer 2 in. Axial Extensometer 22 kip Load Cell
Primary Extensometer:	Laser Extensometer

Note: Specimen failure did not occur

Initial Measurements

Average Diameter:	0.580 in.
Average Thickness:	0.057 in.

Final Measurements

Average Diameter:	0.581 in.
Average Draw Down Thickness:	0.111 in.

Test Results Summary

Peak Load:	1.183 kip
Failure Initiation Load:	N/A
Displacement at Peak:	0.0637 in.
Displacement at Failure Initiation:	N/A

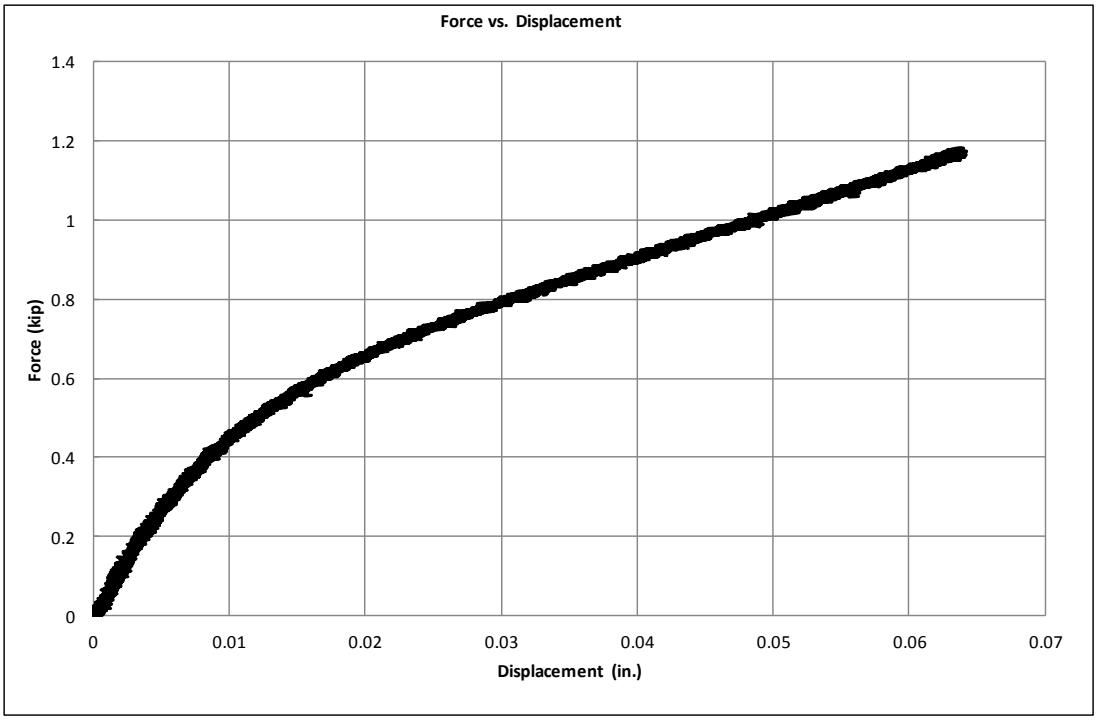

Figure F-38. Test No. SEFT-52 Test Results Summary

MIDWEST ROADSIDE SAFETY FACILITY

Punch Test Summary

Test Information

Test No.	SEFT-53
Specimen Description:	Standard Punch
Specimen Geometry No.:	15
Specimen ID:	120
Test Date:	10/26/2015
Results Folder:	Test Run 104

Testing Procedure

Testing Frame:	Landmark 20 kip
Loading Type:	Punch
Load Rate:	0.0003 in./sec
Grips:	N/A
Grip Pressure:	1000 psi
Fixture:	Compression Platen with Punch Fixture 1 and Punch Head B
Measurement Equipment:	Laser Extensometer 2 in. Axial Extensometer 22 kip Load Cell
Primary Extensometer:	Laser Extensometer

Note: Specimen failure did not occur
Punch rod was offset from center during loading

Initial Measurements

Average Diameter:	0.580 in.
Average Thickness:	0.057 in.

Final Measurements

Average Diameter:	0.579 in.
Average Draw Down Thickness:	0.155 in.

Test Results Summary

Peak Load:	1.726 kip
Failure Initiation Load:	N/A
Displacement at Peak:	0.1090 in.
Displacement at Failure Initiation:	N/A

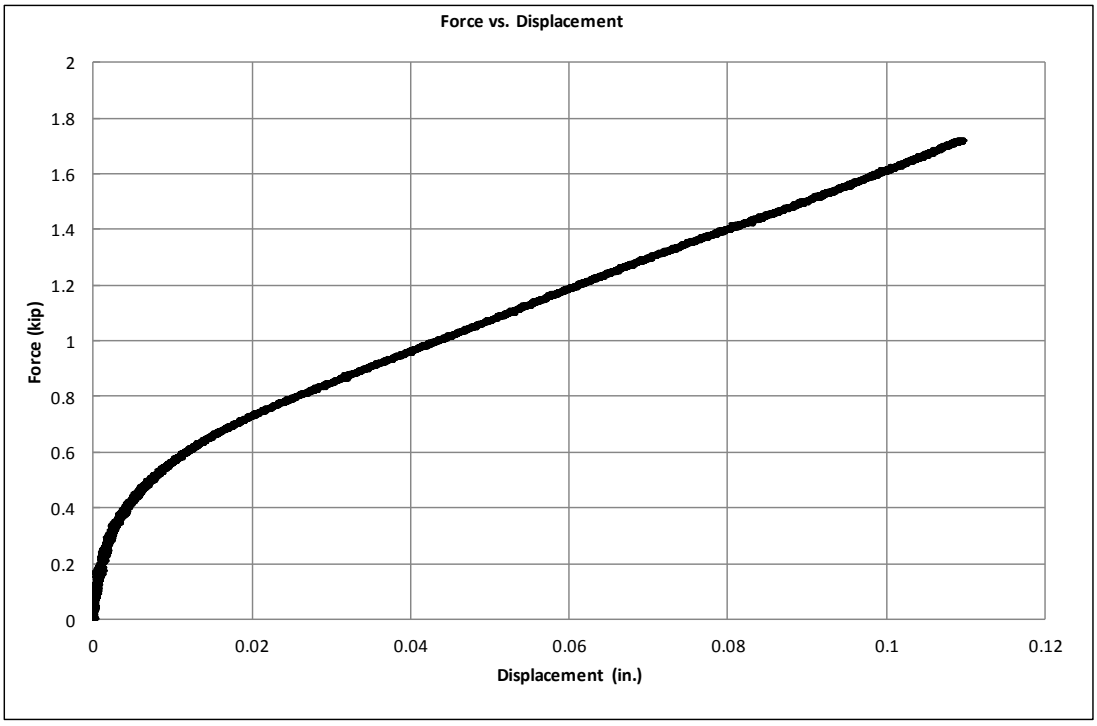

Figure F-39. Test No. SEFT-53 Test Results Summary

MIDWEST ROADSIDE SAFETY FACILITY

Punch Test Summary

Test Information	
Test No.	SEFT-54
Specimen Description:	Standard Punch
Specimen Geometry No.:	15
Specimen ID:	121
Test Date:	10/26/2015
Results Folder:	Test Run 105

Testing Procedure	
Testing Frame:	Landmark 20 kip
Loading Type:	Punch
Load Rate:	0.0003 in./sec
Grips:	N/A
Grip Pressure:	1000 psi
Fixture:	Compression Platten with Punch Fixture 1 and Punch Head B
Measurement Equipment:	Laser Extensometer 2 in. Axial Extensometer 22 kip Load Cell
Primary Extensometer:	Laser Extensometer

Note: Specimen failure did not occur

Initial Measurements	
Average Diameter:	0.580 in.
Average Thickness:	0.057 in.

Final Measurements	
Average Diameter:	0.568 in.
Average Draw Down Thickness:	0.217 in.

Test Results Summary	
Peak Load:	2.896 kip
Failure Initiation Load:	N/A
Displacement at Peak:	0.1864 in.
Displacement at Failure Initiation:	N/A

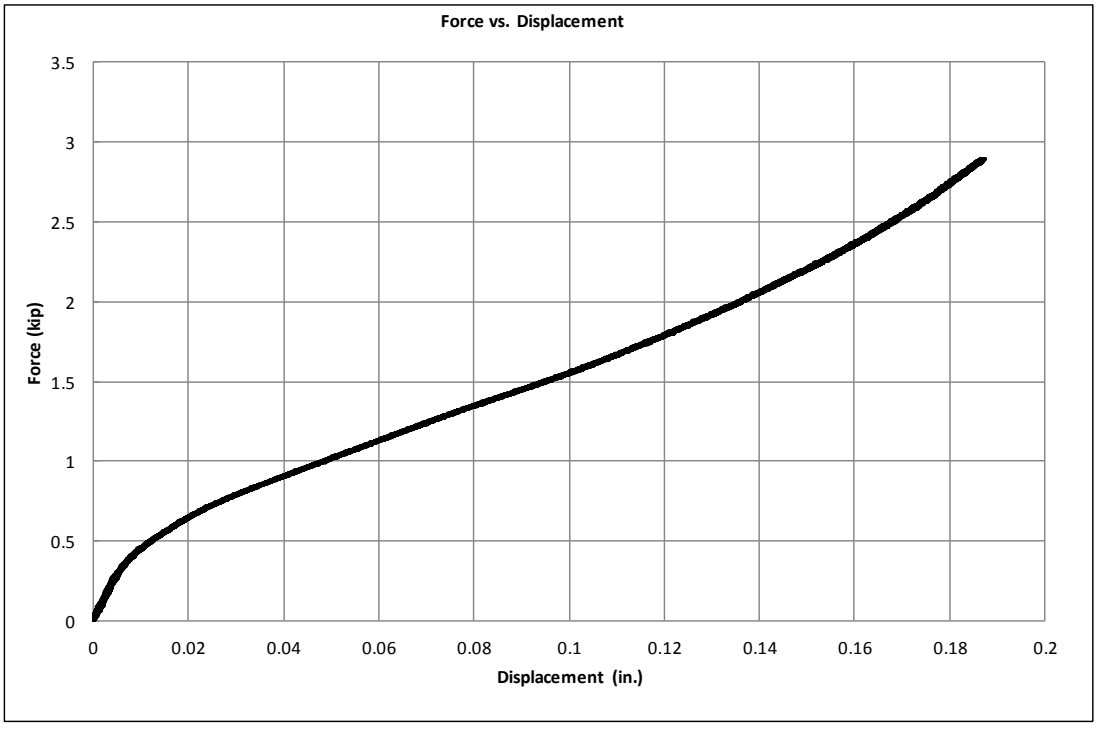

Figure F-40. Test No. SEFT-54 Test Results Summary

MIDWEST ROADSIDE SAFETY FACILITY

Punch Test Summary

Test Information	
Test No.	SEFT-55
Specimen Description:	Standard Punch
Specimen Geometry No.:	15
Specimen ID:	122
Test Date:	10/26/2015
Results Folder:	Test Run 106

Testing Procedure	
Testing Frame:	Landmark 20 kip
Loading Type:	Punch
Load Rate:	0.0004 in./sec
Grips:	N/A
Grip Pressure:	1000 psi
Fixture:	Compression Platen with Punch Fixture 1 and Punch Head B
Measurement Equipment:	Laser Extensometer 22 kip Load Cell
Primary Extensometer:	Laser Extensometer

Initial Measurements		
Average Diameter:	0.580	in.
Average Thickness:	0.057	in.

Final Measurements		
Average Diameter:	0.548	in.
Average Draw Down Thickness:	0.296	in.

Test Results Summary		
Peak Load:	4.144	kip
Failure Initiation Load:	3.948	kip
Displacement at Peak:	0.2407	in.
Displacement at Failure Initiation:	0.2592	in.

Figure F-41. Test No. SEFT-55 Test Results Summary

MIDWEST ROADSIDE SAFETY FACILITY

Punch Test Summary

Test Information	
Test No.	SEFT-56
Specimen Description:	Standard Punch
Specimen Geometry No.:	15
Specimen ID:	123
Test Date:	10/26/2015
Results Folder:	Test Run 107

Testing Procedure	
Testing Frame:	Landmark 20 kip
Loading Type:	Punch
Load Rate:	0.0004 in./sec
Grips:	N/A
Grip Pressure:	1000 psi
Fixture:	Compression Platen with Punch Fixture 1 and Punch Head A
Measurement Equipment:	Laser Extensometer 1 in Axial Extensometer 22 kip Load Cell
Primary Extensometer:	Laser Extensometer

Initial Measurements	
Average Diameter:	0.580 in.
Average Thickness:	0.058 in.

Final Measurements	
Average Diameter:	0.564 in.
Average Draw Down Thickness:	0.291 in.

Test Results Summary	
Peak Load:	4.159 kip
Failure Initiation Load:	4.010 kip
Displacement at Peak:	0.2490 in.
Displacement at Failure Initiation:	0.2598 in.

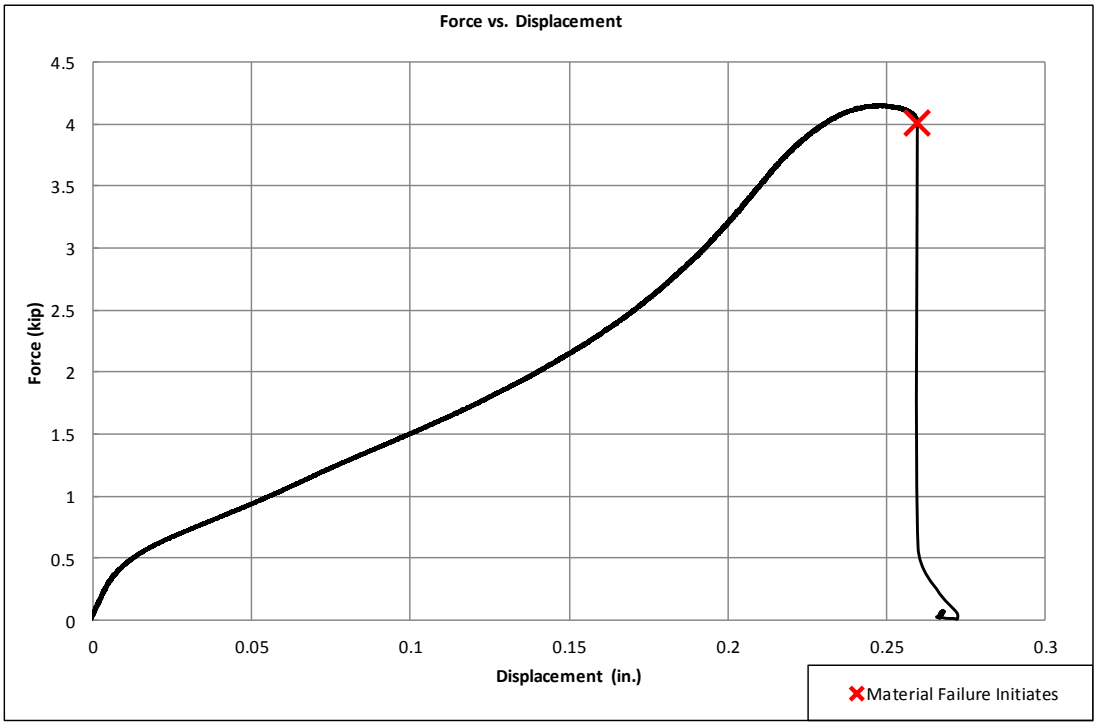

Figure F-42. Test No. SEFT-56 Test Results Summary

MIDWEST ROADSIDE SAFETY FACILITY

Punch Test Summary

Test Information		**Initial Measurements**	
Test No.	SEFT-57	Average Diameter:	0.580 in.
Specimen Description:	Round Punch	Average Thickness:	0.057 in.
Specimen Geometry No.:	16		
Specimen ID:	124		
Test Date:	10/26/2015		
Results Folder:	Test Run 108	**Final Measurements**	
		Average Diameter:	0.547 in.
Testing Procedure		Average Draw Down Thickness:	0.265 in.
Testing Frame:	Landmark 20 kip		
Loading Type:	Punch		
Load Rate:	0.0004 in./sec		
Grips:	N/A		
Grip Pressure:	1000 psi	**Test Results Summary**	
Fixture:	Compression Platen with Punch Fixture 1 and Punch Head A	Peak Load:	4.085 kip
		Failure Initiation Load:	3.738 kip
Measurement Equipment:	Laser Extensometer	Displacement at Peak:	0.1786 in.
	1 in Axial Extensometer	Displacement at Failure Initiation:	0.2091 in.
	22 kip Load Cell		
Primary Extensometer:	Laser Extensometer		

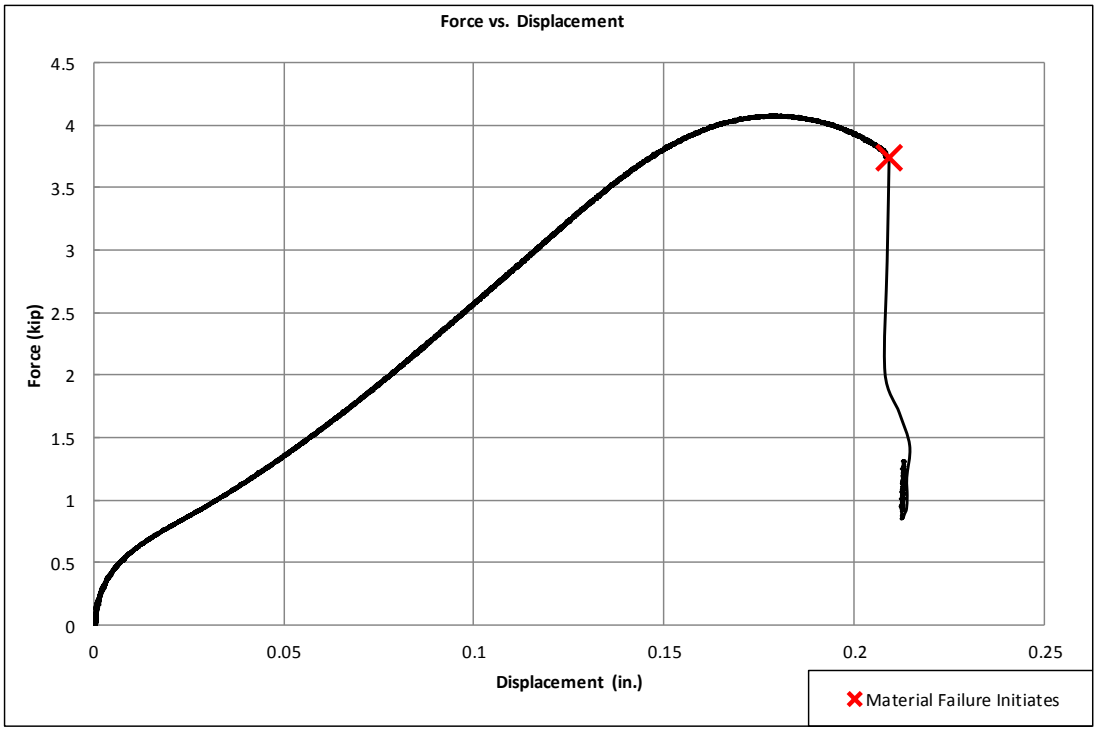

Figure F-43. Test No. SEFT-57 Test Results Summary

MIDWEST ROADSIDE SAFETY FACILITY

Punch Test Summary

Test Information	
Test No.	SEFT-58
Specimen Description:	Round Punch
Specimen Geometry No.:	16
Specimen ID:	125
Test Date:	10/26/2015
Results Folder:	Test Run 109

Testing Procedure	
Testing Frame:	Landmark 20 kip
Loading Type:	Punch
Load Rate:	0.0004 in./sec
Grips:	N/A
Grip Pressure:	1000 psi
Fixture:	Compression Platen with Punch Fixture 1 and Punch Head A
Measurement Equipment:	Laser Extensometer 1 in Axial Extensometer 22 kip Load Cell
Primary Extensometer:	Laser Extensometer

Note: Punch rod was offset from center during loading

Initial Measurements		
Average Diameter:	0.580	in.
Average Thickness:	0.057	in.

Final Measurements		
Average Diameter:	0.569	in.
Average Draw Down Thickness:	0.202	in.

Test Results Summary		
Peak Load:	3.633	kip
Failure Initiation Load:	3.534	kip
Displacement at Peak:	0.1461	in.
Displacement at Failure Initiation:	0.1474	in.

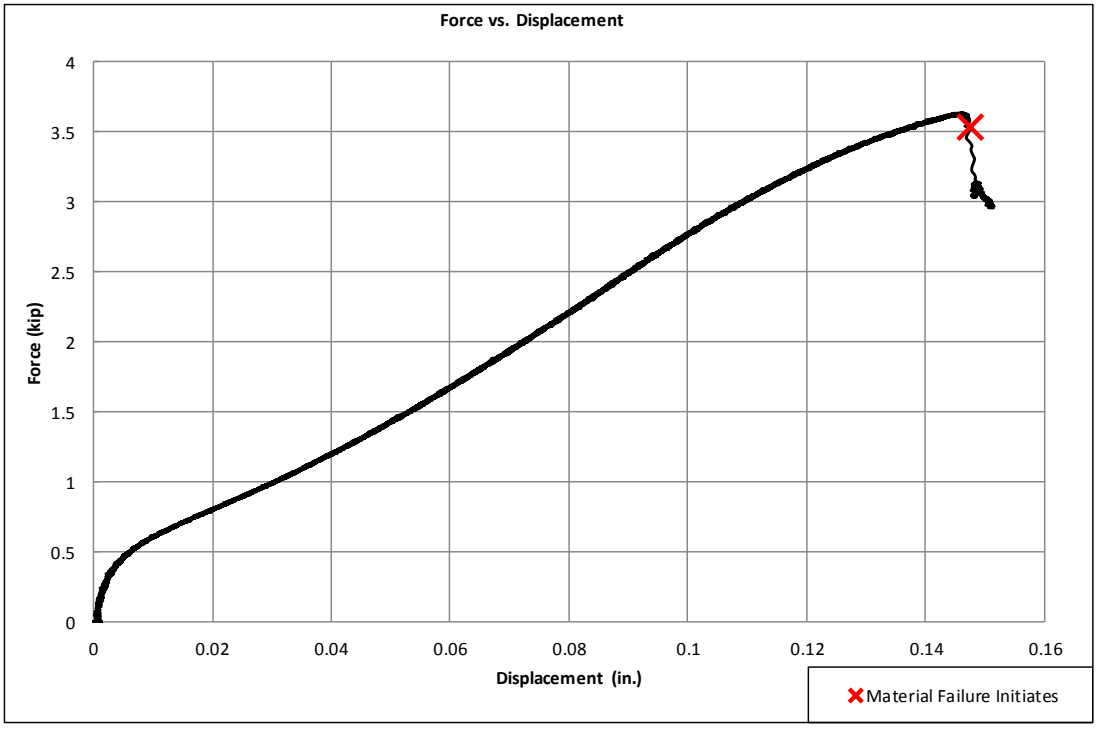

Figure F-44. Test No. SEFT-58 Test Results Summary

MIDWEST ROADSIDE SAFETY FACILITY

Compression Test Summary

Test Information

Test No.	SEFT-59
Specimen Description:	Compression Cylinder
Specimen Geometry No.:	14
Specimen ID:	114
Test Date:	11/2/2015
Results Folder:	Test Run 1

Testing Procedure

Testing Frame:	Criterion 200 kip
Loading Type:	Compression
Load Rate:	0.0004 in./sec
Grips:	N/A
Grip Pressure:	N/A
Fixture:	Compression Platen
Measurement Equipment:	Laser Extensometer 220 kip Load Cell
Primary Extensometer:	Laser Extensometer

Note: Some minor compression platen tilt was present during loading.

Initial Measurements

Average Diameter:	0.489	in.
Initial Area:	4.772	sq. in.
Initial Gauge Length	0.49	in.

Final Measurements

Average Diameter:	0.726	in.
Final Area:	10.526	sq. in.
Increase in Area:	120.6	%

Test Results Summary

Peak Load:	49.480	kip
Displacement at Peak:	0.2595	in.
True Strain at Final	-0.7910	in./in.

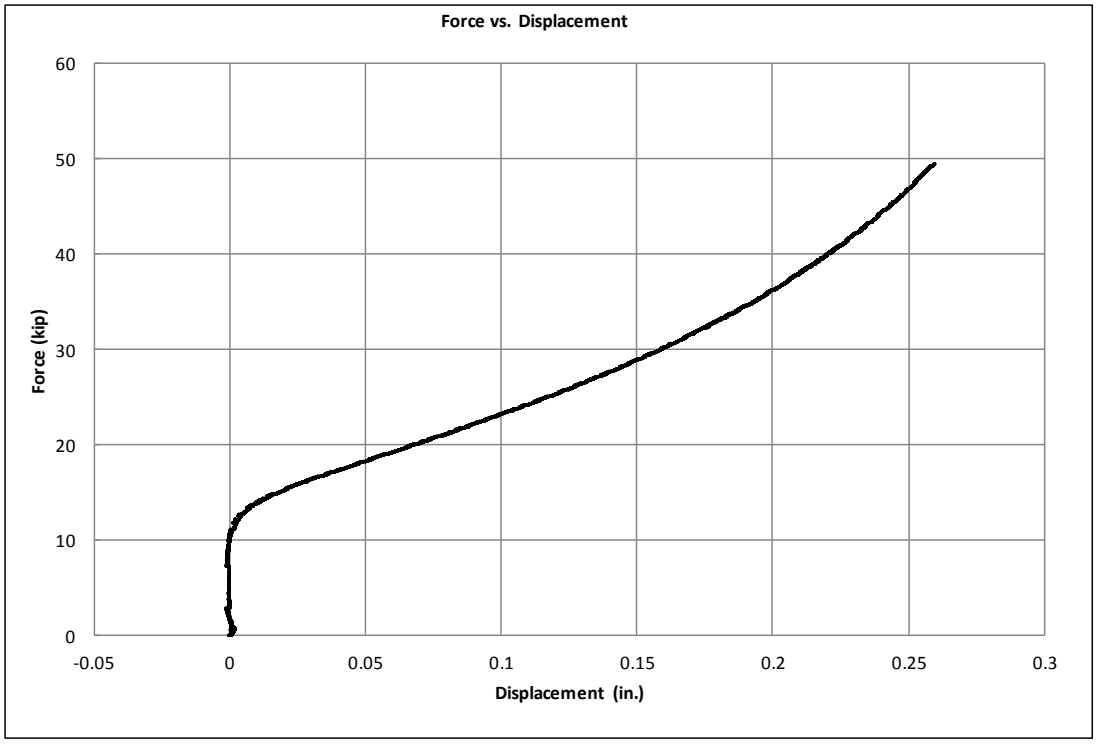

Figure F-45. Test No. SEFT-59 Test Results Summary

MIDWEST ROADSIDE SAFETY FACILITY

Compression Test Summary

Test Information

Test No.	SEFT-60
Specimen Description:	Compression Cylinder
Specimen Geometry No.:	14
Specimen ID:	115
Test Date:	11/2/2015
Results Folder:	Test Run 3

Testing Procedure

Testing Frame:	Criterion 200 kip
Loading Type:	Compression
Load Rate:	0.0004 in./sec
Grips:	N/A
Grip Pressure:	N/A
Fixture:	Compression Platen
Measurement Equipment:	Laser Extensometer 220 kip Load Cell
Primary Extensometer:	Laser Extensometer

Note: Some minor compression platen tilt was present during loading.

Initial Measurements

Average Diameter:	0.489	in.
Initial Area:	4.762	sq. in.
Initial Gauge Length	0.49	in.

Final Measurements

Average Diameter:	0.759	in.
Final Area:	11.498	sq. in.
Increase in Area:	141.4	%

Test Results Summary

Peak Load:	56.253	kip
Displacement at Peak:	0.2820	in.
True Strain at Final	-0.8815	in./in.

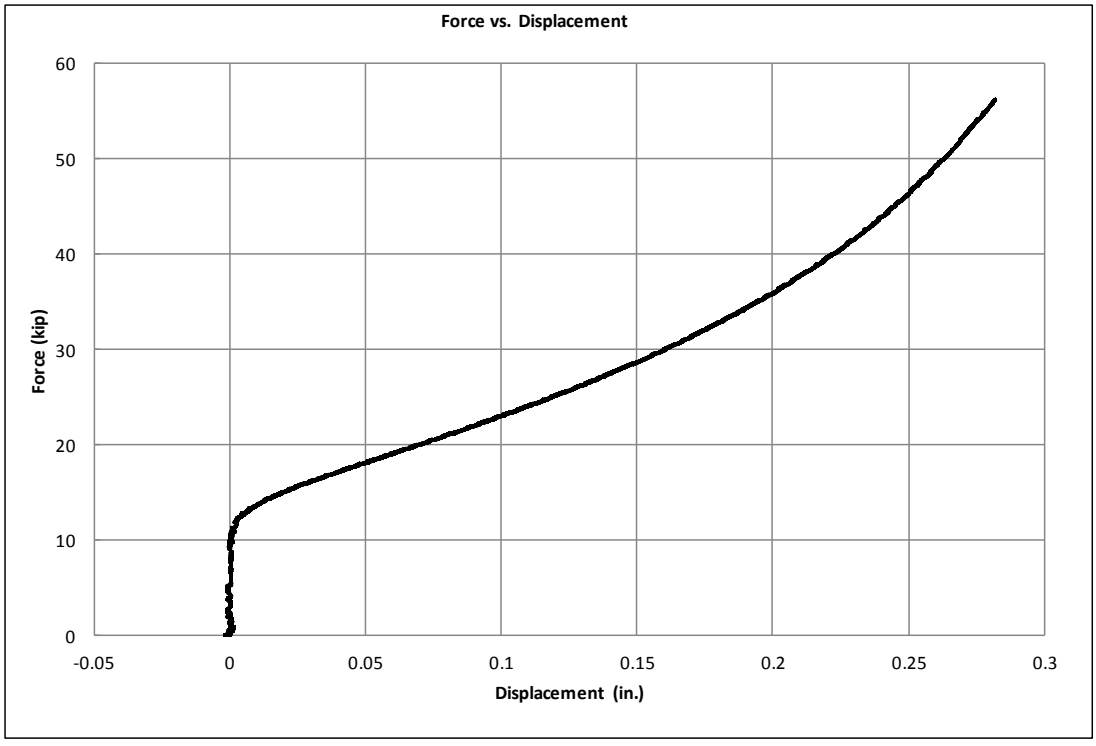

Figure F-46. Test No. SEFT-60 Test Results Summary

MIDWEST ROADSIDE SAFETY FACILITY

Compression Test Summary

Test Information

Test No.	SEFT-61
Specimen Description:	Compression Cylinder
Specimen Geometry No.:	14
Specimen ID:	116
Test Date:	11/2/2015
Results Folder:	Test Run 4

Testing Procedure

Testing Frame:	Criterion 200 kip
Loading Type:	Compression
Load Rate:	0.0004 in./sec
Grips:	N/A
Grip Pressure:	N/A
Fixture:	Compression Platen
Measurement Equipment:	Laser Extensometer
	220 kip Load Cell
Primary Extensometer:	Laser Extensometer

Note: Some minor compression platen tilt was present during loading.

Initial Measurements

Average Diameter:	0.489 in.
Initial Area:	0.189 sq. in.
Initial Gauge Length:	0.49 in.

Final Measurements

Average Diameter:	1.053 in.
Final Area:	0.874 sq. in.
Increase in Area:	363.4 %

Test Results Summary

Peak Load:	165.311 kip
Displacement at Peak:	0.3893 in.
True Strain at Final:	-1.5335 in./in.

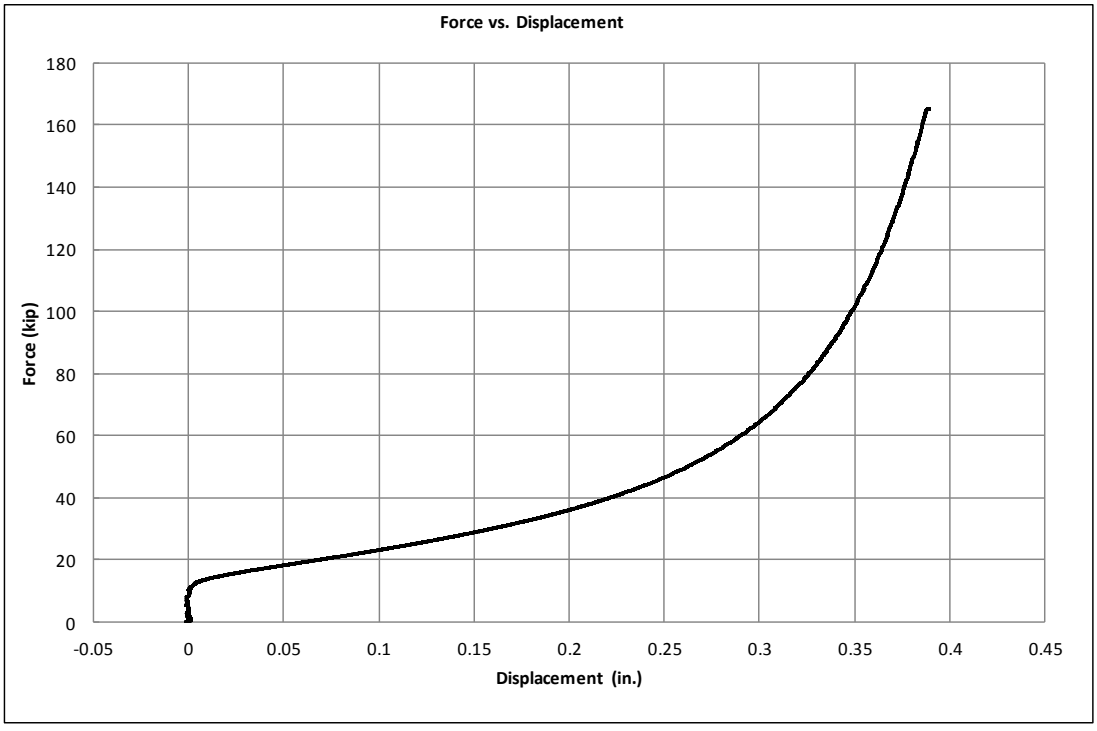

Figure F-47. Test No. SEFT-61 Test Results Summary

MIDWEST ROADSIDE SAFETY FACILITY

Dual Punch Shear Test Summary

Test Information

Test No.	SEFT-62
Specimen Description:	Dual Point Shear
Specimen Geometry No.:	18
Specimen ID:	144
Test Date:	11/9/2015
Results Folder:	Test Run 5

Testing Procedure

Testing Frame:	Criterion 200 kip
Loading Type:	Dual Punch Shear
Load Rate:	0.0004 in./sec
Grips:	N/A
Grip Pressure:	N/A
Fixture:	Dual Point Shear
Measurement Equipment:	Laser Extensometer 220 kip Load Cell
Primary Extensometer:	Laser Extensometer

Initial Measurements

Average Diameter:	0.393 in.
Initial Gauge Length:	2.531 in.

Final Measurements

Test Results Summary

Peak Load:	13.747 kip
Failure Initiation Load:	N/A
Displacement at Peak:	0.0504 in.
Displacement at Failure Initiation:	N/A

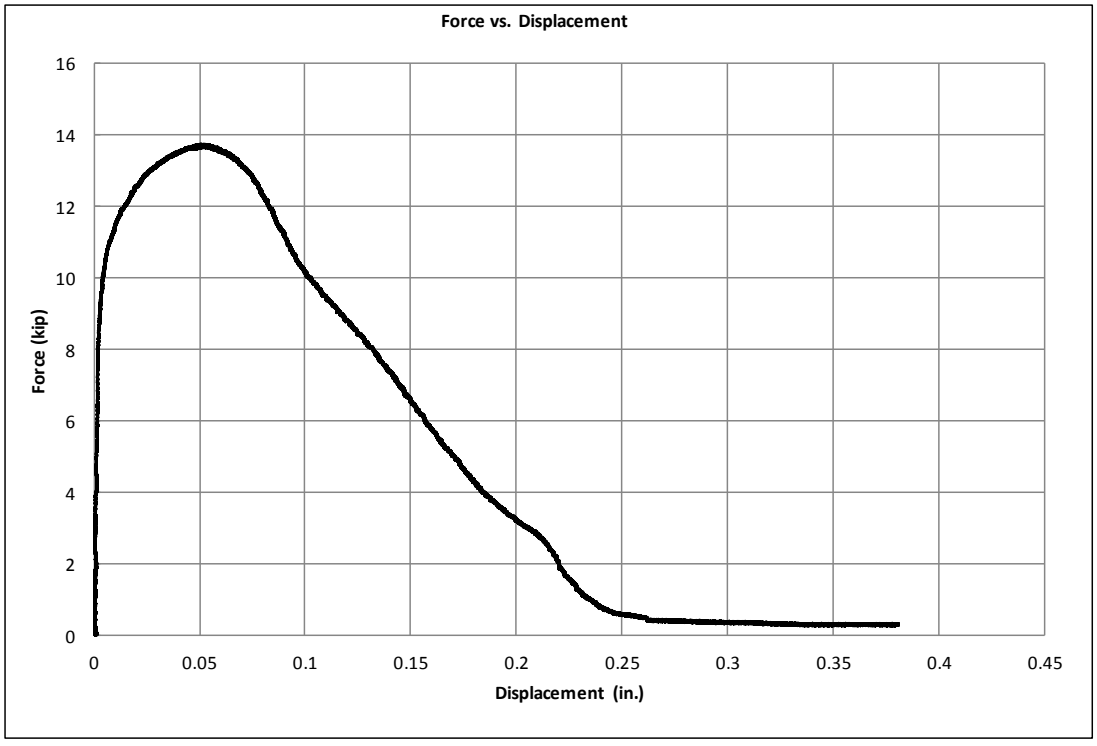

Figure F-48. Test No. SEFT-62 Test Results Summary

MIDWEST ROADSIDE SAFETY FACILITY

Dual Punch Shear Test Summary

Test Information

Test No.	SEFT-63
Specimen Description:	Dual Point Shear
Specimen Geometry No.:	18
Specimen ID:	145
Test Date:	11/9/2015
Results Folder:	Test Run 6

Testing Procedure

Testing Frame:	Criterion 200 kip
Loading Type:	Dual Punch Shear
Load Rate:	0.0004 in./sec
Grips:	N/A
Grip Pressure:	N/A
Fixture:	Dual Point Shear
Measurement Equipment:	Laser Extensometer 220 kip Load Cell
Primary Extensometer:	Laser Extensometer

Initial Measurements

Average Diameter:	0.393 in.
Initial Gauge Length:	2.584 in.

Final Measurements

Test Results Summary

Peak Load:	13.445 kip
Failure Initiation Load:	N/A
Displacement at Peak:	0.0528 in.
Displacement at Failure Initiation:	N/A

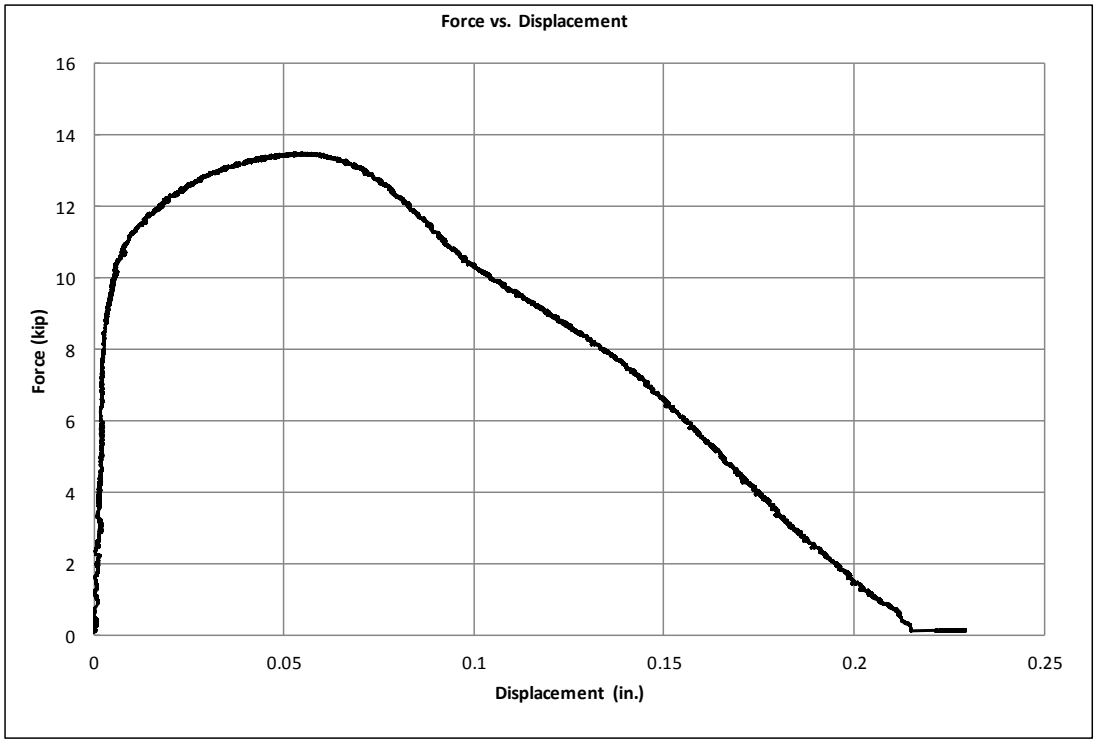

Figure F-49. Test No. SEFT-63 Test Results Summary

MIDWEST ROADSIDE SAFETY FACILITY

Dual Punch Shear Test Summary

Test Information

Test No.	SEFT-64
Specimen Description:	Dual Point Shear
Specimen Geometry No.:	18
Specimen ID:	146
Test Date:	11/9/2015
Results Folder:	Test Run 7

Testing Procedure

Testing Frame:	Criterion 200 kip
Loading Type:	Dual Punch Shear
Load Rate:	0.0004 in./sec
Grips:	N/A
Grip Pressure:	N/A
Fixture:	Dual Point Shear
Measurement Equipment:	Laser Extensometer 220 kip Load Cell
Primary Extensometer:	Laser Extensometer

Initial Measurements

Average Diameter:	0.393 in.
Initial Gauge Length:	2.529 in.

Final Measurements

Test Results Summary

Peak Load:	13.452 kip
Failure Initiation Load:	N/A
Displacement at Peak:	0.0530 in.
Displacement at Failure Initiation:	N/A

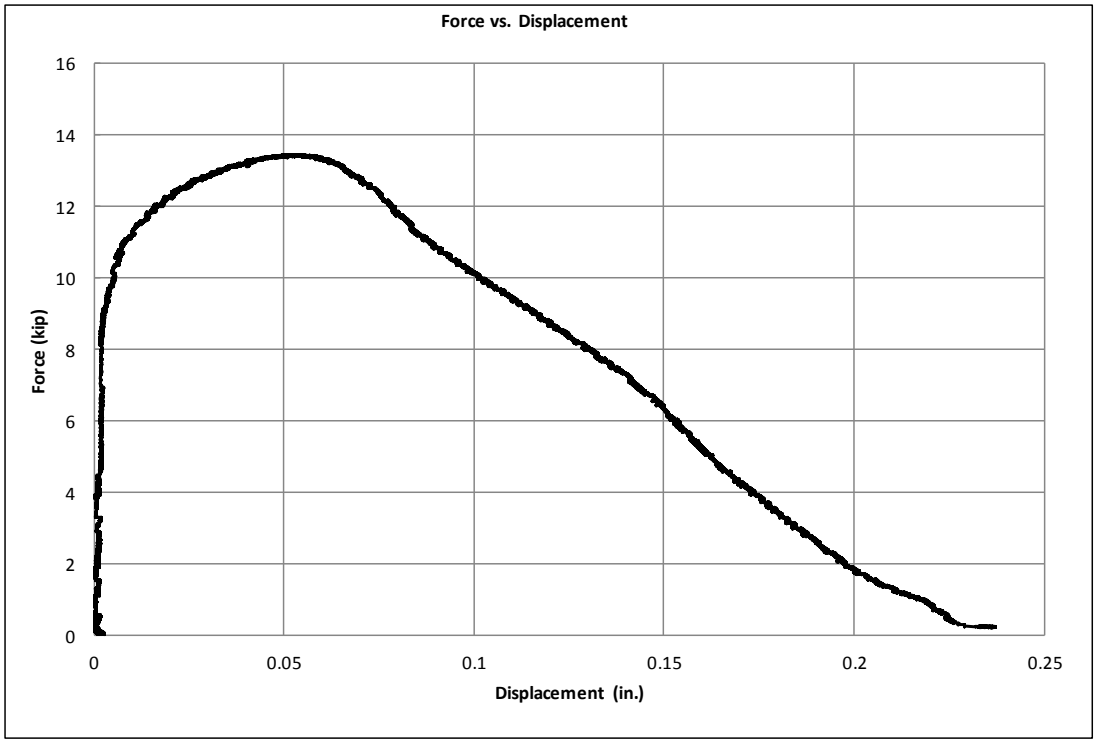

Figure F-50. Test No. SEFT-64 Test Results Summary

MIDWEST ROADSIDE SAFETY FACILITY

Dual Punch Shear Test Summary

Test Information

Test No.	SEFT-65
Specimen Description:	Dual Point Shear
Specimen Geometry No.:	18
Specimen ID:	147
Test Date:	11/9/2015
Results Folder:	Test Run 10

Testing Procedure

Testing Frame:	Criterion 200 kip
Loading Type:	Dual Punch Shear
Load Rate:	0.0004 in./sec
Grips:	N/A
Grip Pressure:	N/A
Fixture:	Dual Point Shear
Measurement Equipment:	Laser Extensometer 220 kip Load Cell
Primary Extensometer:	Laser Extensometer

Initial Measurements

Average Diameter:	0.392 in.
Initial Gauge Length:	2.697 in.

Final Measurements

Test Results Summary

Peak Load:	13.669 kip
Failure Initiation Load:	N/A
Displacement at Peak:	0.0595 in.
Displacement at Failure Initiation:	N/A

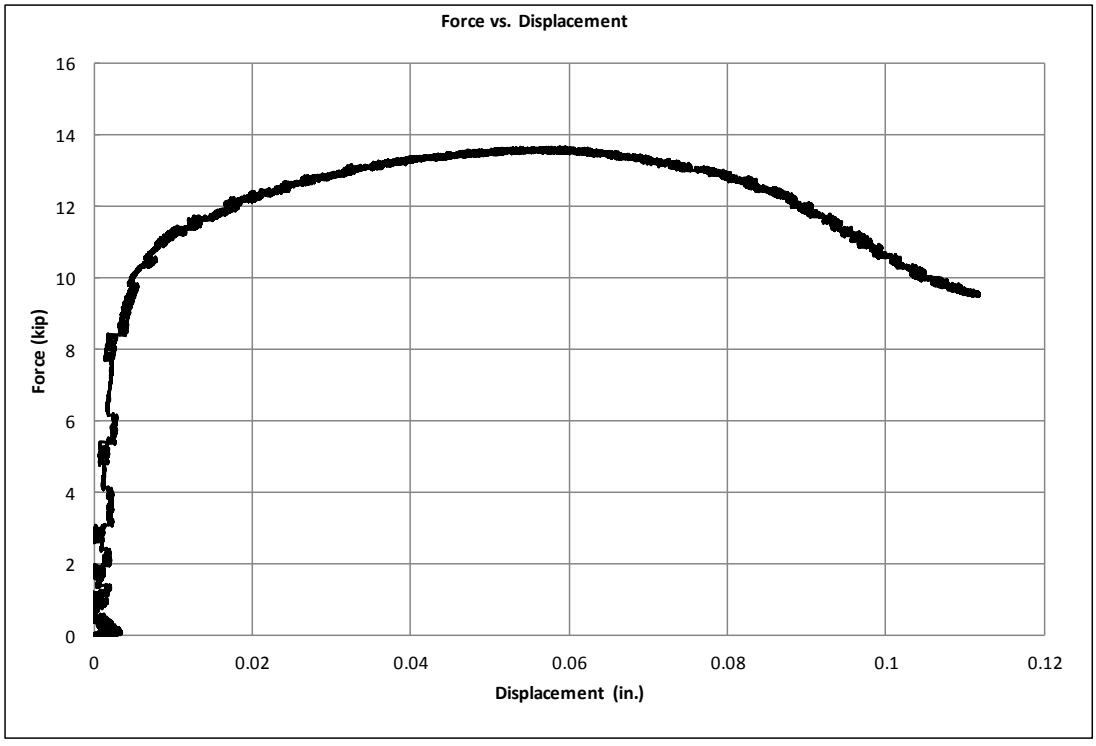

Figure F-51. Test No. SEFT-65 Test Results Summary

MIDWEST ROADSIDE SAFETY FACILITY

Tension Test Summary

Test Information

Test No.	SEFT-66
Specimen Description:	Axial-Symmetric Round Smooth
Specimen Geometry No.:	5
Specimen ID:	156
Test Date:	11/23/2015
Results Folder:	Test Run 117

Testing Procedure

Testing Frame:	Landmark 20 kip
Loading Type:	Tension
Load Rate:	0.00118 in./sec
Grips:	0.43-0.65 in. Serrated Vee
Grip Pressure:	1000 psi
Fixture:	N/A
Measurement Equipment:	2 in. Axial Extensometer Laser Extensometer 22 kip Load Cell
Primary Extensometer:	Laser Extensometer

Initial Measurements

Average Diameter:	0.187	in.
Initial Area:	0.0274	sq. in.
Initial Gauge Length	0.7995	in.

Final Measurements

Average Diameter:	0.100	in.
Final Area:	0.0079	sq. in.
Reduction in Area:	71.1	%
Gauge Length at Failure Initiation:	1.0749	in.

Test Results Summary

Yield Load (0.2% Offset):	1.737	kip
Peak Load:	2.108	kip
Failure Initiation Load:	1.172	kip
Failure Load (ASTM):	1.898	kip
Yield Strength (0.2% Offset):	63.43	ksi
Ultimate Tensile Strength:	76.98	ksi
Engineering Stress at Failure Initiation	42.79	ksi
Engineering Strain at Failure Initiation:	0.3445	in./in.
Engineering Stress at Failure (ASTM):	69.28	ksi
Engineering Strain at Failure (ASTM):	0.2662	in./in.
True Stress at Failure Initiation:	148.06	ksi
True Strain at Failure Initiation:	1.2413	in./in.
Effective Plastic Strain at Failure:	1.2371	in./in.
Young's Modulus:	25,591	ksi

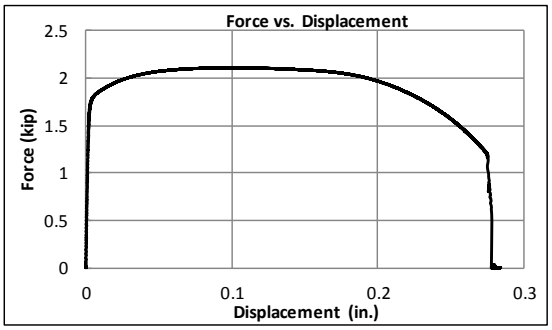

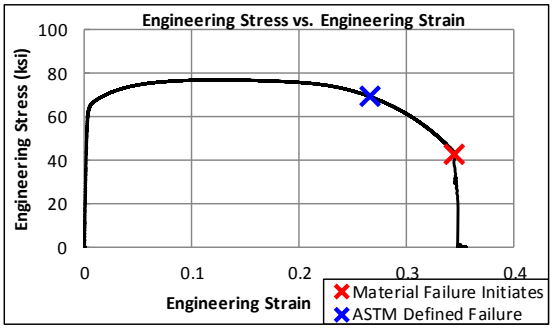

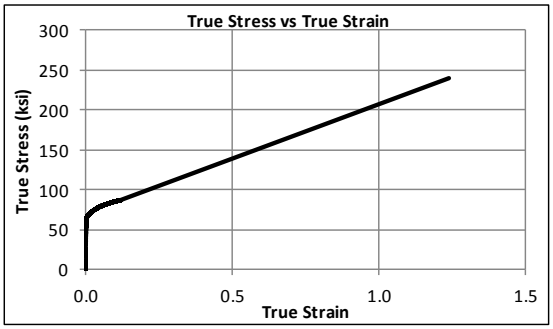

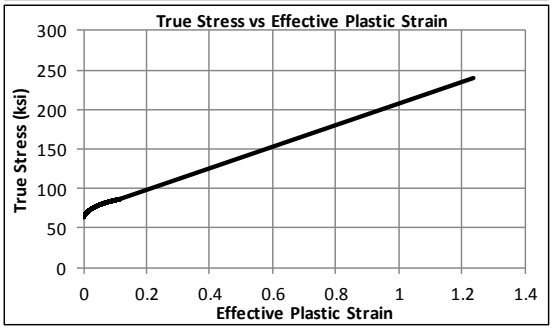

Figure F-52. Test No. SEFT-66 Test Results Summary

MIDWEST ROADSIDE SAFETY FACILITY

Tension Test Summary

Test Information

Test No.	SEFT-67
Specimen Description:	Axial-Symmetric Round Smooth
Specimen Geometry No.:	5
Specimen ID:	157
Test Date:	11/23/2015
Results Folder:	Test Run 118

Testing Procedure

Testing Frame:	Landmark 20 kip
Loading Type:	Tension
Load Rate:	0.00118 in./sec
Grips:	0.43-0.65 in. Serrated Vee
Grip Pressure:	1000 psi
Fixture:	N/A
Measurement Equipment:	2 in. Axial Extensometer Laser Extensometer 22 kip Load Cell
Primary Extensometer:	Laser Extensometer

Initial Measurements

Average Diameter:	0.187	in.
Initial Area:	0.0275	sq. in.
Initial Gauge Length	0.8093	in.

Final Measurements

Average Diameter:	0.100	in.
Final Area:	0.0079	sq. in.
Reduction in Area:	71.4	%
Gauge Length at Failure Initiation:	1.0167	in.

Test Results Summary

Yield Load (0.2% Offset):	1.743	kip
Peak Load:	2.121	kip
Failure Initiation Load:	1.179	kip
Failure Load (ASTM):	1.909	kip
Yield Strength (0.2% Offset):	63.36	ksi
Ultimate Tensile Strength:	77.11	ksi
Engineering Stress at Failure Initiation	42.86	ksi
Engineering Strain at Failure Initiation:	0.2563	in./in.
Engineering Stress at Failure (ASTM):	69.40	ksi
Engineering Strain at Failure (ASTM):	0.1844	in./in.
True Stress at Failure Initiation:	149.71	ksi
True Strain at Failure Initiation:	1.2507	in./in.
Effective Plastic Strain at Failure:	1.2466	in./in.
Young's Modulus:	24,442	ksi

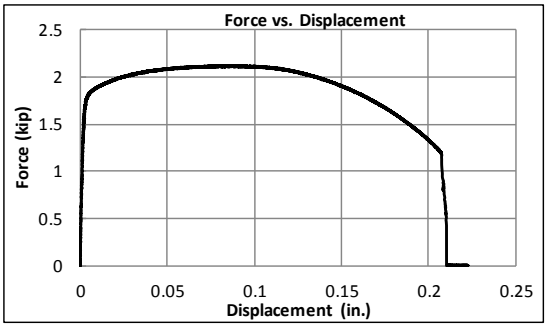

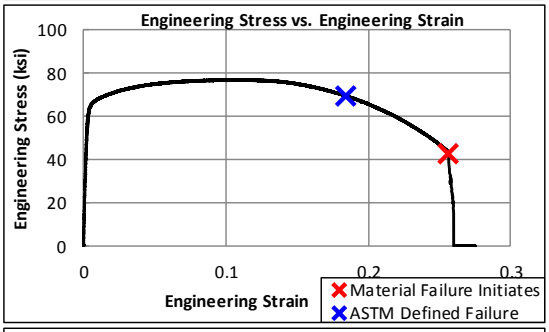

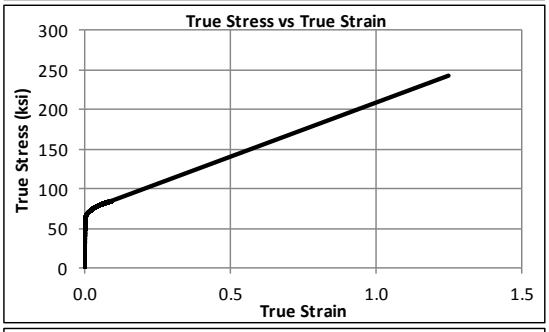

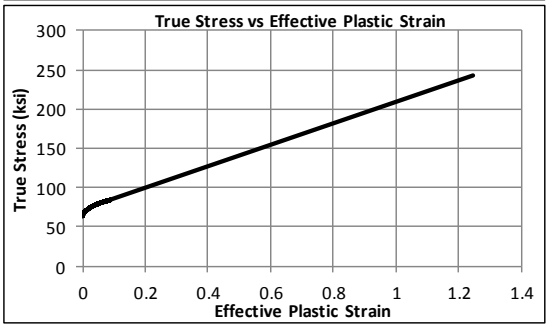

Figure F-53. Test No. SEFT-67 Test Results Summary

MIDWEST ROADSIDE SAFETY FACILITY

Tension Test Summary

Test Information

Test No.	SEFT-68
Specimen Description:	Axial-Symmetric Round Smooth
Specimen Geometry No.:	5
Specimen ID:	158
Test Date:	11/23/2015
Results Folder:	Test Run 119

Testing Procedure

Testing Frame:	Landmark 20 kip
Loading Type:	Tension
Load Rate:	0.00118 in./sec
Grips:	0.43-0.65 in. Serrated Vee
Grip Pressure:	1000 psi
Fixture:	N/A
Measurement Equipment:	2 in. Axial Extensometer Laser Extensometer 22 kip Load Cell
Primary Extensometer:	Laser Extensometer

Initial Measurements

Average Diameter:	0.186	in.
Initial Area:	0.0273	sq. in.
Initial Gauge Length	0.8177	in.

Final Measurements

Average Diameter:	0.100	in.
Final Area:	0.0079	sq. in.
Reduction in Area:	71.1	%
Gauge Length at Failure Initiation:	1.0582	in.

Test Results Summary

Yield Load (0.2% Offset):	1.718	kip
Peak Load:	2.121	kip
Failure Initiation Load:	1.202	kip
Failure Load (ASTM):	1.909	kip
Yield Strength (0.2% Offset):	62.99	ksi
Ultimate Tensile Strength:	77.75	ksi
Engineering Stress at Failure Initiation:	44.06	ksi
Engineering Strain at Failure Initiation:	0.2942	in./in.
Engineering Stress at Failure (ASTM):	69.98	ksi
Engineering Strain at Failure (ASTM):	0.2203	in./in.
True Stress at Failure Initiation:	152.20	ksi
True Strain at Failure Initiation:	1.2397	in./in.
Effective Plastic Strain at Failure:	1.2355	in./in.
Young's Modulus:	23,078	ksi

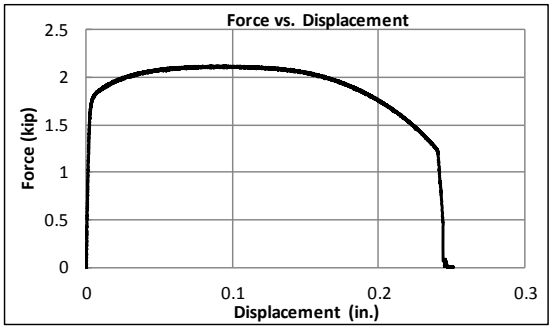

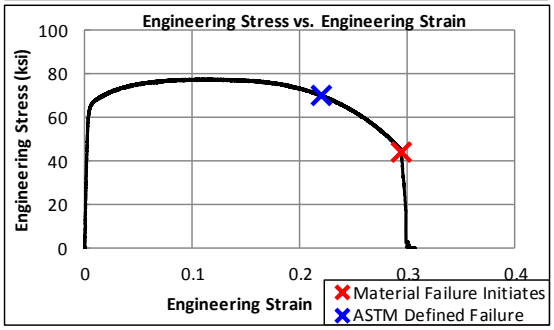

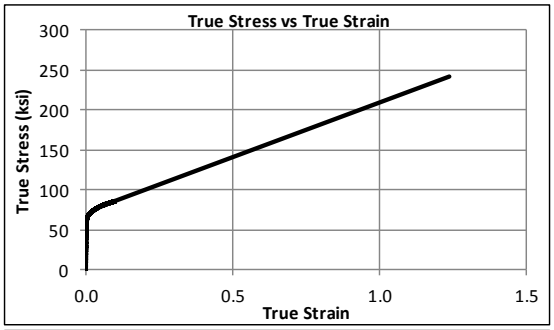

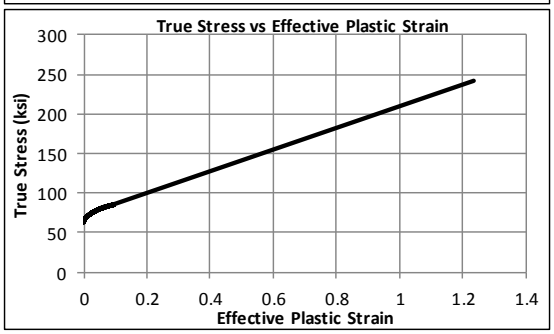

Figure F-54. Test No. SEFT-68 Test Results Summary

MIDWEST ROADSIDE SAFETY FACILITY

Tension Test Summary

Test Information

Test No.	SEFT-69
Specimen Description:	Flat Standard Dog Bone
Specimen Geometry No.:	1
Specimen ID:	018
Test Date:	1/29/2016
Results Folder:	Test Run 120

Testing Procedure

Testing Frame:	Landmark 20 kip
Loading Type:	Tension
Load Rate:	0.0004 in./sec
Grips:	0-0.30 in. Surfalloy
Grip Pressure:	1000 psi
Fixture:	N/A
Measurement Equipment:	1 in. Axial Extensometer Laser Extensometer 22 kip Load Cell
Primary Extensometer:	Laser Extensometer

Initial Measurements

Average Width:	0.120	in.
Average Thickness:	0.029	in.
Initial Area:	0.0035	sq. in.
Initial Gauge Length	0.1596	in.

Final Measurements

Average Width:	0.081	in.
Average Thickness:	0.022	in.
Final Area:	0.0018	sq. in.
Reduction in Area:	50.0	%
Gauge Length at Failure Initiation:	0.2222	in.

Test Results Summary

Yield Load (0.2% Offset):	0.230	kip
Peak Load:	0.279	kip
Failure Initiation Load:	0.190	kip
Failure Load (ASTM):	0.251	kip
Yield Strength (0.2% Offset):	65.41	ksi
Ultimate Tensile Strength:	79.45	ksi
Engineering Stress at Failure Initiation:	53.99	ksi
Engineering Strain at Failure Initiation:	0.3912	in./in.
Engineering Stress at Failure (ASTM):	71.50	ksi
Engineering Strain at Failure (ASTM):	0.2971	in./in.
True Stress at Failure Initiation:	108.05	ksi
True Strain at Failure Initiation:	0.6938	in./in.
Effective Plastic Strain at Failure:	0.6895	in./in.
Young's Modulus:	28,273	ksi

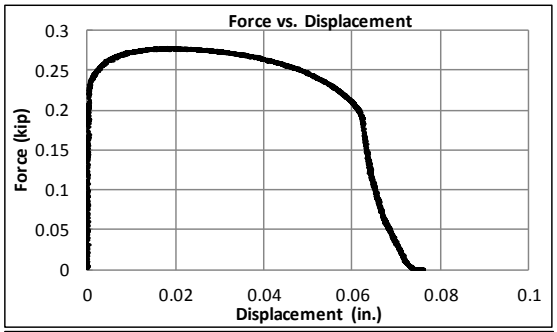

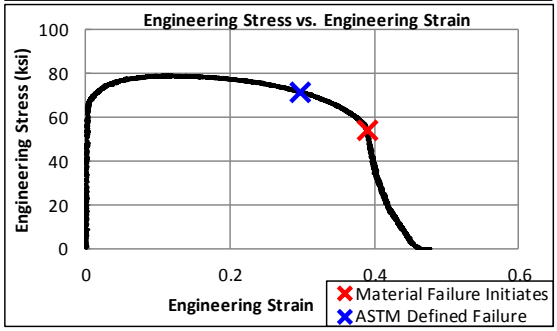

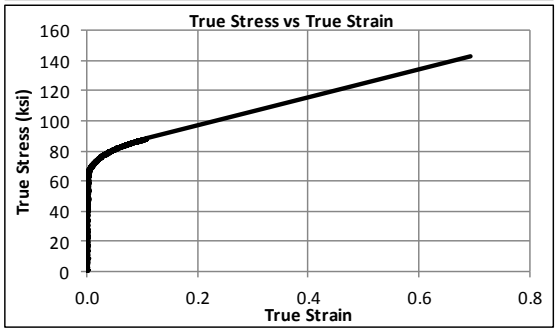

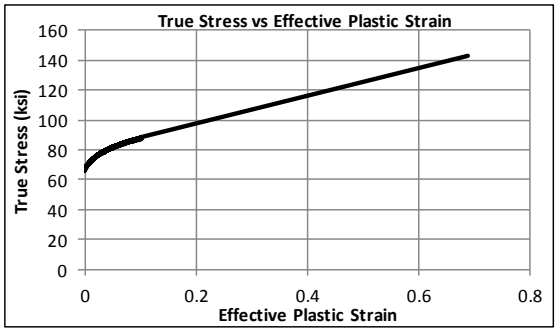

Figure F-55. Test No. SEFT-69 Test Results Summary

MIDWEST ROADSIDE SAFETY FACILITY

Tension Test Summary

Test Information	
Test No.	SEFT-70
Specimen Description:	Flat Standard Dog Bone
Specimen Geometry No.:	1
Specimen ID:	017
Test Date:	1/29/2016
Results Folder:	Test Run 121
Testing Procedure	
Testing Frame:	Landmark 20 kip
Loading Type:	Tension
Load Rate:	0.0004 in./sec
Grips:	0-0.30 in. Surfalloy
Grip Pressure:	1000 psi
Fixture:	N/A
Measurement Equipment:	1 in. Axial Extensometer
	ARAMIS DIC
	22 kip Load Cell
Primary Extensometer:	1 in. Axial Extensometer

Initial Measurements		
Average Width:	0.120	in.
Average Thickness:	0.029	in.
Initial Area:	0.0035	sq. in.
Initial Gauge Length	1.0000	in.
Final Measurements		
Average Width:	0.083	in.
Average Thickness:	0.022	in.
Final Area:	0.0019	sq. in.
Reduction in Area:	46.8	%
Gauge Length at Failure Initiation:	1.0718	in.
Test Results Summary		
Yield Load:	0.224	kip
Peak Load:	0.278	kip
Failure Initiation Load:	0.194	kip
Failure Load (ASTM):	0.250	kip
Displacement at Peak:	0.0274	in.
Displacement at Failure Initiation:	0.0718	in.
Displacement at Failure Load (ASTM):	0.0576	in.
Yield Strength:	64.12	ksi
Ultimate Tensile Strength:	79.33	ksi
Engineering Stress at Failure Initiation:	55.49	ksi
Engineering Stress at Failure (ASTM):	71.40	ksi
True Stress at Failure Initiation:	104.30	ksi
True Strain at Failure Initiation:	0.6310	in./in.
Effective Plastic Strain at Failure:	0.6292	in./in.

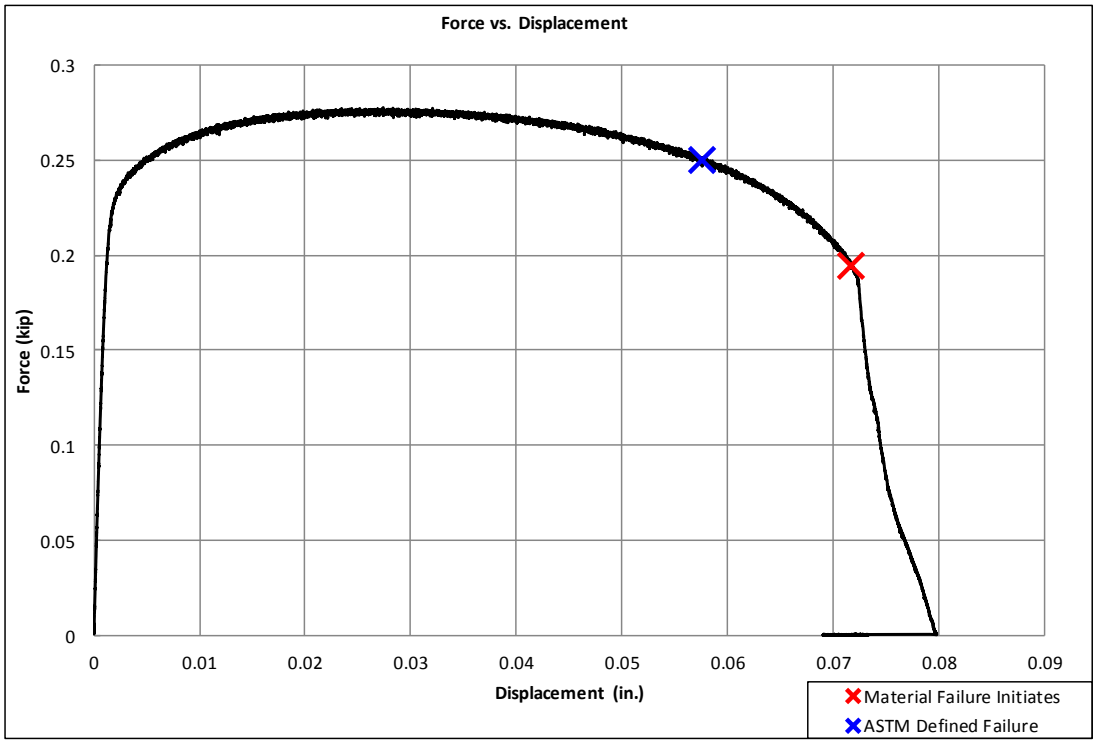

Figure F-56. Test No. SEFT-70 Test Results Summary

MIDWEST ROADSIDE SAFETY FACILITY

Tension Test Summary

Test Information

Test No.	SEFT-71
Specimen Description:	Flat Standard Dog Bone
Specimen Geometry No.:	1
Specimen ID:	020
Test Date:	1/29/2016
Results Folder:	Test Run 122

Testing Procedure

Testing Frame:	Landmark 20 kip
Loading Type:	Tension
Load Rate:	0.0004 in./sec
Grips:	0-0.30 in. Surfalloy
Grip Pressure:	1000 psi
Fixture:	N/A
Measurement Equipment:	1 in. Axial Extensometer
	ARAMIS DIC
	22 kip Load Cell
Primary Extensometer:	1 in. Axial Extensometer

Initial Measurements

Average Width:	0.120	in.
Average Thickness:	0.029	in.
Initial Area:	0.0035	sq. in.
Initial Gauge Length	1.0000	in.

Final Measurements

Average Width:	0.022	in.
Average Thickness:	0.081	in.
Final Area:	0.0018	sq. in.
Reduction in Area:	48.9	%
Gauge Length at Failure Initiation:	1.0710	in.

Test Results Summary

Yield Load:	0.230	kip
Peak Load:	0.278	kip
Failure Initiation Load:	0.191	kip
Failure Load (ASTM):	0.250	kip
Displacement at Peak	0.0289	in.
Displacement at Failure Initiation:	0.0710	in.
Displacement at Failure Load (ASTM):	0.0562	in.
Yield Strength:	65.88	ksi
Ultimate Tensile Strength:	65.88	ksi
Engineering Stress at Failure Initiation:	54.74	ksi
Engineering Stress at Failure (ASTM):	71.73	ksi
True Stress at Failure Initiation:	107.15	ksi
True Strain at Failure Initiation:	0.6717	in./in.
Effective Plastic Strain at Failure:	0.6696	in./in.

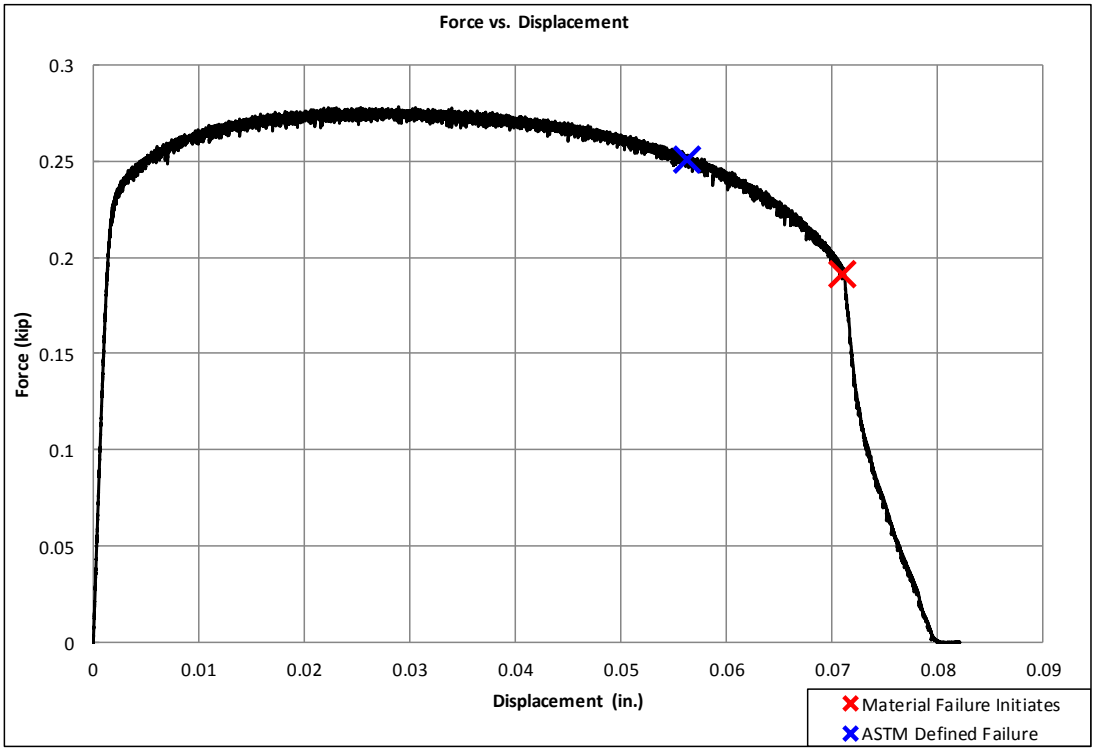

Figure F-57. Test No. SEFT-71 Test Results Summary

MIDWEST ROADSIDE SAFETY FACILITY

Tension Test Summary

Test Information	
Test No.	SEFT-72
Specimen Description:	Flat Standard Dog Bone
Specimen Geometry No.:	1
Specimen ID:	019
Test Date:	1/29/2016
Results Folder:	Test Run 123
Testing Procedure	
Testing Frame:	Landmark 20 kip
Loading Type:	Tension
Load Rate:	0.0004 in./sec
Grips:	0-0.30 in. Surfalloy
Grip Pressure:	1000 psi
Fixture:	N/A
Measurement Equipment:	1 in. Axial Extensometer
	ARAMIS DIC
	22 kip Load Cell
Primary Extensometer:	1 in. Axial Extensometer

Initial Measurements		
Average Width:	0.120	in.
Average Thickness:	0.029	in.
Initial Area:	0.0035	sq. in.
Initial Gauge Length	1.0000	in.
Final Measurements		
Average Width:	0.083	in.
Average Thickness:	0.022	in.
Final Area:	0.0018	sq. in.
Reduction in Area:	49.0	%
Gauge Length at Failure Initiation:	1.0707	in.
Test Results Summary		
Yield Load:	0.228	kip
Peak Load:	0.279	kip
Failure Initiation Load:	0.198	kip
Failure Load (ASTM):	0.251	kip
Displacement at Peak:	0.0273	in.
Displacement at Failure Initiation:	0.0707	in.
Displacement at Failure Load (ASTM):	0.0563	in.
Yield Strength:	64.85	ksi
Ultimate Tensile Strength:	79.30	ksi
Engineering Stress at Failure Initiation:	56.30	ksi
Engineering Stress at Failure (ASTM):	71.37	ksi
True Stress at Failure Initiation:	110.45	ksi
True Strain at Failure Initiation:	0.6739	in./in.
Effective Plastic Strain at Failure:	0.6719	in./in.

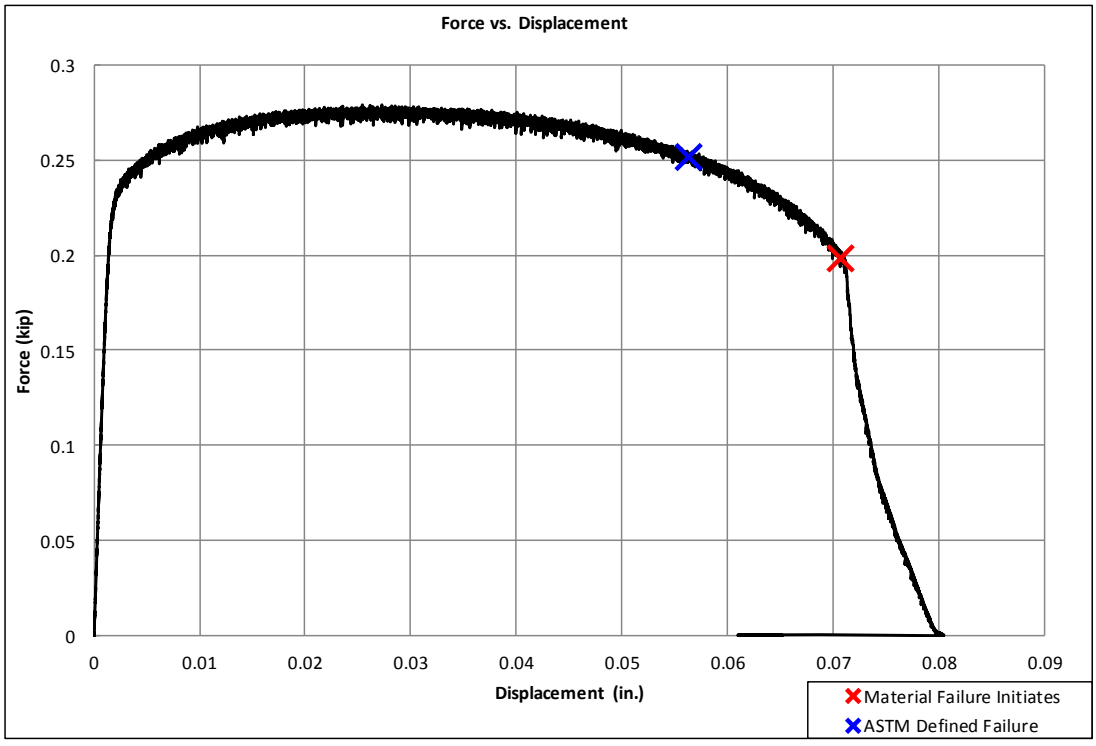

Figure F-58. Test No. SEFT-72 Test Results Summary

MIDWEST ROADSIDE SAFETY FACILITY

Tension Test Summary

Test Information	
Test No.	SEFT-73
Specimen Description:	Flat Large Notch
Specimen Geometry No.:	4
Specimen ID:	044
Test Date:	1/29/2016
Results Folder:	Test Run 124

Testing Procedure	
Testing Frame:	Landmark 20 kip
Loading Type:	Tension
Load Rate:	0.00022 in./sec
Grips:	0-0.30 in. Surfalloy
Grip Pressure:	1000 psi
Fixture:	N/A
Measurement Equipment:	1 in. Axial Extensometer
	ARAMIS DIC
	22 kip Load Cell
Primary Extensometer:	1 in. Axial Extensometer

Initial Measurements		
Average Width:	0.121	in.
Average Thickness:	0.030	in.
Initial Area:	0.0036	sq. in.
Initial Gauge Length	1.0000	in.

Final Measurements		
Average Width:	0.095	in.
Average Thickness:	0.021	in.
Final Area:	0.0020	sq. in.
Reduction in Area:	44.7	%
Gauge Length at Failure Initiation:	1.0343	in.

Test Results Summary		
Yield Load:	0.257	kip
Peak Load:	0.299	kip
Failure Initiation Load:	0.223	kip
Failure Load (ASTM):	0.269	kip
Displacement at Peak:	0.0104	in.
Displacement at Failure Initiation:	0.0343	in.
Displacement at Failure Load (ASTM):	0.0263	in.
Yield Strength:	71.60	ksi
Ultimate Tensile Strength:	83.12	ksi
Engineering Stress at Failure Initiation:	62.04	ksi
Engineering Stress at Failure (ASTM):	74.81	ksi

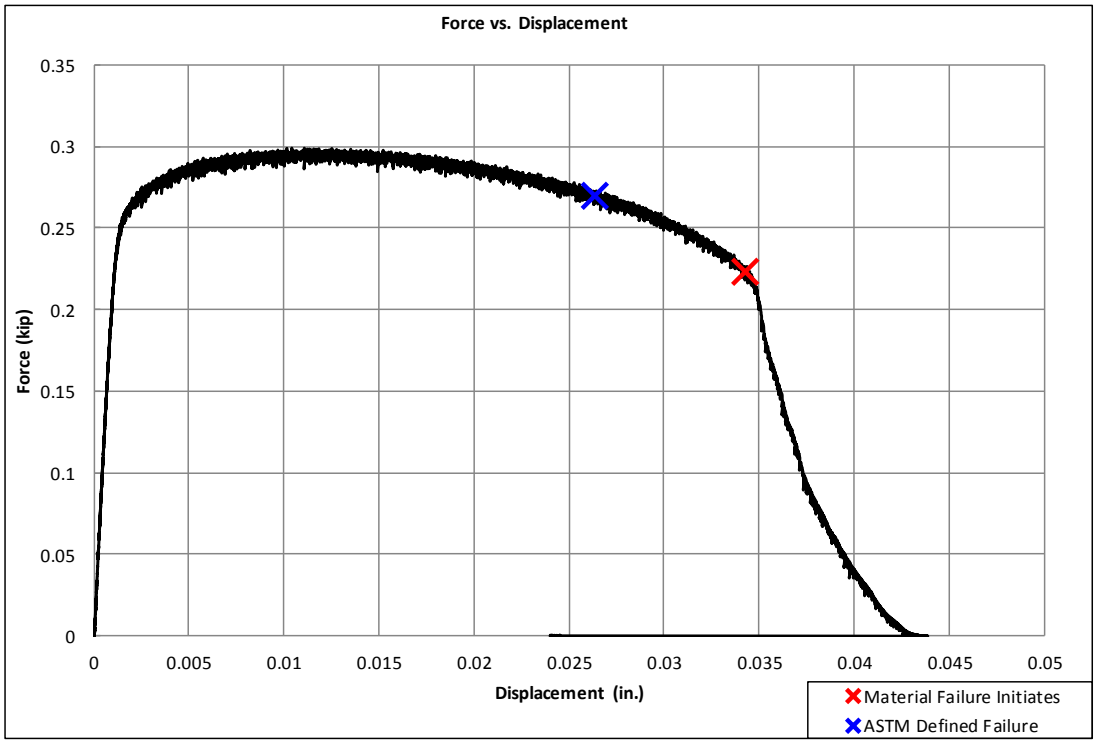

Figure F-59. Test No. SEFT-73 Test Results Summary

MIDWEST ROADSIDE SAFETY FACILITY

Tension Test Summary

Test Information	
Test No.	SEFT-74
Specimen Description:	Flat Standard Dog Bone
Specimen Geometry No.:	1
Specimen ID:	021
Test Date:	2/1/2016
Results Folder:	Test Run 125
Testing Procedure	
Testing Frame:	Landmark 20 kip
Loading Type:	Tension
Load Rate:	0.0004 in./sec
Grips:	0-0.30 in. Surfalloy
Grip Pressure:	1000 psi
Fixture:	N/A
Measurement Equipment:	1 in. Axial Extensometer
	ARAMIS DIC
	22 kip Load Cell
Primary Extensometer:	1 in. Axial Extensometer

Initial Measurements		
Average Width:	0.120	in.
Average Thickness:	0.029	in.
Initial Area:	0.0035	sq. in.
Initial Gauge Length	1.0000	in.
Final Measurements		
Average Width:	0.080	in.
Average Thickness:	0.023	in.
Final Area:	0.0018	sq. in.
Reduction in Area:	47.4	%
Gauge Length at Failure Initiation:	1.0711	in.
Test Results Summary		
Yield Load:	0.222	kip
Peak Load:	0.278	kip
Failure Initiation Load:	0.203	kip
Failure Load (ASTM):	0.250	kip
Displacement at Peak:	0.0284	in.
Displacement at Failure Initiation:	0.0711	in.
Displacement at Failure Load (ASTM):	0.0580	in.
Yield Strength:	63.56	ksi
Ultimate Tensile Strength:	79.53	ksi
Engineering Stress at Failure Initiation:	57.89	ksi
Engineering Stress at Failure (ASTM):	71.58	ksi
True Stress at Failure Initiation:	109.97	ksi
True Strain at Failure Initiation:	0.6417	in./in.
Effective Plastic Strain at Failure:	0.6401	in./in.

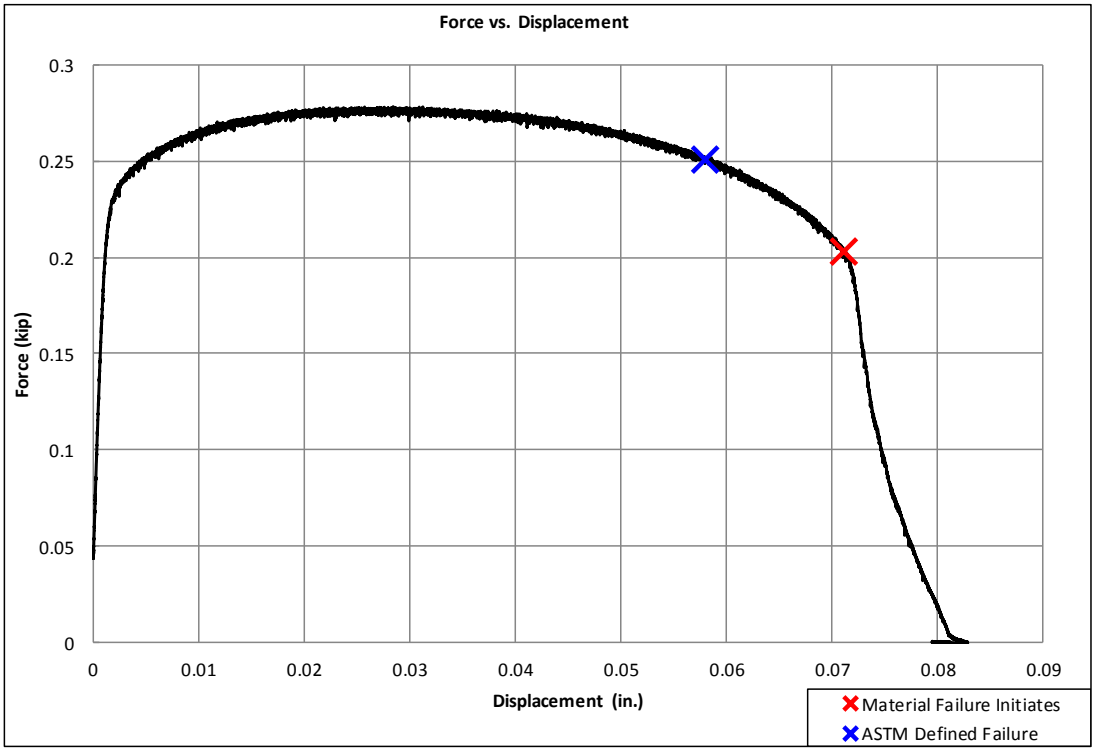

Figure F-60. Test No. SEFT-74 Test Results Summary

MIDWEST ROADSIDE SAFETY FACILITY

Tension Test Summary

Test Information	
Test No.	SEFT-75
Specimen Description:	Flat Large Notch
Specimen Geometry No.:	2
Specimen ID:	044
Test Date:	2/1/2016
Results Folder:	Test Run 126

Testing Procedure	
Testing Frame:	Landmark 20 kip
Loading Type:	Tension
Load Rate:	0.00022 in./sec
Grips:	0-0.30 in. Surfalloy
Grip Pressure:	1000 psi
Fixture:	N/A
Measurement Equipment:	1 in. Axial Extensometer
	ARAMIS DIC
	22 kip Load Cell
Primary Extensometer:	1 in. Axial Extensometer

Initial Measurements		
Average Width:	0.121	in.
Average Thickness:	0.030	in.
Initial Area:	0.0036	sq. in.
Initial Gauge Length	1.0000	in.

Final Measurements		
Average Width:	0.095	in.
Average Thickness:	0.021	in.
Final Area:	0.0020	sq. in.
Reduction in Area:	44.1	%
Gauge Length at Failure Initiation:	1.0352	in.

Test Results Summary		
Yield Load:	0.251	kip
Peak Load:	0.297	kip
Failure Initiation Load:	0.212	kip
Failure Load (ASTM):	0.267	kip
Displacement at Peak:	0.0128	in.
Displacement at Failure Initiation:	0.0352	in.
Displacement at Failure Load (ASTM):	0.0256	in.
Yield Strength:	69.92	ksi
Ultimate Tensile Strength:	82.49	ksi
Engineering Stress at Failure Initiation:	58.97	ksi
Engineering Stress at Failure (ASTM):	74.24	ksi

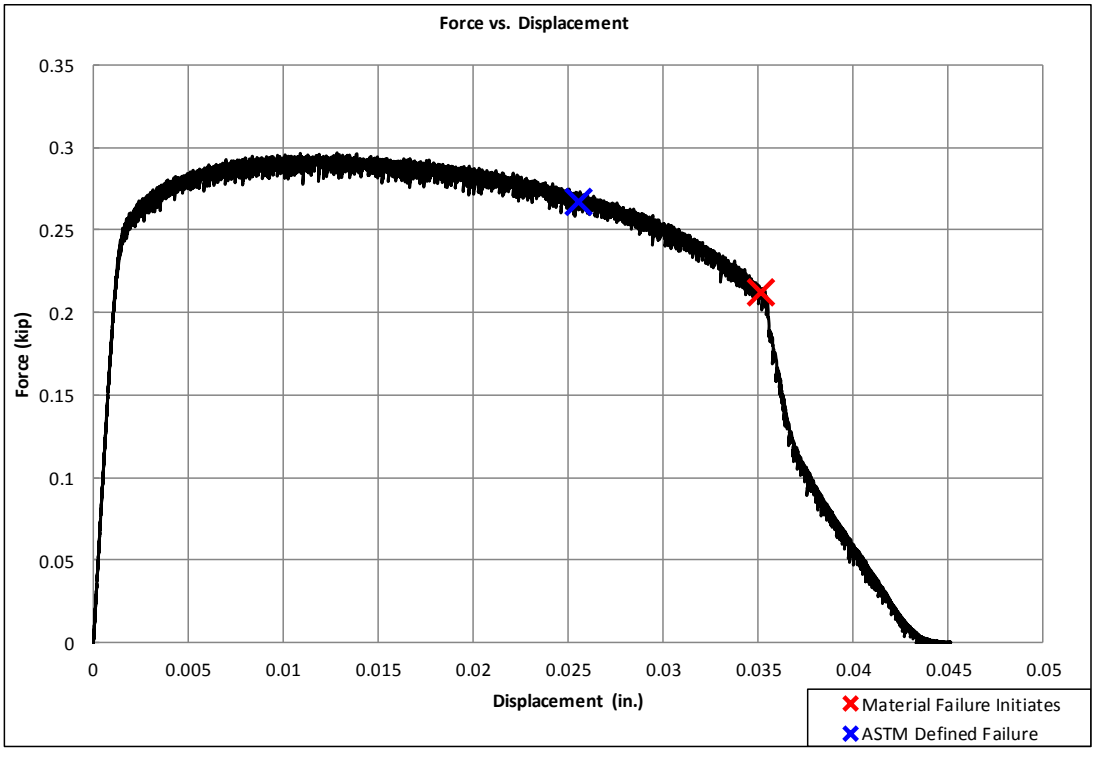

Figure F-61. Test No. SEFT-75 Test Results Summary

MIDWEST ROADSIDE SAFETY FACILITY

Tension Test Summary

Test Information	
Test No.	SEFT-76
Specimen Description:	Flat Standard Dog Bone
Specimen Geometry No.:	1
Specimen ID:	023
Test Date:	2/1/2016
Results Folder:	Test Run 127
Testing Procedure	
Testing Frame:	Landmark 20 kip
Loading Type:	Tension
Load Rate:	0.0004 in./sec
Grips:	0-0.30 in. Surfalloy
Grip Pressure:	1000 psi
Fixture:	N/A
Measurement Equipment:	1 in. Axial Extensometer
	ARAMIS DIC
	22 kip Load Cell
Primary Extensometer:	1 in. Axial Extensometer

Initial Measurements		
Average Width:	0.120	in.
Average Thickness:	0.029	in.
Initial Area:	0.0035	sq. in.
Initial Gauge Length	1.0000	in.
Final Measurements		
Average Width:	0.081	in.
Average Thickness:	0.022	in.
Final Area:	0.0018	sq. in.
Reduction in Area:	49.9	%
Gauge Length at Failure Initiation:	1.0723	in.
Test Results Summary		
Yield Load:	0.226	kip
Peak Load:	0.279	kip
Failure Initiation Load:	0.191	kip
Failure Load (ASTM):	0.251	kip
Displacement at Peak:	0.0277	in.
Displacement at Failure Initiation:	0.0723	in.
Displacement at Failure Load (ASTM):	0.0563	in.
Yield Strength:	64.72	ksi
Ultimate Tensile Strength:	79.66	ksi
Engineering Stress at Failure Initiation:	54.53	ksi
Engineering Stress at Failure (ASTM):	71.70	ksi
True Stress at Failure Initiation:	108.94	ksi
True Strain at Failure Initiation:	0.6920	in./in.
Effective Plastic Strain at Failure:	0.6901	in./in.

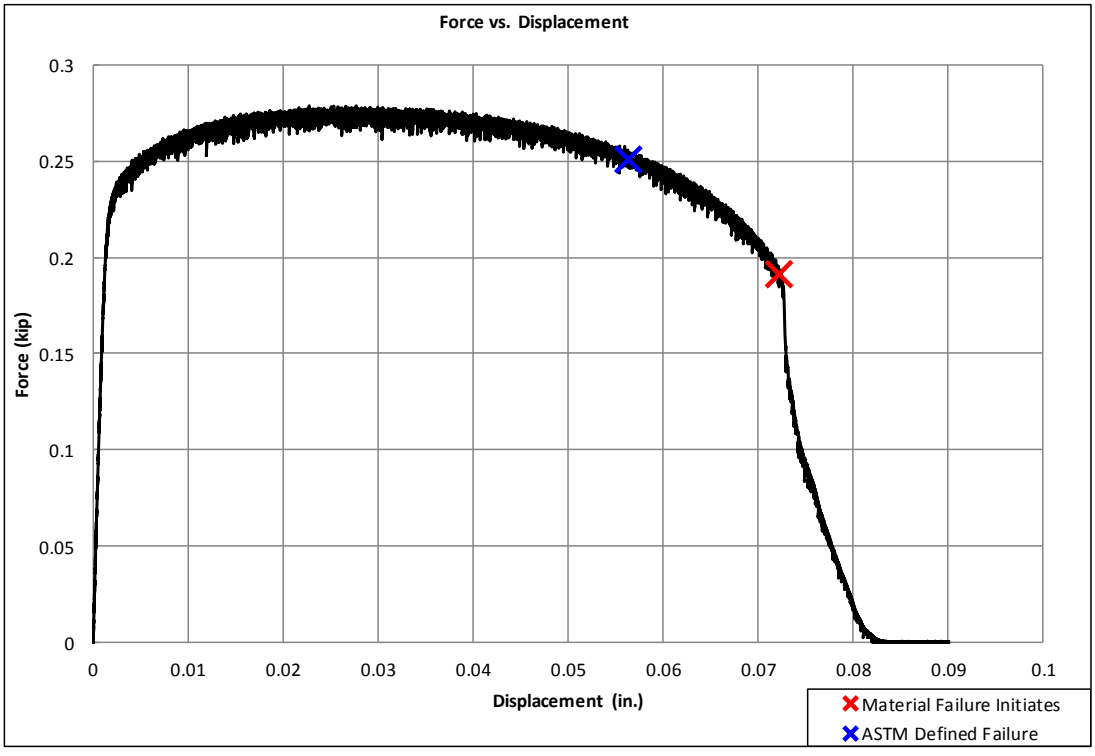

Figure F-62. Test No. SEFT-76 Test Results Summary

MIDWEST ROADSIDE SAFETY FACILITY

Tension Test Summary

Test Information	
Test No.	SEFT-77
Specimen Description:	Flat Standard Dog Bone
Specimen Geometry No.:	1
Specimen ID:	024
Test Date:	2/4/2016
Results Folder:	Test Run 128

Testing Procedure	
Testing Frame:	Landmark 20 kip
Loading Type:	Tension
Load Rate:	0.0004 in./sec
Grips:	0-0.30 in. Surfalloy
Grip Pressure:	1000 psi
Fixture:	N/A
Measurement Equipment:	1 in. Axial Extensometer
	ARAMIS DIC
	22 kip Load Cell
Primary Extensometer:	1 in. Axial Extensometer

Initial Measurements		
Average Width:	0.120	in.
Average Thickness:	0.029	in.
Initial Area:	0.0035	sq. in.
Initial Gauge Length	1.0000	in.

Final Measurements		
Average Width:	0.081	in.
Average Thickness:	0.022	in.
Final Area:	0.0018	sq. in.
Reduction in Area:	49.5	%
Gauge Length at Failure Initiation:	1.0696	in.

Test Results Summary		
Yield Load:	0.229	kip
Peak Load:	0.277	kip
Failure Initiation Load:	0.198	kip
Failure Load (ASTM):	0.249	kip
Displacement at Peak:	0.0274	in.
Displacement at Failure Initiation:	0.0696	in.
Displacement at Failure Load (ASTM):	0.0568	in.
Yield Strength:	64.93	ksi
Ultimate Tensile Strength:	78.36	ksi
Engineering Stress at Failure Initiation:	56.02	ksi
Engineering Stress at Failure (ASTM):	70.53	ksi
True Stress at Failure Initiation:	110.83	ksi
True Strain at Failure Initiation:	0.6823	in./in.
Effective Plastic Strain at Failure:	0.6803	in./in.

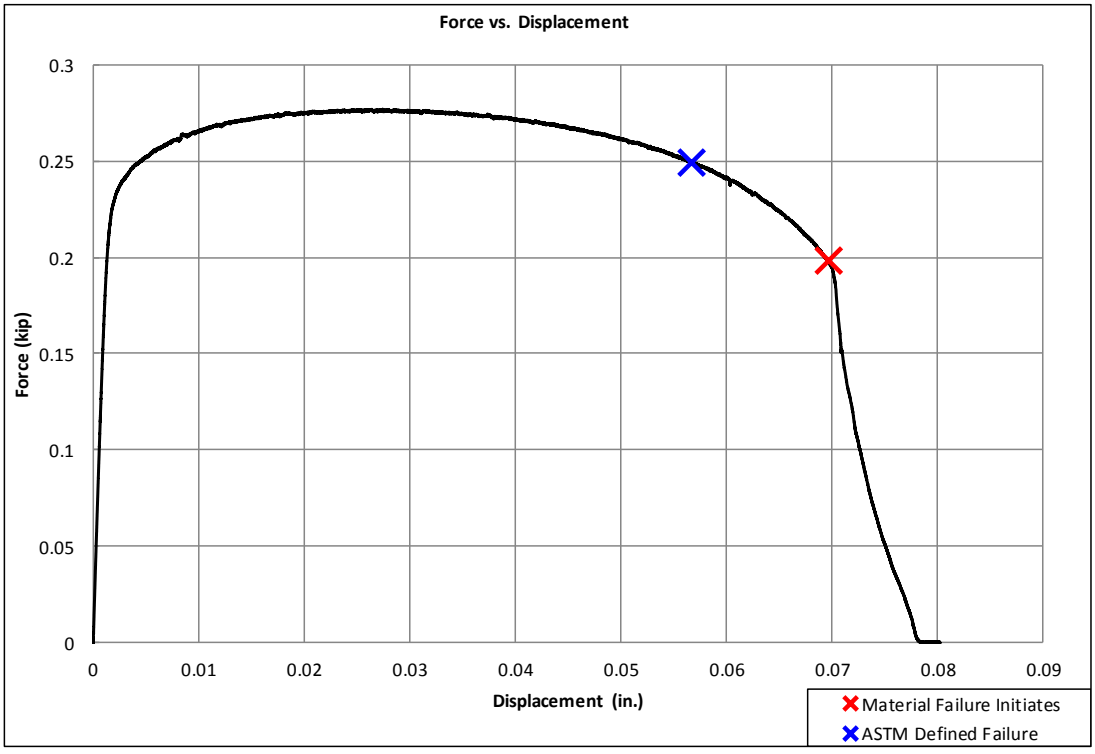

Figure F-63. Test No. SEFT-77 Test Results Summary

MIDWEST ROADSIDE SAFETY FACILITY

Tension Test Summary

Test Information	
Test No.	SEFT-78
Specimen Description:	Notched Round Specimen #4
Specimen Geometry No.:	9
Specimen ID:	086
Test Date:	2/5/2016
Results Folder:	Test Run 129
Testing Procedure	
Testing Frame:	Landmark 20 kip
Loading Type:	Tension
Load Rate:	0.000404 in./sec
Grips:	0.43-0.65 in. Serrated Vee
Grip Pressure:	1000 psi
Fixture:	N/A
Measurement Equipment:	2 in. Axial Extensometer
	ARAMIS DIC
	22 kip Load Cell
Primary Extensometer:	2 in. Axial Extensometer

Initial Measurements		
Average Diameter:	0.188	in.
Initial Area:	0.0278	sq. in.
Initial Gauge Length	2.0000	in.
Final Measurements		
Average Diameter:	0.113	in.
Final Area:	0.0100	sq. in.
Reduction in Area:	64.1	%
Gauge Length at Failure Initiation:	2.0726	in.
Test Results Summary		
Yield Load:	2.215	kip
Peak Load:	2.575	kip
Failure Initiation Load:	1.663	kip
Failure Load (ASTM):	2.317	kip
Displacement at Peak:	0.0127	in.
Displacement at Failure Initiation:	0.0726	in.
Displacement at Failure Load (ASTM):	0.0386	in.
Yield Strength:	79.75	ksi
Ultimate Tensile Strength:	92.70	ksi
Engineering Stress at Failure Initiation:	59.88	ksi
Engineering Stress at Failure (ASTM):	83.43	ksi

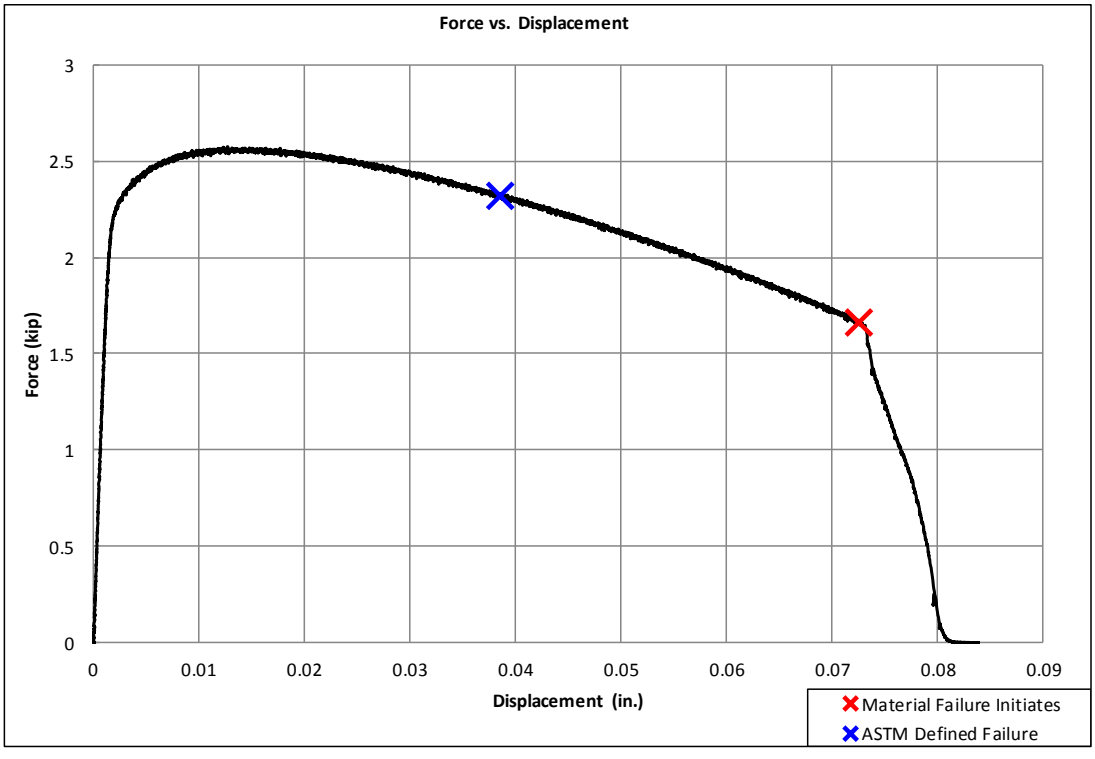

Figure F-64. Test No. SEFT-78 Test Results Summary

MIDWEST ROADSIDE SAFETY FACILITY

Tension Test Summary

Test Information

Test No.	SEFT-79
Specimen Description:	Flat Standard Dog Bone
Specimen Geometry No.:	1
Specimen ID:	022
Test Date:	2/8/2016
Results Folder:	Test Run 130

Testing Procedure

Testing Frame:	Landmark 20 kip
Loading Type:	Tension
Load Rate:	0.0004 in./sec
Grips:	0-0.30 in. Surfalloy
Grip Pressure:	1000 psi
Fixture:	N/A
Measurement Equipment:	1 in. Axial Extensometer
	ARAMIS DIC
	22 kip Load Cell
Primary Extensometer:	1 in. Axial Extensometer

Initial Measurements

Average Width:	0.120	in.
Average Thickness:	0.029	in.
Initial Area:	0.0035	sq. in.
Initial Gauge Length	1.0000	in.

Final Measurements

Average Width:	0.079	in.
Average Thickness:	0.021	in.
Final Area:	0.0017	sq. in.
Reduction in Area:	51.3	%
Gauge Length at Failure Initiation:	1.0701	in.

Test Results Summary

Yield Load:	0.226	kip
Peak Load:	0.276	kip
Failure Initiation Load:	0.196	kip
Failure Load (ASTM):	0.248	kip
Displacement at Peak:	0.0236	in.
Displacement at Failure Initiation:	0.0701	in.
Displacement at Failure Load (ASTM):	0.0568	in.
Yield Strength:	64.72	ksi
Ultimate Tensile Strength:	78.97	ksi
Engineering Stress at Failure Initiation:	56.21	ksi
Engineering Stress at Failure (ASTM):	71.07	ksi
True Stress at Failure Initiation:	115.51	ksi
True Strain at Failure Initiation:	0.7203	in./in.
Effective Plastic Strain at Failure:	0.7186	in./in.

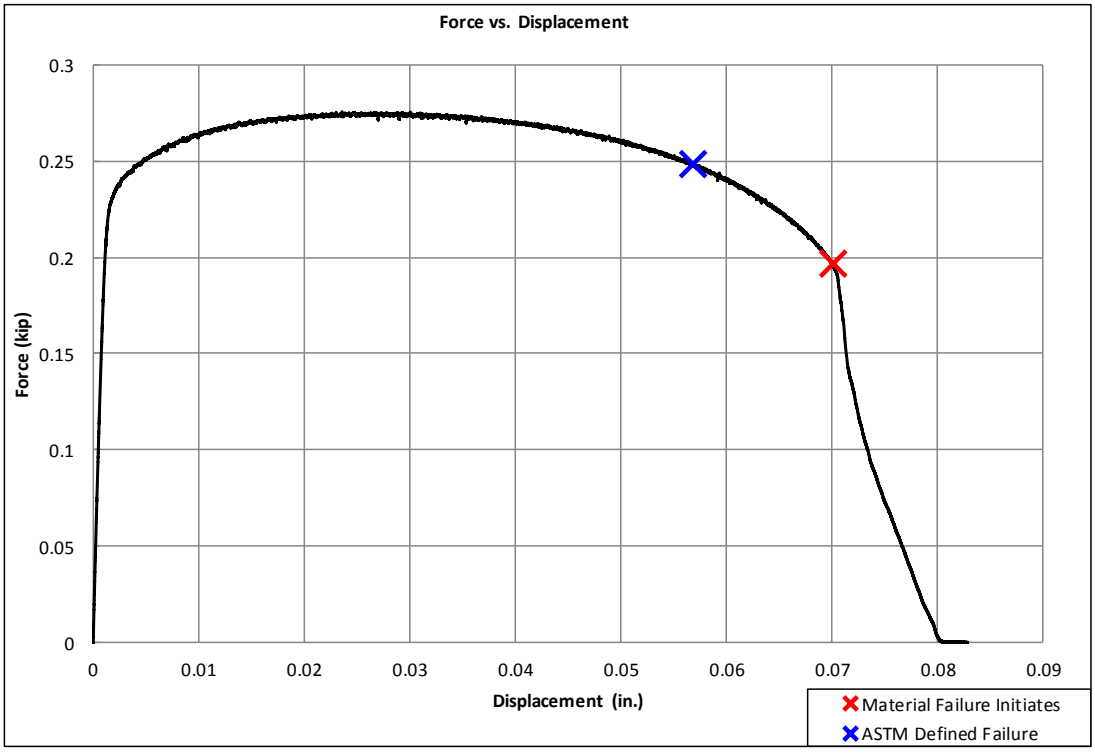

Figure F-65. Test No. SEFT-79 Test Results Summary

MIDWEST ROADSIDE SAFETY FACILITY

Tension Test Summary

Test Information	
Test No.	SEFT-80
Specimen Description:	Notched Round Specimen #3
Specimen Geometry No.:	8
Specimen ID:	080
Test Date:	2/8/2016
Results Folder:	Test Run 131

Testing Procedure	
Testing Frame:	Landmark 20 kip
Loading Type:	Tension
Load Rate:	0.000447 in./sec
Grips:	0.43-0.65 in. Serrated Vee
Grip Pressure:	1000 psi
Fixture:	N/A
Measurement Equipment:	2 in. Axial Extensometer
	ARAMIS DIC
	22 kip Load Cell
Primary Extensometer:	2 in. Axial Extensometer

Initial Measurements		
Average Diameter:	0.188	in.
Initial Area:	0.0279	sq. in.
Initial Gauge Length	2.0000	in.

Final Measurements		
Average Diameter:	0.109	in.
Final Area:	0.0093	sq. in.
Reduction in Area:	66.5	%
Gauge Length at Failure Initiation:	2.0823	in.

Test Results Summary		
Yield Load:	2.149	kip
Peak Load:	2.515	kip
Failure Initiation Load:	1.565	kip
Failure Load (ASTM):	2.264	kip
Displacement at Peak:	0.0168	in.
Displacement at Failure Initiation:	0.0823	in.
Displacement at Failure Load (ASTM):	0.0435	in.
Yield Strength:	77.16	ksi
Ultimate Tensile Strength:	90.30	ksi
Engineering Stress at Failure Initiation:	56.17	ksi
Engineering Stress at Failure (ASTM):	81.27	ksi

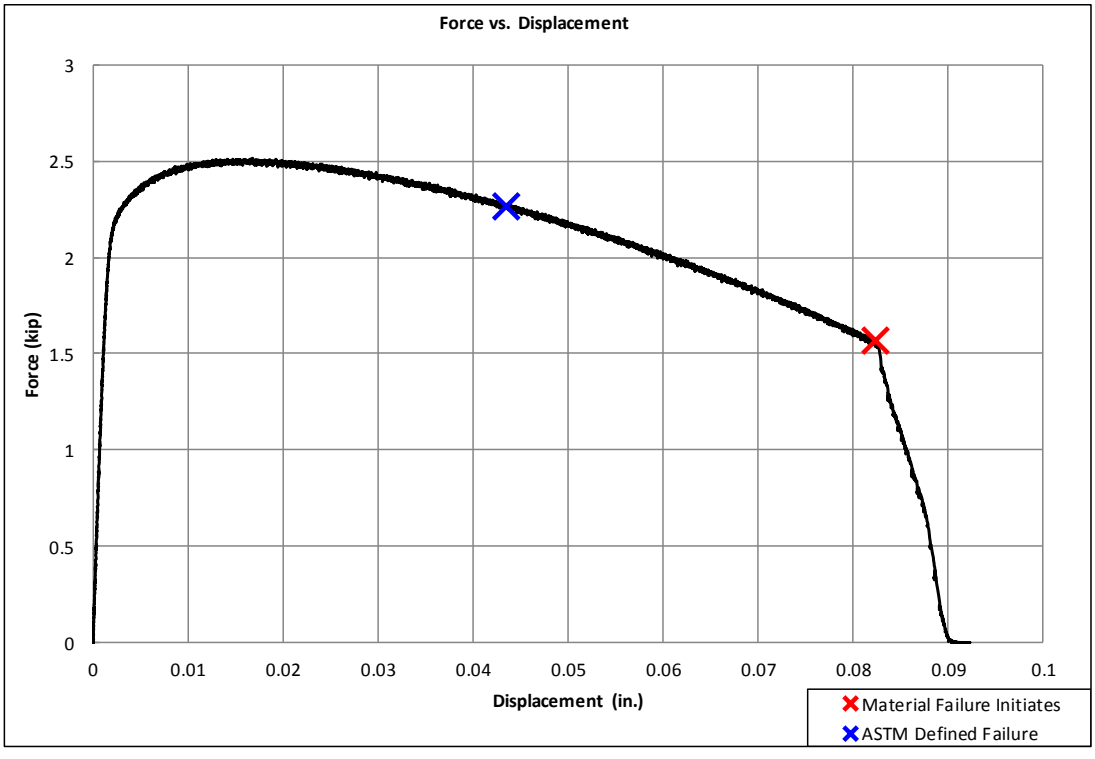

Figure F-66. Test No. SEFT-80 Test Results Summary

MIDWEST ROADSIDE SAFETY FACILITY

Tension Test Summary

Test Information	
Test No.	SEFT-81
Specimen Description:	Thick Dog Bone Specimen
Specimen Geometry No.:	11
Specimen ID:	098
Test Date:	2/8/2016
Results Folder:	Test Run 129

Testing Procedure	
Testing Frame:	Landmark 20 kip
Loading Type:	Tension
Load Rate:	0.0004 in./sec
Grips:	0.28-0.56 in. Flat Diamond Wedge
Grip Pressure:	1000 psi
Fixture:	N/A
Measurement Equipment:	2 in. Axial Extensometer
	ARAMIS DIC
	22 kip Load Cell
Primary Extensometer:	2 in. Axial Extensometer

Initial Measurements		
Average Width:	0.080	in.
Average Thickness:	1.000	in.
Initial Area:	0.0797	sq. in.
Initial Gauge Length	2.0000	in.

Final Measurements		
Average Width:	0.901	in.
Average Thickness:	0.050	in.
Final Area:	0.0448	sq. in.
Reduction in Area:	43.7	%
Gauge Length at Failure Initiation:	2.0719	in.

Test Results Summary		
Yield Load:	5.238	kip
Peak Load:	6.524	kip
Failure Initiation Load:	5.476	kip
Failure Load (ASTM):	5.871	kip
Displacement at Peak:	0.0303	in.
Displacement at Failure Initiation:	0.0719	in.
Displacement at Failure Load (ASTM):	0.0648	in.
Yield Strength:	65.75	ksi
Ultimate Tensile Strength:	81.90	ksi
Engineering Stress at Failure Initiation:	68.74	ksi
Engineering Stress at Failure (ASTM):	73.71	ksi

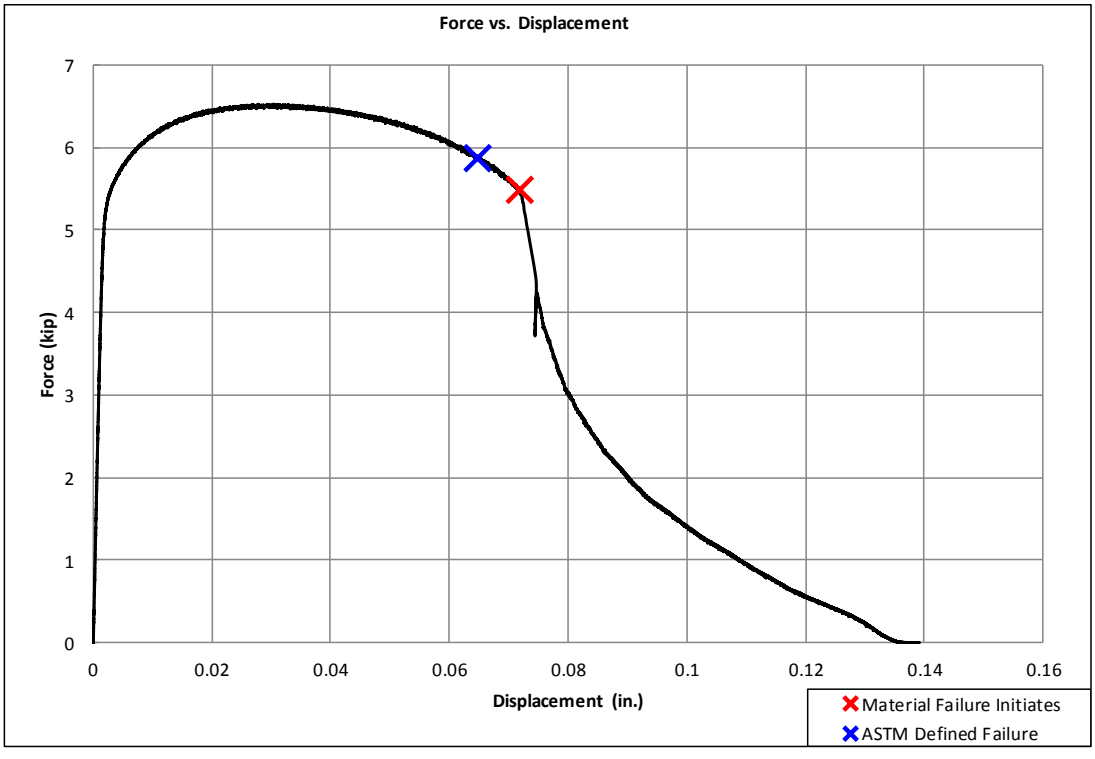

Figure F-67. Test No. SEFT-81 Test Results Summary

MIDWEST ROADSIDE SAFETY FACILITY

Tension Test Summary

Test Information	
Test No.	SEFT-82
Specimen Description:	Notched Round Specimen #5
Specimen Geometry No.:	10
Specimen ID:	092
Test Date:	2/9/2016
Results Folder:	Test Run 131

Testing Procedure	
Testing Frame:	Landmark 20 kip
Loading Type:	Tension
Load Rate:	0.000353 in./sec
Grips:	0.43-0.65 in. Serrated Vee
Grip Pressure:	1000 psi
Fixture:	N/A
Measurement Equipment:	2 in. Axial Extensometer
	ARAMIS DIC
	22 kip Load Cell
Primary Extensometer:	2 in. Axial Extensometer

Initial Measurements		
Average Diameter:	0.189	in.
Initial Area:	0.0281	sq. in.
Initial Gauge Length	2.0000	in.

Final Measurements		
Average Diameter:	0.117	in.
Final Area:	0.0108	sq. in.
Reduction in Area:	61.7	%
Gauge Length at Failure Initiation:	2.0606	in.

Test Results Summary		
Yield Load:	2.360	kip
Peak Load:	2.764	kip
Failure Initiation Load:	1.859	kip
Failure Load (ASTM):	2.488	kip
Displacement at Peak:	0.0118	in.
Displacement at Failure Initiation:	0.0606	in.
Displacement at Failure Load (ASTM):	0.0326	in.
Yield Strength:	83.89	ksi
Ultimate Tensile Strength:	98.28	ksi
Engineering Stress at Failure Initiation:	66.09	ksi
Engineering Stress at Failure (ASTM):	88.46	ksi

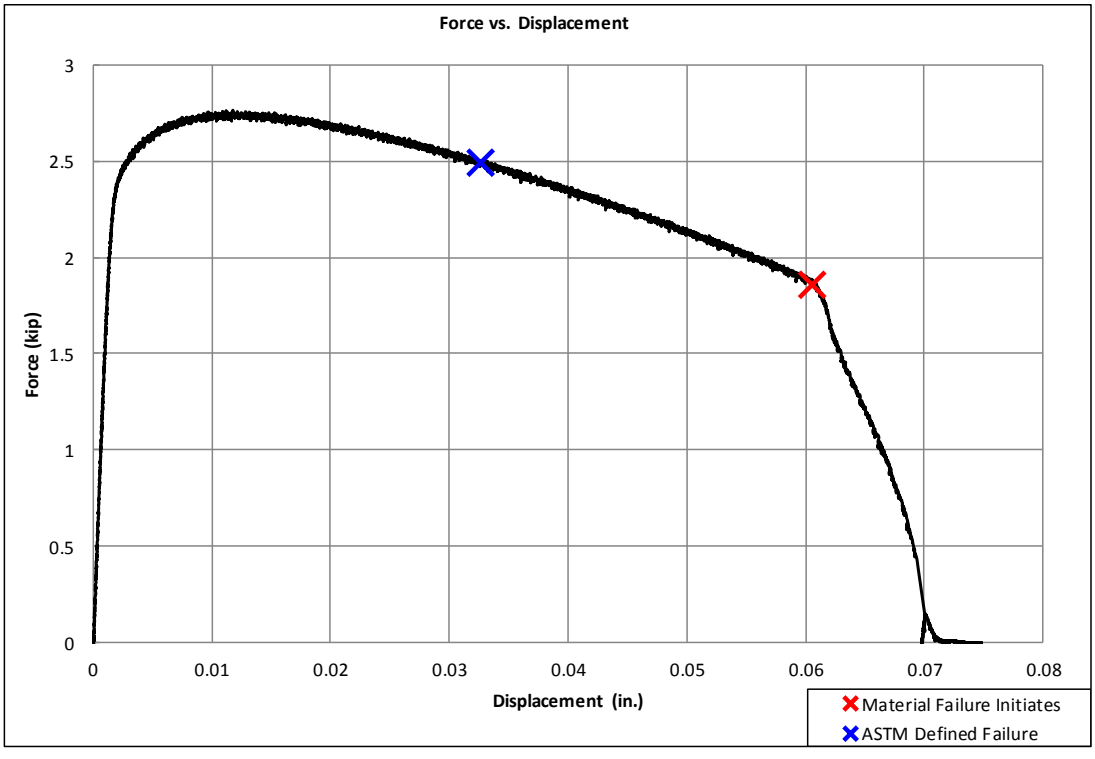

Figure F-68. Test No. SEFT-82 Test Results Summary

MIDWEST ROADSIDE SAFETY FACILITY

Tension Test Summary

Test Information

Test No.	SEFT-83
Specimen Description:	Flat Small Notch
Specimen Geometry No.:	3
Specimen ID:	050
Test Date:	2/9/2015
Results Folder:	Test Run 132

Testing Procedure

Testing Frame:	Landmark 20 kip
Loading Type:	Tension
Load Rate:	0.00017 in./sec
Grips:	0-0.30 in. Surfalloy
Grip Pressure:	1000 psi
Fixture:	N/A
Measurement Equipment:	1 in. Axial Extensometer
	ARAMIS DIC
	22 kip Load Cell
Primary Extensometer:	1 in. Axial Extensometer

Initial Measurements

Average Width:	0.122 in.
Average Thickness:	0.030 in.
Initial Area:	0.0037 sq. in.
Initial Gauge Length	1.0000 in.

Final Measurements

Average Width:	0.102 in.
Average Thickness:	0.021 in.
Final Area:	0.0022 sq. in.
Reduction in Area:	41.1 %
Gauge Length at Failure Initiation:	1.0276 in.

Test Results Summary

Yield Load:	0.259 kip
Peak Load:	0.309 kip
Failure Initiation Load:	0.212 kip
Failure Load (ASTM):	0.278 kip
Displacement at Peak:	0.0088 in.
Displacement at Failure Initiation:	0.0276 in.
Displacement at Failure Load (ASTM):	0.0192 in.
Yield Strength:	70.72 ksi
Ultimate Tensile Strength:	84.31 ksi
Engineering Stress at Failure Initiation:	57.85 ksi
Engineering Stress at Failure (ASTM):	75.88 ksi

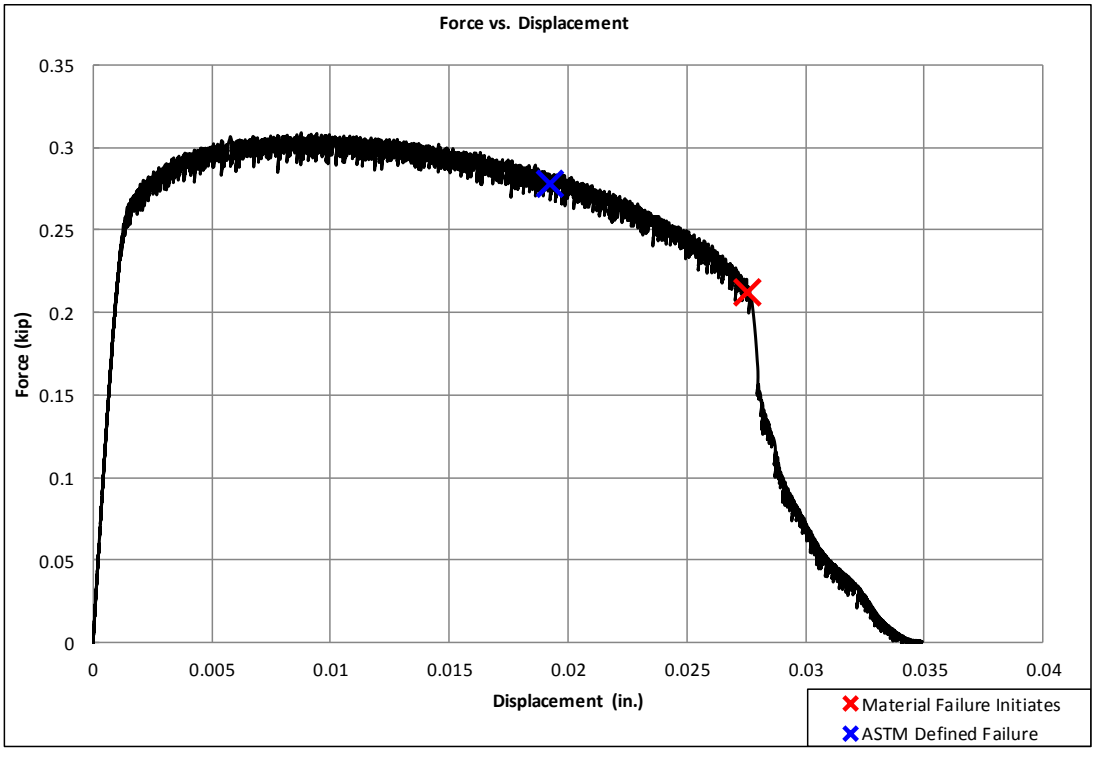

Figure F-69. Test No. SEFT-83 Test Results Summary

MIDWEST ROADSIDE SAFETY FACILITY

Tension Test Summary

Test Information	
Test No.	SEFT-84
Specimen Description:	Flat Sharp Notch
Specimen Geometry No.:	4
Specimen ID:	056
Test Date:	2/9/2016
Results Folder:	Test Run 133

Testing Procedure	
Testing Frame:	Landmark 20 kip
Loading Type:	Tension
Load Rate:	0.000108 in./sec
Grips:	0-0.30 in. Surfalloy
Grip Pressure:	1000 psi
Fixture:	N/A
Measurement Equipment:	1 in. Axial Extensometer
	ARAMIS DIC
	22 kip Load Cell
Primary Extensometer:	1 in. Axial Extensometer

Initial Measurements		
Average Width:	0.120	in.
Average Thickness:	0.029	in.
Initial Area:	0.0035	sq. in.
Initial Gauge Length	1.0000	in.

Final Measurements		
Average Width:	0.115	in.
Average Thickness:	0.019	in.
Final Area:	0.0022	sq. in.
Reduction in Area:	36.4	%
Gauge Length at Failure Initiation:	1.0200	in.

Test Results Summary		
Yield Load:	0.273	kip
Peak Load:	0.316	kip
Failure Initiation Load:	0.213	kip
Failure Load (ASTM):	0.284	kip
Displacement at Peak:	0.0079	in.
Displacement at Failure Initiation:	0.0200	in.
Displacement at Failure Load (ASTM):	0.0135	in.
Yield Strength:	78.17	ksi
Ultimate Tensile Strength:	90.22	ksi
Engineering Stress at Failure Initiation:	60.83	ksi
Engineering Stress at Failure (ASTM):	81.19	ksi

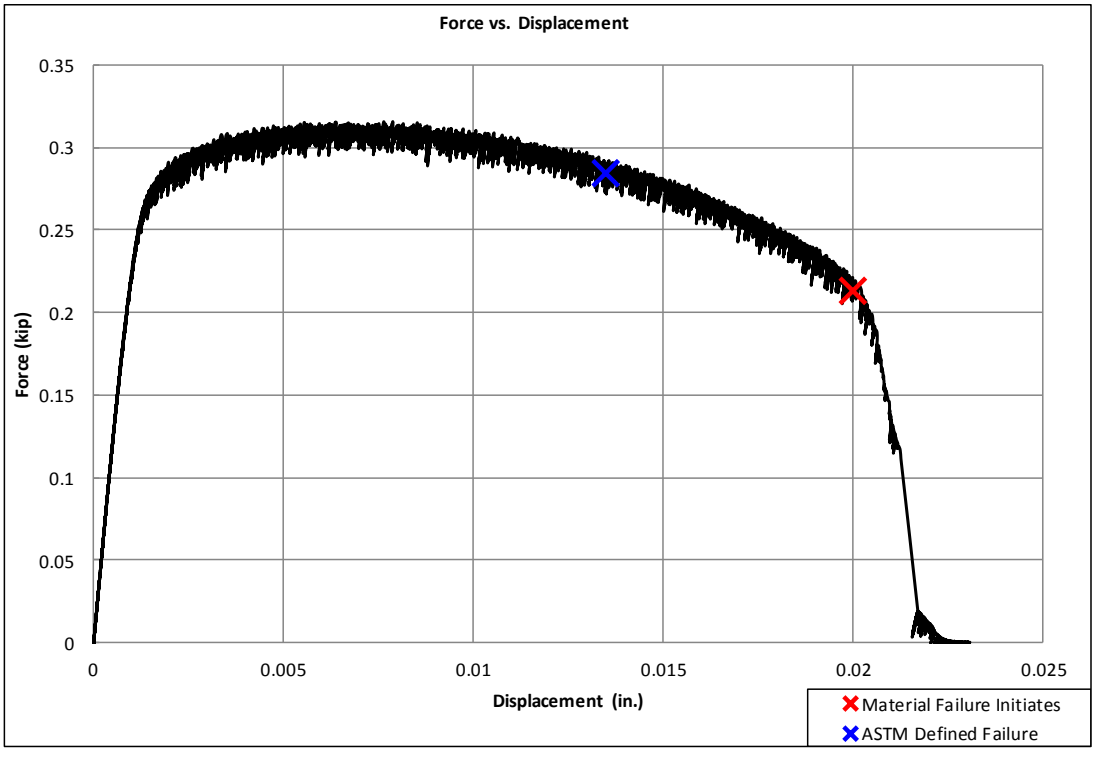

Figure F-70. Test No. SEFT-84 Test Results Summary

MIDWEST ROADSIDE SAFETY FACILITY

Tension Test Summary

Test Information	
Test No.	SEFT-85
Specimen Description:	Thick Large Notch Specimen
Specimen Geometry No.:	13
Specimen ID:	104
Test Date:	2/22/2016
Results Folder:	Test Run 134

Testing Procedure	
Testing Frame:	Landmark 20 kip
Loading Type:	Tension
Load Rate:	0.000312 in./sec
Grips:	0.28-0.56 in. Flat Diamond Wedge
Grip Pressure:	1000 psi
Fixture:	N/A
Measurement Equipment:	2 in. Axial Extensometer
	ARAMIS DIC
	22 kip Load Cell
Primary Extensometer:	2 in. Axial Extensometer

Initial Measurements		
Average Width:	0.080	in.
Average Thickness:	0.999	in.
Initial Area:	0.0802	sq. in.
Initial Gauge Length	2.0000	in.

Final Measurements		
Average Width:	0.053	in.
Average Thickness:	0.895	in.
Final Area:	0.0475	sq. in.
Reduction in Area:	40.8	%
Gauge Length at Failure Initiation:	2.0519	in.

Test Results Summary		
Yield Load:	5.860	kip
Peak Load:	7.060	kip
Failure Initiation Load:	5.592	kip
Failure Load (ASTM):	6.354	kip
Displacement at Peak:	0.0198	in.
Displacement at Failure Initiation:	0.0519	in.
Displacement at Failure Load (ASTM):	0.0425	in.
Yield Strength:	73.05	ksi
Ultimate Tensile Strength:	88.00	ksi
Engineering Stress at Failure Initiation:	69.71	ksi
Engineering Stress at Failure (ASTM):	79.20	ksi

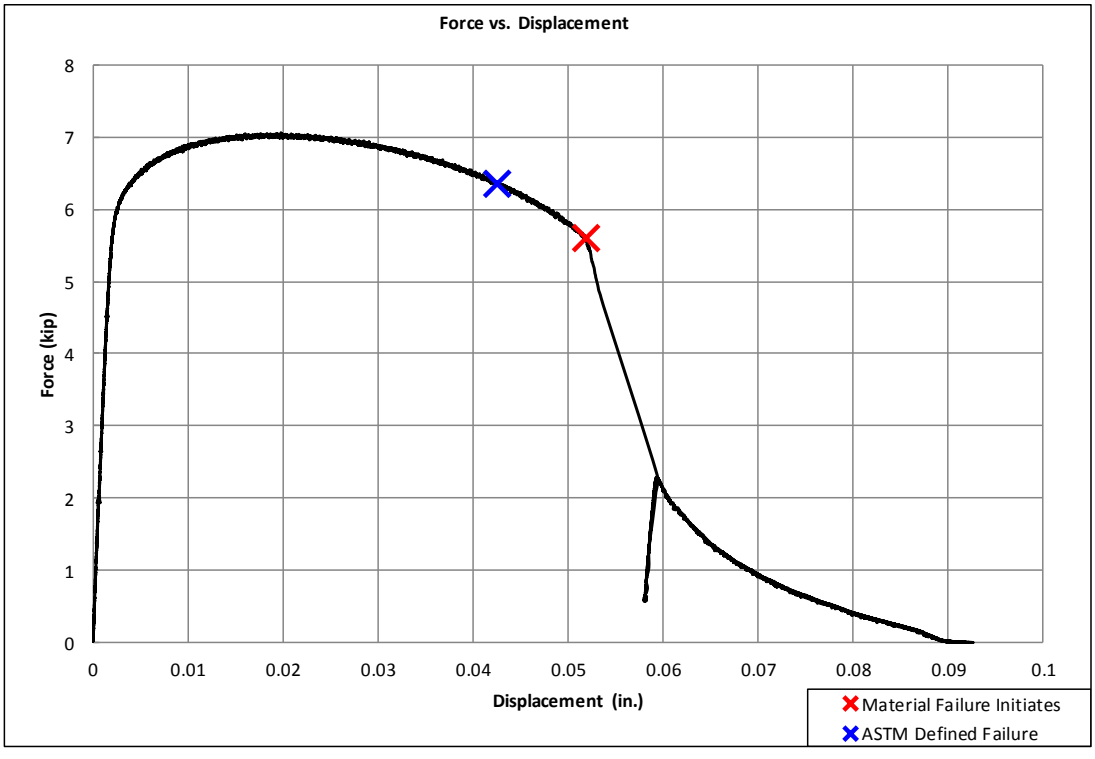

Figure F-71. Test No. SEFT-85 Test Results Summary

MIDWEST ROADSIDE SAFETY FACILITY

Tension Test Summary

Test Information

Test No.	SEFT-86
Specimen Description:	Notched Round Specimen #1
Specimen Geometry No.:	6
Specimen ID:	068
Test Date:	2/22/2016
Results Folder:	Test Run 135

Testing Procedure

Testing Frame:	Landmark 20 kip
Loading Type:	Tension
Load Rate:	0.000564 in./sec
Grips:	0.43-0.65 in. Serrated Vee
Grip Pressure:	1000 psi
Fixture:	N/A
Measurement Equipment:	2 in. Axial Extensometer
	ARAMIS DIC
	22 kip Load Cell
Primary Extensometer:	2 in. Axial Extensometer

Initial Measurements

Average Diameter:	0.187	in.
Initial Area:	0.0276	sq. in.
Initial Gauge Length	2.0000	in.

Final Measurements

Average Diameter:	0.105	in.
Final Area:	0.0087	sq. in.
Reduction in Area:	68.6	%
Gauge Length at Failure Initiation:	2.1042	in.

Test Results Summary

Yield Load:	1.959	kip
Peak Load:	2.291	kip
Failure Initiation Load:	1.359	kip
Failure Load (ASTM):	2.062	kip
Displacement at Peak:	0.0218	in.
Displacement at Failure Initiation:	0.1042	in.
Displacement at Failure Load (ASTM):	0.0575	in.
Yield Strength:	71.02	ksi
Ultimate Tensile Strength:	83.07	ksi
Engineering Stress at Failure Initiation:	49.27	ksi
Engineering Stress at Failure (ASTM):	74.76	ksi

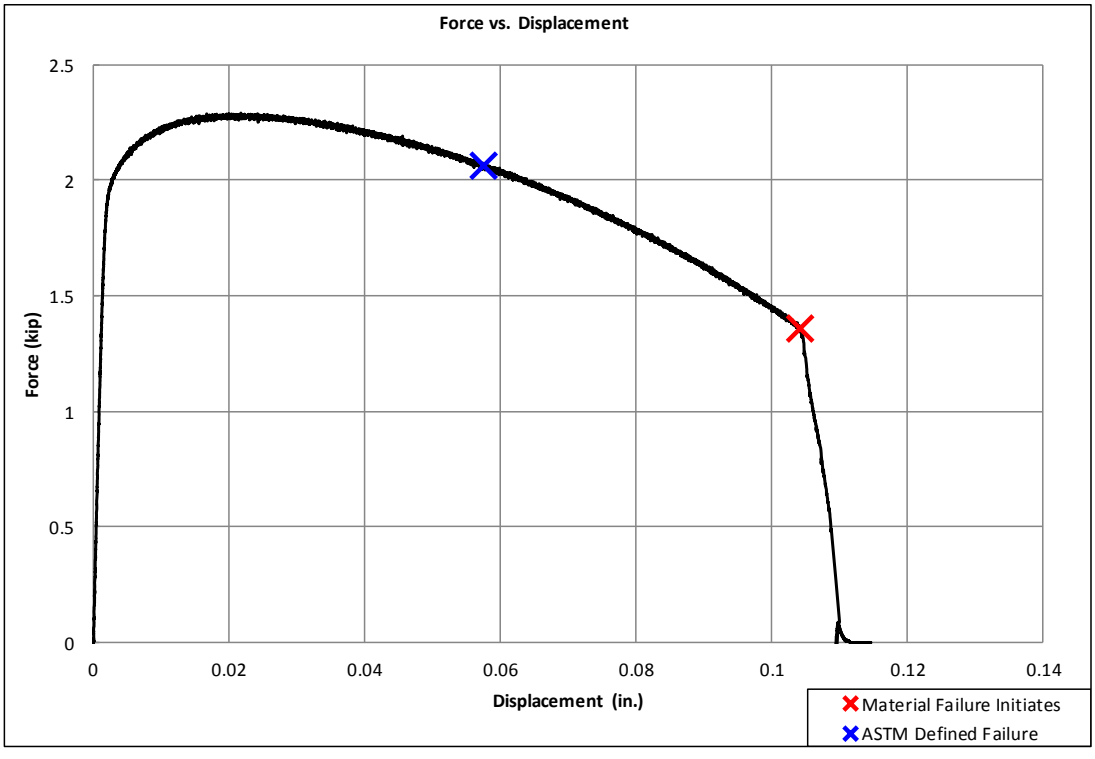

Figure F-72. Test No. SEFT-86 Test Results Summary

MIDWEST ROADSIDE SAFETY FACILITY

Tension Test Summary

Test Information		**Initial Measurements**		
Test No.	SEFT-87	Average Diameter:	0.187	in.
Specimen Description:	Notched Round Specimen #2			
Specimen Geometry No.:	7	Initial Area:	0.0275	sq. in.
Specimen ID:	074	Initial Gauge Length	2.0000	in.
Test Date:	2/22/2016			
Results Folder:	Test Run 136	**Final Measurements**		
		Average Diameter:	0.108	in.
Testing Procedure				
Testing Frame:	Landmark 20 kip	Final Area:	0.0091	sq. in.
Loading Type:	Tension	Reduction in Area:	66.9	%
Load Rate:	0.000496 in./sec	Gauge Length at Failure Initiation:	2.0936	in.
Grips:	0.43-0.65 in. Serrated Vee			
Grip Pressure:	1000 psi	**Test Results Summary**		
Fixture:	N/A	Yield Load:	2.009	kip
Measurement Equipment:	2 in. Axial Extensometer	Peak Load:	2.375	kip
	ARAMIS DIC	Failure Initiation Load:	1.432	kip
	22 kip Load Cell	Failure Load (ASTM):	2.138	kip
		Displacement at Peak:	0.0212	in.
		Displacement at Failure Initiation:	0.0936	in.
Primary Extensometer:	2 in. Axial Extensometer	Displacement at Failure Load (ASTM):	0.0503	in.
		Yield Strength:	73.14	ksi
		Ultimate Tensile Strength:	86.48	ksi
		Engineering Stress at Failure Initiation:	52.15	ksi
		Engineering Stress at Failure (ASTM):	77.83	ksi

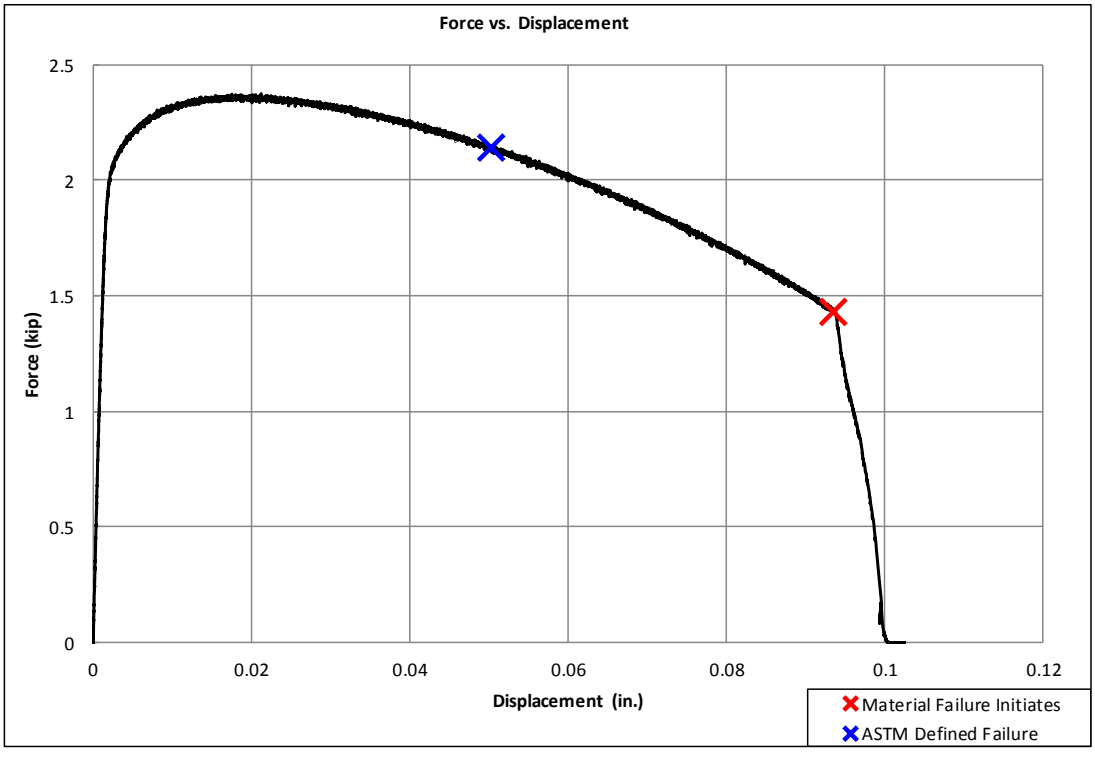

Figure F-73. Test No. SEFT-87 Test Results Summary

MIDWEST ROADSIDE SAFETY FACILITY

Tension Test Summary

Test Information	
Test No.	SEFT-88
Specimen Description:	Axial-Symmetric Round Smooth
Specimen Geometry No.:	5
Specimen ID:	159
Test Date:	2/22/2016
Results Folder:	Test Run 137

Testing Procedure	
Testing Frame:	Landmark 20 kip
Loading Type:	Tension
Load Rate:	0.00118 in./sec
Grips:	0.43-0.65 in. Serrated Vee
Grip Pressure:	1000 psi
Fixture:	N/A
Measurement Equipment:	2 in. Axial Extensometer
	ARAMIS DIC
	22 kip Load Cell
Primary Extensometer:	2 in. Axial Extensometer

Initial Measurements		
Average Diameter:	0.187	in.
Initial Area:	0.0274	sq. in.
Initial Gauge Length	2.0000	in.

Final Measurements		
Average Diameter:	0.092	in.
Final Area:	0.0067	sq. in.
Reduction in Area:	75.6	%
Gauge Length at Failure Initiation:	2.2574	in.

Test Results Summary		
Yield Load:	1.703	kip
Peak Load:	2.087	kip
Failure Initiation Load:	1.199	kip
Failure Load (ASTM):	1.878	kip
Displacement at Peak:	0.1023	in.
Displacement at Failure Initiation:	0.2574	in.
Displacement at Failure Load (ASTM):	0.2003	in.
Yield Strength:	62.16	ksi
Ultimate Tensile Strength:	76.20	ksi
Engineering Stress at Failure Initiation:	43.79	ksi
Engineering Stress at Failure (ASTM):	68.58	ksi
True Stress at Failure Initiation:	179.43	ksi
True Strain at Failure Initiation:	1.4103	in./in.
Effective Plastic Strain at Failure:	1.4077	in./in.

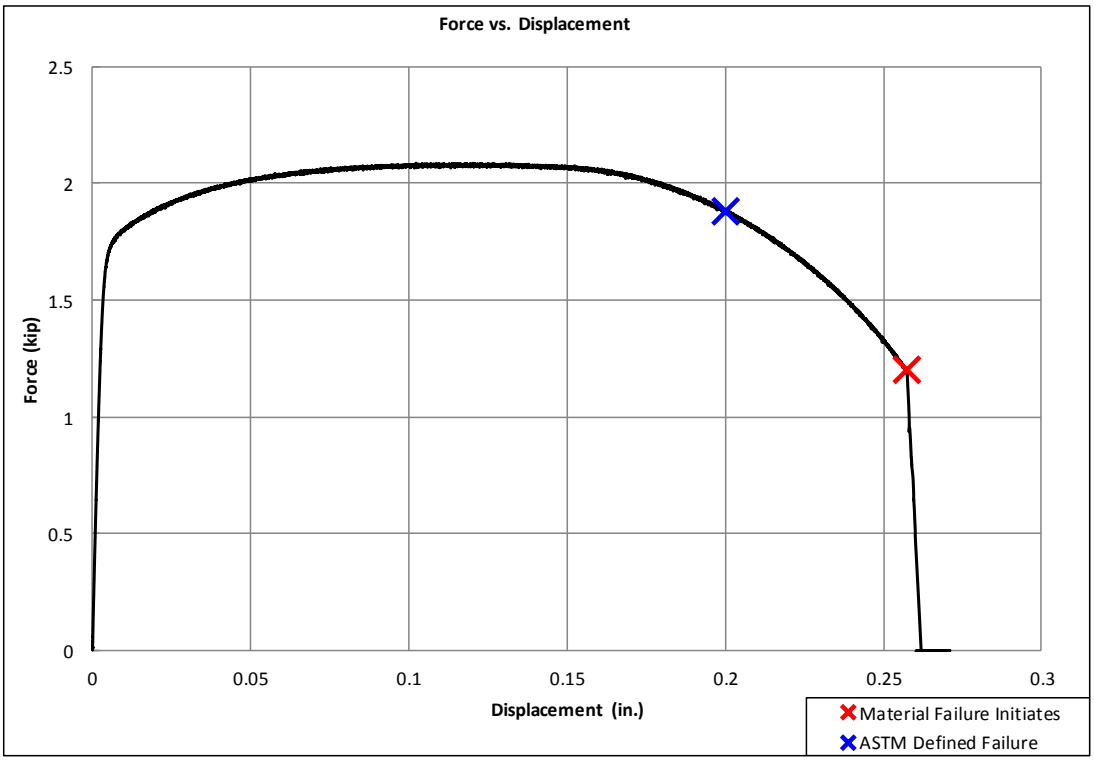

Figure F-74. Test No. SEFT-88 Test Results Summary

MIDWEST ROADSIDE SAFETY FACILITY

Tension Test Summary

Test Information	
Test No.	SEFT-89
Specimen Description:	Axial-Symmetric Round Smooth
Specimen Geometry No.:	5
Specimen ID:	160
Test Date:	2/23/2016
Results Folder:	Test Run 138

Testing Procedure	
Testing Frame:	Landmark 20 kip
Loading Type:	Tension
Load Rate:	0.00118 in./sec
Grips:	0.43-0.65 in. Serrated Vee
Grip Pressure:	1000 psi
Fixture:	N/A
Measurement Equipment:	2 in. Axial Extensometer
	ARAMIS DIC
	22 kip Load Cell
Primary Extensometer:	2 in. Axial Extensometer

Initial Measurements		
Average Diameter:	0.186	in.
Initial Area:	0.0273	sq. in.
Initial Gauge Length	2.0000	in.

Final Measurements		
Average Diameter:	0.091	in.
Final Area:	0.0065	sq. in.
Reduction in Area:	76.2	%
Gauge Length at Failure Initiation:	2.2680	in.

Test Results Summary		
Yield Load:	1.677	kip
Peak Load:	2.092	kip
Failure Initiation Load:	1.189	kip
Failure Load (ASTM):	1.883	kip
Displacement at Peak:	0.1229	in.
Displacement at Failure Initiation:	0.2680	in.
Displacement at Failure Load (ASTM):	0.2091	in.
Yield Strength:	61.41	ksi
Ultimate Tensile Strength:	76.60	ksi
Engineering Stress at Failure Initiation:	43.54	ksi
Engineering Stress at Failure (ASTM):	68.94	ksi
True Stress at Failure Initiation:	183.06	ksi
True Strain at Failure Initiation:	1.4362	in./in.
Effective Plastic Strain at Failure:	1.4338	in./in.

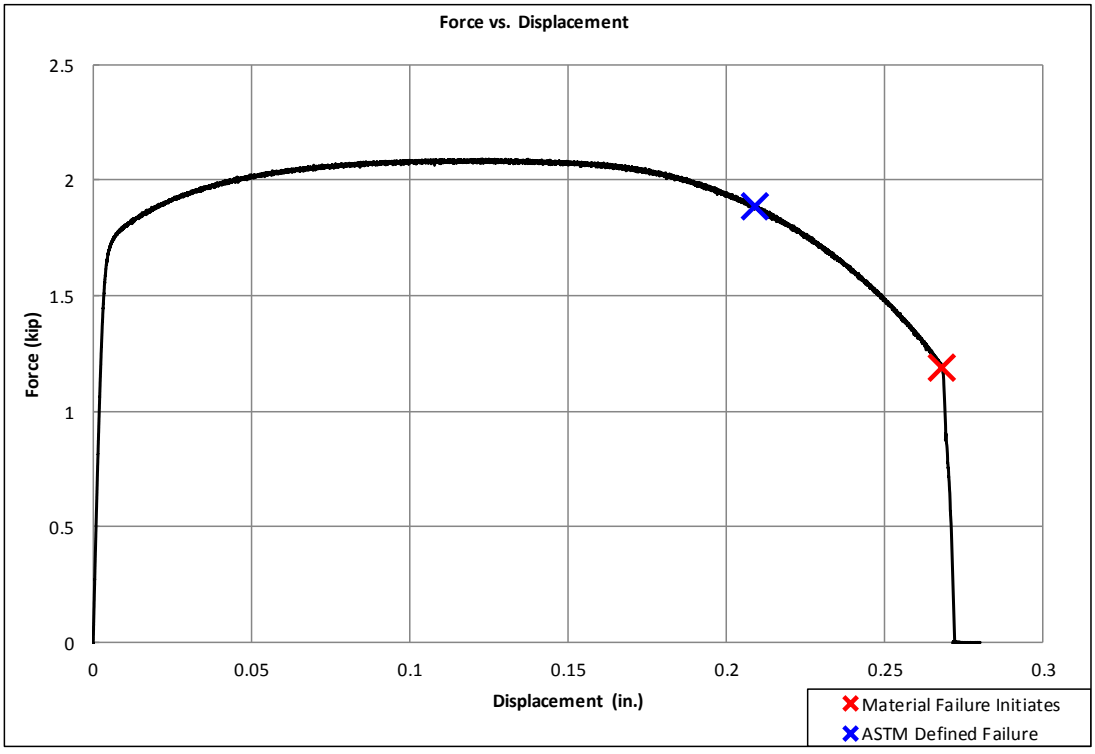

Figure F-75. Test No. SEFT-89 Test Results Summary

MIDWEST ROADSIDE SAFETY FACILITY

Punch Test Summary

Test Information

Test No.	SEFT-90
Specimen Description:	Standard Punch R1
Specimen Geometry No.:	20
Specimen ID:	126
Test Date:	2/24/2016
Results Folder:	Test Run 139

Testing Procedure

Testing Frame:	Landmark 20 kip
Loading Type:	Punch
Load Rate:	0.0003 in./sec
Grips:	N/A
Grip Pressure:	1000 psi
Fixture:	Compression Platen with Punch Fixture 2, R1 Top, and Punch Head R1 A
Measurement Equipment:	Laser Extensometer 1 in Axial Extensometer 22 kip Load Cell
Primary Extensometer:	Laser Extensometer

Initial Measurements

Average Diameter:	0.581 in.
Average Thickness:	0.057 in.

Final Measurements

Average Diameter:	0.557 in.
Average Draw Down Thickness:	0.264 in.

Test Results Summary

Peak Load:	3.147 kip
Failure Initiation Load:	2.850 kip
Displacement at Peak:	0.2005 in.
Displacement at Failure Initiation:	0.2156 in.

Figure F-76. Test No. SEFT-90 Test Results Summary

MIDWEST ROADSIDE SAFETY FACILITY

Punch Test Summary

Test Information

Test No.	SEFT-91
Specimen Description:	Standard Punch Specimen R1
Specimen Geometry No.:	20
Specimen ID:	127
Test Date:	2/24/2016
Results Folder:	Test Run 140

Testing Procedure

Testing Frame:	Landmark 20 kip
Loading Type:	Punch
Load Rate:	0.0013 in./sec
Grips:	N/A
Grip Pressure:	1000 psi
Fixture:	Compression Platen with Punch Fixture 2, R1 Top, and Punch Head R1 A
Measurement Equipment:	Laser Extensometer 1 in Axial Extensometer 22 kip Load Cell
Primary Extensometer:	Laser Extensometer

Initial Measurements

Average Diameter:	0.580 in.
Average Thickness:	0.057 in.

Final Measurements

Average Diameter:	0.556 in.
Average Draw Down Thickness:	0.254 in.

Test Results Summary

Peak Load:	3.270 kip
Failure Initiation Load:	2.991 kip
Displacement at Peak:	0.2019 in.
Displacement at Failure Initiation:	0.2199 in.

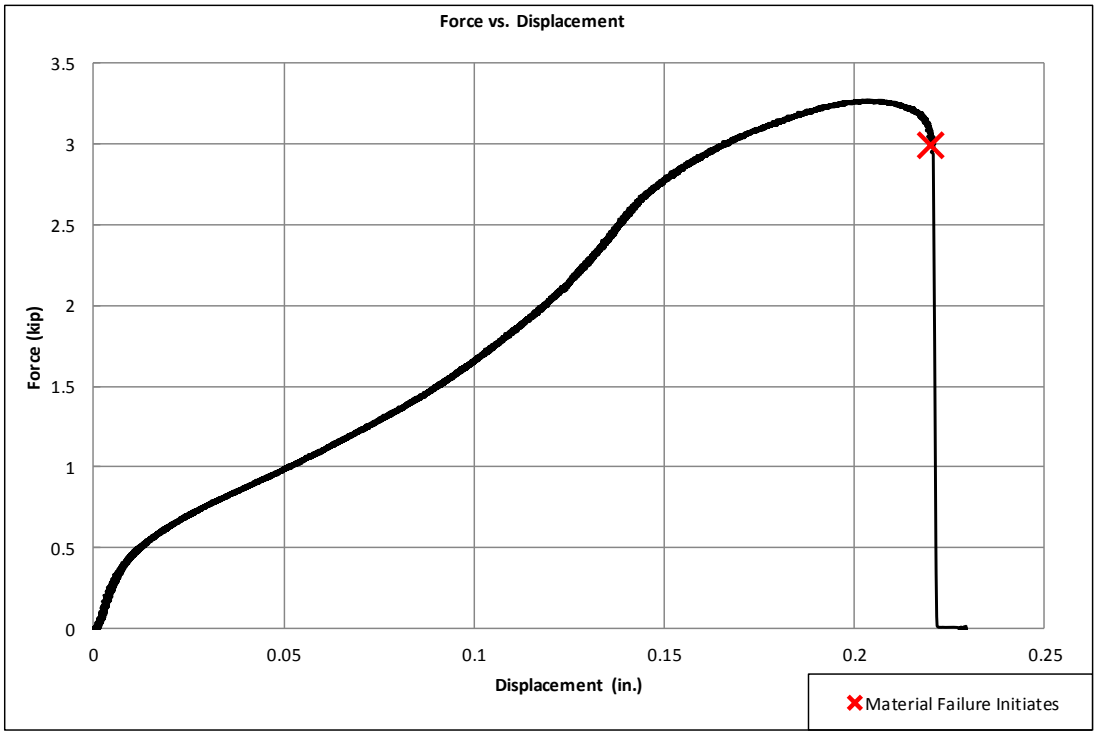

Figure F-77. Test No. SEFT-91 Test Results Summary

MIDWEST ROADSIDE SAFETY FACILITY

Punch Test Summary

Test Information

Test No.	SEFT-92
Specimen Description:	Standard Punch Specimen R1
Specimen Geometry No.:	20
Specimen ID:	128
Test Date:	2/24/2016
Results Folder:	Test Run 141

Testing Procedure

Testing Frame:	Landmark 20 kip
Loading Type:	Punch
Load Rate:	0.0013 in./sec
Grips:	N/A
Grip Pressure:	1000 psi
Fixture:	Compression Platen with Punch Fixture 2, R1 Top, and Punch Head R1 A
Measurement Equipment:	Laser Extensometer 1 in Axial Extensometer 22 kip Load Cell
Primary Extensometer:	Laser Extensometer

Initial Measurements

Average Diameter:	0.580 in.
Average Thickness:	0.057 in.

Final Measurements

Average Diameter:	0.556 in.
Average Draw Down Thickness:	0.255 in.

Test Results Summary

Peak Load:	3.294 kip
Failure Initiation Load:	3.016 kip
Displacement at Peak:	0.2048 in.
Displacement at Failure Initiation:	0.2203 in.

Figure F-78. Test No. SEFT-92 Test Results Summary

MIDWEST ROADSIDE SAFETY FACILITY

Punch Test Summary

Test Information

Test No.	SEFT-93
Specimen Description:	Round Punch Specimen R1
Specimen Geometry No.:	21
Specimen ID:	129
Test Date:	2/24/2016
Results Folder:	Test Run 142

Testing Procedure

Testing Frame:	Landmark 20 kip
Loading Type:	Punch
Load Rate:	0.0013 in./sec
Grips:	N/A
Grip Pressure:	1000 psi
Fixture:	Compression Platen with Punch Fixture 2, R1 Top, and Punch Head R1 A
Measurement Equipment:	Laser Extensometer 1 in Axial Extensometer 22 kip Load Cell
Primary Extensometer:	Laser Extensometer

Initial Measurements

Average Diameter:	0.580 in.
Average Thickness:	0.057 in.

Final Measurements

Average Diameter:	0.553 in.
Average Draw Down Thickness:	0.296 in.

Test Results Summary

Peak Load:	3.110 kip
Failure Initiation Load:	2.525 kip
Displacement at Peak:	0.2016 in.
Displacement at Failure Initiation:	0.2478 in.

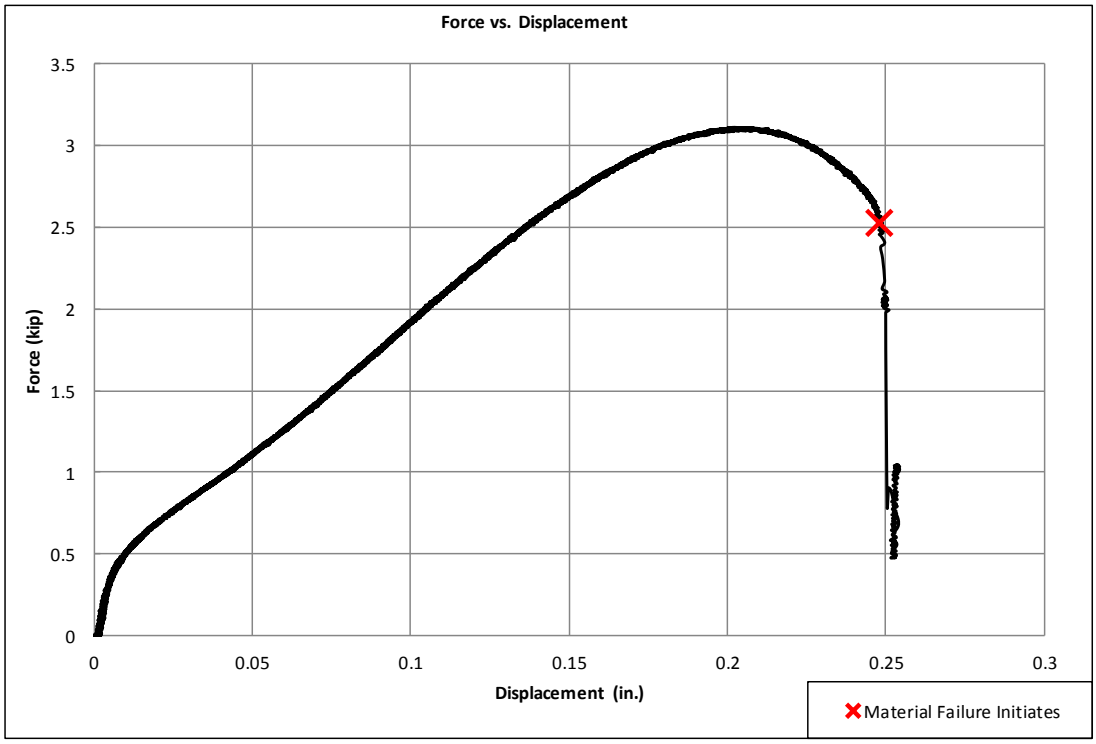

Figure F-79. Test No. SEFT-93 Test Results Summary

MIDWEST ROADSIDE SAFETY FACILITY

Punch Test Summary

Test Information

Test No.	SEFT-94
Specimen Description:	Round Punch Specimen R1
Specimen Geometry No.:	21
Specimen ID:	130
Test Date:	2/24/2016
Results Folder:	Test Run 143

Testing Procedure

Testing Frame:	Landmark 20 kip
Loading Type:	Punch
Load Rate:	0.0013 in./sec
Grips:	N/A
Grip Pressure:	1000 psi
Fixture:	Compression Platen with Punch Fixture 2, R1 Top, and Punch Head R1 A
Measurement Equipment:	Laser Extensometer 1 in Axial Extensometer 22 kip Load Cell
Primary Extensometer:	Laser Extensometer

Initial Measurements

Average Diameter:	0.580 in.
Average Thickness:	0.057 in.

Final Measurements

Average Diameter:	0.549 in.
Average Draw Down Thickness:	0.301 in.

Test Results Summary

Peak Load:	3.111 kip
Failure Initiation Load:	2.604 kip
Displacement at Peak:	0.2088 in.
Displacement at Failure Initiation:	0.2530 in.

Figure F-80. Test No. SEFT-94 Test Results Summary

MIDWEST ROADSIDE SAFETY FACILITY

Punch Test Summary

Test Information

Test No.	SEFT-95
Specimen Description:	Round Punch Specimen R1
Specimen Geometry No.:	21
Specimen ID:	131
Test Date:	2/24/2016
Results Folder:	Test Run 144

Testing Procedure

Testing Frame:	Landmark 20 kip
Loading Type:	Punch
Load Rate:	0.0013 in./sec
Grips:	N/A
Grip Pressure:	1000 psi
Fixture:	Compression Platen with Punch Fixture 2, R1 Top, and Punch Head R1 A
Measurement Equipment:	Laser Extensometer 1 in Axial Extensometer 22 kip Load Cell
Primary Extensometer:	Laser Extensometer

Initial Measurements

Average Diameter:	0.580 in.
Average Thickness:	0.057 in.

Final Measurements

Average Diameter:	0.553 in.
Average Draw Down Thickness:	0.293 in.

Test Results Summary

Peak Load:	3.167 kip
Failure Initiation Load:	2.699 kip
Displacement at Peak:	0.2094 in.
Displacement at Failure Initiation:	0.2422 in.

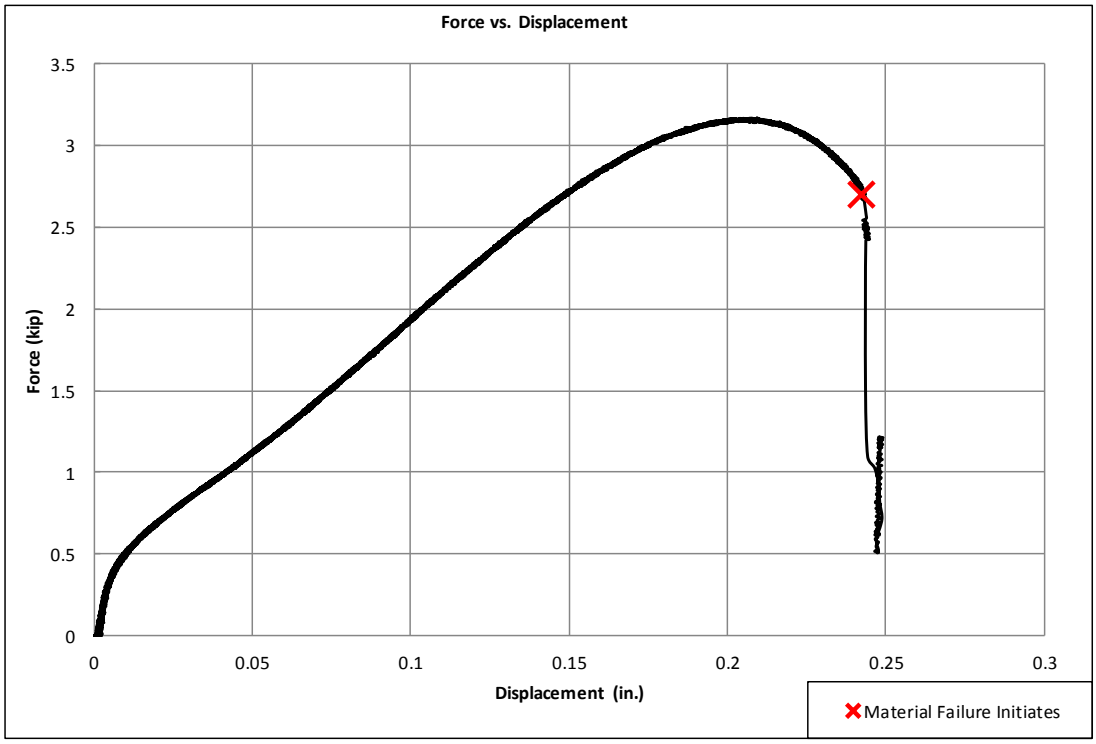

Figure F-81. Test No. SEFT-95 Test Results Summary

MIDWEST ROADSIDE SAFETY FACILITY

Punch Test Summary

Test Information

Test No.	SEFT-96
Specimen Description:	Sharp Punch
Specimen Geometry No.:	17
Specimen ID:	132
Test Date:	2/24/2016
Results Folder:	Test Run 145

Testing Procedure

Testing Frame:	Landmark 20 kip
Loading Type:	Punch
Load Rate:	0.0013 in./sec
Grips:	N/A
Grip Pressure:	1000 psi
Fixture:	Compression Platen with Punch Fixture 2, and Punch Head A
Measurement Equipment:	Laser Extensometer 1 in Axial Extensometer 22 kip Load Cell
Primary Extensometer:	Laser Extensometer

Initial Measurements

Average Diameter:	0.580 in.
Average Thickness:	0.058 in.

Final Measurements

Average Diameter:	0.581 in.
Average Draw Down Thickness:	0.142 in.

Test Results Summary

Peak Load:	4.100 kip
Failure Initiation Load:	3.781 kip
Displacement at Peak:	0.0658 in.
Displacement at Failure Initiation:	0.0857 in.

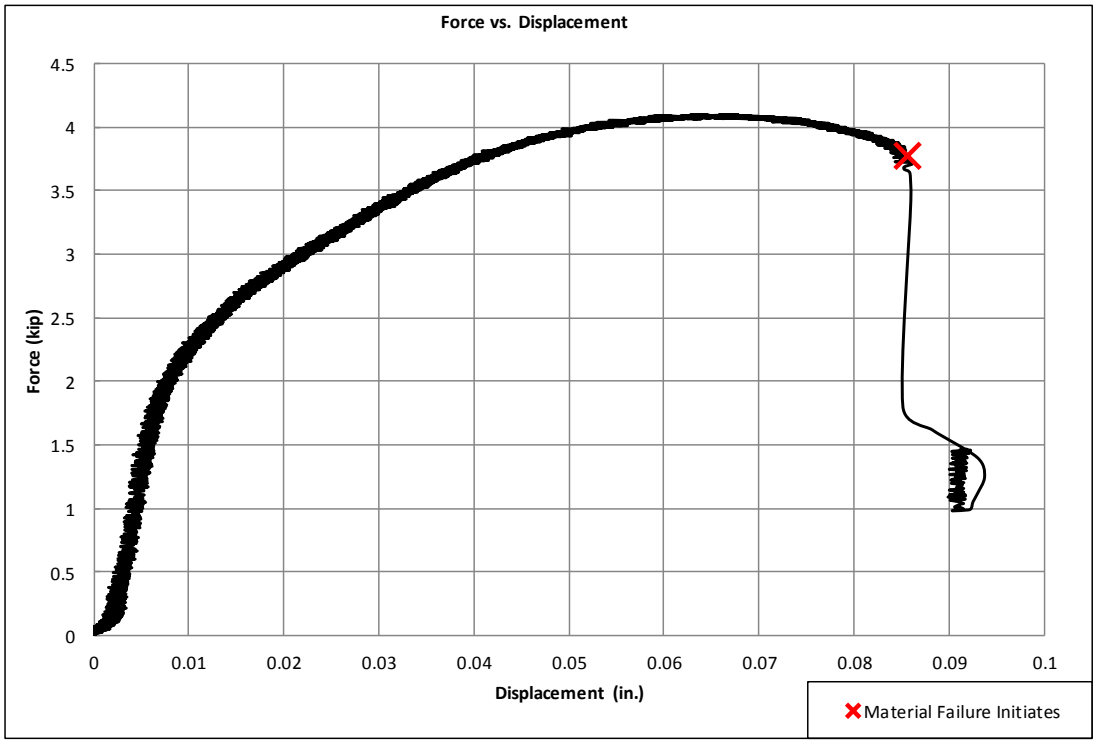

Figure F-82. Test No. SEFT-96 Test Results Summary

MIDWEST ROADSIDE SAFETY FACILITY

Punch Test Summary

Test Information

Test No.	SEFT-97
Specimen Description:	Sharp Punch Specimen
Specimen Geometry No.:	17
Specimen ID:	133
Test Date:	2/24/2016
Results Folder:	Test Run 146

Testing Procedure

Testing Frame:	Landmark 20 kip
Loading Type:	Punch
Load Rate:	0.00054 in./sec
Grips:	N/A
Grip Pressure:	1000 psi
Fixture:	Compression Platen with Punch Fixture 2, and Punch Head A
Measurement Equipment:	Laser Extensometer 1 in Axial Extensometer 22 kip Load Cell
Primary Extensometer:	Laser Extensometer

Initial Measurements

Average Diameter:	0.580 in.
Average Thickness:	0.058 in.

Final Measurements

Average Diameter:	0.581 in.
Average Draw Down Thickness:	0.194 in.

Test Results Summary

Peak Load:	4.054 kip
Failure Initiation Load:	3.571 kip
Displacement at Peak:	0.0628 in.
Displacement at Failure Initiation:	0.0833 in.

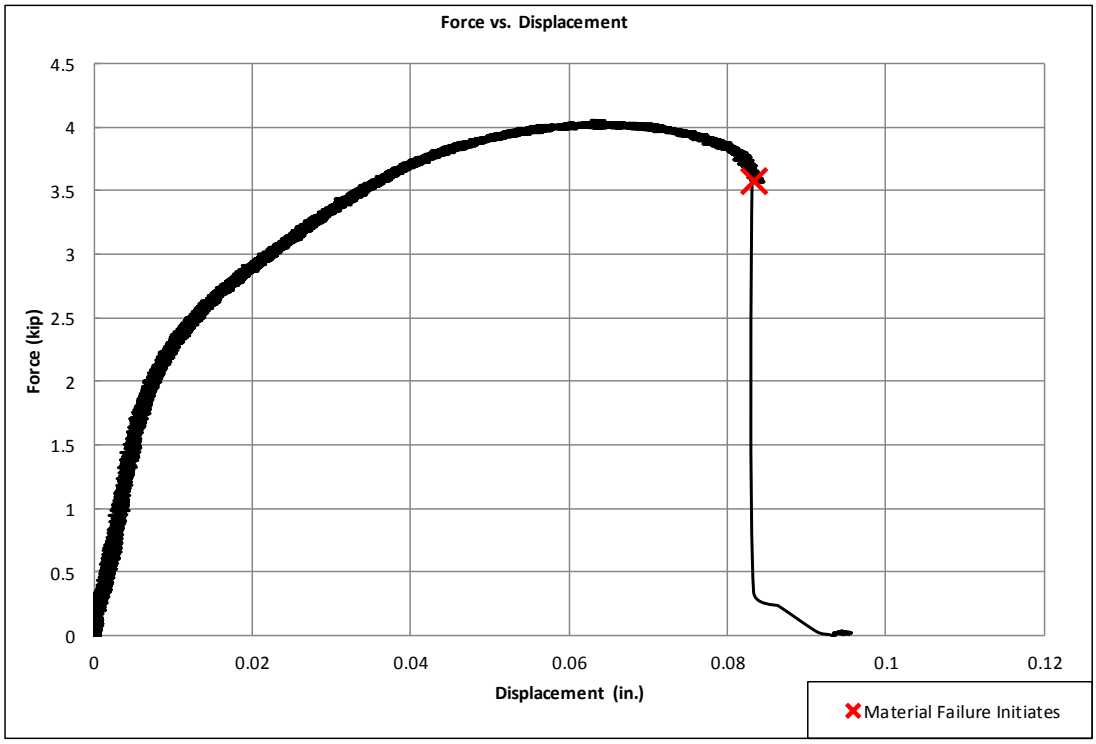

Figure F-83. Test No. SEFT-97 Test Results Summary

MIDWEST ROADSIDE SAFETY FACILITY

Punch Test Summary

Test Information

Test No.	SEFT-98
Specimen Description:	Sharp Punch
Specimen Geometry No.:	17
Specimen ID:	134
Test Date:	2/24/2016
Results Folder:	Test Run 147

Testing Procedure

Testing Frame:	Landmark 20 kip
Loading Type:	Punch
Load Rate:	0.00054 in./sec
Grips:	N/A
Grip Pressure:	1000 psi
Fixture:	Compression Platen with Punch Fixture 2, and Punch Head A
Measurement Equipment:	Laser Extensometer 1 in Axial Extensometer 22 kip Load Cell
Primary Extensometer:	Laser Extensometer

Initial Measurements

Average Diameter:	0.580 in.
Average Thickness:	0.057 in.

Final Measurements

Average Diameter:	0.581 in.
Average Draw Down Thickness:	0.239 in.

Test Results Summary

Peak Load:	4.128 kip
Failure Initiation Load:	3.759 kip
Displacement at Peak:	0.0680 in.
Displacement at Failure Initiation:	0.0863 in.

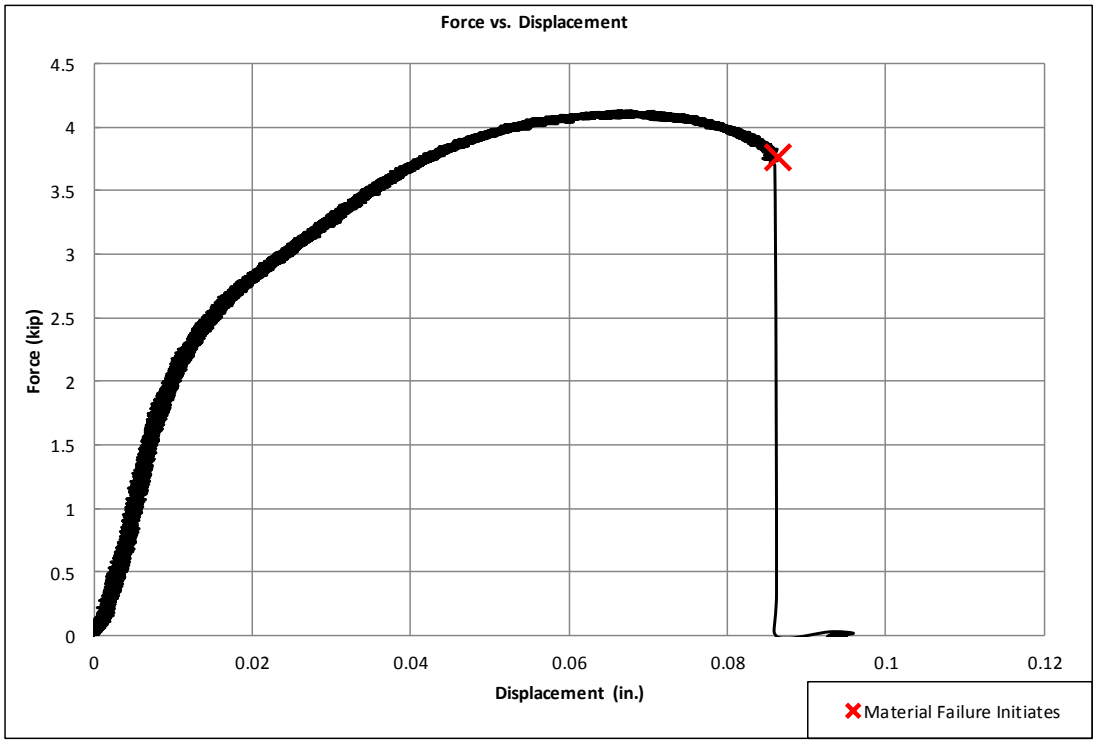

Figure F-84. Test No. SEFT-98 Test Results Summary

MIDWEST ROADSIDE SAFETY FACILITY

Compression Test Summary

Test Information		**Initial Measurements**		
Test No.	SEFT-99	Average Diameter:	0.490	in.
Specimen Description:	Compression Cylinder			
Specimen Geometry No.:	14	Initial Area:	0.1883	sq. in.
Specimen ID:	117	Initial Gauge Length:	0.49	in.
Test Date:	2/25/2016			
Results Folder:	Test Run 21	**Final Measurements**		
		Average Diameter:	0.492	in.
Testing Procedure				
Testing Frame:	Criterion 200 kip	Final Area:	0.1900	sq. in.
Loading Type:	Compression	Increase in Area:	0.9	%
Load Rate:	0.0004 in./sec			
Grips:	N/A			
Grip Pressure:	1000 psi	**Test Results Summary**		
Fixture:	Compression Platen	Yield Load (0.2% Offset):	11.754	kip
Measurement Equipment:	Laser Extensometer	Peak Load:	12.879	kip
	ARAMIS DIC	Displacement at Peak:	0.0098	in.
	220 kip Load Cell	Yield Strength:	62.43	ksi
		True Strain at Final:	-0.0091	in./in.
		Young's Modulus:	5,061	ksi
Primary Extensometer:	Laser Extensometer			

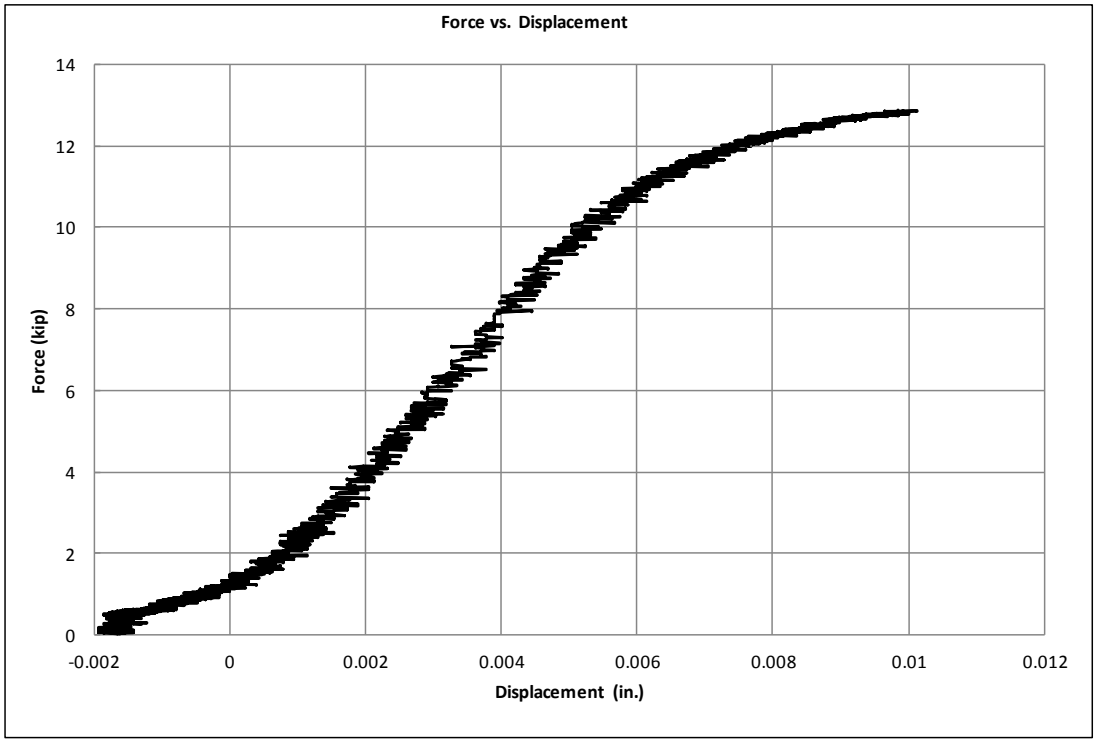

Figure F-85. Test No. SEFT-99 Test Results Summary

MIDWEST ROADSIDE SAFETY FACILITY

Tension Test Summary

Test Information

Test No.	SEFT-101
Specimen Description:	Thick Small Notch Specimen
Specimen Geometry No.:	14
Specimen ID:	110
Test Date:	2/8/2016
Results Folder:	Test Run 130

Testing Procedure

Testing Frame:	Landmark 20 kip
Loading Type:	Tension
Load Rate:	0.00025 in./sec
Grips:	0.28-0.56 in. Flat Diamond Wedge
Grip Pressure:	1000 psi
Fixture:	N/A
Measurement Equipment:	2 in. Axial Extensometer
	ARAMIS DIC
	22 kip Load Cell
Primary Extensometer:	2 in. Axial Extensometer

Initial Measurements

Average Width:	0.081	in.
Average Thickness:	0.999	in.
Initial Area:	0.0809	sq. in.
Initial Gauge Length	2.0000	in.

Final Measurements

Average Width:	0.949	in.
Average Thickness:	0.052	in.
Final Area:	0.0495	sq. in.
Reduction in Area:	38.7	%
Gauge Length at Failure Initiation:	2.0395	in.

Test Results Summary

Yield Load:	6.317	kip
Peak Load:	7.478	kip
Failure Initiation Load:	5.803	kip
Failure Load (ASTM):	6.730	kip
Displacement at Peak:	0.0111	in.
Displacement at Failure Initiation:	0.0395	in.
Displacement at Failure Load (ASTM):	0.0307	in.
Yield Strength:	78.10	ksi
Ultimate Tensile Strength:	92.45	ksi
Engineering Stress at Failure Initiation:	71.75	ksi
Engineering Stress at Failure (ASTM):	83.20	ksi

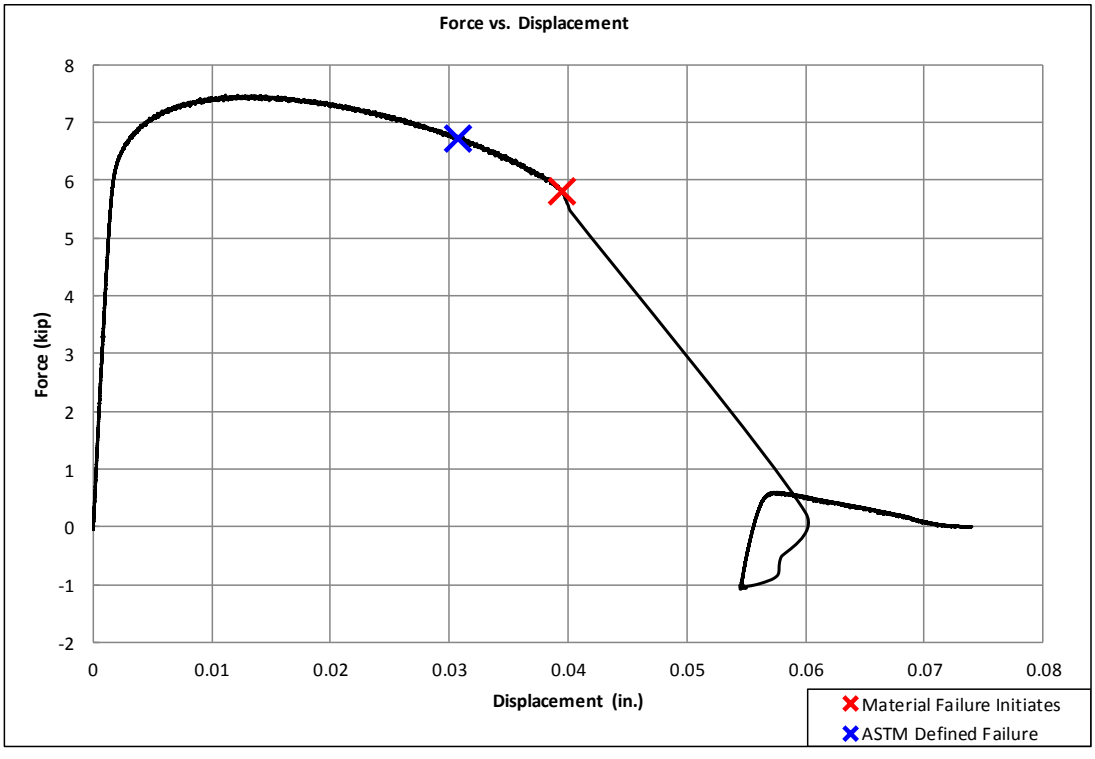

Figure F-86. Test No. SEFT-101 Test Results Summary